Deep Energy Foundations:
Geotechnical Challenges and Design Considerations

Sherif Lotfy Abdel Motaleb Abdelaziz

Dissertation submitted to the faculty of the
Virginia Polytechnic Institute and State University
in partial fulfillment of the requirements for the degree of

Doctor of Philosophy

In
Civil and Environmental Engineering

C.Guney Olgun - Chair
James R. Martin, II - Co-Chair
Joseph E. Dove
Matthew Mauldon

February 1, 2013
Blacksburg, Virginia

Keywords: Geothermal, Energy Piles, Thermo-mechanical, Heat Exchanger, and Thermal Conductivity.

Deep Energy Foundations:
Geotechnical Challenges and Design Considerations

Sherif Lotfy Abdel Motaleb Abdelaziz

ABSTRACT

Traditionally, geothermal boreholes have utilized the ground energy for space heating and cooling. In this system, a circulation loop is placed in a small-diameter borehole typically extending to a depth of 200-300 ft. The hole is then backfilled with a mixture of sand, bentonite and/or cement. The loop is connected to a geothermal heat pump and the fluid inside the loop is circulated. The heat energy is fed into the ground for cooling in the summer and withdrawn from the ground for heating in the winter. Geothermal heat pumps work more efficiently for space heating and cooling compared to air-source heat pumps. The reason is ground-source systems use the ground as a constant temperature source which serves as a more favorable baseline compared to the ambient air temperature.

A significant cost associated with any deep geothermal borehole is the drilling required for installation. Because Energy Piles perform the dual function of exchanging heat and providing structural support, and are only installed at sites where pile foundations are already required, these systems provide the thermal performance of deep geothermal systems without the additional drilling costs. Low maintenance, long lifetime, less variation in energy supply compared to solar and wind power, and environmental friendliness have been cited as additional Energy Pile advantages. Case studies show that they can significantly lower heating/cooling costs and reduce the carbon footprint. Energy cost savings for typical buildings outfitted with Energy Piles could be as much as 70 percent.

The use of Energy Piles has rapidly increased over the last decade, especially in Europe where more than 500 applications are reported. Primary installations have been in Germany, Austria, Switzerland and United Kingdom. Notable projects include the 56-story high Frankfurt Main Tower in Germany, Dock E Terminal Extension at Zurich International Airport in Switzerland and the One New Change building complex in London U.K. Energy piles have seen very little

use in the North America, only a handful of completed projects are known; Marine Discovery Center in Ontario, Canada, Lakefront Hotel in Geneva, New York and the Art Stable building in Seattle, Washington.

Energy Piles are typically installed with cast-in-place technology (i.e. drilled shafts, continuous flight auger piles, micropiles etc.) while some driven pile applications are also reported. Other types of geotechnical structures in contact with the ground, such as shallow foundations, retaining walls, basement walls, tunnel linings and earth anchors, also offer significant potential for harnessing near-surface geothermal energy.

Energy Pile design needs to integrate geotechnical, structural and heat exchange considerations. Geotechnical characteristics of the foundation soils and the level of the structural loads are typically the deciding factors for the selection and dimensioning of the pile foundations. The geothermal heat exchange capacity of an Energy Pile is a key parameter to be considered in design. Thermal characteristics of the ground as well as the heating and cooling loads from the structure need to be considered for the number of piles that will be utilized as heat exchangers. Therefore, the thermal properties of the site need to be evaluated for an Energy Pile application in addition to the traditional geotechnical characterization for foundation design.

Energy Piles bring new challenges to geotechnical pile design. During a heat exchange operation, the pile will expand and contract relative to the soil as heat is injected and extracted, respectively. These relative movements have the potential to alter the shear transfer mechanism at the pile-soil interface. Furthermore, the range of temperature increases near the pile surface, though limited by practical operational guidelines, can have a significant effect on pore pressures generation and soil strength.

This dissertation provides answers for several research questions including the long-term performance of Energy Piles, the applicability of the thermal conductivity tests to Energy Piles. Furthermore, it presents the results and a detailed discussion about the full scale in-situ thermo-mechanical pile load test conducted at Virginia Tech.

To my beloved family

Father

Mather

Wife

Brother

Sisters

Son

Daughter

Acknowledgments

In the name of Allah, the most beneficent and the most merciful.

All my gratitude goes to my dear father, Lotfy Abdel-Motaleb, and my beloved mother, Faten Al-Far, for their unconditional and unlimited love. No words can thank them enough for their invaluable care and the sacrifices they have made, and still make, for me. I have an everlasting debt to them, and to them I dedicate my work and love.

I also dedicate my work to my beloved wife, Hebatollah El-Noby, for all her support. She was always there when I needed support, she has done above and beyond what I asked assuring calm environment for me to focus and work. Heba also is the mother of my two little kids, Mohamed and Malak who motivated me and gave me the power and energy to complete the Ph.D.

I also would like to express my deep appreciation to my Ph.D. advisor Dr. Guney Olgun for all his effort, time and dedication to work with me. Dr. Olgun never hesitated to provide any advice. He has always been on top of things and provided the guidance I needed to accomplish my research in the best way ever. I owe Dr. Olgun a heartfelt thank you for all the patience and understanding during the long discussions throughout my study.

Also, I would like to thank my co-advisor Dr. James Martin and committee members Dr. Joseph Dove and Dr. Matthew Mauldon for their guidance and suggestions.

Additionally, I would like to express my gratitude to my Master's advisor Dr. Montasir Abbas who has been very helpful to me throughout my graduate studies, personally and academically. I learned a lot from him. He always gave me e sincere advice and he was always there for me when I needed him. Thank you!

This research would not be possible without the financial support form the National Science Foundation (NSF) under project number CMMI-0928807. This support is greatly appreciated. I would also like to thank Fatih Catalbas and Pier Luigi Iovino from Layne GeoConstruction for the in-kind installation of the energy piles and assistance during the load test. Mary Ellen Bruce from Deep Foundation Institute (DFI) was instrumental in the coordination of this project with DFI member firms. I would also like to recognize International Society for Micropiles for the Lizzi Scholarship that allowed me to present my research at their 2010 workshop. I would also like to thank Christopher Fox from REHAU and Charles Elks from Mechanical Equipment Sales for all the help during the study. REHAU donated the PEX tubes used in the field test. Mechanical Equipment Sales conducted the thermal conductivity tests.

Moreover, I would like to thank my colleagues Haitham Dawood, Abeera Batool, Tolga Y. Ozudogru and his wife Nazlim C. Ozudogru, Melis Sütman, Ehtesham Mehmood, Abid Mirza, and Ozgur Atlayan for all their support and assistance during my research. Special thanks to my friends, Ahmed Ghoniem, Ismail Zohdy and Abdullah Abdullah for giving me fun and joy when needed throughout my Ph.D.

Table of Content

CHAPTER 1. INTRODUCTION 1

1.1 GENERAL 1

1.2 RESEARCH QUESTIONS 2

CHAPTER 2. LITERATURE REVIEW 4

2.1. DESIGN OF THE GROUND LOOPS 4

2.2. THERMAL ANALYSIS (TEMPERATURE IN THE GROUND) 5

2.2.1. Infinite Line Source Model 5

2.2.2. Finite Line Source Model 7

2.2.3. Hollow Cylindrical Source Model 10

2.2.4. Solid Cylindrical Source Model 10

2.2.5. Model Enhancements 11

(a) Effect of Ground Water Flow 11

(b) Variable Heat Flux 11

(c) Effect of Heat Exchanger Inclination 12

2.3. THERMAL PROPERTIES OF VARIOUS MATERIALS 12

2.3.1. Soil Thermal Properties 13

(a) For unfrozen coarse grained soils 15

(b) For unfrozen fine grained soils 15

(c) For frozen coarse grained soils 16

(d) For frozen fine grained soils 16

2.3.2. The Energy Pile Material 21

(a) Thermal Properties of Concrete 21

(b) Thermal Properties of Steel 24

(c) Thermal Properties for Composite Sections 24

2.3.3. Circulation Tubes Thermal Properties 25

2.3.4. Water/anti-freeze Thermal Properties 25

2.4. THERMO-MECHANICAL BEHAVIOR OF ENERGY PILES 28

2.5. LONG TERM PERFORMANCE 29

2.6. IN-SITU THERMO-MECHANICAL TESTS 31

REFERENCES 33

CHAPTER 3. NUMERICAL MODELING OF THERMAL OPERATION OF HEAT EXCHANGE PILES .. 37

3.1. INTRODUCTION 37

3.2. GENERAL 37

3.3. THERMAL OPERATION OF GROUND ELEMENTS 39
3.4. NUMERICAL MODELING CHALLENGES 42
3.4.1. Modeling the Carrier Fluid *42*
3.4.2. Modeling Circulation Tubes *45*
3.4.3. Initial and Boundary Conditions *46*
3.4.4. Inlet Fluid Temperature *47*
3.5. THREE DIMENSIONAL (3-D) FINITE ELEMENT MODEL 48
3.5.1. Description of the Preliminary Model *50*
3.5.2. Model Validation *51*
3.5.3. Sensitivity Analysis *52*
(a) The estimated thermal performance (thermal energy): 55
(b) Temperature Distribution Along The Pile and in its Vicinity: 56
3.5.4. Effect of Pile Anisotropy *62*
3.6. CONCLUSION 63
REFERENCES 64
CHAPTER 4. MULTILAYER FINITE LINE SOURCE MODEL FOR VERTICAL HEAT EXCHANGERS . 66
4.1. ABSTRACT 66
4.2. INTRODUCTION AND BACKGROUND 66
4.3. LINE SOURCE MODELS 69
4.4. INFINITE LINE SOURCE MODEL 69
4.5. FINITE LINE SOURCE MODEL 70
4.6. MULTILAYER FINITE LINE SOURCE MODEL 70
4.6.1. Main Concept *70*
4.6.2. Effect of the Primary Segment *72*
4.6.3. Effect of Secondary Segments *73*
(a) Composite Section Concept 73
(b) Mathematical Derivation 74
4.6.4. Effect of Layer-Dependent Heat Rate *75*
4.6.5. Interlayer Heat Exchange Adjustment *76*
4.7. MODEL VALIDATION 78
4.8. MODEL GENERALIZATION 82
4.9. SIMPLE LS MODEL WITH THE HEAT RATE ADJUSTMENT 85
4.10. CONCLUSIONS 85
REFERENCES 86

CHAPTER 5. LONG-TERM THERMAL PERFORMANCE OF ENERGY PILES 89

5.1. INTRODUCTION 89

5.2. ANALYSIS OF LONG-TERM PERFORMANCE 89

5.3. DEMONSTRATION EXAMPLE OF THE PROPOSED APPROACH 91

5.3.1. Building Description 91

5.3.2. Building Usage and Occupancy 93

5.3.3. Comfort Temperature 93

5.3.4. Selected Building Locations 93

5.3.5. Energy Analysis for Building Thermal Heating and Cooling Loads 95

5.3.6. Typical Meteorological Year (TMY) Data for Selected Locations 95

5.3.7. Hourly Ground Thermal Loads for the TMY 98

5.3.8. Change Point Analysis to Estimate Heating and Cooling Episodes 107

5.3.9. Sine Wave Equivalency Concept 109

5.4. NUMERICAL MODELING 112

5.5. HEAT EXCHANGE ANALYSIS FOR ONE YEAR 114

5.5.1. Initial Thermal Load 115

5.5.2. The Representative Sine Wave 117

5.6. LONG-TERM ANALYSIS 122

5.7. CONCLUSIONS 127

REFERENCES 127

APPENDIX I : Design weather data for the three selected locations from ASHRAE Fundamentals Handbook (2009) [used under fair use, 2013] 130

APPENDIX II : Principles of Heat Balance Method (HBM) for calculating heating and cooling loads (McQuiston et al. 2004) 134

APPENDIX III : Heat pump operational data 137

APPENDIX IV : Basics of change point analysis (Taylor, 2000) 140

APPENDIX V : Results of the representative change point analysis for each city 142

APPENDIX VI : Comparison for one year analysis 146

APPENDIX VII : Long-term performance at different distances from the pile center for the three selected locations 148

CHAPTER 6. SITE DESCRIPTION AND TESTING PROCEDURES 151

6.1. SITE DESCRIPTION AND SOIL CONDITIONS 151

6.2. TEST SETUP 152

6.2.1. General Setup and Pile Installation 152

6.2.2. Lab Tests on Cement Cubes and Cylinders 158

6.3. TESTING EQUIPMENT 160
6.3.1. Mechanical Loading Frame *161*
6.3.2. Thermal Loading Equipment *163*
(a) Temperature Controlling Equipment 163
(b) Heat Rate Control Equipment 165
6.4. VARIOUS FIELD TESTS 167
REFERENCES 167
APPENDIX VIII : Soil profile from drilling data 169
APPENDIX IX : Grain size analysis and Atterberg limits for the top soil layer 175
APPENDIX X : Calibration sheets of the hydraulic pump 180
CHAPTER 7. IN-SITU THERMAL RESPONSE TESTS 182
7.1. INTRODUCTION 182
7.1. GENERAL 182
7.1.1. ASHRAE Procedure *183*
7.1.2. Dutch Procedure *184*
7.2. DATA PROCESSING 184
7.2.1. Applied Power and Calorimetric Power during the Test *184*
7.2.2. Ambient Temperature Interference *185*
7.2.3. Undisturbed Ground Temperature *187*
7.2.4. Ground Thermal Properties *188*
(a) Infinite Line Source Model 188
(b) Cylindrical Source Model 189
(c) Parameter Matching Techniques 191
7.3. VIRGINIA TECH THERMAL CONDUCTIVITY TESTS 194
7.3.1. Undisturbed Ground Temperature (T_o) *197*
7.3.2. Measured Fluid Temperatures (T_f) *200*
7.4. DATA PROCESSING 203
7.4.1. Ignoring the Ambient Temperature Interference *204*
(a) Infinite Line Source Model 204
(b) Parameter Matching 208
7.4.2. Considering the Ambient Temperature Interference *211*
7.5. VALIDATION 212
7.6. MODIFIED DUTCH THERMAL CONDUCTIVITY TEST 214
7.6.1. Theoretical Concept *214*

7.6.2. Virginia Tech Modified Dutch Thermal Response Test *217*

(a) Test Set Up 217

(b) Data Processing 219

REFERENCES 221

APPENDIX XI : Temperature along Pile 3 during TCT 1 and along the Test Pile TCT 4. 224

APPENDIX XII : Parameter matching with no ambient air correction using the infinite line source model, the finite line source model, and the cylindrical source model. Results include; undisturbed ground temperature, the effective thermal conductivity of the ground, and the thermal resistance of the heat exchanger 229

APPENDIX XIII : Parameter matching with ambient air correction using the infinite line source model, the finite line source model, and the cylindrical source model. Results include; percentage of the heat exchanged (loss) with the ambient air, the effective thermal conductivity of the ground, and the thermal resistance of the heat exchanger. 242

CHAPTER 8. THERMO-MECHANICAL PILE LOAD TESTS 255

8.1. INTRODUCTION 255

8.2. MECHANICAL LOADING PHASE 255

8.2.1. Loading Procedure *256*

8.2.2. Load-Displacement Relation *256*

8.2.3. Measured Strain Profiles *257*

8.2.4. Mechanical Load Profile *260*

(a) Pile Tangent Modulus 260

(b) Load Profile from Measured Strains 261

(c) Residual Loads and the True Load Profile 262

8.3. THERMAL LOADING PHASE 265

8.3.1. Loading Procedure *265*

(a) Controlled Inlet Fluid Temperature Tests 266

(b) Controlled Heat Rate Tests 266

8.3.2. Thermal Loads *267*

8.3.3. Thermal Response *269*

(a) Undisturbed Ground Temperature 270

(b) Reference Temperature and Thermal Recovery 271

(c) Temperature Change Along The Test Pile 273

(d) Location-Dependent Temperature Measurements 276

8.4. THERMO-MECHANICAL SUPERIMPOSED EFFECTS 279

8.4.1. Soil-Structure Interaction of Energy Piles *279*

8.4.2. Measured Thermal Strains *280*

8.4.3. Location-Dependent Thermal Strains *282*
8.4.4. Measured Thermal Strain Profiles *284*
8.4.5. Pile Head Movements and Neutral Point *289*
8.4.6. Thermal load profiles *290*
8.4.7. Superimposed Thermo-Mechanical Load Profiles *293*
8.4.8. Thermal Load Recovery *296*
8.5. NUMERICAL MODELING OF FIELD TESTS 297
8.5.1. Concept of Uncoupled Thermo-Mechanical Modeling of Energy Piles *297*
(a) Mechanical Analysis 298
(b) Thermal Analysis 301
(c) Superimposed Thermo-Mechanical Analysis 304
(d) Limitations of The Analytical Approach 307
8.5.2. Decoupled Finite Element Approach for Energy Piles *308*
8.5.3. Load-Displacement Curves *308*
(a) Boundary Conditions, Initial Conditions, and Meshing 316
(b) Model Validation 318
8.5.4. Modeling Virginia Tech Thermo-Mechanical Tests *322*
REFERENCES 331
APPENDIX XIV : Temperature along the Test Pile During Various Thermo-Mechanical Tests 334
APPENDIX XV : Thermal strains along the pile segment embedded in the silty sand layer during various thermo-mechanical tests 339
CHAPTER 9. CONCLUSIONS AND POTENTIALS FOR FUTURE RESEARCH 344
9.1. GENERAL 344
9.2. MULTI-LAYER FINITE LINE SOURCE MODEL 345
9.3. NUMERICAL AND ANALYTICAL MODELING OF ENERGY PILES 345
9.4. LONG-TERM THERMAL PERFORMANCE 346
9.5. THERMAL CONDUCTIVITY TESTING 346
9.6. THERMO-MECHANICAL BEHAVIOR OF ENERGY PILES 347

List of Figures

Figure 2.1. Different heat sources (a) point source, and (b) infinite line source. 6

Figure 2.2. Finite line source (FLS) model with finite homogeneous medium 9

Figure 2.3. Thermal conductivity against dry density and water content for frozen and unfrozen soils (adapted from Brandl, 2006 - used under fair use, 2013): (a) coarse-grained frozen soil; (b) coarse-grained unfrozen soil; (c) fine-grained frozen soil; (d) fine-grained unfrozen soil. 22

Figure 2.4. Heat transfer coefficient for different water/propylene glycol mixtures for 25.4 mm (1 inch) tube and flow rate of 11 liter/min (2.9 gpm). 28

Figure 2.5. Thermally induced soil-pile interaction during Energy Pile operation adapted from (Bourne-Webb et al., 2009 - used under fair use, 2013) 30

Figure 2.6. Time evolution of ground temperature 31

Figure 3.1. Details of Ground Coupled Heat Pump (Siegenthaler, 2010 - used under fair use, 2013) 38

Figure 3.2. Heat transfer mechanisms in ground elements (Not to scale). 40

Figure 3.3. Heat transfer coefficients for different water/propylene glycol mixtures for 1 inch tube and flow rate of 11 liter/min (3 gpm). 44

Figure 3.4. Modeled Energy Pile and its surrounding soil. 49

Figure 3.5. Finite element model validation against the solid cylindrical analytical model at the pile soil interface. 52

Figure 3.6. Annual average ambient air temperature variation at Blacksburg, VA using 15.5^{o}C average and 14^{o}C swing 54

Figure 3.7. Initial and final temperature profiles for the three models used to examine the effect of boundary conditions on thermal modeling results. 55

Figure 3.8. Total output energy versus time in logarithmic scale 56

Figure 3.9. Temperature distribution at the mid length of the modeled pile at; (a) surface Insulation, (b) constant temperature, and (c) varying ground temperature. 58

Figure 3.10. Temperature profile for the three models at; (a) pile-soil interface, and (b) 0.25m – 1 ft away from the pile-soil interface. 59

Figure 3.11. Temperature change profile for the three models at; (a) pile-soil interface, and (b) 0.25m – 1 ft away from the pile-soil interface. 60

Figure 3.12. Temperature variation along the radial distance for different orientations at the mid-length of the pile by the end of the modeled month for the three considered models. 62

Figure 3.13. Effect of modeling Energy Piles as a thermally anisotropic material using model 3 (thermal surface insulation and constant initial temperature) 63

Figure 4.1. Multilayer finite line source model; (a) effect of the primary segment, and (b) effect of the secondary segments. 72

Figure 4.2. Soil stratification for the example used in the model validation. 78

Figure 4.3. Validation of the proposed layer dependent heat rate formula (Eq. 3-15). 79

Figure 4.4. Temperature change at different times for the example used in the model validation using finite element model (FE), Multilayer FLS model with all adjustments, and infinite line source (ILS) model with the heat rate adjustment at; (a) interface of heat exchanger and the soil, (b) 0.5m away from the interface, and (c) 2.5m away from the interface. 81

Figure 4.5. Temperature change for the example used in model validation at the center of the upper and the lower soil layers versus radial distance from the heat exchanger interface using the proposed multilayer FLS model and finite element model. 82

Figure 4.6. Heat rate in each soil layer for different analyses. 84

Figure 4.7. Generalization of the proposed FLS model using temperature changes in a two-layered soil profile at; (a) soil-heat exchanger interface, and (b) 2.5m away from the interface. 85

Figure 5.1. Design office building used in the demonstration example for the proposed long-term analysis procedure. 92

Figure 5.2. Ambient air dry bulb temperature for the selected locations. 97

Figure 5.3. Hourly variation for ground thermal loads at the three selected locations for a typical metrological year (TMY) 106

Figure 5.4. Ground thermal load profiles for the selected locations with the non-dominating load set at the beginning of the year. The red sine waves are developed following Lazzari et al. (2010) approach; the green sine waves are developed using the sine wave equivalency concept. 111

Figure 5.5. Sketch of the Energy Pile used in the analysis. 113

Figure 5.6. Results of finite element model (COMSOL) versus Infinite Line Source (ILS) model 114

Figure 5.7. The effect of the initial thermal load on the predicted temperature change at the center of the pile by the end of one-year analysis. 116

Figure 5.8. Effect of ground temperature at the beginning of the 2nd thermal load on the respective predicted ground temperature. 116

Figure 5.9. Temperature changes at the pile center estimated using the actual ground loads (Q_{actual}), the sine wave based on Lazzari et al. approach, and the equivalent sine wave sine wave ($Q_{equivalent}$) for; (a) Charlotte, NC; (b) Chicago, IL; and (c) Austin, TX. 119

Figure 5.10. Comparison between models performed using the actual ground loads (Q_{actual}), and sine waves based on equivalent sine wave concept ($Q_{equivalent}$) for; (a) Charlotte, NC, and Austin, TX, (b) Chicago, IL. 121

Figure 5.11. Ground temperature variation at the center of the pile for the selected locations assuming 30 years of operation. 124

Figure 5.12. Indices of heap pump performance for the selected locations over time. 125

Figure 5.13. Temperature recovery at the center of the pile for the selected locations assuming 30 years of operation. 126

Figure 6.1. General location of the test site with respect to Virginia Tech main campus in Blacksburg, VA [from Google maps - used under fair use, 2013] 151

Figure 6.2. Soil cuttings taken while drilling the Test Pile hole. 152

Figure 6.3. Virginia Tech Energy Pile Test Setup. 153
Figure 6.4. Drill bit and hummer used for drilling different piles and observation points. 154
Figure 6.5. Installing circulation tubes and pressure testing them before backfilling. 155
Figure 6.6. RocTest EM-5 concrete embedded strain gauge. 156
Figure 6.7. Installing the EM-5 Instrumentation in the Test Pile (Pile 1) and observation point 4 157
Figure 6.8. Quality control of the cement mortar. 158
Figure 6.9. Measuring the volume of broken cement specimens for dry density calculations. 159
Figure 6.10. Results of compressive tests on cement cubes and cylinders. 159
Figure 6.11. Measured dry density of the cement mortar used in different field test elements. 160
Figure 6.12. Loading frame and reference beam. 163
Figure 6.13. Temperature controlling equipment. 165
Figure 6.14. Heat rate controlling equipment Mechanical Equipment Sales, Inc. system. 166
Figure 7.1. Schematic of in-situ thermal conductivity test set up. 186
Figure 7.2. Dimensionless G-function. 190
Figure 7.3. Thermal insulation used to reduce the heat exchanged with the ambient in each test. 195
Figure 7.4. Estimating the undisturbed ground temperature from the average fluid temperature during the initialization phase of each thermal conductivity test. 198
Figure 7.5. Undisturbed ground temperature measured before the beginning of the testing program. 199
Figure 7.6. Effect of thermo-mechanical tests on the undisturbed ground temperature measured during TCT 2 and TCT 3. 200
Figure 7.7. Measured inlet and outlet fluid temperatures for various thermal conductivity tests conducted following the ASHRAE procedure. 201
Figure 7.8. Averaged fluid temperature and ambient air temperature for various thermal conductivity tests conducted following the ASHRAE procedure. 202
Figure 7.9. The calorimetric power applied to the fluid estimated using Eq. 7-4.c, and the ambient air temperature measured in each test. 203
Figure 7.10. Processing the results of thermal conductivity tests using; (a) forward processing, and (b) backward processing. 205
Figure 7.11. Results of the considered thermal conductivity tests using logarithmic scale for the time. 206
Figure 7.12. Ground effective thermal conductivity estimated using the infinite line source model for the forward and the backward processing. 206
Figure 7.13. Thermal resistance of the heat exchanger estimated using the infinite line source model for the forward and the backward processing (T_o = 14.5ºC/58.1ºF). 207

Figure 7.14. Effect of the ground thermal conductivity and the thermal resistance of the heat exchanger on one another. 210

Figure 7.15. The actual applied power corrected for the heat lost to the ambient air versus the applied power with not correction and the ambient air temperature. 213

Figure 7.16. Validating the results of the parameter matching including the correction for the heat exchanged with the ambient air using finite element modeling of the four considered tests. 214

Figure 7.17. Proposed online modification of the inlet fluid temperature to account for the heat exchanged with the ambient air. 216

Figure 7.18. Fluid temperature during the initialization phase used to estimate the undisturbed ground temperature (T_o). 217

Figure 7.19. Measured fluid and air temperatures during the modified Dutch thermal conductivity test performed at Virginia Tech. 218

Figure 7.20. The ambient air and the power applied in the modified Dutch thermal conductivity test conducted at Virginia Tech, estimated using the fluid temperatures near the ground surface (T_{in} and T_{out}) and using the fluid temperatures near the testing equipment (T^*_{in} and T^*_{out}). 219

Figure 7.21. Measured fluid and air temperatures using logarithmic scale for the time. 220

Figure 7.22. The average fluid temperature estimated using the 2-dimensional finite element model versus the average fluid temperature measured in-situ. 221

Figure XI.1. Temperature at different depths along the center of Pile 3 during TCT 1 225

Figure XI.2. Temperature change at different depths along the Test Pile during TCT 3 226

Figure XI.3. Temperature along the Pile 3 at different times during TCT 1 227

Figure XI.4. Temperature along the Test Pile at different times during TCT 3 228

Figure XII.1. Undisturbed ground temperature estimated using various models incorporated in the parameter matching framework with no ambient air effects considered for TCT1 230

Figure XII.2. Ground effective thermal conductivity estimated using various models incorporated in the parameter matching framework with no ambient air effects considered for TCT1 231

Figure XII.3. Thermal resistance of the heat exchanger estimated using various models incorporated in the parameter matching framework with no ambient air effects considered for TCT1 232

Figure XII.4. Undisturbed ground temperature estimated using various models incorporated in the parameter matching framework with no ambient air effects considered for TCT2 233

Figure XII.5. Thermal conductivity estimated using various models incorporated in the parameter matching framework with no ambient air effects considered for TCT2 234

Figure XII.6. Thermal resistance of the heat exchanger estimated using various models incorporated in the parameter matching framework with no ambient air effects considered for TCT2 235

Figure XII.7. Undisturbed ground temperature estimated using various models incorporated in the parameter matching framework with no ambient air effects considered for TCT3 236

Figure XII.8. Thermal conductivity estimated using various models incorporated in the parameter matching framework with no ambient air effects considered for TCT3 237

Figure XII.9. Thermal resistance of the heat exchanger estimated using various models incorporated in the parameter matching framework with no ambient air effects considered for TCT3 238

Figure XII.10. Undisturbed ground temperature estimated using various models incorporated in the parameter matching framework with no ambient air effects considered for TCT4 239

Figure XII.11. Thermal conductivity estimated using various models incorporated in the parameter matching framework with no ambient air effects considered for TCT4 240

Figure XII.12. Thermal resistance of the heat exchanger estimated using various models incorporated in the parameter matching framework with no ambient air effects considered for TCT4 241

Figure XIII.1. Thermal conductivity of the ground estimated using various models incorporated in the parameter matching framework with no ambient air effects considered for TCT1 243

Figure XIII.2. Thermal resistance of the heat exchanger estimated using various models incorporated in the parameter matching framework with no ambient air effects considered for TCT1 244

Figure XIII.3. Percentage of applied heat transferred to the ground estimated using various models incorporated in the parameter matching framework with no ambient air effects considered for TCT1 245

Figure XIII.4. Thermal conductivity of the ground estimated using various models incorporated in the parameter matching framework with no ambient air effects considered for TCT2 246

Figure XIII.5. Thermal resistance of the heat exchanger estimated using various models incorporated in the parameter matching framework with no ambient air effects considered for TCT2 247

Figure XIII.6. Percentage of applied heat transferred to the ground estimated using various models incorporated in the parameter matching framework with no ambient air effects considered for TCT2 248

Figure XIII.7. Thermal conductivity of the ground estimated using various models incorporated in the parameter matching framework with no ambient air effects considered for TCT3 249

Figure XIII.8. Thermal resistance of the heat exchanger estimated using various models incorporated in the parameter matching framework with no ambient air effects considered for TCT3 250

Figure XIII.9. Percentage of applied heat transferred to the ground estimated using various models incorporated in the parameter matching framework with no ambient air effects considered for TCT3 251

Figure XIII.10. Thermal conductivity of the ground estimated using various models incorporated in the parameter matching framework with no ambient air effects considered for TCT4 252

Figure XIII.11. Thermal resistance of the heat exchanger estimated using various models incorporated in the parameter matching framework with no ambient air effects considered for TCT4 253

Figure XIII.12. Percentage of applied heat transferred to the ground estimated using various models incorporated in the parameter matching framework with no ambient air effects considered for TCT4 254

Figure 8.1. Pile head movement-load curves for 1st and 2nd load tests. 257

Figure 8.2. Measured strains along the pile during the 1st and the 2nd load tests..... 259

Figure 8.3. Tangent modulus for the Test Pile at different depths from the results of the 1st and the 2nd load tests. 261

Figure 8.4. Estimated load profiles along the pile for each loading step of the first load test. 262

Figure 8.5. Residual load development in drilled shafts; black arrows show the relative magnitude of settlements for the soil and the shaft while red arrows show the direction of the frictional forces. .. 263

Figure 8.6. Measured, residual, and true load profiles along the Test Pile at the ultimate heat load of the first load test. 264

Figure 8.7. Measured load profiles along the pile for each step of the second load test. 265

Figure 8.8. Measured inlet and outlet fluid temperatures in each thermo-mechanical test. 268

Figure 8.9. Undisturbed ground temperature measured in early August 2011 prior to any thermal activity at the test site. 270

Figure 8.10. Initial ground temperature for each thermo-mechanical test. 272

Figure 8.11. Temperature change along the Test Pile at the end of T-MT 3 and T-MT 4; and along Pile 3 at the end a thermal conductivity test. 273

Figure 8.12. Temperature change along the Test Pile at the end of various steps of the thermal load of T-MT 1 and T-MT 2. 275

Figure 8.13. Effect of the relative locations of the temperature gauge and the ground loops on the measured temperatures. 276

Figure 8.14. Temperature change around the Test Pile at the end of; (a) T-MT 1 and T-MT 2, and (b) T-MT 3 and T-MT 4. 279

Figure 8.15. Concept of temperature self-compensating strain gauges. 282

Figure 8.16. The effect of the gage's relative location within the pile cross-section on measured thermal strains. 284

Figure 8.17. Blocked thermal strain profiles along the Test Pile at the end of T-MT 3, and T-MT 4. 285

Figure 8.18. Blocked thermal strain profiles along the Test Pile at the end of each thermal load step of T-MT 1 and T-MT 2. 286

Figure 8.19. Schematic for cases where uniform thermal strains are expected. 288

Figure 8.20. Pile head movement due to different thermal loads in T-MT 1 and T-MT 2. 289

Figure 8.21. Thermal load profiles along the Test Pile at the end of T-MT 3, and T-MT 4. 290

Figure 8.22. Thermal load profiles along the Test Pile at the end of each thermal load step of T-MT 1 and T-MT 2. 292

Figure 8.23. Thermo-mechanical load profile for each thermal step in T-MT 1. 294

Figure 8.24. Thermo-mechanical load profile for each thermal step in T-MT 2. 295

Figure 8.25. Thermal and structural load recovery after T-MT 1. 296

Figure 8.26. Thermal load recovery for T-MT 2, T-MT 3, and T-MT 4. 297

Figure 8.27. Load carrying mechanisms of piles under mechanical compressive and tensile loads. 298

Figure 8.28. Load-transfer curves for the unit shaft friction and the unit base resistance (Frank and Zhao, 1982 - used under fair use, 2013) 299

Figure 8.29. Spring analogy for analyzing the mechanical response in a pile foundation (Knellwolf et al. 2011- under fair use, 2013). 300

Figure 8.30. Effects of fixity of pile ends on the thermal displacement along the pile. 302

Figure 8.31. Effect of thermal heating load on Energy Piles (Knellwolf et al. 2011 - used under fair use, 2013). 303

Figure 8.32. Thermo-mechanical response for the pile shaft friction. 306

Figure 8.33. Thermo-mechanical response for the base resistance. 307

Figure 8.34. Stiffness of the soil springs (K_{soil}) for finite element modeling of the load-transfer curves. . 309

Figure 8.35. Spring stiffness-displacement curve from the load-transfer curve of the unit shaft friction. 310

Figure 8.36. Spring stiffness-displacement curve from the load-transfer curve of the unit base resistance. 311

Figure 8.37. Thermal stiffness of soil springs along the shaft of Energy Piles. 313

Figure 8.38. Thermal stiffness of the soil springs along the pile shaft for finite element modeling. 314

Figure 8.39. Thermal stiffness of soil springs at the base of Energy Piles. 316

Figure 8.40. Mechanical analysis of Energy Piles in decoupled finite element models. 317

Figure 8.41. Thermal analysis of Energy Piles in decoupled finite element models. 318

Figure 8.42. Validating the proposed finite element approach with the EPFL thermo-mechanical in-situ test results (Laloui et al., 2006 - used under fair use, 2013). 321

Figure 8.43. Validating the proposed finite element approach with the Lambeth College thermo-mechanical in-situ test results (Bourne-Webb et al., 2009 - used under fair use, 2013). 322

Figure 8.44. Displacement-dependent soil spring stiffness. 324

Figure 8.45. Comparison between the distributions of the mechanical load along the Test Pile from the finite element models and the in-situ measurements. 325

Figure 8.46. Comparison between the thermal strains from the finite element model and the in-situ measurements for T-MT 1. 327

Figure 8.47. Comparison between the thermal strains from the finite element model and the in-situ measurements for T-MT 2. 328

Figure 8.48. Comparison between the thermo-mechanical loads from the finite element model and the in-situ measurements for T-MT 1. 329

Figure 8.49. Comparison between the thermo-mechanical loads from the finite element model and the in-situ measurements for T-MT 2. 330

Figure XIV.1. Temperature along the Test Pile during T-MT 1 335
Figure XIV.2. Temperature along the Test Pile during T-MT 2 336
Figure XIV.3. Temperature along the Test Pile during T-MT 3 337
Figure XIV.4. Temperature along the Test Pile during T-MT 4 338
Figure XV.1. Thermal induced strains along the Test Pile during T-MT 1 340
Figure XV.2. Thermal induced strains along the Test Pile during T-MT 2 341
Figure XV.3. Thermal induced strains along the Test Pile during T-MT 3 342
Figure XV.4. Thermal induced strains along the Test Pile during T-MT 4 343

List of Tables

Table 2-1. Typical values for the thermal properties of soils (Clarke et al., 2008 - used under fair use, 2013). 14

Table 2-2. Typical proposed values for κ (Côte and Konrad, 2005 - used under fair use, 2013) 18

Table 2-3. Typical values for ß and η proposed by Côte and Konrad (2005 - used under fair use, 2013) 19

Table 2-4. Typical thermal conductivity for different soils (from Salomone and Marlowe, 1989 - used under fair use, 2013). 21

Table 2-5. Specific heat and heat capacity of concrete (ACI, 2002 - used under fair use, 2013) 24

Table 2-6. Thermal properties of HDPE and PEX tubes. 25

Table 2-7. Heat transfer coefficient in W/m^{2}·°C for different water/propylene glycol mixtures for 1 inch tube and flow rate of 11 liter/min (2.9 gpm). 27

Table 2-8. Summary of the two reported Energy Piles field tests. 32

Table 3-1. Analytical models for ground coupled heat exchangers 41

Table 3-2. Thermal properties of HDPE and PEX tubes. 45

Table 3-3. Boundary conditions for heat transfer problems in Energy Piles. 46

Table 3-4. Liquid temperature change through ground coupled heat pumps (Kavanaugh and Rafferty, 1997 - used under fair use, 2013). 48

Table 3-5. Parameters used in the preliminary models. 51

Table 4-1. Summary of thermal properties of the layers used in model generalization. 83

Table 5-1. Components of exterior and interior walls, roof, and floor (McQuiston et al., 2004 - used under fair use, 2013). 92

Table 5-2. Summary of weather design data for the three selected locations 94

Table 5-3. Building heating and cooling loads at the three selected locations 95

Table 5-4. Balance point temperature analysis for the selected locations under occupied and unoccupied conditions. 99

Table 5-5. Temperature bins for each selected location 100

Table 5-6.a) Ground thermal loads for Charlotte, NC. 103

Table 5-6.b) Ground thermal loads for Chicago, IL. 104

Table 5-6.c) Ground thermal loads for Austin, TX. 105

Table 5-7. Results of the change point analysis in the ground thermal loads for the selected locations . 108

Table 5-8. Amplitudes of different sine waves used to represent ground thermal loads 110

Table 5-9. Geo-material, fluid, tube, and pile thermal properties included in the model. 114

Table 5-10. Temperature change (ΔT) at the pile center from the three modeled ground heating loads Q_{actual}, $Q_{equ.}$, and Lazzari et al. (2010) analyses. 120

Table 6-1. Components inside each Energy Pile..... 156

Table 6-2. Instrumentation and ground loop type and configuration in each test element. 157

Table 6-3. Estimated thermal conductivity of different elements 160

Table 6-4. Virginia Tech field testing program. 167

Table 7-1. Equivalent diameters and thermal resistances for Polyethylene U-tubes (Kavanaugh and Rafferty, 1997 - used under fair use, 2013) 191

Table 7-2. Typical values of $\boldsymbol{Fsc}$ (Kavanaugh and Rafferty, 1997 - used under fair use, 2013) 191

Table 7-3. List of Virginia Tech thermal conductivity tests..... 196

Table 7-4. Average and standard deviation of the ground effective thermal conductivity and the thermal resistance of the heat exchanger estimated using the infinite line source model for the forward and the backward processing. 208

Table 7-5. Summary of the parameter matching for the considered four tests using the infinite line source, the finite line source, and the cylindrical source model following the forward and the backward processing techniques. 209

Table 7-6. Summary of the parameter matching using the corrected power for the considered four tests using the infinite line source, the finite line source, and the cylindrical source model following the forward and the backward processing techniques. 212

Table 8-1. Virginia Tech thermo-mechanical tests performed on the Test Pile (Pile 1) as part of the testing program. 255

Table 8-2. Thermal properties of the two ground layers considered in the numerical model. 276

Table 8-3. Soil properties for different soils encountered at the test sites of Laloui et al. (2006) and Bourne-Webb et al. (2009). 320

Table 8-4. Ultimate unit shaft friction for each silty sand sublayers estimated for T-MT 1 and T-MT 2. 323

Table 8-5. Temperature change for modeling various thermal steps. 326

CHAPTER 1. INTRODUCTION

1.1 General

Traditionally, geothermal boreholes have utilized the ground energy for space heating and cooling. In this system, a circulation loop is placed in a small-diameter borehole typically extending to a depth of 200-300 ft. The hole is then backfilled with a mixture of sand, bentonite and/or cement. The loop is connected to a geothermal heat pump and the fluid inside the loop is circulated. The heat energy is fed into the ground for cooling in the summer and withdrawn from the ground for heating in the winter. Geothermal heat pumps work more efficiently for space heating and cooling compared to air-source heat pumps. The reason is ground-source systems use the ground as a constant temperature source which serves as a more favorable baseline compared to the ambient air temperature.

Over the past 20 years, this ground coupling concept has been expanded from geothermal borehole systems to the use of building foundation elements as heat exchangers. Energy Piles in particular are an innovative technology that combines geothermal heat exchange and structural foundation support. In this hybrid system, geothermal loops are integrated into the deep foundation elements, such as piles, piers, or drilled shafts, that are already in place to provide structural support.

A major cost associated with any deep geothermal borehole is the drilling required for installation. Because Energy Piles perform the dual function of exchanging heat and providing structural support, and are only installed at sites where pile foundations are already required, these systems provide the thermal performance of deep geothermal systems without the additional drilling costs. Low maintenance, long lifetime, less variation in energy supply compared to solar and wind power, and environmental friendliness have been cited as additional Energy Pile advantages. Case studies show that they can significantly lower heating/cooling costs and reduce carbon footprint. Energy cost savings for typical buildings outfitted with Energy Piles could be as much as 70 percent.

The use of Energy Piles has rapidly increased over the last decade, especially in Europe where more than 500 applications are reported. Primary installations have been in Germany, Austria, Switzerland and United Kingdom. Notable projects include the 56-story high Frankfurt Main Tower in Germany, Dock E Terminal Extension at Zurich International Airport in Switzerland and the One New Change building complex in London U.K. Energy piles have seen very little use in the North America, only a handful of completed projects are known; Marine Discovery Center in Ontario, Canada, Lakefront Hotel in Geneva, New York and the Art Stable building in Seattle, Washington.

Energy Piles are typically installed with cast-in-place technology (i.e. drilled shafts, continuous flight auger piles, micropiles etc.) while some driven pile applications are also reported. Other types of geotechnical structures in contact with the ground, such as shallow foundations, retaining walls, basement walls, tunnel linings and earth anchors, also offer significant potential for harnessing near-surface geothermal energy.

The use of Energy Piles extends beyond space heating and cooling. Energy Piles can be used to collect and store heat energy for de-icing bridge decks in the winter. The piles or drilled shafts used to support the bridge can in turn be used to store and withdraw heat energy. Heat can be collected from the asphalt pavement over the summer and stored in the ground using the deep foundations. During the winter, this stored energy can then be reclaimed to heat and de-ice the

bridge deck. There is a potential to further integrate geothermal energy into the bridge substructure by placing geothermal loops in the bridge abutments which would increase the thermal mass available for storing heat.

This simple application demonstrates how versatile Energy Piles can be and the possible significance of their contribution to sustainable structures. Current practices of deicing concrete bridges involve chemical salts, which can be harmful to the environment and lead to accelerated corrosion of the bridge deck and reinforcing steel. Energy Piles could eliminate the need for deicing salts on many bridges, extending their service life while providing a safe roadway for motorists.

Energy Pile design needs to integrate geotechnical, structural and heat exchange considerations. Geotechnical characteristics of the foundation soils and the level of the structural loads are typically the deciding factors for the selection and dimensioning of the pile foundations. The geothermal heat exchange capacity of an Energy Pile is a key parameter to be considered in design. Thermal characteristics of the ground as well as the heating and cooling loads from the structure need to be considered for the number of piles that will be utilized as heat exchangers. Therefore, the thermal properties of the site need to be evaluated for an Energy Pile application in addition to the traditional geotechnical characterization for foundation design.

Energy Piles bring new challenges to geotechnical pile design. During a heat exchange operation, the pile will expand and contract relative to the soil as heat is injected and extracted, respectively. These relative movements have the potential to alter the shear transfer mechanism at the pile-soil interface. Furthermore, the range of temperature increases near the pile surface, though limited by practical operational guidelines, can have a significant effect on pore pressures generation and soil strength.

1.2 Research Questions

Several geotechnical related research questions rise due to utilizing the piles as heat exchanger elements including;

1. What is the design temperature that should be used while accounting for the thermal effects on the mechanical performance of the piles? This temperature should correspond to the most critical stresses and deformations that may take place in the pile due to the combined thermo-mechanical effects. A good estimate of this temperature requires a good predication of the long-term thermal performance of the piles.
2. How can the long-term thermal performance be reliably predicted? Numerical modeling is the most suitable approach to predicate the long-term thermal performance of energy piles. However, several issues should be considered while conducting such models;
    a. How to efficiently account for the short term variation of the applied heating rate including the hourly and the daily variation?
    b. How to obtain a good estimate of the thermal properties of the various materials included in the model?
    c. How to design a system that is efficient and sustainable? This requires assuring that the ground temperature recovers in an acceptable short time period after turning the system down to assure that future generations will be able to reutilize the geothermal energy.
3. What are the thermal stresses expected while the piles are subjected to heating and cooling cycles?

4. How the degrees of fixation at the pile head and toe as well as the frictional resistance affect the thermal strains and stresses in an energy piles?
5. How to predicate the thermo-mechanical behavior of energy piles?
6. What is the effect of the temperature change on the soil response and consequently on the pile behavior?

The work reported in this dissertation attempts to answer the first five-questions. While the sixth question is being investigated by other researchers since it requires significant efforts in laboratory experiments.

Chapter 2 of this dissertation summarizes the background needed to conduct research in the energy foundation area including the simplified method to estimate the length of the ground loops, available analytical models to analyze the thermal performance of the piles, estimating the thermal properties of various materials using simple correlations, and the reported thermo-mechanical pile load tests.

Chapter 3 presents a detailed numerical modeling technique proposed to conduct finite element modeling of energy piles. In this chapter, the effect of using various initial and boundary conditions was investigated as well as considering the pile as a thermally anisotropic material. Furthermore, approaches to account for the effect of the carrier fluid and the walls of the ground loops without physically modeling these domains are presented in this chapter. Additionally, Chapter 4 provides a newly developed analytical model that can be used in lieu of the finite element models to estimate the temperature changes in and around energy piles embedded in stratified soils.

Chapter 5 utilizes the findings of the finite element modeling in predicting the long-term thermal performance of the system. In this chapter, the daily and hourly heating rate variation was accounted for using a newly developed concept titled the “equivalent sine wave”. Furthermore, the thermal recovery of the ground temperature after terminating the operation of the system is also investigating by the end of that chapter.

Chapter 6 describes the full scale testing facility used to examine the applicability of thermal conductivity tests to energy piles as well as the thermo-mechanical behavior of energy piles. Chapter 7 summarizes the findings of various thermal conductivity tests and discusses the effect of various loops and the loop length of the estimated thermal properties of the ground estimated using the traditional testing techniques. Moreover, a modification to the testing procedure is proposed by the end of the chapter to improve the accuracy of the obtained testing results which consequently simplify the data processing afterwards. Finally, Chapter 8 summarizes the findings of thermo-mechanical load tests and the observed behavior of the tested energy pile.

CHAPTER 2. LITERATURE REVIEW

2.1. Design of the Ground Loops

This section outlines briefly the general procedure followed to design the ground loops for geothermal systems. The detailed procedure is outlined by Kavanaugh and Rafferty (1997). The most common approach followed to size the ground loops is that proposed by Ingersoll et al. (1948) which is based on a simple steady-state heat transfer equation. In this approach, the large thermal mass of the ground surrounding the ground loops are assumed to damp the daily and the monthly thermal pulses. Thus, the annual net heat transferred to the ground is sufficient to approximate the thermal performance of the system. The fundamental steady-state heat transfer coefficient used to approximate the length of the ground loops is;

$$q = \frac{L(T_g - T_w)}{R} \qquad \text{Eq. 2-1}$$

Where L is the length of the ground loop, R is the total thermal resistance of the system to the applied thermal load q, T_g is the undisturbed ground temperature, and T_w is the temperature of the carrier fluid.

Eq. 2-1 is rearranged to solve for the ground loop length (L) and account for the variable applied heat rate (q) using a series of constant heat rate pulses. Thus, the thermal resistance is divided into time-dependent resistances. These time-dependent resistances correspond to various thermal pulses in q-series. Furthermore, another term is added to account for the thermal resistance of the pipe pall and interfaces between the pipe and the fluid and the pile and the ground. These modifications give;

$$L_c = \frac{q_a R_{ga} + (q_{lc} - 3.41\overline{W}_c)(R_b + \mathrm{PLF_m} R_{gm} + R_{gd} F_{sc})}{T_g - \frac{T_{wi} - T_{wo}}{2} - T_p} \text{ for cooling loads (Imperial units)} \qquad \text{Eq. 2-2}$$

And;

$$L_h = \frac{q_a R_{ga} + (q_{lh} - 3.41\overline{W}_h)(R_b + \mathrm{PLF_m} R_{gm} + R_{gd} F_{sc})}{T_g - \frac{T_{wi} - T_{wo}}{2} - T_p} \text{ for heating load (Imperial units)} \qquad \text{Eq. 2-3}$$

Or,

$$\mathrm{L_c} = \frac{\mathrm{q_a R_{ga}} + (\mathrm{q_{lc}} - \overline{\mathrm{W}}_\mathrm{c})(\mathrm{R_b} + \mathrm{PLF_m R_{gm}} + \mathrm{R_{gd} F_{sc}})}{\mathrm{T_g} - \frac{\mathrm{T_{wi}} - \mathrm{T_{wo}}}{2} - \mathrm{T_p}} \text{ for cooling loads (SI units)} \qquad \textbf{Eq. 2-4}$$

And,

$$\mathrm{L_h} = \frac{\mathrm{q_a R_{ga}} + (\mathrm{q_{lh}} - \overline{\mathrm{W}}_\mathrm{h})(\mathrm{R_b} + \mathrm{PLF_m R_{gm}} + \mathrm{R_{gd} F_{sc}})}{\mathrm{T_g} - \frac{\mathrm{T_{wi}} - \mathrm{T_{wo}}}{2} - \mathrm{T_p}} \text{ for heating load (SI units)} \qquad \text{Eq. 2-5}$$

Where;

L_c :the length of the ground loop required to satisfy the cooling capacity,
L_h: the length of the ground loop required to satisfy the heating capacity,
q_a: net annual average heat transfer to the ground,
q_{lc}: the building design cooling load,
q_{lh}: the building design heating load,
R_{ga}: effective thermal resistance of the ground annual pulse,

R_{gd}: effective thermal resistance of the ground daily pulse,
R_{gm}: effective thermal resistance of the ground monthly pulse,
R_b: thermal resistance of the heat exchanger,
T_{wi}: the temperature of the fluid entering the heat pump, i.e. outlet of the ground loop,
T_{wo}: the temperature of the fluid leaving the heat pump, i.e. inlet of the ground loop,
T_p: temperature penalty for interference of adjacent heat exchangers,
$\bar{W}_c$: power input at design cooling load,
$\bar{W}_h$: power output at design heating load.

For Imperial units L_c and L_h are in feet; q_a, q_{lc}, q_{lh} are in Btu/hr; R_{gd}, R_{gm} and R_b are in hr·ft·°F/Btu; T_{wi}, T_{wo} and T_p are in °F; and $\bar{W}_c$ and $\bar{W}_h$ are in Btu/hr. While for SI units L_c and L_h are in meters; q_a, q_{lc}, q_{lh} are in Watts; R_{gd}, R_{gm} and R_b are in m·°C/Watts; T_{wi}, T_{wo} and T_p are in °C; and $\bar{W}_c$ and $\bar{W}_h$ are in Watts.

The heat transfer rates, building loads, and temperature penalties are positive for heating in the Eq. 2-2 and Eq. 2-3 and negative for cooling (Kavanaugh and Rafferty, 1997). Moreover, these two formulas consider a long-term effect which is represented by the annual pulse, an average monthly pulse, and a short-term effect which is represented by the daily pulse. The final length is governed by the minimum of Eq. 2-2 and Eq. 2-3 (Kavanaugh and Rafferty, 1997).

2.2. Thermal Analysis (Temperature in the Ground)

2.2.1. Infinite Line Source Model

The infinite line source (ILS) model is a direct application of Lord Kelvin's heat source to ground heat exchangers. This model relays on the fact that any line can be treated as numerous points positioned next to each other. Thus, it starts with calculating the temperature change at specific location in an infinite homogeneous medium based on the formula of point heat source, then using integration to account for the effect of other point sources at that desired location.

The following general assumptions were made for the derivation of this model as well as all the following models;

1) The ground is regarded as a homogeneous medium and its thermo-physical properties do not change with temperature,
2) The medium has a uniform initial temperature,
3) The heating rate per unit length is constant from the starting instant.

Ingersoll et al. (1948) showed that the temperature change at a distance *r* from a point heat-source emitting instantaneously Q units of heat at a time τ as shown in Figure 2.1.a can be calculated as follows;

$$\Delta T = \left(\frac{Q\alpha}{k}\right)\left(\frac{1}{2\sqrt{\pi\alpha\tau}}\right)^3 e^{-\rho^2/4\alpha\tau} \qquad \text{Eq. 2-6}$$

Where;
α : thermal diffusivity of the medium (soil),
k : thermal conductivity of the medium (soil),
τ : time,
ρ : distance between the point source and location of interest.

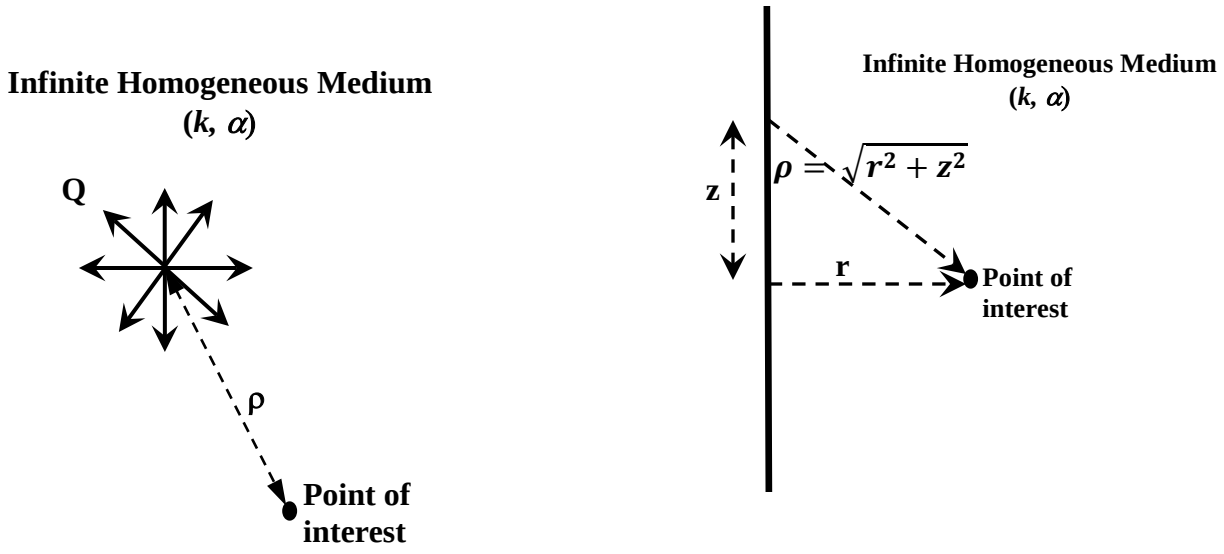

(a) (b)

Figure 2.1. Different heat sources (a) point source, and (b) infinite line source.

The following integration is then used to estimate the temperature change due to an infinite line-source. Again, the line-source is represented by adjacent points which for each one of them the distance to the location of interest are $\rho = \sqrt{r^2 + z^2}$ as shown in Figure 2.1.b which result is;

$$\Delta T = \int_{-\infty}^{\infty} \left(\frac{q\prime\alpha}{k}\right)\left(\frac{1}{2\sqrt{\pi\alpha\tau}}\right)^3 e^{-(r^2+z^2)/4\alpha\tau}\,.\,dz \qquad \text{Eq. 2-7}$$

Where, q' is the emitted heating units released per unit length of the line source. Thus,

$$\Delta T = \left(\frac{q\prime\alpha}{k}\right)\left(\frac{1}{2\sqrt{\pi\alpha\tau}}\right)^3 e^{-r^2/4\alpha\tau} \int_{-\infty}^{\infty} e^{-z^2/4\alpha\tau}\,.\,dz = \frac{q\prime}{4\pi k\tau}\, e^{-r^2/4\alpha\tau} \qquad \text{Eq. 2-8}$$

When the source is emitting continuously from time 0 to *t*, the change of temperature can be estimated as;

$$\Delta T = \frac{q'}{4\pi k} \int_0^t \frac{e^{-r^2/4\alpha\tau}}{\tau}\,.\,d\tau$$

Setting $\beta = r/2\sqrt{\alpha\tau}$, thus

$$\frac{d\beta}{d\tau} = \left(\frac{r}{2}\right)\left(\frac{1}{\alpha^{0.5}}\right)\left(\frac{1}{-2}\right)\left(\frac{1}{\tau^{1.5}}\right)$$

$$\frac{d\tau}{\tau} = \left(\frac{-4}{r}\right)(\alpha^{0.5})(\tau^{0.5}).\, d\beta = -2\frac{d\beta}{\beta}$$

Therefore,

$$\Delta T = \frac{q'}{2\pi k}\int_{\beta}^{\infty}\frac{e^{-\beta^2}}{\beta}.\, d\beta \qquad \text{Eq. 2-9}$$

The integration minimum and maximum limits were determined by substituting in β using $\tau = 0$, and $\tau = t$, respectively. The above formula is the final relation to be used to estimate the change of temperature in an infinite homogeneous medium assuming that the heat exchanger is an infinite line source. This model has the following limitations;

1) It is only applicable if the soil stratification does not affect thermal properties significantly since it assumes a single homogeneous medium. As will appear later, this limitation is applied for all available analytical methods.
2) This model does not count for the case of groundwater flow. This point is also a shortage for all other analytical models. Some modifications to the ILS model was provided by Carslaw and Jaeger (1959) to account for groundwater flow conditions. The details of the later modifications are beyond scope of this document; therefore it is not discussed here.
3) It depends on a single value for the heat rate (q') which is not the case for the real operation of heat exchangers and energy foundations.
4) It is assumed that the thermal properties of the homogeneous infinite medium do not change with temperature. This is an acceptable assumption since for the typical range of temperature change occurring with energy foundation applications, the change is soil thermal properties is not significant (Balland and Arp, 2005).
5) FLS model does not represent the limited length of general heat exchangers and Energy Piles. The limited length causes the edge effect which is a reduction in the temperature change at the edges of the line. This axial effect is found to be significant for time $t \approx H^2/180\alpha$ for a single line source, where H is the length of the heat exchanger (Lamarche and Beauchamp, 2007). This limiting time is even less if there is an interaction between different line sources (Lamarche and Beauchamp, 2007).
6) Representing heat exchanger as a line does not provide accurate results in the short time periods and for the case of large diameter heat exchangers such as Energy Piles.

2.2.2. Finite Line Source Model

Heat exchangers as well as Energy Piles are not infinite. They have a limited length. Therefore, the ILS model is insufficient to model such elements. Another model that is also based on representing heat exchanger as a line is the finite line source (FLS) model. In this model, heat exchanger is represented by a finite line which in turn is represented by different points. The idea behind FLS model is similar to ILS model which is integrating point source model over the length of the line. For the FLS model, the integration is limited to the length of the heat exchanger.

FLS model also considers a finite homogeneous medium which is not the case for ILS model. To take this point into consideration which affects the results at the edges, an imaginary line source is considered. That imaginary line source is identical to the main line source (length,

and heat rate), except that it has an opposite heat rate. For instance, if the main line is injected heat to the ground then the imaginary line is sucking heat and vice versa. This ensures that the boundary of the medium (ground surface) keeps a constant temperature same as its initial one throughout the period concerned which is an assumption for such model.

Here below is the full derivation for the general FLS model. The derivation starts from the point source model similar to ILS model as follows (Ingersoll et al., 1948);

$$\Delta T = \left(\frac{Q\alpha}{k}\right)\left(\frac{1}{2\sqrt{\pi\alpha\tau}}\right)^3 e^{-\rho^2/4\alpha\tau} = \frac{\left(\frac{Q\alpha}{k}\right)}{8(\pi^{3/2})(\alpha^{3/2})(\tau^{3/2})}\, e^{-\rho^2/4\alpha\tau} \qquad \text{Eq. 2-10}$$

For the case of a point source operating from time $\tau = 0$ to time $\tau = t$, the above formula is integrated over the operating time as follows;

$$\Delta T = \frac{\left(\frac{Q\alpha}{k}\right)}{8(\pi^{3/2})(\alpha^{3/2})}\int_0^t \left(e^{-\rho^2/4\alpha\tau}\right)\left(\tau^{-3/2}\right).d\tau$$

Using $\beta = \rho\ /2\sqrt{\alpha\tau}$, thus

$$d\tau = \left(\frac{-4}{\rho}\right)\left(\alpha^{1/2}\right)\left(\tau^{3/2}\right).d\beta$$

$$\Delta T = \frac{\left(\frac{Q\alpha}{k}\right)}{8(\pi^{3/2})(\alpha^{3/2})}\int_0^t \left(e^{-\beta^2}\right)\left(\tau^{-3/2}\right)\left(\frac{-4}{\rho}\right)\left(\alpha^{1/2}\right)\left(\tau^{3/2}\right).d\beta$$

$$\Delta T = \frac{\left(\frac{Q\alpha}{k}\right)}{2(\pi^{3/2})\alpha\rho}\int_\beta^\infty \left(e^{-\beta^2}\right).d\beta$$

$$\Delta T = \left(\frac{Q}{4\pi k\rho}\right)\left(\frac{2}{\sqrt{\pi}}\right)\int_\beta^\infty \left(e^{-\beta^2}\right).d\beta$$

But, $\left(\frac{2}{\sqrt{\pi}}\right)\int_\beta^\infty \left(e^{-\beta^2}\right).d\beta = erfc(\beta) = erfc\left(\frac{\rho}{2\sqrt{\alpha t}}\right)$, thus

$$\Delta T = \left(\frac{Q}{4\pi k\rho}\right) erfc\left(\frac{\rho}{2\sqrt{\alpha t}}\right)$$

For a finite line source which extends to *H* length, the above formula is integrated over its length as follows;

$$\Delta T = \left(\frac{q'}{4\pi k}\right)\int_0^H \frac{\left[erfc\left(\frac{\rho}{2\sqrt{\alpha t}}\right)\right]}{\rho}.d\rho$$

Including the effect of the finite homogeneous medium, the above formula is transformed to;

$$\Delta T = \left(\frac{q'}{4\pi k}\right)\int_0^H \left\{\frac{\left[erfc\left(\frac{\rho}{2\sqrt{\alpha t}}\right)\right]}{\rho} - \frac{\left[erfc\left(\frac{\rho'}{2\sqrt{\alpha t}}\right)\right]}{\rho'}\right\}.d\rho$$

From Figure 2.2, values of ρ and ρ' can be substituted in the above equation as follows;

$$\Delta T = \left(\frac{q'}{4\pi k}\right)\int_0^H \left\{\frac{\left[erfc\left(\frac{\sqrt{r^2+(z-h)^2}}{2\sqrt{\alpha t}}\right)\right]}{\sqrt{r^2+(z-h)^2}} - \frac{\left[erfc\left(\frac{\sqrt{r^2+(z+h)^2}}{2\sqrt{\alpha t}}\right)\right]}{\sqrt{r^2+(z+h)^2}}\right\}.dh \qquad \text{Eq. 2-11}$$

This relation is the general FLS model. This model has the same limitations of the ILS model except that it counts for the edge effects as well as the finite homogeneous medium.

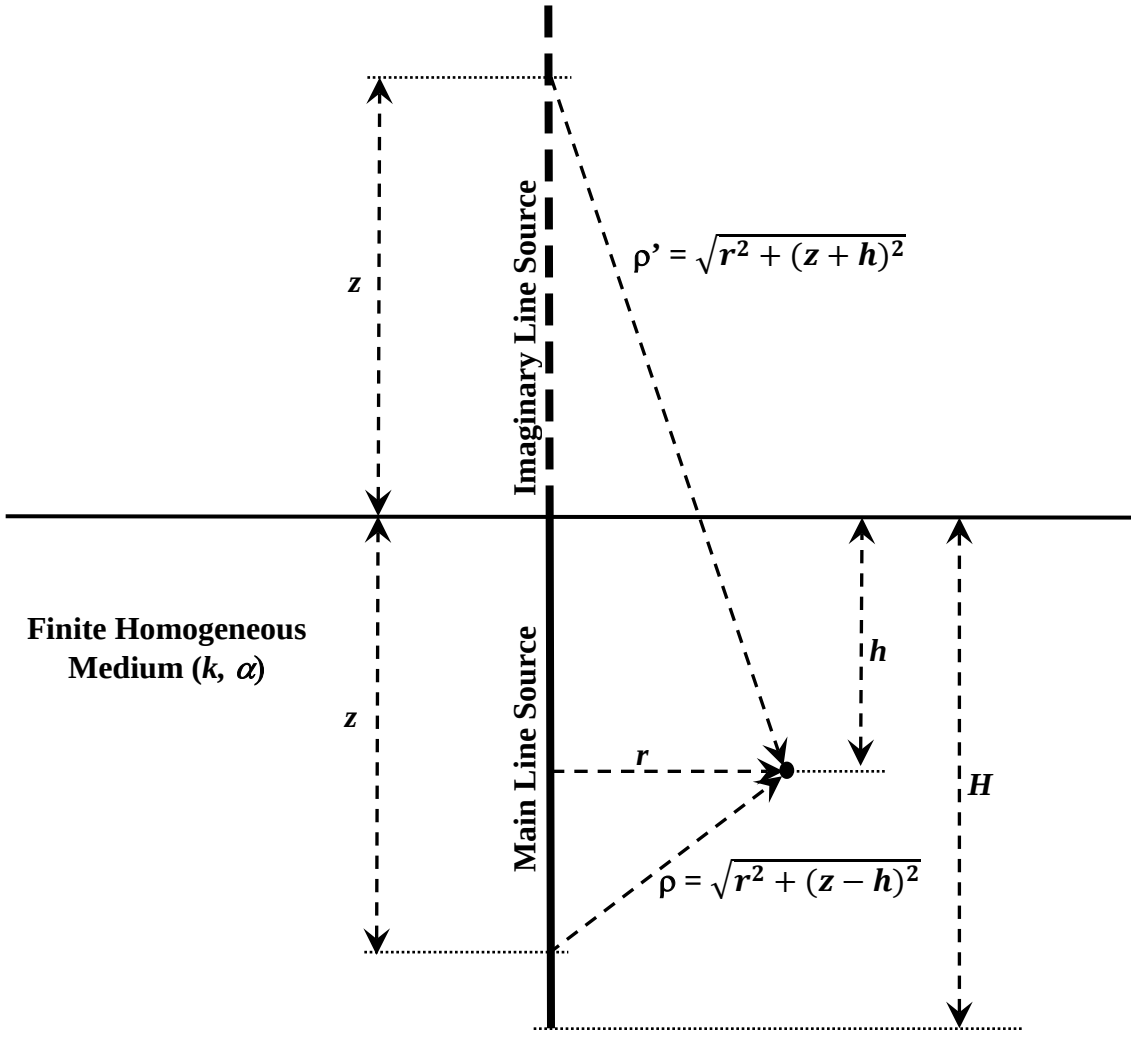

Figure 2.2. Finite line source (FLS) model with finite homogeneous medium

2.2.3. Hollow Cylindrical Source Model

Hollow cylindrical source (HCS) model is quite complicated compared to the ILS and FLS models. HCS model is recommended over the latter two models in cases where the time is too short or the pipe diameter is too large. Ingersoll et al. (1948) described these cases using a conditional relation of $\alpha t/r_b^2 < 20$. In this model the heat exchanger (Energy Pile) is represented with a hollow cylinder which has a diameter equals to that of the heat exchanger. Thus, pile material is not modeled and therefore the temperature profile inside the cylinder (pile) cannot be estimated. Here below is the general formula of the HCS model;

$$\Delta T = \frac{q'}{k\pi^2} \int_0^\infty \frac{e^{-\beta^2 F_o} - 1}{\beta^2 \cdot \{J_1^2(\beta) - Y_1^2(\beta)\}} \cdot [\{J_0(p\beta) \cdot Y_1(\beta)\} - \{J_1(\beta) \cdot Y_0(p\beta)\}] \cdot d\beta$$

Where;

F_o: Fourier number = $\alpha t/r_b^2$

J_0, J_1: Bessel functions of the first kind of order 0 and 1, respectively

Y_0, Y_1: Bessel functions of the second kind of order 0 and 1, respectively

p: Dimensionless distance = r/r_b

r_b: Borehole radius

Ingersoll et al. (1948) simplified the above form as follows;

$$\Delta T = \frac{q'}{k} G(z, p) \qquad \text{Eq. 2-12}$$

Value of $G(z, p)$ function is given in a tabulated form (Ingersoll et al., 1948). While, Hellstrom (1991) provided a correlation function of F_o to represent $G(z, p)$. Hellstrom correlation is as follows;

$$\ln(G) = -2.052271 + \{0.36081 \times \ln(F_o)\} - \{0.023922 \times \ln^2(F_o)\} + \{0.679 \times 10^{-3} \times \ln^3(F_o)\} \qquad \text{Eq. 2-13}$$

The HCS model shares the same limitation of ILS model listed about except the last two as it counts for the effect of the diameter of the heat exchanger and the end effects. The additional limitation here, as mentioned earlier, is that the temperature inside heat exchanger cannot be estimated.

2.2.4. Solid Cylindrical Source Model

In this model the cylinder is no longer a cavity, it is assumed to be filled with a medium identical to that out of the cylinder so that the whole infinite domain is composed of a homogeneous medium (Man et al., 2010). This model is considered a more general model as it counts for all the deficiencies of other models. The solid cylindrical source model is provided as follows (Man et al., 2010);

$$\Delta T = \frac{q'k}{\alpha}\int_0^t \int_0^H \frac{1}{8\left[\sqrt{\pi\alpha t}\right]^3} I_0\left[\frac{r r_b}{2\alpha t}\right]\left\{ e^{-\left[\frac{r^2+r_b^2+(z'-z)^2}{4\alpha t}\right]} - e^{-\left[\frac{r^2+r_b^2+(z'+z)^2}{4\alpha t}\right]} \right\} \cdot dz'dt \qquad \text{Eq. 2-14}$$

Where;

r: Radial coordinates of the location of interest,

z: Depth coordinates of the location of interest,

$I_0[x] = \frac{1}{\pi}\int_0^\pi e^{(x\cdot\cos\varphi)} \cdot d\varphi$

The only deficiency of this model is that it works only for the homogeneous medium which is not the case for almost all the heat exchanger applications.

2.2.5. Model Enhancements

Different improvements for the four main analytical models described above have been reported in the literature. This section is to summarize such improvements as follows;

(a) Effect of Ground Water Flow

An improvement by Carslaw and Jaeger (1959) and Sutton et al. (2003) accounts for water flow in the horizontal direction at a constant speed along the entire borehole length. The infinite line-source model was coupled with groundwater flow producing the moving line-source model. Groundwater flow is expected to have a noticeable effect mostly for heat exchangers in granular materials (Marcotte and Pasquier, 2008). This model estimates the change of ground temperature at time *t* and distance *r* along angle θ is given by Sutton et al. (2003) as follows;

$$\Delta T = \frac{q'}{4\pi k} e^{(P_e \bar{r}\cos\theta)/2}\left(\int_0^\infty \frac{e^{-u-b/u}}{u}\cdot du - \int_0^{\bar{r}^2/4F_0} \frac{e^{-u-b/u}}{u}\cdot du\right) \qquad \text{Eq. 2-15}$$

Where;

P_e: Peclet number = $U_e r_b/\alpha$

U_e: Effective underground water velocity = $\left(\emptyset c_f/c\right)U$

r_b: Borehole radius

α: thermal diffusivity

$\emptyset$: porosity expressed as a fraction

c_f: specific heat of the ground water

c: specific heat of the soil

U: underground water velocity

$\bar{r} = r/r_b$

r: distance to center of borehole

θ: angle between the flow direction and the direction of the horizontal line joining the borehole axis to the point where ground temperature is computed

$b = P_e^2\bar{r}^2/16$

(b) Variable Heat Flux

In general applications of heat exchangers, the heat transfer rate between the heat exchanger and ground around it varies continuously due to the variations of heating/cooling load. Thus the constant heat flux infinite line source solutions presented above must be adapted for a variable heat flow situation. Ingersoll et al. (1948) suggested that the solution presented above of ILS

model should be divided into time intervals for the different heat rates and the heat rate for each time interval can be visualized as constant, i.e. step load. Then, by superposition, the resulting temperature differences are added for each interval. By quoting the idea of superposition principle and step load, the constant heat flux line source solutions can be used to express the temperature response in ground with different heat rates at different times (Weibo et al., 2009).

(c) Effect of Heat Exchanger Inclination

For some situations, heat exchangers are inclined. The inclination of heat exchangers has an effect on the temperature change. This effect was first considered by Cui et al. (2006) who used the FLS model to incorporate the effect of inclination for single heat exchanger as well as multiple incline line sources. Cui et al. (2006) model for a single inclined line source is given as follows;

$$\Delta T = \frac{q'}{4\pi k}\int_0^H \left\{ \frac{\operatorname{erfc}\left(\frac{r_+}{2\sqrt{\alpha t}}\right)}{r_+} - \frac{\operatorname{erfc}\left(\frac{r_-}{2\sqrt{\alpha t}}\right)}{r_-} \right\} \cdot ds \qquad \text{Eq. 2-16}$$

Where;

$r_+ = \sqrt{(x - x_0 - s\sin\alpha\cos\beta)^2 + (y - y_0 - s\sin\alpha\sin\beta)^2 + (z - s\cos\alpha)^2}$

$r_- = \sqrt{(x - x_0 - s\sin\alpha\cos\beta)^2 + (y - y_0 - s\sin\alpha\sin\beta)^2 + (z + s\cos\alpha)^2}$

α : inclined angle of borehole

β : direction angle of borehole

x, y, z : coordinates of point of interest

Marcotte and Pasquier (2009) extended the above model for the case of having the head of heat exchanger below ground surface as follows;

$$\Delta T = \frac{q'}{4\pi k}\left(\int_{x_1}^{x_2} \frac{\operatorname{erfc}\left(\frac{d(x,x_0)}{2\sqrt{\alpha t}}\right)}{d(x,x_0)} \cdot dx - \int_{y_1}^{y_2} \frac{\operatorname{erfc}\left(\frac{d(y,x_0)}{2\sqrt{\alpha t}}\right)}{d(y,x_0)} \cdot dy \right) \qquad \text{Eq. 2-17}$$

Where;

x, x_0 : underground points

x_1, x_2 : points at the beginning and end of the real borehole

y_1, y_2 : points at the beginning and end of the image borehole

The above formula allows the heat exchanger head to be at any location within the infinite homogeneous medium and therefore, it solves for the case of having it below ground surface.

2.3. Thermal Properties of Various Materials

This section discusses the thermal properties of different materials being used in geothermal Energy Piles. These materials include the pile material (such as concrete, steel…etc.), soils and rocks, the material of the tube, and water/anti-freeze mixture. In one hand, the thermal properties of these different materials control the thermal performance of Energy Piles and therefore, they are important to be well estimated before designing or simulating these systems. On the other hand, stresses within and at the pile/soil interface are being affected by the thermal

operation. Therefore, it is important to estimate these properties accurately in order to have reliable predications of the mechanical performance of the system.

Thermal conductivity, thermal diffusivity, heat capacity and coefficient of thermal expansion are considered the most important thermal properties for all materials involved in energy foundations. Thermal conductivity refers to amount of energy being transferred within a material. The coefficient of thermal conductivity *(k)* is a measure of the rate at which heat (energy) passes perpendicularly through a unit area of homogeneous material of unit thickness for a temperature difference of one degree (ACI, 2002). Typical units for coefficient of thermal conductivity is W/(m·K) in SI system, and Btu/(hr·ft·°F) in Imperial units.

The heat capacity (C) is defined as the amount of heat necessary to raise the temperature of a given mass one degree. Heat capacity can also be defined as the amount of energy stored in a specific mass of a material per unit change in temperature (Brandl, 2006). It is generally used as another indicator of thermal mass which is often used in energy codes. The heat capacity is simply calculated as the product of a mass and its specific heat (C_p), i.e. $C = \boldsymbol{\gamma C_p}$. Heat capacity is a very important parameter when non-steady solutions are to control, which is the case for Energy Piles/foundations. The specific heat (C_p) is the heat capacity per unit mass of a material. The thermal diffusivity *(α)* indicates how quickly a material changes temperature. In other words, thermal diffusivity describes the distance and velocity of penetration of a temperature wave into a material. A high thermal diffusivity indicates that heat transfer through a material will be fast and the amount of heat storage will be small. On the other hand, materials with low thermal diffusivity respond slowly to an imposed temperature difference. Thermal diffusivity is calculated as follows;

$$\boldsymbol{\alpha = \frac{k}{\gamma C_p}} \qquad \text{Eq. 2-18}$$

Where k is the thermal conductivity coefficient, γ is the density, and C_p is the specific heat. Typical unit for thermal diffusivity is square unit length per unit time (m^2/sec).

According to the definitions of thermal conductivity (k) and heat capacity (C), the thermal diffusivity can be seen now as the ratio between the thermal conductivity and the heat capacity of the material. This ratio refers to how fast the heat transfer in a material reaches equilibrium. For instance, when the amount of energy penetrating the material is high (refereeing to a high value of k) compared to the amount of energy that the material can store (refereeing to heat capacity), thus it is expected to have that material reach equilibrium quite fast. This is the case of having a value of the thermal diffusivity that is relatively high. The opposite is true for lower values of thermal diffusivity. This analogy will be used to determine the effect of the concrete on the thermal performance of Energy Piles later in this section.

The coefficient of thermal expansion of any material describes how much a material will expand for each degree of temperature change. This coefficient is important for the pile material but not as much important for the soil. The coefficient of thermal expansion for the concrete and the steel are found to be slightly different and thus it is necessary to estimate the coefficient of the thermal expansions of the composite section of the reinforcement concrete forming the pile cross-section.

2.3.1. Soil Thermal Properties

Soil thermal properties, i.e. coefficient of thermal conductivity, heat capacity and density are temperature-dependent parameters. These parameters are all coupled with soil thermal diffusivity (Brandl, 2006), as appears in Eq. 2-19. However, the temperature dependency of

these parameters is considered negligible for a temperature range from -30 to 30 ℃ (-22 to 86 ℉) (Balland and Arp, 2005). This range is exactly the same temperature range within which Energy Piles operate for most of US. Thus, soil thermal properties for Energy Pile applications can reasonably be assumed independent of temperature.

Since geothermal Energy Piles as well as all energy foundations in general, deal with a transient heat transfer problem within the soil mass, the heat capacity for the soil is a key factor in the design and modeling processes for these elements. However, the determination of the soil specific heat capacity (which is directly used to estimate the heat capacity) did not receive much attention to the knowledge of the authors. Rees et al. (2000) reported that the specific heat capacity for a soil can be estimated simply by adding the specific heat capacities of the different constituents according to their volume fraction time their densities as follows;

$$c_p = x_1\rho_1 c_{p_1} + x_2\rho_2 c_{p_2} + x_3\rho_3 c_{p_3} \qquad \text{Eq. 2-19}$$

Where c_{p_1},c_{p_2}, and c_{p_3} are the specific heat capacities of the three soil constituents, i.e. solids, water, and air, respectively. x_1, x_2, and x_3 donate the volume fractions of the three soil constituents, and ρ_1, ρ_2, and ρ_3 are densities.

The soil specific heat capacity can be determined in the lab using the method described by Brandl (2006) in which water/soil mixtures are to be prepared at different temperatures. Given constant total thermal energy for both water and soil and the known specific heat capacity of water, then soil specific heat capacity can be estimated. In addition to these two previous references (Brandl, 2006; Rees et. al., 2000), not much other literature about heat capacity of soils was found. Table 2-1 summarizes typical soil specific heat capacities (Clarke et al., 2008).

Table 2-1. Typical values for the thermal properties of soils (Clarke et al., 2008 - used under fair use, 2013).

Soil Type	Water Content %	Bulk Density		Dry Density		Specific Heat Capacity	
		kg/m^3	pcf	kg/m^3	pcf	J/kg·K	Btu/lb·℉
Sandy CLAY	26.5	1890	118	1494	93	1696	0.405
Soft grey fine sandy CLAY	54.6	1650	103	1067	67	2646	0.632
Stiff dark grey sandy gravelly CLAY	10.1	2299	143	2088	130	1141	0.273
Very soft grey fine sandy CLAY	46.2	1711	107	1170	73	2362	0.564
Grey Limestone	0.1	2690	167	2687	168	803	0.192
Dry coarse SAND	0	1800	112	1800	112	800	0.191
Saturated coarse SAND	20.2	2080	130	1730	108	1483	0.354
Dry fine SAND	0	1600	100	1600	100	800	0.191
Saturated fine SAND	24.6	2010	125	1613	101	1632	0.461
Dry medium SAND	0	1700	106	1700	106	800	0.191
Saturated medium SAND	20.2	2080	130	1730	108	1483	0.354

Soil thermal conductivity, on the other hand, has been the main concern for researchers from different disciplines such as engineering, agriculture, geosciences etc. As a result, different standard procedures to measure thermal conductivity of soils in the lab were developed, for instance ASTM C518 (ASTM, 2010), ASTM C1113 (ASTM, 2009), and ASTM D5334 (ASTM, 2008). Hence, the scope of this dissertation does not include measuring thermal conductivity of soils via lab testing; these standards are not summarized within this context.

Soil thermal conductivity is a very important parameter for the analysis of Energy Piles. Therefore, an extensive literature review of the available empirical and semi-empirical methods for estimating thermal conductivity of soils from other easily measured parameters will be presented herein.

The thermal conductivity of soils was found to be highly affected by the soil density (unit weight), water content, degree of saturation, quartz content, organic content, and mineral composition (Lu et al., 2007). Different relationships were developed to correlate thermal conductivity of soils to several or all of these factors. Farouki (1982) investigated the applicability and the sensitivity for models developed before 1982 including Smith (1942), Kersten (1949), Mickley (1951), Gemant (1952), De Vries (1952, 1963), Van Rooyen and Winterkorn (1959), Kunii and Smith (1960), Woodside and Messmer (1961), McGaw (1969), and Johansen (1975). The comparison was performed for both fine and coarse grained soils in the unfrozen and frozen states. The unfrozen state includes dry, saturated, and partially saturated cases. Methods by Kersten, Mickley, Gemant, De Vries, Van Rooyen, McGaw and Johansen were listed to be applicable for unfrozen soils, while methods by Kersten, Mickley, De Vries, and Johansen were listed to be applicable for frozen soils. Methods by Kunii-Smith and Woodside were applicable for soils at either the saturated state or dry state (Farouki, 1982). Below are listed a summary of findings from Farouki (1982):

(a) For unfrozen coarse grained soils

- The use of Kersten method should be limited to coarse soils with intermediate quartz content (around 60% of the soil solids).
- Gemant method is applicable if degree of saturation is above 0.2.
- De Vries method provides better results than Johansen at lower values of degree of saturation (between 0.1 to 0.2).
- Van Rooyen method provides the best results for degree of saturation less than 0.1.
- Mickley and McGaw methods have generally similar results. They both neglect the effect of moist within the soil mass which makes them unreliable for the estimation of thermal conductivity of coarse soils.
- Johansen method gives good predictions for soils with varied quartz content at degree of saturation above 0.2. Thus, its results are acceptable for the saturated case (degree of saturation equal 1.0).
- On summary, above degree of saturation of 0.2 Johansen method is advised to be used. For degree of saturation from 0.1 to 0.2, De Vries method provides the best fit while below degree of saturation of 0.1, Van Rooyen method should be used.

(b) For unfrozen fine grained soils;

- For degree of saturation below 0.3, Kersten method gives deviations that are either too high or too low. For the rest of degree of saturation range, the deviation is the highest of all other methods.

- Johansen method at low values of the degree of saturation provides better agreement than Kersten. For medium and high degree of saturations, this method is believed to be better than Kersten given that some modifications should be applied.
- All other methods result on an unacceptable deviations and scatters.
- On summary, in the degree of saturation range between 0.1 to 0.2, Johansen method is advised to be used but its value should be increased by 5%. For degree of saturation below 0.1, Johansen method with an increase of 15% is advised. For higher degree of saturation (>0.2), Johansen method should be applied without any modification for the results.

(c) For frozen coarse grained soils;

- Kersten method gives predictions that are generally much too high for frozen sands, gravels, and crushed rocks having low quartz content. On the other had it gives too low predictions for sand and crushed materials with high quartz content. Even for materials with intermediate quartz content, this method shows conflicting trends.
- Above degree of saturation of 0.1, Johansen method gives good and adequate predictions for frozen sands, gravels, and crushed rocks of any quartz content. However, there are some exceptions for several crushed rocks.
- De Vries method generally gives good agreement above degree of saturation of 0.8 but even so there are some exceptions.
- Mickley method gives good agreement for gravel and crushed rocks with degree of saturation above 0.3, and for sands with degree of saturation above 0.6.

(d) For frozen fine grained soils;

- Kersten method gives good predictions up to a degree of saturation of 0.9 above which its results are considerably over predicted.
- Johansen method shows a tendency to over predict thermal conductivity for degree of saturation below 0.1 above which the predicted results are good and adequate.
- Above degree of saturation of 0.4, De Vries method gives values very similar to Johansen.
- Mickley method is considered to the worst predictor of all and only gives reasonable results at high values of the degree of saturation (around 0.8) but even then shows some excessive deviations.

For the scope of this dissertation, only saturated (unfrozen and frozen) case will be considered. Therefore, Farouki (1982) findings for saturated soils (degree of saturation equals 1.0) are summarized here below:

- For saturated unfrozen coarse soils, methods by Johansen, De Vries, Kunii-Smith, McGaw, Gemant, and Woodside provide the best predictions.
- For saturated unfrozen fine soils, methods by Johansen, De Vries, Woodside, Kunii-Smith, McGaw, Gemant, and Mickley are more or less equally applicable. However, the Johansen method is suggested the first choice.
- For frozen saturated coarse soils, the best methods to use are Johansen, De Vries, Mickley, Woodside, and Kunii-Smith. All of these methods provide good agreement.
- For frozen saturated fine soils, Johansen and De Vries give the best agreement and are capable of taking into account the effect of the unfrozen water content.

As appear from the previous discussion. Method by Johansen (1975) is recommended for all saturated unfrozen and frozen soils. This method is recommended by Farouki (1982) to be the best method for the prediction of thermal conductivity due to its reliable results for all saturated soils as well as its simplicity compared to all other methods. Furthermore, Johansen method gave the best overall prediction results for sands and fine-grained soils available in the literature (Côté and Konrad, 2005). It is important to infer that Farouki (1982) considered that results of a certain method are sufficient and reliable if the estimated values were within about ± 25% of its true value. He attributed this to the expected variation of thermal conductivity for the same soil in the field because of the lack of homogeneity. This is important when prediction methods (including Johansen method) being used to estimate the thermal conductivity of soils for numerical modeling. Therefore, it is recommended to perform a sensitivity analysis on values of thermal conductivity being used in any numerical model to examine the effect of the expected variation.

Johansen Method for prediction of soils thermal conductivity will be used in the work reported in this context, when needed. Therefore, the exact methodology is summarized here. This method uses the concept of normalized thermal conductivity with the thermal conductivity of dry and saturated states as follow;

$$k = k_{dry} + k_r\left(k_{sat} - k_{dry}\right) \quad \text{Eq. 2-20}$$

Where:

k : actual thermal conductivity,

k_{dry} and k_{sat} : thermal conductivity of the soil in dry and saturated states, respectively

k_r: normalized thermal conductivity.

Johansen (1975) provided correlations to estimate the normalized thermal conductivity in W/m·℃ from the degree of saturation (S_r) as follow;

$k_r = 0.7\log(S_r) + 1$ for unfrozen medium and fine sands and $S_r > 0.05$ Eq. 2-21

$k_r = \log(S_r) + 1$ for unfrozen fine grained soils and $\boldsymbol{S_r} > 0.1$ Eq. 2-22

$k_r = S_r$ for frozen medium and fine sands and fine grained soils Eq. 2-23

Furthermore, Johansen (1975) used the geometric mean method to estimate thermal conductivity of soils at the saturation state (k_{sat}). The geometric mean method can be summarized as follows;

$k_{sat(u)} = k_s^{1-n_u} k_w^{n_u}$ for unfrozen saturated soils in W/m·℃ Eq. 2-24

$k_{sat(f)} = k_s^{1-n_f} k_i^{n_f}$ for frozen saturated soils in W/m·℃ Eq. 2-25

Where:

$k_{sat(u)}$: thermal conductivity of saturated unfrozen soil.

$k_{sat(f)}$: thermal conductivity of saturated frozen soil.

$k_s,\ k_w, and\ k_i$: thermal conductivities of solid particles, 0.60 W/m·℃ (0.347 Btu/hr·ft·°F) for water and 2.24 W/m·℃ (1.294 Btu/hr·ft·°F) for ice.

n_u : porosity of unfrozen soil.

n_f : Porosity of frozen soil, which can be estimated as $[1.09\, n_u/(1 + 0.09\, n_u)]$ (Côte and Konrad, 2005)

Another correlation to estimate the thermal conductivity of solid particles (k_s) was provided by Johansen (1975). The proposed correlation depended on separating soil solids into quartz content and other minerals. The thermal conductivity for quartz was assumed to be 7.70 W/m·℃ (4.45 Btu/hr·ft·°F), while a value of 2 W/m·℃ (1.15 Btu/hr·ft·°F) was assigned to all other forming minerals when quartz content is more than 20%. When quartz content is less than 20%, the thermal conductivity of the other forming minerals was to be raised to a value of 3 W/m·℃ (1.73 Btu/hr·ft·°F). Therefore, correlation to estimate thermal conductivity of solids was written as follow:

$$k_s = \begin{cases} 2.0^{1-q} \times 7.7^{q} & \Rightarrow \ q > 0.2 \\ 3.0^{1-q} \times 7.7^{q} & \Rightarrow \ q \leq 0.2 \end{cases} \qquad \text{Eq. 2-26}$$

Where; q is the volume fraction of quartz in the solid particles.

Johansen (1975) also proposed the following correlation to estimate the thermal conductivity for dry soils in which the SI units were used;

$$k_{dry} = \frac{0.137\rho_b + 0.0647}{2.7 - 0.947\rho_b} \ [\frac{\mathrm{W}}{\mathrm{m}\cdot℃}] \text{ for fine soils and sands} \qquad \text{Eq. 2-27}$$

Where ρ_b is the bulk density of the soil in g/cm^3.

Côte and Konrad (2005) noticed that Eq. 2-21, Eq. 2-22, and Eq. 2-23 do not meet the lower and upper limits for the normalized thermal conductivity (k_r) which are:

Lower limit is for dry soil: $S_r = 0 \ \Rightarrow \ k_r = 0 \ \Rightarrow \therefore k = k_{dry}$

Upper limit is for saturated soil: $S_r = 1 \ \Rightarrow \ k_r = 1 \ \Rightarrow \therefore k = k_{sat}$

Therefore, Côte and Konrad (2005) developed another correlation for normalized thermal conductivity of soils that meets the upper and the lower limits stated above. This correlation was written as follows;

$$k_r = \frac{\kappa S_r}{1 + (\kappa - 1)S_r} \qquad \text{Eq. 2-28}$$

Where κ is an empirical parameter used to account for different soil types in the frozen and the unfrozen states. Table 2-2 shows proposed values for κ.

Table 2-2. Typical proposed values for κ (Côte and Konrad, 2005 - used under fair use, 2013)

Soil type	κ	
	unfrozen	**frozen**
Gravels and coarse sands	4.60	1.70
Medium and fine sands	3.55	0.95
Silty and clayey soils	1.90	0.85
Organic fibrous soils (peat)	0.60	0.25

Furthermore, Côte and Konrad (2005) provided another correlation to estimate thermal conductivity of dry soils given soil porosity (n) which was written as follow;

$$k_{dry} = ß \times 10^{-\eta n} \text{ in } \mathrm{W/m}\cdot℃ \qquad \text{Eq. 2-29}$$

Where ß (in W/m·℃) and η are material parameters accounting for the particle shape effect. Table 2-3 presents typical values for ß and η for different geo-materials.

Table 2-3. Typical values for ß and η proposed by Côte and Konrad (2005 - used under fair use, 2013)

Material	ß (W/m·℃)	η
Rocks and gravels	1.70	1.80
Natural mineral soils	0.75	1.20
Organic fibrous soils (peat)	0.30	0.87

Another effort to improve the performance of Johansen model was proposed by Balland and Arp (2005). Balland and Arp (2005) improved Johansen model by:

1) First, improving estimate of thermal conductivity of soils k_s via considering thermal conductivity of the organic matter with the soil solids. This was performed via modifying Eq. 2-30.

$$k_s = \begin{cases} k_{om}^{q_{om}} \times 7.7^{q} \times 2.0^{1-q-q_{om}} & \Rightarrow \ q > 0.2 \text{ in W/m} \cdot ℃ \\ k_{om}^{q_{om}} \times 7.7^{q} \times 3.0^{1-q-q_{om}} & \Rightarrow \ q \leq 0.2 \text{ in W/m} \cdot ℃ \end{cases} \quad \text{Eq. 2-30}$$

Where, k_{om} is the thermal conductivity of the organic matter with soil solids and q_{om} is the volumetric fraction of organic matter within the soil solids.

2) Improving correlation to estimate thermal conductivity for soils in the dry state as follows;

$$k_{dry} = \frac{(0.053k_s - k_{air})\rho_b + 2.7k_{air}}{2.70 - 0.947\rho_b} \text{ in W/m} \cdot ℃ \quad \text{Eq. 2-31}$$

Where,
k_{air} : thermal conductivity of air in W/m · ℃,
ρ_b : bulk density of the soil in g/cm^3

3) Improving normalized thermal conductivity of soils (k_r) by including organic matter in the formulation as follows;

$$k_r = S_r^{0.5(1+q_{om}-\alpha V_{sand}-V_{cf})} \left[\left(\frac{1}{1+e^{-\beta S_r}}\right)^3 - \left(\frac{1-S_r}{2}\right)^3\right]^{1-q_{om}} \text{ for unfrozen soils in W/m} \cdot ℃ \quad \text{Eq. 2-32}$$

$$k_r = S_r^{(1+q_{om})} \text{ for frozen or partially frozen soils in W/m} \cdot ℃ \quad \text{Eq. 2-33}$$

Where; α and β are adjustable parameters with values of 0.24±0.04, and 18.3±1.1, respectively. V_{sand} and V_{cf} donate the volumetric fractions of sand and coarse fragments within the soil solids, respectively.

Balland and Arp (2005) improved the predictions of the soil thermal conductivity using the pre-mentioned formulations. It, however, require more inputs to the model such as thermal conductivity and volumetric fraction of the organic matter within the soil solids. This increases the complexity of the model and it is believed to have less effect on the results given the level of accuracy described earlier associated with Johansen's model (±25% of the true value of the thermal conductivity).

Another improvement of Johansen's model was proposed by Lu et al. (2007) within which the correlations for the normalized thermal conductivity (k_r) and thermal conductivity of dry soils were replaced with the following formulations;

$$k_r = e^{\left(\alpha\left[1-S_r^{(\alpha-1.33)}\right]\right)} \text{ in W/m} \cdot ℃ \quad \text{Eq. 2-34}$$

$$k_{dry} = -0.56n + 0.51 \text{ in W/m} \cdot ℃ \quad \text{Eq. 2-35}$$

Where, α is a soil texture dependent parameter, 1.33 is a shape parameter, and n is the soil porosity. It should be noticed that Eq. 2-35 is recommended for soils having porosity between 0.2 and 0.6. Lu et al. (2007) reported α values of 0.96 and 0.27 for the coarse grained and fine grained soils, respectively.

Other different models developed by researchers with an agricultural background are available in the literature. These models, however, consider only soils at very shallow depths, less than 0.60 m (2.0 ft). One of these models that show a potential application for deep foundations is the one proposed by Usowicz et al. (2006). This model shows a great attempt to determine soil thermal conductivity from cone penetration resistance and the water content (or air-filled porosity). The validity of this model for deeper soils needs to be examined by comparing the data available from cone penetration in-situ tests conducted at deep depths where soil samples were examined in the lab to determine the true thermal conductivity.

An extensive comparison between Johansen (1975), and its modifications (i.e. Côte and Konrad, 2005; Balland and Arp, 2005; and Lu et al., 2007) was reported by Tarnawski et al. (2009). This comparison suggested that the later model (Lu et al., 2007) gives the most suitable predictions for all soils included in the study. For the scope of the work reported in this dissertation, these different methods will be considered based upon the availability of the input data for each one. The estimated results will then be compared with the figure provided by Brandl (2006) which is adapted and shown here in Figure 2.3. Moreover, the obtained estimated thermal conductivities will be compared with the typical values provided by Salomone and Marlowe (1989) which are presented in Table 2-4. These typical values were found to be in good agreement with Brandl graph using typical values for soil dry densities, for instance typical dry density for sands and clays are about 1800, and 1500 kg/m^3 (112 and 94 pcf), respectively (Terzaghi et al., 1996), which according to Brandl's figure correspond to a saturated thermal conductivity for sands and clays of about 2.45 W/m·℃ (1.42 Btu/hr·ft·°F) and 1.35 W/m·℃ (0.78 Btu/hr·ft·°F), respectively.

Table 2-4. Typical thermal conductivity for different soils (from Salomone and Marlowe, 1989 - used under fair use, 2013).

Thermal Texture Class (Soil Type)	Thermal Conductivity		Thermal Diffusivity	
	W/(m·℃)	Btu/(ft·hr·°F)	cm^2/sec	ft^2/day
Sand (or gravel)	0.77	0.44	0.0045	0.42
Silt	1.67	0.96	--	--
Clay	1.11	0.64	0.0054	0.50
Loam	0.91	0.52	0.0049	0.46
Saturated Sand	2.50	1.44	0.0093	0.86
Saturated Silt or Clay	1.67	0.96	0.0066	0.61

The typical values for the thermal conductivity of different soils proposed by Salomone and Marlowe (1989) are used in the preliminary numerical models where no field samples were taken. These values will also be used when general numerical models are being analyzed to investigate specific thermal, mechanical, or thermo-mechanical behavior of Energy Piles/foundations.

2.3.2. The Energy Pile Material

Energy Piles are typically made of concrete (either cast in-situ or precast concrete) or closed ended driven steel piles. The cast in-situ Energy Piles are similar in their construction concept to drilled shafts except that tubes for fluid circulation are attached to the steel cage before lowering it down to the bottom of the drilled hole. Precast Energy Piles are identical to precast driven piles but again with tubes for fluid circulation are installed within the pile vicinity before casting the concrete. As reported by Brandl (2006), driven reinforced concrete Energy Piles represented the majority of Energy Piles however, a steadily increase in the percentage of bored Energy Piles since the year of 2000 was observed. The closed ended driven piles are typically driven into the ground, circulation tubes are then lowered and the pile core (i.e. around tubes) is backfilled with either concrete or granular material (Morino and Oka, 1994). Thus, the thermal properties for concrete, steel used to form the cage, as well as steel forming pile walls for the closed ended piles are considered in this discussion. The previous section covered the thermal properties for granular materials that may be used as backfilling inside the closed ended piles.

(a) Thermal Properties of Concrete

The thermal conductivity of the concrete can be determined using the procedure described in ASTM C177 (ASTM, 2013) . Numerous testing programs have shown that the coefficient of thermal conductivity for the concrete *(k_c)* depends on the aggregate types used in the concrete mixture (ACI, 2002). A general formula for estimating the coefficient of thermal conductivity for concrete was provided by Valore (1980) as follows:

$$k_c = 0.5e^{0.02\gamma_o} \text{ (Imperial units)} \quad \text{Eq. 2-36}$$

$$k_c = 0.072e^{0.00125\gamma_o} \text{ (S.I. units)} \quad \text{Eq. 2-37}$$

Where γ_o is the oven-dry density in lb/ft^3 (or pcf) for Imperial units or kg/m^3 for S.I. Units.

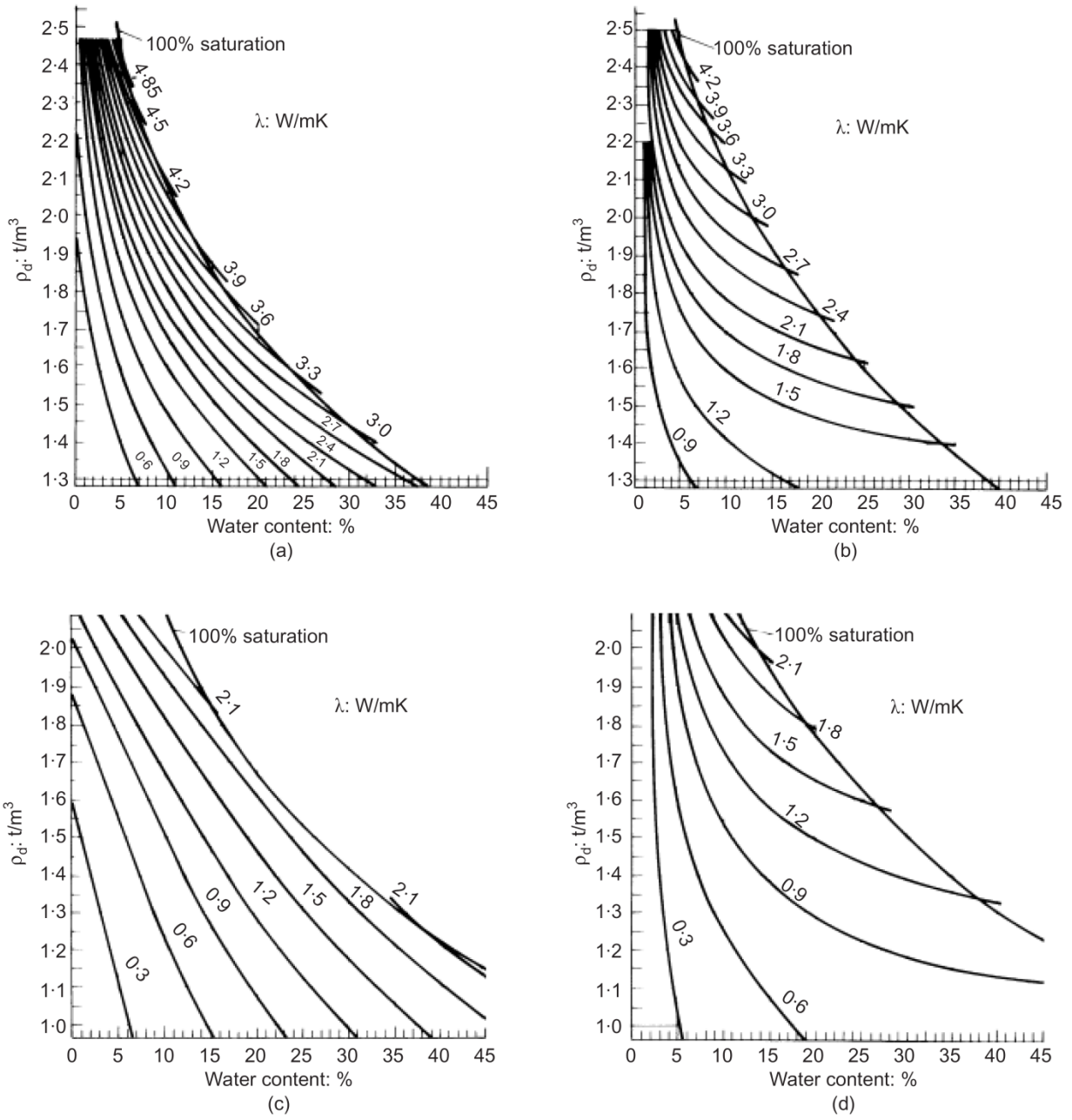

Figure 2.3. Thermal conductivity against dry density and water content for frozen and unfrozen soils (adapted from Brandl, 2006 - used under fair use, 2013): (a) coarse-grained frozen soil; (b) coarse-grained unfrozen soil; (c) fine-grained frozen soil; (d) fine-grained unfrozen soil.

The thermal conductivity values obtained using the above formula for concrete mixtures having an oven-dry densities from 320 to 1600 kg/m^3 (20 to 100 pcf) correlate better to test data than for concrete mixtures outside this density range (Valore, 1980). In addition to that, the above formula does not include the effect of moisture on the thermal conductivity of the concrete. Moisture was found to affect such property significantly (Plonski, 1973a, b; Tye and

Spinney, 1976; Valore, 1958). Different methods to consider the effect of moisture were presented in ACI (2002). An accurate way is as follows:

$$k_c(corrected) = k_c\left[1 + \frac{(6\gamma_m - \gamma_0)}{\gamma_0}\right] \quad \text{Eq. 2-38}$$

Where γ_m and γ_0 are densities of concrete in moist and oven-dry conditions, respectively.

ACI (2002) provides typical moisture correction factors for the thermal conductivity of the concrete based on the type of aggregates used in the mixture. For most concrete mixtures, a single factor of 1.20 can be applied to the oven-dry (k_c) values as suggested by Valore (1980). Then Eq. 2-36, and Eq. 2-37 become;

$$k_c = 0.6e^{0.02\gamma_0} \ (\text{Imperial units}) \quad \text{Eq. 2-39}$$
$$k_c = 0.0865e^{0.00125\gamma_0} \ (\text{S. I. units}) \quad \text{Eq. 2-40}$$

Typical concrete being used for construction purposes has a typical moist density of about 2400 kg/m^3 (150 pcf) corresponding to a typical dry density of about 2250 kg/m^3 (140 pcf) (ACI, 2002). Using the typical dry density value with Eq. 2-39 and Eq. 2-40, the coefficient of thermal conductivity is estimated to be 1.44 W/(m·℃) or 0.80 Btu/(hr·ft·°F). Typical concrete thermal conductivity is about 1.40 W/(m·℃) (ACI, 2002; Clarke et al., 2008) which agrees with the estimated value.

The thermal diffusivity of the concrete as reported by the ACI (ACI) is considered low (ACI, 2002). The typical value for the thermal diffusivity of the concrete is about 0.007 cm^2/sec (0.027 ft^2/hr) (Clarke et al., 2008), which is consistent with the thermal diffusivity of saturated sands and clays proposed by Salomone and Marlowe (1989) and presented in Table 2-4, i.e. 0.0093 and 0.0066 cm^2/sec (0.036 and 0.026 ft^2/hr), respectively. Based on these typical values, the concrete is expected to reduce the thermal performance of Energy Piles (foundations) constructed in sandy soils. On the other hand, the thermal performance of concrete piles constructed in clayey soils is not affected much, if at all, by the concrete properties and therefore that effect can be neglected. Table 2-5 shows suggested values for heat capacity of the concrete. The values presented in this table agree with these reported by Banks (2008). ACI (2002) suggested that a reasonable specific heat capacity for the concrete may be assumed as 840 J/kg·K (0.20 Btu/lb·°F), while Banks (2008) reported that it is about 800 J/kg·K (0.19 Btu/lb·°F) for most rock.

Comparing the obtained approximate coefficient of thermal conductivity for traditional concrete with these for different soils presented in Table 2-4, it can be inferred that concrete generally has a thermal conductivity equal to or less than that of saturated soils. Therefore, it is expected to have the concrete reduces the performance of Energy Piles (foundations) which agrees with the previous thermal diffusivity discussion.

Some publications mistakenly reported that the thermal conductivity of concrete is higher than saturated soils, or generally better thermal properties for the concrete if compared to those for soils (Brandl, 2006). This confusion is due to the fact that mechanical engineers have been reporting concrete as a good construction material due to its good thermal properties. In the mechanical engineering context, good thermal properties refer to the low thermal diffusivity and conductivity of the concrete which help to insulate buildings from the outside extreme climatic conditions. For energy foundations, this low thermal properties work against the desired heat transfer as discussed earlier.

Table 2-5. Specific heat and heat capacity of concrete (ACI, 2002 - used under fair use, 2013)

Material	Density, kg/m^3 (pcf)	Specific heat capacity, J/kg·K (Btu/lb·°F)	Heat capacity, MJ/m^3·K (Btu/ft^3·°F)
Mortar	1922 (120)	840 (0.20)	1.61 (24.0)
Concrete	1280 (80)	880 (0.21)	1.13 (16.8)
	1440 (90)	880 (0.21)	1.27 (18.9)
	1600 (100)	880 (0.21)	1.41 (21.0)
	1760 (110)	880 (0.21)	1.55 (23.1)
	1922 (120)	880 (0.21)	1.70 (25.2)
	2082 (130)	920 (0.22)	1.92 (27.3)
	2240 (140)	920 (0.22)	2.06 (29.4)

It is very critical to realize that using grout instead of concrete (such as for anchoring applications) will cause a more dramatic effect on the thermal performance of Energy Piles. Grout typically refers to water/cement mixture without any aggregates added. Typical thermal properties for traditional grout are as follow (from Clarke et al., 2008);

Thermal conductivity of grout = 0.7 W/m·℃ (0.4 Btu/hr · ft · °F)

Specific heat capacity of grout = 7500 J/kg·K (1.79 Btu/lb·°F)

(b) Thermal Properties of Steel

The thermal properties of steel are highly related to its temperature as presented by Banovic et al. (2005). This report, however, presents thermal properties of steel in response to fire as it is concerned with the performance of World Trade Center construction materials.

Similar to soils, thermal properties for steel can be assumed constant for the narrow temperature range within which Energy Piles/foundations operate. Typical values for such properties are as follows (ASHRAE, 2009);

Density = 7861 kg/m^3 (490 pcf)

Thermal conductivity = 52.0 W/m·℃ (30 Btu/hr·ft·°F)

Specific heat capacity= 510 J/(kg·℃ (0.122 Btu/lb·°F)

Heat capacity = 4.00 MJ/m^3·℃ (59.6 Btu/ft^3·°F)

(c) Thermal Properties for Composite Sections

For the case of reinforcement concrete or closed ended driven piles backfilled with either concrete or granular material, the effective overall pile thermal conductivity can be estimated using various methods for estimating effective thermal conductivity of composite materials. Extensive review for the available methods is reported by Mutnuri (2006). Typically, Energy Piles were modeled as a thermally isotropic material (Laloui, 2006) rather than changing the thermal conductivity between the transverse and the longitudinal directions. As will appear in the following chapters of this dissertation, Energy Piles should not be modeled as a thermally anisotropic material because this anisotropy does not affect the thermal and mechanical behavior of the pile.

A simplified and accurate method to estimate the effective thermal conductivity for composite materials in the transverse direction is the inverse rule of mixtures which can be written as follows (Mutnuri, 2006);

$$\frac{1}{k_{pile,T}} = \frac{(1-\varphi)}{k_{concrete}} + \frac{\varphi}{k_{steel}} \quad \text{Eq. 2-41}$$

Where φ is the percentage of reinforcement steel of the total cross sectional area = $\frac{A_s}{A_{total}}$

While the effective overall thermal conductivity for composite concrete/steel piles in the longitudinal direction is easily estimated using rule of mixture as follows (Mutnuri, 2006);

$$k_{pile,L} = (1-\varphi)k_{concrete} + \varphi\, k_{steel} \quad \text{Eq. 2-42}$$

2.3.3. Circulation Tubes Thermal Properties

Two different tube types are being used in energy foundations in general, high density polyethylene (HDPE), and cross-linked polyethylene (PEX). The typical thermal properties for these two materials are listed in Table 2-6.

Table 2-6. Thermal properties of HDPE and PEX tubes.

Tube Type	Thermal Conductivity W/m·℃ (Btu/hr·ft·°F)	Specific Heat Capacity J/kg·℃ (Btu/lb·°F)
HDPE	0.42-0.51 (0.242-0.30)*	2300 (0.549)*
PEX	0.41 (0.236) *	2300 (0.549)*

* REHAU (2010)

It appears from Table 2-6 that HDPE and PEX have the same thermal properties and therefore, their thermal performance is expected to be the same.

2.3.4. Water/anti-freeze Thermal Properties

Different antifreezes are being used in general geothermal applications including, methanol, ethylene glycol, and propylene glycol. The antifreeze is mixed with water using a typical antifreeze volumetric percentage between 5 to 20%. The exact percentage is controlled by the minimum expected operational fluid temperature for a specific project which is highly related to the project location (weather), and heating and cooling loads.

The thermal properties of the water/antifreeze mixture (density, thermal conductivity, specific heat, and viscosity) are significantly related to the fluid temperature. ASHRAE Handbook (ASHRAE, 2009) presents the thermal properties of different water/antifreeze mixtures as functions of temperature. Knowing these properties helps to determine the flow condition (laminar or turbulent) inside the circulation tubes. This flow condition is determined using Reynolds number (R_e) which is determined as follows for circular tubes:

$$R_e = \frac{\rho V D_H}{\mu} \quad \text{Eq. 2-43}$$

Where;

ρ : density of the fluid,

V : mean fluid velocity,

D_H : hydraulic diameter of the pile = diameter of circular tubes

μ : dynamic viscosity of the fluid.

The laminar flow condition takes place when Reynolds number is less than 2300, while turbulent flow condition takes place when Reynolds number is more than 4000. When Reynolds number is between 2300 and 4000, the flow is in the transition or the critical zone within which the flow condition is controlled by other factors such as tube roughness, and flow uniformity. It

is not easy to determine the exact flow condition within transition zone as this point is still under investigation by hydrologists (Munson et al., 2002).

During the design of the geothermal heat exchangers, the general intent is to have a turbulent flow condition inside the tubes. This is because turbulent flow enhances the heat exchange process which increases the efficiency and the performance of the system. A simple way to look at this issue is through the heat transfer coefficient (h). Heat transfer coefficient is used in calculating the heat transfer typically by convection between a flowing fluid and a stationary solid which is exactly the case for the fluid inside circulation tubes in geothermal applications. The higher the heat transfer coefficient, the more the heat transferred between the fluid and the solid. The heat transfer coefficient (h) is estimated as follows (Incropera, 2007);

$$h = \frac{4.3\, k_{fluid}}{d} \text{ for laminar flow conditions} \qquad \text{Eq. 2-44}$$

$$h = 0.023 \times R_e^{(4/5)} \times P_r^{(1/3)} \times \frac{k_{fluid}}{d} \text{ for turbulent flow condition} \qquad \text{Eq. 2-45}$$

where;

k_{fluid} : thermal conductivity of water/antifreeze mixture

d : diameter of the tube

P_r : Prandtl number = $\frac{C_p \mu}{k_{fluid}}$

C_p : specific heat of the fluid

μ : dynamic viscosity.

Table 2-7 presents calculated heat transfer coefficients for different water/propylene glycol mixtures at different temperature. The green zone represents laminar flow conditions, while red zone represents turbulent flow conditions. Also, the same data are present in Figure 2.4.

Table 2-7. Heat transfer coefficient in $W/m^2 \cdot °C$ for different water/propylene glycol mixtures for 1 inch tube and flow rate of 11 liter/min (2.9 gpm).

Temp. °C	Concentrations in Volume Percent Propylene Glycol (%)								
	10	20	30	40	50	60	70	80	90
-34						41	36	33	30
-29					46	41	37	34	31
-23					46	42	37	34	31
-18				52	47	42	38	34	31
-12			59	53	48	43	38	34	31
-7		0	60	54	48	43	39	35	32
-1		34	61	55	49	44	39	35	32
4	-	-	63	56	50	44	39	35	32
10	843	-	63	57	50	45	40	35	32
16	920	-	-	57	51	45	40	36	32
21	993	787	-	58	52	46	40	36	32
27	1071	855	-	-	52	46	40	36	32
32	1149	923	723	-	53	46	41	36	33
38	1224	992	785	-	-	47	41	36	33
43	1299	1058	846	672	-	47	41	36	33
49	1371	1125	908	728	-	-	41	36	33
54	1442	1191	967	781	619	-	-	37	33
60	1510	1255	1028	833	664	-	-	37	33
66	1573	1318	1083	885	708	577	-	-	33
71	1648	1384	1138	932	751	617	-	-	33
77	1716	1441	1196	984	795	656	520	-	-
82	1793	1504	1247	1026	840	695	549	-	-
88	1850	1561	1300	1077	877	731	580	476	-
93	1914	1624	1343	1114	919	767	610	504	-
99	1963	1674	1381	1153	953	804	638	528	-
104	2016	1728	1433	1192	991	835	666	553	428
110	2074	1766	1469	1229	1021	867	695	578	450
116	2125	1807	1515	1272	1054	896	720	602	469
121	2190	1856	1542	1302	1092	926	745	626	491

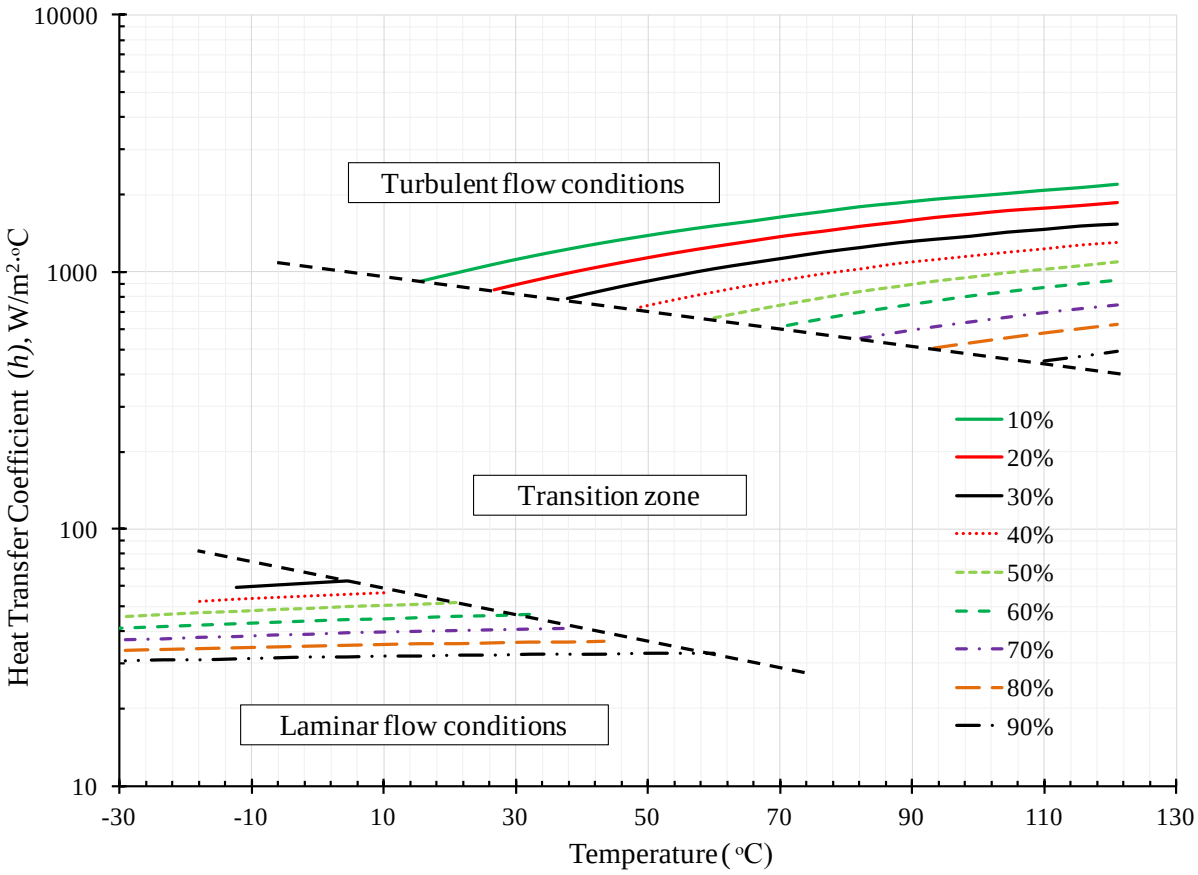

Figure 2.4. Heat transfer coefficient for different water/propylene glycol mixtures for 25.4 mm (1 inch) tube and flow rate of 11 liter/min (2.9 gpm).

As can be seen from Figure 2.4, heat transfer coefficients for turbulent flow are significantly higher than these for laminar flow. Therefore, turbulent flow will result in better heat transfer compared to laminar flow.

Examining the geothermal tubes have diameters ranging between 19 mm (¾ inch) to 25.4 mm (1.0 inch), typical flow rate of 11 lit/min (2.9 gpm), and an antifreeze volumetric percentage of 10%, it can be easily found that Reynolds number for this case is higher than 4000 (minimum of 4580 at -1 ℃) for the entire operational temperature range indicating that turbulent flow is ensured during the system operation. This is also the case when the upper antifreeze percentage (i.e. 20%) is used.

2.4. Thermo-Mechanical Behavior of Energy Piles

In addition to heat exchange operation, Energy Piles also require geotechnical design to account for coupled thermo-mechanical soil-structure interaction effects on foundation performance, especially over long time periods. One of the major long-term behavioral questions is what effect repeated heating and cooling cycles have on the shear transfer mechanism between the Energy Piles and the surrounding soil. Specifically, contraction or expansion of the piles during heating or cooling may lead to changes in pile side friction (and ultimate load-carrying capacity) or distress in the concrete. It is of particular interest whether the

thermally-induced additional stresses (compression stresses during heating or tensile stresses during cooling) on the pile would be critical for design.

Contraction or elongation occurs in Energy Piles due to thermal elastic expansion, in which thermal strain ε_t occurs during a temperature change in proportion to a coefficient of thermal expansion ($\varepsilon_t = \alpha_T \Delta T$). The actual amount of thermal expansion or contraction for an Energy Pile will depend upon site-specific soil-structure interaction effects, as the surrounding soil and pile head and tip restraints provide a confining effect.

These coupled thermo-mechanical loads produce a unique stress profile as illustrated in the two sets of schematics in Figure 2.5. The left figure illustrates the change in stresses along the pile due to heating operations. As the pile expands due to heating, the net effect is an increased load experienced by the pile. This trend has been confirmed by field and numerical results (Laloui et al., 2006). When an Energy Pile is loaded under a structural load the largest compression stress occurs at the top of the pile. The load along the pile is transferred to the surrounding soil and the compression stresses are reduced with depth as shown in the left schematic. If the temperatures within the pile are increased due to injection of heat energy from the upper structure (left diagram), the pile will elongate. Simply, a floating pile will tend to expand about its mid-points, as shown in the central schematic. The relative displacement of the pile with respect to the soil will alter the stress transfer between the pile and the soil. Upward relative movement of the pile due to heating will result in downdrag forces from the soil. This heating induced interaction results in an increase in compressive stresses throughout the pile, and an increase in side friction. The coupled response produces a near uniform stress profile in the upper portion of the pile as shown in the upper right schematic. Bourne-Webb et al. (2009) and Laloui et al. (2006) indicated that in some cases the total stresses could be twice as high as those from the structural load alone especially in cases where the displacement of the pile toe is restrained such as in the case of an end-bearing pile. Although the side friction will increase uniformly with depth during heating, the direction of the side shear force will be opposite on either side of the mid-point of the pile since it is assumed to expand from the mid-point.

A reverse trend occurs for cooling operations and may result in tensile stresses along pile cross section. As the piles are cooled as heat energy is extracted from the ground, the pile will tend to contract. Because the structural load is reduced toward the bottom, negative compressive forces (tensile forces) could begin to dominate the axial stresses in the piles foundation if the cooling load is high enough (Bourne-Webb et al., 2009). This coupled response is illustrated in the right set of diagrams. Pile contraction will lead to a reduction in radial stresses and decrease in skin friction as well. There is concern that repeated heating and cooling cycles over long time periods may lead to a cumulative decrease in skin friction or relax the normal stresses on the pile surface. Observations from recent Energy Pile field tests reported by Bourne-Webb et al. (2009) and Laloui and Nuth (2006) indicate measured strain profiles that are similar to the stress profiles shown in Figure 2.5.

2.5. Long Term Performance

Energy Piles like any ground coupled heat exchanger (GCHE) are designed to operate for a long period of time, typically 30 years of operation is considered in the design. The long term performance of GCHEs is a very important point for the thermal design of the system which consequently should be considered in the geotechnical design of Energy Piles. However, long term performance has been considered in the thermal design of geothermal boreholes by

including a long-term energy pulse in the design equation (Kavanaugh and Rafferty, 1997) due to difficulty of accurately modeling such performance.

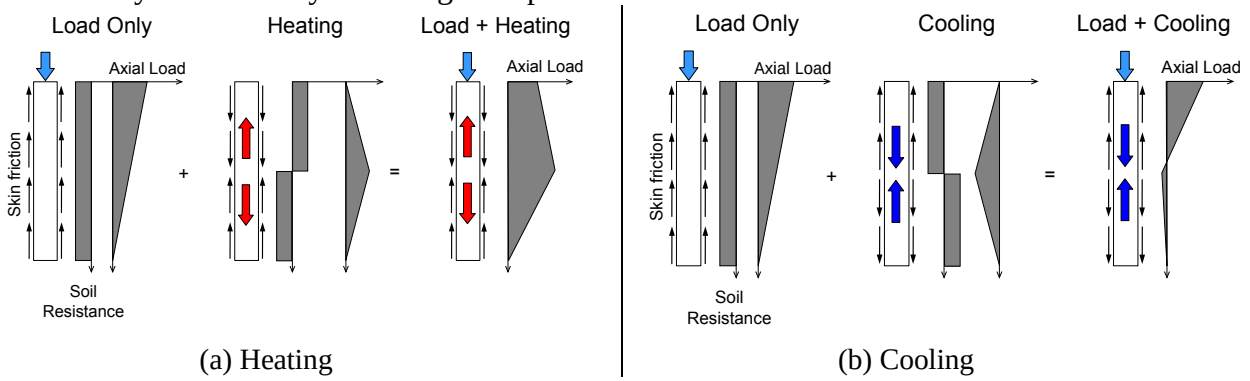

(a) Heating (b) Cooling

Figure 2.5. Thermally induced soil-pile interaction during Energy Pile operation adapted from (Bourne-Webb et al., 2009 - used under fair use, 2013)

As shown in Figure 2.6, there is the question as to how the Energy Pile operation, run over the life cycle of the structure, will change the temperature gradients around the pile, and in turn, affect the heat exchange capacity and efficiency of operations (i.e., the entire soil mass is gradually heated up or cooled down). Similarly, if imbalanced thermal loads are induced over long time periods, and/or if key soil parameters are altered by these loadings, the foundation system might undergo differential movements.

Recently, Lazzari et al. (2010) presented a 2D finite element modeling approach for the long term performance of geothermal heat exchangers. Lazzari et al. (2010) were mainly concerned with the temperature of the fluid inside the ground loops which in fact determines if the system is operational for the desired period or not. If the temperatures fall below the freezing temperature of the fluid, then the system is not operational anymore. In their analyses, different sine waves representing different thermal load patterns were used. The year was divided into heating for the first six month and cooling for the last six months. One sine wave was used to represent heating dominant systems so heating power was assigned for the first six months and no power in the remaining six months. Another type of sine wave was used for cooling dominant systems with no power for the first six months and cooling power for the last six. The last group of sine waves is used for systems that have heating and cooling demands. Balanced as well as unbalanced heating/cooling demands were considered for this latter group. The findings of this study indicate that properly designed geothermal borehole systems can operate for 30 years without falling below the freezing point.

It is expected the ground to progressively heat for cooling dominant systems as a result of unbalanced heat injection into the ground. Similarly the ground will cool in areas where building heating is dominant.

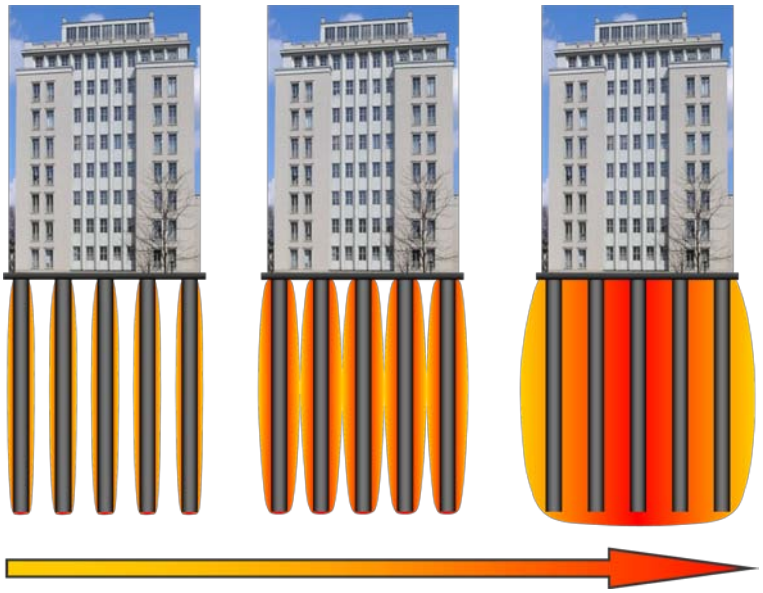

Figure 2.6. Time evolution of ground temperature

2.6. In-situ Thermo-Mechanical Tests

There are two other reported full scale field tests performed on Energy Piles; the first is by a group from Switzerland lead by Laloui (Laloui and Nuth, 2006; Laloui et al., 2006), the second is a group from Cambridge University in England lead by Soga (Bourne-Webb et al., 2009). Table 2-8 summarizes the details of each one of these tests along with a summary of their key findings.

Another effort to investigate the behavior of Energy Piles and their feasibility is being performed by a group of researchers at University of Colorado at Boulder led by McCartney (McCartney et al., 2010; McCartney and Rosenberg, 2011). McCartney's group focuses on centrifuge modeling of Energy Piles and developing T-z curves for the tested piles. The results of the centrifuge modeling of Energy Piles show an increase in the overall pile capacity when piles were heated. This increase in pile capacity was attributed to the fact that the soils used in the centrifuge were not full saturated which has different behavior under raising temperatures than that explained earlier for piles in saturated clays (McCartney and Rosenberg, 2011). It is expected to have the capacity of Energy Piles embedded in saturated clays to reduce due to the decrease in the clay strength caused by undrained heating.

Table 2-8. Summary of the two reported Energy Piles field tests.

#	Research Group	Publiched Papers	Pile Dimensions	Soil Deposit	Measurments	Loading History	Summary of Obtained Restults
1	Laloui, Switzerland	* Numerical Modeling of some features of heat exchange pile (2006) * Experimental and numerical investigations of the behaviour of a heat exchanger pile (2006)	diameter 88cm, Length 25.8m	* Alluvial soil (0m ~ 12m) * Sandy Gravelly Moraine (12m ~ 21.8m) * Bottom Moraine (21.8m ~ 25.2m) * Molasse (25.2m ~ 25.8m) * GWT is near ground surface	* Vertical strains * Temperature * Radial strains * Load at pile tip	* Mechanical load achieved by dead weight of building * Thermal load achieved by heating device * Thermal and mechanical loads were applied separately and alternately to decouple their effects * Test (1) was only thermal test with temp. difference of 21C with 12 days heating and 16 days cooling * Six other tests were thermo-mechanical tests with temp. change of 15C * Max. mechanical load was 1300kN at the end of the construction	* Temperature distribution along pile in heating and cooling are uniform which supports the assumption that the pile acts as an infinitely long heat sink/source. * Strains are not uniform during the heating period and are influenced by the friction along the pile shaft * All strains casued by heating were reversed by cooling, i.e. thermo-ealstic response was observed * Radial strains showed that contact between pile and surrounding soil was still maintained * Mechanical load affects mostly the top of the pile, while thermal load creates rather larger axial stresses at the toe. * The axial load in the pile approximately doubled with respect to the head load suring the applied thermal cycle. * Temperature change of 1C results in an additional temerpature-induced verticle force on the order of 100kN
2	Soga, UK	* Energy pile test at Lambeth College, London: geotechnical and thermodynamic aspects of pile response to heat cycles (2009)	diameter 60cm, Length 23m	* Superficial layer of Made Ground (0m ~ 1.5m) * River Terrace Deposits (1.5m ~ 5.5m) * London Clay formation (5.5m ~ below pile toe) * GWT is at about 3m below ground level	* Vertical strains * Temperature * Ambient air temp * Temp. of supply and return fluids at the heat pump * Load and movement at the pile head	* Working load for test pile was 1200kN * Temperature range applied during the thermal test period is -6C to +56C	* At normal operating temperatures and with respect to short cycles of cooling, freezing at the pile/soil interface is unlikely to develop. * Temperature change is uniform over pile length, and thus pile expandes/contacts about "null" point at mid-depth if both pile ends are free. * When cooling cycle is applied to the pile, if both ends of the pile are free to move, then along the upper part of the shaft, shear stress on the pile/soil interface will be mobilised in the same sense as that mobilised by compression loading applied at the pile head, while shear stress will be in the opposite sense in the lower part of the pile. * When a heating cycle is applied, the reverse effect to a cooling cycle will develop. * Cooling reduces axial loads along pile shaft, while heating increases such loads. * The end restraint conditions acting on the energy pile in relation to the magnitude of change in apparent pile loading and mobilised shaft friction caused by temperature change

References

American Concrete Institute, ACI (2002) "Guide to thermal properties of concrete and Masonry Systems," No. ACI 122R-02, p 21.

American Society of Heating, Refrigerating, and Engineers Air-Conditioning (2009) "2009 ASHRAE handbook fundamentals." Atlanta, GA: American Society of Heating, Refrigeration and Air-Conditioning Engineers.

American Society for Testing Materials (2013) "C 117: Standard Test Method for Steady-State Heat Flux Measurements and Thermal Transmission Properties by Means of the Guarded-Hot-Plate Apparatus," ASTM International, West Conshohocken, PA, 2013, DOI: 10.1520/C0117-13, www.astm.org.

American Society for Testing Materials (2010) "C 518: Standard Test Method for Steady-State Thermal Transmission Properties by Means of the Heat Flow Meter Apparatus," ASTM International, West Conshohocken, PA, 2010, DOI: 10.1520/C0518-10, www.astm.org.

American Society for Testing Materials (2009) "C 1133: Standard Test Method for Thermal Conductivity of Refractories by Hot Wire (Platinum Resistance Thermometer Technique)," ASTM International, West Conshohocken, PA, 2009, DOI: 10.1521/C1113-09, www.astm.org.

American Society for Testing Materials (2008) "C 5334: Standard Test Method for Determination of Thermal Conductivity of Soil and Soft Rock by Thermal Needle Probe Procedure," ASTM International, West Conshohocken, PA, 2008, DOI: 10.1520/D5334-08, www.astm.org.

Balland, V., and P.A. Arp (2005) "Modeling soil thermal conductivities over a wide range of conditions," *Journal of Environmental Engineering and Science*, Vol. 4, No. 6, pp 549-558.

Banovic, S.W., C.N. McCowan, and W.E. Luecke (2005) "Physical Properties of Structural Steels," *Federal Building and Fire Safety Investigation of the World Trade Center Disaster, NIST NCSTAR 1-3E*.

Bourne-Webb, P. J., K. Soga, T. Amis, C. Davidson, P. Payne, and B. Amatya (2009) "Energy pile test at Lambeth College, London: geotechnical and thermodynamic aspects of pile response to heat cycles," *Géotechnique*, Vol. 59, No. 3, pp 237-248.

Brandl, H. (2006) "Energy foundations and other thermo-active ground structures," *Géotechnique*, Vol. 56, No. 2, pp 81-122.

Carslaw, H.S., and J.C. Jaeger (1959) *Conduction of Heat in Solids*: 2nd Edition, Oxford University Press, USA.

Clarke, B. G., D. Nicholson, and A. Agab (2008) "Model specification to determine thermal conductivity of soils," *Proceedings of the ICE - Geotechnical Engineering*, Vol. 161, No. 3, pp 161-168.

Côté, J., and J.M. Konrad (2005) "A generalized thermal conductivity model for soils and construction materials," *Canadian Geotechnical Journal*, Vol. 42, No. 2, pp 443-458.

Cui, P., H. Yang, and Z. Fang (2006) "Heat transfer analysis of ground heat exchangers with inclined boreholes," *Applied Thermal Engineering*, Vol. 26, No. 11-12, pp 1169-1175.

De Vries, D.A. (1952) "The thermal conductivity of soil," *Mededelingen van de Landbouwhogeschool te Wageningen*, Vol. 52, No. 1, pp 1-73.

De Vries, D.A. (1963) "Thermal properties of soils," In: W.R. Van Wijk, Ed., *Physics of plant environment*. Amsterdam: North-Holland Publishing Co.

Engineering ToolBox, "Thermal Conductivity of Some Common Materials and Gases." N.p., n.d. Web. 07 Apr. 2010. <http://www.engineeringtoolbox.com/>.

Farouki, O. T. (1982) "Evaluation of methods for calculation soil thermal conductivity." Hanover, New Hampshire: U.S. Army Cold Regions Research and Engineering Laboratory, p 82.

Gemant, A. (1952) "How to compute thermal soil conductivities," *Heating, Piping and Air Conditioning*, Vol. 24, No. 1, pp 122-123.

Hellstrom, G. (1991) "Ground Heat Storage: Thermal Analyses of Duct Storage Systems." Lund, Sweden: University of Lund.

Incropera, F.P. (2007) *Fundamentals of heat and mass transfer*, Hoboken, NJ: John Wiley.

Ingersoll, L.R., H.J. Plass, and M. Wis (1948) "Theory of the Ground Pipe Heat Source for the Heat Pump," *Heating, Piping & Air Conditioning*, Vol. 20, No. 7, pp 119-123.

Johansen, O. (1975) "Thermal conductivity of soils." Norway: Trondheim University.

Kavanaugh, S., and K. Rafferty (1997) *Ground Source Heat Pumps: Design of Geothermal Systems for Commercial and Institutional Buildings*, Atlanta, Georgia: American Society of Heating, Refrigerating, and Air-Conditioning Engineers, Inc.

Kersten, M.S. (1949) "Laboratory research for the determination of the thermal properties of soils," *Arctic Construction and Frost Effects Laboratory Technical Report 23*.

Kunii, D., and J.M. Smith (1960) "Heat transfer characteristics of porous rocks," *American Institute of Chemical Engineers Journal*, Vol. 6, No. 1, pp 71-78.

Laloui, L., and M. Nuth (2006) "Numerical modeling of some features of heat exchange pile," *Geotechnical Special Publications*, No. 153, pp 189-194.

Laloui, L., M. Nuth, and L. Vulliet (2006) "Experimental and numerical investigations of the behaviour of a heat exchanger pile," *International Journal for Numerical and Analytical Methods in Geomechanics*, Vol. 30, No. 8, pp 763-781.

Lamarche, L., and B. Beauchamp (2007) "A new contribution to the finite line-source model for geothermal boreholes," *Energy and Buildings*, Vol. 39, No. 2, pp 188-198.

Lazzari, S., A. Priarone, and E. Zanchini (2010) "Long-term performance of BHE (borehole heat exchanger) fields with negligible groundwater movement," *Energy*, Vol. 35, No. 12, pp 4966-4974.

Lu, S., T. Ren, Y. Gong, and R. Horton (2007) "An Improved Model for Predicting Soil Thermal Conductivity from Water Content at Room Temperature," *Journal of Soil Science Society of America*, Vol. 71, No. 1, pp 8-14.

Man, Y., H. Yang, N. Diao, J. Liu, and Z. Fang (2010) "A new model and analytical solutions for borehole and pile ground heat exchangers," *International Journal of Heat and Mass Transfer*, Vol. 53, No. 13-14, pp 2593-2601.

Marcotte, D., and P. Pasquier (2008) "Fast fluid and ground temperature computation for geothermal ground-loop heat exchanger systems," *Geothermics*, Vol. 37, No. 6, pp 651-665.

Marcotte, D., and P. Pasquier (2009) "The effect of borehole inclination on fluid and ground temperature for GLHE systems," *Geothermics*, Vol. 38, No. 4, pp 392-398.

McCartney, J.S., D. LaHaise, T. Lahaise, and J. Rosenberg (2010) "Application of Geoexchange Experience to Geothermal Foundations," In: M. Hussein, W. Camp, and J. Anderson, Eds., *The Art of Foundation Engineering Practice*: ASCE Geotechnical Special Publication, No. 198, pp 411-422.

McCartney, J.S., and J.E. Rosenberg (2011) "Impact of heat exchange on side shear in thermo-active foundations," In: J. Han, and D.E. Alzamora, Eds., *Geo-Frontiers 2011: Advances in Geotechnical Engineering*: ASCE Geotechnical Special Publichation, No. 211, pp 488-498.

McGaw, R. (1969) "Heat conduction in saturated granular materials," *Effects of temperature and heat on engineering behavior of soils, Highway Research Board Special Report 103*, pp 114-131.

Mickley, A.S. (1951) "The thermal conductivity of mosit soil," *American Institute of Electrical Engineers Transactions*, Vol. 70, pp 1789-1797.

Morino, K., and T. Oka (1994) "Study on heat exchanged in soil by circulating water in a steel pile," *Energy and Buildings*, Vol. 21, pp 65-78.

Munson, B.R., D.F. Young, and T.H. Okiishi (2002) *Fundamentals of fluid mechanics*, New York: Wiley.

Mutnuri, B (2006) "Thermal Conductivity Characterization of Composite Materials," *Mechanical Engineering*. Morgantown, West Virginia: West Virginia University, p 69.

Plonski, W. (1973a) "Thermal conductivity and moisture content of autoclaved aerated concrete," *Symposium on Lightweight Concrete, CEB Polish National Group/Engineering Committee, National Academy of Sciences*, pp 362-371.

Plonski, W. (1973b) "Thermal Conductivity and Moisture Content of Lightwight Aggregate Concrete," *Symposium on Lightweight Concrete, CEB Polish National Group/Engineering Committee, National Academy of Sciences*, pp 137-148.

REHAU (2010) "Ground Loop Heat Exchange System", Interenal Report.

Rees, S. W., M. H. Adjali, Z. Zhou, M. Davies, and H. R. Thomas (2000) "Ground heat transfer effects on the thermal performance of earth-contact structures," *Renewable and Sustainable Energy Reviews*, Vol. 4, pp 213-265.

Salomone, L.A., and J.I. Marlowe (1989) "Soil and Rock Classification for the Design of Ground-Coupled Heat Pump Systems," *Field Manual, EPRI CU-6600*.

Smith, W.O. (1942) "The thermal conductivity of dry soil," *Soil Science*, Vol. 53, pp 435-459.

Sutton, M.G., D.W. Nutter, and R.J. Couvillon (2003) "A ground resistance for vertical bore heat exchangers with groundwater flow," *Transactions of the ASME Journal of Energy Resources Technology*, Vol. 125 No. 3, pp 183-189.

Tarnawski, V. R., W. H. Leong, and T. Momose (2009) "Assessing the impact of quartz content on the prediction of soil thermal conductivity," *Géotechnique*, Vol. 59, No. 4, pp 331-338.

Terzaghi, K., R.B. Peck, and G. Mesri (1996) *Soil Mechanics in Engineering Practice*: John Wiley & Sons.

Tye, R.P., and S.C. Spinney (1976) "Thermal Conductivity of Concrete: Measurement Problems and Effect of Moisture," Vol. presented at meeting of Commission of BI of Institute International Du Froid, Washington, D.C., Sept. 14-15, Dynatech R/D Company, Cambridge.

Usowicz, B., J. Lipiec, and A. Ferrero (2006) "Prediction of soil thermal conductivity based on penetration resistance and water content or air-filled porosity," *International Journal of Heat and Mass Transfer*, Vol. 49, No. 25-26, pp 5010-5017.

Valore, R. C., Jr. (1958) "Insulating Concretes," *ACI Journal*, Vol. 53, No. 5, pp 509-535.

Valore, R. C., Jr. (1980) "Calculation of U-Values of Hollow Concrete Masonry," *Concrete International*, Vol. 2, No. 2, pp 40-63.

Van Rooyen, M., and H.F. Winterkom (1959) "Structural and testural influences on thermal conductivity of soils," *Highway Research Board Proceedings*, pp 576-621.

Weibo, Y., S. Mingheng, and C. Zhenqian (2009) "A variable heat flux line source model for boreholes in ground coupled heat pump," *Power and Energy Engineering Conference, 2009. APPEEC 2009. Asia-Pacific*, pp 1-4.

Woodside, W., and J.H. Messmer (1961) "Thermal conductivity of porous media," *Journal of Applied Physics*, Vol. 32, No. 9, pp 1688-1706.

CHAPTER 3. NUMERICAL MODELING OF THERMAL OPERATION OF HEAT EXCHANGE PILES

3.1. Introduction

Geotechnical engineers are the responsible to ensure the safety and the durability of the foundation system against any anticipated failure. Due to the complexity of the actual performance of Energy Piles, a common way followed to design these systems is to use a factor of safety higher than normal in the geotechnical design (Knellwolf et al., 2011). Another design approach is to use numerical models to predict the expected thermo-mechanical response of the foundation system. Using these numerical models, a more reliable and economical design can be achieved. However, modeling Energy Piles requires a good understanding of different techniques associated with the thermal performance taking place within the pile. This chapter discusses the details of modeling this thermal performance and advanced analytical techniques used to simplify the numerical models.

3.2. General

In order to model the thermal performance of Energy Piles, and explore their long term performance, a clear understanding of various system components, the materials used, and the operation of each component is required. Any ground coupled heat pump (GCHP) system is divided into three parts; the first represents the distribution system in the building, the second represents the ground elements, and the last is the heat pump connecting the building side to the ground elements. The former part is concerned with estimating the thermal loads of the building and the designing the distribution system such as the ducts, etc. Designing the distribution system is the responsibility of the HVAC engineer and is beyond the scope of this dissertation. Chapter 5 presents a comprehensive simplified method for estimating the building thermal loads and the procedure followed to convert these building loads into ground thermal loads. The thermal operation of the ground element was discussed in Chapter 2 in details and is summarized in Section 3.3.

The heat pump that is used to connect the building system and the ground elements is known as the ground source heat pump (GSHP). The heat pump is either a water-to-water pump or a water-to-air pump. Water-to-water GSHPs exchange the thermal energy between two fluids; one from the building side and the other from the ground side. While water-to-air GSHPs exchange the thermal energy between a circulating fluid from the ground loop side and the air from the building side. Both GSHPs are commonly being present in the market, and the choice of the most appropriate one for a particular project depends on the project needs. For instance, when the system is to provide hot water to the building than the water-to-water system is preferred over the water-to-air system. On the other hand, the water-to-air pump is used if raising air quality inside the building in intended.

GSHPs operate using a standard vapor-compression refrigeration cycle which typically consists of an evaporator, a compressor, a condenser, an extension valve, and a circulating refrigerant as shown in Figure 3.1. As the refrigerant moves around the cycle, it changes from vapor to liquid and vice versa in a continuous process. When a liquid refrigerant evaporates, it absorbs heat from its surroundings. Conversely, when the refrigerant vapor condenses back to a liquid, it releases heat to its surroundings (Siegenthaler, 2010).

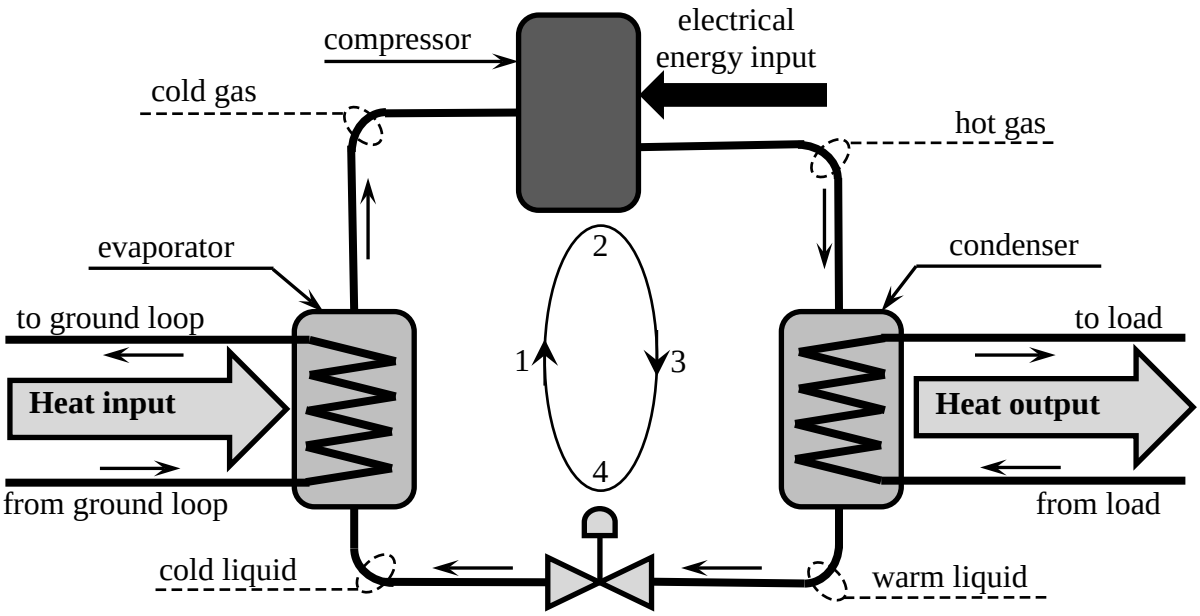

Figure 3.1. Details of Ground Coupled Heat Pump (Siegenthaler, 2010 - used under fair use, 2013)

The following specific steps describe the thermodynamic process of the heat exchange taking place inside the ground source heat pump which is explained by the numbers at the center of Figure 3.1 (Siegenthaler, 2010). These steps describe the building heating mode in which the geothermal energy is used to heat up the buildings environment. Thus, the ground temperature is reduced in this model while the temperature of the air inside the building is increased. The refrigerant cycle is as follows;

1. The liquid refrigerant enters the evaporator as a low-temperature, low-pressure liquid. It passes across the surface of copper tubing through which water or water/antifreeze mixture from the ground loops. Because the liquid refrigerant is several degrees colder than the water/antifreeze mix, the former absorbs heat from the latter. The absorbed heat causes the cold refrigerant to vaporize.
2. The cold refrigerant gas then passes to the electrically operated compressor, where its pressure and temperature are significantly increased. The temperature of the hot refrigerant gas line leaving the compressor reaches between 60℃ - 76.7℃ (140 °F - 170 °F).
3. The hot gas flows on to the condenser, where it passes across another copper coil carrying water or air from the building side. Because the refrigerant gas is warmer than the fluid from the building side, heat moves from the gas to the water. This causes the refrigerant to condense back to a liquid, but still remain at the relatively high pressure.
4. Finally, the liquid refrigerant flows from the condenser to the thermal expansion valve. As it flows through this valve, its pressure is reduced, and its temperature drops immediately. The refrigerant is now back to the same condition it started from at the base of the evaporator. It is ready to repeat this cycle as long as the compressor is running.

The building cooling mode requires the heat to be absorbed from the building environment and injected to the ground which is performed by reversing the direction of the refrigerant cycle.

Commercial GCHPs have the ability to make such reversal in which the condenser becomes an evaporator, the evaporator becomes a condenser, and the compressor works in the two directions.

3.3. Thermal Operation of Ground Elements

As explained in the above section, a cold fluid leaves the heat pump and enters the ground loops (labeled "to ground loops" in Figure 3.1) in the building heating mode while a heated fluid is injected to the ground loops in the building cooling mode. A thermal gradient is developed due to the difference between the temperature of the fluid injected to the ground and the ground temperature. The fluid inside the circulation tubes exchanges heat with the ground loops by convection at the inner surface of the tube. Then, heat conduction through the tube wall takes place till the outer surface of the tube at which the heat continues to propagate within the pile material by conduction till reaching the pile-soil interface. At the pile soil interface, the heat is transferred within the soil mass primarily by conduction and by heat convection if a ground water flow exists. These mechanisms of heat transfer between the Energy Pile and the ground are shown in Figure 3.2. As schematically shown in the Figure 3.2, heat transfer occurs in two directions reflecting the heat injected into the ground during building cooling mode (the dark arrows) and the heat extracted from the ground during building heating mode (white arrows).

Thus, the numerical analyses used to model the heat exchange between Energy Piles and the surrounding soils should account for all these components. These models should start with a good estimate of the inlet fluid temperature which is based on the thermal loads of the building. This inlet fluid temperature is used as the triggering factor for the entire thermal operation. Furthermore, reasonable estimates of the thermal properties of all the materials including the soil, the pile, the tube, and the circulating fluid should be used in the model to obtain reliable results. Chapter 2 presents a detailed discussion about different analytical approaches followed to determine the thermal properties of each of the considered materials.

Several Analytical models to predicate the temperature at any point in the ground due to the operation of ground heat exchangers (GCHE) are available. These models usually are preferred over the numerical models due to their simplicity, and savings in the computational costs. These analytical models are divided into two main categories; the first are the models that handle the domain inside the pile which includes the pile material, the tubes, and the fluid while the second are the models handling the domain outside the pile which form the soil layers. These two categories are connected through the temperature change at the pile-soil interface which is estimated at a specific operational time using a model from the second category then is utilized to estimate the distribution of the fluid temperature along the tubes using a model from the first category. This procedure can be easily programmed and reasonable estimations of the temperature of the outlet fluid as well as the temperature within and around the pile can be estimated in a timely manner. Table 3-1 summarizes the most usable models in each of the two categories. It should be noticed that the inside-pile model reported by Zeng et al. (2003) has an error in the equations listed in the original paper and the corrected equations obtained from the authors of the original publication are presented in Table 3-1.

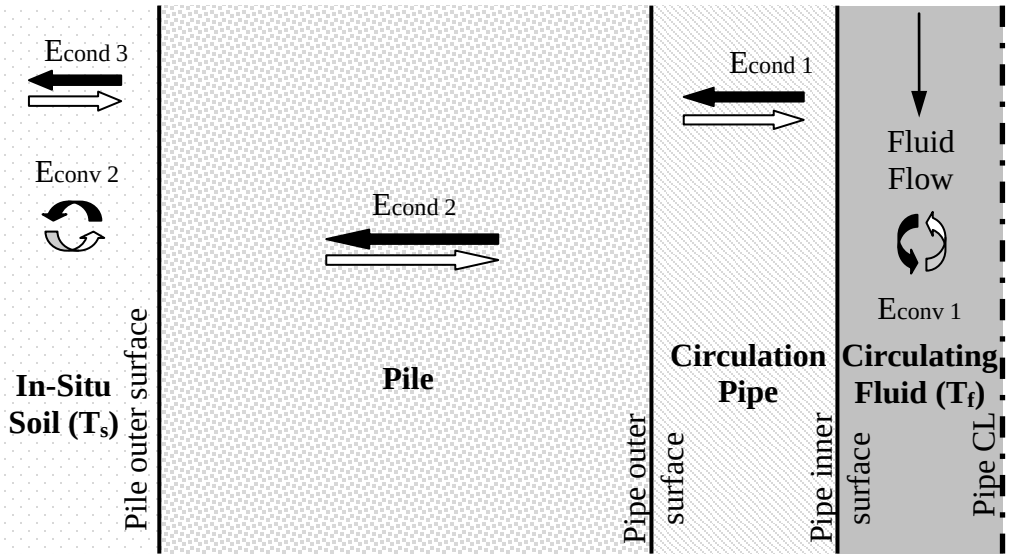

Figure 3.2. Heat transfer mechanisms in ground elements (Not to scale).

Although these analytical models are easy and more convenient to be used, they have some limitations that preclude their applicability for most of the cases. These limitations include;

1. All the out-pile models assume homogeneous soil which means that these models cannot be used for stratified grounds,
2. The finite line source (FSC) model assumes that the heat exchanger was backfilled with a material identical to the soil surrounding the pile. Therefore it is not applicable to grouted piles/boreholes,
3. These models ignore the impact of convection due to ground water flow; if any,
4. These models use a constant value for the heat rate (q') which is not the case for the real operation of heat exchangers and energy foundations.

There are several efforts to overcome these limitations (Carslaw and Jaeger, 1986; Cui et al., 2006; Ingersoll et al., 1948). These efforts are successful but they only handle one of the limitations. Therefore for a more general case, numerical modeling is preferred over anyone of the analytical models because it can easily account for most the factors observed at a site.

Table 3-1. Analytical models for ground coupled heat exchangers

Model name and reference	Mathematical Model
Temperature inside the pile (Zeng et al, 2003)	For Single U-Tube*; $\Theta_d(Z) = \mathrm{ch}(\beta Z) - \frac{1}{\beta S_{12}}\left[\left(\frac{S_{12}}{S_1}+1\right) - \frac{\beta S_1 \cdot \mathrm{ch}(\beta) - sh(\beta)}{\beta S_1 \cdot \mathrm{ch}(\beta) + sh(\beta)}\right]\mathrm{sh}(\beta Z)$ $\Theta_u(Z) = \frac{\beta S_1 \cdot \mathrm{ch}(\beta) - sh(\beta)}{\beta S_1 \cdot \mathrm{ch}(\beta) + sh(\beta)}\mathrm{ch}(\beta Z) - \frac{1}{\beta S_{12}}\left[1 - \left(\frac{S_{12}}{S_1}+1\right)\frac{\beta S_1 \cdot \mathrm{ch}(\beta) - sh(\beta)}{\beta S_1 \cdot \mathrm{ch}(\beta) + sh(\beta)}\right]\mathrm{sh}(\beta Z)$ $\Theta'' = \frac{\beta S_1 \cdot \mathrm{ch}(\beta) - sh(\beta)}{\beta S_1 \cdot \mathrm{ch}(\beta) + sh(\beta)}$ The details of the model are in the reference paper.
Infinite Line Source Model, ILS (Ingersoll et al., 1948)	$\Delta T = \frac{q'}{2\pi k}\int_{\beta}^{\infty}\frac{e^{-\beta^2}}{\beta}.d\beta$
Finite Line Source Model, FLS (Ingersoll et al., 1948)	$\Delta T = \left(\frac{q'}{4\pi k}\right)\int_0^H \left\{\frac{\left[erfc\left(\frac{\sqrt{r^2+(z-h)^2}}{2\sqrt{\alpha t}}\right)\right]}{\sqrt{r^2+(z-h)^2}} - \frac{\left[erfc\left(\frac{\sqrt{r^2+(z+h)^2}}{2\sqrt{\alpha t}}\right)\right]}{\sqrt{r^2+(z+h)^2}}\right\}.dh$
Finite Hollow Cylindrical Model, FHC (Ingersoll et al., 1948)	$\Delta T = \frac{q'}{k\pi^2}\int_0^{\infty}\frac{e^{-\beta^2 F_o}-1}{\beta^2\cdot\{J_1^2(\beta)-Y_1^2(\beta)\}}\cdot[\{J_0(p\beta)\cdot Y_1(\beta)\}-\{J_1(\beta)\cdot Y_0(p\beta)\}]\cdot d\beta$
Finite Solid Cylindrical Model, FSC (Man et al., 2010)	$\Delta T = \frac{q'k}{\alpha}\int_0^t\int_0^H \frac{1}{8\left[\sqrt{\pi\alpha t}\right]^3} I_0\left[\frac{rr_b}{2\alpha t}\right]\left\{e^{-\left[\frac{r^2+r_b^2+(z'-z)^2}{4\alpha t}\right]} - e^{-\left[\frac{r^2+r_b^2+(z'+z)^2}{4\alpha t}\right]}\right\}\cdot dz'dt$

*For double tubes in parallel and in series configurations, check the original paper.

3.4. Numerical Modeling Challenges

In this section, the challenges encountered while modeling Energy Piles numerically are presented and the detailed approaches followed to overcome these challenges are discussed. Energy Piles can be modeled using three dimensional finite element or finite difference models (Marcotte and Pasquier, 2008). Furthermore, two dimensional models can be used should a uniform ground is assumed. Section 3.5 presents the details of using three dimensional finite element models to estimate the performance of Energy Piles.

3.4.1. Modeling the Carrier Fluid

Modeling the fluid is performed to estimate the temperature of the fluid along the tube length and more importantly, to apply the thermal load to the ground through heat convection between the fluid and the inner surface of the ground loops as discussed earlier. The heat rate applied from the fluid to the tubes depends on the fluid velocity in the three dimension space, since the total applied heat (q) is estimated as;

$$\boldsymbol{q} = \mathrm{M} \cdot \boldsymbol{C_p} \cdot \Delta \boldsymbol{T_f} = \left(\boldsymbol{\rho_f} \cdot \mathbf{G}\right) \cdot \boldsymbol{C_p} \cdot \Delta \boldsymbol{T_f} = \left(\boldsymbol{\rho_f} \cdot \boldsymbol{U} \cdot \mathbf{A_{in-tube}}\right) \cdot \boldsymbol{C_p} \cdot \Delta \boldsymbol{T_f} \qquad \text{Eq. 3-1}$$

Where M**:** Mass flow rate = volumetric flow rate × fluid density (ρ_f),

G : Volumetric flow rate = velocity of the flow (U) × area of the inner tube ($\mathbf{A_{in-tube}}$),

C_p: the heat capacity of the circulating fluid,

ΔT_f : the difference between the fluid temperature at the inlet and outlet of the ground loop.

Eq. 3-1 is commonly used to estimate the applied heating power using measured inlet and outlet fluid temperatures. When 3-D finite element models are used, the inner area of the ground loop ($\mathbf{A_{in-tube}}$) is geometrically built in the model and therefore is not needed in the Eq. 3-1. Furthermore, the fluid velocity and the temperature change have three components in the three dimensions. Thus, Eq. 3-1 can be rewritten for finite element use as;

$$\boldsymbol{q} = \boldsymbol{\rho_f} \cdot \boldsymbol{C_p} \cdot \left(\boldsymbol{u}\Delta \boldsymbol{T_{fx}} + \boldsymbol{v}\Delta \boldsymbol{T_{fy}} + \boldsymbol{w}\Delta \boldsymbol{T_{fz}}\right) \qquad \text{Eq. 3-2}$$

Where u, v, w: flow velocity components in x, y and z directions, respectively.

Since the temperature change in each direction depends on the location along the ground loop and the finite element model is used to estimate the fluid temperature along the loop, the change in the temperature of the fluid in each direction is simplified as the tangential derivative of the fluid temperature in x, y, and z dimensions. Thus, Eq. 3-2 can be rewritten in its final form that can be implemented in the finite element model as;

$$\boldsymbol{q} = \boldsymbol{\rho_f} \cdot \boldsymbol{C_p} \cdot \left(\boldsymbol{u}\boldsymbol{T_{fTx}} + \boldsymbol{v}\boldsymbol{T_{fTy}} + \boldsymbol{w}\boldsymbol{T_{fTz}}\right) \qquad \text{Eq. 3-3}$$

Two different modeling approaches can be used to estimate the fluid temperature and to use it in applying the heating power (q) to the ground. The first is to model the actual fluid flow while the second is to have the effect of the fluid built in the model without modeling the fluid physically. Modeling the fluid domain in 2-D space is doable; however it generates numerical instability and convergence problems in 3-D models due to the high aspect ratio of the elements used to discretize the fluid domain. Thus, the second modeling approach is adopted for all the 3-D models reported in this dissertation.

In this technique, analytical methods are used to estimate normalized fluid temperature distribution along the length of the tube. This normalized fluid temperature distribution refers to the relative dissipation of the heat at each point along the tube length. For instance, no heat is

expected to dissipate at the inlet of the tube while the dissipated heat at the outlet of the tube is expected to be 100%. Zeng et al. (2003) showed that for a single tube about 60% of heat is dissipated along the pipe leg that contains the downward flow and the remaining 40% is dissipated along the other pipe leg; while for double tubes configuration, the downward flow pipe dissipates about 62.5% and the upward flow pipe dissipates the remaining 37.5%. This agrees with the general rule of thumb which proposes that the downward flow pipe dissipates about 2/3 of the heating energy, while the upward flow pipe dissipates 1/3 of the heating energy (Austin, 1998). Therefore for simplicity purposes, the rule of thumb is adopted in all the analysis performed by dividing the tube into two portions; the first is from the inlet till the midpoint within the U-section and the second is from the midpoint till the outlet. Thus, a reliable estimate of the heat dissipated at any point along the ground loop can be estimated using a steady state analysis of a thin conductive layer representing the inner surface of the tube. In this analysis, an inlet fluid temperature of 1 ^{o}K at the inlet, 0.33 ^{o}K at the midpoint of the tube, and 0 ^{o}K at the outlet are forced while no heat is allowed to be exchanged with the surrounding mediums. Thus, the normalized fluid temperature in the three dimensions ($\mathrm{vel_x}, \mathrm{vel_y}$, and $\mathrm{vel_z}$) are estimated. These components of the normalized fluid temperature are then used to determine the fluid velocity in x, y, and z as;

$$U = G/\mathrm{A_{in-tube}}$$

$$vel_{total} = \sqrt{(vel_x)^2 + \left(vel_y\right)^2 + (vel_z)^2}$$

$$u = (U \cdot vel_x)/vel_{total}$$

$$v = \left(U \cdot vel_y\right)/vel_{total}$$

$$w = (U \cdot vel_z)/vel_{total}$$

Thus, Eq. 3-3 can be used as a defined heating rate boundary condition at the inner surface of the ground loop given the known velocity field at any point along the tube. However, the temperature of the fluid is not expected to be equal to that of the inner surface of the tube due to the convection nature of the heat transfer. Thus, a convective boundary condition is needed to represent the heat applied from the fluid to the pipe as well as from the pipe to the fluid. Theoretically, these two heating rates are equal and opposite in direction. However since the fluid is modeled as a thin conductive layer rather than a domain, the heat rate applied from the pipe to the thin conductive layer representing the fluid should be higher and the difference is the area-volume ratio between the thin conductivity layer and the actual fluid domain. Heat transfer coefficients are utilized to apply the heating load the conductive heat from the fluid to the pipe and from the pipe to the fluid. The heat applied from the fluid to the pipe (q_1) and the heat applied from the pipe to the fluid (q_2) are thus estimated as;

$$\left.\begin{aligned} q_1 &= h_1\left(T_f - T_p\right) \\ q_2 &= h_2\left(T_p - T_f\right) \end{aligned}\right\} \quad \text{Eq. 3-4}$$

Where the convection heat transfer coefficient from the fluid to the pipe (h_1) is estimated using the general formulas based on the flow condition, i.e. laminar flow or turbulent flow (Incropera, 2007). These formulas are as follows;

$$\boldsymbol{h_1} = \frac{\mathbf{4.3}\, \boldsymbol{k_{fluid}}}{\boldsymbol{d}} \text{ for laminar flow} \quad \text{Eq. 3-5}$$

$$\boldsymbol{h_1 = 0.023 \times R_e^{(4/5)} \times P_r^{(1/3)} \times \frac{k_{fluid}}{d}}$$ for turbulent flow Eq. 3-6

Where, k_{fluid} is the thermal conductivity of circulating fluid, d is the inner diameter of the tube, P_r is Prandtl number = $\frac{C_{p_{fluid}} \cdot \mu_{fluid}}{k_{fluid}}$, R_e is Reynolds number = $\frac{\rho_{fluid} \cdot U \cdot \mathrm{d}}{\mu_{fluid}}$, and μ_{fluid} is the dynamic viscosity of the fluid.

The flow condition is determined using Reynolds number (R_e) such that the flow is laminar when $R_e \leq 2300$, while it is turbulent when $R_e \geq 4000$. For $2300 < R_e < 4000$, the flow is in the transition or the critical region within which the flow condition is controlled by other factors such as tube roughness, and flow uniformity. It is not easy to determine the exact flow condition within transition zone as this point is still under investigation by hydrologists (Munson et al., 2002). Generally speaking for geothermal energy applications, the flow inside the circulation tubes is intended to be turbulent due to the high values of the coefficient of heat transfer (h) associated with turbulent flow as shown in Figure 3.3 which represents the heat transfer coefficient for the laminar and the turbulent flow conditions given by Eq. 3-5 and Eq. 3-6.

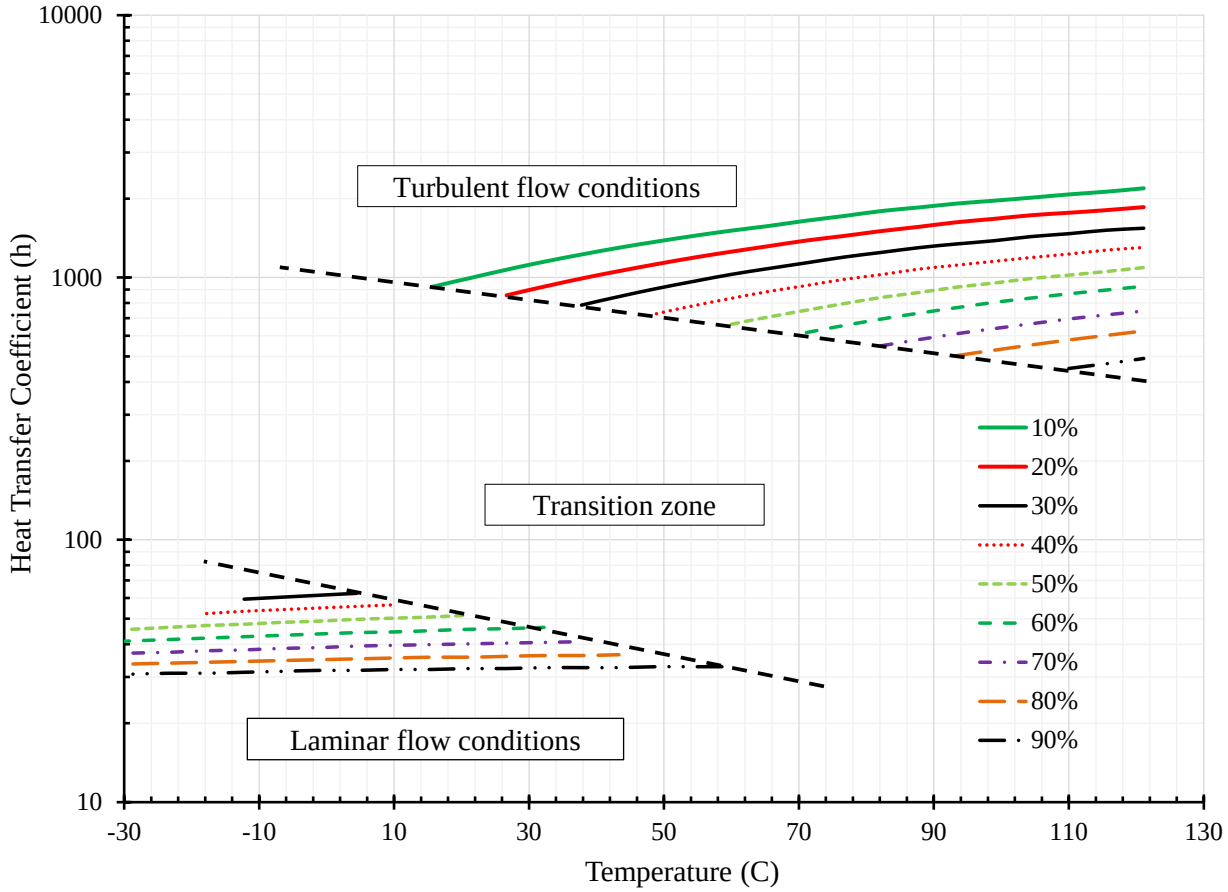

Figure 3.3. Heat transfer coefficients for different water/propylene glycol mixtures for 1 inch tube and flow rate of 11 liter/min (3 gpm).

The thermal properties of the fluid, i.e. density (ρ_{fluid}), specific heat capacity ($C_{P_{fluid}}$), thermal conductivity (k_{fluid}), and dynamic viscosity (μ_{fluid}), depend on the type and the volume percentage of the antifreeze used in the mixture. Different antifreezes are being used in general

geothermal applications including, methanol, ethylene glycol, and propylene glycol. The antifreeze is mixed with water using a conventional antifreeze volumetric percentage between 5 to 20%. The exact percentage is controlled by the least expected operational fluid temperature for a specific project which is highly related to the climatic conditions at the project location, and heating and cooling loads. ASHRAE handbook (2009) presents the thermal properties of different water/antifreeze mixtures as functions of temperature. For modeling purposes, the properties of the fluid are assumed constant and independent of the temperature because traditional geothermal applications achieve about 5.5℃ temperature change between the inlet and the outlet fluids. This temperature difference according to Figure 3.3 causes a small variation (less than 10%) of the heat transfer coefficient (h) and thus, assuming content properties is sufficient.

The heat transfer coefficient from the pipe to the fluid (h_2) is then estimated using the area-volume ratio between the thin conductivity layer and the actual fluid domain as discussed earlier. This ratio can be estimated as;

$$\frac{\text{Surface area of the thin conductive layer}}{\text{Volume of the actual fluid domain}} = \frac{\pi d L_p}{\pi (d^2/4) L_p} = \frac{4}{d}$$

Thus;

$$h_2 = \frac{4}{d} h_1$$

3.4.2. Modeling Circulation Tubes

Two different tube types are being used in energy foundations, the high density polyethylene (HDPE), and the cross-linked polyethylene (PEX-a). The typical thermal properties for these two materials are listed in Table 3-2 which shows that HDPE and PEX have about the same thermal properties and therefore, their performance is expected to be the same. In other words, the choice between anyone of these tubes does not affect the thermal performance of the piles. Thermal conductivity tests performed at Virginia Tech on heat exchangers with the two tube types show that the type of the tube has no effect of the thermal resistance of the heat exchanger as presented in Chapter 7.

Table 3-2. Thermal properties of HDPE and PEX tubes.

Tube Type	Thermal Conductivity W/m·℃ (Btu/hr·ft·°F)	Specific Heat Capacity J/kg·℃ (Btu/lb·°F)	Density kg/m^3 (pcf)
HDPE	0.42–0.51 (0.242-0.30)	2300 (0.549)	950 (59.3)
PEX	0.41 (0.236)	2300 (0.549)	950 (59.3)

The typical sizes of the polyethylene tubes used in geothermal applications are from 19 mm (¾ inch) to 50.8 mm (2 inches) . The wall thickness for these tubes is less than 6.3 mm (0.25 inch). This small wall thickness causes instability and convergence problems for the numerical solver and requires a very large number of tiny elements to discretize such narrow domain in order to overcome these issues. These tiny elements cannot be easily connected to the elements discretizing the pile domain causing a difficulty in finding a globally accepted mesh for the numerical solvers.

One way to overcome these issues is to account for the thermal resistance taking place within the tube wall without physically modeling the wall. This is performed by correcting the convection heat transfer coefficient (h_1) described earlier to include the tube wall thermal

resistance (Austin, 1998; Kavanaugh and Rafferty, 1997). Thus the corrected heat transfer coefficient would be between the fluid and the outer surface of the tubes rather than the inner surface of the tubes. This is performed by estimating the pipe thermal resistance (R_p) and the fluid convection resistance (R_c) then combining them together to determine the corresponding heat transfer coefficient from the fluid to the outside cylinder pipe wall (h_{eq}) as follows;

$$R_p = \frac{r_o\, Ln\left(\frac{r_o}{r_i}\right)}{2k_p} \qquad \text{and} \qquad R_c = \frac{1}{h_1\left(\frac{r_i}{r_o}\right)} \qquad \text{thus, } h_{eq} = \frac{1}{R_p + R_c}$$

Where, r_o is the outer radius of the circulation tubes, r_i is the inner radius of the circulation tubes, k_p is the thermal conductivity of the tube material, and h is the convection heat transfer coefficient between the fluid and the inner surface of the tubes estimated using formulas provided earlier. This approach is adopted in all the 3-D models reported in this dissertation.

3.4.3. Initial and Boundary Conditions

As for any numerical modeling, the choice of the appropriate boundary conditions for the entire problem is significant. Analyzing the thermal operation of geothermal Energy Piles is a transient problem in which not only the selection of the boundary condition is crucial, but also the choice of reliable initial condition is critical.

Different boundary conditions exist for heat transfer problems including heat transfer in Energy Piles. These boundary conditions include insulation, free flux, assigned specific temperatures, continuity, and symmetry. Assigning reasonable conditions to different boundaries is an important task that significantly affects the analysis outputs, which is the case for the use of numerical models in any discipline. Table 3-3 presents the physical meaning of each of the previously mentioned heat transfer boundary conditions as well as the location at which each one of these boundaries is assigned, if any, within Energy Pile models.

Table 3-3. Boundary conditions for heat transfer problems in Energy Piles.

Boundary Condition	Description	Use in Energy Pile modeling
Insulation/symmetry	All heat transfer mechanisms across the boundary have been disabled. This means that there is no temperature gradient across the boundary and no mass flow in the normal direction.	• All external boundaries of the model (sides and bottom), except surface. • Ground surface for the sensitivity analysis reported later.
Convective flux	Similar to insulation/symmetry boundary condition except that it only allows for convection heat transfer mode to occur over the boundary.	• Not Used
Assigned constant temperature	Assigning a prescribed constant temperature at a boundary.	• Ground surface for the sensitivity analysis reported later.
Continuity	The default setting for interior boundaries which means that the heat flux in the normal direction is continues across the boundary.	• Interior boundaries along pile-soil interface.

Assigning appropriate ground surface boundary conditions causes confusion for those who are new to this field. It is important to recognize the differences between conventional ground coupled heat exchangers (GHEX) and Energy Piles to resolve this confusion. GHEX are holes drilled into the ground which are provided with single or double circulation tubes and backfilled with either the native soils or a mixture of sand and cement. The ground surface around GHEX is typically subjected to the ambient air temperature rather than being insulated (i.e. assigned ambient air temperature). On the other hand, Energy Piles (and generally energy foundations) are placed below structures, as their main functionality is to serve as load carrying elements for such structures. And since it is common practice to insulate the ground floor from the foundation soils, the right ground surface boundary condition for Energy Pile/foundation models is insulation. However, assigning the ambient air temperature as a boundary condition at the ground surface is recommended when modeling thermal conductivity tests since no structure is rested on the tested Energy Pile yet, or where the ground surface above and around the piles is not insulated. For simplicity, the use of constant ground surface temperature was reported in the literature (Laloui et al., 2006). The selected constant temperature is the average temperature over a considered period.

Moreover, the initial conditions are another source of confusion. Laloui et. al. (2006) used a constant temperature profile as an initial condition for his models. However, ground temperature before the beginning of the thermal application of energy foundations is not constant. In fact, ground temperature varies with depth according to the ambient air temperature and soil thermal properties (Kusuda and Achenbach, 1965). The effect of different boundary and initial conditions on the thermal performance of Energy Piles is investigated as explained as part of the sensitivity analysis reported in Section 3.5.3.

3.4.4. Inlet Fluid Temperature

Modeling the thermal operation of Energy Piles starts with the temperature of the fluid entering the ground loops as discussed before. This temperature is assigned as an initial condition to the numerical model and varies over time to represent the desired operation. Therefore, right inlet fluid temperature should be utilized in the numerical models for reliable predictions of the system performance. The inlet fluid temperature depends on the thermal performance of the above-ground side of the system including the thermal loads of the building and the heat pump operation. Thus, it is expected to have these two factors affecting the assessment of the inlet fluid temperature.

Kavanaugh and Rafferty (1997) presented a simple approach to estimate the inlet fluid temperature. This approach is based on selecting the temperature of the fluid going to the heat pump, which is the outlet fluid from ground loops, such that it achieves the highest possible performance of the heat pump. Kavanaugh and Rafferty (1997) mentioned that choosing the temperature of the fluid entering the heat pump too close to the average ground temperature will produce higher system efficiency, but the resulting ground loop length will be very long and so, unreasonably expensive. On the other hand, choosing this temperature far away from the average ground temperature results in a small, inexpensive ground loop, but the capacity of the heat pumps is significantly reduced in heating mode. They suggested that selecting the temperature of the fluid entering the heat pump ($t_{hp-in} = t_{loop-out}$) to be within 11℃ to 16.5℃ (20°F – 30°F) higher than the average ground temperature in the cooling mode, and 5.5℃ to 11℃ (10°F – 20°F) lower than the average ground temperature in the heating mode. These recommendations are good compromise between the initial overhead cost of the system and the overall system efficiency in most regions of the U.S.

The temperature of the fluid leaving heat pump, which is entering ground loop $t_{hp-out} = t_{loop-in}$, is then estimated as a function of the liquid flow rate (Q_{flow}), heat pump capacity ($\overline{W}$), and the power input (q) as follows (Kavanaugh and Rafferty, 1997);

$$\boldsymbol{t_{hp-out}}(°\text{F}) = \boldsymbol{t_{hp-in}}(°\text{F}) - \frac{\boldsymbol{q\left(\frac{Btu}{hr}\right) - 3.412\overline{W}(\text{Watts})}}{\left[\boldsymbol{60 \times \rho_{fluid}(\text{lb/gal}) \times C_{P_{fluid}}(\text{Btu/lb}\cdot°\text{F})}\right] \times \boldsymbol{Q_{flow}(\text{gpm})}} \quad \text{Eq. 3-7}$$

Where the value used for q can be either the block heat gain or loss as long as the proper sign convection is followed. In Eq. 3-7, heating loads are considered positive while cooling loads are considered negative. Thus for the real operation of any geothermal system, the temperature of the fluid entering ground loops ($t_{loop-in}$) varies with time due to the variation of the heating/cooling loads. The variation of $t_{loop-in}$ intends to keep t_{hp-in} within the recommended limits to ensure the required efficiency of the system.

A much simpler way to estimate the temperature of the fluid entering the ground loops is based on the rule of thumb that Kavanaugh and Rafferty (1997) summarized as a function of only the system flow (Q_{flow}) as shown in Table 3-4.

Table 3-4. Liquid temperature change through ground coupled heat pumps (Kavanaugh and Rafferty, 1997 - used under fair use, 2013).

System flow, Q_{flow} (gpm/ton)	Temperature rise in cooling (°C/°F)	Temperature drop in heating (°C/°F)
3.0	5.5/10	3.3/6
2.5	7.2/13	3.8-4.4/7-8
2.0	8.3/15	5/9

3.5. Three Dimensional (3-D) Finite Element Model

This section describes the 3-D finite element models used to analyze the thermal behavior of Energy Piles. The model consists of two domains, a pile domain and a soil domain as shown in Figure 3.4. The former represents the material of the Energy Pile considered and includes the U-shaped ground loops built-in. The walls of the tubes were not modeled due to meshing difficulties and the numerical solver instability. They, however, are considered in the model using the technique discussed in Section 3.4.2. The soil domain refers to the soil around the pile and, in fact, several domains can be used to represent stratified ground. The pile and its surrounding soils are assumed to be in contact during the considered modeled period. No ground water flow was considered in these preliminary analyses for the sake of simplicity and for better interpretation of the results. Therefore, the soil domain was modeled as a solid material considering the soil average thermal conductivity, specific heat capacity, and density; rather than modeling it as a porous medium.

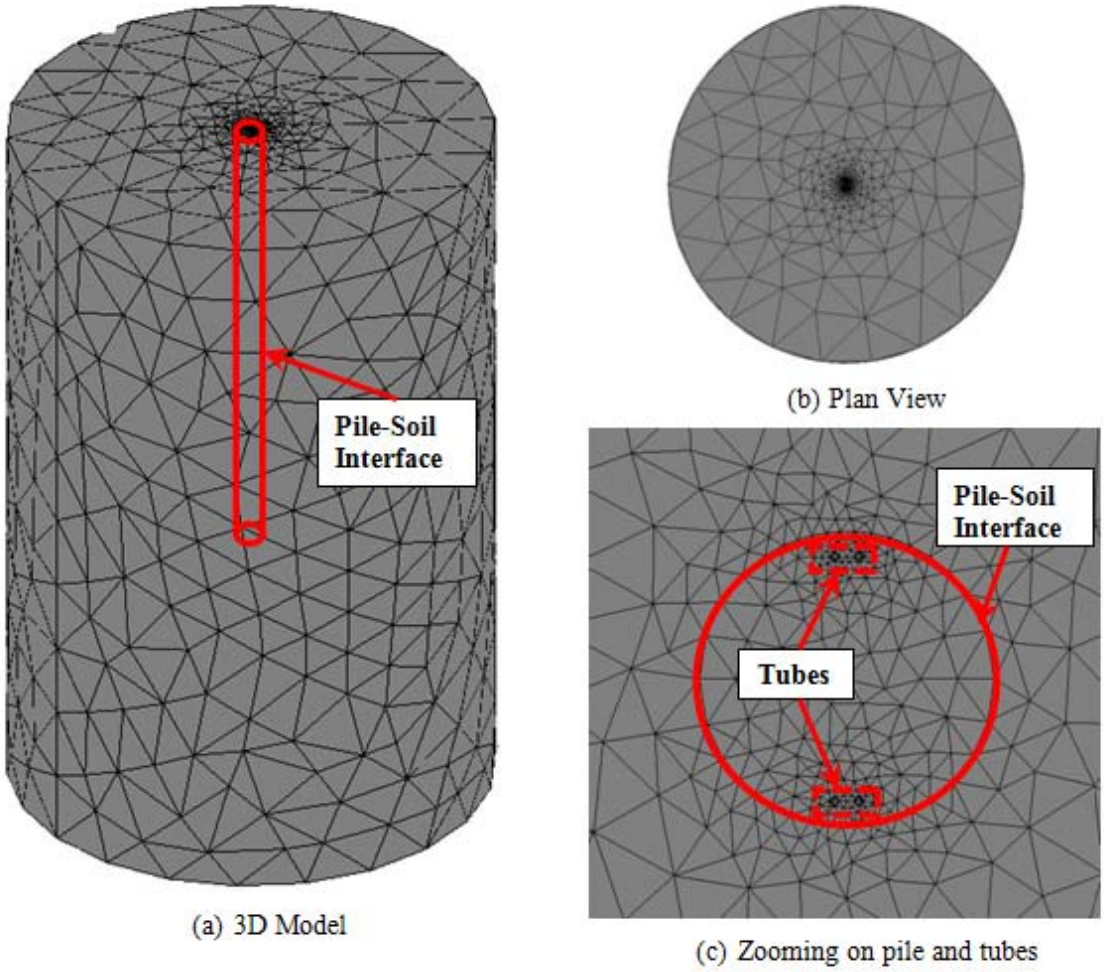

Figure 3.4. Modeled Energy Pile and its surrounding soil.

As can be seen in Figure 3.4, the soil domain is modeled as a cylinder around the pile. This shape was selected to reduce the total number of elements discretizing the soil domain which consequently reduces the computational cost and time. The radius and the depth of the soil domain cylinder were selected such that the initial ground temperatures along the domain boundaries are not affected by the thermal operation of the pile during the modeled period. Thus, initial models with large soil domain cylinders with about 50 m (164 ft) radius and 100 m (328 ft) depth were analyzed and it was gradually reduced until reaching to an optimal dimensions that cause no thermal interference at the boundaries. The results of these initial modeling efforts showed that the thermal interference in the ground due to the pile operation is a cylinder around the modeled pile with a maximum radius of about 7.5 m (24.6 ft) and maximum depth of 6 m (19.7 ft) below pile toe for thermal load duration of 30 days. Thus, the analyses reported in this chapter were based on a cylindrical soil domain with a radius of 10 m (32.8 ft), and a depth of 10m (32.8 ft) below pile toe. Larger soil domains are used when the long term performance of the piles is considered as presented in Chapter 5.

Zeng et al. (2003) indicated that heat transfer mechanism inside the pile domain is slow and minor; therefore steady state analysis was recommended to analyze such domain. On the other

hand, transient analysis was recommended to analyze the heat transfer in the surrounding soils (Zeng et al., 2003). These recommendations were based on a typical geothermal borehole dimensions which are 0.10 - 0.20 m (0.33-0.66 ft) in diameter and 40 - 200 m (131-656 ft) in length. Energy Piles are significantly larger than geothermal boreholes since they follow the typical range for deep foundations, i.e. 0.5 - 4 m (1.5-13 ft) in diameter and from 15 - 60 m (48.2-200 ft) in length. For these dimensions, that transient analysis controls the pile domain as well as the soil domain (Laloui et al., 2006). Therefore, all the analyses reported in this thesis are based on a transient analysis for both domains.

3.5.1. Description of the Preliminary Model

The pile modeled in the analyses reported in this section is 0.6 m in diameter and 20 m in length. The pile was provided with double 1 inch circulation tubes placed on opposing sides of the pile as shown in Figure 3.4 (c). The distance from the tube centerlines to the pile-soil interface is 5 cm providing about 4 cm of a clear distance from the outer perimeter of the tube to pile-soil interface. Moreover, the distance between the two legs of the each tube is 5 cm. All these dimensions were selected based on the common practice. Furthermore, neither the fluid nor the tube walls were included in the model due to the difficulties in meshing these domains and the numerical instability they cause. Their effect, however, was considered in the model following the procedure described in Section 3.4.1 and Section 3.4.2, respectively.

Sensitivity analysis is conducted to examine the impact of setting various boundary and initial conditions on the predicted thermal response of Energy Piles as discussed in Section 3.5.3. Moreover, the modeled pile was selected to be a reinforced concrete pile with a steel average area of 3% of the total pile cross sectional area. This percentage is then used to estimate the thermal conductivity of the pile in the transverse direction ($k_{pile,T}$) and in the longitudinal direction ($k_{pile,L}$) using the rule of mixtures and its inverse discussed in Chapter 2. Based on typical thermal conductivity values of 1.4 W/m·℃ (0.8 Btu/hr·ft·°F) for the concrete and 52 W/m·℃ (30 Btu/hr·ft·°F) for the steel, the pile thermal conductivities in the transverse and longitudinal directions are 1.44 and 2.9 W/m·℃ (0.83 and 1.66 Btu/hr·ft·°F), respectively. The effect of considering the pile thermal anisotropy while modeling the thermal operation of Energy Piles was not reported in the literature. Thus, the effect of the thermal anisotropy of the pile is also investigated in the sensitivity analysis reported in this chapter as presented in Section 3.5.4.

In these preliminary models, the carrier fluid is a glycol/water mixture with 10% propylene circulated at an average flow rate 11 lit/min (2.9 gpm). For the given tube dimensions and the properties of the fluid mixture at the modeled temperature range, turbulent flow inside the tubes is developed since R_e is about 10,000. Furthermore, the soil considered in these preliminary analyses is a saturated, homogeneous, and isotropic sand layer with an average thermal conductivity of 2.5 W/m·℃ (1.44 Btu/hr·ft·°F). Table 3-5 summarizes all the parameters used in the preliminary study reported in this section.

Table 3-5. Parameters used in the preliminary models.

Parameter	Assigned value
Soil (Saturated sand)	
Thermal conductivity	2.50 W/m·℃ ‖ 1.44 Btu/hr·ft·°F
Specific heat capacity	1500 J/kg·℃ ‖ 0.358 Btu/lb·°F
Density	1520 kg/m^3 ‖ 94.8 pcf
Pile	
Length	20 m ‖ 65.6 ft
Diameter	60 cm ‖ 23.5 inches
Material	Reinforced concrete (3% steel)
Density	2500 kg/m^3 ‖ 156 pcf
Specific heat capacity	880 J/kg·℃ ‖ 0.21 Btu/lb·°F
Thermal conductivity (transverse direction)	1.44 W/m·℃ ‖ 0.83 Btu/hr·ft·°F
Thermal conductivity (longitudinal direction)	2.90 W/m·℃ ‖ 1.67 Btu/hr·ft·°F
Fluid	
Glycol type and percentage	10% Propylene glycol
Density @ 35 ℃	1002.56 kg/m^3 ‖ 65.58 pcf
Specific heat capacity @ 35 ℃	4103.0 J/kg·℃ ‖ 0.98 Btu/lb·°F
Viscosity @ 35 ℃	9.9×10^{-4} Pa·sec ‖ 2.0610^{-5} lb·sec/ft^2
Thermal conductivity@ 35 ℃	0.56 W/m·℃ ‖ 0.33 Btu/hr·ft·°F
Tube	
Type and commercial dimension	PEX 25.4 mm ‖ 1 inch
Outer diameter	28.5 mm ‖ 1.125 inch
Inner diameter	22.4 mm ‖ 0.88 inch
Thermal conductivity	0.41 W/m·℃ ‖ 0.237 Btu/hr·ft·°F
Equivalent heat transfer coefficient	
Pipe thermal resistance (R_p)	4.30×10^{-3} m·℃/W ‖ 7.44 ft·°F·hr/Btu
Reynolds number (R_e)	9802
Fluid convection resistance (R_c)	9.80×10^{-4} m·℃/W ‖ 16.96 ft·°F·hr/Btu
Fluid original heat transfer coefficient (h_i)	1300 W/m^2·℃ ‖ 228.94 Btu/hr·ft^2·°F
Equivalent heat transfer coefficient (h_{eq})	190 W/m^2·℃ ‖ 33.46 Btu/hr·ft^2·°F

3.5.2. Model Validation

The described model technique was validated using one of the finite solid cylindrical analytical model (Man et al., 2010) presented in Chapter 2. In order to validate the finite element model, the thermal properties of the soil were assigned to the pile domain since the analytical model assumes that the native soils were used to backfill the pile. Furthermore, a constant ground surface temperature was assumed to comply with the analytical model assumption of constant surface temperature. The selected surface temperature was set equal to 15.5℃ (59.9°F) which is the average ground temperature at Blacksburg, VA. The same temperature was used as an initial condition for the soil and the pile domains.

Moreover, all the available analytical models including Man et al. (2010) consider a constant rate of heating which requires a constant difference between the fluid temperature at the inlet and the outlet of the ground loops. This is assured using the "boundary coupling variables" in COMSOL which allows the outlet fluid temperature for a particular time step to be used as the

fluid temperature at the loop inlet for the following time steps after adding a preselected temperature difference of 5℃ (9 ℉) to the output fluid temperature.

The results of the validation are presented in Figure 3.5 which shows the temperature change at the pile-soil interface. In this figure; the dimensionless temperature change is defined as $\frac{(T_{f-in}-T_{f-out})\cdot k_s}{q}$, and the dimensionless depth is defined $\frac{Depth}{Pile\ radius}$. It can be seen in Figure 3.5 that the results of the numerical model fit with the analytical model. Also it can be inferred that the longer the heating period, the better the agreement between the analytical and the finite element models. This is due to the interaction between the two modeled tubes that behaves separately at the early times which as time progresses start to behave like the single cylinder considered in the analytical model.

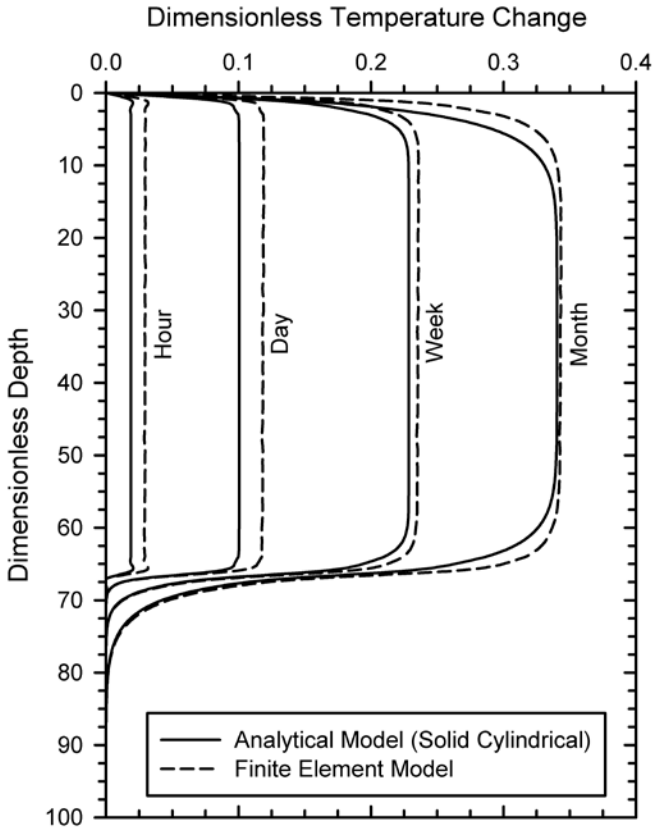

Figure 3.5. Finite element model validation against the solid cylindrical analytical model at the pile soil interface.

3.5.3. Sensitivity Analysis

To examine the impact of assigning different ground surface boundary conditions and initial conditions to the finite element models of Energy Piles, a sensitivity analysis was conducted in which three one-month heating models each with a different initial or boundary conditions than the others were studied. These models are;

1. Model 1: considers the varying ambient air temperature as the ground surface boundary condition and the actual ground temperature profile at the beginning of the thermal operation as the initial condition in the pile and the soil domains. This actual ground temperature distribution was obtained from an initial model in which the thermal properties of the

ground were assigned to the pile domain to represent the site prior to constructing the pile. In this initial model, the varying air temperature over a full year was assigned as a boundary condition at the ground surface. The variation of the ambient air temperature at Blacksburg, VA was used in the initial model and it was estimated using Kusuda and Achenbach (1965) formula which is based on the average air temperature and the annual temperature fluctuation at the considered location as shown in Eq. 3-8;

$$T = T_{mean} - T_{amp} \cdot e^{-z\sqrt{\frac{\pi}{\alpha t_{cycle}}}} \cdot \cos\left[\frac{2\pi}{t_{cycle}}\left(t_{current} - t_{shift}\right) - z\sqrt{\frac{\pi}{\alpha t_{cycle}}}\right] \quad \text{Eq. 3-8}$$

where

T: temperature at depth of interest,

T_{mean}: mean surface temperature (average air temperature),

T_{amp}: amplitude of the surface temperature (difference between maximum and minimum air temperature),

D: depth of interest,

α: thermal diffusivity of the ground,

t_{cycle}: the period of soil temperature cycle (365 days),

$t_{current}$: current day of the year,

t_{shift}: day of the year with the minimum surface temperature.

The average air temperature and the annual temperature fluctuation at Blacksburg, VA are 15.5℃ (59.9°F) and 14℃ (57.2°F), respectively. It is assumed that the thermal operation started when ground heating typical occurs, i.e. cooling of the air inside the building. According to Kusuda and Achenbach (1965), the maximum ground heating at Blacksburg, VA takes place at the beginning of August which corresponds to the maximum ambient temperature as shown in Figure 3.6. The model considers a one month thermal period starting 15 days prior to the maximum ambient temperature, and ends 15 days after such temperature as highlighted in red in Figure 3.6.

2. Model 2: uses a pre-assigned constant ground surface temperature equals to the annual average ground temperature. The same value of the annual average ground temperature is also used as an initial ground condition. For Blacksburg, VA, the annual average ground temperature is 15.5℃ (59.9°F) which is the same as the average annual ambient air temperature.

3. Model 3: uses insulation as the surface conditions and the constant annual average ground temperature which is 15.5℃ (59.9°F) as initial conditions. This boundary condition is considered to be valid for modeling Energy Piles since these elements are placed underneath a building which is thermally insulated from the ground.

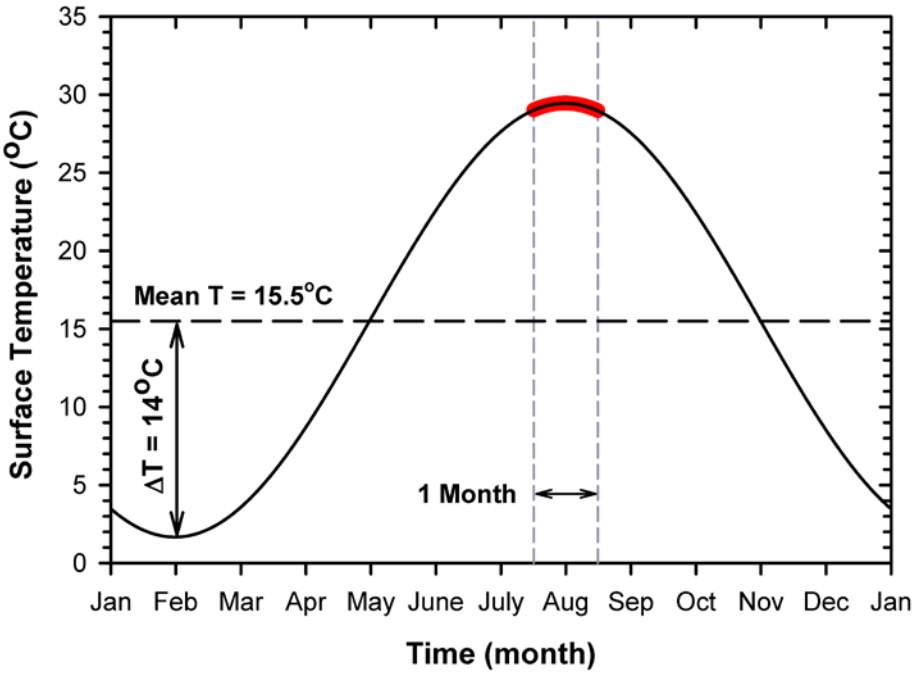

Figure 3.6. Annual average ambient air temperature variation at Blacksburg, VA using 15.5°C average and 14°C swing

A solver time step of one-hour was used in all these models and thus a solution for each hour of the modeled month was obtained. The temperature of the inlet fluid was set to 35℃ (95°F) which is assumed constant over the modeled month. This temperature is selected based on the usual recommended value for the fluid temperature of an operating GCHP system in Blacksburg, VA as discussed earlier. The recommended average design temperature for the fluid entering the heat pump at Blacksburg, VA is about 29.5℃ (85.1°F) which is 14℃ (25.2°F) above ground temperature. For 11 lit/min (2.9 gpm), the temperature of the fluid leaving the heat pump and entering the ground loops is 5.5℃ (10°F) higher than the entering fluid temperature as presented in Section 3.4.4. Therefore, a reasonable value for the inlet fluid temperature at Blacksburg, VA is 35℃ (95°F) which is 19.5℃ (35.1°F) more than the average ground temperature.

Figure 3.7 shows the selected initial and surface conditions for each one of the considered models. Furthermore, this figure also compares the temperature profiles at the soil domain boundary by the end of the modeled month for Model 1 to the undisturbed ground temperature profile. It can be inferred that the temperature distribution at the boundary of the model is not affected by the operation of the pile as the two distributions fit together proving that the model was extended enough to ensure no thermal interference at the boundary.

The sensitivity of the predicted thermal performance of the modeled pile to assigning different initial and boundary conditions was investigated using two indicators;

1. The thermal energy injected to the ground form the modeled pile,
2. The temperature distribution along, within, and around the pile.

The former is used as an indicator for the thermal performance while, the latter is important when the geotechnical and/or the structural design of the pile are considered. The findings of the

sensitivity analysis are presented in terms of comparisons between the estimated thermal energy and temperature distributions from the three considered models as shown in the following sections.

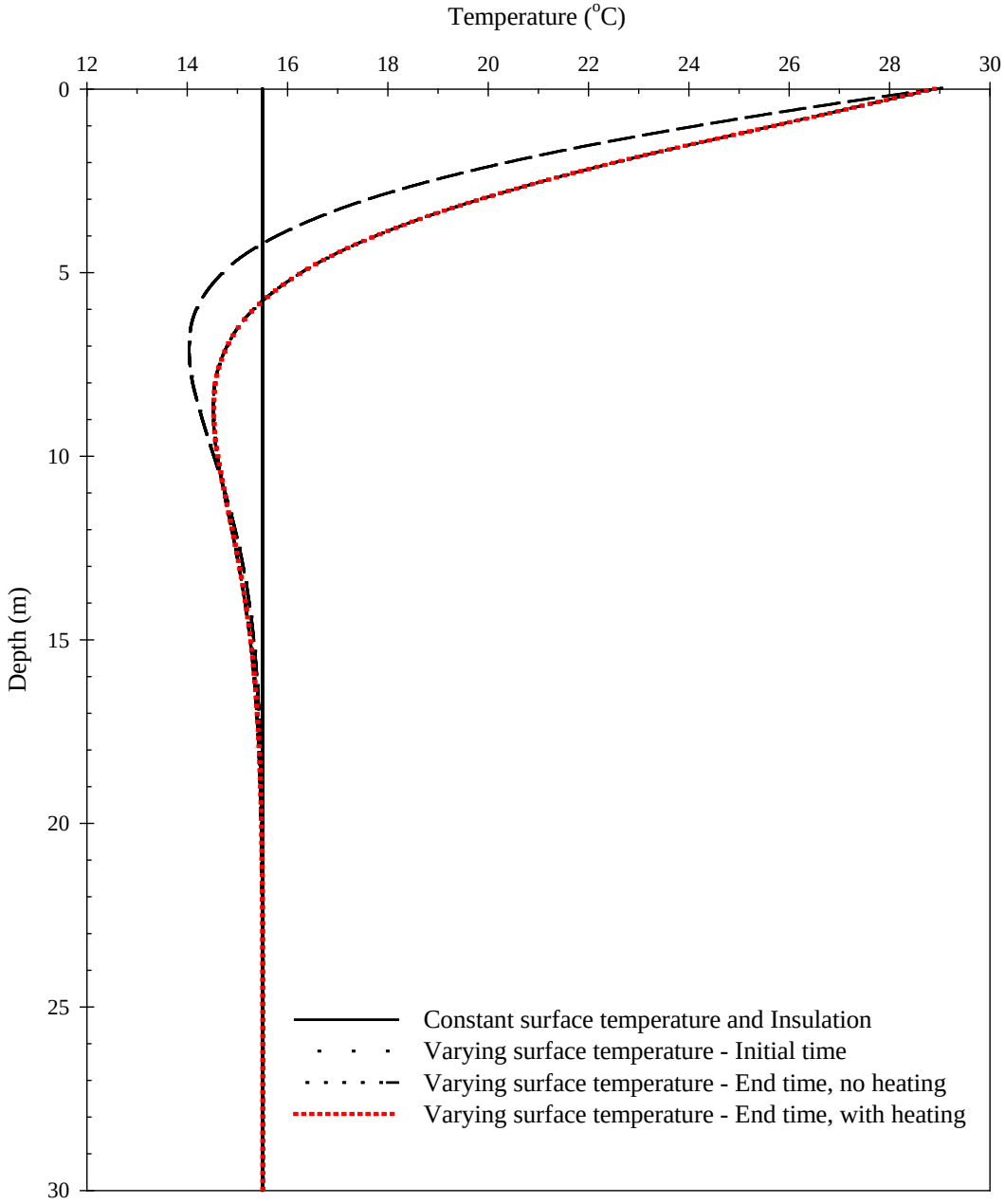

Figure 3.7. Initial and final temperature profiles for the three models used to examine the effect of boundary conditions on thermal modeling results.

(a) The estimated thermal performance (thermal energy):

The thermal performance of the three models described earlier was evaluated by referring to the energy injected to the ground and its decay over time as well as the change in the system efficiency over time. The total output energy from the pile was estimated as the summation of

the output energy from each individual tube of the modeled two tubes. The energy produced out of each single tube at a certain time was estimated using Eq. 3-1.

As mentioned earlier, the inlet fluid temperature ($T_{f\text{-}in}$) was kept constant at 35℃ (95°F) over the modeled one-month duration. Figure 3.8 presents the total output energy and the decay of the efficiency over time. It can be inferred from this figure that the energy output for the three considered scenarios decreases with time which is also pronounced in the decay of the overall system efficiency over time. It should be noticed that the rate of the total output energy decay decreases with time for the three models, i.e. higher energy decay takes place at the beginning of the thermal operation while smaller decay occurs after longer operation periods. The same performance was observed for efficiency loss with time, i.e. the increase in the loss of efficiency continues with time.

More importantly, Figure 3.8 reveals that the initial and boundary conditions has no effect on the predicted thermal performance for short term periods since all the models gave the same output energy. While for longer durations, the effect of the assigned initial and boundary conditions is more pronounced as a deviation of the results was observed. Furthermore, the model that considered surface insulation (Model 3) represents the average of the three models over the long term. The model considering the seasonal variation of the surface and initial temperatures (Model 2) was found to be about 10% less than the other two cases due to the increase in the ground temperature caused by the ambient air temperature included this model. Thus, it is concluded that the initial and the boundary conditions has a significant effect on the predicted thermal performance in the long term.

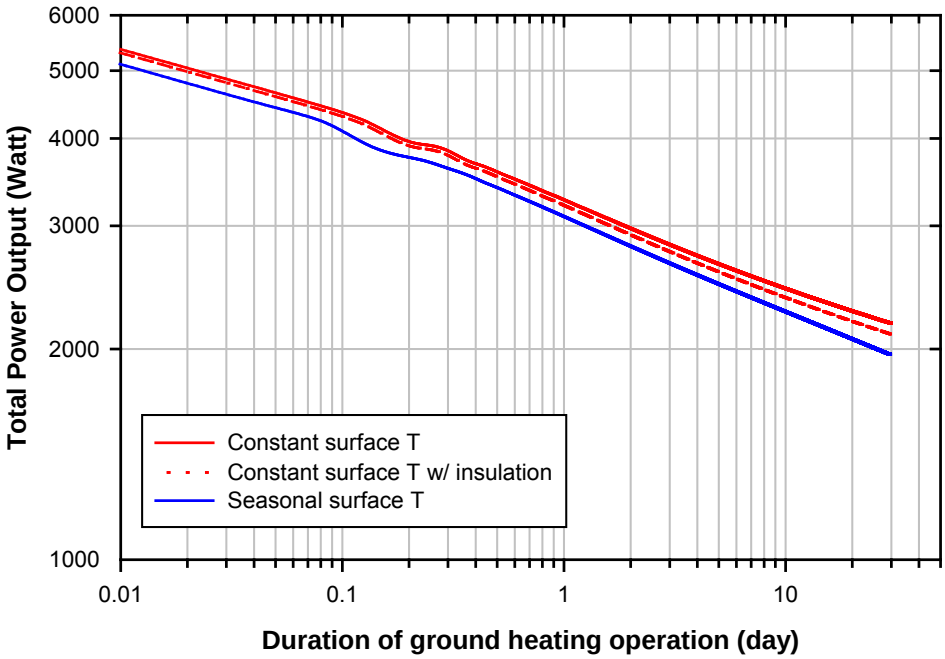

Figure 3.8. Total output energy versus time in logarithmic scale.

(b) Temperature Distribution Along The Pile and in its Vicinity:

The geotechnical design of Energy Piles depends on the stress state within the soil around the pile. The thermal operation of Energy Piles has a significant impact on such stress state (McCartney et al., 2010). Therefore, it is necessary to understand the thermal response and

temperature changes around the pile as well as the effect of different boundary and initial conditions on that response.

Figure 3.9 shows the temperature contours around the pile after 1 hour, 1 day, 1 week, and 1 month from the beginning of the ground heating at the mid-length of the pile for the three considered scenarios. The pile is represented in Figure 3.9 using a red line. As can be seen in this figure, each tube behaves independently for short time periods of 1 hour causing localized small temperature interference around its own self. This concentration of the temperature interference around the tubes for the short periods would cause a non-uniform frictional resistance around the pile perimeter. This issue is of an interest and will be considered in future research.

With the time evolution, the two tubes begin to interact together and thus the temperature bulb grows around the pile. Temperature contours within and near the pile are not circles; in fact they take an elliptical shape. On the other hand, the contours away from the pile for all times are circles. This response at far-away distances is expected since the soil averages out the effect of the individual tubes. The effect of tube interaction is significant at shorter distances,; while at far-away distances, the effect of the temperature concentrations around the tubes is reduced by the soil thermal resistance causing the far away points to act as if the heat was produced by a single source rather than two nearby sources.

Figure 3.10 and Figure 3.11 show the averaged temperature profile and the averaged temperature change profile produced from each model at the pile-soil interface, respectively. Model 2 which considers constant surface and initial temperatures is included in these figures even though it does not reflect the reality by any means just to match the general method used in previous studies (Laloui et al., 2006) to the actual cases. The temperature profiles and the temperature change profiles are almost the same for all the three models except for the top 10 m (3 ft). The temperature change is factor controlling the thermo-mechanical response of Energy Piles. The constant surface temperature and the varying surface temperature models resulted in less temperature changes within the top 10 m (3 ft) compared to the surface insulation model. The varying surface temperature model produces higher temperature changes for about the middle 10 m (3 ft) of the pile.

The effect of the initial and boundary conditions on the temperature around the pile is investigated using a radial temperature profiles as shown in Figure 3.12 for the three considered models. This figure reveals that the temperature at different orientations in the pile varies due to the existence of the ground loops. However, as the distance from the pile center increases the effect of the tubes vanishes. More importantly, it can be inferred from this figure that the temperature around the pile is not affected by the initial and the boundary condition which is expected since the amount of the heat injected to the ground is the sole factor affecting the temperature at a given point in the ground. And since the three models provided close output powers (within 10%), the predicted temperatures in the soil mass were not significantly affected. Thus, it is concluded that the initial and the surface conditions significantly affect the temperature in the pile and at its surface but have a slight effects on the temperature in the soil mass.

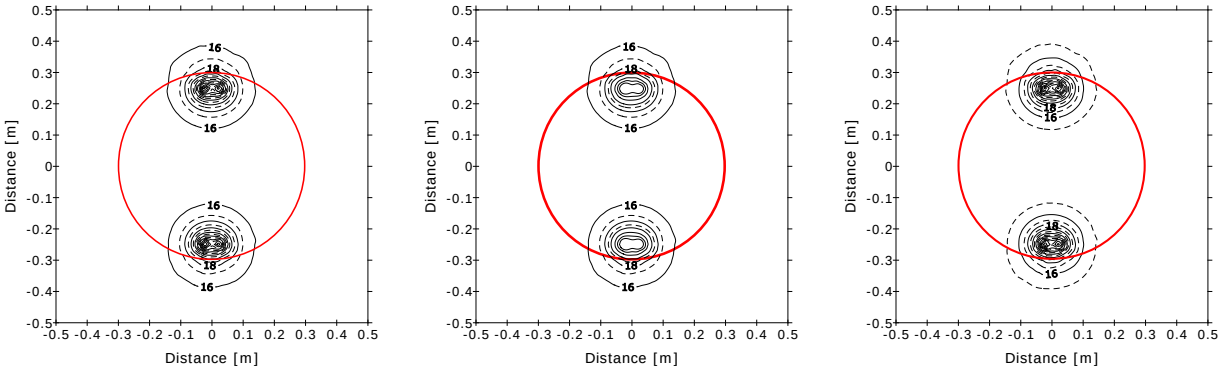

(a-1) One hour (b-1) One hour (c-1) One hour

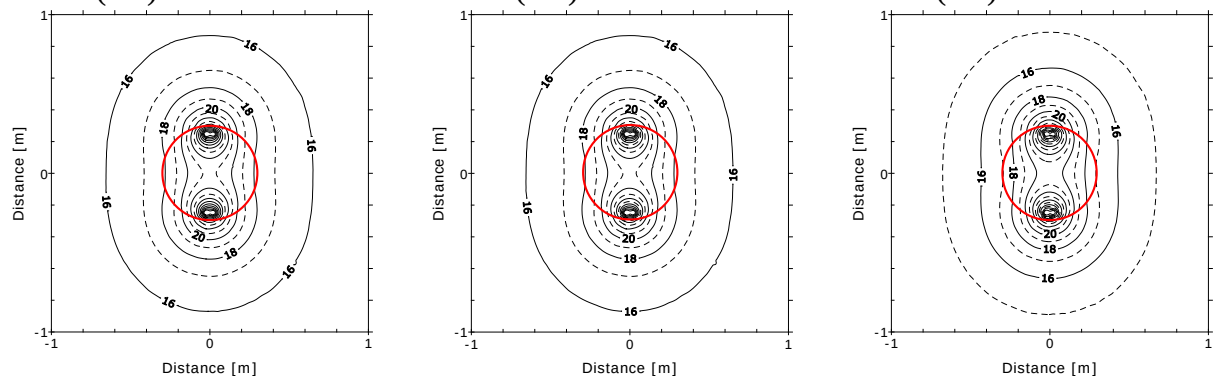

(a-2) One day (b-2) One day (c-2) One day

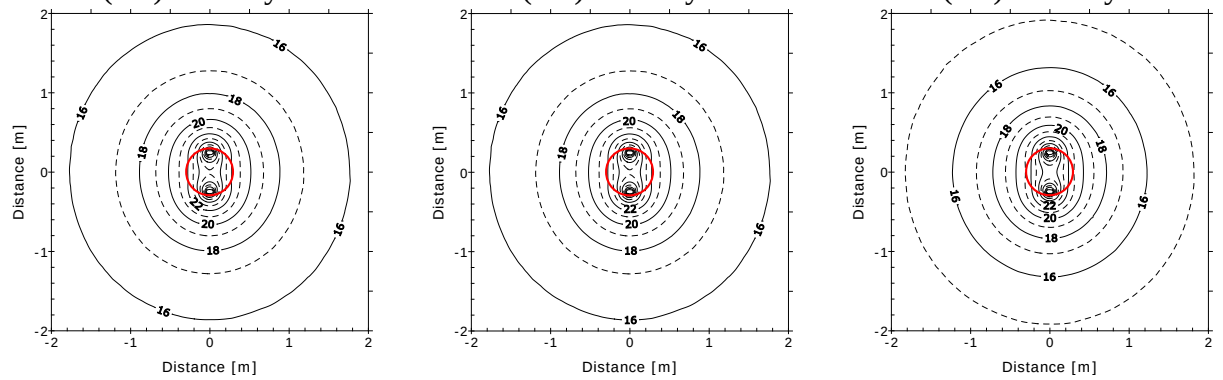

(a-3) One week (b-3) One week (c-3) One week

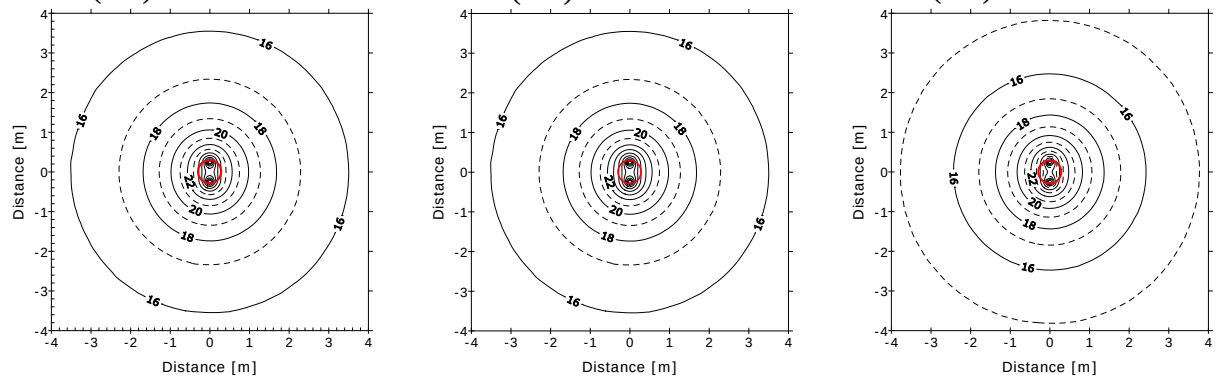

(a-4) One month (b-4) One month (c-4) One month

Figure 3.9. Temperature distribution at the mid length of the modeled pile at; (a) surface Insulation, (b) constant temperature, and (c) varying ground temperature.

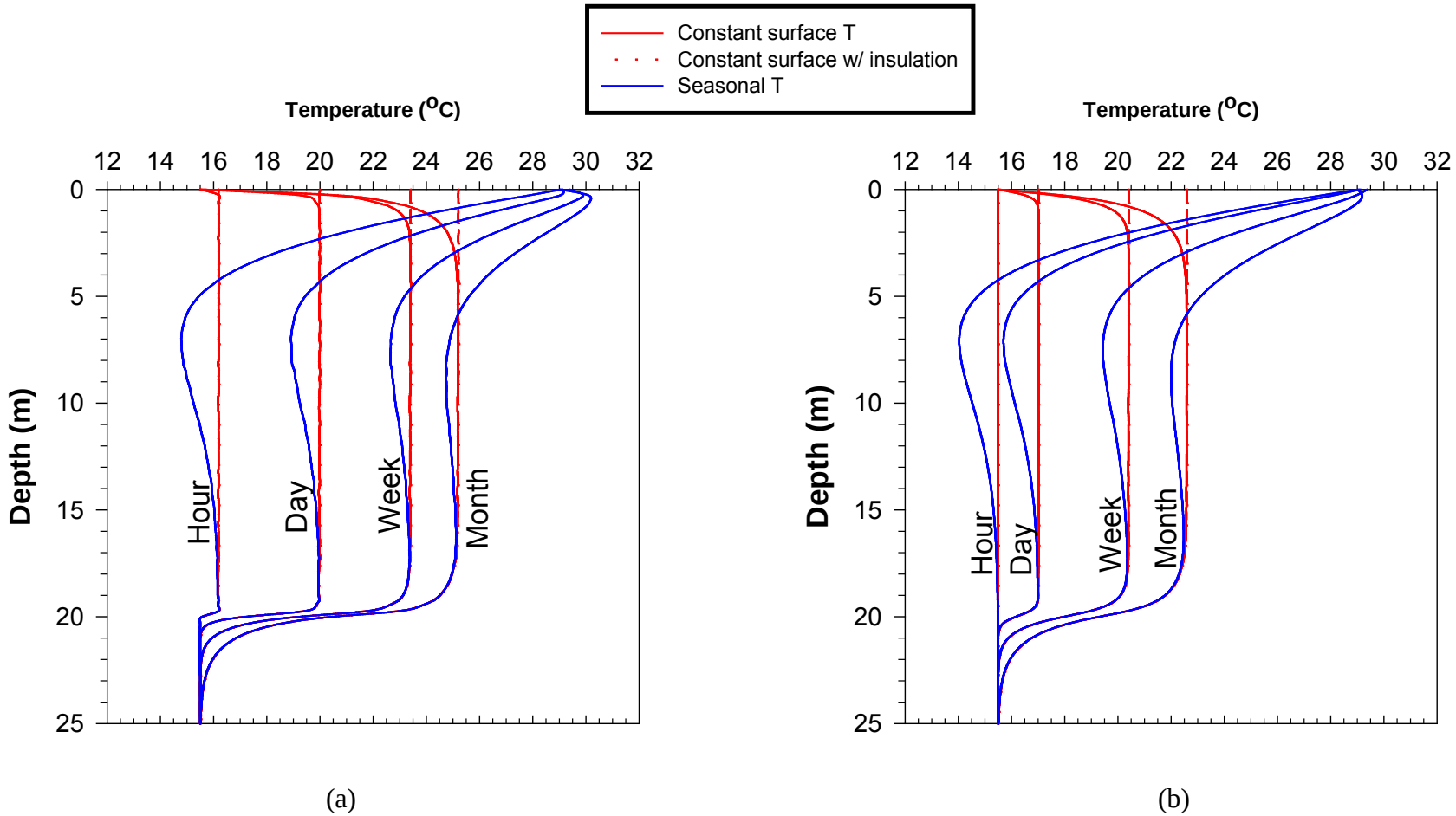

Figure 3.10. Temperature profile for the three models at; (a) pile-soil interface, and (b) 0.25m – 1 ft away from the pile-soil interface.

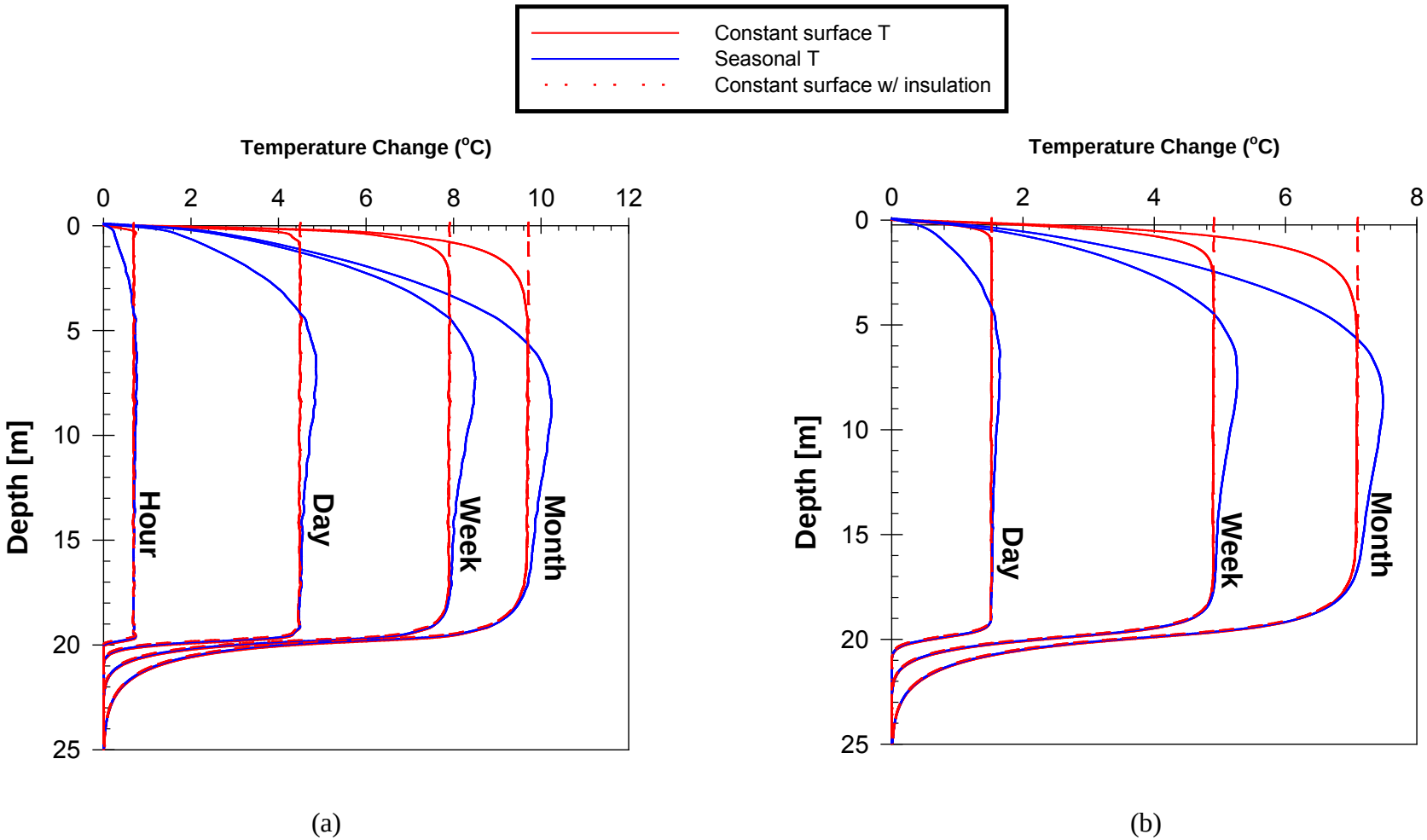

(a) (b)

Figure 3.11. Temperature change profile for the three models at; (a) pile-soil interface, and (b) 0.25m – 1 ft away from the pile-soil interface.

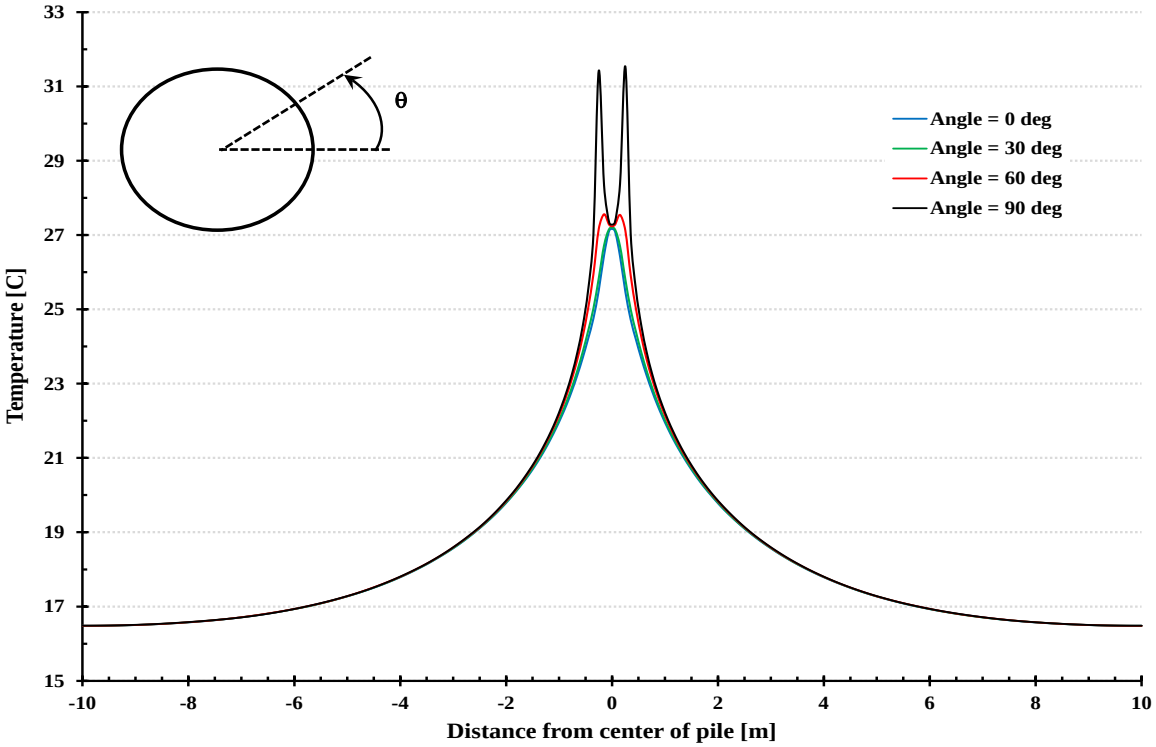

(a) Seasonal surface and initial temperature variation – Model 1

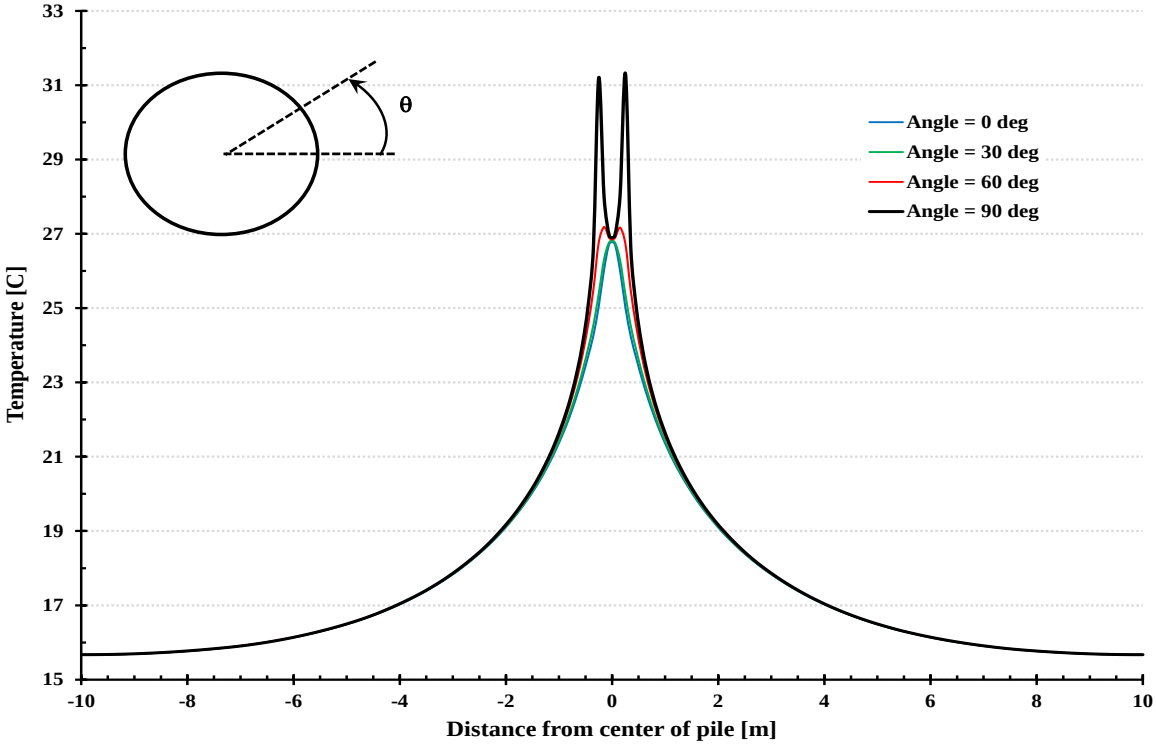

(b) Constant initial and surface temperatures – Model 2

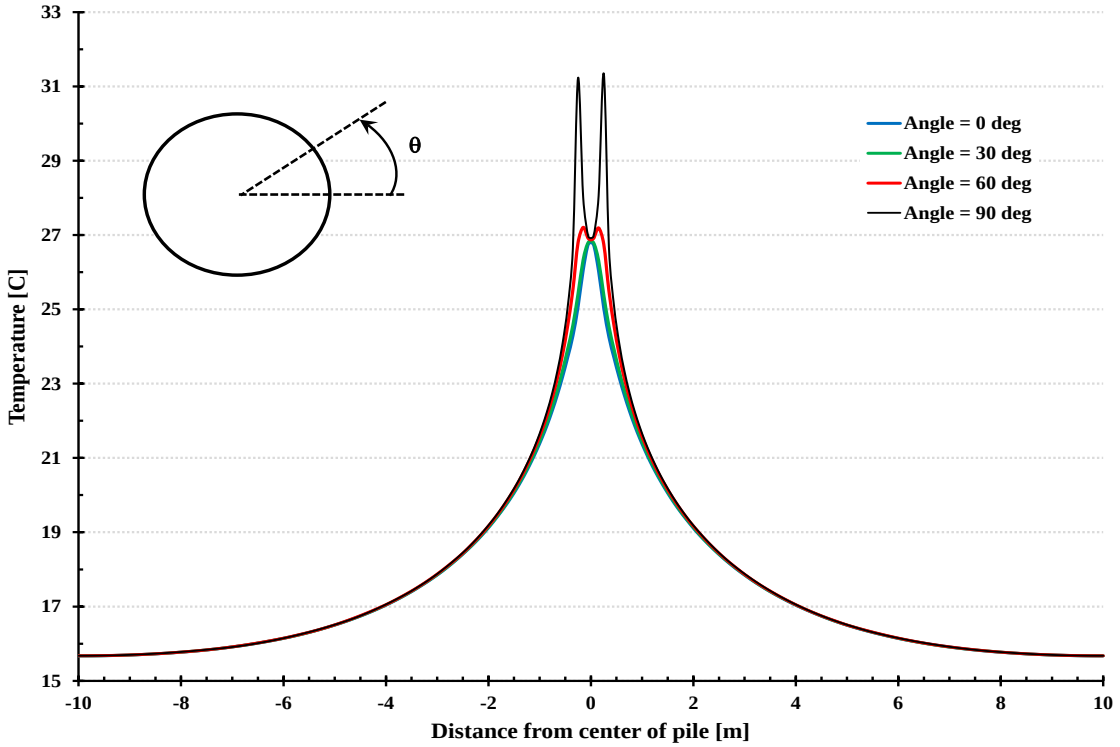

(c) Constant initial and surface insulation – Model 3

Figure 3.12. Temperature variation along the radial distance for different orientations at the mid-length of the pile by the end of the modeled month for the three considered models.

3.5.4. Effect of Pile Anisotropy

Energy Piles, as described earlier, are not a thermally isotropic material due to the effect of the longitudinal steel reinforcement. The effect of the thermal anisotropy on the general thermal performance of Energy Piles was never reported before. In this study, a finite element model using COMSOL package was performed considering the thermal anisotropy of Energy Piles. In this model, the actual value of the longitudinal thermal conductivity of the pile reported in Table 3-5 was used for the longitudinal direction while the transverse thermal conductivity was used for all the radial directions. The surface insulation model (Model 3) was selected as the base reference for the comparison.

Figure 3.13 presents the averaged temperature profile at the pile soil interface for the isotropic thermal insulation model and the anisotropic thermal insulation model. It is clear from this figure that the thermal anisotropy of Energy Piles did not have any effect of the pile thermal performance. This is also confirmed via comparing the output power of the two models which were found to be the same over the entire modeled month. Thus, it can be informed that modeling Energy Piles as thermally isotropic material is acceptable.

Furthermore, Figure 3.13 suggests that uniform temperature distribution is developed along the pile due to its thermal operation. This uniform distribution is expected to take place if the ground was homogeneous since stratified grounds produce temperature difference along the pile as presented in Chapter 3. Thus, 2-D finite element models can be used to predict the thermal performance of Energy Piles if the ground is assumed homogeneous. The details of using 2-D finite element models are presented in Chapter 7 since these models are used to examine the long term thermal performance of Energy Piles.

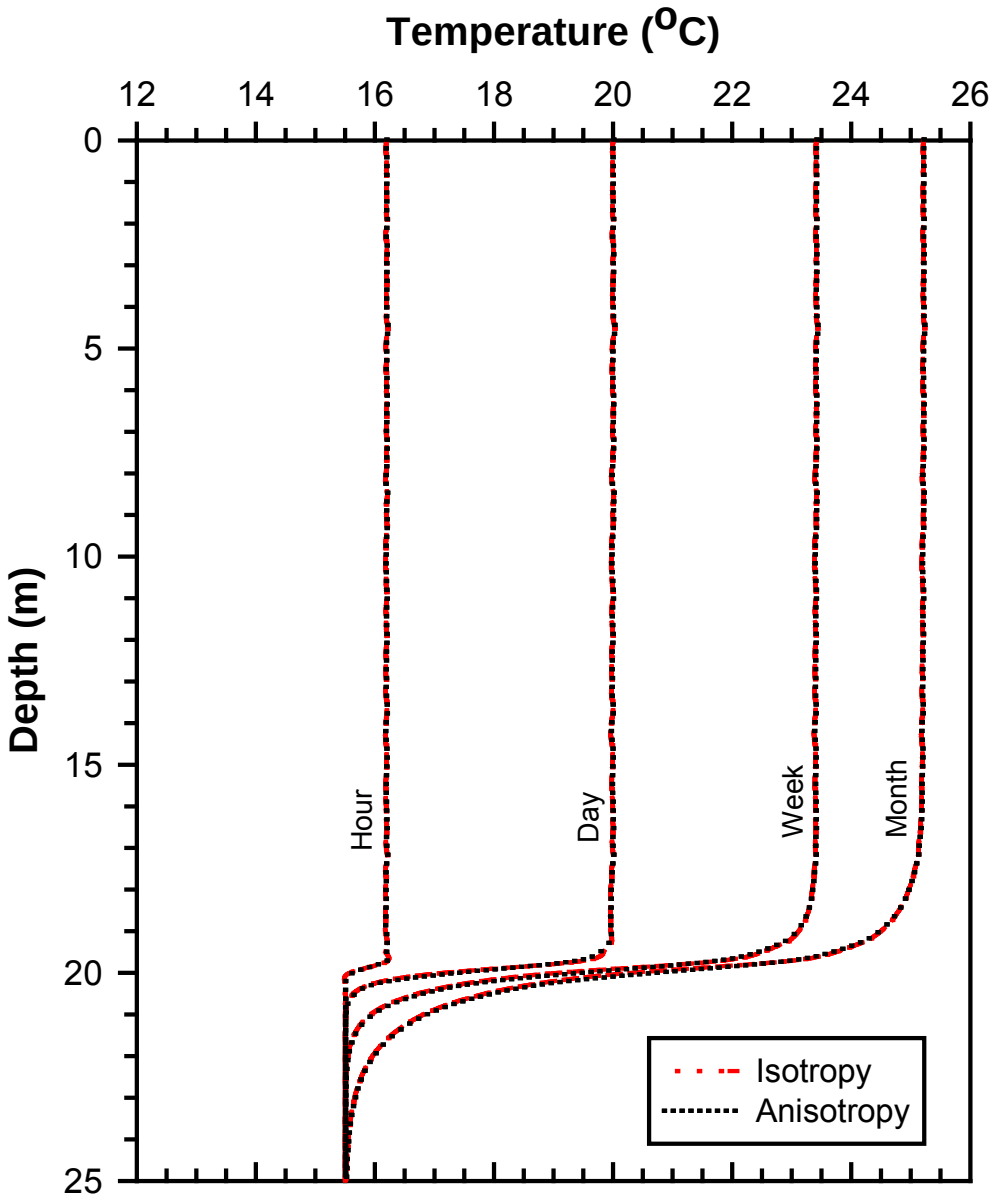

Figure 3.13. Effect of modeling Energy Piles as a thermally anisotropic material using model 3 (thermal surface insulation and constant initial temperature).

3.6. Conclusion

The results of the presented finite element models show that;

1. Accurate estimation of the thermal properties of various materials involoved in the geothermal systems is required. Laboratory and in-situ testing can be used to provide the required thermal properties. The thermal properties of these materials can be considered as temperature independent properties due to the narrow variation expected in these properties within the temperature range for geothermal applications.
2. The surface boundary conditions should be with respect to the expected actual operation of the ground heat exchanger. For instance, the actual variation of the ambient air

temperature should be considered for geothermal boreholes. While for Energy Piles underneath a well insulated building, surface insulation should be used.

3. The temperature change along the considered Energy Pile does not change significantly and thus 2D finite element models are sufficient to present the average thermal response.
4. The Anisotropy of Energy Piles due to using steel reinforcement along the pile is not of significant effect on the overall thermal performance of the pile.
5. The transverse thermal properties of the pile material control the expected performance.

References

American Society of Heating, Refrigerating, and Engineers Air-Conditioning (2009) "2009 ASHRAE handbook fundamentals." Atlanta, GA: American Society of Heating, Refrigeration and Air-Conditioning Engineers.

Austin, W. A. (1998) "Development of an in situ system for measuring ground thermal properties," Mechanical Engineering. Stillwater, Oklahoma Oklahoma State University, p 177.

Carslaw, H.S., and J.C. Jaeger (1986) Conduction of Heat in Solids: 2nd Edition, Oxford University Press, USA.

Cui, P., H. Yang, and Z. Fang (2006) "Heat transfer analysis of ground heat exchangers with inclined boreholes," Applied Thermal Engineering, Vol. 26, No. 11-12, pp 1169-1175.

Incropera, F.P. (2007) Fundamentals of heat and mass transfer, Hoboken, NJ: John Wiley.

Ingersoll, L.R., H.J. Plass, and M. Wis (1948) "Theory of the Ground Pipe Heat Source for the Heat Pump," Heating, Piping & Air Conditioning, Vol. 20, No. 7, pp 119-123.

Kavanaugh, S., and K. Rafferty (1997) Ground Source Heat Pumps: Design of Geothermal Systems for Commercial and Institutional Buildings, Atlanta, Georgia: American Society of Heating, Refrigerating, and Air-Conditioning Engineers, Inc.

Knellwolf, C., H. Peron, and L. Laloui (2011) "Geotechnical Analysis of Heat Exchanger Piles," Journal of Geotechnical and Geoenvironmental Engineering.

Kusuda, T., and P.R. Achenbach (1965) "Earth temperature and thermal diffusivity at selected stations in United States," American Society of Heating, Refrigerating and Air-Conditioning Engineers (ASHRAE) Transactions, Vol. 71, No. 1, pp 61-75.

Laloui, L., M. Nuth, and L. Vulliet (2006) "Experimental and numerical investigations of the behaviour of a heat exchanger pile," International Journal for Numerical and Analytical Methods in Geomechanics, Vol. 30, No. 8, pp 763-781.

Man, Y., H. Yang, N. Diao, J. Liu, and Z. Fang (2010) "A new model and analytical solutions for borehole and pile ground heat exchangers," International Journal of Heat and Mass Transfer, Vol. 53, No. 13-14, pp 2593-2601.

Marcotte, D., and P. Pasquier (2008) "Fast fluid and ground temperature computation for geothermal ground-loop heat exchanger systems," Geothermics, Vol. 37, No. 6, pp 651-665.

McCartney, J.S., D. LaHaise, T. Lahaise, and J. Rosenberg (2010) "Application of Geoexchange Experience to Geothermal Foundations," In: M. Hussein, W. Camp, and J. Anderson, Eds., The

Art of Foundation Engineering Practice: ASCE Geotechnical Special Publication, No. 198, pp 411-422.

Munson, B.R., D.F. Young, and T.H. Okiishi (2002) Fundamentals of fluid mechanics, New York: Wiley.

Siegenthaler, J. (2010) "It all adds up: Tracking energy flows in a ground-source heat pump.," Plumbing and Mechanical, p 6.

Zeng, H., N. Diao, and Z. Fang (2003) "Heat transfer analysis of boreholes in vertical ground heat exchangers," International Journal of Heat and Mass Transfer, Vol. 46, No. 23, pp 4467-4481.

CHAPTER 4. MULTILAYER FINITE LINE SOURCE MODEL FOR VERTICAL HEAT EXCHANGERS

4.1. Abstract

This paper introduces a finite line source model for vertical heat exchangers considering a layered soil profile. The existing analytical models assume a homogeneous soil profile, where the thermal properties of the ground along the entire length of the heat exchanger are uniform. This assumption can yield unreliable results since the typical length of heat exchangers is 60-100 meters (200-300 feet) and stratified ground is expected over this length. In the approach presented herein, the heat exchanger is divided into a number of segments to represent various soil layers along its length. Heat exchange induced temperature change at a certain location within the soil formation is obtained by summing up the individual contributions of all these segments. The effect of the heat exchanger segment within the soil layer around itself is estimated using the finite line source model. Furthermore, the finite line source model is applied on transformed sections for estimating the contributions of heat exchanger segments at locations outside their domains. The proposed model also incorporates two adjustments; the first accounts for the different heat rates within soil layers while the second adjustment considers the heat exchanged in the vertical direction between soil layers. Estimated results using the proposed model agree with the results obtained from a calibrated finite element analysis. The proposed procedure is promising and can also be adapted within the framework of cylindrical models.

4.2. Introduction and Background

Ground-coupled heat pump (GCHP) systems are utilized as an efficient sustainable energy technology for heating and cooling of buildings. This system consists of circulation tubes embedded horizontally or vertically in trenches or pre-drilled holes in the ground known as ground heat exchangers (GHE). The hole is backfilled with the native soil or thermally enhanced grout. The tubes are connected to a heat pump and a circulating pump at the ground surface which circulates water/antifreeze mixture in the tubes. GHEs are designed to inject or collect a certain amount of thermal energy via the circulating fluid.

The design of any heating and air conditioning system and other system components is performed by first estimating the energy demands of the building. In addition to the typical duct work design, the design of GCHP systems requires sizing of the heat pump and optimizing the heat exchanger length. The length of the heat exchanger depends mainly on the energy demands of the building, the type of the selected heat exchanger (vertical or horizontal), the thermal properties of the ground, and the undisturbed ground temperature. Therefore, the design of a GCHP system incorporates the building energy demands and heat exchange capacity of the ground. Estimating the building energy demands has been investigated by numerous researchers since early eighties (McQuiston and Spitler, 1992; Pedersen et al., 1998) and has gone through significant improvements from simplified energy analyses (day hours, and bin method) to

detailed building energy simulations (ASHRAE, 2009; Pedersen et al., 1998). Thus, the available techniques to estimate the building energy demands are considered adequate. On the other hand, the available analytical methods (line and cylindrical source models) related to modeling the heat exchange behavior in the ground are still constrained by several simplifying assumptions and uncertainties. One of these constraints is the homogeneous soil profile assumption (Carslaw and Jaeger, 1986; Ingersoll et al., 1948).

The design of GHE involves two sets of analyses, one concerned with the domain inside the heat exchanger (tubes, infill material, fluid) and the other with the domain outside the heat exchanger (surrounding ground). The former analysis aims to estimate the fluid temperature along the length of the heat exchanger considering the short circuit taking place due to the interaction between the two legs of the tubes (Zeng et al., 2003). The temperature at GHE/ground interface is used as a boundary condition for estimating the fluid temperature profile (Zeng et al., 2003). The interface temperature at any time is estimated from the latter analysis for the ground temperature outside the GHE. The fluid temperature is estimated by adding the heat loss taking place inside the GHE to the interface temperature assuming that the heat exchange inside the GHE has reached to its steady state condition which is represented by the borehole thermal resistance. The borehole thermal resistance is assessed by considering a series of thermal resistances including the convective resistance between the fluid and the inner tube surface, the conductive resistance of the tube walls, short circuit effect between down and up legs of the tubes, as well as the conductive resistance of the borehole backfill material (Man et al., 2010).

Different analytical models have been developed to simulate the heat conduction in the soil outside the GHE assuming no heat convection due to ground water flow. The infinite line source (ILS) model was developed by Ingersoll and Plass (1948) to estimate the temperature changes in an infinite homogeneous medium due to an infinite line GHE. A few years later, Ingersoll et al. (1954) proposed the infinite cylindrical source (ICS) model accounting for the cylindrical nature of the GHE. Then, the finite line source (FLS) model was proposed by Eskilson (1987) which considers the end effects of the heat exchanger. Lamarche and Beauchamp (2007) suggested improvements to the solution of the FLS method to decrease computational burden. Zeng et al. (2002) also used this model to study the long-term thermal behavior of geothermal vertical GHEs. Lee and Lam (2007) proposed a three-dimensional numerical model for ground GHEs, and compared their results to those obtained by the FLS and ICS models. Marcotte and Pasquier (2008) devised a computationally efficient method for the hourly temperature calculation with the FLS model. Furthermore, Marcotte and Pasquier (2009) used the FLS model to evaluate the influence of borehole inclination on the performance of a GHE system.

All of the above models are based on several simplifying assumptions including; (1) Homogeneous soil profile with temperature independent thermo-physical properties, (2) Uniform initial ground temperature, (3) Constant heat rate per unit length over the system operational period, and (4) No heat convection due of the ground water flow.

Numerous efforts have been reported to overcome the limitations associated with these simplifications. For instance, Bandos et al. (2009) developed an analytical FLS model accounting for the effects of the geothermal gradient and of the temperature changes at the soil surface. Carslaw and Jaeger (1959) and Sutton et al. (2003) proposed a moving line-source model to account for the convection effects due to ground water flow. Also, Weibo et al. (2009) showed that the concept of superposition can be used to account for varying heat rate per unit length. These improvements help in the analysis of cases not conforming to the basic assumptions listed earlier. However, these methods assume a single homogeneous layer which may not be a realistic representation of GCHP applications. The typical length of a GHE ranges between 60 – 100 meters (200 – 300 ft). The ground over this length is not homogeneous and in fact stratified ground with different thermal properties is expected. The overall thermal performance of any GHE is controlled by the average thermal properties of all soils encountered along its length. Thus, assuming a single homogeneous layer having these average thermal properties is an acceptable simplification for GHE applications.

The latest generation of heat exchangers is the use of deep foundations (piles and drilled shafts) to serve as vertical GHEs, known generally as energy piles. Piles are used mainly to transfer structural loads from a building to deep stiffer soils/rocks. These concrete elements are integrated with embedded circulation tubes so that they can operate as heat exchangers in addition to their structural support functionality. This dual function of energy piles reduces the initial cost of having two different systems.

The geotechnical design of pile foundations is based on estimating the ultimate shear resistance along the pile shaft (shaft resistance) and the ultimate bearing resistance at the pile toe (toe resistance). These shaft and toe resistances depend on the strength and stiffness of the soils in which the pile is embedded. The total shaft resistance is estimated by summing the shaft resistances from different soil layers along the pile length. Therefore, the mechanical properties of different soil layers should be known for the completion of the geotechnical design. Mitchell (1969) showed that the soil temperature affects the mechanical properties of soils and that most soils can potentially lose strength and become weaker under elevated temperatures. Thus, it is required to estimate the expected temperature change caused by the thermal operation of energy piles for each soil layer along the shaft so that temperature effects on mechanical properties can be incorporated in the geotechnical design process.

The use of a thermal analytical model which is based on the assumption of a homogeneous medium (ILS, FLS, or ICS) causes an underestimation or an overestimation of the temperature changes within different soil layers depending on the respective thermal properties of these layers. For underestimated temperature change, overestimated soil strength will be used in the geotechnical design producing unsafe foundation elements, while overestimating the temperature change will cause an overdesigned and uneconomical foundation system. One way to obtain accurate temperature changes in a stratified soil profile is to use numerical models such as finite element or finite difference analysis. These analyses are expensive and time consuming. Another

way is to develop a simple analytical model that accounts for a layered ground profile. This paper intends to relax the assumption of the homogenous medium for the finite line source model, one of the commonly used analytical models. A layered soil profile analysis will help in better approximations of the system performance and thus more reliable and optimized systems can be designed. The technique presented in this paper can be easily extended to the cylindrical source model, which will increase the accuracy of the predicted performance.

4.3. Line Source Models

The line source model is a direct application of Lord Kelvin's heat source model to ground heat exchangers (Kelvin, 1880). This model relies on the principle of superposition where a line can be treated as a combination of sequentially positioned points. Thus, it starts with calculating the temperature change at specific location in an infinite homogeneous medium based on the formula of point heat source, then using integration along a line to account for the effect of other point sources at that location of interest. The model is called infinite line source model (ILS) when the integral of the point source formula is performed on a line with an infinite length. When a line with a finite length is considered, the model is called finite line source model (FLS), which is used to account for the end effects of ground heat exchangers.

4.4. Infinite Line Source Model

Ingersoll and Plass (1948) showed that the temperature change at a distance *r* from a point heat-source emitting instantaneously $\boldsymbol{q'}$ units of heat at a time τ can be calculated as follows;

$$\Delta \boldsymbol{T} = \left(\frac{\boldsymbol{q'\alpha}}{\boldsymbol{k}}\right)\left(\frac{\boldsymbol{1}}{\boldsymbol{2\sqrt{\pi\alpha\tau}}}\right)^{\boldsymbol{3}} \boldsymbol{e^{-\rho^2/4\alpha\tau}} \qquad \textbf{Eq. 4-1}$$

Where;

α : thermal diffusivity of the soil,

k : thermal conductivity of the soil,

τ : time,

ρ : distance between the point source and the location of interest.

Integrating Eq. 3-1 over distance extending from negative infinity to positive infinity and considering the heat rate is applied over a time period (*t*), then the infinite line source model becomes:

$$\Delta \boldsymbol{T} = \frac{\boldsymbol{q'}}{\boldsymbol{2\pi k}} \int_{\boldsymbol{\beta}}^{\infty} \frac{\boldsymbol{e^{-\beta^2}}}{\boldsymbol{\beta}} . \boldsymbol{d\beta} \qquad \textbf{Eq. 4-2}$$

Where $\beta = r/2\sqrt{\alpha\tau}$

4.5. Finite Line Source Model

For this model, the integration of Eq. 3-1 is performed over the limited length of the heat exchanger. The end effect of the GHE at the ground surface is included in the FLS model by considering an imaginary line source which is obtained by mirroring the original source around the ground surface plane. This imaginary source is identical to the real source, except that it has an opposite heat rate that cancels the effect of the heat exchanger ensuring that no temperature change takes place at the ground surface. Thus, the null temperature change at the ground surface has become one of the main cornerstones of the FLS model.

The FLS model can easily be derived by integrating Eq. 3-1 over the length of the heat exchanger and including the identical yet opposite imaginary source. The final form of the FLS model equation is;

$$\Delta \boldsymbol{T} = \left(\frac{\boldsymbol{q'}}{\boldsymbol{4\pi k}}\right) \int_{\boldsymbol{0}}^{\boldsymbol{H}} \left\{ \frac{\left[\mathrm{erfc}\left(\frac{\boldsymbol{\rho}}{\boldsymbol{2\sqrt{\alpha t}}}\right)\right]}{\boldsymbol{\rho}} - \frac{\left[\mathrm{erfc}\left(\frac{\boldsymbol{\rho'}}{\boldsymbol{2\sqrt{\alpha t}}}\right)\right]}{\boldsymbol{\rho'}} \right\} . \boldsymbol{d\rho} \qquad \text{Eq. 4-3}$$

Where, ρ and ρ' are the distances from the actual and imaginary sources to the point of concern, respectively. H is the finite length of the heat exchanger.

4.6. Multilayer Finite Line Source Model

As mentioned earlier both ILS and FLS models assume a single homogeneous layer, which is not the case for the real applications of GCHP systems, and energy piles. This section presents an improvement to the finite line source model with which the temperature change in layered soil profiles can be approximated. This improvement can be accompanied with other modifications to have a more generalized model.

4.6.1. Main Concept

The proposed model is based on dividing the GHE into a number of segments each distinctly embedded in a single soil layer. Thus, the number of GHE segments is equal to the number of soil layers along its length. The superposition concept is utilized to estimate the change in temperature at a specific point in the soil formation by adding the contributions of all GHE segments at that location.

The finite line source model presented in Eq. 3-3 can be used only when the top of the heat exchanger is at the ground surface. When the GHE is divided into segments, a more general form of Eq. 3-3 is needed for each segment embedded below ground surface. This generalized form was proposed by Marcotte and Pasquier (2009) who developed it to account for an inclined finite line source and for cases when the top of the GHE is located below the ground surface. This generalized equation is presented as follows (Marcotte and Pasquier, 2009):

$$\Delta \boldsymbol{T}(\boldsymbol{p_0}, \boldsymbol{t}) = \left(\frac{\boldsymbol{q'}}{\boldsymbol{4\pi k}}\right) \left(\int_{\boldsymbol{p_1}}^{\boldsymbol{p_2}} \frac{\mathrm{erfc}\left\{\frac{\boldsymbol{d(\delta, p_0)}}{\boldsymbol{2\sqrt{\alpha t}}}\right\}}{\boldsymbol{d(\delta, p_0)}} \boldsymbol{d\delta} - \int_{\boldsymbol{p_1'}}^{\boldsymbol{p_2'}} \frac{\mathrm{erfc}\left\{\frac{\boldsymbol{d(\delta', p_0)}}{\boldsymbol{2\sqrt{\alpha t}}}\right\}}{\boldsymbol{d(\delta', p_0)}} \boldsymbol{d\delta'} \right) \qquad \text{Eq. 4-4}$$

Where;

δ, δ' : integration variables ($\delta = [x, y, z]$, and $\delta' = [x', y', z']$)

p_0 : coordinates of the point being considered (x_o, y_o, z_o)

p_1, p_2: coordinates of the points at the beginning and at the end of the real GHE, i.e. $p_1 = (x_1, y_1, z_1)$ and $p_2 = (x_2, y_2, z_2)$

p_1', p_2': coordinates of the points at the beginning and at the end of the imaginary GHE, i.e. $p_1' = (x_1', y_1', z_1')$ and $p_2' = (x_2', y_2', z_2')$

The first integration term in Eq. 3-4 is for the real heat source while the second is for its imaginary source. Moreover, it should be noticed that the integrations in Eq. 3-4 are for the coordinates of the GHE in the three dimensional space. For a vertical GHE which is considered here, only a two dimensional space is required and therefore points p_1, p_2, p_1', p_2' all lie on a vertical line representing the GHE. In other words; the integrations will be along the vertical axis only, i.e. $\delta = z, \delta' = z', p_1 = z_1, p_2 = z_2, p_1' = z_1',$ and $p_2' = z_2'$..

Several assumptions were made when the generalized FLS model presented in Eq. 3-4 was developed (Marcotte and Pasquier, 2009) such as, (a) uniform initial ground temperature, (b) constant ground surface temperature, (c) temperature independent thermo-physical properties of each layer, and (d) constant heat rate per unit length.

For estimating the temperature change at a point in a specific layer; (1) primary segment is defined as the GHE segment embedded within that layer; and (2) secondary segments are the GHE segments embedded in the other layers. For example, for a given point A in Table 4-1, layer 2 is the primary segment as the GHE segment embedded in, whereas GHE segments embedded in layers 1 and 3 are the secondary segments for point A.

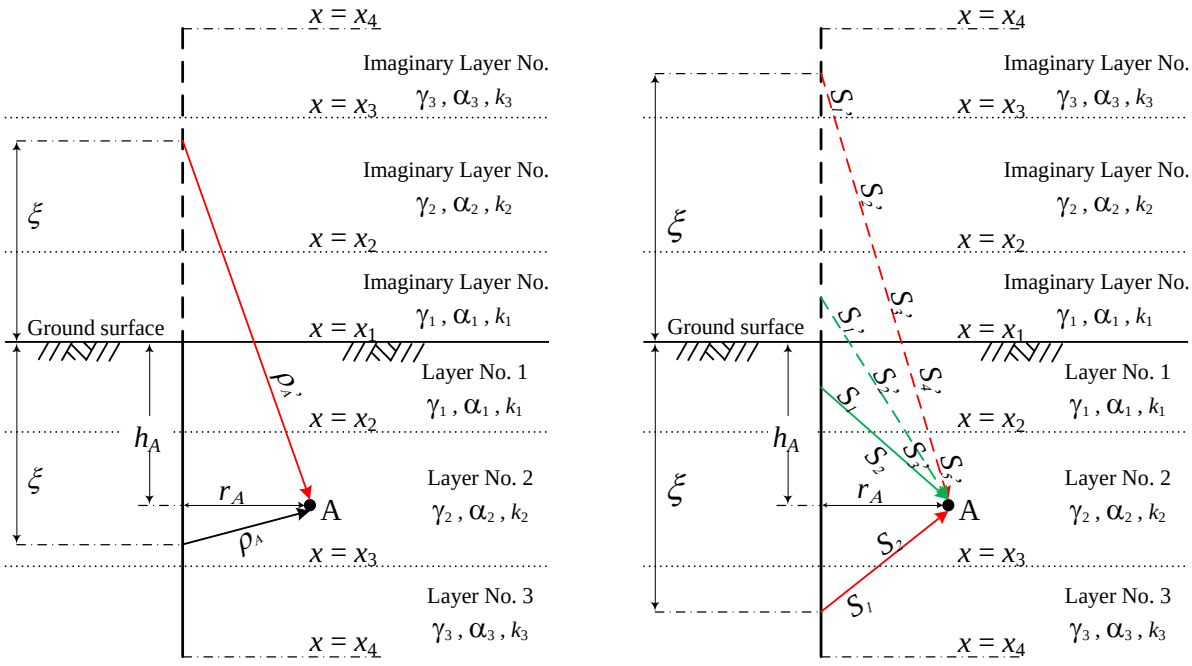

Figure 4.1. Multilayer finite line source model; (a) effect of the primary segment, and (b) effect of the secondary segments.

4.6.2. Effect of the Primary Segment

The effect of the primary segment at the point of interest is obtained using Eq. 3-4. The thermal properties of the soil layer where the primary segment is embedded are used to calculate this effect, since the energy wave will only propagate in this layer. Therefore, for point *A* in Figure 4.1-a, the effect of the primary segment can be estimated as;

$$\Delta \boldsymbol{T_{1-A}} = \left(\frac{\boldsymbol{q'}}{\boldsymbol{4\pi k_2}}\right) \int_{\boldsymbol{x_2}}^{\boldsymbol{x_3}} \left\{ \frac{\left[\operatorname{erfc}\left(\frac{\boldsymbol{\rho_A}}{\boldsymbol{2\sqrt{\alpha_2 t}}}\right)\right]}{\boldsymbol{\rho_A}} - \frac{\left[\operatorname{erfc}\left(\frac{\boldsymbol{\rho'_A}}{\boldsymbol{2\sqrt{\alpha_2 t}}}\right)\right]}{\boldsymbol{\rho'_A}} \right\} . \boldsymbol{d\rho} \qquad \text{Eq. 4-5}$$

Where $\rho_A = \sqrt{(\xi - h_A)^2 + r_A^2}$ and $\rho'_A = \sqrt{(\xi + h_A)^2 + r_A^2}$, therefore Eq. 3-5 becomes;

$$\Delta \boldsymbol{T_{1-A}} = \left(\frac{\boldsymbol{q'}}{\boldsymbol{4\pi k_2}}\right) \int_{\boldsymbol{x_2}}^{\boldsymbol{x_3}} \left\{ \frac{\left[\operatorname{erfc}\left(\frac{\sqrt{(\xi - h_A)^2 + r_A^2}}{2\sqrt{\alpha_2 t}}\right)\right]}{\sqrt{(\xi - h_A)^2 + r_A^2}} - \frac{\left[\operatorname{erfc}\left(\frac{\sqrt{(\xi + h_A)^2 + r_A^2}}{2\sqrt{\alpha_2 t}}\right)\right]}{\sqrt{(\xi + h_A)^2 + r_A^2}} \right\} . \boldsymbol{d\xi} \qquad \text{Eq. 4-6}$$

Following the same approach for other segments when they are treated as the primary contributing segment with respect to points lying within their corresponding layers, the general primary segment equation can be written as;

$$\Delta \boldsymbol{T}_{\boldsymbol{1-layer\,(j)}} = \left(\frac{\boldsymbol{q'}}{\boldsymbol{4\pi k_j}}\right) \int_{\boldsymbol{x_j}}^{\boldsymbol{x_{j+1}}} \left\{ \frac{\left[\operatorname{erfc}\left(\frac{\sqrt{(\xi-h)^2+r^2}}{2\sqrt{\alpha_j t}}\right)\right]}{\sqrt{(\xi-h)^2+r^2}} - \frac{\left[\operatorname{erfc}\left(\frac{\sqrt{(\xi+h)^2+r^2}}{2\sqrt{\alpha_j t}}\right)\right]}{\sqrt{(\xi+h)^2+r^2}} \right\} . \boldsymbol{d\xi} \qquad \text{Eq. 4-7}$$

4.6.3. Effect of Secondary Segments

The distinction between the primary segment and secondary segments has been introduced due to the fact that, for a given soil layer, the effect from the primary segment is concerned in that layer only, whereas all other segments are contributing through transformed composite paths.

(a) Composite Section Concept

The contributions of secondary segments at the point of interest are also determined with Eq. 3-4 using the thermal properties of a composite section. For each source point within a secondary segment, laws of composite materials are used to estimate the thermal properties of the composite section corresponding to that source point. Thermal properties of each layer encountered along the energy path from that specific source point towards the point of interest are used to evaluate the composite properties of the path. The three main thermal properties of interest are the density (γ), thermal conductivity (*k*), and specific heat capacity (C_p) which are transferred into a single composite section as follows;

$$\left.\begin{aligned} \boldsymbol{\gamma_{comp.}} &= \sum_{\boldsymbol{i=1}}^{\boldsymbol{N}} \frac{\boldsymbol{S_i}}{\sum_i \boldsymbol{S_i}} \boldsymbol{\gamma_i} \\ \frac{\boldsymbol{1}}{\boldsymbol{k_{comp.}}} &= \sum_{\boldsymbol{i=1}}^{\boldsymbol{N}} \frac{\left(\frac{\boldsymbol{S_i}}{\sum_i \boldsymbol{S_i}}\right)}{\boldsymbol{k_i}} \\ \boldsymbol{C_{P_{comp.}}} &= \sum_{\boldsymbol{i=1}}^{\boldsymbol{N}} \boldsymbol{C_{P_i}} \frac{\boldsymbol{M_i}}{\sum_i \boldsymbol{M_i}} = \sum_{\boldsymbol{i=1}}^{\boldsymbol{N}} \boldsymbol{C_{P_i}} \frac{\boldsymbol{S_i \gamma_i}}{\sum_i \boldsymbol{S_i \gamma_i}} \end{aligned}\right\} \qquad \text{Eq. 4-8}$$

Where;

S_i : distance that the energy wave travels in layer *i*

N : number of layers in the energy path

γ_i : density of layer *i*

k_i : thermal conductivity of layer *i*

C_{P_i} : specific heat capacity of layer *i*

M_i : mass of layer $i = V_i \gamma_i = S_i \gamma_i$

V_i : volume of layer *i* in the path of energy wave propagation

Using the thermal properties of the composite section, the composite thermal diffusivity ($\alpha_{comp.}$) can be estimated as follows;

$$\boldsymbol{\alpha_{comp.}} = \frac{\boldsymbol{k_{comp.}}}{\boldsymbol{C_{P_{comp.}}\gamma_{comp.}}} \qquad \text{Eq. 4-9}$$

(b) Mathematical Derivation

Since the collective effect of all the secondary segments is evaluated on a point by point basis, we base our derivation on the point source model. Point heat source equation mentioned in Eq. 3-1 is simplified as follows;

$$\Delta T = \left(\frac{q'\alpha}{k}\right)\left(\frac{1}{2\sqrt{\pi\alpha\tau}}\right)^3 e^{-\rho^2/4\alpha\tau} = \frac{\left(\frac{q'\alpha}{k}\right)}{8(\pi^{3/2})(\alpha^{3/2})(\tau^{3/2})}\, e^{-\rho^2/4\alpha\tau}$$

For the case of a point source operating from time $\tau = 0$ to time $\tau = t$, the above formula is integrated over that time period as follows;

$$\Delta T = \frac{\left(\frac{q'\alpha}{k}\right)}{8(\pi^{3/2})(\alpha^{3/2})}\int_0^t \left(e^{-\rho^2/4\alpha\tau}\right)\left(\tau^{-3/2}\right).d\tau$$

Let $\beta = \rho/2\sqrt{\alpha\tau}$, thus $\Delta T = \left(\frac{q'}{4\pi k\rho}\right)\left(\frac{2}{\sqrt{\pi}}\right)\int_\beta^\infty \left(e^{-\beta^2}\right).d\beta$

Since $\left(\frac{2}{\sqrt{\pi}}\right)\int_\beta^\infty \left(e^{-\beta^2}\right).d\beta = \text{erfc}(\beta) = \text{erfc}\left(\frac{\rho}{2\sqrt{\alpha t}}\right)$, thus the equation becomes:

$$\boldsymbol{\Delta T} = \left(\frac{\boldsymbol{q'}}{\boldsymbol{4\pi k\rho}}\right)\text{erfc}\left(\frac{\boldsymbol{\rho}}{\boldsymbol{2\sqrt{\alpha t}}}\right) \qquad \text{Eq. 4-10}$$

When the thermal properties of various composite sections corresponding to each point in a secondary segment and the finite length of the segment are considered, Eq. 3-10 should be integrated over the length of the real source segment and its imaginary source as follows;

$$\boldsymbol{\Delta T_{2-ij}} = \frac{\boldsymbol{q'}}{\boldsymbol{4\pi}}\int_{x_i}^{x_{i+1}}\left\{\left[\left(\frac{\boldsymbol{1}}{\boldsymbol{k_{comp.}\rho}}\right)\text{erfc}\left(\frac{\boldsymbol{\rho}}{\boldsymbol{2\sqrt{\alpha_{comp.}t}}}\right)\cdot\boldsymbol{d\rho}\right] - \left[\left(\frac{\boldsymbol{1}}{\boldsymbol{k'_{comp.}\rho'}}\right)\text{erfc}\left(\frac{\boldsymbol{\rho'}}{\boldsymbol{2\sqrt{\alpha'_{comp.}t}}}\right)\cdot\boldsymbol{d\rho'}\right]\right\}$$

Eq. 4-11

Where;

ΔT_{2-ij}: is the temperature change due to secondary segment embedded in layer (*i*) at a point located in the main layer (*j*)

$\rho = \sum_{i=1}^{N} S_i$ and $\rho' = \sum_{i=1}^{N} S'_i$

Figure 4.1.b shows an example of the effect of secondary segments on layers 1 and 3 at point (*A*) located within layer 2. The distances (*S* and *S'*) can easily be calculated using trigonometry. Thus, the effect of all secondary segments can be obtained as follows;

$$\Delta \boldsymbol{T}_{\mathbf{2-layer}\ j} = \sum_{i=1}^{N} \left(\frac{q'}{4\pi}\right) \int_{x_i}^{x_{i+1}} \left\{ \left(\frac{1}{k_{comp.}\rho}\right) \operatorname{erfc}\left(\frac{\rho}{2\sqrt{\alpha_{comp.}t}}\right) \cdot \boldsymbol{d\rho} - \left(\frac{1}{k'_{comp.}\rho'}\right) \operatorname{erfc}\left(\frac{\rho'}{2\sqrt{\alpha'_{comp.}t}}\right) \cdot \boldsymbol{d\rho'} \right\}$$

Eq. 4-12

Where;

N : Number of secondary segments = total number of layers – 1

The total temperature change at a specific point is then estimated by adding that of the primary segment (ΔT_1) and effects of secondary segments (ΔT_2) as follows;

$$\Delta \boldsymbol{T} = \Delta \boldsymbol{T_1} + \Delta \boldsymbol{T_2}$$ Eq. 4-13

4.6.4. Effect of Layer-Dependent Heat Rate

The analytical models discussed above and the one presented herein utilize the heat rate at the face of the GHE to estimate temperatures at a distance from the GHE face. The heat rate per unit length (q') is expected to vary from one layer to another due to differences in the thermal properties of these layers. Therefore, it is critical to realistically estimate the variation of heat rate at different soil layers within the profile.

The rate of heat exchange at the GHE-soil interface is affected by the thermal properties of the soil layer at that specific location as well as the heat transfer processes within the GHE. Heat energy is transmitted through the circulation fluid to the borehole loop and through the grout it reaches the GHE-soil interface. Properties of the elements within GHE such as the borehole loop and the grout are uniform along its length. Therefore, the thermal processes within the GHE are expected to result in a uniform heat emanation at different depths. Heat conduction beyond the face of the GHE would be controlled by the respective thermal properties of each layer. Therefore, we developed an approach to estimate the layer dependent heat rate based on the weighted distribution using the respective thermal properties as well as the near-uniform distribution along the length of the GHE.

The ground temperature change using infinite line source (ILS) model is estimated by integrating the point heat source equation over an infinite length followed by another integral over the operation time of the system. The first integral of the point source model over the infinite length presented in Eq. 3-14 shows that at the source (at *r*=0) the heat rate is only related to the thermal conductivity of the medium and the expected temperature change. This suggests that thermal conductivity of any layer is the thermal property controlling the temperature increase and the heat rate from that layer at the GHE-soil interface.

$$\Delta T = \int_{-\infty}^{\infty} \left(\frac{q'\alpha}{k}\right)\left(\frac{1}{2\sqrt{\pi\alpha\tau}}\right)^3 e^{-(r^2+z^2)/4\alpha\tau}\,.\,dz = \frac{q'}{4\pi k\tau}\, e^{-r^2/4\alpha\tau} \qquad \text{Eq. 4-14.a}$$

Thus, at the source *r=0* then:

$$q' = 4\pi k\tau\Delta T \qquad \text{Eq. 3-14.b}$$

Different soil layers with varying thermal properties are encountered outside the borehole domain whereas the material properties are uniform within the GHE. Therefore, the varying heat rate between soil layers is accounted for using the expression;

$$q_i' = \frac{1}{2}\Big(\underbrace{q'}_{\text{Uniform inside GHE}} + \underbrace{\frac{k_i Q}{\sum_{i=1}^{m}(k_i L_i)}}_{\text{Limiting layer dependent outside GHE}} \Big) = \frac{q'}{2}\left(1 + k_i \frac{\sum_{i=1}^{m} L_i}{\sum_{i=1}^{m}(k_i L_i)}\right) \qquad \text{Eq. 4-15}$$

where;

q_i' : layer dependent heat rate per unit length for layer *i*

q' : average heat rate per unit length of heat exchanger

Q: total heat rate = $q' \sum_{i=1}^{m} L_i$

m : number of ground layers.

This expression essentially averages the expected uniform heat rate inside the GHE and the weighted heat rate distribution because of the different soil layers around the GHE. The first term in the right hand side of Eq. 3-15 is used to account for the constant uniform heat rate inside the borehole domain; while the second reflects the effect of the outside varying soil layers on the layer ability to exchange heat. Validity of this empirical expression is discussed in the following sections, where the results of the numerical analyses are presented.

4.6.5. Interlayer Heat Exchange Adjustment

The formulation presented above only considers heat conduction in the radial direction due to GHE operation and ignores the heat transfer between various soil layers due to internal gradients in the vertical direction. For this reason, we are introducing the interlayer adjustment, which is based on heat conduction analysis within a two-layer composite section due to the temperature gradient near the interface of two layers.

A two-layer composite section is used to account for the heat exchanged between different soil formations in the vertical direction. This composite section considers the transition zone near the interface between soil formations. The thickness of each layer forming the composite section is bounded by the interface between the considered soil formations and the depth at

which the transition zone starts in the layer of interest. To estimate this depth; the layer dependent heat rates obtained from Eq. 3-15 are used in Eq. 3-7, and Eq. 3-12 to develop a preliminary temperature change profile at a given radial distance from the GHE. The beginning of the transition zone in the considered layer is determined using this preliminary temperature profile as the depth at which the temperature change within the soil layer starts to deviate 5% from the mid-layer temperature change.

The final temperatures at the boundaries of the composite section (i.e. beginning of the transition zone in each soil formation) are equal to the initial ground temperature plus the temperature change estimated using the preliminary analysis. The solution for heat conduction through a two-layer composite section given constant surface temperatures was provided by Carslaw and Jaeger (1959). This solution is based on estimating the effective thermal resistance of the section (*R*), which is given as follows;

$$\boldsymbol{R} = \frac{\boldsymbol{LT_{upper}}}{\boldsymbol{k_{upper}}} + \frac{\boldsymbol{LT_{lower}}}{\boldsymbol{k_{lower}}} \qquad \text{Eq. 4-16}$$

Where LT_{upper}, and LT_{lower} are the thicknesses of transition zones in the upper and the lower soil formations, respectively. Also, k_{upper}, and k_{lower} are the thermal conductivities of the upper and lower soil layers, respectively. Using the effective thermal resistance (*R*), the heat flux through the composite section (q_z) can then be estimated as follows;

$$\boldsymbol{q_z} = -(\boldsymbol{T_{lower}} - \boldsymbol{T_{upper}})/\boldsymbol{R} \qquad \text{Eq. 4-17}$$

Where T_{lower} is the temperature of the external surface at the lower bounding depth, and T_{upper} is the temperature of the external surface at the upper bounding depth.

Assuming that there is no contact resistance between the two layers of the composite section and there is no generated or dissipated heat within these layers, the heat flux (q_z) along the whole composite section is constant. The heat flux through the upper and the lower layers can be estimated as follows;

$$\left.\begin{aligned} \boldsymbol{q_z} = \boldsymbol{q_{upper}} &= -(\boldsymbol{T_{interface}} - \boldsymbol{T_{upper}})\frac{\boldsymbol{k_{upper}}}{\boldsymbol{LT_{upper}}} \\ \boldsymbol{q_z} = \boldsymbol{q_{lower}} &= -(\boldsymbol{T_{lower}} - \boldsymbol{T_{interface}})\frac{\boldsymbol{k_{lower}}}{\boldsymbol{LT_{lower}}} \end{aligned}\right\} \qquad \text{Eq. 4-18}$$

Using any one of the formulas presented in Eq. 3-18, the interface temperature ($T_{interface}$) and consequently the temperature change at the interface ($\Delta T_{interface}$) can be estimated. The smooth variation of the temperature change in the transition zone was performed by fitting exponential functions.

It should be noticed that, the procedure used for the interlayer heat exchange effect utilizes the steady state solution for heat exchange in a two-layer composite section with known surface temperatures. However, the surface temperatures used in that analysis are obtained from a

transient analysis using the proposed multilayer FLS model. Thus, the steady state solution is used in a transient framework making it reliable to provide the transition between different layers at different times.

4.7. Model Validation

The validation of the proposed multilayer FLS model, the layer-dependent heat rate adjustment, and the adjustment for interlayer heat exchange is performed by comparing the results of this proposed analytical model to the results of a finite element (FE) analysis for identical soil stratifications.

A ground stratification consisting of two soil formations is used to validate the proposed analytical model. These two soil layers are a saturated clay formation on top of a saturated sand formation. The clay formation extends from the ground surface to a depth of 10 m (32.8 ft) at which the sand formation starts and extends till the end of the ground profile. Figure 4.2 shows the ground stratification used in the model validation. The total length of the heat exchanger is 20 m (65.6 f) with its head located at the ground surface. This heat exchanger length is selected to represent a typical energy pile, an application behind the motivation to develop such a multilayer FLS model.

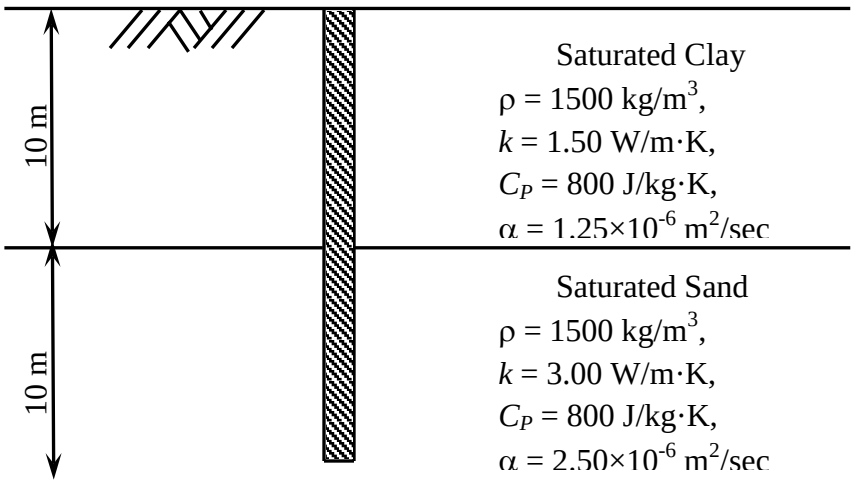

Figure 4.2. Soil stratification for the example used in the model validation.

The FE analysis was performed using COMSOL Multiphysics v4.2a (2011). The total heat exchange rate is 2900 W (9895 Btu/hr) with an average heat rate per unit length of 145 W/m. The heating of the carrier fluid was simulated by maintaining a constant temperature difference between the inlet and the outlet of the tubes. The heat rate per unit length was selected to be higher than typical heat rates used in GCHP applications (50-80 W/m) in order to have a wider zone of influence around the heat exchanger, while maintaining a reasonable simulation time. The FE model was calibrated using the finite line source (FLS) model for a one-layer system and

the calibration results were presented in Chapter 3 as well as Abdelaziz et al. (2011), and Olgun et al. (2010).

Initially, the proposed formula for the layer dependent heat rate given in Eq. 3-15 is validated by comparing it with the heat rate in each layer obtained from the FE model as shown in Figure 4.3. Figure 4.3 also shows that the proposed formulation for the layer dependent heat rate agrees with the FE results.

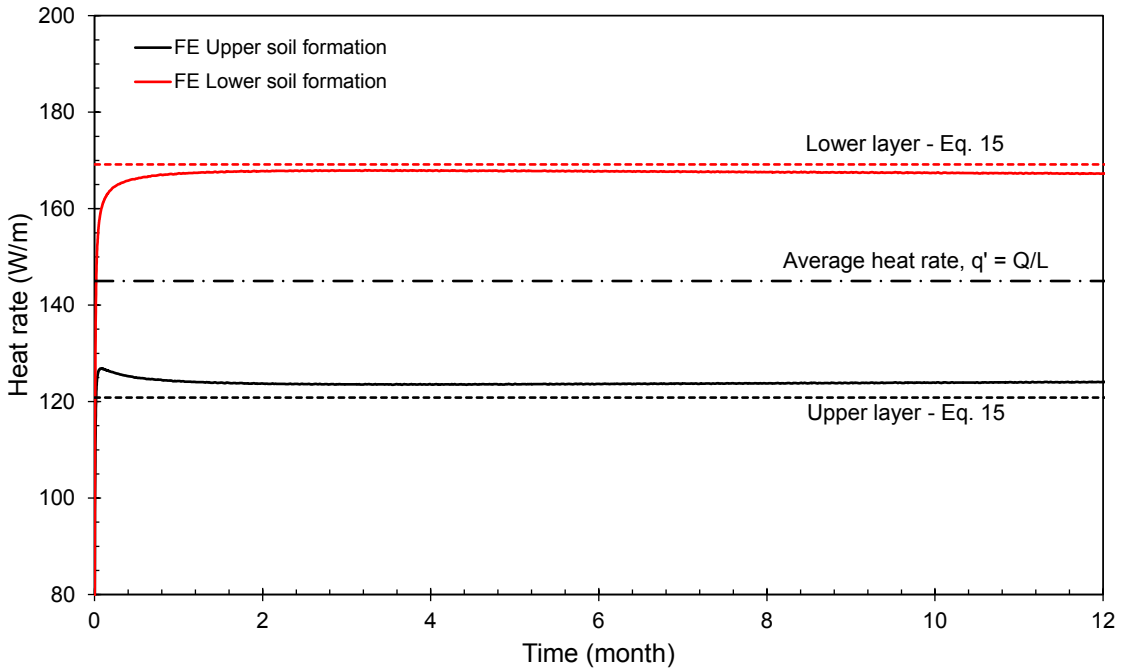

Figure 4.3. Validation of the proposed layer dependent heat rate formula (Eq. 3-15).

The results of the FE model and the proposed analytical model were compared at three different locations (GHE/soil interface, 0.5 m (1.6 ft) away from the interface, and 2.5 m (8.2 ft) away from the interface) for three time periods; 1 day, 1 week, and 1 month. The comparison of the results are presented in Figure 4.4. It can be seen in this figure that the temperature change profiles estimated using the proposed multilayer FLS model agree well with the finite element results for all time-distance combinations.

Figure 4.5 shows the radial temperature change profiles starting from the heat exchanger interface at the mid-layer depths of each formation for different times; 1 day, 1 week, and 1 month estimated using the proposed multilayer FLS model and finite element analysis. The radial profiles presented in this figure show that the model was successfully able to predict the temperature change for any time-distance combination.

It is noticed from Figure 4.4 that for the example used here, the temperature change in the upper layer is higher than that in the lower layer at the interface for 1 day, 1 week, and 1 month and at 0.5 m (1.6 ft) away for 1 week, and 1 month. For all times at 2.5 m (8.2 ft) away from the

interface and for 1 day at 0.5m (1.6 ft) away from the interface, this behavior is reversed. To physically explain this change in behavior, the thermal conductivities of the two formations are used. The lower formation has a thermal conductivity higher than the upper formation. This indicates a smaller thermal resistance of the lower formation compared to a higher thermal resistance of the upper formation. Thus, a wider zone of thermal influence is expected in the lower formation for a given operational period, which can be seen in Figure 4.5 for all considered operational periods. Moreover, higher ultimate temperature changes (at distance = 0m) are expected in layers with higher thermal resistance which is also seen in Figure 4.5 as a higher temperature change at distance = 0m in the upper formation. Therefore, the response is reversed at a certain distance for a given operational period, which is seen in the temperature change profiles presented in Figure 4.4.

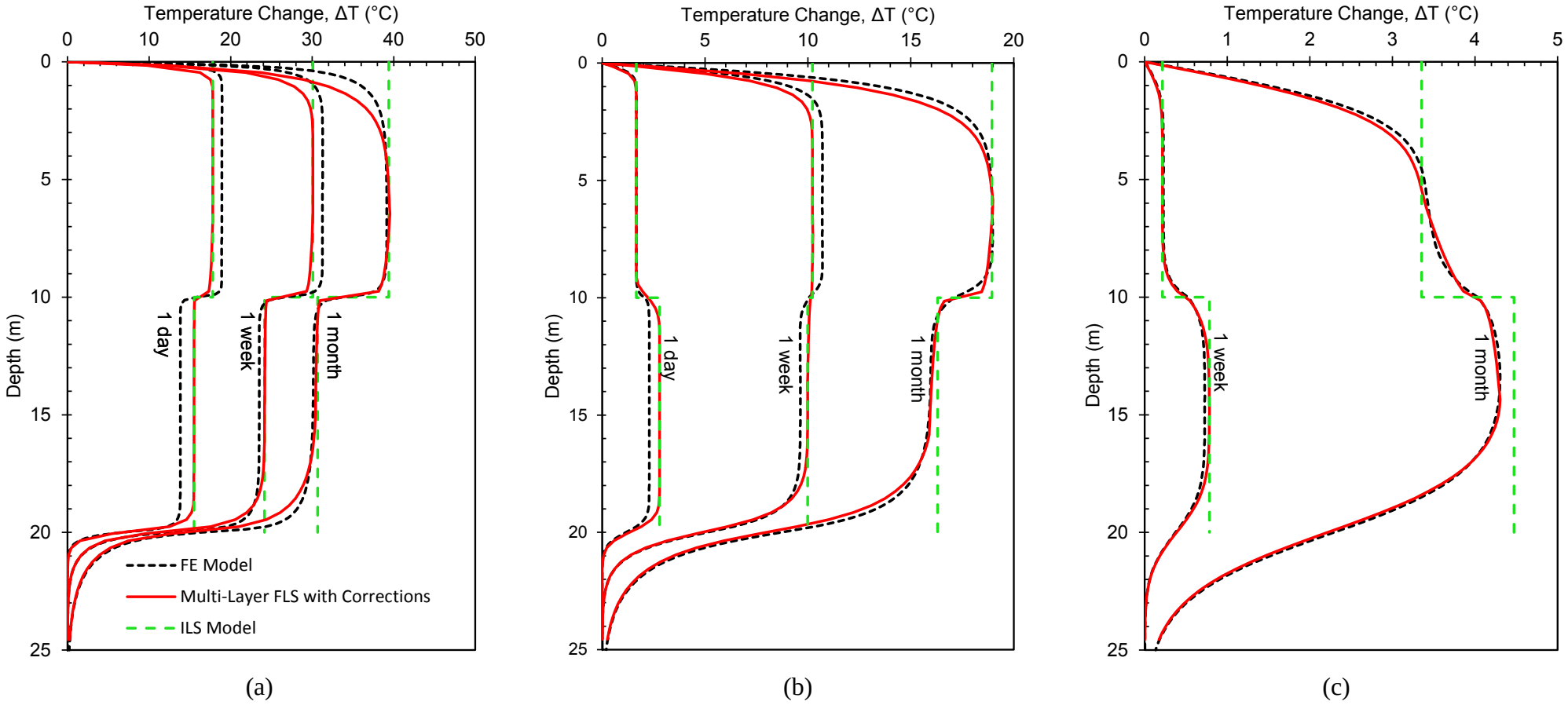

Figure 4.4. Temperature change at different times for the example used in the model validation using finite element model (FE), Multilayer FLS model with all adjustments, and infinite line source (ILS) model with the heat rate adjustment at; (a) interface of heat exchanger and the soil, (b) 0.5m away from the interface, and (c) 2.5m away from the interface.

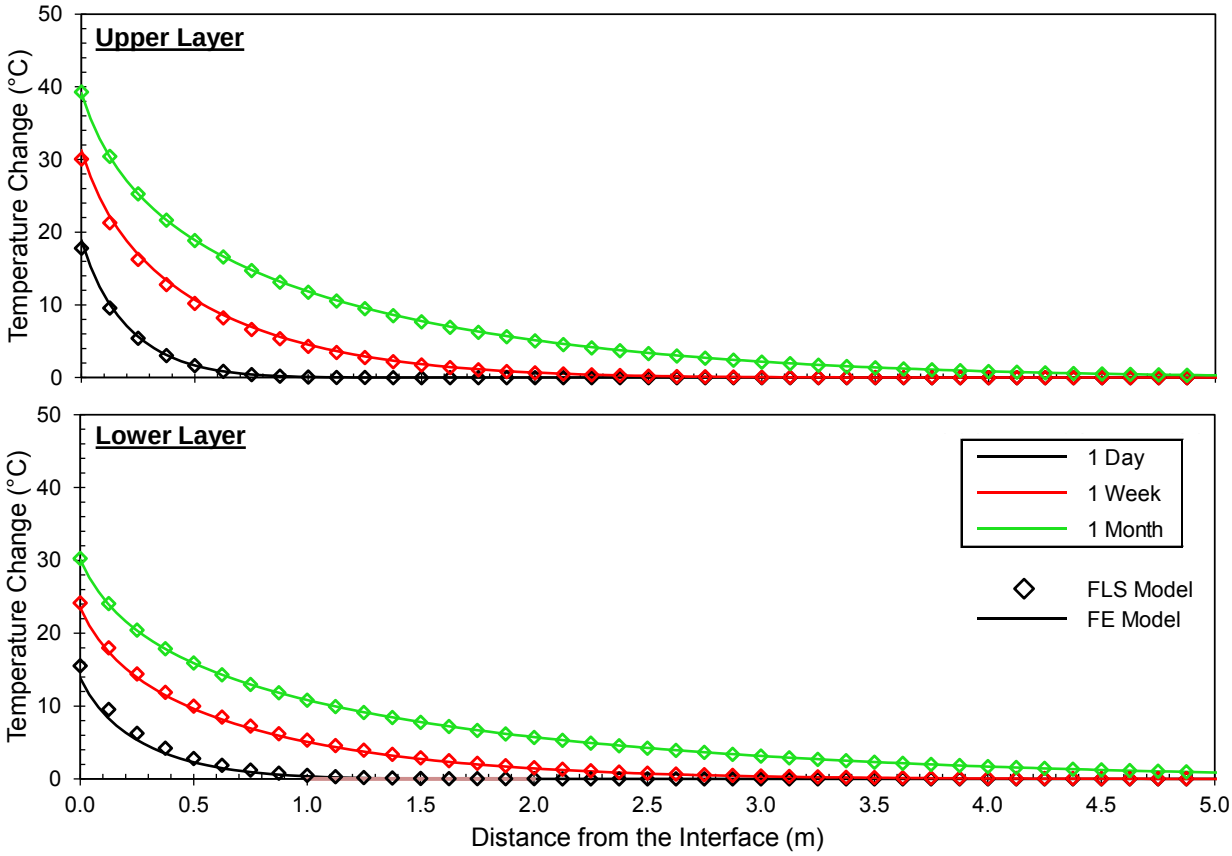

Figure 4.5. Temperature change for the example used in model validation at the center of the upper and the lower soil layers versus radial distance from the heat exchanger interface using the proposed multilayer FLS model and finite element model.

4.8. Model Generalization

The FLS model is intended to be applicable for any ground stratification. Thus, the generality of the model is examined by comparing the temperature changes estimated using the proposed model with the temperature changes from finite element analyses considering a series of ground conditions.

The thermal properties of the two formations in the example used in the model validation were varied such that they cover a wide range of soils and rocks. The thermal conductivity of the upper formation was varied between 0.5 to 1.5 W/m·℃ (0.289-0.867 Btu/hr·ft·°F), while that for the lower formation was varied between 0.5 to 8.0 W/m·℃ (0.289-4.622 Btu/hr·ft·°F). The lower formation was selected to have a wider range for the thermal conductivity than the upper formation because a rock formation can exist underneath a soil formation. The density and the heat capacity of the two formations were also varied in accordance to the assumed soil such that they provide a variation in the thermal diffusivity ranging from 3.0×10^{-7} to 1.7×10^{-6} m^2/sec (0.01-

0.0057 ft^2/hr). Table 4-1 presents the considered thermal properties for the two formations in the thirty-two analyses used to explore the generality of the proposed multilayer FLS model.

The finite element analysis was repeated for each soil/rock combination with different thermal properties listed in Table 4-1. The heat rate at each layer was obtained from the FE analysis and compared to the layer-dependent heat rate estimated using Eq. 3-15. These results are comparatively presented in Figure 4.6. On average, relative difference between the heat rate proposed in the FLS model and the computed heat rate in the FE were found to be 3.8% and 2.2% for the upper and lower layers, respectively. The bar chart in Figure 4.6 shows the relative error for each analysis. It is concluded that the heat rate adjustment used in the proposed FLS model based on the thermal properties provides a good estimate of the heat rate in each soil layer for a wide range of soils and rocks.

Table 4-1. Summary of thermal properties of the layers used in model generalization.

	Upper Layer		Lower Layer		Ratio		Upper Layer		Lower Layer		Ratio
	Thermal Properties		Thermal Properties		Thermal		Thermal Properties		Thermal Properties		
Run #	k_1	α_1	k_2	α_2	k_2/k_1	Run #	k_1	α_1	k_2	α_2	k_2/k_1
1	1.50	1.25E-06	0.50	4.17E-07	0.33	17	1.50	1.25E-06	6.00	1.20E-06	4.00
2	1.50	1.25E-06	1.00	8.33E-07	0.67	18	1.50	1.25E-06	8.00	1.60E-06	5.33
3	1.50	1.25E-06	1.50	1.25E-06	1.00	19	1.50	1.25E-06	4.00	8.00E-07	2.67
4	1.50	1.25E-06	2.00	1.67E-06	1.33	20	1.50	1.25E-06	6.00	1.20E-06	4.00
5	1.50	1.25E-06	2.50	2.08E-06	1.67	21	1.50	1.25E-06	8.00	1.60E-06	5.33
6	1.50	1.25E-06	3.00	2.50E-06	2.00	22	1.50	1.25E-06	4.00	4.00E-07	2.67
7	1.50	1.25E-06	0.50	3.13E-07	0.33	23	1.50	1.25E-06	6.00	6.00E-07	4.00
8	1.50	1.25E-06	1.00	6.25E-07	0.67	24	1.50	1.25E-06	8.00	8.00E-07	5.33
9	1.50	1.25E-06	1.50	9.38E-07	1.00	25	0.50	4.17E-07	0.50	4.17E-07	1.00
10	1.50	1.25E-06	2.00	1.25E-06	1.33	26	0.50	4.17E-07	1.00	8.33E-07	2.00
11	1.50	1.25E-06	2.50	1.56E-06	1.67	27	0.50	4.17E-07	1.50	9.38E-07	3.00
12	1.50	1.25E-06	3.00	1.88E-06	2.00	28	0.50	4.17E-07	2.00	1.25E-06	4.00
13	1.50	1.25E-06	4.00	1.60E-06	2.67	29	0.50	4.17E-07	2.50	1.56E-06	5.00
14	1.50	1.25E-06	6.00	2.40E-06	4.00	30	1.00	8.33E-07	1.00	8.33E-07	1.00
15	1.50	1.25E-06	8.00	3.20E-06	5.33	31	1.00	8.33E-07	2.00	1.67E-06	2.00
16	1.50	1.25E-06	4.00	8.00E-07	2.67	32	0.75	6.25E-07	1.50	9.38E-07	2.00

1 Thermal conductivities k_1 and k_2 are in W/m·℃

2 Thermal diffusivities α_1 and α_2 are in m^2/sec

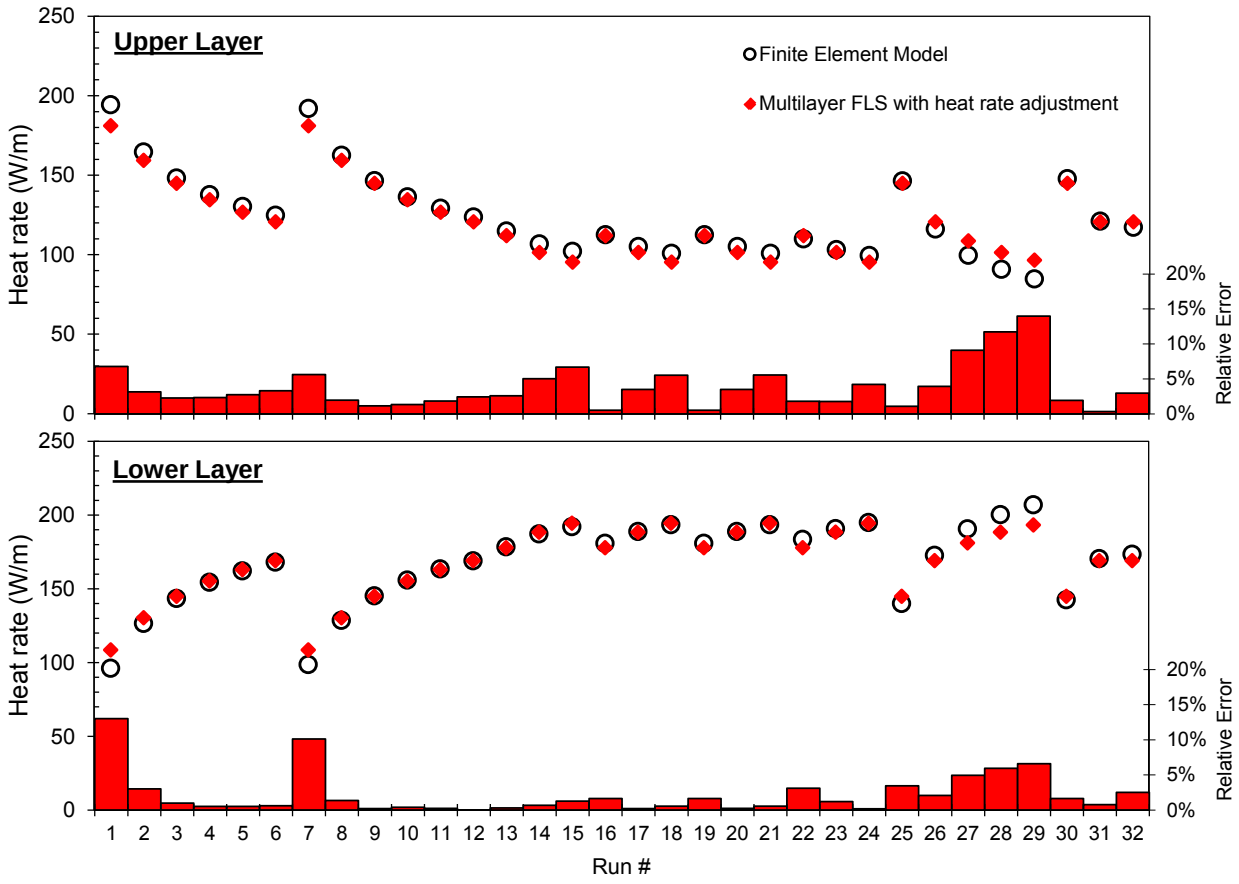

Figure 4.6. Heat rate in each soil layer for different analyses.

Moreover, the temperature change estimated using the proposed FLS model was also used to examine the model generality. It is shown in Figure 4.4 that the proposed FLS model provides good estimates of the temperature changes in each of the two layers in the considered example, i.e. analysis number 6 in Table 4-1. For other analyses listed in Table 4-1, Figure 4.7 shows temperature changes in the upper and lower layers resulted from the finite element analysis and the proposed FLS model for one week, and one month at the soil-exchanger interface and at 2.5m (8.2 ft) away. As seen in Figure 4.7, the proposed FLS model has a good agreement of the temperature change for the wide range of thermal conductivities shown in Table 4-1. Although it is not presented in Figure 4.6, good agreement in temperature change was also observed for other time-distance combinations. From Figure 4.4 and Figure 4.7, it can be inferred that the proposed FLS model is a general one and can be used for any soil formation.

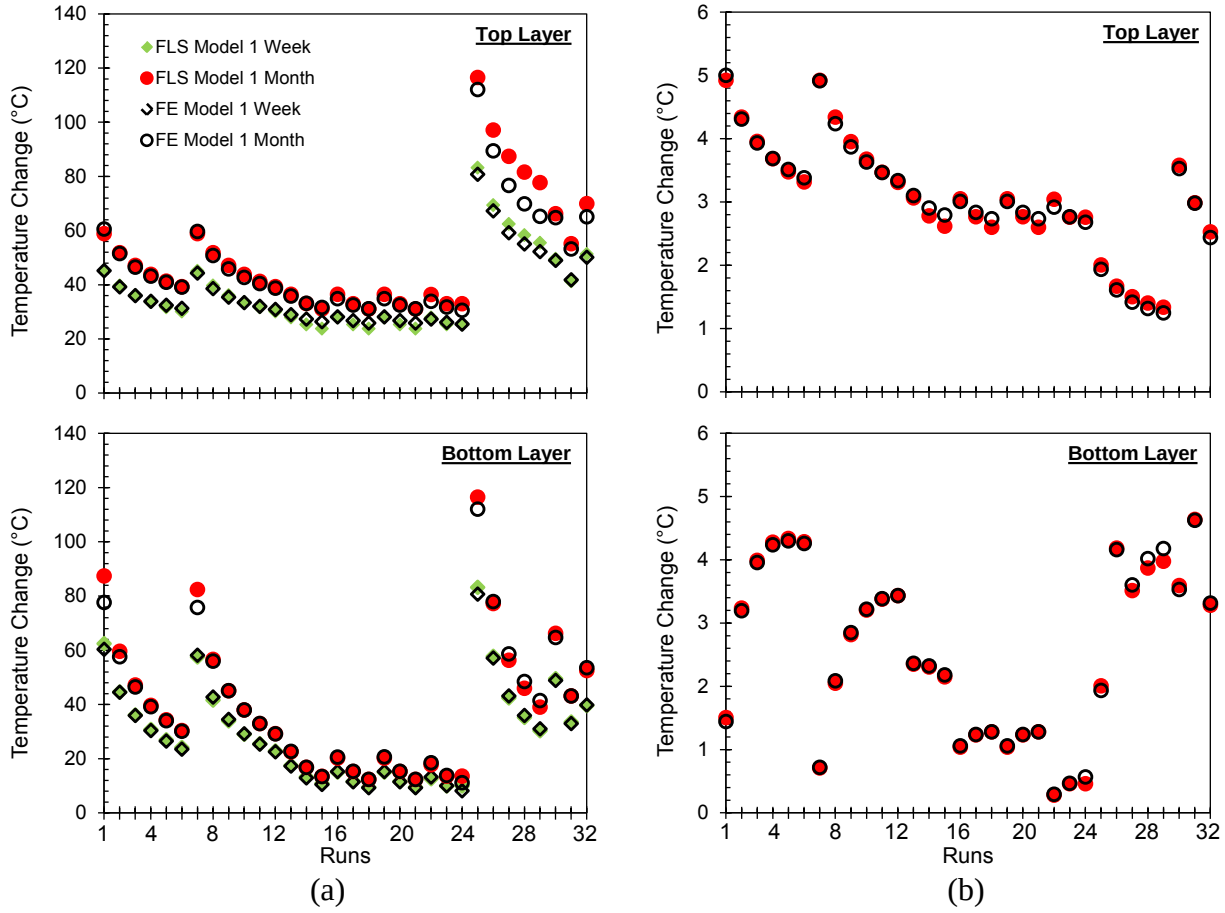

Figure 4.7. Generalization of the proposed FLS model using temperature changes in a two-layered soil profile at; (a) soil-heat exchanger interface, and (b) 2.5m away from the interface.

4.9. Simple LS Model with the Heat Rate Adjustment

The use of the infinite line source model proposed by Ingersoll et al. (1954) to estimate the temperature change in different layers is examined as a simplification for the proposed multilayer FLS model. The heat rate in the original formula of the infinite line source was modified for each layer using Eq. 3-15. Figure 4.4 shows a comparison between the use of the proposed multilayer FLS model and the original ILS model for the example used in the model validation section. It can be seen from this figure that the original ILS model when used with the adjusted heat rate for each soil layer gives the average temperature change in the layer. This simplification can be used to get a quick estimate of the temperature changes in layered soil profiles.

4.10. Conclusions

The design of ground coupled heat pump (GCHP) systems and energy piles which is a relatively new GHE technology depends on the estimation of temperature changes in the ground

around such elements. Currently several analytical models including infinite line source (ILS), finite line source (FLS), infinite cylindrical source (ICS), and finite cylindrical source (FCS) models are utilized for this purpose. All of these models are based on the assumption of a homogeneous medium, which does not reflect the likely conditions around borehole heat exchangers as well as energy piles due to their lengths. This assumption can potentially result in the overdesign of the GCHP systems and therefore this paper presents an approach where ground stratification is considered.

The work presented in this paper proposes a multilayer FLS model which uses the concept of superposition to determine temperature change within different layers. The heat exchanger is divided into different segments and the effect of each segment at a point in the profile is superimposed to find the total temperature change. Variation of heat rate within each soil layer with different thermal properties is accounted for using an expression based on weighted distribution of the total heat rate. The results of the proposed multilayer are validated and the generality of the approach was verified by comparing the heat rate and temperature change in a two-layered soil profile with combinations of varying thermal properties for the layers, covering a wide range of geomaterials.

References

Abdelaziz, S.L., C.G. Olgun, and J.R. Martin (2011) "Design and operational considerations of geothermal energy piles," In: J. Han, and D.E. Alzamora, Eds., Geo-Frontiers 2011: Advances in Geotechnical Engineering. Dallas, TX: ASCE Geotechnical Special Publication, No. 211, pp 450-459.

ASHRAE (2009). "ASHRAE handbook fundamentals." American Society of Heating, Refrigeration and Air-Conditioning Engineers. Access Date: February 23, 2011. Web page: <http://www.knovel.com/knovel2/Toc.jsp?BookID=2809>.

Bandos, T.V., Montero, Á., Fernández, E., Santander, J.G., Isidro, J.M., Pérez, J., Fernández de Córdoba, P.J.F., Urchueguía, J.F. (2009). Finite line-source model for borehole heat exchangers: effect of vertical temperature variations. Journal of Geothermics, vol. 38, pp. 263 – 270.

Carslaw, H., Jaeger, J. (1959). Conduction of Heat in Solids, 2nd ed. Oxford University Press, Oxford, U.K., 510 p.

COMSOL (2011). “Introduction to COMSOL Multiphysics: Version 4.2a” Reference Manual and Tutorial, COMSOL Inc., Burlington MA.

Eskilson, (1987). Thermal Analysis of Heat Extraction Boreholes. Ph.D. Thesis. University of Lund, Lund, Sweden. 264 p.

Ingersoll, L.R., Plass, H.J. (1948). Theory of the ground pipe heat source for the heat pump. Journal of Heating, Piping and Air conditioning, vol. 20, pp. 119 – 122.

Ingersoll, L.R., Zobel, O.J., Ingersoll, A.C. (1954). Heat Conduction with Engineering Geological and other Applications. Mc Graw-Hill, New York, NY, USA, p. 325.

Kelvin, W.T. (1880). Compendium of the Fourier mathematics for the conduction of heat in solids and the mathematically allied physical subjects of diffusion of fluids and transmission of electric signals through submarine cables. Journal of Math. and Physics, vol. 2, pp. 41.

Kusuda, T., Achenbach, P.R. (1965). Earth Temperature and Thermal Diffusivity at Selected Stations in the United States. ASHRAE Transactions, vol. 71, Part 1.

Lamarche, L., Beauchamp, B. (2007). A new contribution to the finite line-source model for geothermal boreholes. Journal of Energy and Buildings, vol. 39, pp. 188 – 198.

Lee, C.K., Lam, H.N. (2007). Computer simulation of borehole ground heat exchangers for geothermal heat pump systems. Journal of Renewable Energy, vol. 33, pp. 1286 – 1296.

Marcotte, D., Pasquier, P. (2008). Fast fluid and ground temperature computation for geothermal ground-loop heat exchanger systems. Journal of Geothermics, vol. 37, pp. 651 - 665.

Marcotte, D., Pasquier, P. (2009). The effect of borehole inclination on fluid and ground temperature for GLHE systems. Journal of Geothermics, vol. 38, pp. 392 – 398.

Man, Y., Yang, H., Diao, N., Liu, J., Fang, Z. (2010). A new model and analytical solutions for borehole and pile ground heat exchangers. International Journal of Heat and Mass Transfer, vol. 53, pp. 2593 – 2601.

McQuiston, F. C., and J. D. Spitler (1992) Cooling and heating load calculation manual, Atlanta: American Society of Heating, Refrigerating Air-Conditioning, Engineers, ASHRAE.

Mitchell, J. K. (1969). “Temperature effects on the engineering properties and behavior of soils.” Highway Research Board Special Report, report number 103, pp. 9-28.

Olgun, C.G., Sezen. A., Martin, J.R., Abdelaziz, S.L. (2010) “Renewable Energy Applications in Geotechnical Engineering.” Invited Keynote Lecture, ZM13, 13th National Conference on Soil Mechanics and Geotechnical Engineering, September 30-October 1, 2010, Istanbul, Turkey.

Pedersen, C. O., D. E. Fisher, J. D. Spitler, and R. J. Liesen (1998) Cooling and Heating Load Calculation Principles, Atlanta, GA: American Society of Heating, Refrigerating and Air-Conditioning Engineers, Inc.

Sutton, M., Nutter, D., Couvillion, R. (2003). A ground resistance for vertical bore heat exchangers with groundwater flow. Journal of Energy Resources Technology, vol. 125, pp. 183 – 189.

Weibo, Y., Mingheng, S., Zhenqian, C. (2009). A variable heat flux line source model for boreholes in ground coupled heat pump. Proceedings of 2009 Asia-Pacific Power and Energy Engineering Conference (APPEEC), pp. 2242 – 2245.

Zeng, H.Y., Diao, N.R., Fang, Z.H. (2002). A finite line-source model for boreholes in geothermal heat exchangers. Journal of Heat Transfer – Asian Research, vol. 31, pp. 558 - 567.

Zeng, H.Y., Diao, N.R., Fang, Z.H. (2003). Heat transfer analysis of boreholes in vertical ground heat exchangers. International Journal of Heat and Mass Transfer, vol. 46, pp. 4467 – 4481.

CHAPTER 5. LONG-TERM THERMAL PERFORMANCE OF ENERGY PILES

5.1. Introduction

Long-term performance of geothermal systems such as deep vertical boreholes and shallow horizontal trenches is one of the challenges that need to be addressed for the optimum design of these types of systems. As explained in Chapter 2, typically a long-term energy pulse is considered to account for the long-term heat exchange behavior of these systems in addition to the daily energy pulse to consider the short-term effects (Kavanaugh and Rafferty, 1997). Another way to consider long-term effects is to perform a comprehensive energy analysis for the building and the geothermal system using one of the commercially available computer packages (ASHRAE, 2009). This approach necessitates the integration of the geothermal system design with building energy analysis, which can be time consuming and not computationally feasible. Therefore, it is not commonly performed for small-scale geothermal systems for residential and small commercial buildings.

The pile design procedure is based on estimating the ultimate resistance of the pile which is the sum of the shaft resistance and the toe resistance. These resistances depend mainly on the strength of the soils around the pile. As discussed in Chapter 2, the soil strength is temperature dependent and progressive temperature changes can lead migration of the pore fluid and deformations around an energy pile. Therefore, it is critical to study the progression of temperatures within the soil mass around an energy pile during its operational period.

In this section, a newly developed method to account for the long-term effects is presented. With this approach, the temperature changes around an energy pile can be estimated and used for the geotechnical design of the pile. Long-term progression of temperatures around an energy pile can also have implications for the efficiency of heat exchange operations. This chapter starts with a brief description of the methods used to estimate heating and cooling loads of a building, followed by a detailed energy analysis to estimate the hourly ground thermal loads. Then, an approach to simplify these hourly thermal loads is presented using the developed concept of sine wave equivalency. The sine wave approach developed here presents a robust procedure to estimate the respective amplitudes and durations of heating and cooling episodes for any building using the change point statistical analysis. This procedure significantly improves the current state-of-the-art since the reported methods on long-term performance methodologies assume heating and cooling episodes each with 6 month duration over a year (Lazzari et al., 2010.

Afterwards, a series of finite element analyses are performed and the results are presented for an operational period of 30 years using the equivalent sine wave approach. These analyses demonstrate the applicability of the equivalent sine wave approach to simulate long-term energy pile behavior. The broader results from these analyses have implications about the long-term heat exchange performance of energy piles under different climatic conditions.

5.2. Analysis of Long-Term Performance

The methodology developed for analyzing the long-term thermal performance of energy piles is outlined below. In this analysis, three measures of system performance were used: (*a*) temperature changes in the ground around the energy pile, (*b*) the coefficient of performance (COP), and (*c*) the thermal recovery period.

1. Design thermal loads (heating and cooling) of the building under consideration are estimated using the weather data for the building location, interior and exterior building components/materials, lighting features, building occupancy and usage. The ASHRAE Fundamentals Handbook (2009) provides weather data for nationwide weather stations. Occupied and unoccupied building conditions are considered when building occupancy is expected to affect the design thermal loads, for example cases like office buildings, and schools.
2. The optimum capacity ground coupled heat pump (GCHP) is selected using iterations listed below;
    a. A specific GCHP is initially selected,
    b. GCHP operation interacts with building thermal loads as these operations generate heat and this heat is added to the fluid. Therefore, the effect of GCHP operation is considered in estimating ground thermal loads. The heat energy from the GCHP is subtracted from the building heating load for the ground cooling load, and added to the building cooling load for the ground heating load.
    c. The GCHP is then confirmed functional by comparing its capacity to the ultimate ground thermal loads, otherwise another GCHP is selected and the design process is repeated.
3. As mentioned in Step 2, the ground thermal loads are estimated by accounting for the effect of the energy generated due to the operation of the heat pump. In building heating mode, the ground cooling load is estimated by subtracting the energy generated by the selected GCHP from the building heating load. In the building cooling mode, the ground heating is estimated by adding the energy generated by the selected GCHP to the building cooling load. Afterwards, the hourly ground thermal loads for a full year is then developed based on the design ground thermal loads and the ambient air temperature using the bin method (McQuiston et al., 2004).
4. Heating and cooling episodes are estimated from the approximated hourly ground thermal loads using the change point statistical analysis. The results of this analysis define two distinct periods; the first is when the seasonal ground thermal load switches from cooling dominant load (winter) to heating dominant load (summer), while the second is when the seasonal ground thermal load switches from heating dominant load (summer) to cooling dominant load (winter).
5. A representative annual sine wave for the ground thermal loads is developed to simplify the numerical modeling process. This annual sine wave is composed of one half of a sine wave applied over the heating period, and another half of a sine wave applied over the cooling period. The amplitudes and durations of the two half sine waves depend on the respective heating and cooling demands at each season. The change from seasonal heating to cooling is determined using the change point analysis and hence the duration of half sine waves over a year. The amplitudes of the half sine waves are estimated using the equivalent area concept. This concept is based on equating the area of one half of a sine wave to the area of the hourly ground load time history for the same thermal load.
6. Perform the long-term performance using the obtained representative annual sine wave.

Several intermediate analyses were performed to finalize this presented methodology including; (a) comparison between the temperature changes estimated using the equivalent sine wave and those obtained using the estimated hourly ground thermal loads for one year analysis to confirm that the proposed sine wave captures the average system response; (*b*) comparison

between the temperature changes estimated using the sine waves proposed by Lazzari et al. (2010) which are widely used in the long-term analysis of GCHP systems and the estimated hourly ground thermal loads for one year analysis intending to present the current inaccuracy in long-term modeling; and (*c*) analyses to investigate the effect of the assumed initial thermal load on the predicated long term performance.

5.3. Demonstration Example of the Proposed Approach

As described above, this approach is developed to model the long-term performance of GCHE systems with specific focus on energy piles. The approach incorporates climate data with the energy use within a building to estimate seasonal energy demand and the corresponding ground thermal loads. Ground thermal loads are further represented by a simplified seasonal heating and cooling loads with respective amplitudes and durations. This simplified energy demand is used to investigate the long-term heat exchange behavior with numerical analyses.

These analyses were performed for a typical office building at three locations with different climate profiles. Detailed building description is discussed including the geometry, wall components, usage, and occupancy of the building. The information required to estimate the building thermal loads are also included in this section. Afterwards, ground thermal loads are determined by accounting for the effect of the ground coupled heat pump and heat exchange operations. Hourly ground thermal loads are estimated from the building energy analysis and the separation of heating and cooling episodes over the year is determined using the change point statistical analysis. At the end, the hourly ground thermal loads are converted to equivalent representative sine waves to be used in the long term performance analysis. Using sine wave thermal loads instead of the hourly loads reduces the computational time and cost significantly.

5.3.1. Building Description

An office building is presented to exemplify the proposed methodology for investigating the long-term thermal performance of energy piles. A hypothetical single floor office building consisting of four equal size square rooms (25 m^2) and a corridor (10 m long and 2 m wide) is selected as a demonstration example. The ceiling height of the building is 3 m. The building is aligned such that the corridor is in the south-north (SN) direction. All of the exterior walls have 1.5 m × 1 m windows. Figure 5.1 presents a plan view of this building and its orientation. The typical compositions of exterior and interior walls, roof, and floor for this building type are selected based on available recommendations as summarized in Table 5-1 (McQuiston et al., 2004).

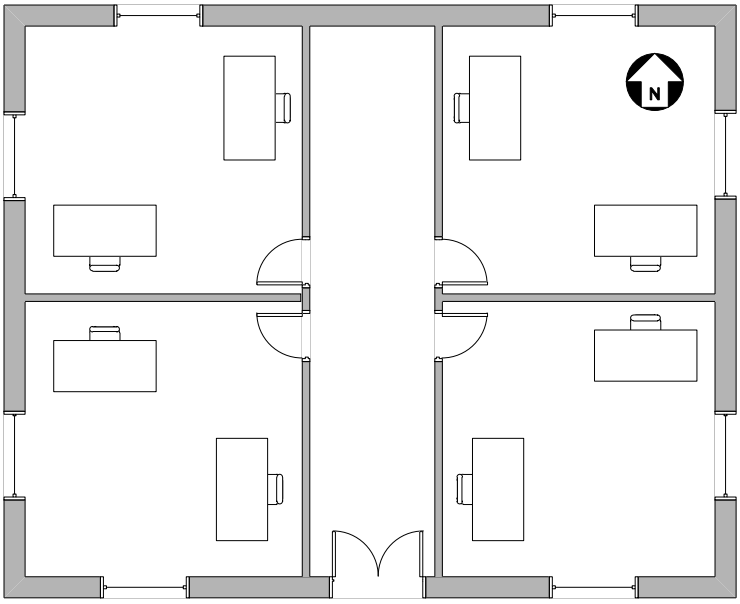

Figure 5.1. Design office building used in the demonstration example for the proposed long-term analysis procedure.

Table 5-1. Components of exterior and interior walls, roof, and floor (McQuiston et al., 2004 - used under fair use, 2013).

Layer		Layer Thickness, t (mm)	Thermal Conductivity, K (W/m·°C)	Heat Capacity, C_p (kJ/kg·°C)	Density, γ (kg/m^3)
Exterior Walls	Facing Brick 3"	76.2	0.87	0.79	1600
	Air Gap 2"	50.8	0.29	1.00	2
	Insulation 3"	76.2	0.04	0.84	91
	Concrete Block 6"	152.4	0.21	1.05	944
Interior Walls	Plaster 0.5"	12.7	0.16	0.84	720
	Concrete Block 4"	101.6	1.63	0.92	2096
	Plaster 0.5"	12.7	0.16	0.84	720
Roof	Stone Chippings 0.5"	12.7	1.44	1.67	880
	Felt 3/8"	9.525	0.17	1.67	1120
	Insulation 2"	50.8	0.04	0.84	32
	Cast Concrete 4"	101.6	1.73	0.92	2304
Floor	Cast Concrete 8"	203.2	1.73	0.92	2304
	Screed 2.75"	69.85	1.40	0.88	1920
	Vinyl Tiles 0.2"	5.08	0.61	1.26	800

5.3.2. Building Usage and Occupancy

Full building occupancy is assumed between 8:00 am and 6:00 pm on weekdays. A room is considered fully occupied when used by two people. The 132W typical total heat gain from the people in office buildings is assumed (McQuiston et al., 2004). This total heat gain is composed of 73 W of sensible heat transferred to the space and 59 W of latent heat generated within and instantly transferred to the space. The sensible heat gain is divided into 70% radiant gain transferred instantly to the space, and 30% delayed convective gain (McQuiston et al., 2004).

Lights and equipment contribute significantly to the heat gain of the building. Light heat gain depends on the type of the lamps and lighting features with a typical total peak value of 24 W/m^2 for office buildings (McQuiston et al., 2004). This amount is divided into 30% convective heat transferred directly to the space, and 70% heat radiated initially to the room contents and walls then to the space by air convection. Full light usage coincides with the building full occupancy between 8:00 am and 6:00 pm on weekdays. At all other times including weekends, a 10% light usage is assumed.

Equipment heat gain for office buildings is about 10 W/m^2 (McQuiston et al., 2004) which is the recommended value for preliminary design when specific information about the actual equipment usage is not known. It is divided into 60% sensible heat gain out of which 70% is radiation and 30% is convection, and 40% latent heat gain (McQuiston et al., 2004). Equipment heat is generated only when the building is occupied from 8:00 am and 6:00 pm on weekdays.

Another source of thermal load is the air infiltration from outside of the building to the inside. Numerous approaches are available to estimate the thermal load due to infiltration (McQuiston et al., 2004). The air-change method is a simplified approach in which the number of air changes per hour (ACH) is used to estimate the infiltration rate by multiplying it by the gross space volume. The range for the ACH is between 0.5 for very low infiltration and 2 for very high infiltration (McQuiston et al., 2004). The average of these two extremes (ACH = 1.25) is assumed for the considered building. Infiltration thermal loads are then estimated by multiplying the obtained infiltration rate by the temperature difference between the ambient air and the desired comfort temperature. The infiltration is assumed to occur 24 hours a day.

5.3.3. Comfort Temperature

McQuiston et al. (2004) recommend a design indoor temperature around 22°C (71.6°F) which is used for the occupied building condition in the two modes of operation (heating and cooling). For the unoccupied building conditions, the building energy consumption is attempted to be reduced by decreasing the indoor temperature to 15°C (59°F) in heating mode and increasing it to 32°C (89.6°F) in cooling mode.

5.3.4. Selected Building Locations

Three typical locations are considered to investigate different cases of long-term performance of ground coupled heat exchange systems ; (1) location where the design ground thermal loads are balanced, (2) location where the ground thermal load is heating dominant, and (3) location where the ground thermal load is cooling dominant. Thus, three locations in the United States are included in this study where each one of them represents one of these hypothetical cases. The selected locations are Charlotte, NC representing the balanced load case, Chicago, IL representing the heating dominant case, and Austin, TX representing the cooling dominant case. The design weather data for each one of the selected locations are taken from the ASHRAE Fundamentals Handbook (2009). The design data for the three selected locations are summarized in Table 5-2 and a copy of the weather data is presented in Appendix I.

Table 5-2. Summary of weather design data for the three selected locations

Location	Atm. Pressure kPa (psi)	Ground Temp. °C (°F)	Summer Conditions				Winter Conditions			
			Dry Bulb °C (°F)	Wet Bulb °C (°F)	Wind Direction degrees Clockwise from N	Wind Speed m/s (mph)	Dry Bulb °C (°F)	Wet Bulb °C (°F)	Wind Direction degrees Clockwise from N	Wind Speed m/s (mph)
Charlotte, NC	98.52 (14.29)	16.7 (62.0)	34.5 (94.1)	23.7 (74.6)	240	3.3 (7.4)	-6.4 (20.5)	-8.6 (16.5)	20	2.68 (6.0)
Chicago, IL	99.08 (14.37)	10 (50.0)	33.4 (92.1)	23.8 (74.9)	220	5.63 (12.6)	-18.7 (-1.6)	-20.3 (-4.6)	300	5.36 (12.0)
Austin, TX	99.49 (14.43)	24 (75.2)	37.6 (99.7)	23.9 (75.0)	190	3.66 (8.2)	-3.8 (25.2)	-6.0 (21.2)	10	3.17 (7.1)

5.3.5. Energy Analysis for Building Thermal Heating and Cooling Loads

Heat Balance Method (HBM) is used to estimate the building thermal loads by solving three different balancing formulas simultaneously (McQuiston et al., 2004; Pedersen et al., 1998). These three balancing formulas are; (*1*) Heat balance for exterior surfaces, (*2*) Heat balance for interior surfaces, and (*3*) Heat balance for the zone air. The exterior surface formula balances the heat conduction at the exterior surfaces with the summation of heat generated form the adsorbed solar energy, ambient air convection, and radiation at each surface. The interior surface formula balances the heat conduction at the interior surfaces with the summation of heat collected from the adsorbed solar energy, zone air convection, and radiation at each surface. The zone air formula balances the building heating and cooling thermal loads with the total rate of heat from occupants, lights, equipment, zone air convection, and infiltration. Appendix II provides a summary of the Heat Balance Method.

Solving these heat balance equations requires an iterative process because these equations are interdependent. The HvacLoadExplorer program implements the iterative scheme proposed by Pedersen et al. (1998) to perform the heat balance analysis. This program was used to estimate the thermal loads for the considered building at the three selected locations.

The clearness and the ground reflectivity are two parameters used to account for the solar energy effect on the building thermal loads. They are needed to accomplish the heat balance analysis, thus typical design values for the clearness and the ground reflectivity at the considered locations are used.

Table 5-3 presents the calculated thermal loads for the building at the three selected locations under occupied and unoccupied conditions. As shown in Table 5-3; (*1*) Heating and cooling loads for the occupied building in Charlotte, NC are very similar in magnitude (11% more heating load), (*2*) Chicago, IL has about 78% more heating load, and (*3*) Austin, TX has about 33% more cooling load. No cooling load is required for the unoccupied building at the three locations because the unoccupied set temperature (i.e. 32°C) is very close to the design summer dry bulb making ventilation sufficient to cool the space down to this desired set temperature.

Table 5-3. Building heating and cooling loads at the three selected locations

Location	Heating Load (Watts)		Cooling Load (Watts)	
	Occupied	Unoccupied	Occupied	Unoccupied
Charlotte, NC	17,945	4,720	16,155	0
Chicago, IL	24,135	10,700	13,550	0
Austin, TX	14,350	1,655	19,010	0

5.3.6. Typical Meteorological Year (TMY) Data for Selected Locations

The estimated building thermal loads are based on the design ambient dry bulb temperature for the three selected locations given by ASHRAE Fundamentals Handbook (2009). Thus, the variation of the ambient dry bulb temperature and its relation to the estimated thermal loads should be accounted for while predicting the long-term performance of GCHP systems.

The variation of the ambient dry bulb over a year is used to estimate the hourly thermal loads of the selected building. Analyses are based on the typical meteorological year (TMY). The TMY consists of twelve meteorological months (January through December), each of which has the most critical hourly ambient measurements out of 30 years records for the respective month is the year (Wilcox and Marion, 2008). The ambient measurements in the TMY include;

dry bulb temperature, wet bulb temperature, solar values, wind speed and direction (Wilcox and Marion, 2008). The TMY database has few missing data for some hours which were filled with interpolated values (Wilcox and Marion, 2008). The variation of the dry bulb over the TMY is assumed to repeat for every year included in the long-term analysis implying that the building thermal loads do not change from one year to another. The ambient dry bulb variations for the selected locations were obtained from the latest meteorological database, the TMY3, from the National Solar Radiation Data Base website (http://rredc.nrel.gov/solar/old_data/nsrdb/1991-2005/tmy3/). Figure 5.2 presents the ambient dry bulb temperature over a typical year for the selected three locations.

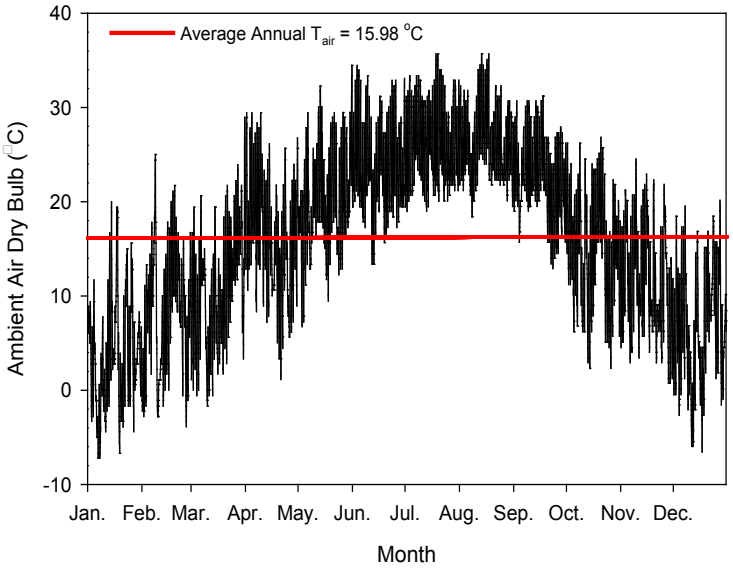

(1)Charlotte, NC

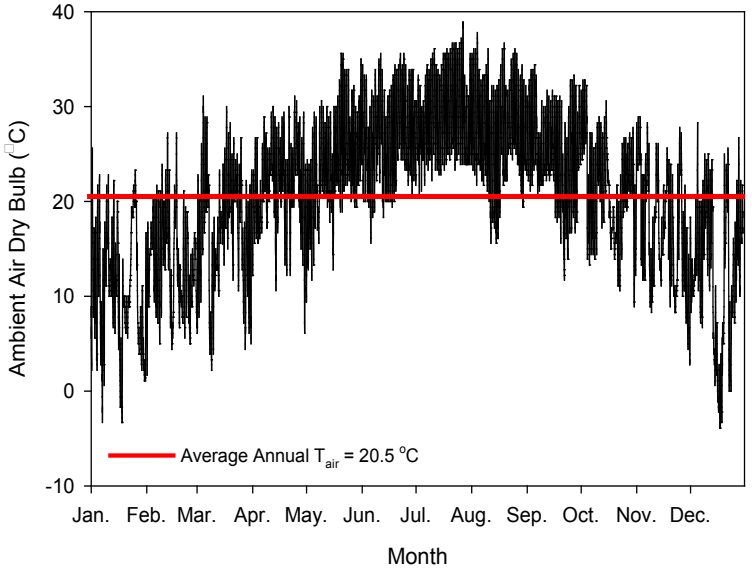

(3) Austin, TX

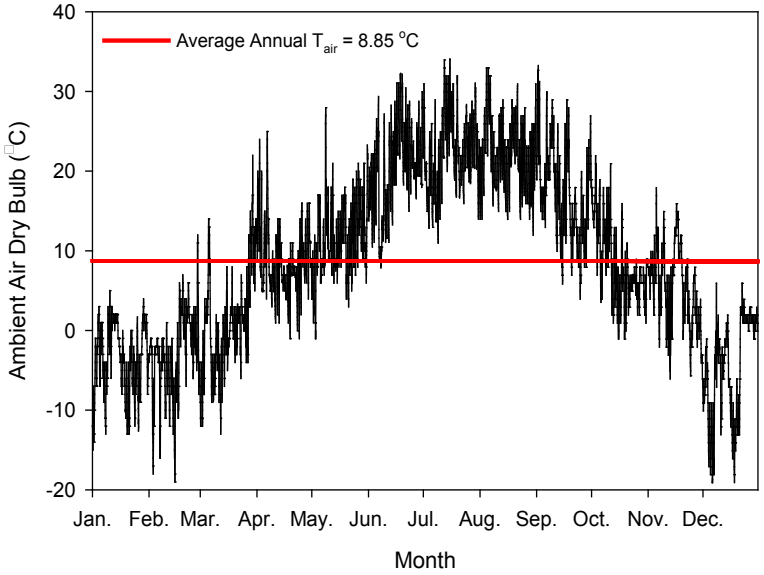

(2) Chicago, IL

Figure 5.2. Ambient air dry bulb temperature for the selected locations.

5.3.7. Hourly Ground Thermal Loads for the TMY

The obtained design heating and cooling loads for the building correspond to a single ambient temperature for each mode (heating or cooling) which is the design dry bulb temperature for that mode. When the ambient temperature varies from the design temperature, the building thermal load is expected to vary accordingly. For instance, the building requires less heating load when the ambient temperature is above the design heating dry bulb temperature. Also, the building requires less cooling load when the ambient temperature is below the design cooling dry bulb temperature. If 2kW heating load was estimated for a building assuming a design heating dry bulb of -2°C, then the operational heating load when the ambient temperature is 0°C is less than the design 2kW. Similarly for cooling load, If 1.5kW cooling load was estimated for a building assuming a design cooling dry bulb of 40°C, then the operational cooling load when the ambient temperature is 32°C is less than the design 1.5kW. At given ambient temperatures, no heating or cooling loads are required. For heating mode, the ambient temperature at which no heating is needed is less than the design comfort temperature due to the internal heat gains. While for cooling, the ambient temperature at which no cooling is needed is slightly more than the design comfort temperature due to the natural ventilation. These temperatures are known as the balance temperatures (ASHRAE, 2009).

In order to model the long-term performance of geothermal systems, the time variation of the thermal load is required. The ambient temperature variation is used to obtain such time variation of the thermal load by using a predefined relationship between the ambient temperature and the building thermal loads (heating and cooling). A linear relationship is usually assumed due to its simplicity (ASHRAE, 2009). This linear relationship is defined by estimating the thermal loads corresponding to at least two ambient temperatures; the first is the design ambient temperature at which the thermal load is the design load, while the second is the balance temperature at which no thermal load is needed. Thus, estimating the balance temperature for both heating and cooling modes under occupied and unoccupied conditions is essential to fully define the assumed linear relation and consequently establishing the thermal load-time variation.

The procedure outlined in the ASHRAE Fundamentals Handbook (2009) is implemented to estimate the balance temperature for the different cases considered. In this procedure, the heat gains (q_{gain}) from occupants, lights, and equipment for both occupied and unoccupied conditions are estimated. For occupied building, the heat gain comes from people, lights, and equipment, while for unoccupied building, only the assumed operational light is included in the heat gain estimation. Thus, for the considered building the heat gain is estimated as;

$$q_{gain-occupied} = 4\,rooms \times [(132\,Watts) + (\{24Watts/m^2 + 10Watts/m^2\} \times 25m^2)] = 3928\,Watts \cong 3930\,Watts$$

$$q_{gain-unoccupied} = 4\,rooms \times [0.1 \times 10Watts/m^2 \times 25m^2] = 100\,Watts$$

The building heat loss coefficient (K_{tot}), defined as the ratio between the design thermal load and the design indoor and outdoor temperature difference, is then estimated. For cooling mode, ventilation can be enough when the ambient and the desired indoor temperatures are close (McQuiston et al., 2004). Thus, a 10% reduction in the temperature difference between the indoor and the outdoor is recommended to account for the ventilation effects (ASHRAE, 2009). This correspond to a 10% increase in the calculated K_{tot} (ASHRAE, 2009).

Thereafter, the balance point temperature is estimated as;

$$t_{bal} = t_{indoor-design} - \frac{q_{gain}}{K_{tot,or\ max}}$$

Table 5-4 presents the estimated balance temperatures for the occupied and unoccupied conditions under heating and cooling modes for the three selected locations.

Table 5-4. Balance point temperature analysis for the selected locations under occupied and unoccupied conditions.

Location	Occupied Heating			Unoccupied Heating		
	ΔT (°C)	K_{tot} (Watt/°C)	t_{bal} (°C)	ΔT (°C)	K_{tot} (Watt/°C)	t_{bal} (°C)
Charlotte, NC	28.4	631.87	15.8	21.4	220.56	14.5
Chicago, IL	40.7	593.00	15.4	33.7	317.51	14.7
Austin, TX	25.8	556.20	14.9	18.8	88.03	13.9

Location	Occupied Cooling			Unoccupied Cooling*		
	ΔT (°C)	K_{max} (Watt/°C)	t_{bal} (°C)	ΔT (°C)	K_{max} (Watt/°C)	t_{bal} (°C)
Charlotte, NC	12.5	1418.12	19.2	--	--	--
Chicago, IL	11.4	1307.46	19.0	--	--	--
Austin, TX	15.6	1340.45	19.1	--	--	--

* No unoccupied cooling loads for the three locations.

The estimated balance temperatures presented in Table 5-4 show interesting trends which can be explained as;

1) The internal heat gain raises the indoor temperature causing the heating balance temperatures to be less than the design indoor comfort temperature.
2) The more the internal heat gain is, the less the expected heating balance temperature for a specific indoor design temperature. However, the estimated heat balance temperatures, defined as the temperatures at which no heating or cooling loads are required, for the occupied building ($q_{gain-occupied} = 3930W$) are more than those for the unoccupied building ($q_{gain-unoccupied} = 100W$). The change in the reference indoor temperature, 22°C for occupied and 15°C for unoccupied, is the reason for the observed lower unoccupied heating balance temperature.
3) The cooling balance temperature is that temperature below which no cooling system is needed, in other words ventilation is sufficient to cool down the space. To move the extra internal heat gain out of the building by ventilation, the ambient temperature should be less than the design indoor comfort temperature creating a thermal gradient from inside to outside of the building. Thus, the cooling balance temperature should be less than the design comfort indoor temperature which is seen in Table 5-4.

Using the estimated heat balance temperatures and assuming a linear relationship between the ambient temperature and the thermal load, the thermal load corresponding to any ambient temperature ($q_{t_{amp.}}$) is given by;

$$q_{t_{amp.}} = q_{design} \times \left(\frac{t_{bal} - t_{amp.}}{t_{bal} - t_{amp.design}} \right)$$

Where; $t_{amp.design}$ is the design ambient temperature from Table 5-2, q_{design} is the design thermal load from Table 5-3, and t_{bal} is the corresponding balance temperature from Table 5-4.

The hourly variation of the building thermal load is developed using the hourly ambient temperature data from the typical meteorological year (TMY) along with the above formula. The building operational model is determined based on the comparison of the hourly ambient temperatures for any selected location and the heating/cooling balance temperatures. There we establish the conditions such as, heating mode for $t_{amp} < t_{bal\text{-}heating}$, cooling mode for $t_{amp.} > t_{bal\text{-}cooling}$, and ventilation for $t_{bal\text{-}heating} > t_{amp.} > t_{bal\text{-}cooling}$.

If every ambient temperature from the TMY is used then the resulting thermal load will oscillate every hour of the year which will cause numerical instability in the finite element analyses. Ambient temperature bins are used to reduce the oscillation of the thermal load over time and to improve the stability of the finite element analyses(ASHRAE, 2009). The extreme limits for the bins are the rounded minimum and maximum ambient temperatures from the TMY database as presented in Table 5-5 for the three considered locations in which a bin width of 2.5°C is used. Each record of the hourly ambient temperatures in the TMY database is categorized into the corresponding temperature bin.

Table 5-5. Temperature bins for each selected location

Location	Ambient Temperatures from the TMY Database (°C)		Bin Temperature Limits (°C)		Number of Temperature Bins
	Min.	Max.	Min.	Max.	
Charlotte, NC	-7.2	35.6	-7.5	37.5	18
Chicago, IL	-19	34.1	-20	35	22
Austin, TX	-3.9	38.9	-5	40	18

For each ambient temperature bin, the respective thermal load is estimated using the mean bin temperature in the formula presented earlier. The thermal load for a specific temperature bin is assigned to all ambient temperatures that belong to that bin. Since several consecutive hours are expected to belong to the same temperature bin (i.e. no sudden changes), a more stable thermal load time history is developed. Table 5-6 presents the results of the energy analyses for the building at the three selected locations using the temperature bin approach.

The long-term performance of geothermal loops depends directly on the ground thermal loads rather than the building thermal loads. Ground thermal load is based on the building thermal load and the operational characteristics of the selected heat pump as it is a combined measurement of the building thermal load and the heat generated from the heat pump operations. On the other hand, selecting a heat pump is based on the ultimate ground thermal load. Therefore, the heat pumps for the considered locations are selected based on the ultimate building load then confirmed to provide the ultimate ground load. For Charlotte, NC; and Chicago, IL heat pumps with capacity of 21.1 kW (6 tons) at an entering fluid temperature of 19 °C (66.2 °F) are used. While, for Austin, TX a heat pump with capacity of 17.58 kW (5 tons) at an entering fluid temperature of 22°C (71.6 °F) is used.

The capacity of the GCHP in heating and cooling modes depends on the entering water temperature (EWT) as presented in the heat pump characteristic curves in Appendix III.

Kavanaugh and Lambert (2004) procedure is used to estimate the EWT for each ambient temperature bin. In this approach, the design value of the EWT is assumed at the design ambient temperature while the EWT is slightly offset from the undisturbed ground temperature for no thermal load case. For flow rate of 11.4 lit/min (3 gpm), the recommended temperature offset for the no thermal load case is 6°C in cooling mode and -6°C in heating mode (Kavanaugh and Lambert, 2004; Kavanaugh and Rafferty, 1997). The EWT for each ambient temperature bin is estimated assuming a linear relationship between the EWT and the ambient temperature as presented in Table 5-6. The approximated EWT for each ambient temperature bin and the heat pump characteristic curves are used to estimate the capacity, the coefficient of performance (COP), and the energy efficiency ratio (EER) of the heat pump for that bin.

For Charlotte and Austin, the heat generated by the heat pump is estimated using the COP for heating mode and the EER for cooling mode as follows;

For building heating (i.e. ground cooling);

$$COP = \frac{\text{Energy transferred for heating the building } (Q_H)}{\text{Heat pump input electrical energy } (W)} \rightarrow \therefore\ W = \frac{Q_H}{COP}$$

but; Q_H = Ground thermal cooling load $\left(Q_{gc}\right) + W$
thus; $Q_{gc} = Q_H - W$

For building cooling (i.e. ground heating);

$$EER = \frac{\text{Building cooling load } (Q_C)\ in\ (BTU/hr)}{\text{Heat pump input energy } (W)\ in\ (watts)} \rightarrow \therefore\ W = \frac{Q_C \times 3.412\left(\text{watts}/(Btu/hr)\right)}{EER}$$

but; Q_C = Ground thermal heating load $\left(Q_{gh}\right) - W$
thus; $Q_{gh} = Q_C + W$

It should be noticed that the ground heating load corresponds to the building cooling load, and the ground cooling load corresponds to the building heating load. In the building cooling mode, the air temperature inside the building is more than the desired comfort temperature thus energy are extracted from the building and injected to the ground causing a ground heating mode. Similarly in the building heating mode, the air temperature inside the building is less than the desired comfort temperature thus heat is withdrawn from the ground and injected to the building causing a ground cooling mode. The heat pump operation injects additional heat to the system which shifts the ground thermal load for the building thermal load as follows; (1) In the building heating mode, the additional heat injected into the system due to the heat pump operation helps to provide some of the requried building heating load which causes the ground cooling load to be less than the building heating load, and (2) On the contrary, in the building cooling mode the heat injected to the system due to the heat pump operation increases the amount of heat required to be injected to the ground which causes the ground heating load to be more than the building cooling load. The effect of the heat pump operation is observed in different ways in the three considered locations; (1) Balanced building design thermal loads for Charlotte were observed as shown in Table 5-3, but the ultimate ground heating load is about double the ultimate ground cooling load; (2) The building design load for Chicago is heating

dominant but the ultimate ground thermal loads are balanced; and (3) for Austin, the ground heating load is dominating .

Ground thermal loads for each of the considered location are shown in Figure 5.3. In this figure, ground heating is assumed negative while ground cooling is assumed positive. Hourly variation of ground thermal load is obtained by matching the ambient temperature for each hour with a specific temperature bin. Then the corresponding occupied or unoccupied ground thermal loads are assigned based on the predefined occupancy periods. It should be noticed that while developing this figure, the ground thermal loads are divided by an assumed ground loop length of 450 m for Charlotte, 350 m for Chicago, and 525 m for Austin. These loop lengths were selected such that the maximum ground thermal load per unit loop length is less than 50 W/m as suggested by Brettmann et al. (2010), and Kavanaugh and Rafferty (1997). The actual value of the maximum ground thermal load per unit length depends on the long-term performance of the GCHP system which is being investigated in this chapter. When designing a geothermal ground loop, the value of this maximum heating rate needs to be confirmed and adjusted, if needed, based on the results of the long-term analysis. ,

Table 5-6.a) Ground thermal loads for Charlotte, NC.

Bin temperature range (°C)		Bin reference temp. (°C)	H or C	Building's thermal load (Watts)		EWT (°C)	Heat pump capacity (Watts)	COP	EER	Heat pump additional power (Watts)		Ground heat load (Watts)	
min.	max.			O	U					O	U	O	U
-7.5	-5	-6.25	H	17824	4686	8.38	18385	3.18	--	5604	1473	12219	3213
-5	-2.5	-3.75	H	15801	4123	8.65	18458	3.19	--	4946	1290	10855	2832
-2.5	0	-1.25	H	13779	3560	8.91	18531	3.21	--	4293	1109	9486	2450
0	2.5	1.25	H	11757	2996	9.17	18604	3.22	--	3647	929	8110	2067
2.5	5	3.75	H	9734	2433	9.43	18677	3.24	--	3006	751	6728	1682
5	7.5	6.25	H	7712	1870	9.70	18750	3.25	--	2371	575	5341	1295
7.5	10	8.75	H	5690	1306	9.96	18823	3.27	--	1741	400	3948	906
10	12.5	11.25	H	3667	743	10.22	18896	3.28	--	1117	226	2550	517
12.5	15	13.75	H	1645	180	10.49	18969	3.30	--	499	54	1146	125
15	17.5	16.25	--	--	--	--	--	--	--	--	--	--	--
17.5	20	18.75	--	--	--	--	--	--	--	--	--	--	--
20	22.5	21.25	C	2131	--	23.74	22646	--	16.09	452	--	2582	--
22.5	25	23.75	C	4777	--	25.03	23004	--	15.72	1037	--	5814	--
25	27.5	26.25	C	7423	--	26.32	23362	--	15.33	1652	--	9075	--
27.5	30	28.75	C	10069	--	27.62	23721	--	14.93	2301	--	12370	--
30	32.5	31.25	C	12715	--	28.91	24079	--	14.52	2988	--	15703	--
32.5	35	33.75	C	15361	--	30.20	24438	--	14.11	3715	--	19076	--
35	37.5	36.25	C	18007	--	31.49	24796	--	13.69	4488	--	22495	--

H : Heating
C : Cooling
O : Occupied
U : Unoccupied
EWT : Entering water temperature
COP : Coefficient of performance of heat pump in the heating mode
EER : Energy efficiency ratio for the heat pump in the cooling mode

Table 5.6.b) Ground thermal loads for Chicago, IL.

Bin temperature range (°C)		Bin reference temp. (°C)	H or C	Building's thermal load (Watts)		EWT (°C)	Heat pump capacity (Watts)	COP	EER	Heat pump additional power (Watts)		Ground heat load (Watts)	
min.	max.			O	U					O	U	O	U
-20	-17.5	-18.75	H	24170	10716	1.66	16522	2.81	--	4302	1907	15567	6902
-17.5	-15	-16.25	H	22400	9915	1.83	16569	2.82	--	3973	1759	14453	6397
-15	-12.5	-13.75	H	20629	9114	2.01	16617	2.83	--	3647	1611	13335	5891
-12.5	-10	-11.25	H	18858	8312	2.18	16664	2.84	--	3323	1465	12213	5383
-10	-7.5	-8.75	H	17088	7511	2.35	16711	2.85	--	3001	1319	11086	4873
-7.5	-5	-6.25	H	15317	6710	2.52	16759	2.86	--	2681	1174	9955	4361
-5	-2.5	-3.75	H	13546	5908	2.69	16806	2.87	--	2363	1031	8820	3847
-2.5	0	-1.25	H	11776	5107	2.86	16854	2.88	--	2048	888	7681	3331
0	2.5	1.25	H	10005	4306	3.03	16901	2.88	--	1734	746	6537	2813
2.5	5	3.75	H	8234	3505	3.20	16949	2.89	--	1422	605	5389	2294
5	7.5	6.25	H	6464	2703	3.38	16996	2.90	--	1113	465	4238	1772
7.5	10	8.75	H	4693	1902	3.55	17044	2.91	--	805	326	3082	1249
10	12.5	11.25	H	2922	1101	3.72	17091	2.92	--	500	188	1922	724
12.5	15	13.75	H	1152	300	3.89	17139	2.93	--	196	51	759	197
15	17.5	16.25	--	--	--	--	--	--	--	--	--	--	--
17.5	20	18.75	--	--	--	--	--	--	--	--	--	--	--
20	22.5	21.25	C	2121	--	17.23	20841	--	17.73	204	--	2529	--
22.5	25	23.75	C	4472	--	18.60	21221	--	17.42	438	--	5348	--
25	27.5	26.25	C	6824	--	19.97	21600	--	17.10	681	--	8186	--
27.5	30	28.75	C	9176	--	21.34	21980	--	16.75	935	--	11045	--
30	32.5	31.25	C	11528	--	22.71	22360	--	16.38	1201	--	13929	--
32.5	35	33.75	C	13879	--	24.08	22740	--	15.99	1481	--	16840	--

H : Heating
C : Cooling
O : Occupied
U : Unoccupied
EWT : Entering water temperature
COP : Coefficient of performance of heat pump in the heating mode
EER : Energy efficiency ratio for the heat pump in the cooling mode

Table 5.6.c) Ground thermal loads for Austin, TX.

Bin temperature range (°C)		Bin reference temp. (°C)	H or C	Building's thermal load (Watts)		EWT (°C)	Heat pump capacity (Watts)	COP	EER	Heat pump additional power (Watts)		Ground heat load (Watts)	
min.	max.			O	U					O	U	O	U
-5	-2.5	-3.75	H	14312	1650	15.67	15260	3.58	--	3994	461	10317	1190
-2.5	0	-1.25	H	12397	1416	15.98	15337	3.60	--	3444	393	8954	1023
0	2.5	1.25	H	10483	1182	16.30	15413	3.62	--	2898	327	7585	855
2.5	5	3.75	H	8568	948	16.61	15490	3.63	--	2357	261	6211	687
5	7.5	6.25	H	6653	713	16.92	15567	3.65	--	1822	195	4831	518
7.5	10	8.75	H	4739	479	17.23	15644	3.67	--	1292	131	3447	349
10	12.5	11.25	H	2824	245	17.54	15720	3.69	--	766	66	2058	178
12.5	15	13.75	H	910	11	17.85	15797	3.70	--	246	3	664	8
15	17.5	16.25	--	--	--	--	--	--	--	--	--	--	--
17.5	20	18.75	--	--	--	--	--	--	--	--	--	--	--
20	22.5	21.25	C	2237	--	30.93	19019	--	13.87	550	--	2787	--
22.5	25	23.75	C	4802	--	31.99	19281	--	13.53	1211	--	6013	--
25	27.5	26.25	C	7366	--	33.06	19543	--	13.18	1907	--	9273	--
27.5	30	28.75	C	9931	--	34.12	19806	--	12.83	2640	--	12571	--
30	32.5	31.25	C	12496	--	35.19	20068	--	12.49	3414	--	15910	--
32.5	35	33.75	C	15060	--	36.25	20330	--	12.14	4231	--	19292	--
35	37.5	36.25	C	17625	--	37.31	20592	--	11.80	5095	--	22720	--
37.5	40	38.75	C	20190	--	38.38	20855	--	11.47	6008	--	26198	--

H : Heating
C : Cooling
O : Occupied
U : Unoccupied
EWT : Entering water temperature
COP : Coefficient of performance of heat pump in the heating mode
EER : Energy efficiency ratio for the heat pump in the cooling mode

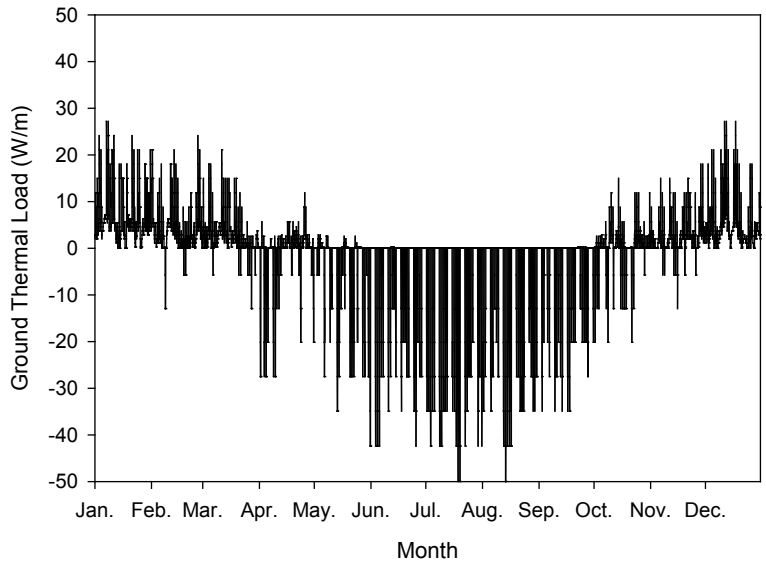

(1) Charlotte, NC

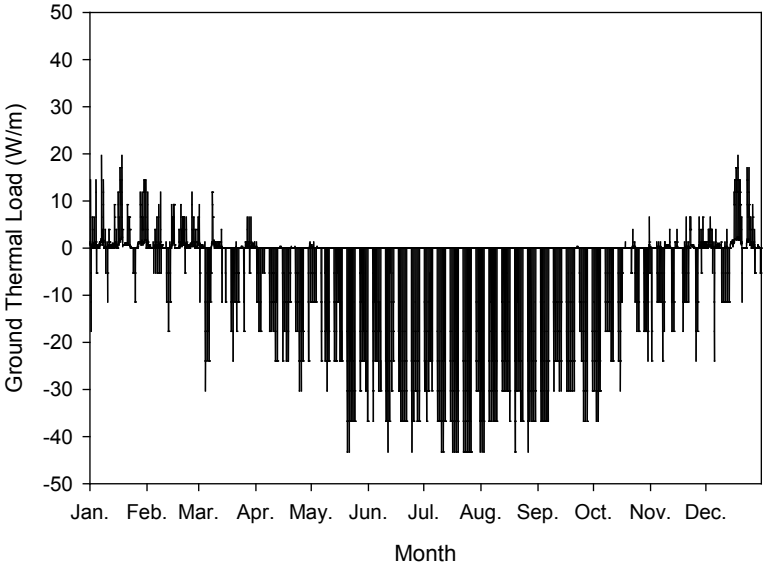

(3) Austin, TX

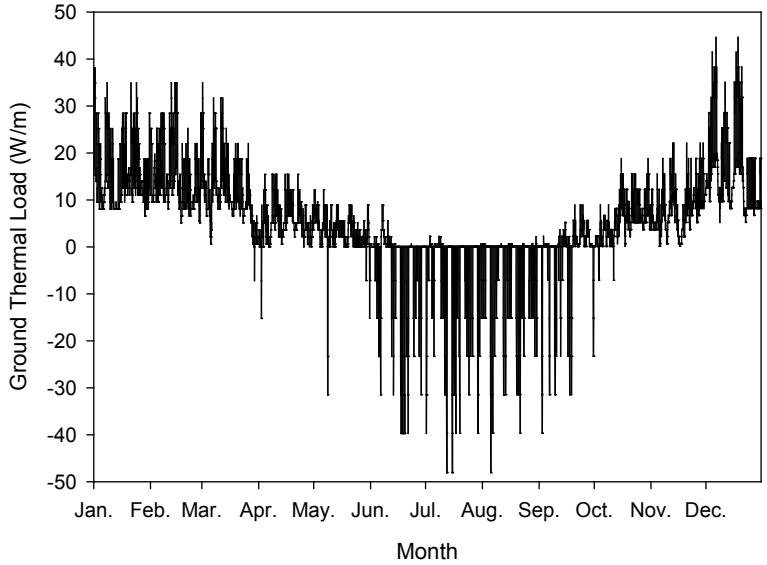

(2) Chicago, IL

Figure 5.3. Hourly variation for ground thermal loads at the three selected locations for a typical metrological year (TMY)

5.3.8. Change Point Analysis to Estimate Heating and Cooling Episodes

The period over which the ground is being heated or cooled varies from one location to another. Near-equal duration ground heating and cooling episodes for Charlotte, longer ground cooling episode for Chicago, and longer ground heating episode for Austin are observed as shown in Figure 5.3. Despite this observation of varying heating/cooling episodes, recently reported long-term analyses consider an equal 6 month long heating and cooling episodes over a year (Lazzari et al., 2010). In their baseline analysis, Lazzari et al. (2010) used equal amplitudes of the heating and cooling loads. These amplitudes are estimated from the peak ground thermal load and the selected loop length. Furthermore, they run additional analyses to analyze long-term performance where the respective amplitudes of heating and cooling are varied based on the maximum amplitudes of the heating and cooling during the year. The detailed approach presented in this chapter demonstrates the shortcomings behind the simplifying assumption of the earlier Lazzari et al. (2010) method.

Our purpose is to represent the ground thermal load with two half sine waves, one for heating and the other for cooling. For this purpose we need to determine where the ground thermal load transitions from heating to cooling during the year. As shown, the ground thermal load has varying amplitudes during heating and cooling episodes which both can be of varying durations over a year. It is possible to visually make this assessment. However, we need to develop a systematic approach to determine these respective amplitudes and durations. In our approach to delineate the heating and cooling episodes over each year we utilized the change point statistical analysis. This is a robust technique to characterize the trend of data that varies over time (Hinkley and Schechtman, 1987; Hinkley, 1971; Page, 1955, 1957; Pettit, 1980; Taylor, 2000). Appendix IV summarizes the princplies of implementing the change point analysis to capture the point of change within any data set. The change-point analyzer software by Tayler Enterprises is used to perform the analyses for the considered locations.

A change point analysis is performed for each considered location for the hourly ground thermal loads averaged over a certain time interval. Data averaging is used because the change from heating to cooling is a seasonal change rather than an hourly or a daily change. The change point analysis is repeated for various averaging periods. The initial averaging period is 24 hours with an averaging time step of one day. Additional change point analyses are performed for different averaging windows. Inthe first analysis data are averaged every day while in the second analysis the data are averaged every two days and so forth.

Numerous change points are detected by the change point analysis. Each change point indicates a time after which the average ground load is significantly different from the preceding average load. Two change points are of special interest; the first is when the average ground thermal load changes from positive ground cooling to negative ground heating (from winter to summer), and the other is when the change from negative ground heating to positive ground cooling takes place (from summer to winter). These two change points are summarized in Table 5-7 for the three selected locations for various averaging intervals.

The representative change points are taken from the analysis that has the least averaging period with no dependency errors. The details of the error dependency are provided in Appendix V. Two-day averaging period was the minimum averaging duration that provided no dependency errors for Charlotte; while for Austin and Chicago, three-day averaging period is needed to eliminate the dependency error. Moreover, the second change point was not captured when six and seven days averaging periods were used for Austin suggesting that the longer the averaging period, the more crude the analyses got to capture the change. Appendix V presents

the results of the representative analyses (2 days for Charlotte, and 3 days for Austin and Chicago) for each selected location.

Table 5-7. Results of the change point analysis in the ground thermal loads for the selected locations

Averaging period (days)	Charlotte, NC				Chicago ,IL				Austin, TX			
	Change point (days)		Thermal load episode (days)		Change point (days)		Thermal load episode (days)		Change point (days)		Thermal load episode (days)	
	1	2	H	C	1	2	H	C	1	2	H	C
1	--	--	--	--	--	--	--	--	--	--	--	--
2	84	296	212	153	--	--	--	--	--	--	--	--
3	84	270	186	179	144	285	141	224	63	348	285	80
4	84	296	212	153	144	256	112	253	60	223	288	77
5	80	295	215	150	155	255	100	265	60	350	290	75
6	84	276	192	173	156	264	108	257	60	**	**	**
7	84	273	189	176	161	287	126	239	7	**	**	**

1 and 2 : 1st change point from ground cooling to ground heating (end of winter), and the 2nd change point from ground heating to ground cooling (end of summer)
H : ground heating, C: ground cooling
-- : Not reliable results, i.e. dependent error
** : The 2nd change point is not captured

The results of the change point analyses suggest that;

1. For Charlotte, the ground heating and cooling episodes are 7 months and 5 months respectively,
2. For Chicago, the ground heating and cooling episodes are about 4 months and 8 months respectively,
3. For Austin, the ground heating and cooling episodes are about 9 months and 3 months respectively.

Based on these results, the equal 6 months heating/cooling episodes are considered acceptable for cases when the building thermal loads are balanced such as Charlotte. For locations where one thermal load (either heating or cooling) dominates, it is recommended to perform a change point analysis for the ground thermal loads to get a better estimate of the actual heating and cooling episodes. More importantly this demonstrates the limitations of the Lazzari method to analyze long-term performance of GCHP systems. The assumption of equal duration (i.e. 6 month) heating and cooling episodes is only valid for cases where heating and cooling loads are balanced where long-term effects will be negligible if any. The method has a fundamental fallacy in estimating durations where seasonal energy demands are unbalanced and long-term effects are expected. If a quick, rough estimate of these periods is needed; a period of 8 to 9 months for the dominating load and 4 to 3 months for the non-dominating load can be used.
Ground thermal load time history for the considered locations shown in Figure 5.3 were reproduced having the non-dominant load at the beginning of the year as shown in Figure 5.4. More discussion about the requirement for having the non-dominant load at the beginning of simulation is presented in the following section.

5.3.9. Sine Wave Equivalency Concept

Modeling the long term performance of GCHP systems is based on representing the ground thermal loads as sine waves, either balanced or unbalanced (Lazzari et al., 2010). This representation of the ground thermal loads assists in reducing the computational time and making these long-term analyses feasible. Lazzari et al. (2010) proposed a method to model the long-term performance of GCHP systems based on three main assumptions; (1) Equal 6 months heating and cooling episodes, (2) Ground thermal loads are repeated every year throughout the entire duration of the considered long-term analysis, and (3) Ground cooling always occurs before ground heating. In their work, Lazzari et al. (2010) performed a series of parametric analyses to investigate the effect of having balanced ground heating and cooling loads as well as unbalanced ground loads. For balanced ground loads, Lazzari et al. (2010) used the maximum acceptable design values (30 to 50 W/m) as the amplitude for both ground heating and ground cooling sine waves. They considered the unbalanced ground heating and cooling loads by varying the amplitude of the ground heating load only. In other words, the amplitude of the heating load is reduced to simulate unbalanced loading as the amplitude of the ground cooling load was maintained the same as the balanced load analysis. Thus, Lazzari et al. (2010) only considered locations at which the building thermal loads are balanced or when the building is heating dominant such as Chicago. However, the reduction of the heating load amplitude to account for unbalanced thermal loads was performed arbitrarily and no justification was provided for such reduction. Furthermore, the fixed 6 month durations of the heating and cooling episodes were not changed when the unbalanced ground thermal loads were considered.

The previous section examined the validity of the first assumption of Lazzari et al. (2010) approach and presented a detailed procedure to estimate the relative durations of heating and cooling episodes. The second assumption simply considers repeating weather cycles over years implying a stationary building energy demand. As discussed above, the ground thermal loads are based on the building energy demand which is a function of the weather, building utilization, usage habits of the occupants, building contents and characteristics of its components. Thus, this assumption is required to be able to predicate the long term performance of GCHP systems and thus it is assumed in the approach proposed in this chapter.

The sequence of heating and cooling episodes and the amplitudes of these loads require more investigations to ensure that the sine wave used in the long-term analysis represents the average actual operation of the GCHP system. Therefore, two halves of sine waves (one for heating and one for cooling) were developed following the Lazzari approach for each one of the considered locations as shown with the red line in Figure 5.4. For these waves, equal 6 months heating/cooling episodes are used giving a sine wave frequency of 2π/year or 1.9924×10^{-7} rad/sec for each of the heating and cooling episodes. The amplitudes of the heating and cooling loads for these waves are taken as the maximum respective thermal loads for the considered location. Even though the Lazzari method does not provide any systematic approach to select the respective amplitudes of heating and cooling episodes we selected the amplitudes of the half sine waves to match the computed maximum ground thermal load per loop length. This way the respective ground thermal loads consistently represented. For Chicago even though Lazzari et al. (2010) suggest the use of ground cooling before ground heating, this sequence was reversed here to match the proposed procedure of having the non-dominating thermal load first. More discussions about this procedure are reported in the following sections.

Another sine wave called Q_{equ} wave is also developed for each location as shown with the green line in Figure 5.4. The Q_{equ} waves are based on the equivalent sine wave concept. The

amplitude of the half sine wave is determined by equating the area of the ground thermal load within that episode with the area under the corresponding half sine wave. This is done separately for the heating and cooling episodes throughout their respective durations. The frequencies of the heating and cooling sine waves are estimated as $2\pi/P$, where P is the duration of the thermal load episode. The following formula is derived to estimate the sine wave amplitude for heating and cooling ground loads which is summarized in Table 5-8 along with the relative durations for each selected location.

$$Equivelent\ ground\ thermal\ load\ amplitude\ = \frac{\sum_{i=1}^{n} q_i}{12 \times P}$$

where; q_i: hourly ground thermal load (heating or cooling)

P: Thermal load duration in days
n: Number of thermal load hours = $P\ \times 24$

It is recognized that the use of a sine wave for the long term performance inherently imposes continuous application of the thermal load throughout the year, while there will be specific times during the year in which heating or cooling will not be necessary. The respective amplitude of each episode of the Q_{equ} sine wave accounts for the effect of these non-operational times.

Table 5-8. Amplitudes of different sine waves used to represent ground thermal loads

Location	Amplitudes of Lazzari et al. (2010) sine waves [Watts/m]		Frequencies of $Q_{equ.}$ sine waves (rad/sec.)		Amplitudes of $Q_{equ.}$ sine waves (Watts/m)	
	Heating	Cooling	Heating	Cooling	Heating	Cooling
Charlotte, NC	-49.989	27.154	1.715e-7	2.376e-7	-10.275	8.519
Chicago, IL	-48.115	44.476	3.578e-7	1.623e-7	-7.606	21.308
Austin, TX	-43.276	19.652	1.262e-7	4.722e-7	-11.312	2.709

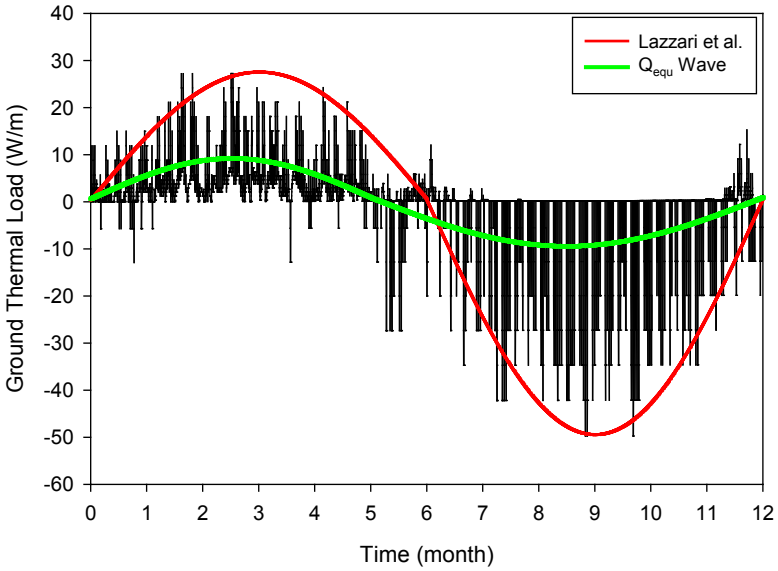

(1) Charlotte, NC

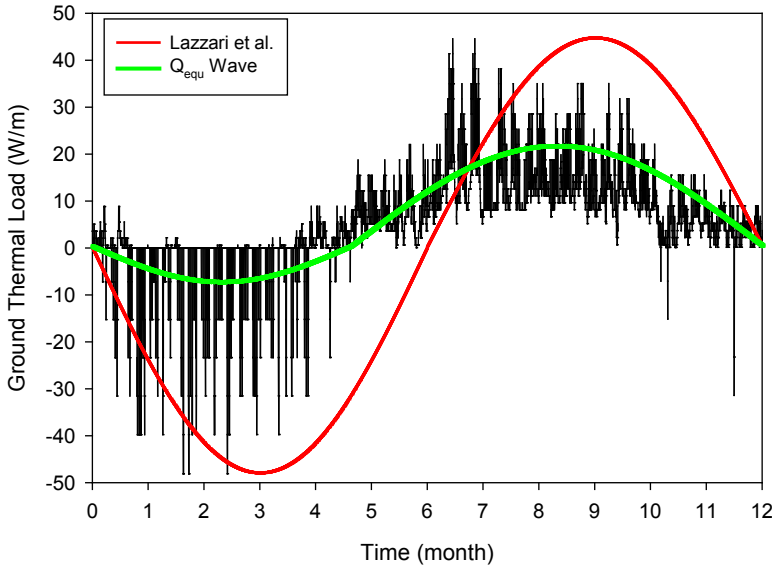

(2) Chicago, IL

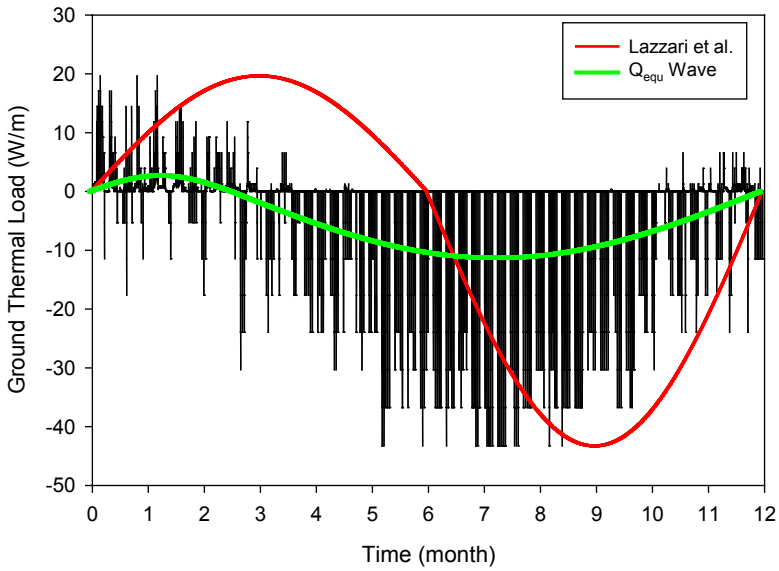

(3) Austin, TX

Figure 5.4. Ground thermal load profiles for the selected locations with the non-dominating load set at the beginning of the year. The red sine waves are developed following Lazzari et al. (2010) approach; the green sine waves are developed using the sine wave equivalency concept.

5.4. Numerical Modeling

As concluded in Chapter 3, modeling the operation of GCHP systems is sufficiently done using 2-D cross sectional numerical models. This is justified by the fact that the majority of the heat exchanged by the GCHE in general, and explicitly energy piles is in the radial direction; therefore, 3-D models are not necessary for estimating temperature changes in and around the piles. The 2-D modeling technique presented by Lazzari et al. (2010) is adopted and implemented using COMSOL finite element package (COMSOL, 2011).

The energy pile modeled here is assumed to be 50 cm in diameter, surrounded by a homogeneous, isotropic soil medium. The pile was assumed to have double 1.25 inch PEX tubes placed in opposing sides as shown in Figure 5.5. The distance between the upward and the downward tube branches is 10 cm (4 inches) measured from the center of the tubes. The initial ground temperature was set to the value reported in Table 5-2 for each selected location.

It should be noticed that the proposed model provides the average fluid temperature of the upward and the downward flows rather than the individual temperatures of these flows (Lazzari et al., 2010). This is because the heat rate per unit length is equally distributed between all tubes assuming that 50% of the total heat is exchanged by the downward flow while the other 50% is exchanged by the upward flow. The 50% distribution ratio is acceptable for these models since the actual ratio has a minor effect on the estimated temperature changes in and around the pile as discussed in Chapter 3.

A free boundary condition is assumed at the model external boundaries. However, the extent of the models (distance x in Figure 5.5) was selected such that no thermal interaction occurs across the external boundaries. Models considering free thermal external boundaries were compared to other models in which the external boundaries were set to the undisturbed ground temperature in order to confirm that the selected extent of the model is sufficient for no thermal interaction across the external boundaries. Based on this comparison, it is found that 20 meters are needed to assure no thermal interaction for one year of operation, while 200 meters are required for 30 years.

The ground thermal load is assigned as a heat source in the fluid domain using (Lazzari et al., 2010);

$$Q_{H\ or\ C} = \frac{-q_{H\ or\ C}}{4\pi r_i^2}$$

where; $Q_{H\ or\ C}$: is the heat assigned within the fluid domain in the model in W/m^3,
$q_{H\ or\ C}$: is the ground thermal load (H: heating, or C: cooling) in W/m,
r_i : is the internal radius of the tubes in m

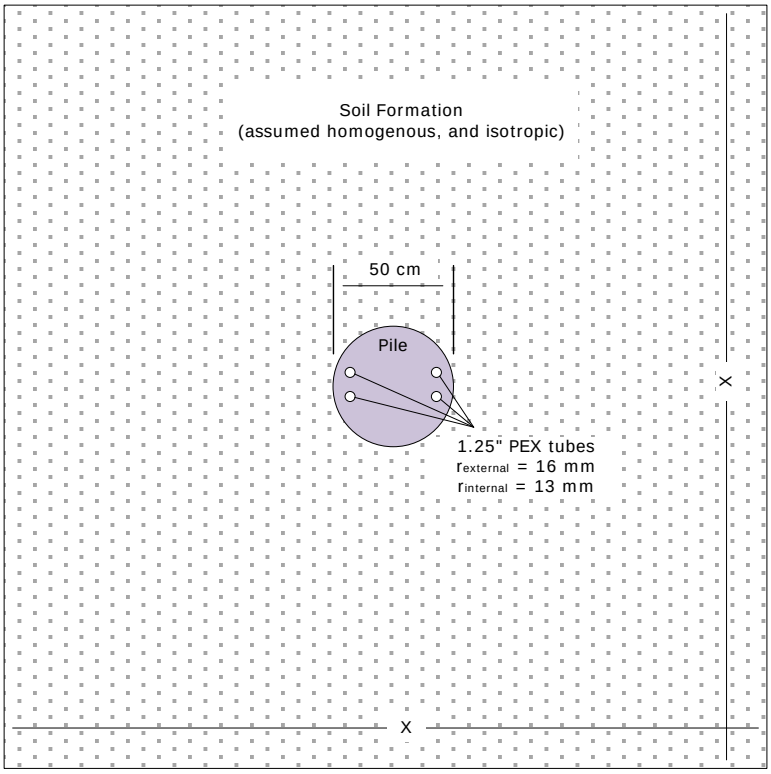

Figure 5.5. Sketch of the energy pile used in the analysis.

The heat convection between the fluid and the inner tube wall, the heat conduction in the tube walls, and the heat conduction in and around the pile are all considered in the model (Lazzari et al., 2010). No heat convection due to ground water flow is assumed. The circulation fluid is modeled as a solid domain with a high thermal conductivity value (k_{fluid} = *100 W/m·K*) and the actual density and heat capacity of water. This large fluid thermal conductivity is used to assure uniform fluid temperature inside the tube. Table 5-9 summarizes the values of different parameters used in the model.

The numerical model is validated using the infinite line source (ILS) analytical model (Ingersoll et al., 1948). A constant ground thermal load (q_H) of 20W/m was applied to the circulating fluid in the numerical model for one month and the temperature changes at different distances from the pile were compared to those predicted using the ILS model as shown in Figure 5.6. As seen in this figure, the temperature changes estimated using the numerical model are in good agreement with the respective temperature changes estimated using the ILS model for times more than 1 day. For times less than 1 day, the error between the two models is about 2 °C at 0.5 m away from the pile center; this error decreases as the distance from the pile increases. This observed error at close-by distances is due to the limitation of the ILS model since this model does not account for the cylindrical shape of the pile which is considered in the numerical model by using the actual pile geometry. The effect of the cylindrical shape of the pile is averaged out at large distances and thus the two models agree better.

Table 5-9. Geo-material, fluid, tube, and pile thermal properties included in the model.

Quantity	Value
Internal radius of PEX tubes [mm]	13
External radius of PEX tubes [mm]	16
Pile radius [mm]	250
Thermal conductivity of PEX tube [W/m·K]	0.4
Specific heat capacity of PEX tube [J/kg·K]	2300
Density of PEX tube [kg/m^3]	940
Concrete thermal conductivity [W/m·K]	1.44
Concrete heat capacity per unit volume [MJ/m^3·K]	1.41
Soil thermal conductivity [W/m·K]	1.4
Soil heat capacity per unit volume [MJ/m^3·K]	2.16
Fluid density [kg/m^3]	1031.8
Fluid specific heat capacity [J/kg·K]	3891

* heat capacity per unit volume = density × specific heat

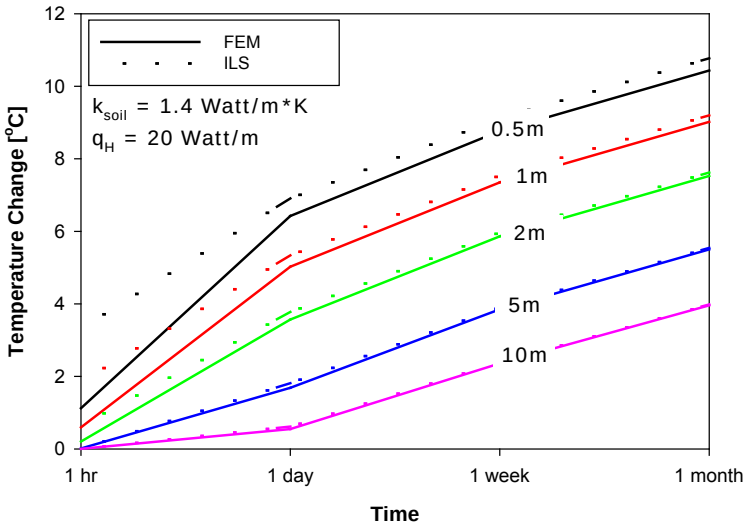

Figure 5.6. Results of finite element model (COMSOL) versus Infinite Line Source (ILS) model

5.5. Heat Exchange Analysis for One Year

The use of the actual ground thermal load (Q_{actual}) in a long term analysis is computationally expensive; furthermore, parametric analyses cannot be conducted because Q_{actual} is building dependent. On the contrary, the use of sine-wave ground thermal loads saves time and allows performing parametric analyses by varying the sine wave amplitude and duration. The selection of the representative sine wave should be made carefully such that the ground temperature changes estimated using the sine wave thermal load agree with those estimated using the actual thermal load. The results of one-year COMSOL analyses performed using the Q_{actual} thermal load, the equivalent sine wave Q_{equ} thermal load, and the sine wave developed using Lazzari et al. (2010) procedure were compared to select either the Q_{equ} sine wave or Lazzari et al. (2010) sine wave for the long term performance analyses. The sine wave that gives the best agreement with the ground temperature changes predicted using the Q_{actual} thermal load is selected for the

long term performance analyses. All the one-year models are performed as described in the previous section using half an hour (30 minutes) time step for the numerical solver.

5.5.1. Initial Thermal Load

One of the long term modeling challenges is the initial thermal load. As mentioned earlier, Lazzari et al. (2010) always unjustifiably considered the ground cooling load at the beginning of all their reported long term analyses. In this section, the importance of selecting the most representative initial thermal load is investigated. As mentioned earlier, it should be noticed that the sine wave that represents Lazzari et al. (2010) for Chicago was modified to have the ground heating load first to match the non-dominating thermal load approach proposed by the end of this section. This modification is believed not to affect the overall accuracy of Lazzari et al. (2010) approach; It, however, makes the comparison between this sine wave and the Q_{equ} sine wave simpler.

Figure 5.7 shows the temperature variation for Austin, TX at the center of the pile over a one year period obtained using the amplitudes and durations of the equivalent sine wave Q_{equ} and considering the following scenarios; (1) An initial heating load followed by a cooling load shown by the dotted black line, (2) An initial cooling load followed by a heating load shown by the dotted red line. For these two scenarios, the ground temperature in and around the pile estimated at the end of the first thermal load (heating for scenario 1, and cooling for scenario 2) is used as an initial condition for the following thermal load (cooling for scenario 1, and heating for scenario 2). Figure 5.7 also shows the temperature variation for another two superimposed thermal load scenarios; one starts with heating load followed by cooling load (the solid black line), and the other starts with cooling load followed by heating load (the solid red line). The superimposed scenarios were developed by using the undisturbed ground temperature as the initial condition to estimate the temperature variation due to the heating load only, and due to the cooling load only. The estimated ground temperature changes for heating and cooling loads were then superimposed one after the other to represent the heating-cooling and the cooling-heating scenarios.

As expected, the two superimposed thermal load scenarios resulted in the same temperature change at the end of the modeled year since it is simple superposition. On the other hand, the scenarios accounting for the effect of the initial thermal load on the following thermal load (the dotted lines) deviated from one another. Moreover, the ground temperatures estimated form the latter scenarios match those estimated from the respective superimposed scenarios for the initial thermal loads, and deviated from these respective superimposed scenarios for the final thermal load. This is due to the change of the initial ground temperature at the beginning of the final thermal load. This effect can be explained using the sketches in Figure 5.8.

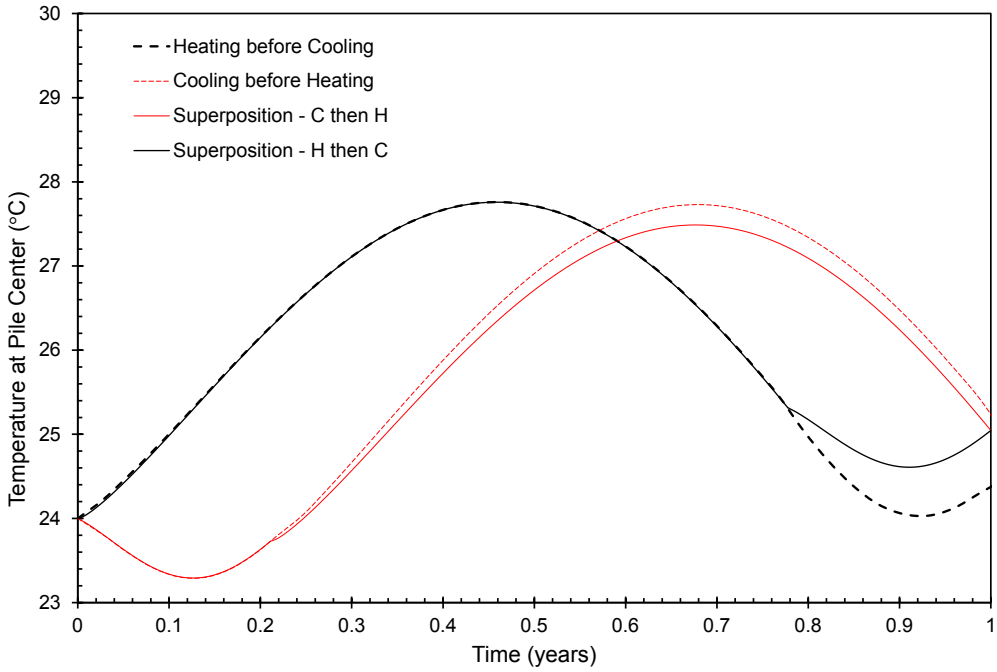

Figure 5.7. The effect of the initial thermal load on the predicted temperature change at the center of the pile by the end of one-year analysis.

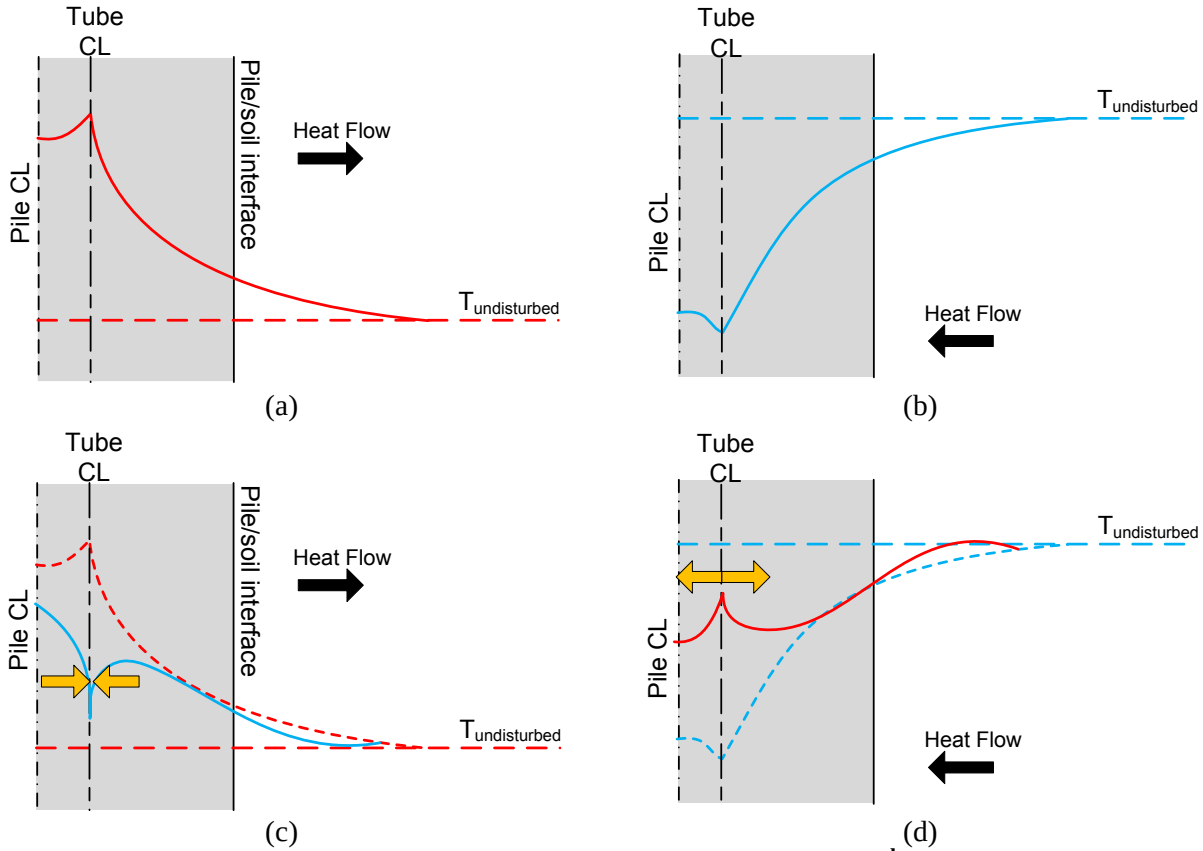

Figure 5.8. Effect of ground temperature at the beginning of the 2nd thermal load on the respective predicted ground temperature.

When only heating load is applied using the undisturbed ground temperature as the initial condition, the heat flows away from the pile as shown in Figure 5.8-a. The opposite is true, when the cooling load is applied using the undisturbed ground temperature as the initial condition the heat flows towards the pile as shown in Figure 5.8-b. For the case of cooling after heating as in Figure 5.8-c, in addition to the heat dissipation away from the pile another heat is being directed to the tubes which decreases the temperature at all points in and around the pile compared to using the superposition. Similarly, for the case of heating after cooling as shown in Figure 5.8-d, heat it being directed away from the tubes which is resisted by the heat directed to the pile causing more temperature buildup in and around the pile. The proportions of heat loss for heating-cooling scenario and heat gain for cooling-heating scenario depend of the relative heat gain and heat loss during the initial thermal load, respectively.

Examining for the effect of the initial thermal load on the estimated final ground temperature change at the end of a one year analysis, analyses considering the initial thermal load to be the heating load and others considering it to be the cooling load were performed for all three locations. When the Q_{equ} model begins with the ground heating load at the start of the year, the temperature change by the end of the modeled year at the center of the pile were found to be -0.56°C, -2.14°C, and 0.31°C for Charlotte, Chicago, and Austin, respectively. For Austin, the observed 0.31°C average annual temperature change at the pile center is quite small for the large difference between the dominant ground heating load (11.3 W/m over 9 months) and the non-dominant ground cooling load (2.7 W/m over 3 months). Furthermore, the observed annual average temperature change for Charlotte (-0.56°C) is not expected since the dominant load is the ground heating load (10.3 W/m over 7 months). Similar unexpected response for Chicago was obtained when the ground cooling load was used at the beginning of the year.

The temperature changes trend were found reasonable when the non-dominant ground thermal load is considered at the beginning of the year as shown in Figure 5.9, Figure 5.10, and Table 5-10. The non-dominant thermal load is defined as the load with the least sine wave amplitude and duration. For example; the ground cooling load is the non-dominant load for Charlotte and Austin, while the ground heating load is the non-dominant for Chicago. Thus, it is suggested that the non-dominant thermal load should be used as the initial thermal load to capture the right system behavior which is adopted in all analyses reported in the preceding sections.

5.5.2. The Representative Sine Wave

Figure 5.9 presents the estimated temperature changes at the center of the pile obtained from the Q_{actual} analysis, the $Q_{equ.}$ analysis, and the sine wave based on Lazzari et al. (2010) analysis. Similar comparisons at 1 m and 10 m away from the center of the pile are shown in Appendix VI. It is observed from Figure 5.9 that the analysis performed using the sine wave which was developed based on Lazzari et al. (2010) produces temperature changes that do not represent the actual system operation obtained by the Q_{actual} analysis. Even though, the general response of cooling the ground then heating it was captured by Lazzari et al. (2010) sine wave, the magnitude of the temperature change is significantly amplified for all three locations. On the other hand, the temperature changes estimated using the equivalent sine wave Q_{equ} analysis represents the average response of the GCHP system since it agrees with the results from the Q_{actual} analysis as shown in Figure 5.9 and in Table 5-10. Furthermore, Figure 5.10 shows the temperature change along a line extending from the center of the pile to 15m away from the center at the end of one year of thermal operation. In this figure, it is shown that the temperature changes estimated using the equivalent sine wave and the operational thermal loads are in good

agreement at the pile center as well as in its vicinity. Thus, the sine waves developed using the equivalency concept are more accurate than Lazzari et al. (2010) and therefore they will be used for the long term analyses.

Moreover it is noticed in Table 5-10 that despite the huge difference in the heating thermal load between Charlotte, NC and Austin, TX, the temperature change estimated using the equivalent sine waves at the end of the year for these two locations are very close. However, Figure 5.10 shows a larger thermal influence zone around the pile in Austin, TX (about 14m) compared to this in Charlotte, NC (about 7m). This larger influenced zone refers to the higher injected thermal energy in the ground. Thus, it can be inferred that the temperature change at the center of the pile should not be used solely to judge the overall performance of the system.

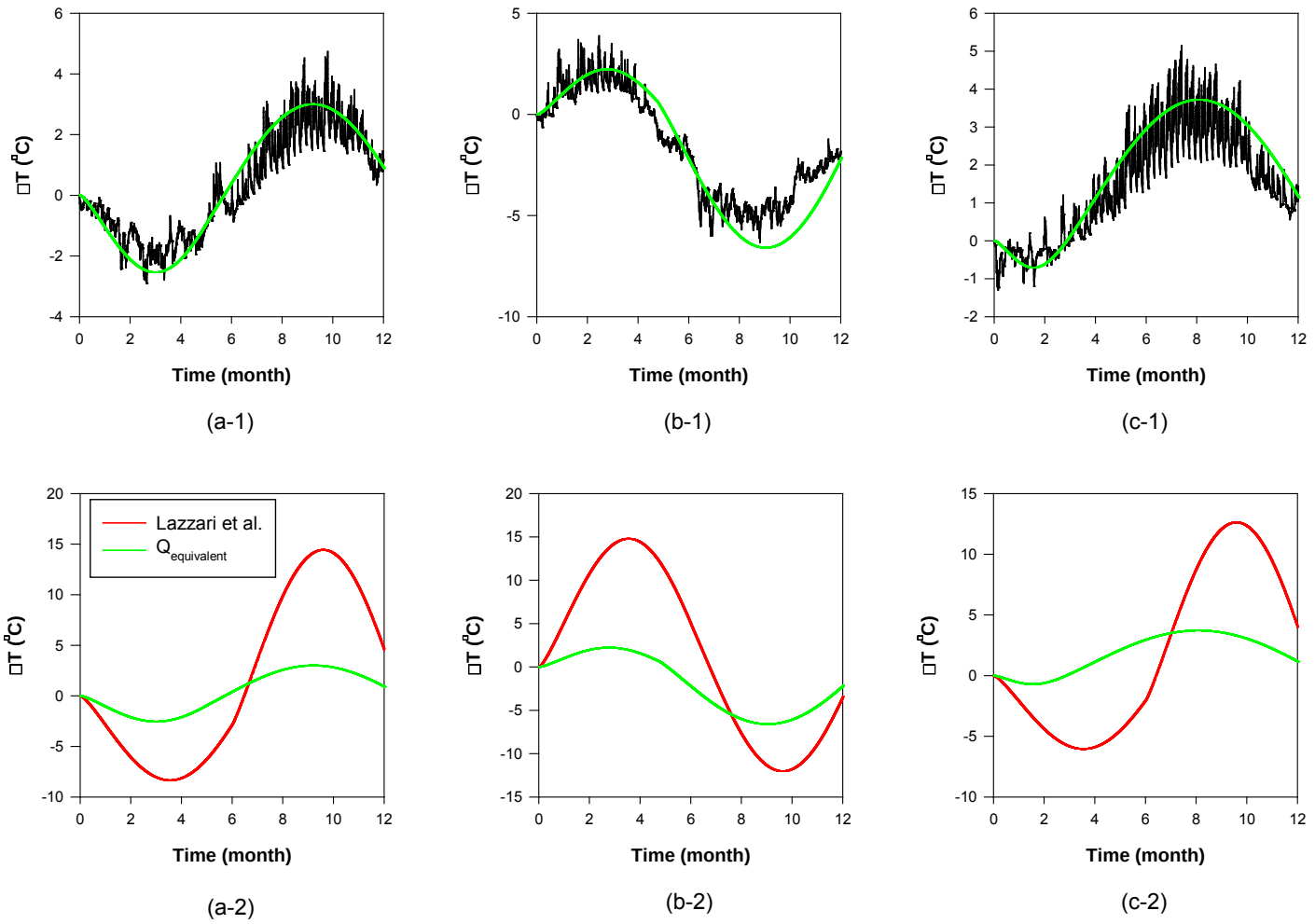

Figure 5.9. Temperature changes at the pile center estimated using the actual ground loads (Q_{actual}), the sine wave based on Lazzari et al. approach, and the equivalent sine wave sine wave ($Q_{equivalent}$) for; (a) Charlotte, NC; (b) Chicago, IL; and (c) Austin, TX.

Table 5-10. Temperature change (ΔT) at the pile center from the three modeled ground heating loads Q_{actual}, $Q_{equ.}$, and Lazzari et al. (2010) analyses.

Location	Q_{actual} analysis			$Q_{equ.}$ analysis			Lazzari et al. (2010) sine wave			Absolute error at the end of the year	
	End of a year	Mid-heating	Mid-cooling	End of a year	Mid-heating	Mid-cooling	End of a year	Mid-heating	Mid-cooling	Q_{equ}	*Lazzari et al. (201)*
Charlotte, NC	1.12	2.86	-2.25	0.89	2.87	-2.45	4.50	13.81	-8.06	0.23	3.38
Chicago, IL	-1.82	1.94	-4.9	-2.14	2.16	-6.34	-3.41	14.28	-11.38	0.32	1.59
Austin, TX	1.39	3.85	-0.59	1.14	3.61	-0.68	3.99	12.10	-5.83	0.25	2.6

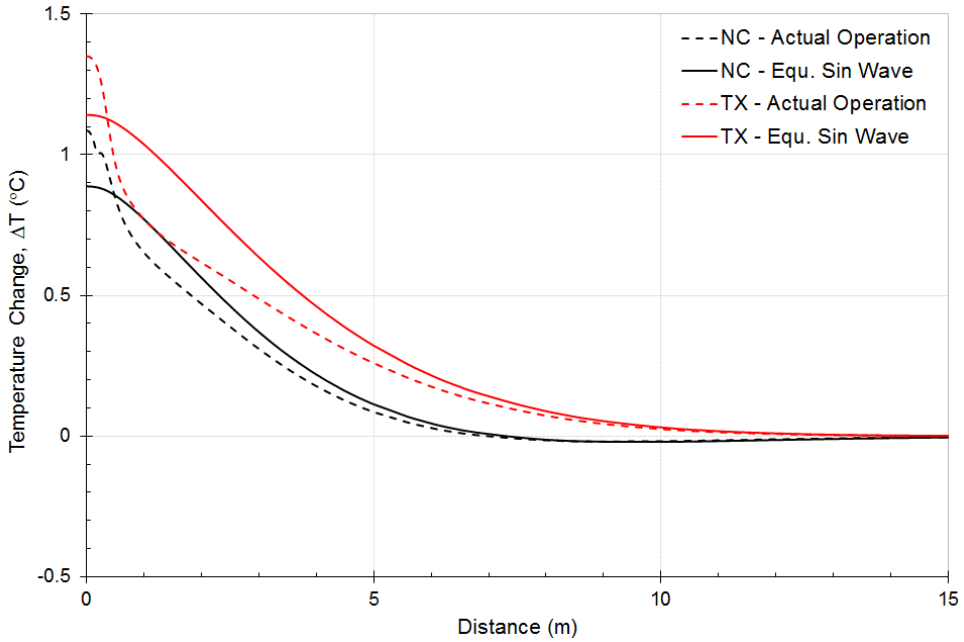

(a)

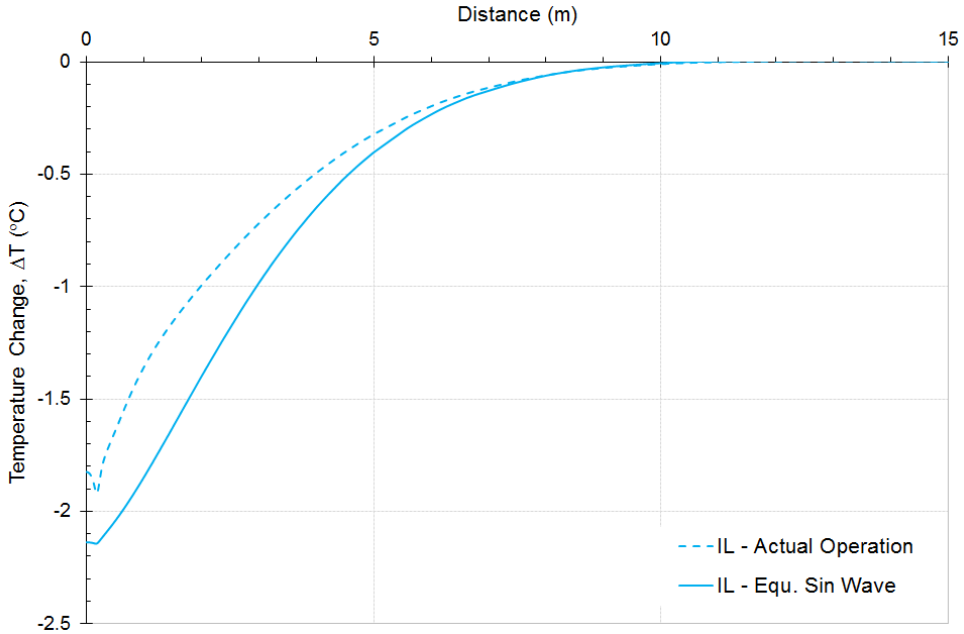

(b)

Figure 5.10. Comparison between models performed using the actual ground loads (Q_{actual}), and sine waves based on equivalent sine wave concept ($Q_{equivalent}$) for; (a) Charlotte, NC, and Austin, TX, (b) Chicago, IL.

5.6. Long-Term Analysis

The sine waves developed using the equivalent sine wave concept (Q_{equ}) for Austin, TX and Chicago, IL are used to perform the long term thermal analysis of the GCHP system for the these cities. Since the sine wave for Charlotte, NC is not fully balanced as intended to be, a hypothetical fully balanced sine wave is used to examine the long-term performance of energy piles. This hypothetical sine wave has amplitudes of 10 W/m for heating and cooling episodes which were assumed 6 month each. The Q_{equ} sine waves for the three selected locations and the hypothetical balanced sine wave are assumed to be repeated for every operational year. The total long term period considered in these models is 150 years; the first 30 years are the system operational period. The remaining 120 years are modeled with no thermal load applied to the ground in order to investigate the thermal recovery period. The recovery time is an indication of how sustainable the system is (Rybach et al., 2000; Signorelli et al., 2005) because it refers to the time duration after which the system can be reused with its full capacity by future generations.

Rybach and Eugster (2002), and Signorelli et al. (2005) reported that for a building operating 30 years in the heating mode, the time required for the ground temperature to recover to its initial undisturbed value is 30 years for a single heat exchanger and 70 years for a borehole array. The ambient seasonal variation at the ground surface contributes to the recovery period (shortening it) and thus it was accounted for in the recovery period estimations reported by Rybach and Eugster (2002), and Signorelli et al. (2005). Energy piles are constructed underneath a building with a thermally insulated ground floor making the solar energy effect not significant for the recovery period estimation. And since the thermal gradients controlling the heat transfer during recovery are those developed in the radial direction at the end of the operational period, the recovery period for energy piles can be accurately estimated using the 2D cross sectional models considered in this chapter.

Figure 5.11 shows the temperature variation at the pile center for the selected locations and the hypothetical sine wave. For the later, the average ground temperature does not change over years as shown in Figure 5.11.a. On the other hand for locations where one thermal load dominates (Chicago as a cooling dominant, and Austin as a heating dominant), the average ground temperature varies significantly in the first decade (10 years) then reaches to stability. The same observations were found when the ground temperatures at different distances from the pile center are considered as shown in Appendix VII. Furthermore, it is observed that the yearly variation of the ground temperature reduces as the distance from the pile increases as shown in Appendix VII. Similar conclusions were reported by Rybach and Eugster (2002), and Signorelli et al. (2005) for building heating operation (ground cooling mode).

Moreover, Figure 5.12 shows the reduction in the heap pump performance indices for the Austin and Chicago. The coefficient of performance (COP) is used for Chicago because it is cooling dominating nature while the energy efficiency ratio (EER) is used for Austin and Charlotte because the heating load is the dominant. The decrease in the performance index for Charlotte (EER) is smaller than those observed for Austin and Chicago suggesting a more dependable system.

The geotechnical design of energy piles is based on the frictional and toe resistances of the pile. Such resistances depend on the soil strength which is affected by the soil temperature. For normally and slightly over consolidated clays, the soil strength is reduced by the temperature increase and therefore; (1) for balanced thermal loads, modeling only one year is sufficient to obtain the optimum (maximum and minimum) ground temperatures for estimating the soil strength, (2) for locations where ground cooling is dominating, the lower soil strength is at the

initial undisturbed temperature, and (3) for locations where ground heating is dominating, the critical case is the long term operation which requires knowing the desired system life to get a good estimate of the maximum and minimum ground temperature. It is, however, enough to model the first 10 years of ground heating since the variation of the ground temperature after this period is repeatable and can be accounted for by adding 1 ^{o}C to the ground temperature after 10 years.

Figure 5.13 shows the temperature recovery at the pile center for Austin, Chicago, and for the hypothetical balanced sine wave. A strong recovery takes place immediately after switching off the heat pump followed by decay in the recovery rate with time. Furthermore, the temperature recovery at different distances for the same location takes the same time period to reach to the full recovery line defined by Rybach and Eugster (2002), and Signorelli et al. (2005). The full recovery line is defined as the ground temperature that deviates by at most ± 0.1 ^{o}C from the undisturbed ground temperature.

Balanced thermal loads and periods produce the shortest recovery time which is less than 1 year as opposed to the heating dominant (76 years for Austin) and cooling dominant (104 years for Chicago) locations. The temperature recovery for Charlotte is in between the fully balanced load and the unbalanced behavior (about 15 years). Therefore, it is highly recommended to attempt to have balanced heating and cooling loads when possible.

The recovery period for building heating operation (ground cooling) was found to be 104 years for Chicago. This result is significantly higher than the 30 years recovery period reported by Rybach and Eugster (2002), and Signorelli et al. (2005). The difference is attributed to the effect of solar energy recharge for boreholes which is not the case for energy piles.

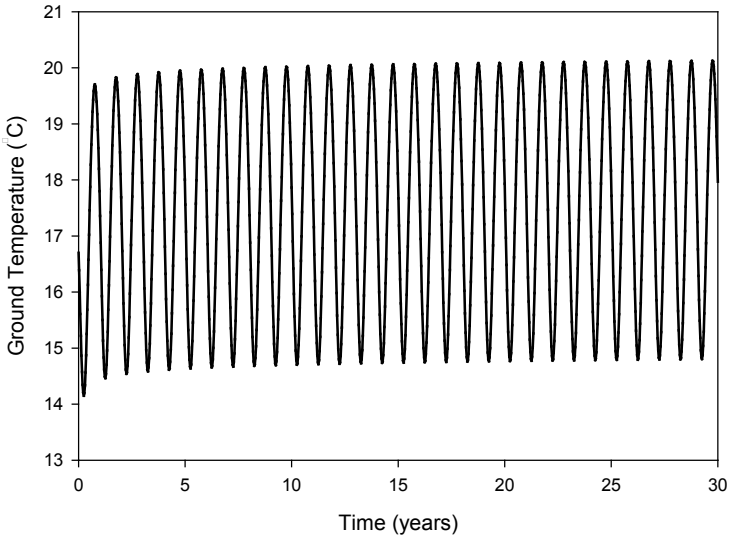

(a) Charlotte, NC

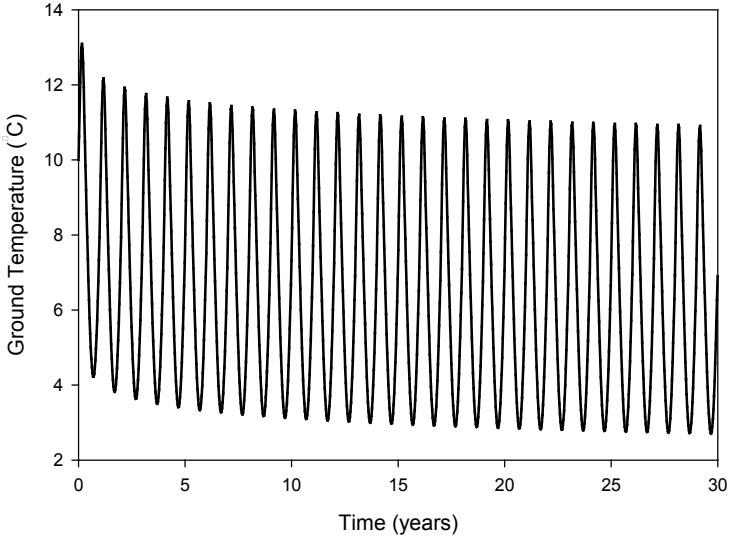

(b) Chicago, IL

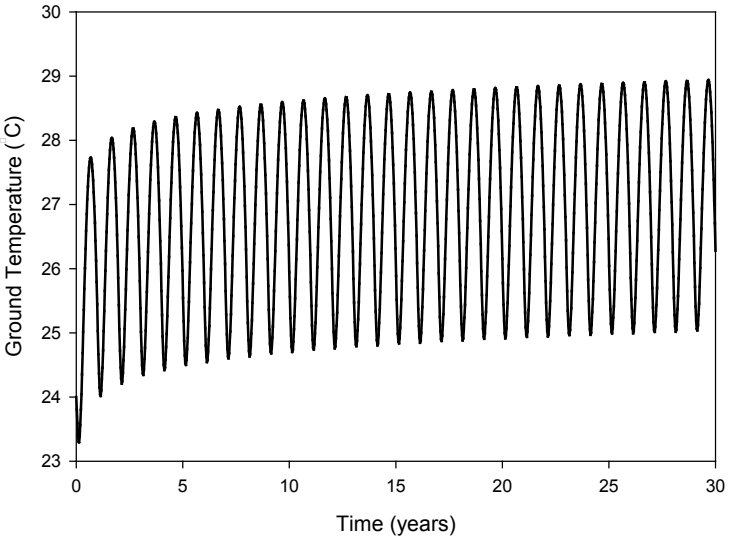

(c) Austin, TX

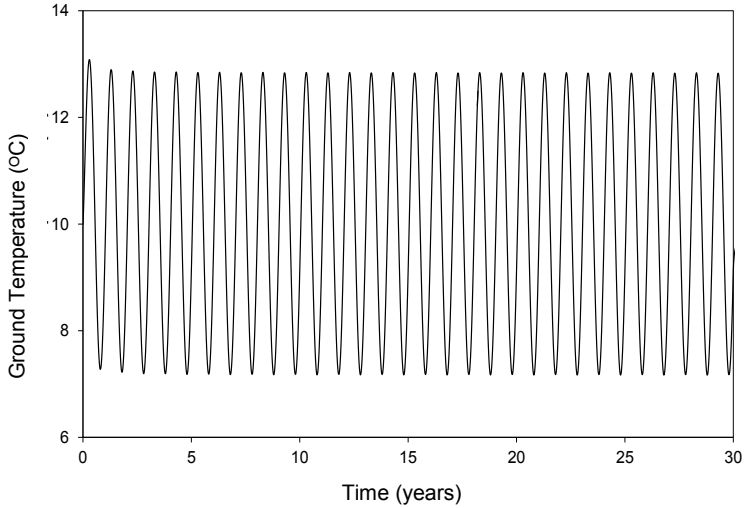

(d) Hypothetical Balanced Sine Wave

Figure 5.11. Ground temperature variation at the center of the pile for the selected locations assuming 30 years of operation.

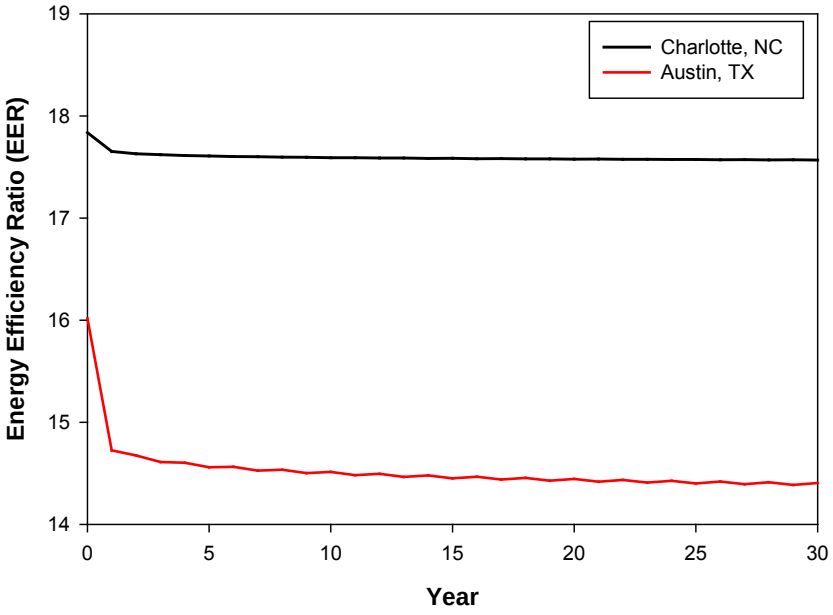

(a) Austin

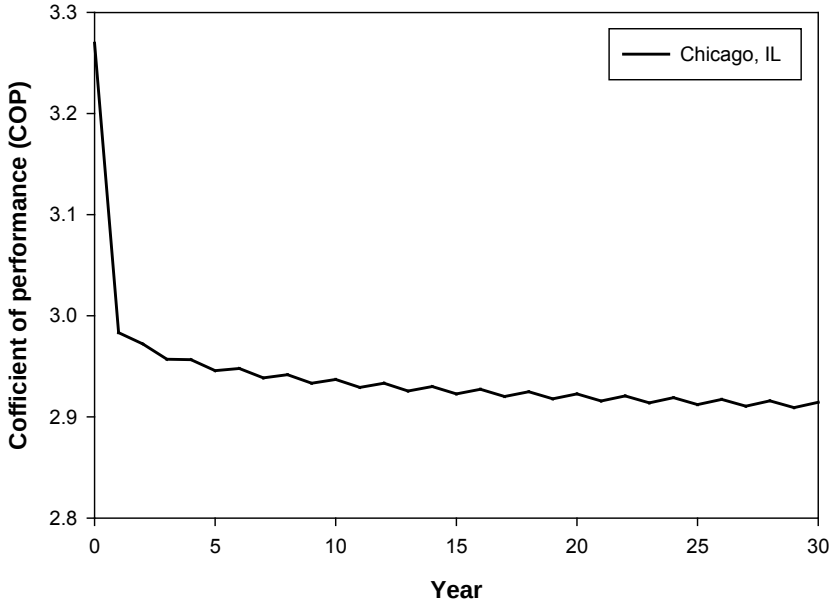

(b) Chicago

Figure 5.12. Indices of heap pump performance for the selected locations over time.

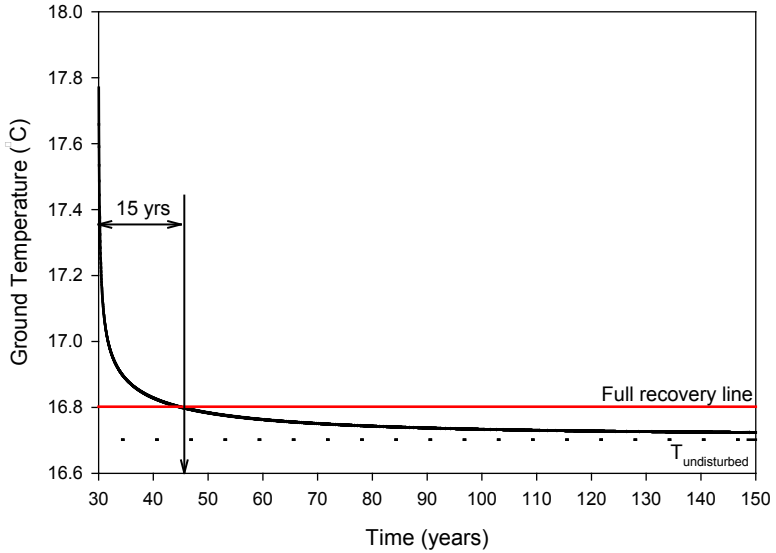

(a) Charlotte, NC

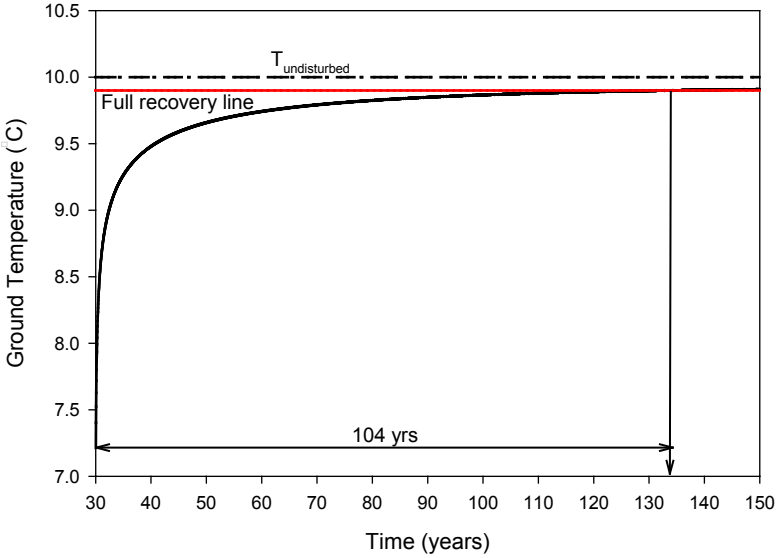

(b) Chicago, IL

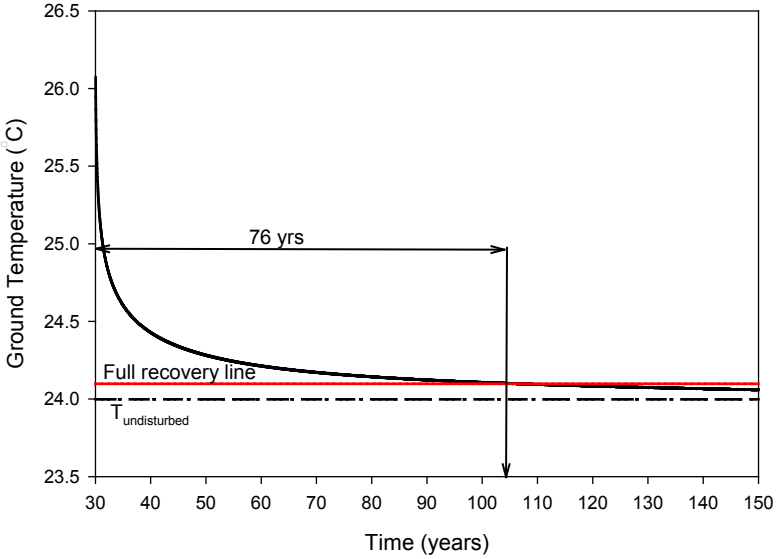

(c) Austin, TX

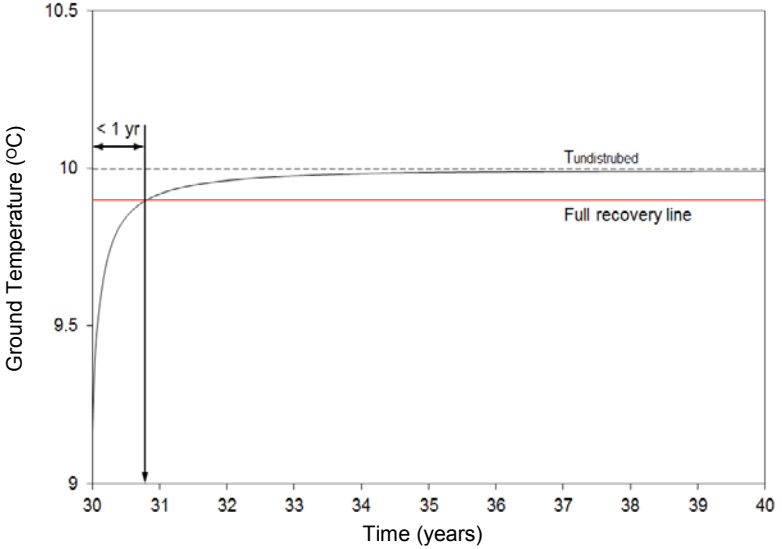

(d) Hypothetical Balanced Sine Wave

Figure 5.13. Temperature recovery at the center of the pile for the selected locations assuming 30 years of operation.

5.7. Conclusions

The procedure outlined in this chapter is a simplified approach to investigate the long term performance of energy piles. It, however, can be used to predicate the long term performance of general borehole heat exchangers except that the recovery period will not be accurate as the model does not account for the solar recharging energy.

Several conclusions were derived from the analyses reported here;

1. Modeling long term performance of geothermal system can be done using sine wave simplifications,
2. The selection of the representative sine wave to be included is a critical process and the procedure outlined in the chapter can be used for this. However, the following general rules can be used to simplify the analysis;
   a. The maximum ground thermal loads are to be reduced to 30% of their values and the reduced ground thermal loads are to be used as the amplitude for the sine waves,
   b. When heating and cooling loads are balanced, heating and cooling periods can be assumed equal and each is 6 months,
   c. When heating and cooling loads are not balanced with one dominating than the other, 9 months period for the dominating load is to be used and 3 months for the non-dominating load.
3. When the soil strength is reduced as the temperature increases (which is the most common case), one can conclude that; (a) for locations where balanced heating and cooling load exist, modeling only one year is sufficient to obtain the optimum (maximum and minimum) ground temperatures which are then to be used to estimate the soil strength either in the lab via thermo-mechanical testing apparatus or using the available correlations, (b) for locations where ground cooling is dominating, the critical case is at the beginning of the thermal operation and thus no modeling is required, and (c) for locations where ground heating is dominating, the critical case is the long term operation which requires knowing the desired system life to get a good estimate of the maximum and minimum ground temperature. It is, however, enough to model the first 10 years of ground heating since the ground temperature increase after this period is minimal and can be accounted for by adding $1^{o}C$ to the ground temperature after 10 years.
4. When energy piles are used, an attempt to have balanced heating and cooling loads should be made to assure a reasonable recovery period which assures the sustainability of the system. This could be performed by utilizing the system to provide the minimum of the heating or the cooling thermal loads and providing the additional loads using another means. In other words, hybrid system is recommended when ground couple heat pumps are considered.

References

American Society of Heating, Refrigerating, and Engineers Air-Conditioning (2009) "2009 ASHRAE handbook fundamentals." Atlanta, GA: American Society of Heating, Refrigeration and Air-Conditioning Engineers.

Brettmann, T., T. Amis, and M. Kapps (2010) "Thermal Conductivity Analysis of Geothermal Energy Piles," *the Geotechnical Challenges in Urban Regeneration Conference*. London, UK: DFI and EFFC, pp 1-6.

COMSOL (2011) "Introduction to COMSOL Multiphysics: version 4.2," *Reference Manual and Tutorial, COMSOL Inc, Burlington MA.*

Hinkley, D., and E. Schechtman (1987) "Conditional bootstrap methods in the mean-shift model," *Biometrika*, Vol. 74, pp 85-93.

Hinkley, D.V. (1971) "Inference about the change-point from cumulative sum tests," *Biometrika*, Vol. 58, pp 509-523.

Ingersoll, L.R., H.J. Plass, and M. Wis (1948) "Theory of the Ground Pipe Heat Source for the Heat Pump," *Heating, Piping & Air Conditioning*, Vol. 20, No. 7, pp 119-123.

Kavanaugh, S. P., and S. E. Lambert (2004) "A bin method energy analysis for ground-coupled heat pumps," *ASHRAE Transactions: Symposia*, Vol. AN-04-8-1, No. RP-1217, pp 535-542.

Kavanaugh, S., and K. Rafferty (1997) *Ground Source Heat Pumps: Design of Geothermal Systems for Commercial and Institutional Buildings*, Atlanta, Georgia: American Society of Heating, Refrigerating, and Air-Conditioning Engineers, Inc.

Lazzari, S., A. Priarone, and E. Zanchini (2010) "Long-term performance of BHE (borehole heat exchanger) fields with negligible groundwater movement," *Energy*, Vol. 35, No. 12, pp 4966-4974.

McQuiston, F. C., J. D. Parker, and J. D. Spitler (2004) *Heating, ventilating, and air conditioning : analysis and design*, New York: Wiley.

Page, E.S. (1955) "A test for a change in a parameter occuring at an unknown point," *Biometrika*, Vol. 42, pp 523-527.

Page, E.S. (1957) "On problems in which a change in parameter occurs at an unknown point," *Biometrika*, Vol. 44, pp 248-252.

Pedersen, C. O., D. E. Fisher, J. D. Spitler, and R. J. Liesen (1998) *Cooling and Heating Load Calculation Principles*, Atlanta, GA: American Society of Heating, Refrigerating and Air-Conditioning Engineers, Inc.

Pettit, A.N. (1980) "A simple cumulative sum type staistic for the change-point problem with zero-one observations," *Biometrika*, Vol. 67, pp 79-84.

Rybach, L., and W.J. Eugster (2002) "Sustainability aspects of geothermal heat pumps," *27th workshop on geothermal reservoir engineering*. Stanford University, Stanford, California, pp 1-6.

Rybach, L., T. Megel, and W.J. Eugster (2000) "At what time scale are geothermal resources renewable?," *world geothermal congress 2000*. Kyushu e Tohoku, Japan; May 28 - June 10.

Signorelli, S., T. Kohl, and L. Rybach (2005) "Sustainability of production from borehole heat exchanger fields," *World Geothermal Congress 2005*. Antalya, Turkey; 24-29 April 2005.

Tayler Enterprises, Inc. "Change-Point Analyzer Software," *http://www.variation.com/cpa/index.html*.

Taylor, W. (2000) "Change point analysis: a powerful new tool for detecting changes," *http://www.variation.com/cpa/tech/changepoint*.

Wilcox, S., and W. Marion (2008) "Users Manual for TMY3 Data Sets," In: National Renewable Energy Laboratory NREL, Ed. Golden, Colorado: NREL National Renewable Energy Laboratory, p 50.

Appendix I
Design weather data for the three selected locations
from ASHRAE Fundamentals Handbook (2009)
[used under fair use 2013]

WASHINGTON DC DULLES INT'L AR, VA, USA

WMO#: 724030

Lat: 38.94N Long: 77.45W Elev: 325 StdP: 14.52 Time Zone: -5.00 (NAE) Period: 82-06 WBAN: 93738

Annual Heating and Humidification Design Conditions

Coldest Month	Heating DB		Humidification DP/MCDB and HR						Coldest month WS/MCDB				MCWS/PCWD to 99.6% DB	
			99.6%			99%			0.4%		1%			
	99.6%	99%	DP	HR	MCDB	DP	HR	MCDB	WS	MCDB	WS	MCDB	MCWS	PCWD
1	10.7	15.7	-3.1	4.7	15.8	1.9	6.1	20.3	25.1	33.4	23.0	33.2	6.1	310

Annual Cooling, Dehumidification, and Enthalpy Design Conditions

Hottest Month	Hottest Month DB Range	Cooling DB/MCWB						Evaporation WB/MCDB						MCWS/PCWD to 0.4% DB	
		0.4%		1%		2%		0.4%		1%		2%			
		DB	MCWB	DB	MCWB	DB	MCWB	WB	MCDB	WB	MCDB	WB	MCDB	MCWS	PCWD
7	20.5	93.5	75.1	90.8	74.3	88.2	73.0	77.7	88.8	76.5	86.6	75.3	84.3	9.0	290

Dehumidification DP/MCDB and HR								Enthalpy/MCDB						Hours
0.4%			1%			2%		0.4%		1%		2%		8 to 4 &
DP	HR	MCDB	DP	HR	MCDB	DP	HR	MCDB	Enth	MCDB	Enth	MCDB	Enth	MCDB	55/69
74.5	130.5	82.0	73.5	126.0	80.8	72.5	121.9	79.8	41.2	89.0	40.0	87.2	38.9	84.5	712

Extreme Annual Design Conditions

Extreme Annual WS			Extreme Max	Extreme Annual DB				n-Year Return Period Values of Extreme DB							
				Mean		Standard deviation		n=5 years		n=10 years		n=20 years		n=50 years	
1%	2.5%	5%	WB	Min	Max	Min	Max	Min	Max	Min	Max	Min	Max	Min	Max
20.5	18.3	16.4	84.0	1.1	97.1	8.2	3.5	-4.8	99.6	-9.6	101.6	-14.2	103.5	-20.2	106.0

Monthly Climatic Design Conditions

			Annual	Jan	Feb	Mar	Apr	May	Jun	Jul	Aug	Sep	Oct	Nov	Dec
Temperatures, Degree-Days and Degree-Hours	Tavg		55.1	33.3	36.4	43.9	54.0	62.9	71.7	76.4	75.0	67.3	55.7	46.3	36.8
	Sd			10.42	8.95	9.65	8.51	7.49	6.16	4.97	5.37	7.24	8.02	9.01	9.76
	HDD50		1848	528	389	241	51	2	0	0	0	1	33	177	426
	HDD65		4735	984	800	656	344	132	15	1	3	58	306	562	874
	CDD50		3704	9	9	53	171	402	652	819	776	521	209	66	17
	CDD65		1119	0	0	4	14	67	217	355	314	128	18	2	0
	CDH74		10773	0	1	51	229	767	2056	3482	2915	1091	165	15	1
	CDH80		4139	0	0	12	61	241	756	1512	1179	353	24	1	0
Monthly Design Dry Bulb and Mean Coincident Wet Bulb Temperatures	0.4%	DB		66.7	69.0	81.1	86.8	89.7	93.8	97.0	96.4	93.5	83.2	76.1	69.8
		MCWB		59.3	55.8	62.8	66.6	71.2	74.3	76.1	76.2	73.7	68.4	63.0	61.4
	2%	DB		60.9	61.5	72.1	80.5	86.1	90.3	93.8	92.8	87.7	78.7	70.2	62.6
		MCWB		55.2	52.9	57.5	63.3	69.9	73.9	75.7	74.9	71.8	66.4	60.0	56.1
	5%	DB		53.9	56.2	66.2	75.3	82.5	87.5	91.0	89.7	83.9	74.6	66.0	56.7
		MCWB		47.2	48.0	54.9	60.9	68.3	72.7	75.3	73.6	69.9	63.9	58.9	51.4
	10%	DB		47.8	51.0	60.8	70.4	78.1	84.6	88.2	86.6	80.5	70.4	61.9	51.8
		MCWB		42.2	44.4	51.2	58.0	65.6	71.5	74.0	72.5	68.5	61.7	55.0	46.1
Monthly Design Wet Bulb and Mean Coincident Dry Bulb Temperatures	0.4%	WB		61.9	59.7	64.4	69.0	75.4	78.0	79.9	78.9	76.2	71.5	66.2	62.9
		MCDB		64.5	64.2	77.2	81.3	86.1	88.8	91.2	90.5	86.5	78.2	71.3	67.3
	2%	WB		55.5	54.3	60.4	65.9	72.4	76.2	78.1	77.2	74.4	69.2	63.3	57.7
		MCDB		60.0	59.6	69.2	76.3	82.3	86.4	89.3	88.3	82.9	75.5	68.0	61.6
	5%	WB		48.1	49.5	56.5	62.7	70.0	74.9	77.0	75.9	72.8	66.4	59.9	52.6
		MCDB		52.5	55.0	63.9	72.1	78.8	84.0	87.3	85.5	79.9	72.4	64.8	55.8
	10%	WB		42.8	45.3	52.3	59.9	67.6	73.3	75.7	74.6	71.0	63.5	56.1	46.4
		MCDB		47.0	50.5	60.1	69.0	75.9	81.4	84.5	83.2	77.1	68.8	60.8	50.6
Mean Daily Temperature Range		MDBR		17.2	18.7	20.8	22.9	22.1	21.2	20.5	20.5	21.2	22.8	20.7	17.6
	5% DB	MCDBR		24.7	27.2	30.0	31.1	27.9	24.4	24.3	24.0	24.8	27.1	25.7	24.0
		MCWBR		18.2	18.9	18.0	16.2	13.5	10.5	9.3	9.2	11.1	15.6	17.3	18.2
	5% WB	MCDBR		21.6	22.6	25.6	25.7	23.2	21.0	20.6	20.6	20.1	21.8	20.6	20.5
		MCWBR		17.9	17.6	17.3	14.7	12.5	10.0	9.0	9.1	10.3	13.9	16.3	17.7
Clear Sky Solar Irradiance	taub			0.313	0.344	0.394	0.404	0.462	0.523	0.544	0.576	0.418	0.365	0.333	0.311
	taud			2.422	2.228	2.065	2.085	1.932	1.808	1.787	1.687	2.160	2.303	2.401	2.477
	Ebn,noon			273	276	272	277	262	245	239	226	262	266	263	266
	Edh,noon			29	39	49	50	60	67	68	73	44	35	29	26

CDD*n* Cooling degree-days base n°F, °F-day
CDH*n* Cooling degree-hours base n°F, °F-hour
DB Dry bulb temperature, °F
DP Dew point temperature, °F
Ebn,noon } Clear sky beam normal and diffuse hori-
Edh,noon } zontal irradiances at solar noon, Btu/h/ft2
Elev Elevation, ft
Enth Enthalpy, Btu/lb
HDD*n* Heating degree-days base n°F, °F-day
Hours 8/4 & 55/69 Number of hours between 8 a.m. and 4 p.m with DB between 55 and 69 °F
HR Humidity ratio, grains of moisture per lb of dry air
Lat Latitude, °
Long Longitude, °
MCDB Mean coincident dry bulb temperature, °F
MCDBR Mean coincident dry bulb temp. range, °F
MCDP Mean coincident dew point temperature, °F
MCWB Mean coincident wet bulb temperature, °F
MCWBR Mean coincident wet bulb temp. range, °F
MCWS Mean coincident wind speed, mph
MDBR Mean dry bulb temp. range, °F
PCWD Prevailing coincident wind direction, °, 0 = North, 90 = East
Period Years used to calculate the design conditions
Sd Standard deviation of daily average temperature, °F
StdP Standard pressure at station elevation, psi
taub Clear sky optical depth for beam irradiance
taud Clear sky optical depth for diffuse irradiance
Tavg Average temperature, °F
Time Zone Hours ahead or behind UTC, and time zone code
WB Wet bulb temperature, °F
WBAN Weather Bureau Army Navy number
WMO# World Meteorological Organization number
WS Wind speed, mph

AUSTIN/BERGSTROM, TX, USA

WMO#: 722540

Lat: 30.18N Long: 97.68W Elev: 495 StdP: 14.43 Time Zone: -6.00 (NAC) Period: 82-06 WBAN: 13904

Annual Heating and Humidification Design Conditions

Coldest Month	Heating DB		Humidification DP/MCDB and HR						Coldest month WS/MCDB				MCWS/PCWD to 99.6% DB	
	99.6%	99%	99.6%			99%			0.4%		1%			
			DP	HR	MCDB	DP	HR	MCDB	WS	MCDB	WS	MCDB	MCWS	PCWD
1	25.2	29.6	10.7	9.7	34.3	16.6	13.0	40.2	25.8	46.9	23.8	48.1	7.1	10

Annual Cooling, Dehumidification, and Enthalpy Design Conditions

Hottest Month	Hottest Month DB Range	Cooling DB/MCWB						Evaporation WB/MCDB						MCWS/PCWD to 0.4% DB	
		0.4%		1%		2%		0.4%		1%		2%			
		DB	MCWB	DB	MCWB	DB	MCWB	WB	MCDB	WB	MCDB	WB	MCDB	MCWS	PCWD
8	22.5	99.7	75.0	97.8	75.1	95.9	75.4	79.1	89.9	78.3	89.0	77.7	88.4	8.2	190

Dehumidification DP/MCDB and HR									Enthalpy/MCDB						Hours
0.4%			1%			2%			0.4%		1%		2%		8 to 4 &
DP	HR	MCDB	DP	HR	MCDB	DP	HR	MCDB	Enth	MCDB	Enth	MCDB	Enth	MCDB	55/69
76.8	142.0	81.8	75.9	137.8	81.1	75.2	134.5	80.8	42.8	89.5	42.1	89.1	41.4	88.4	657

Extreme Annual Design Conditions

Extreme Annual WS			Extreme Max	Extreme Annual DB				n-Year Return Period Values of Extreme DB							
				Mean		Standard deviation		n=5 years		n=10 years		n=20 years		n=50 years	
1%	2.5%	5%	WB	Min	Max	Min	Max	Min	Max	Min	Max	Min	Max	Min	Max
20.9	18.8	16.9	84.9	19.3	103.4	6.0	3.0	15.0	105.6	11.4	107.3	8.1	109.0	3.7	111.2

Monthly Climatic Design Conditions

		Annual	Jan	Feb	Mar	Apr	May	Jun	Jul	Aug	Sep	Oct	Nov	Dec
Temperatures, Degree-Days and Degree-Hours	Tavg	68.7	51.0	54.0	61.2	69.1	75.9	81.3	83.9	84.9	79.4	70.4	60.7	51.1
	Sd		9.39	9.57	8.28	7.06	5.30	3.64	2.79	3.15	5.91	7.57	9.28	10.29
	HDD50	300	102	61	12	0	0	0	0	0	0	1	16	108
	HDD65	1654	444	322	173	43	2	0	0	0	2	36	190	442
	CDD50	7108	132	173	359	572	804	938	1052	1083	881	634	337	143
	CDD65	2989	10	14	55	165	341	488	587	618	433	205	61	12
	CDH74	32215	54	110	383	1333	3057	5431	7079	7793	4663	1854	404	54
	CDH80	15566	5	19	75	388	1190	2645	3834	4393	2283	661	71	2
Monthly Design Dry Bulb and Mean Coincident Wet Bulb Temperatures	0.4% DB		79.1	82.2	86.0	91.9	95.7	99.3	101.6	102.5	102.8	93.3	86.1	79.0
	0.4% MCWB		60.9	62.3	65.6	71.2	74.2	75.5	74.1	75.1	75.3	72.9	69.4	65.4
	2% DB		74.9	77.2	81.5	87.4	91.5	96.1	99.1	100.0	96.9	90.1	81.9	75.1
	2% MCWB		62.9	62.3	65.8	69.3	73.7	76.1	74.9	75.1	75.0	72.3	68.4	64.7
	5% DB		71.5	73.3	78.4	84.2	89.4	93.4	96.9	98.3	94.0	87.1	78.9	72.1
	5% MCWB		61.7	61.6	65.0	68.9	74.5	75.4	75.2	75.3	74.5	71.6	67.2	63.3
	10% DB		67.7	70.0	74.9	81.6	86.6	91.6	94.7	96.3	91.2	83.6	75.3	68.9
	10% MCWB		59.9	61.4	64.0	68.6	73.5	75.8	75.4	75.6	74.0	70.4	66.6	62.0
Monthly Design Wet Bulb and Mean Coincident Dry Bulb Temperatures	0.4% WB		69.4	69.4	72.0	76.0	79.1	80.0	80.2	80.1	79.2	77.7	73.3	70.4
	0.4% MCDB		73.0	74.2	78.7	83.8	88.0	91.0	91.1	91.4	89.6	85.5	79.7	74.6
	2% WB		67.1	67.6	70.1	74.2	77.5	78.5	78.7	78.7	78.0	76.2	71.7	68.4
	2% MCDB		71.3	72.1	76.0	81.7	86.8	89.3	89.6	90.1	88.0	83.7	77.6	72.3
	5% WB		64.5	65.9	68.7	72.7	76.2	77.8	78.0	78.0	77.2	75.0	70.4	66.1
	5% MCDB		69.5	70.0	74.2	79.9	85.0	88.5	88.7	89.6	86.9	82.1	75.8	70.4
	10% WB		60.5	63.4	67.2	71.2	75.0	77.0	77.2	77.3	76.3	73.4	68.8	63.2
	10% MCDB		66.4	68.0	72.8	77.9	83.2	87.2	87.7	89.0	85.9	79.8	73.9	68.0
Mean Daily Temperature Range		MDBR	21.2	21.2	21.6	21.2	19.7	19.9	21.1	22.5	21.7	21.9	21.6	21.9
	5% DB	MCDBR	27.5	27.0	24.5	24.2	21.9	22.5	24.7	25.2	24.4	24.6	23.5	25.2
		MCWBR	17.4	15.9	13.4	11.8	8.3	6.7	5.8	6.0	7.3	10.0	12.9	16.8
	5% WB	MCDBR	20.2	20.0	18.0	17.9	18.3	19.5	20.4	21.7	19.7	18.2	18.0	19.9
		MCWBR	15.5	14.2	11.5	9.9	8.2	7.1	6.2	6.3	6.9	9.0	11.9	15.7
Clear Sky Solar Irradiance	taub		0.340	0.357	0.370	0.400	0.424	0.444	0.450	0.457	0.426	0.371	0.351	0.335
	taud		2.404	2.328	2.291	2.204	2.177	2.141	2.139	2.114	2.216	2.388	2.413	2.467
	Ebn,noon		283	287	290	284	276	269	267	264	269	279	276	279
	Edh,noon		33	38	41	46	48	49	49	50	44	35	32	30

CDD*n* Cooling degree-days base n°F, °F-day
CDH*n* Cooling degree-hours base n°F, °F-hour
DB Dry bulb temperature, °F
DP Dew point temperature, °F
Ebn,noon } Clear sky beam normal and diffuse hori-
Edh,noon } zontal irradiances at solar noon, Btu/h/ft2
Elev Elevation, ft
Enth Enthalpy, Btu/lb
HDD*n* Heating degree-days base n°F, °F-day
Hours 8/4 & 55/69 Number of hours between 8 a.m. and 4 p.m with DB between 55 and 69 °F
HR Humidity ratio, grains of moisture per lb of dry air
Lat Latitude, °
Long Longitude, °
MCDB Mean coincident dry bulb temperature, °F
MCDBR Mean coincident dry bulb temp. range, °F
MCDP Mean coincident dew point temperature, °F
MCWB Mean coincident wet bulb temperature, °F
MCWBR Mean coincident wet bulb temp. range, °F
MCWS Mean coincident wind speed, mph
MDBR Mean dry bulb temp. range, °F
PCWD Prevailing coincident wind direction, °, 0 = North, 90 = East
Period Years used to calculate the design conditions
Sd Standard deviation of daily average temperature, °F
StdP Standard pressure at station elevation, psi
taub Clear sky optical depth for beam irradiance
taud Clear sky optical depth for diffuse irradiance
Tavg Average temperature, °F
Time Zone Hours ahead or behind UTC, and time zone code
WB Wet bulb temperature, °F
WBAN Weather Bureau Army Navy number
WMO# World Meteorological Organization number
WS Wind speed, mph

CHICAGO MIDWAY AP, IL, USA

WMO#: 725340

Lat: 41.79N Long: 87.75W Elev: 617 StdP: 14.37 Time Zone: -6.00 (NAC) Period: 82-06 WBAN: 14819

Annual Heating and Humidification Design Conditions

Coldest Month	Heating DB		Humidification DP/MCDB and HR						Coldest month WS/MCDB				MCWS/PCWD to 99.6% DB	
	99.6%	99%	99.6%			99%			0.4%		1%			
			DP	HR	MCDB	DP	HR	MCDB	WS	MCDB	WS	MCDB	MCWS	PCWD
1	-1.6	4.3	-12.0	2.9	-0.4	-6.0	4.1	5.9	27.5	25.6	24.9	28.5	12.0	300

Annual Cooling, Dehumidification, and Enthalpy Design Conditions

Hottest Month	Hottest Month DB Range	Cooling DB/MCWB						Evaporation WB/MCDB						MCWS/PCWD to 0.4% DB	
		0.4%		1%		2%		0.4%		1%		2%			
		DB	MCWB	DB	MCWB	DB	MCWB	WB	MCDB	WB	MCDB	WB	MCDB	MCWS	PCWD
7	15.9	92.1	74.9	89.6	73.3	86.5	71.9	78.0	88.3	76.2	85.4	74.4	83.1	12.6	220

Dehumidification DP/MCDB and HR									Enthalpy/MCDB						Hours
0.4%			1%			2%			0.4%		1%		2%		8 to 4 &
DP	HR	MCDB	DP	HR	MCDB	DP	HR	MCDB	Enth	MCDB	Enth	MCDB	Enth	MCDB	55/69
75.0	134.1	84.3	73.0	125.5	82.2	71.8	120.2	80.9	41.9	89.0	40.0	85.4	38.3	83.2	632

Extreme Annual Design Conditions

Extreme Annual WS			Extreme Max WB	Extreme Annual DB				n-Year Return Period Values of Extreme DB							
				Mean		Standard deviation		n=5 years		n=10 years		n=20 years		n=50 years	
1%	2.5%	5%		Min	Max	Min	Max	Min	Max	Min	Max	Min	Max	Min	Max
24.4	21.2	19.2	85.3	-8.2	97.3	7.5	3.8	-13.6	100.0	-17.9	102.2	-22.1	104.4	-27.6	107.1

Monthly Climatic Design Conditions

			Annual	Jan	Feb	Mar	Apr	May	Jun	Jul	Aug	Sep	Oct	Nov	Dec
Temperatures, Degree-Days and Degree-Hours		Tavg	51.6	25.7	30.0	38.8	50.1	60.8	70.6	75.7	73.8	66.2	54.2	41.6	29.8
		Sd		11.28	10.52	10.48	9.68	8.81	7.66	5.77	5.77	8.09	8.66	9.52	11.56
		HDD50	2791	755	563	379	112	10	0	0	0	2	55	283	632
		HDD65	5930	1219	981	815	458	192	34	1	5	83	349	701	1092
		CDD50	3356	0	2	30	115	346	618	798	736	489	185	32	5
		CDD65	1022	0	0	1	11	63	202	334	277	120	14	0	0
		CDH74	8680	0	0	11	113	561	1857	3040	2132	863	103	0	0
		CDH80	2982	0	0	2	29	162	665	1161	695	250	18	0	0
Monthly Design Dry Bulb and Mean Coincident Wet Bulb Temperatures	0.4%	DB		55.6	60.6	74.6	84.2	88.7	93.4	97.5	94.6	90.6	82.5	70.0	62.9
		MCWB		51.1	51.3	61.1	65.3	70.6	74.7	78.4	77.1	72.0	66.3	58.1	59.3
	2%	DB		48.1	53.8	68.0	76.9	84.3	90.4	92.9	90.6	86.1	76.8	64.0	55.2
		MCWB		44.4	47.3	57.0	62.3	68.5	72.5	75.9	75.3	69.9	62.8	57.0	50.9
	5%	DB		43.0	47.1	61.4	71.7	80.9	87.5	89.7	87.0	82.3	72.3	61.0	48.9
		MCWB		39.2	42.1	52.7	58.7	66.1	71.5	74.4	73.8	68.2	60.8	55.1	45.3
	10%	DB		39.0	43.3	54.9	65.9	75.8	83.7	86.4	83.7	79.3	67.7	56.6	44.1
		MCWB		36.1	39.2	47.6	55.5	63.3	69.6	72.7	72.0	66.5	58.8	51.2	40.0
Monthly Design Wet Bulb and Mean Coincident Dry Bulb Temperatures	0.4%	WB		53.2	54.4	63.1	68.2	74.3	78.3	81.8	80.1	75.4	68.8	62.2	59.5
		MCDB		55.7	57.2	72.8	79.1	84.4	88.5	91.8	90.4	85.0	77.1	65.1	62.1
	2%	WB		44.9	47.1	58.3	64.4	71.3	75.6	78.4	77.7	72.8	65.6	59.0	52.0
		MCDB		47.4	52.8	65.9	73.6	81.1	85.4	88.9	87.2	81.6	72.7	63.5	54.8
	5%	WB		39.8	42.6	53.4	60.1	68.6	73.3	76.6	75.6	70.7	62.6	55.7	45.5
		MCDB		42.7	46.8	60.5	69.4	77.0	83.6	86.5	83.3	79.1	70.0	60.2	48.2
	10%	WB		36.4	39.0	48.1	56.3	65.7	71.4	74.7	73.8	68.7	59.8	51.5	40.0
		MCDB		38.9	43.2	55.1	65.2	73.7	81.2	83.7	81.3	76.6	66.9	56.0	43.5
Mean Daily Temperature Range		MDBR		12.4	12.9	14.8	17.0	18.0	17.5	15.9	14.9	16.5	16.1	13.3	12.0
	5% DB	MCDBR		15.9	18.4	23.4	24.9	22.6	20.5	19.1	18.3	19.8	22.2	18.4	16.6
		MCWBR		13.5	14.1	15.7	14.6	11.9	9.5	8.6	8.3	9.4	12.7	14.6	14.3
	5% WB	MCDBR		15.8	17.0	21.8	22.6	20.4	19.0	17.8	16.2	17.1	18.6	17.2	15.3
		MCWBR		14.0	13.9	16.5	15.6	12.9	10.5	9.7	8.4	9.8	12.3	15.6	14.4
Clear Sky Solar Irradiance		taub		0.305	0.349	0.397	0.420	0.446	0.464	0.457	0.457	0.416	0.368	0.339	0.311
		taud		2.344	2.123	2.004	1.986	1.970	1.982	2.043	2.030	2.130	2.248	2.290	2.363
		Ebn,noon		267	267	267	269	264	259	260	256	258	258	249	253
		Edh,noon		30	41	51	55	57	56	53	52	44	36	31	28

CDD*n* Cooling degree-days base n°F, °F-day
CDH*n* Cooling degree-hours base n°F, °F-hour
DB Dry bulb temperature, °F
DP Dew point temperature, °F
Ebn,noon } Clear sky beam normal and diffuse hori-
Edh,noon } zontal irradiances at solar noon, Btu/h/ft2
Elev Elevation, ft
Enth Enthalpy, Btu/lb
HDD*n* Heating degree-days base n°F, °F-day
Hours 8/4 & 55/69 Number of hours between 8 a.m. and 4 p.m with DB between 55 and 69 °F
HR Humidity ratio, grains of moisture per lb of dry air
Lat Latitude, °
Long Longitude, °
MCDB Mean coincident dry bulb temperature, °F
MCDBR Mean coincident dry bulb temp. range, °F
MCDP Mean coincident dew point temperature, °F
MCWB Mean coincident wet bulb temperature, °F
MCWBR Mean coincident wet bulb temp. range, °F
MCWS Mean coincident wind speed, mph
MDBR Mean dry bulb temp. range, °F
PCWD Prevailing coincident wind direction, °, 0 = North, 90 = East
Period Years used to calculate the design conditions
Sd Standard deviation of daily average temperature, °F
StdP Standard pressure at station elevation, psi
taub Clear sky optical depth for beam irradiance
taud Clear sky optical depth for diffuse irradiance
Tavg Average temperature, °F
Time Zone Hours ahead or behind UTC, and time zone code
WB Wet bulb temperature, °F
WBAN Weather Bureau Army Navy number
WMO# World Meteorological Organization number
WS Wind speed, mph

Appendix II
Principles of Heat Balance Method (HBM) for calculating heating and cooling loads (from McQuiston et al. 2004)

For a zone of six surfaces; four walls, a roof, and a floor; the energy components that should be considered in the balance equations are (1) the solar energy coming through the windows, (2) heat conducted through the exterior walls and the roof, and (3) internal heat gains due to lights, equipment, and occupants. The heat balance equation for an exterior surface *j* can be written as follows;

$$q''_{conduction,ext,j,\theta} = q''_{solar,ext,j,\theta} + q''_{convection,ext,j,\theta} + q''_{radiation,ext,j,\theta}$$

where;

$q''_{conduction,ext,j,\theta}$: conduction heat flux through the wall at the exterior surface at time θ

$q''_{solar,ext,j,\theta}$: absorbed solar heat flux at the exterior surface at time θ

$q''_{convection,ext,j,\theta}$: convection heat flux between the ambient air and exterior wall surface at time θ

$q''_{radiation,ext,j,\theta}$: thermal radiation heat flux at the exterior wall surface at time θ

Similarly, the interior surface heat balance on the *j* surface at time θ is;

$$q''_{conduction,int,j,\theta} = q''_{solar,int,j,\theta} + q''_{convection,int,j,\theta} + q''_{radiation,int,j,\theta}$$

where;

$q''_{conduction,int,j,\theta}$: conduction heat flux through the wall at the interior surface at time θ

$q''_{solar,int,j,\theta}$: absorbed solar heat flux at the interior surface at time θ

$q''_{convection,int,j,\theta}$: convection heat flux between the zone air and interior wall surface at time θ

$q''_{radiation,int,j,\theta}$: thermal radiation heat flux at the interior wall surface at time θ

It should be noticed that $q''_{conduction,ext,j,\theta}$ is not equal to $q''_{conduction,int,j,\theta}$ unless steady state heat transfer conditions exist.

The last balance equation is for the zone air which is assumed to have negligible thermal storage capacity and thus;

$$\sum_{j=1}^{N} A_j q''_{convection,in,j,\theta} + q_{infiltration,\theta} + q_{system,\theta} + q_{internal,conv,\theta} = 0$$

where;

A_j : area of the *j*th surface,

$q_{infiltration,\theta}$: heat gain due to infiltration,

$q_{system,\theta}$: heat gain due to heating/cooling system,

$q_{internal,conv,\theta}$: convection portion of internal heat gains due to people, lights, or equipment

McQuiston et al. (2004) includes the formulation for all the terms stated above.

Based on the balance equation for the exterior surface, the final expression for the external surface temperature of the *j*th wall is;

$$t_{es,j,\theta} = \frac{Y_o t_{is,j,\theta} - H_{ext,j,\theta} + \alpha G_t + h_c t_o + h_{h-g} t_g + h_{r-sky} t_{sky}}{X_o + h_c + h_{h-g} + h_{r-sky}}$$

where;

$t_{es,j,\theta}$: exterior temperature of surface *j* at time θ

Y_o : conduction transfer function (CTF) coefficient,

X_o : exterior CTF coefficient,

$t_{is,j,\theta}$: interior temperature of surface j at time θ

α : solar absorptivity of the surface,

G_t : total solar irradiation incident on the surface,

h_c : convection coefficient between the air and exterior wall surface which is function of wind speed and temperature difference between the exterior surface and the outside air,

t_o : air temperature,

t_g : ground temperature

t_{sky} : effective sky temperature,

h_{h-g} : linearized view factor from the surface to the ground which is a function of the tilt angle of the surface from horizontal,

h_{r-sky} : linearized view factor from the surface to the sky which is a function of the tilt angle of the surface from horizontal,

$H_{ext,j,\theta}$: a term that relates the exterior surface temperature at the current time θ to historical surface temperatures,

As can be seen if the previous formula, the interior surface temperature is an input to calculate the exterior surface temperature. Therefore, the interior surface temperature should be defined in order to solve for the exterior surface temperature. From the heat balance equation for the interior surface, the interior surface temperature final formula is as follows;

$$t_{is,j,\theta} = \frac{q^{"}_{solar,int,j,\theta} + Y_o t_{es,j,\theta} + H_{in,j,\theta} + h_c t_i + h_{r,j} t_{f,j} + q^{"}_{balance} + q^{"}_{radiation-ihg,in,j,\theta}}{Z_o + h_c + h_{r,j}}$$

where;

$H_{in,j,\theta}$: a term that relates the interior surface temperature at the current time θ to historical surface temperatures,

$q^{"}_{radiation-ihg,in,j,\theta}$: interior heat gain due to radiation from people, lights, and equipment,

$t_{f,j}$: an area-emissivity-weighted temperature,

$h_{r,j}$: radiation coefficient,

$q^{"}_{balance}$: balancing factor,

Z_o : interior CTF coefficient,

It is clear from the above formulation for the temperature of the interior surface that this temperature is a function of the exterior surface temperature. Therefore, an iterative solution is required to solve to these two temperatures since each one depends on the other. Also, an internal iterative process is also required to solve for each temperature known the other because the heat coefficients involved in calculating each temperature depend on the desired temperature.

These iterative processes are being guided via the zone air heat balance equation. The zone air heat balance equation relates the temperature of all internal surfaces to the desired zone temperature (i.e. set temperature) via a similar formula like the ones for exterior and interior wall surfaces. The program HvacLoadExplorer is used to perform all these iterations and provide the final heating and cooling loads required to balance the three formulations. Heating and cooling loads are calculated using the zone air heat balance equation once all temperatures (exterior, interior, and zone air) converge.

Appendix III
Heat pump operational data

For Chicago and Charlotte;

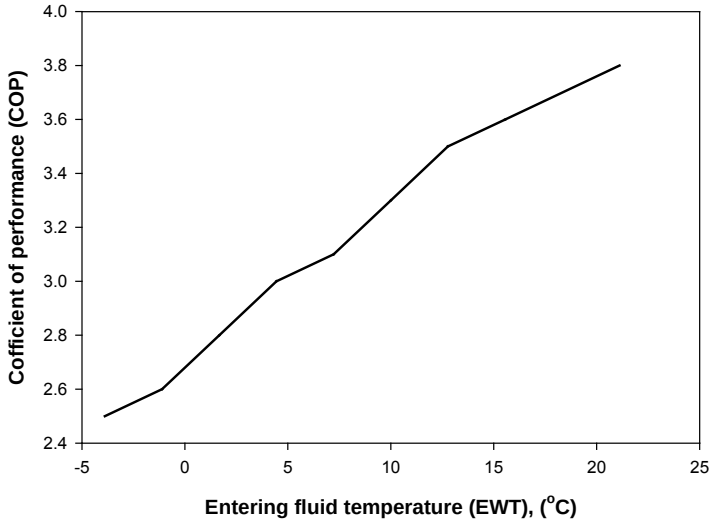

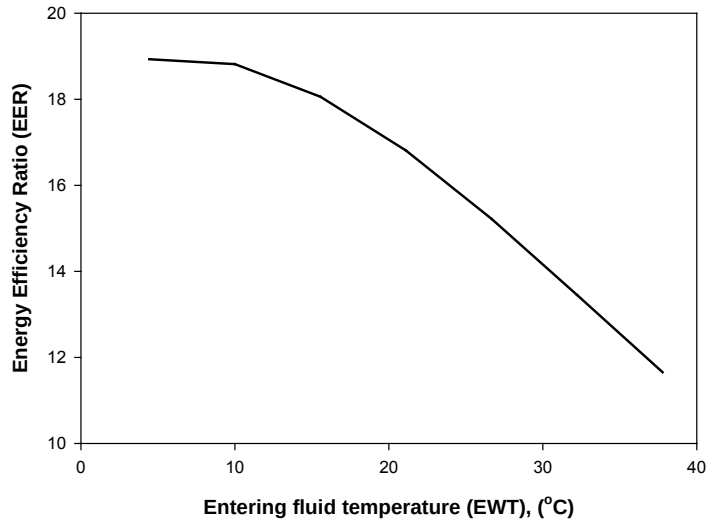

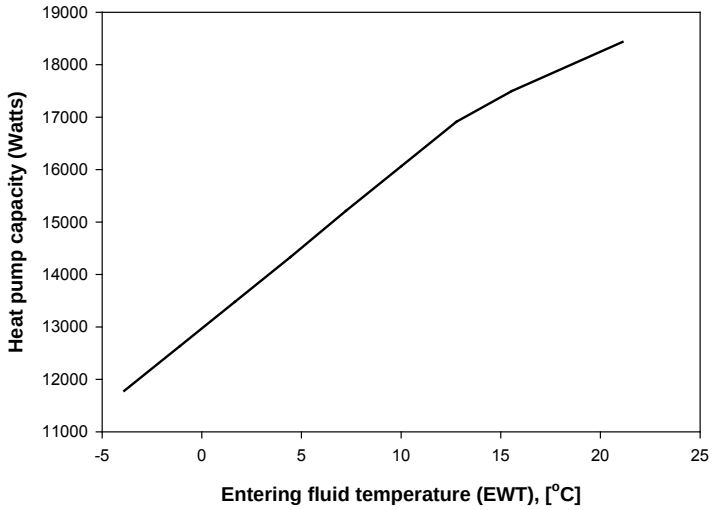

For Austin:

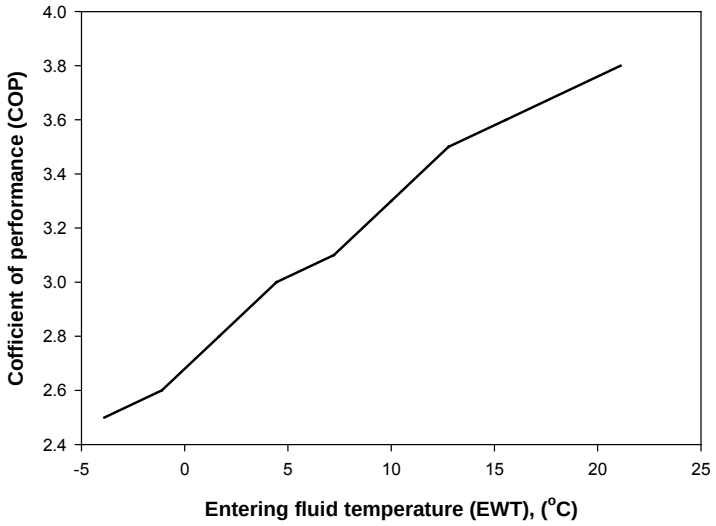
Cofficient of performance (COP)
4.0
3.8
3.6
3.4
3.2
3.0
2.8
2.6
2.4
-5
0
5
10
15
20
25
Entering fluid temperature (EWT), (°C)

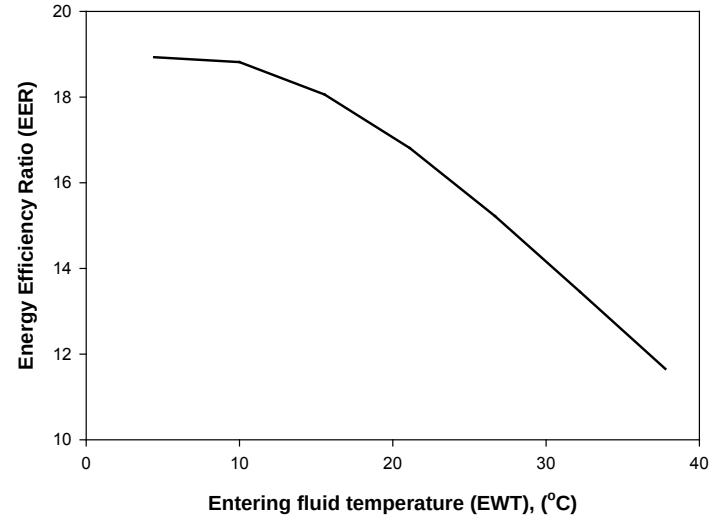
Energy Efficiency Ratio (EER)
20
18
16
14
12
10
0
10
20
30
40
Entering fluid temperature (EWT), (°C)

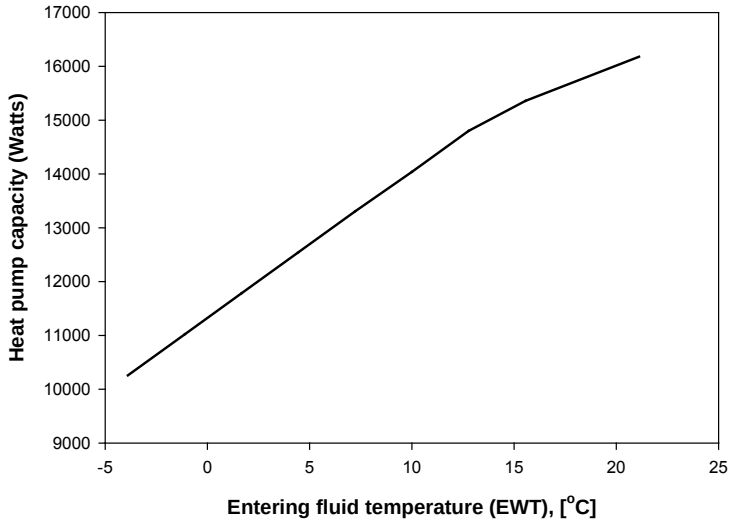
Heat pump capacity (Watts)
17000
16000
15000
14000
13000
12000
11000
10000
9000
-5
0
5
10
15
20
25
Entering fluid temperature (EWT), [°C]

Appendix IV
Basics of change point analysis (Taylor, 2000)

The change point analysis includes two main steps;

1. capturing that a change has occurs,
2. defining the point where the change occurred.

Capturing the change:

The change point analysis uses a combination of cumulative sums and bootstrapping to capture the changes. To explain this, lets assumed an n-values of data X_n. For this data, the cumulative sums are named S_n where;

$S_n = S_{n-1} + (X_i - \bar{X})$ for all i = 1, 2, 3, ... n.

and $\bar{X} = \frac{\sum_{i=1}^{n} X_i}{n}$

Then an estimate of the magnitude of the change is estimated as follows;

$S_{diff} = S_{max} - S_{min}$

where;

$S_{max} = \max_{i=0,1,...n} S_i$ and $S_{min} = \min_{i=0,1,...n} S_i$

Then bootstrap analysis starts by randomly reordering the original *n* data, then calculating the cumulative sums (S_n^0) corresponding to that reordered data, and then the magnitude of change (S_{diff}^0) corresponding to that reordered data is to be estimated.

The bootstrap analysis is to be repeated (*m*) times. The number of bootstraps (*k*) for which the magnitude of change (S_{diff}^m) is less than the magnitude of change for the actual data set (S_{diff}) is to be counted. Then the confidence level that a change has occurred is estimated as;

Confidence level = k/m %

If the confidence level is 90% or more, then a change has definitely occurred.

Determining the change point:

Once a change has been detected and confirmed, the determination of the location of the change is performed by determining the last point before the change occurred (*c*) as follows;

$$|S_c| = \max_{i=0,1,...n} |S_i|$$

This S_c is the point furthest from zero.

While the above procedure generally works well, an improvement is made via treating the changes detected by the above procedure as a set of candidate change-points. Once this set is generated, all the change-points and their confidence levels are re-estimated. A backward elimination procedure is then use to eliminate those points that no longer test significant. When a point is eliminated, the surrounding change-points are re-estimated along with their significance levels. This reduces the rate of false detections.

Appendix V
Results of the representative change point analysis for each city

Charlotte, NC

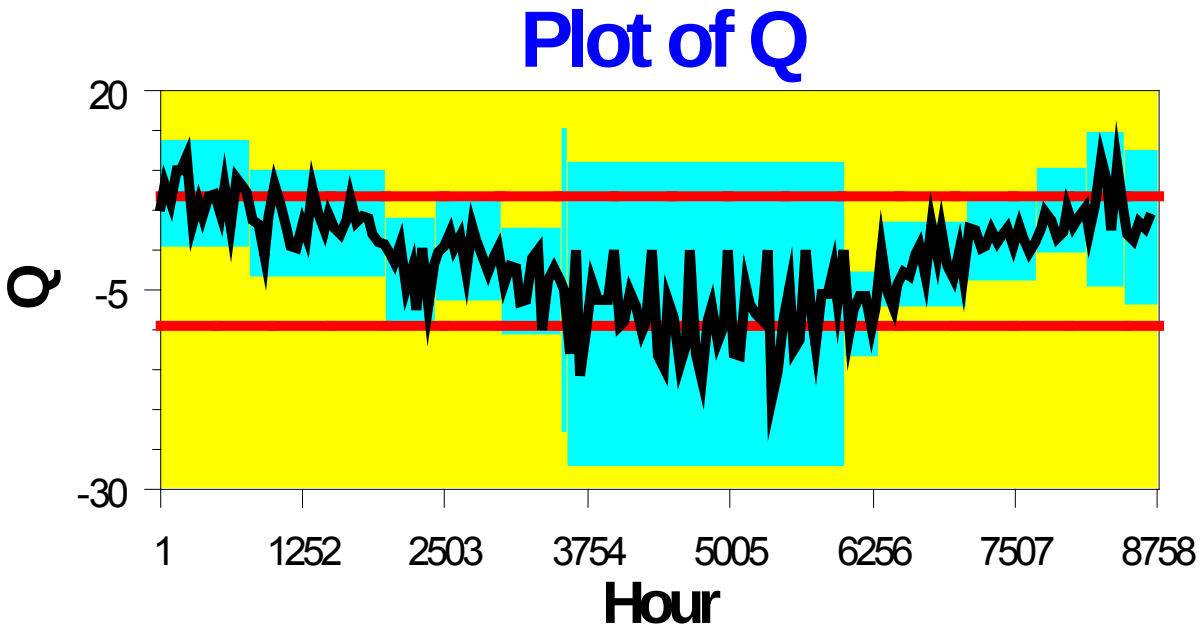

Plot for the average ground thermal load (Q) over the averaging period versus time, hours

Table of Significant Changes for Q

Confidence Level for Candidate Changes = 50%, Confidence Level for Inclusion in Table = 90%, Confidence Interval = 95%, Bootstraps = 1000, Without Replacement, MSE Estimates

Hour	Confidence Interval	Conf. Level	From	To	Level
817	(625, 1057)	100%	7.0792	3.4569	2
2017	(1969, 2113)	100%	3.4569	-2.5699	1
2449	(2065, 2593)	93%	-2.5699	0.28243	5
3025	(2929, 3265)	94%	0.28243	-3.7906	4
3601	(3457, 5233)	97%	-3.7906	-7.9251	3
6337	(5905, 6433)	100%	-7.9251	-1.7552	2
7105	(6673, 7153)	94%	-1.7552	1.6197	4
7729	(7729, 8257)	99%	1.6197	5.085	3
8497	(7777, 8545)	94%	5.085	2.8365	5

Chicago, IL

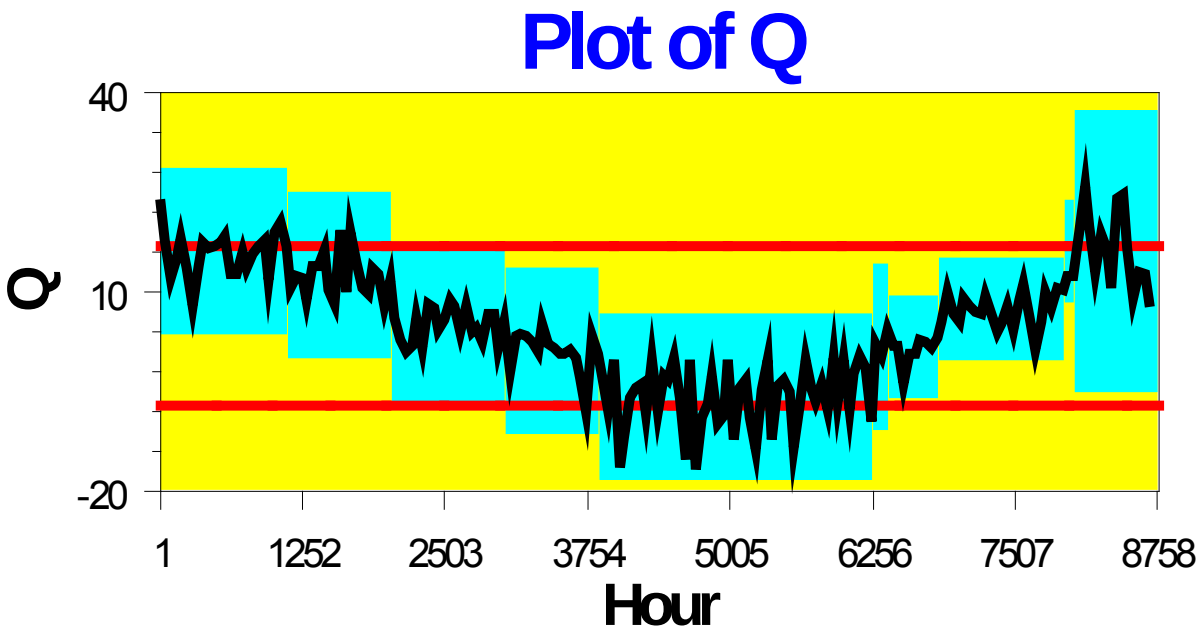

Plot for the average ground thermal load (Q) over the averaging period versus time, hours

Table of Significant Changes for Q

Confidence Level for Candidate Changes = 50%, Confidence Level for Inclusion in Table = 90%, Confidence Interval = 95%, Bootstraps = 1000, Without Replacement, MSE Estimates

Hour	Confidence Interval	Conf. Level	From	To	Level
1153	(673, 1537)	95%	16.093	12.539	2
2065	(1969, 2113)	100%	12.539	5.1848	1
3073	(2833, 3409)	100%	5.1848	1.1605	4
3889	(3793, 4177)	100%	1.1605	-5.6852	5
6289	(6001, 6337)	100%	-5.6852	1.6504	4
6865	(6865, 6961)	100%	1.6504	7.4257	2
7969	(7969, 8209)	100%	7.4257	16.203	3

Austin, TX

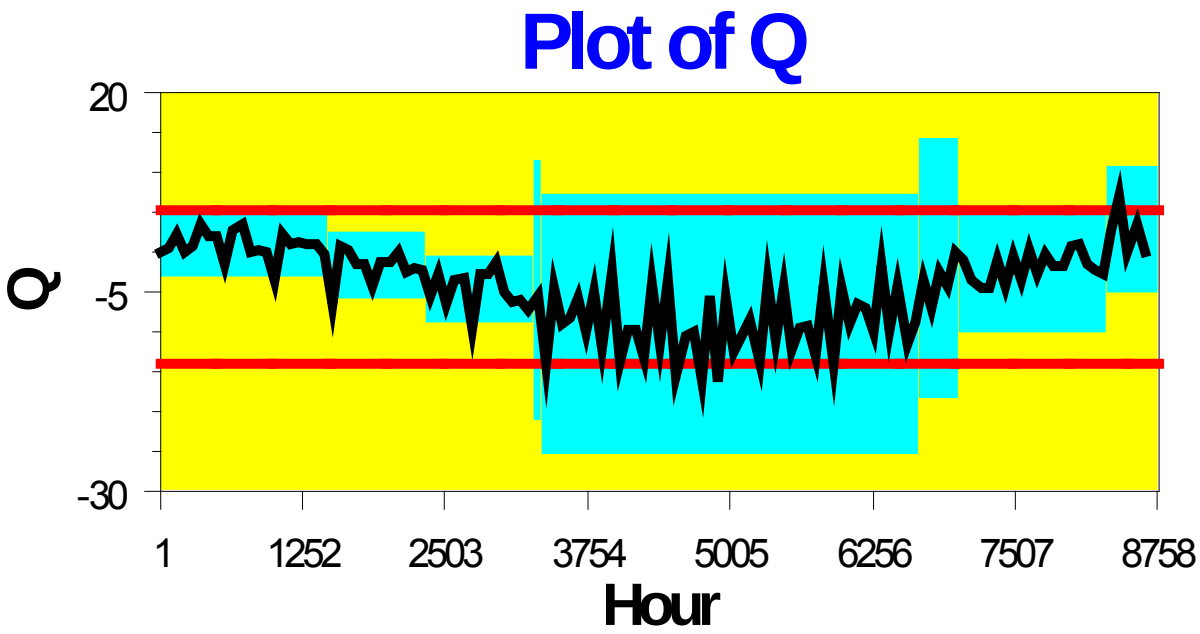

Plot for the average ground thermal load (Q) over the averaging period versus time, hours

Table of Significant Changes for Q

Confidence Level for Candidate Changes = 50%, Confidence Level for Inclusion in Table = 90%, Confidence Interval = 95%, Bootstraps = 1000, Without Replacement, MSE Estimates

Hour	Confidence Interval	Conf. Level	From	To	Level
1513	(1225, 1873)	99%	1.0289	-1.7335	2
2377	(2089, 2881)	100%	-1.7335	-4.6888	1
3385	(3241, 4393)	99%	-4.6888	-8.8947	3
6697	(6409, 6769)	100%	-8.8947	-2.0811	2
8353	(8137, 8497)	98%	-2.0811	2.8087	3

Appendix VI
Comparison for one year analysis

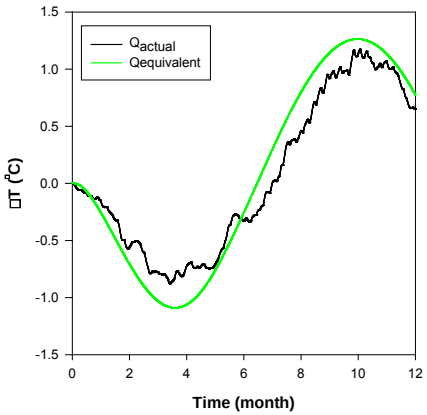

(a-1)

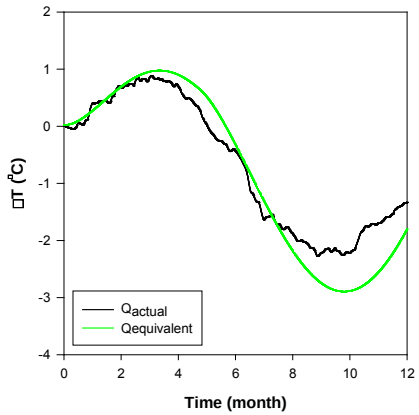

(b-1)

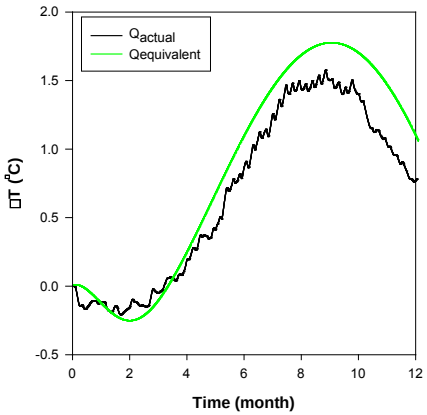

(c-1)

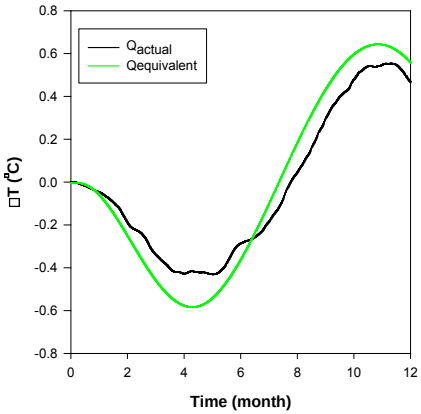

(a-2)

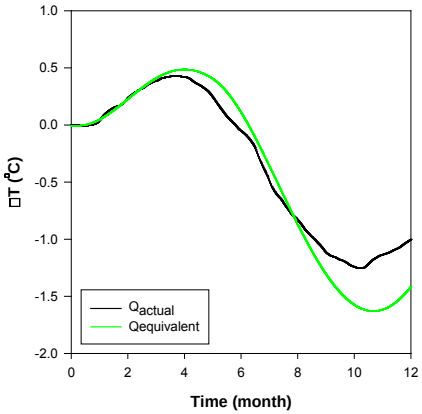

(b-2)

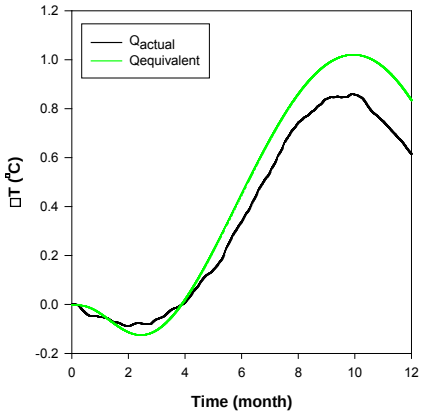

(c-2)

Comparison between models performed using the actual ground loads (Q_{actual}), and sine waves based on equivalent sine wave concept ($Q_{equivalent}$) for; (a) Charlotte, NC, (b) Chicago, IL, and (c) Austin, TX. Upper row (1) is for the temperature change at a distance of 1 m from the pile center, while lower row (2) is for the temperature change at a distance of 2 m from the pile center.

Appendix VII
Long-term performance at different distances from the pile center for the three selected locations

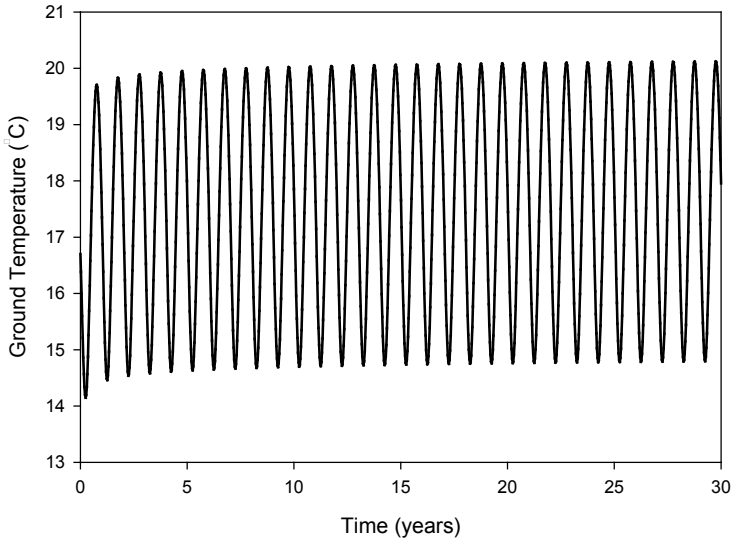

(a) Charlotte, NC

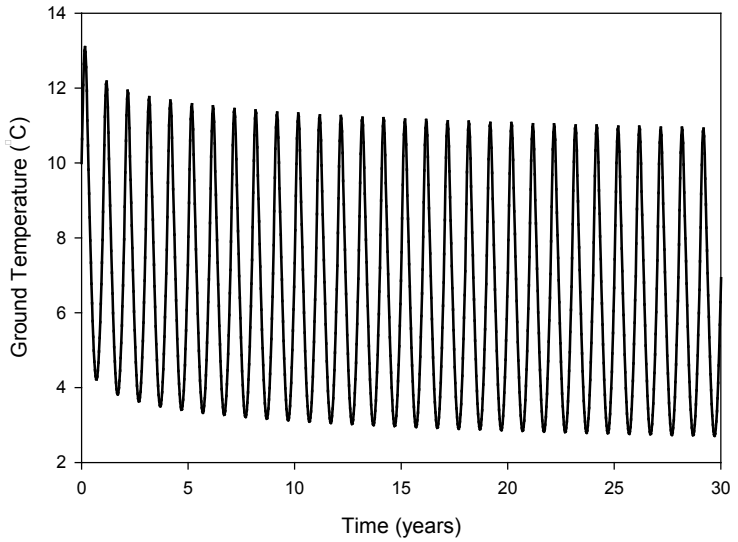

(b) Chicago, IL

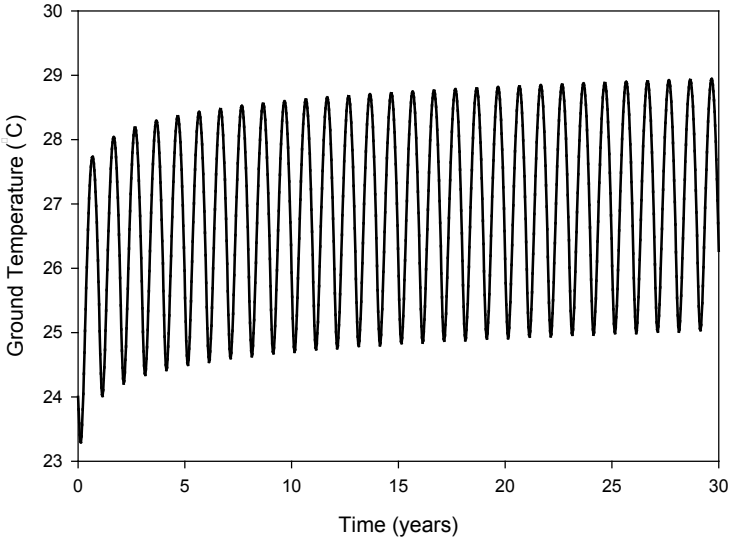

(c) Austin, TX

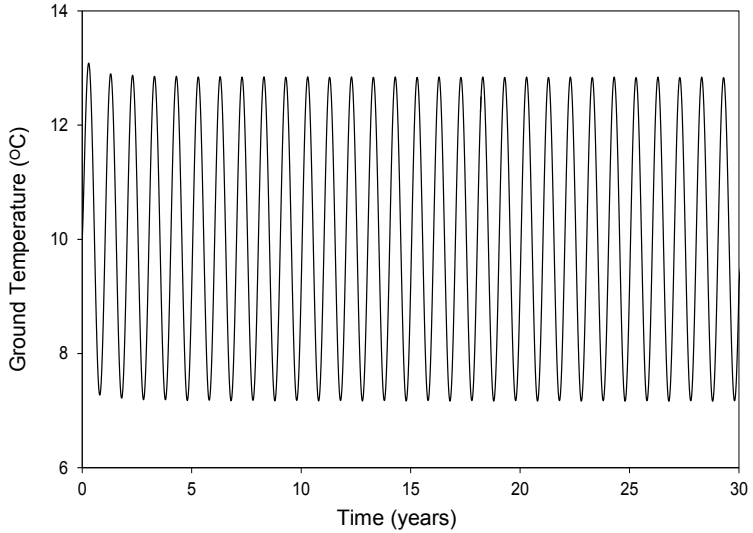

(d) Hypothetical Balanced Sine Wave

Ground temperature variation at the <u>surface of the pile</u> for the selected locations assuming 30 years of operation.

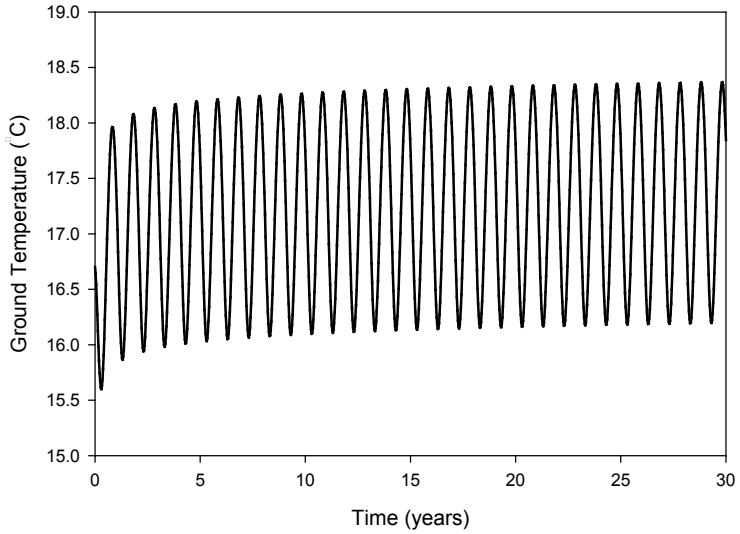

(a) Charlotte, NC

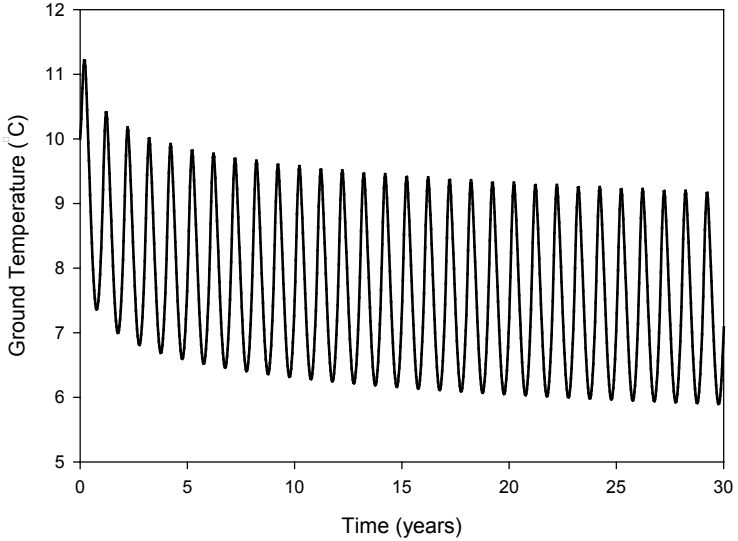

(b) Chicago, IL

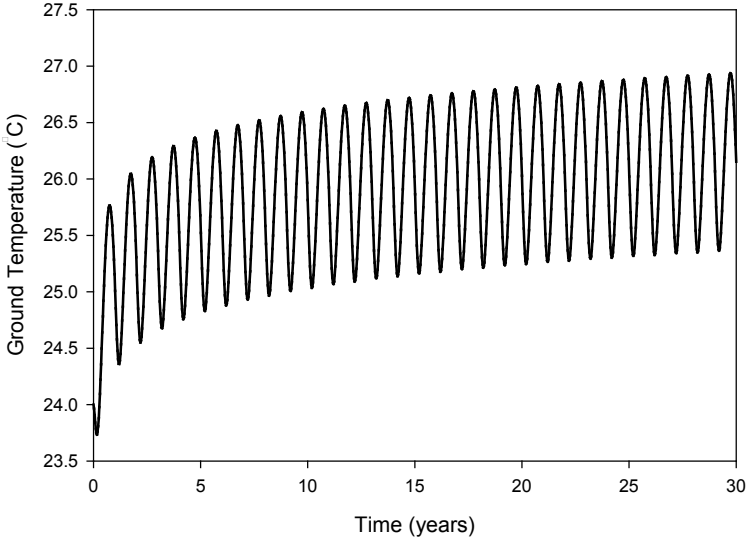

(c) Austin, TX

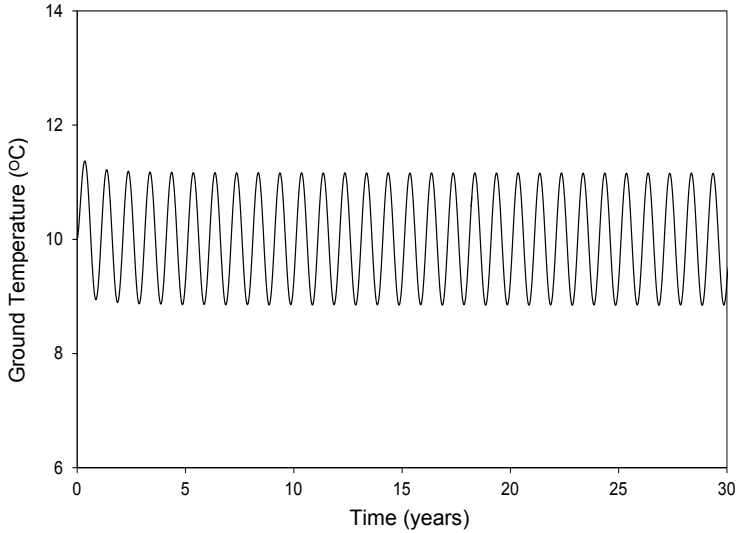

(d) Hypothetical Balanced Sine Wave

Ground temperature variation at <u>1 m away from the center of the pile</u> for the selected locations assuming 30 years of operation.

CHAPTER 6. SITE DESCRIPTION AND TESTING PROCEDURES

A series of full scale field tests were performed at Virginia Tech to investigate the thermo-mechanical behavior of Energy Piles. Furthermore, additional tests were performed to investigate the applicability of in-situ thermal conductivity tests originally developed for small diameter and deep geothermal boreholes on Energy Piles as well as comparing the performance of Energy Piles constructed providing different tube material and configurations.

This chapter presents a description of the ground conditions at the test site and the test set up. In addition, detailed descriptions of various equipment used during different testing phases are also presented, including the frame used for loading the Test Pile, the custom-made temperature controlling equipment, and the heat-rate controlling equipment provided by the Mechanical Equipment Sales, Inc. A list of various tests performed within this testing program is also provided. Procedures and results of different tests are discussed in the following chapters. Chapter 7 presents the results for thermal conductivity tests, and Chapter 8 presents the results of the thermo-mechanical pile load tests.

6.1. Site Description and Soil Conditions

The test site is located 6.5 km (4 miles) away from the main campus of Virginia Tech in the south west direction as shown in Figure 6.1. The test set up was constructed next to the Geotechnical Engineering Facility in Prices Fork road.

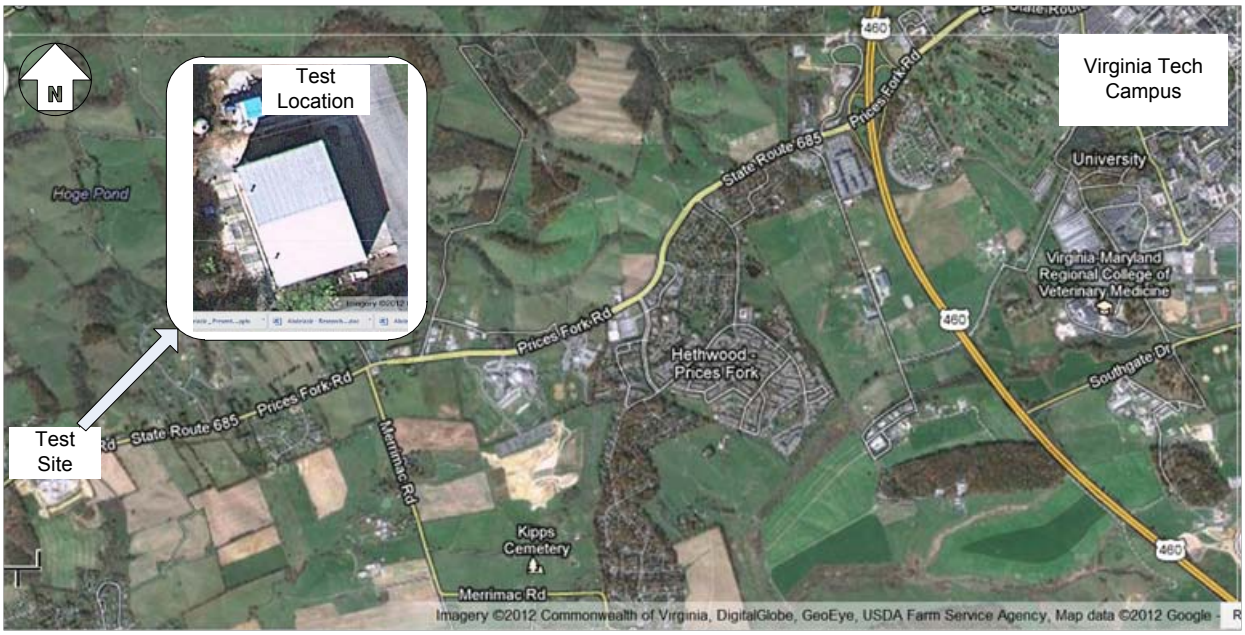

Figure 6.1. General location of the test site with respect to Virginia Tech main campus in Blacksburg, VA [from Google maps - used under fair use, 2013] .

Ground conditions at the test site were inferred from the drilling operations during the installation of different elements in the test setup (i.e. energy piles, and observation points). Based on this drilling information, the ground at the test site was found to consist of a silty sand layer underlain by a shale layer. The silty sand layer extends from the ground surface to a depth ranging from 12.8 m (42 ft) to 18.9 m (62 ft). The shale was encountered below the silty sand

layer till the end of drilling. Appendix VIII includes the detailed soil profile at the location of different elements. It should be noticed that no ground water table was reported in the logs shown in Appendix VIII because drilling was performed using water (as will be discussed later) which affected the actual level of ground water table. Ground water, however, was recognized while drilling by the change in the echo of the drill bit. Such change was always found deep into the shale layer suggesting that the top silty sand layer is unsaturated.

The consistency of each of the two main soil layers over the entire test site was confirmed with the penetration rate of the drill bit along with the blown-up cuttings. It took 3-4 minutes to drill 3 m (10 ft) in the silty sand layer and about 5-6 minutes to drill the same length in the shale layer. This penetration rate was observed in all piles and observation points drilled at the test site revealing to some extent the consistency of the main soil layers over the entire site. Figure 6.2 shows the silty sand soil cuttings taken while drilling the Test Pile.

Figure 6.2. Soil cuttings taken while drilling the Test Pile hole.

Three samples were collected from soil cuttings and were used in the lab to perform sieve analysis and Atterberg limits. The liquid and the plastic limits for the fine content of the soil cuttings were evaluated as 33.4%, and 24.5%, respectively, as presented in Appendix IX. The top soil layer was found to classify as poorly graded sand with silt (SP-SM) according to the ASTM D2487 for Unified Soil Classification System (ASTM, 2011).

6.2. Test Setup

6.2.1. General Setup and Pile Installation

Five piles were constructed in May 2010 at the test site. All piles are 30.5 m (100 ft) in length and 25 cm (10 inches) in diameter. The distance between any two adjacent piles is 2.5 m (8 ft). Figure 6.3 presents the layout of the test setup. The thermo-mechanical load test was performed in Pile 1 which is titled "*the Test Pile*" in Figure 6.3. In addition to these piles, four temperature observation points were installed within the test area. Observation point 2 was installed far away from all energy piles to monitor the ground temperature variations due to

climate. Observation points 1 and 2 extend 30.5 m (100 ft) deep into the ground. While observation points 3 and 4 extend 12 m (40 ft) and 36.5 m (120 ft) in the ground, respectively.

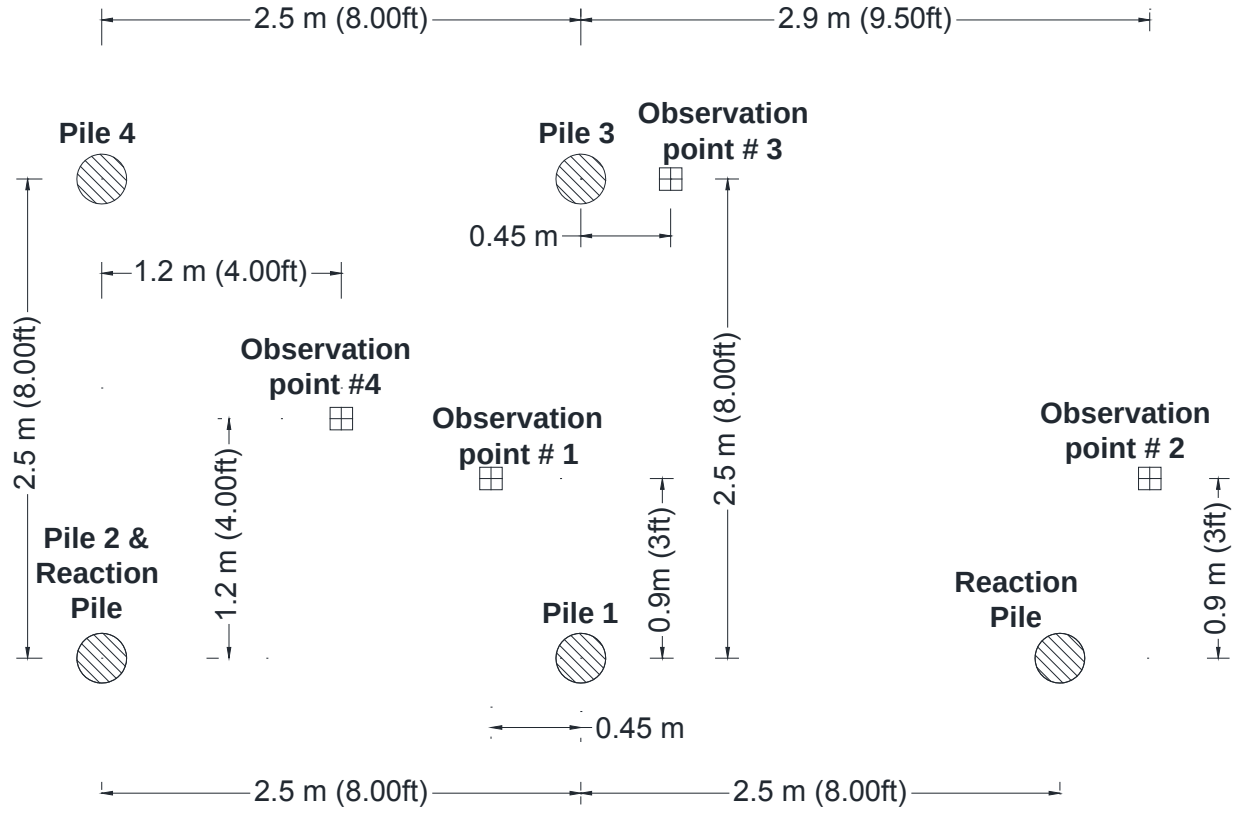

Figure 6.3. Virginia Tech Energy Pile Test Setup.

The percussion rotary blasting drilling technique was used for drilling all the piles and observation points. In this technique, a piston-driven hammer is used to drive a hollow steel drill bit into the ground. The drill bit has thick tungsten rods at the bottom representing the cutting face of the bit. Figure 6.4 shows the drill rig and the hummer used in the drilling. The cuttings are blown up the outside of the rods using air or combination of air and a fluid. At the initial drilling stages of this project, air was used to blow up the cuttings out of the drilled hole which was found to be difficult because the overburden soils were sticky and plugged the air flow path. Thus, water was introduced to assist the blowing up operation. Moreover, water is used to cool down the drill bit while drilling in the shale. Steel casing was used to support the overburden soils while drilling. This casing was pulled out of the ground from all observation points and all piles except the Test Pile (Pile 1). A steel casing with a total length of 9.75 m (32 ft) was left at the upper section of the Test Pile.

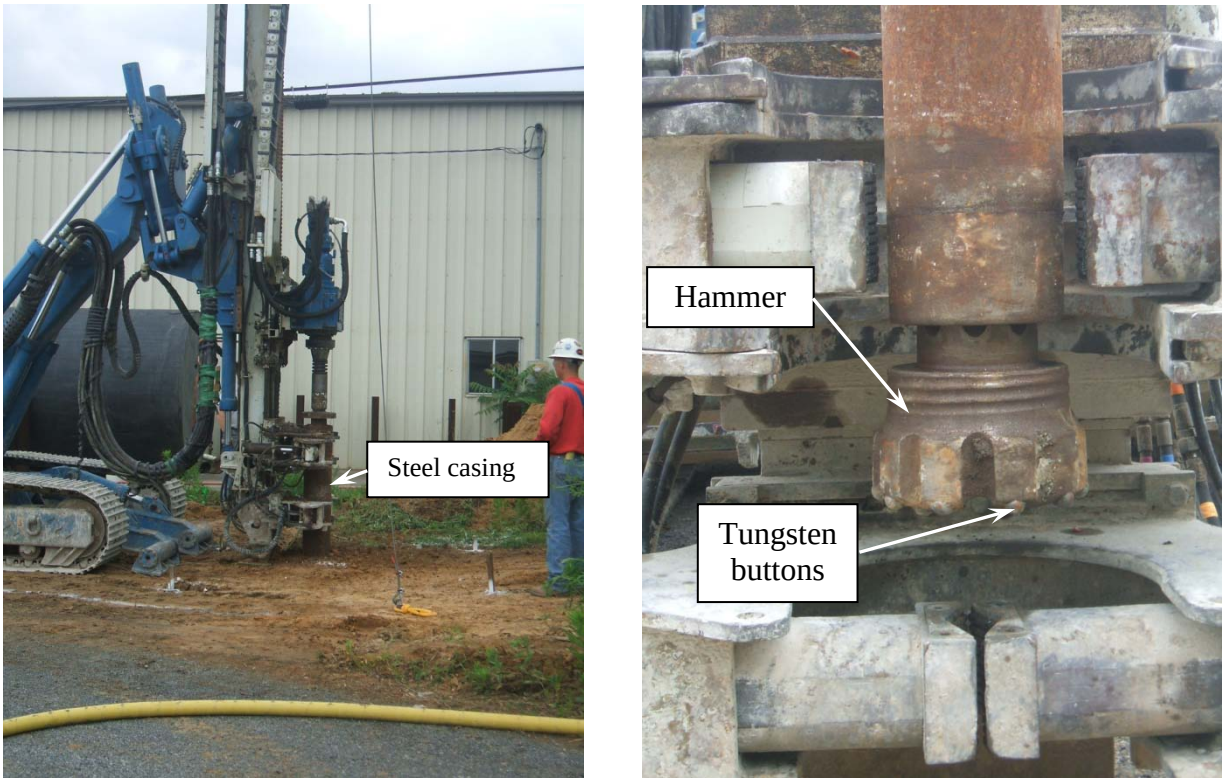

(a) positioning drill rig (b) Drill bit and hammer

Figure 6.4. Drill bit and hummer used for drilling different piles and observation points.

A fifth pile with no circulation tubes was installed as a second reaction pile during the load test. Four piles were switched to energy piles via providing them with circulation tubes. Different tube types (HDPE and PEX), and configurations (single and double) were used to investigate their effect on the heat exchange capacity of energy piles. The tubes for each pile were placed in the borehole after drilling and before backfilling. The distance between tube legs was maintained using 50 mm (1.97 inches) plastic cylindrical spacers spaced 1 m (3 ft) apart along the tube length. All tubes were pressure tested after being placed and before backfilling to assure that no cracks or holes in the tube walls were caused during the mobilization and installation. The pressure test was performed by installing valves at both ends of the tube above ground, filling the tube with water and then applying a pressure of 550 kPa (80 psi) to the water using an air pump while the valves were closed and monitoring the pressure loss over a period of 30 minutes as shown in Figure 6.5. No significant pressure drop was observed for all installed tubes over the testing period. The maximum pressure drop was 4 psi indicating good tube integrity. Table 6-1 presents tube types and configurations installed in each energy pile (pile title is as presented in Figure 6.3).

A 25.4 mm (1-inch) tremie pipe for grouting was taped and lowered with the circulation tubes in all piles. Moreover, a 38 mm (1.5 inch) steel bar was also lowered with the tubes in Test Pile (Pile 1) and Pile 2 (Reaction Pile). The total length of the steel bar was achieved by connecting 3 m (10 ft) pieces together using high strength couplings as shown in Figure 6.5. A 38 mm (1.5 inch) steel bar was also installed in the other reaction pile which does not have any tubes.

(a) Cylindrical spacers for the U-tube

(c) pressure testing

(b) tube installation

(d) connecting the steel bars

Figure 6.5. Installing circulation tubes and pressure testing them before backfilling.

Two of the energy piles (Piles 1 and 3 in Figure 6.3) were provided with strain gauges with temperature sensors at every 3 m (10 ft). RocTest Model EM-5 concrete embedded strain gauges shown in Figure 6.6 were used. The gauges in the Test Pile (i.e. Pile 1) were taped to the concentric steel bar at the desired depths as shown in Figure 6.7. The tap was placed around the centered pot of the gauges assuring the verticality of the gauge and leaving the two end flanges free to move so that strains in the concrete can be accurately measured. The EM-5 gauges for Pile 3 were installed in position by placing a mark in the gauge's cable such that having this mark at the ground surface assures the right depth of the gauge as shown in Figure 6.7. The verticality of these gauges was assured using straps around the legs connecting the flanges with the central pot. These straps are attached to the gauges' cable band. The straps were not strongly tightened to assure the flanges would be free to mode with the development of deformations.

Table 6-1. Components inside each Energy Pile

Pile	Tube type	Tube configuration
Pile 1 (Test Pile)	HDPE	S
Pile 2	HDPE	S
Pile 3	PEX	S
Pile 4	PEX	D

* HDPE : is High Density Polyethylene, PEX: crossed-linked Polyethylene tubes,
** S : single ground loop, D : double ground loops,
** The outside diameter of HDPE tubes is 19mm (¾ inches) and 32 mm (1¼ inches) for PEX tubes .

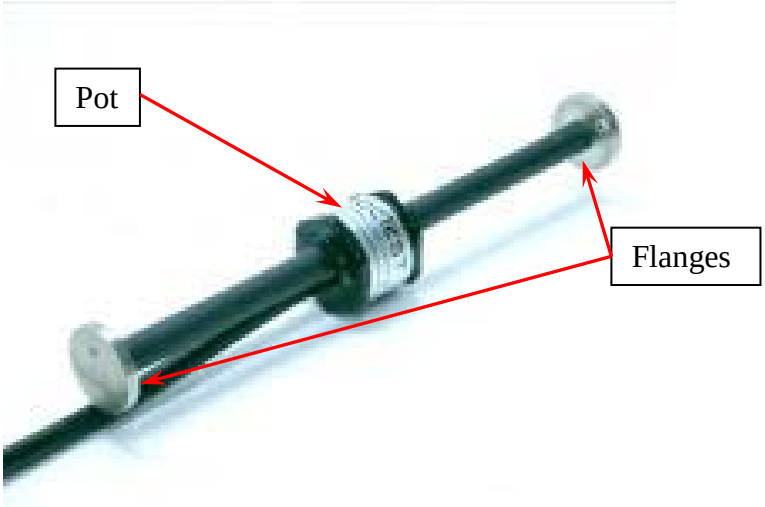

Figure 6.6. RocTest EM-5 concrete embedded strain gauge.

All observation points were provided with thermistors to monitor ground temperature during testing. Table 6-2 presents the Instrumentation provided in each observation well and energy piles. The mentioned insulation technique for EM-5 gauges in Pile 3 was followed to assure the right depth of the thermistors in all observation points. After installing the thermistors in each observation point, the hole was backfilled with sand by damping it from the ground surface. Pile 4 was also backfilled by damping sand from the ground surface.

All strain gauges and thermistors were connected to a data collection system. The data collection system consists of a data logger which has two reading channels. The data logger was connected to three multiplexers to increase number of channels. Each multiplexer has a total of 128 channel enabling either 64 two-channel gauges or 32 four-channel gauges. The strain gauges used in pile 1 and pile 3 have four channels; two for strain readings and two for temperature readings. All thermistors used in observation points and temperature sensors have only two channels for temperature. Every sensor requires 2 seconds per reading summing up to 116 seconds for a total of 58 sensors. Thus the data logger was programmed to record readings every 2 minutes.

Table 6-2. Instrumentation and ground loop type and configuration in each test element.

Element	Depth	Tube		Sensor type	Depths of Sensors (m)
		Type	S or D*		
Pile 1 (Test Pile)	30.5 m (100 ft)	19 mm (¾ inch) HDPE	S	Thermocouple	3, 6, 9, 12, 15, 18, 21, 24, 27, 30.5
Pile 2	30.5 m (100 ft)	19 mm (¾ inch) HDPE	S	-	-
Pile 3	30.5 m (100 ft)	25.4 mm (1 inch) PEX	S	Thermocouple	3, 6, 9, 12, 15, 18, 21, 24, 27, 30.5
Pile 4	30.5 m (100 ft)	25.4 mm (1 inch) PEX	D	-	-
Observation Well 1	30.5 m (100 ft)	-	-	Thermistors	3, 6, 9, 12, 15, 18, 23, 24, 27, 30.5
Observation Well 2	30.5 m (100 ft)	-	-	Thermistors	3, 6, 9, 12, 15, 18, 23, 24, 27, 30.5
Observation Well 3	15 m (50 ft)	-	-	Thermistors	3, 6, 10.6, 15
Observation Well 4	36.5 m (120 ft)	-	-	Thermistors	3, 6, 9, 12, 15, 18, 21, 24, 27, 30.5, 33.5, 36.5

* S: single tube, and D: double tubes.

(a) Taping EM-5 gauge to steel bar in the Test Pile (b) Mark at the ground surface for OP 4

Figure 6.7. Installing the EM-5 Instrumentation in the Test Pile (Pile 1) and observation point 4

Piles 1, 2, and 3, and the reaction pile were all backfilled with cement mortar from bottom to top using 25.4mm (1 inch) tremie pipe. The tremie pipe was extracted out of the pile upon casting the concrete. The cement mortar was prepared in-situ by mixing cement with water. The quality and consistency of the cement mortar was confirmed while grouting by maintaining the specific gravity of the mortar constant at 1.9 revealing a mortar density of 1.9 g/cm^3 (118.6 pcf) as shown in Figure 6.8. Moreover, 50 mm (2 inches) sided cement cubes and cylinders with 45 mm (1.8 inch) diameter and 91 mm (3.6 inch) in length were taken as samples and tested in the lab.

6.2.2. Lab Tests on Cement Cubes and Cylinders

The cement cube and cylinder samples taken while grouting were kept submerged in the lab under controlled room temperature of 20℃ until they were tested. Compressive tests were performed to measure the compressive strength at 7 days and 28 days after sampling of each element. Figure 6.10 shows the results of compressive tests on different cubical and cylindrical specimens from different testing elements. In general, the strength of the cylindrical specimens is less than the cubical specimens at the same age. Also as expected, the strength of both cubical and cylindrical specimens at 7 days is less than that at 28 days. For the Test Pile, the average cubical strength at age of 28 days is 54.6 MPa (7.9 ksi).

After finishing the compressive testing of all the specimens, the dry densities of broken pieces were determined by drying the soaked samples in the oven for 24 hours and measuring their dry weights upon removal from the oven. Each specimen was then submerged in a graduated cylinder filled with water and the volume of the specimen is determined. Figure 6.9 shows one of the cement cubes while measuring its volume in the lab. Figure 6.11 presents the measured dry densities for different elements involved in the project.

(a) checking specific gravity of the cement mortar

(b) cubes for lab testing

Figure 6.8. Quality control of the cement mortar.

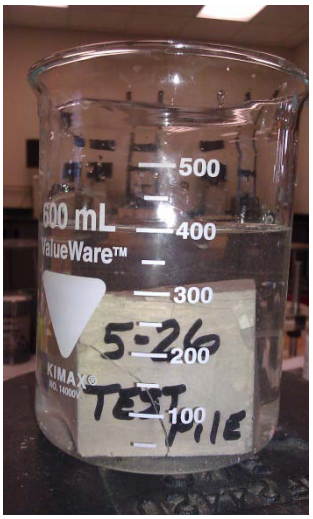

Figure 6.9. Measuring the volume of broken cement specimens for dry density calculations.

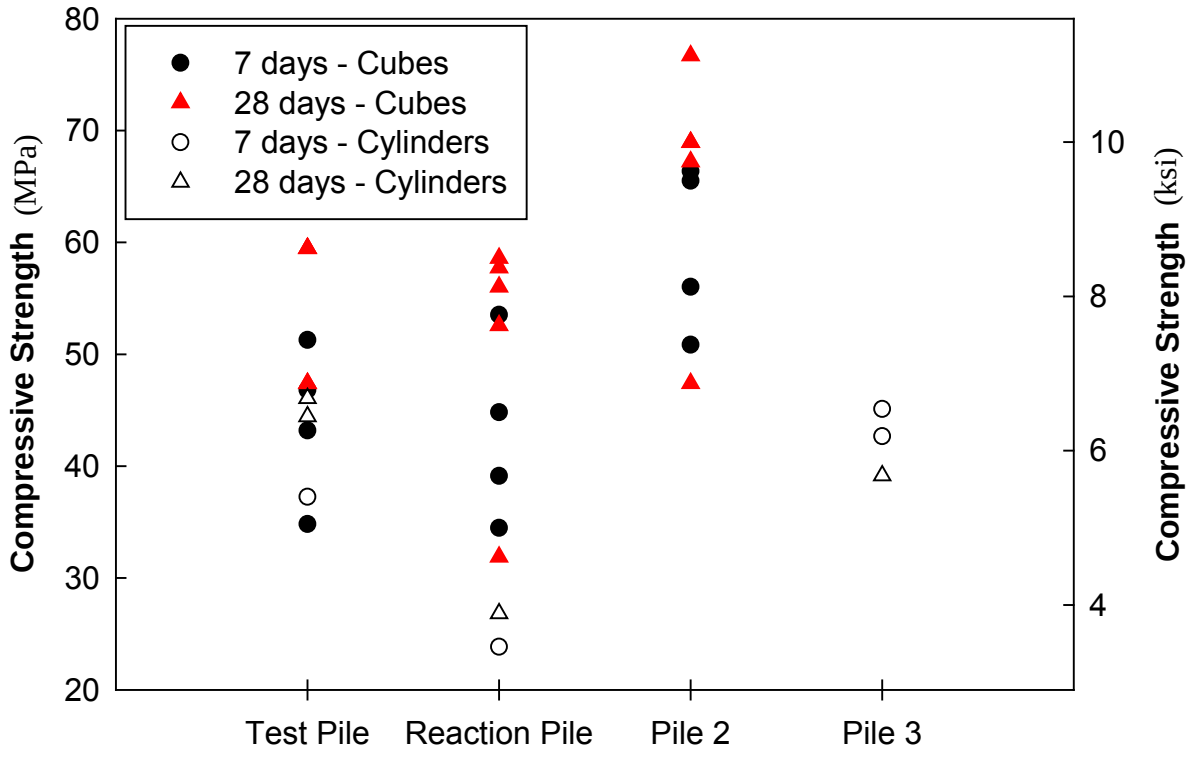

Figure 6.10. Results of compressive tests on cement cubes and cylinders.

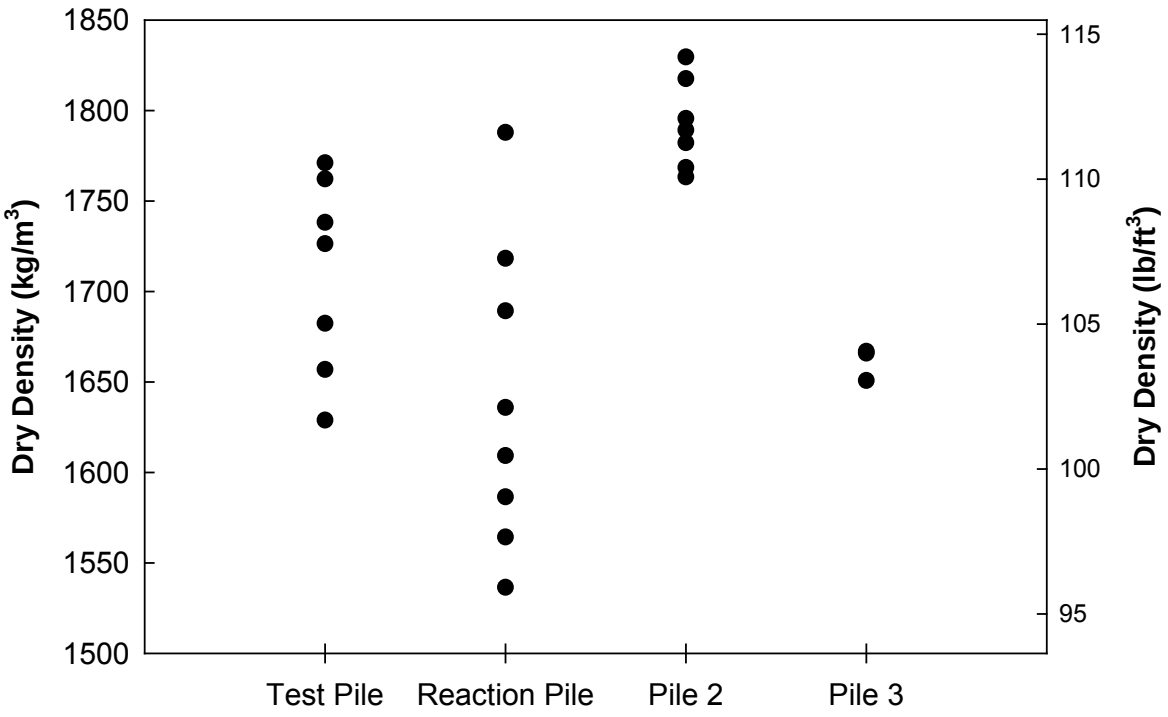

Figure 6.11. Measured dry density of the cement mortar used in different field test elements.

The average dry density of cement cubes and cylinders for each element is then used with the ACI formula to estimate the thermal conductivity of the grout used in each test element (American Concrete Institute, 2002). Table 6-3 shows the estimated thermal conductivity of each element. These thermal conductivity values will be used later to estimate the thermal conductivity of the composite section of each element which will be used in analyzing the results of different tests.

Table 6-3. Estimated thermal conductivity of different elements

Element	Average dry density, kg/m^3 (pcf)	Thermal conductivity of grout*, W/m·℃ (Btu/hr·ft·°F)
Test Pile	1709.4 (106.71)	0.73 (0.42)
Reaction Pile	1640.94 (102.44)	0.67 (0.39)
Pile 2	1792.23 (111.89)	0.81 (0.47)
Pile 3	1661.13 (103.70)	0.69 (0.40)

*Thermal conductivity $k_c = 0.0865 \cdot e^{0.00125d}$ in W/m·K and $k_c = 0.6 \cdot e^{0.02d}$ in Btu·in/hr·ft^2·°F (American Concrete Institute, 2002)

6.3. Testing Equipment

Detailed descriptions of the mechanical loading frame used to apply the structural load to the pile, the temperature controlling equipment, and the heat rate controlling equipment are provided in this section.

6.3.1. Mechanical Loading Frame

The Test Pile was subjected to structural load using a hydraulic ram (Simplex 620 ton) pressurized by a hydraulic pump (Power Team # PE55A Model C). The hydraulic pump was calibrated by the contractor before starting the field experiment as shown in Appendix X. The hydraulic ram is centered on the top of the pile and reacts against a steel I-beam. The steel beam has 60 cm (2 ft) flanges and two 90 cm (3 ft) webs. The two webs were centrally welded to the flanges at a distance of 30 cm (1 ft) from each other. The thicknesses of the flanges and the webs are 25 mm (1 inch), and 20 mm (0.75 inch), respectively.

Prior to loading the Test Pile, the steel beam was laid to rest at its ends on wooden ledgers and then connected to the two reaction piles using steel bars, plates and nuts. Each reaction pile was subjected to tensile loads using a small hydraulic ram connected to the hydraulic pump. The tensile load on each reaction pile was 75 tons (150 kips) which is half the maximum load in the Test Pile (i.e. 150 tons or 300 kips). The wooden ledgers were used to transfer this loads to the top of the ground surface.

The circulation tubes and the sensor cables were passed through the center of the hydraulic ram and circular holes in the flanges of the steel beam and attached to the top of the I-beam. The Test Pile, reference beam, and dial gauges were covered inside an enclosure to protect them from the weather (rain, snow, sun, etc) during the test period. Moreover, the test site was covered with a 5 inch thick layer of pea gravel for access.

Four dial gauges were set up around the Test Pile. Starret Dial indicators with range from 0-127mm (0-5 inches) and 0.0254mm (0.001 inch) gradation were used. These dial gauges were attached to a 4.8 m (16 ft) long reference beam. The reference beam was anchored to the ground by four posts set 2.4 m (8 ft) away from the Test Pile and perpendicular to the steel I-beam. Figure 6.12 shows the used loading frame and reference beam.

(a) Load frame

(b) Tensioning of the reaction piles

(c) Test frame and the shed

(d) Dial gauges and reference beam under the shed

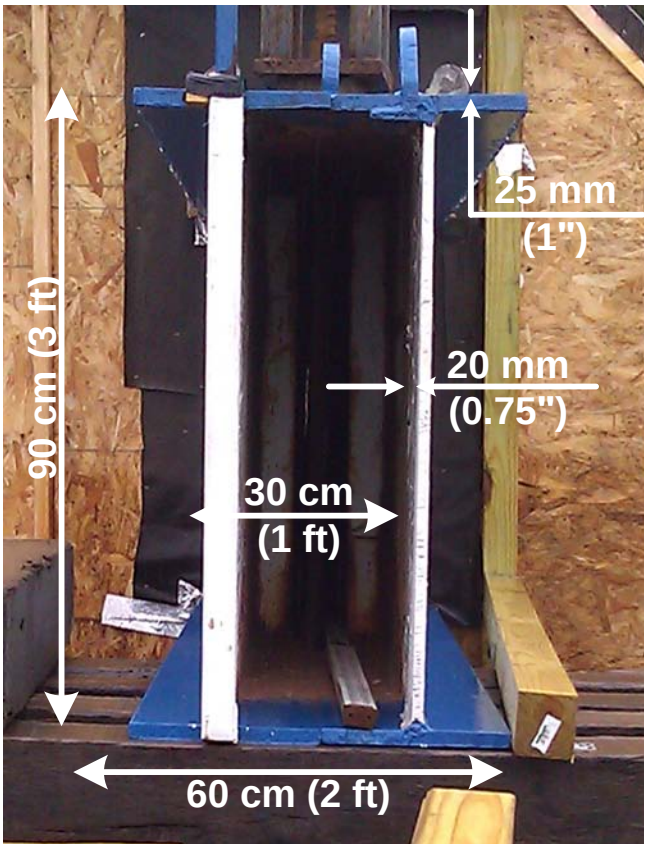

(e) Cross section of the I-beam

Figure 6.12. Loading frame and reference beam.

6.3.2. Thermal Loading Equipment

Two sets of equipment were used to apply controlled heating and cooling loads; the first controls the temperature of the inlet fluid while the second controls the amount of heat rate transferred to the ground. Here below is a detailed description of each one of these machines.

(a) Temperature Controlling Equipment

This machine is custom made at Virginia Tech. The temperature of the fluid entering the ground loops (referred to as the inlet fluid) is controlled by the means of a temperature controller. The temperature controller unit used in this machine has two LED screens; one shows the set temperature and another shows the current fluid temperature. The set temperature is the desired inlet fluid temperature and it can be adjusted using the up and down buttons in the temperature controller. The current fluid temperature is the actual temperature of the inlet fluid measured using internal temperature sensors. The accuracy of measuring the two temperatures is 0.5 ℃ (0.9 °F). As the unit is functionally operating, the two temperatures in the LED need to be identical except immediately after changing the set temperature during testing.

The temperature controller unit has four main fluid lines; to-process and from-process lines, a water supply line, and a drain line. The to-process line is where the water leaves the temperature controller and enters the ground loops, while the from-process line is where the returning water from the ground loops enters the temperature controller. The water supply and drain lines are important for the operation of the unit. The temperature controller used in the

machine requires pressurized water with a minimum pressure of 137.9 kPa (20 psi) to be supplied through the water supply line. An auxiliary pump was used to provide the required pressure in the water supply line. The temperature of the water in the water supply line needs to be less than the desired set temperature by about 5 ℃ (9 ℉). This temperature difference represents the amount of heat transferred to the fluid by the internal pump installed in the temperature controller unit. The temperature controller uses the water supply line when it is initially turned on to saturate the to-process and the from process lines along with the ground loops with an automatic venting process. Once the lines are saturated, the temperature controller shuts down the water supply line and uses it only when cooling is necessary (i.e. set temperature is less that the current fluid temperature).

Heating is performed by turning on the built-in heater. On the other hand, the temperature controller cools the loop-inlet fluid by draining some of the water from the loops through the drain line and mixing water from the water supply line with what remains in the loops. It maintains the same pressure in the line when performing this water exchange process not to affect the overall functionality of the system. Therefore for cooling of the inlet fluid, the temperature of the fluid in the water supply line has to be less than the newly adjusted set temperature as stated earlier. The water for the water supply line is provided from a water tank through the auxiliary pump. The auxiliary pump is a typical deep well pump. The temperature of the water in the water tank was maintained between -3 ℃ and 1 ℃ (26.6 ℉ to 33.8 ℉) by continuously dumping ice in the tank once the temperature rises above 1 ℃ (33.8 ℉). The temperature controller and the water tank were installed inside an insulated wooden box while the auxiliary pump was installed on the top of the box. The wooden box was covered inside the enclosure to protect it from the weather.

A flow meter was installed in the to-process line to measure the flow rate in the loops. The flow rate was controlled using a valve installed before the flow meter. Moreover, temperature sensors were installed in the to-process and the from-process lines to continuously measure the inlet and the outlet fluid temperatures. These sensors were connected to the data logger used for the in-ground strain gauges and thermistors. Moreover, all tubes above the ground surface were insulated to assure minimum interaction with the surrounding ambient weather. Figure 6.13 shows different components of the temperature control machine.

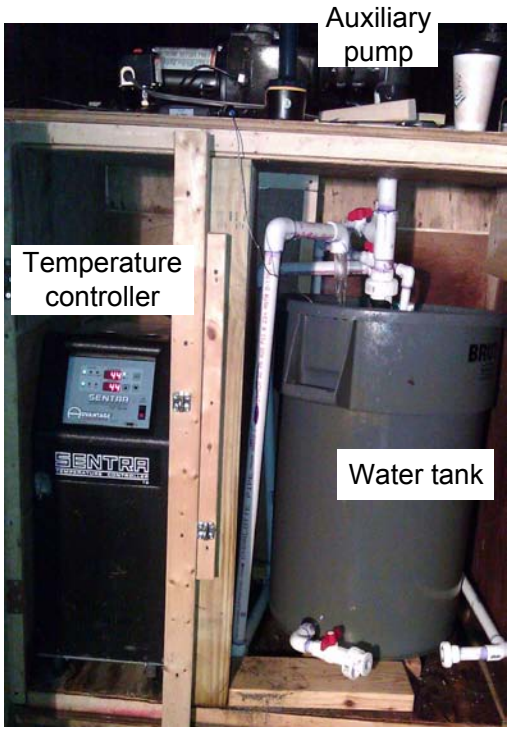

(a) Wooden box and different components of the temperature control system

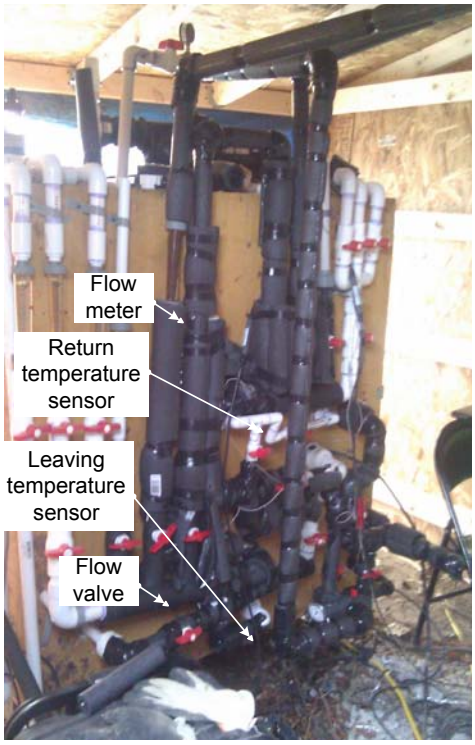

(b) Flow meter and temperature sensors

Figure 6.13. Temperature controlling equipment.

(b) Heat Rate Control Equipment

This equipment was provided in-hind by Mechanical Equipment Sales. The equipment is a trailer mounted test station used for typical ASHRAE thermal conductivity tests (Kavanaugh et al., 2001). The trailer has two partitions thermally insulated from each other; the first contains all electronic pieces including a computer, a data logger, power switches for different system components, heaters and flow valves. The second partition contains a 20 kW diesel powered generator used to power the test station and a water tank used to saturate the ground loops. Figure 6.14 shows the two sections of the trailer.

Six heaters were installed in this testing station (two 1 kW, one 2 kW, one 3 kW, one 4 kW, and one 5 kW) providing the ability to apply a total power of 16 kW to the circulating fluid. Each heater has a separate power switch such that the operator can decide which heaters to turn on based on the tested ground loop length and the required heat rate. These heaters were divided into two groups; each group was installed inside a 50 mm (2 inches) diameter polyethylene (PE) pipe. These large diameter pipes were placed in the fluid line leaving the test station followed by temperature sensors to measure the leaving fluid temperature after heating. Other temperature sensors were installed in the return line to measure the fluid temperature after exchanging heat with the ground. All water lines in the trailer including the large diameter pipes were insulated with 25.4mm (1 inch) closed-cell insulation to reduce the interaction with the weather.

The electrical generator in the test trailer has a voltage regulator to assure minimal variation in the voltage applied to the electrical heaters. Regulating the voltage of the heater is essential to ensure the application of a controlled heat rate to the circulating fluid.

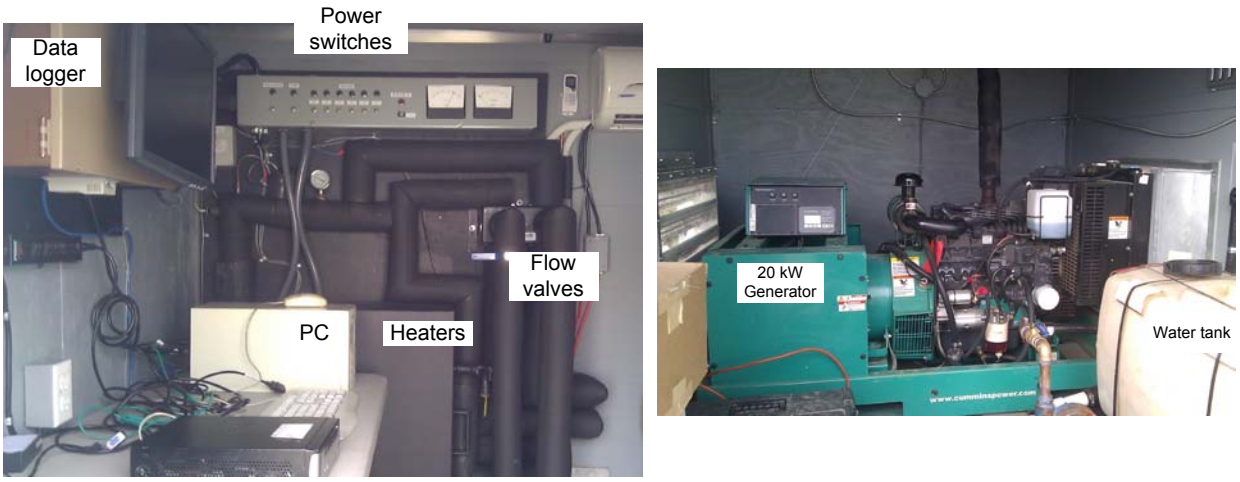

(a) First section; PC, data logger, and power switches

(b)Second section; electrical generator and water tank

Figure 6.14. Heat rate controlling equipment Mechanical Equipment Sales, Inc. system.

Along with monitoring leaving and returning fluid temperatures, the voltage and the amperage of all operating heaters and circulating pump were also monitored with a monitoring system with a redundant data logger and a PC. The PC and the monitoring system were powered by an uninterruptible power supply (UPS) with monitoring to verify the accuracy of the measurements.

The water was circulated in the ground loops with an air-cooled circulation pump (Armstrong model E9). An air-cooled pump was used to minimize any thermal loading transferred to the fluid by the pump during testing. However, the contractor was asked to perform a verification test in which the amount of thermal energy transferred to the fluid due to the operation of the circulating pump is measured. In this test, the leaving fluid line and the returning fluid line were connected bypassing the normal test borehole and the connecting tubes were insulated. The test was performed inside the contractor's warehouse to limit the ambient temperature effects. The test computer was set to record with only the circulating pump operating (i.e. no heaters were operating) for a total test duration of 6.75 hours. An average flow rate of 4 lit/min (1.06 gpm) was used in the test to assure reasonable temperature measurements given the sensitivity of the temperature sensors and the data logger.

The theoretical heat generated from the pump was first estimated by multiplying the pump average voltage (244.9 volts) and average amperage (0.7 amp) providing an average theoretical pump heat of 0.17 kW. This theoretical pump heat would have transferred completely to the fluid if the circulation pump was a water cooled pump, while for an air-cooled pump the pump heat transferred to the fluid is expected to be significantly less than this theoretical value. The average pump heat transferred to the fluid is estimated from the results of this verification test as follows;

$$Ave.pump\ heat(kW) = \frac{500 \times Ave.\ flow\ rate\ (gpm) \times \Delta T_{average}(°\mathrm{F})}{3.412\ \left(\frac{Btu}{hr} \rightarrow W\right) \times 1000(W \rightarrow kW)}$$

The average temperature difference between the leaving and the returning fluids $\Delta T_{average}$ was found to be 0.17℃ (0.31 °F) giving 0.048 kW of an average pump heat transferred to the fluid. This additional heating from the pump is not significant for typical geothermal loops

which are 90 ~150 m (300 ~ 500 ft) in length since the applied power by the electrical heaters for these loops is about 6.5kW which means that the pump heat is about 0.75% of the applied power. For the tests performed using this equipment at Virginia Tech, the geothermal loops are 30.5 m (100 ft) in length which requires a typical applied heater power of about 2 kW based on 20 W/ft rule recommended by ASHRAE (Kavanaugh et al., 2001). Therefore, the pump heat represents about 2.4% of the applied heat which is significant and thus it is decided to consider the pump heat while processing the results of thermal conductivity tests performed using this machine.

6.4. Various Field Tests

This section lists different tests included in Virginia Tech field testing program. The detailed procedure for each test and the results of such tests are presented and discussed in Chapter 8 for thermo-mechanical tests and Chapter 7 for thermal conductivity tests.

Five thermal conductivity tests were performed on different piles. Four of these tests (one test for each energy pile in Figure 6.3) were performed using ASHRAE recommended procedure which suggests applying constant heating rate during the entire test period. The fifth test was performed on the Test Pile (Figure 6.3) following the Dutch approach (Witte et al., 2002) in which a constant temperature difference between the inlet and the outlet fluids is maintained throughout the testing period.

The ASHRAE (ASHREA, 2009) and the Dutch (Witte et al., 2002) thermal conductivity tests performed on the Test Pile were conducted when the pile was subjected to the structural load. Thus, these tests were also considered as thermo-mechanical tests with different ways of applying the thermal load. In addition, two thermo-mechanical pile load tests were performed in which the thermal load was applied by assigning a constant inlet fluid temperature using the temperature controlling equipment. The second test was performed because of a failure in one of the tube connections at the end of the first test which did not allow for enough time applying the extreme temperature which will be discussed in the following chapters. It was also used as a baseline to check the repeatability of the results. Table 6-4 presents a list of the field tests performed for this study.

Table 6-4. Virginia Tech field testing program.

Test	Duration		Procedure and Equipment	Element	General notes
	From	To			
TCT 1	Aug. 22, 2011	Aug. 25, 2011	Heat rate controlling equipment	Pile 3	
TCT 2	Nov. 16, 2011	Nov. 19, 2011		Pile 4	
TCT 3	Dec. 16, 2011	Dec. 18, 2011		Pile 2	
TCT 4	Jan. 18, 2012	Jan. 20, 2012		Test Pile	Considered as T-MT 3
TCT 5	Feb. 18, 2012	Feb. 20, 2012	Temperature controlling equipment	Test Pile	Considered as T-MT 4
T-MT 1	Oct. 27, 2011	Nov. 11, 2011		Test Pile	
T-MT 2	Nov. 21, 2011	Dec. 9, 2011		Test Pile	

*TCT: Thermal conductivity test, T-MT: Thermo-Mechanical test.

References

American Concrete Institute, ACI (2002) "Guide to thermal properties of concrete and Masonry Systems," No. ACI 122R-02, p 21.

ASHRAE (2002) "Methods for Determining Soil and Rock Formation Thermal Properties from Field Tests," *ASHRAE Research Summary - ASHRAE 1118-TRP*: American Society of Heating, Refrigerating and Air-Conditioning Engineers.

American Society for Testing Materials (2011), "D2487: Standard Practice for Classification of Soils for Engineering Purposes (Unified Soil Classification System)," ASTM International, West Conshohocken, PA, 2011, DOI: 10.1520/D2487-11, www.astm.org.

Kavanaugh, S.P., Xie, L. and Martin, C. (2001). Investigation of Methods for Determining Soil and Rock Formation from Short Term Field Tests. ASHRAE1118-TRP, American Society of Heating, Refrigerating and Air-Conditioning Engineers, Inc., 77 p.

Witte, H. J. L., G. J. van Gelder, and J. D. Spitler (2002) "In situ measurement of ground thermal conductivity-A dutch Perspective," *ASHRAE Transactions*, Vol. 108, No. 1, pp 263-272.

Appendix VIII

Soil profile from drilling data

Observation Point #1			
Date: 05/19/2010 Time: 3:15PM			
Contractor: Layne GeoConstruction			
Driller: Fred		Logger: Sherif	
Symbol	Depth (ft)	Depth (m)	Description
	33.0	10	Silty Clayey SAND, light Brown, plastic, sticky soil Drilling started with air, but at depth of 10m (33 ft) drilling with water was used to simplify taking the hammer out of the ground.
	47.0	14	
	100	30.5	Weak weathered SHALE End of the hole

Observation Point #2			
Date: 05/20/2010 Time: 12:00PM			
Contractor: Layne GeoConstruction			
Driller: Fred		Logger: Sherif	
Symbol	Depth (ft)	Depth (m)	Description
	58	17.7	Silty Clayey SAND, light Brown, plastic, sticky soil
	100	30.5	Weak weathered SHALE End of the hole

Reaction Pile (no Instrumentation)			
Date: 05/22/2010 Time: 9:30AM			
Contractor: Layne GeoConstruction			
Driller: Fred		Logger: Sherif	
Symbol	Depth (ft)	Depth (m)	Description
	1.0		Asphalt layers
	47	14.3	Silty Clayey SAND, light Brown, plastic, sticky soil
	100	30.5	Weak weathered SHALE End of the hole

REHAU PEX Pile - Double Tube (Pile 4)			
Date: 05/24/2010 Time: 8:30AM			
Contractor: Layne GeoConstruction			
Driller: Fred		Logger: Sherif	
Symbol	Depth (ft)	Depth (m)	Description
			Silty Clayey SAND, light Brown, plastic, sticky soil
	49	14.9	
			Very soft soil from 14.9m (49 ft) to 17.4 m (57 ft)
	57	17.4	
	62	18.9	
			Weak weathered SHALE
	100	30.5	End of the hole

Reaction Pile HDPE (Pile 2)			
Date: 05/25/2010 Time: 8:15AM			
Contractor: Layne GeoConstruction			
Driller: Fred		Logger: Sherif	
Symbol	Depth (ft)	Depth (m)	Description
	47	14.3	Silty Clayey SAND, light Brown, plastic, sticky soil
	100	30.5	Weak weathered SHALE End of the hole

REHAU PEX Single Tube Pile + Instrumentations (Pile 3)			
Date: 05/25/2010 Time: 3:00PM			
Contractor: Layne GeoConstruction			
Driller: Fred		Logger: Sherif	
Symbol	Depth (ft)	Depth (m)	Description
	30	9.15	Silty Clayey SAND, light Brown, plastic, sticky soil
	34	10.4	Boulder from 9.15m (30ft) to 10.4m (34ft)
	57	17.4	
	100	30.5	Weak weathered SHALE End of the hole

Test Pile - HDPE Tube + Instrumentations (Pile 1)			
Date: 05/26/2010 Time: 8:00AM			
Contractor: Layne GeoConstruction			
Driller: Fred		Logger: Sherif	
Symbol	Depth (ft)	Depth (m)	Description
	42	12.8	Silty Clayey SAND, light Brown, plastic, sticky soil
	100	30.5	Weak weathered SHALE End of the hole

Observation Point #3			
Date: 05/23/2010 Time: 8:00AM			
Contractor: Layne GeoConstruction			
Driller: Fred		Logger: Sherif	
Symbol	Depth (ft)	Depth (m)	Description
	50	15.3	Silty Clayey SAND, light Brown, plastic, sticky soil End of the hole

Central Observation Point #4			
Date: 05/27/2010 Time: 8:20AM			
Contractor: Layne GeoConstruction			
Driller: Fred		Logger: Sherif	
Symbol	Depth (ft)	Depth (m)	Description
	41	12.5	Silty Clayey SAND, light Brown, plastic, sticky soil
	50	15.3	Weak weathered Fractured SHALE good quality rock started at 50ft
	82	25	very strong rock at 82ft
	120	36.6	End of the hole

Appendix IX

Grain size analysis and Atterberg limits for the top soil layer

Plastic Limit

Sample	Weight of can (gm)	Weight of wet soil + can (gm)	Weight of dry soil + can (gm)	Weight of wet soil (gm)	Weight of dry soil (gm)	Weight of water (gm)	PL
1	11.09	24.17	21.6	13.08	10.51	2.57	24.5
2	11.13	23.77	21.21	12.64	10.08	2.56	25.4
3	11.84	26.11	23.37	14.27	11.53	2.74	23.8
						Average =	24.5

Liquid Limit

Sample	Weight of can (gm)	Weight of wet soil + can (gm)	Weight of dry soil + can (gm)	Weight of wet soil (gm)	Weight of dry soil (gm)	Weight of water (gm)	Moisture content, *w* (%)	Number of blows
1	11.84	23.82	20.86	11.98	9.02	2.96	32.82	30
2	11.14	24.74	21.23	13.6	10.09	3.51	34.79	16
3	11.93	29.55	25.12	17.62	13.19	4.43	33.59	23

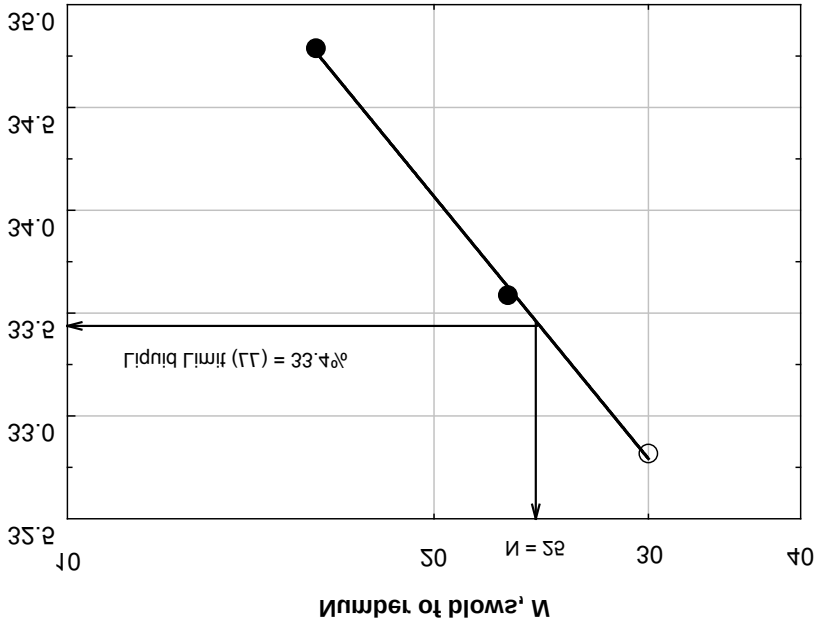

LL = 33.5%
PI = LL - PL = 8.9%
This soil falls below the A-line

Sample # 1

Pan weight (gm) = 164.8
Dry soil + Pan (gm) = 666.9
Dry soil (gm) = 502.1

Seive #	Seive opening (mm)	Weight of Pan + retained soil (gm)	Weight of soil retained on each sieve (gm)	Percent of mass retained on each sieve	Cumulative percent retained	Percent finer
4	4.750	165.8	1	0.20	0.20	99.80
10	2.000	173.7	8.9	1.77	1.97	98.03
20	0.850	181.3	16.5	3.29	5.26	94.74
40	0.425	259.4	94.6	18.84	24.10	75.90
60	0.250	324.1	159.3	31.73	55.83	44.17
100	0.150	246.1	81.3	16.19	72.02	27.98
200	0.075	261.1	96.3	19.18	91.20	8.80
Bottom pan	-	208.4	43.6	--	--	--
		final wt (gm) =	501.5	=> loss =	0.12%	

D_{10} = 0.080 mm
D_{30} = 0.162 mm
D_{60} = 0.337 mm

C_u = 4.233
C_c = 0.982
% fines = 8.80
USCS : **SP - SM**

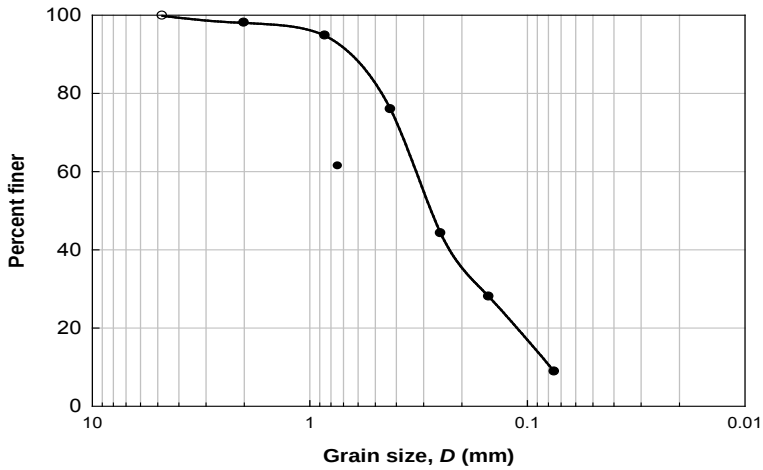

Sample # 2

Pan weight (gm) = 486.5
Dry soil + Pan (gm) = 961.5
Dry soil (gm) = 475

Seive #	Seive opening (mm)	Weight of Pan + retained soil (gm)	Weight of soil retained on each sieve (gm)	Percent of mass retained on each sieve	Cumulative percent retained	Percent finer
4	4.750	488.2	1.7	0.36	0.36	99.64
10	2.000	492.4	5.9	1.24	1.60	98.40
20	0.850	500.6	14.1	2.97	4.57	95.43
40	0.425	584.1	97.6	20.55	25.12	74.88
60	0.250	645.8	159.3	33.54	58.65	41.35
100	0.150	563	76.5	16.11	74.76	25.24
200	0.075	568.5	82	17.26	92.02	7.98
Bottom pan	-	524.1	37.6	--	--	--
		final wt (gm) =	474.7	=> loss =	0.06%	

D_{10} = 0.084 mm
D_{30} = 0.180 mm
D_{60} = 0.347 mm

C_u = 4.146
C_c = 1.108
% fines = 7.98
USCS : **SP - SM**

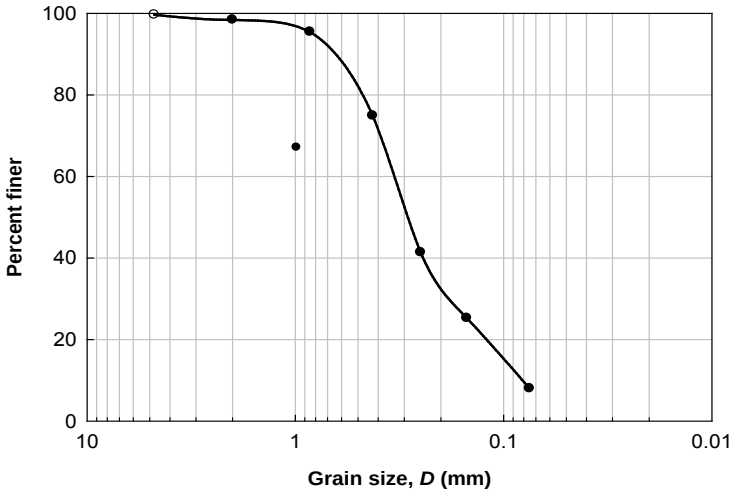

Sample # 3

Pan weight (gm) = 164.9
Dry soil + Pan (gm) = 1234.1
Dry soil (gm) = 1069.2

Seive #	Seive opening (mm)	Weight of Pan + retained soil (gm)	Weight of soil retained on each sieve (gm)	Percent of mass retained on each sieve	Cumulative percent retained	Percent finer
4	4.750	174.1	9.2	0.86	0.86	99.14
10	2.000	188.3	23.4	2.19	3.05	96.95
20	0.850	204.2	39.3	3.68	6.72	93.28
40	0.425	403.6	238.7	22.33	29.05	70.95
60	0.250	500.3	335.4	31.37	60.42	39.58
100	0.150	325.8	160.9	15.05	75.47	24.53
200	0.075	344.2	179.3	16.77	92.24	7.76
Bottom pan	-	246.2	81.3	--	--	--
		final wt (gm) =	1067.5	=> loss =	0.16%	

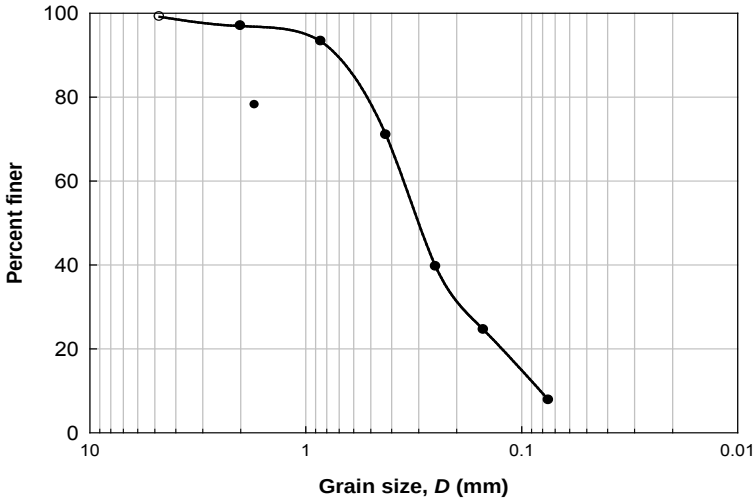

D_{10} = 0.085 mm
D_{30} = 0.186 mm
D_{60} = 0.364 mm

C_u = 4.281
C_c = 1.122
% fines = 7.76
USCS : **SP - SM**

Appendix X

Calibration sheets of the hydraulic pump

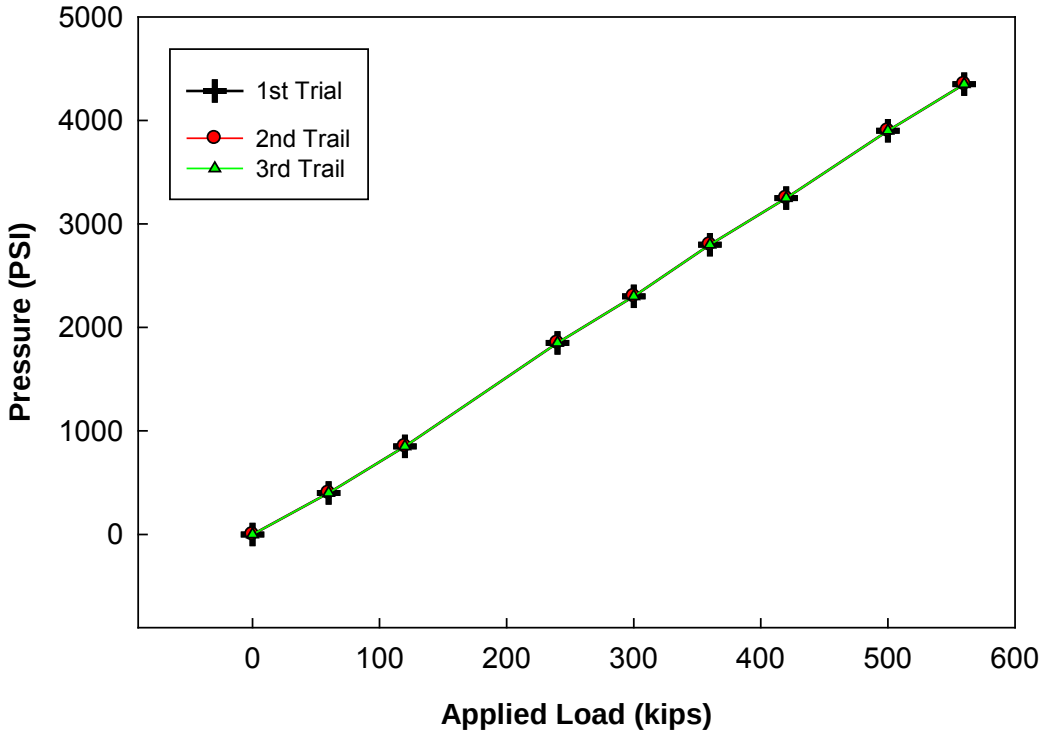
5000
4000
3000
2000
1000
0
Pressure (PSI)
1st Trial
2nd Trail
3rd Trail
0
100
200
300
400
500
600
Applied Load (kips)

CHAPTER 7. IN-SITU THERMAL RESPONSE TESTS

7.1. Introduction

The undisturbed ground temperature, the ground thermal conductivity and diffusivity, and the thermal resistance of the heat exchanger are required in order to design ground-coupled heat exchangers as discussed in Chapter 2. If the ground loops are embedded in stratified ground, the average thermal conductivity and diffusivity of various layers encountered along the length of the loops are used in the design. These measured thermal properties are indicative of the system properties representing effective and average ground response.

Furthermore, the length of the ground loops depends on the heat exchange capacity of the heat exchanger. The thermal resistances of various components of the heat exchanger control this heat exchange capacity. The summation of the resistances of the different components including the convective resistance of the fluid, the tube resistance, and the resistance of the backfilling material is known as the thermal resistance of the heat exchanger which is also required in the design formulations. The thermal resistance of the heat exchanger defines the temperature change produced by the resistance of a unit area of the heat exchanger to the flow of unit heat energy. Thus, estimating this collective term is necessary to estimate the length of the ground loops.

The most reliable way to estimate the parameters required for the design of the ground coupled heat exchangers is conducting in-situ thermal conductivity tests. This chapter presents the standards followed to perform such tests; followed by a detailed discussion about different techniques to process the results and to estimate the desired design parameters. Thereafter, various thermal conductivity tests performed as part of this study are presented along with the estimation of the effective thermal properties of the ground at the test site.

7.1. General

Subjecting the ground to a thermal load, through heating/cooling of the carrier fluid then circulating it in the ground loops, produces temperature changes in the ground. The rate at which the ground temperature varies at a point in the ground depends on the distance between this point and the exchanger-soil interface, the applied thermal load, the thermal properties of the ground, and the thermal resistance of the heat exchanger. Based on the definition of the thermal resistance of the heat exchanger mentioned earlier, the change of the fluid temperature inside the ground loops (ΔT_f) is related to the temperature change at the exchanger-soil interface (ΔT_b), the applied thermal load per unit area (q), and the thermal resistance of the heat exchanger (R_b) as follows;

$$\Delta T_f(t) = \Delta T_b(t) + q \cdot R_b \qquad \text{Eq. 7-1}$$

Thus, the fluid temperature at any time (T_f) can be estimated provided that the initial fluid temperature is known. As discussed later, the carrier fluid is circulated in the ground loops for an initialization time period without applying any thermal load. At the end of this initialization period, the fluid temperature converges to the undisturbed ground temperature (T_o) which, therefore, can be treated as the initial reference temperature. Hence, the fluid temperature at a given time (T_f) is estimated by adding the undisturbed ground temperature (T_o) to Eq.7-1 as follows;

$$T_f(t) = \Delta T_b(t) + q \cdot R_b + T_o \quad \text{Eq. 7-2}$$

In thermal conductivity tests, a constant thermal load per unit area (q) is applied into the carrier fluid and the average fluid temperature (T_f) over the testing period is recorded. Furthermore, the undisturbed ground temperature (T_o) is estimated using the initialization period as discussed earlier. Thus, the temperature change at the exchanger-soil interface and the thermal resistance of the heat exchanger are the two unknowns in Eq.7-2. Various analytical and numerical models are used to estimate the temperature change at the exchanger-soil interface (ΔT_b). These models are function of the thermal properties of the ground and thus they are used, accompanied with the measured fluid temperature, to estimate the thermal properties of the ground as well as the thermal resistance of the heat exchanger by solving Eq.7-2. The data processing technique is generally titled with reference to the model used to estimate ΔT_b.

In this section, the details of the two available standards for applying the constant thermal load in the in-situ thermal conductivity tests are presented. The first procedure is outlined by the American Society of Heating, Refrigerating, and Air-Conditioning Engineers (ASHREA, 2009), while the second is proposed by Witte et al. (2002).

7.1.1. ASHRAE Procedure

The thermal load according to the ASHRAE procedure is always heating and is applied to the carrier fluid in the ground loops at a constant rate using electrical heaters. The carrier fluid used in the ASHRAE thermal conductivity tests is generally water since the fluid temperature does not fall below freezing and thus, no need for using anti-freeze. The power applied by the electrical heaters to the carrier fluid is fixed by maintaining constant voltage and amperage in the heaters using electrical regulators. Below are listed the requirements of the ASHRAE standards (ASHRAE, 2002);

- The thermal conductivity test needs to be initiated at least after 5 days from constructing the heat exchanger in formations with thermal conductivity less than 1.7 W/m·℃ (0.98 BTU/hr·ft °F), or 3 days if the formation has higher thermal conductivity;
- The undisturbed ground temperature needs to be measured at the end of an initial time period over which the water is to be circulated in the loops without any applied heating loads;
- The total testing duration should range from 36 to 48 hours;
- A constant heat power ranging from 50 to 80 W/m (about 15 to 25 W/ft) needs to be applied over the entire testing period;
- The standard deviation and the maximum spikes of the heating power applied to the electrical heaters should not be more than 1.5% and 10% of the average power, respectively;
- The inlet fluid temperature, the outlet fluid temperature, and the voltage and the amperage applied to the heating elements and the circulation pump should be recorded during the test;
- The flow rate, the diameter and the depth of the heat exchanger, tube dimensions and type, the specifications of the filling material are additional measurements that are suggested to increase the accuracy of the estimated ground thermal properties;

- The flow rate at which the carrier fluid is circulated is selected such that it results in 3 to 7℃ (5.4 to 12.6 °F) of a t emperature difference between the inlet and the outlet fluid temperatures;
- In case of retesting the same heat exchanger, the loop temperature should return to within ±0.3℃ (±0.54°F) of the ground temperature prior to the initial test.

7.1.2. Dutch Procedure

The Dutch perspective for conducting thermal conductivity tests presented by Witte et al. (2002) is based on maintaining a constant temperature difference between the fluid entering and leaving the ground loop over the testing period. The calorimetric power applied to the fluid is estimated as;

$$\text{Power (W)} = \mathrm{V} \cdot C_p \cdot \Delta T_f = \mathbf{V} \cdot C_p \cdot \left(T_{f-in} - T_{f-out}\right) \quad \text{Eq. 7-3}$$

Where;

V: Mass flow rate in kg/sec = volumetric flow rate (m^3/sec)×fluid density (kg/m^3),

C_p: Specific heat in J/kg·℃,

ΔT_f: Temperature difference between the fluid entering the ground loop (T_{f-in}) and the fluid leaving the ground loop (T_{f-out}).

Thus, the applied power does not change as the fluid flow rate (**V**) and the temperature difference (ΔT_f) are maintained constant which is the idea behind the Dutch procedure for thermal response testing. In the Dutch perspective, heating loads or cooling loads can be used. Heating loads are applied by setting the temperature of the fluid entering the ground loop to be more than the temperature of the fluid leaving the ground loop. While, cooling loads are applied by setting the temperature of the fluid entering the loop to be less than the temperature of the fluid leaving the loops. Section 7.7 presents a modification for the Dutch procedure which enhances the estimated design parameters.

7.2. Data Processing

This section presents different techniques used to process the data recorded during thermal conductivity tests for estimating various design parameters. A discussion about the average power required to process the test data is presented first followed by the effect of the ambient on the actual power applied into the ground. The procedure followed to estimate the undisturbed ground temperature is presented next after which different analytical models used to estimate the effective thermal properties of the ground are discussed in details.

7.2.1. Applied Power and Calorimetric Power during the Test

The power applied during the testing period (q) is required to process the test data. There are three approaches to estimate the average applied power if the test is performed according to the ASHRAE procedure (ASHRAE, 2009). The average power can be assumed equal to; (1) the power applied to the electrical heaters, (2) the summation of the power applied to the electrical heaters and the circulation pump, and (3) the calorimetric power applied to the circulation fluid using Eq.7-3. The power applied to the electrical heaters is approximated as the multiplication of the voltage and the amperage provided to the heaters in operation; similarly, the power applied to the circulation pump equals the voltage times the amperage provided to that pump. Only the third approach can be used to estimate the applied power in the Dutch procedure since there are

no electrical heaters used in this technique. Eq. 7-4 presents the three approaches discussed earlier.

$$\text{Power (W)} = \begin{cases} V_{heater} \times A_{heater} & \text{(a)} \\ (V_{heater} \times A_{heater}) + (V_{pump} \times A_{pump}) & \text{(b)} \\ \text{V} \cdot C_p \cdot \Delta T_f & \text{(c)} \end{cases} \quad \text{Eq. 7-4}$$

The first and the second approaches evaluate the power applied to the fluid by the heaters and the circulation pump assuming a 100% efficient system. This assumption is not valid since the heaters, the temperature gauges, and the circulation pump are installed inside the trailer housing the logging system and all other electrical components. The ground loops are connected to the trailer using tubes that are thermally insulated. This insulation reduces the interaction between the fluid inside the tubes above the ground and the ambient but does not prohibit it; thus heat loss/gain takes place in the system due to this ambient interaction. Furthermore, additional heat loss/gain takes place inside the trailer due to interacting with the air inside the testing trailer. Since the calorimetric power estimated using the third approach is based on actual measurements of the fluid temperatures, it is considered the most accurate and thus is recommended to be used while processing the results of any thermal conductivity test. It, however, should be noticed that the power from the third approach is estimated using the fluid temperatures measured by temperature gauges installed inside the testing trailer. The fluid temperatures right at the inlet and the outlet of the ground loops differ from those measured inside the trailer due to the heat exchanged with the ambient air. Therefore, the power from the third approach still does not represent the actual power applied to the ground and thus requires a modification to estimate the actual power. Section 7.3.2 presents a procedure to approximate the actual power applied to the ground using the fluid temperatures measured inside the testing trailer and the ambient temperature. This procedure corrects the evaluated power and uses advanced processing techniques to estimate the design parameters. A modification to the testing practice is proposed in Section 7.7 to provide this actual power directly from the test measurements thus no power corrections or advanced processing techniques are needed.

7.2.2. Ambient Temperature Interference

As mentioned in the previous section, the temperature of the inlet (T_{in}^*) and the outlet (T_{out}^*) fluids are measured using temperature gauges installed inside the testing trailer. Similarly, the electrical amperages and the voltages provided to the electrical heaters and the circulation pumps are recorded using the logging system inside the testing trailer. The trailer is connected to the ground loops using thermally insulated tubes with a total length of *D* as shown in Figure 7–1. The heat exchange between the fluid inside these insulated tubes above the ground surface and the ambient is inevitable due to the lack of having an ideal thermal insulation. The direction of this heat exchange depends on the temperatures of the ambient air and the fluid; the fluid losses heat if its temperature is higher than the ambient air temperature, and it gains heat if its temperature is less than the ambient air tempeature (Bandos et al., 2011). Consequently, the temperature of the fluid at the entrance (T_{in}) and at the exit (T_{out}) of the ground loops are different than the temperatures measured inside the trailer (T_{in}^* and T_{out}^*). Thus, the actual power applied to the ground differs from this estimated using the input to the electrical heaters or the calorimetric power estimated using the fluid temperatures measured inside the trailer as in Eq.7.4. Small heat flow through the insulation complicates the estimation of the ground effective thermal properties since the estimated properties for this case depend on the time interval used for the evaluation (Bandos et al., 2011).

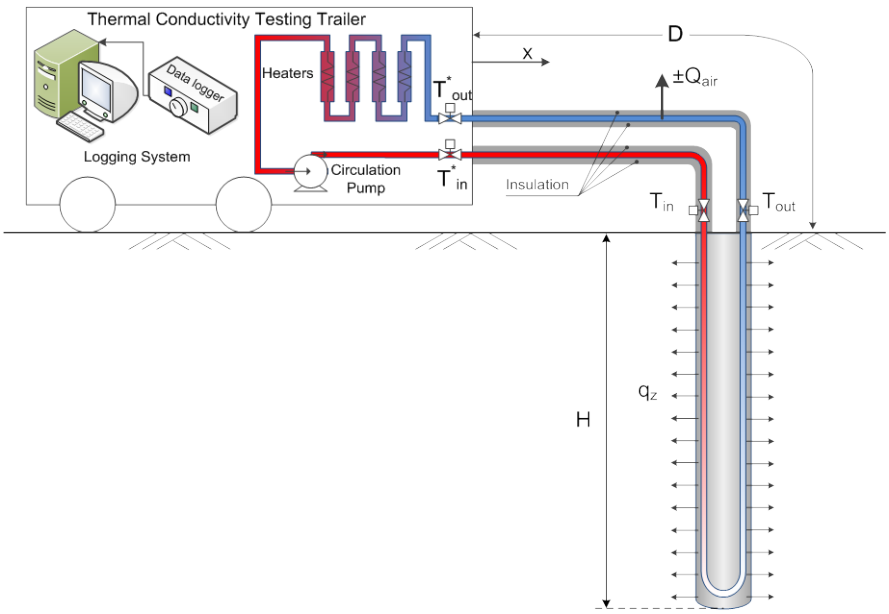

Figure 7.1. Schematic of in-situ thermal conductivity test set up.

Bandos et al. (2011) proposed an analytical procedure to account for the heat exchanged between the fluid in the tubes above the ground surface and the ambient air. This procedure depends on estimating the total heat applied to the fluid (Q_f) as the summation of the heat exchanged with the ambient (Q_{air}) and the actual heat injected to the ground ($q_z H$) as shown schematically in Figure 7–1 and presented in Eq.7-5.

$$Q_f = Q_{air} + q_z H \qquad \text{Eq. 7-5}$$

This total applied heat can also be estimated using Eq.7-3 as the calorimetric power applied to the fluid, i.e. $Q_f = \mathrm{V} \cdot C_p \cdot (T^*_{in} - T^*_{out})$. On the other hand, the calorimetric power estimated based on the fluid temperatures at the inlet and the outlet of the ground loops represents the actual power applied to the ground ($q_z H$). Thus;

$$q_z H = \mathrm{V} \cdot C_p \cdot (T_{in} - T_{out}) \qquad \text{Eq. 7-6}$$

Bandos et al. (2011) proposed a quasi steady-state analysis for the heat exchange with the ambient air and showed that the convection equations governing the heat exchanged between the fluid and the ambient are;

$$VC_p \frac{dT_f^{\downarrow}(\mathrm{x},t)}{d\mathrm{x}} = \frac{T_a(t) - T_f^{\downarrow}(\mathrm{x},t)}{R_a} \qquad \text{Eq. 7-7}$$

$$-VC_p \frac{dT_f^{\uparrow}(\mathrm{x},t)}{d\mathrm{x}} = \frac{T_a(t) - T_f^{\uparrow}(\mathrm{x},t)}{R_a} \qquad \text{Eq. 7-8}$$

Where;

x : Distance along the tube above the ground surface ($0 \leq \mathrm{x} \leq D$);

T_a : Ambient air temperature;

R_a : Thermal resistance between the fluid and the ambient air;

$T_f^{\downarrow}$: Temperature of the fluid in the tube above the ground surface in which the flow is entering the ground loops; thus, $T^*_{in} = T_f^{\downarrow}(\mathrm{x} = 0)$, and $T_{in} = T_f^{\downarrow}(\mathrm{x} = D)$;

$T_f^{\uparrow}$: Temperature of the fluid in the tube above the ground surface in which the flow is leaving the ground loops; thus, $T_{out}^* = T_f^{\uparrow}(\mathrm{x} = 0)$, and $T_{out} = T_f^{\uparrow}(\mathrm{x} = D)$.

The solution for the Eq. 7-7 and Eq. 7-8 was found to be;

$$\left.\begin{aligned} T_{in} &= T_{in}^* e^{-\mu} + T_a(1 - e^{-\mu}) \\ T_{out} &= T_{out}^* e^{\mu} + T_a(1 - e^{\mu}) \end{aligned}\right\} \quad \text{Eq. 7-9}$$

μ is the system parameter that represents the percentage of the heat exchanged with the ambient air. Thus, μ is equal to zero for ideally perfect insulation and is more than zero for non-ideal insulations. This parameter is independent of the flow direction since it is an average value that depends on the fluid and air temperature regardless of the flow direction. This parameter was estimated as (Bandos et al., 2011);

$$\mu = \frac{D}{R_a V C_p} \quad \text{Eq. 7-10}$$

Substituting from Eq. 7-9 into Eq. 7-6, the actual power applied to the ground is estimated as;

$$q_z(\mu, t)H = \mathrm{V} \cdot C_p \cdot [2T_a(t)\ sinh(\mu) - T_{out}^* e^{\mu} + T_{in}^* e^{-\mu}] \quad \text{Eq. 7-11}$$

And thus, the average fluid temperature is given as;

$$\bar{T}_f(\mu, t) = \frac{T_{in}(t) + T_{out}(t)}{2} = T_a(t)[1 - cosh(\mu)] + \frac{T_{out}^* e^{\mu} + T_{in}^* e^{-\mu}}{2} \quad \text{Eq. 7-12}$$

To estimate the system parameter (μ); it is assumed that the percentage of the heat exchanged with the ambient is *p*. Therefore;

$$Q_{air}(t) = p \cdot Q_f(t)$$

Thus,

$$\mu = p \frac{\langle T_{in}^*(t) - T_{out}^*(t) \rangle_{\text{avg. over t}}}{\langle T_{in}^*(t) + T_{out}^*(t) - 2T_a(t) \rangle_{\text{avg. over t}}} \quad \text{Eq. 7-13}$$

Eq.7-13 is used to estimate the system parameter μ which is then used along with the measured fluid and temperatures in Eq.7-11 to estimate the change of the actual power applied to the ground over the test period (*t*). The estimate actual power and its variation over the test period are then used within an advanced parameter matching technique to estimate the ground and the heat exchanger thermal properties as discussed in Section 7.3.4.

7.2.3. Undisturbed Ground Temperature

The undisturbed ground temperature is one of the design parameters required in order to estimate the length of the ground loops (Kavanaugh and Rafferty, 1997). Field testing is the most accurate method to evaluate the average undisturbed in-situ ground temperature (T_o) over a proposed length of the ground loops. This is performed by an initial phase in which the carrier fluid is circulated for a period of time ranging from 2 to 6 hours with no applied thermal loads.

The inlet fluid and the outlet fluid temperatures converge to the average in-situ undisturbed ground temperature by the end of the initialization phase.

7.2.4. Ground Thermal Properties

The effective thermal properties of the ground, the thermal resistance of the heat exchanger, and the undisturbed ground temperature are related to the measured average fluid temperature and to one another as shown Eq. 7-2. In this equation, the temperature change at the exchanger-soil interface is required. Various analytical models are used to estimate this temperature change and thus processing the thermal conductivity test results are performed according to these models. In this section, a detailed discussion about each of these models is presented followed by the respective procedure to estimate the three required parameters.

(a) Infinite Line Source Model

This model represents the ground loops as a line centered at the heat exchanger axis. It utilizes the line source model (Carslaw and Jaeger, 1986) derived in Chapter 2 to estimate the thermal properties of the ground and the thermal resistance of the borehole. Mogensen (1983) was the first to apply this model in processing the results of thermal conductivity tests. This is the most commonly used approach because of its simplicity and quick and reliable results (Monzó, 2011).

The temperature change at a distance r from the line source after applying constant heat rate (q) for time (t) is given by;

$$\Delta T(r,t) = \frac{q}{4\pi k}\int_{\frac{r^2}{4\alpha t}}^{\infty}\frac{e^{-u}}{u}\cdot du \qquad \text{Eq. 7-14}$$

Where;

r: radius from line source;

t: time after start of heat injection,

q: heat injection rate per unit length of the heat exchanger,

k: thermal conductivity of the ground,

α: thermal diffusivity of the ground.

For $\frac{\alpha t}{r^2} \geq 5$, Mogensen (1983) suggested approximating the integral in Eq. 7-14 as;

$$\int_{\frac{r^2}{4\alpha t}}^{\infty}\frac{e^{-u}}{u}\cdot du = ln\left(\frac{4\alpha t}{r^2}\right) - \gamma \qquad \text{Eq. 7-15}$$

Where; γ: Euler constant = 0.5772

Thus setting the distance r equal to the radius of the heat exchanger and substituting from Eq. 7-15 into Eq. 7-2, the average fluid temperature can be estimated as;

$$T_f(t) = \frac{q}{4\pi k}\left[ln\left(\frac{4\alpha t}{r^2}\right) - \gamma\right] + q\cdot R_b + T_o \qquad \text{Eq. 7-16}$$

Collecting terms and rearranging Eq. 7-16 to a more usable form, it can be presented as;

$$T_f(t) = \frac{q}{4\pi k}\left[ln\left(\frac{4\alpha}{r^2}\right) - \gamma\right] + q\cdot R_b + T_o + \frac{q}{4\pi k}ln(t) \qquad \text{Eq. 7-17}$$

Notice that the first three terms on the right hand side of Eq. 7-17 are constant over time as long as the heat rate is maintained constant. The last term in Eq. 7-17 is the only one that varies with time. Thus, this equation can be simplified using a line equation as;

$$y = m\cdot\ ln(t) + b \qquad \text{Eq. 7-18}$$

Where;

y: average fluid temperature = $T_f(t)$,

m: the slope of the line which is related to the thermal conductivity of the ground = $\boldsymbol{\frac{q}{4\pi k}}$,

b: the magnitude of the fluid temperature when the time is zero which is the ordinate at the origin = $q\left[\frac{1}{4\pi k}\left(ln\left(\frac{4\alpha}{r^2}\right)-\gamma\right)+R_b\right]+T_o$.

Thus, the effective thermal conductivity of the ground can be estimated using the slope of the estimated line as follows;

$$k=\frac{q}{4\pi m} \qquad \text{Eq. 7-19}$$

While an average thermal resistance of the heat exchanger can be estimated using the intercept (b) as follows;

$$R_b=\frac{b-T_o}{q}-\frac{1}{4\pi k}\left[ln\left(\frac{4\alpha}{r^2}\right)-\gamma\right] \qquad \text{Eq. 7-20}$$

(b) Cylindrical Source Model

The cylindrical source model estimates the temperature changes at any point in the ground representing the ground loops as an infinite cylinder surrounded by a homogeneous soil with constant properties under a constant heat rate. The heat transfer between the heat exchanger and the ground is assumed to be purely heat conduction (Carslaw and Jaeger, 1986; Ingersoll et al., 1948; Yang et al., 2010).

The temperature change in the ground at a distance *r* after applying the constant heat rate q for time *t* is estimated as;

$$\Delta T(r,t)=\frac{q}{k}\cdot G(F_o) \qquad \text{Eq. 7-21}$$

Where;

F_o : Fourier number $=\frac{\alpha t}{r^2}$

G : dimensionless G-function $=\frac{\gamma-ln(4F_o)-\frac{F_o}{2}[ln(F_o)-\gamma+1]}{4\pi}$ which also can be obtained from Figure 7–2.

Kavanaugh and Rafferty (1997) proposed a procedure to use the cylindrical source model in estimating the effective thermal conductivity and the effective thermal diffusivity of the ground. In this procedure, the conductivity and the diffusivity cannot be directly calculated but values for these parameters are assumed and verified. The effective thermal resistance of the ground under a daily heat pulse is to be estimated as shown in Eq. 7-22.

$$R_{gd}(\text{m}\cdot{}^\circ\text{C/W})=\left[\frac{L_c\times\left(T_o-\frac{T_{in}-T_{out}}{2}\right)}{-W_c}-R_b\right]\times\frac{1}{F_{sc}} \quad \text{(in SI units)}$$

$$R_{gd}(\text{hr}\cdot\text{ft}\cdot{}^\circ\text{F/Btu})=\left[\frac{L_c\times\left(T_o-\frac{T_{in}-T_{out}}{2}\right)}{-3.41W_c}-R_b\right]\times\frac{1}{F_{sc}} \quad \text{(in Imperial units)} \qquad \text{Eq. 7-22}$$

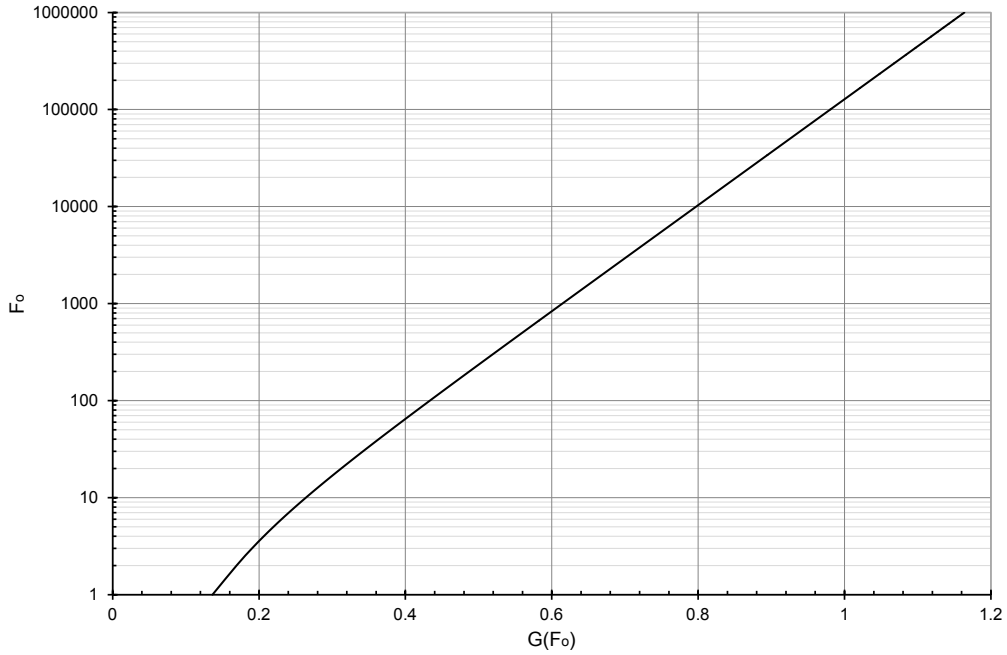

Figure 7.2. Dimensionless G-function.

Where;

L_c: Length of the heat exchanger in meters for SI units or feet for Imperial units,

W_c : Average applied heating power in Watts for SI and Imperial units,

R_b : Thermal resistance of the heat exchanger in m·℃/W for SI unit or in hr·ft·°F/Btu for Imperial unit that can be estimated from Table 7-1 based on an approximated values for the thermal conductivity of the ground and the backfilling as well as the heat exchanger and loop dimensions,

T_o : Undisturbed ground temperature in ℃ for SI units or °F for Imperial units,

T_{in} : Temperature of fluid entering the ground loops ℃ for SI units or °F for Imperial units,

T_{out} : Temperature of fluid leaving the ground loops ℃ for SI units or °F for Imperial units,

F_{sc} : Factor depending on the loop arrangement and flow rate that can be obtained from Table 7-2.

After estimating the thermal resistance of the ground under the daily heating pulse (R_{gd}), values for the ground effective thermal conductivity and diffusivity are assumed and used to estimate the Fourier number which is then used to estimate the dimensionless g-function. The ground resistance corresponding to the assumed values of the effective thermal properties of the ground is then estimated as;

$$R_g = {}^{G}/_{k_g} \qquad \text{Eq. 7-23}$$

The ground thermal resistance estimated from Eq. 7-23 is compared to the approximated thermal resistance of the ground from Eq. 7-22. If these two values are not within a preset acceptable tolerance, various values for the effective thermal properties of the ground should be assumed and iterations are repeated until meeting within the acceptable tolerance. Upon convergence, the effective thermal ground properties are the most representative properties.

This procedure is significantly slow and requires several iterations to estimate the required design parameters. Thus, it is not commonly used in practice. Rather, parameter matching techniques based on the cylindrical source model are used instead. Therefore, this procedure was not used to process the results of Virginia Tech thermal conductivity tests.

Table 7-1. E quivalent diameters and thermal resistances for Polyethylene U-tubes (Kavanaugh and Rafferty, 1997 - used under fair use, 2013)

U-tube Dia. (Eqv. Dia.)	SDR	Thermal resistance of the heat exchanger (m·°C/W) || (hr·ft·°F/Btu)							
		For Water flows above 7.5 lit/min (2.0 gpm)		20% Prop. Glycol flow 11.4 lit/min (3.0 gpm)		20% Prop. Glycol flow 19 lit/min (5.0 gpm)		20% Prop. Glycol flow 38 lit/min (10.0 gpm)	
19 mm (¾ in.)	SDR 11	0.052	0.09	0.069	0.12	Not Recommended		Not Recommended	
	SDR 9	0.064	0.11	0.087	0.15	Not Recommended		Not Recommended	
	SDR 40	0.058	0.10	0.081	0.14	Not Recommended		Not Recommended	
25.4 mm (1.0 in.)	SDR 11	0.052	0.09	0.081	0.14	0.058	0.10	Not Recommended	
	SDR 9	0.064	0.11	0.092	0.16	0.069	0.12	Not Recommended	
	SDR 40	0.058	0.10	0.087	0.15	0.064	0.11	Not Recommended	
31.75 mm (1¼ in.)	SDR 11	0.052	0.09	0.087	0.15	0.069	0.12	0.052	0.09
	SDR 9	0.064	0.11	0.098	0.17	0.087	0.15	0.064	0.11
	SDR 40	0.052	0.09	0.087	0.15	0.069	0.12	0.052	0.09
38.1 mm (1½ in.)	SDR 11	0.052	0.09	0.092	0.16	0.087	0.15	0.052	0.09
	SDR 9	0.064	0.11	0.104	0.18	0.098	0.17	0.064	0.11
	SDR 40	0.046	0.08	0.081	0.14	0.081	0.14	0.046	0.08

Table 7-2. Typical values of F_{sc} (Kavanaugh and Rafferty, 1997 - used under fair use, 2013)

Loop configuration	Single loop		Double loops		Three loops	
Flow rate	3 gpm/ton	2 gpm/ton	3 gpm/ton	2 gpm/ton	3 gpm/ton	2 gpm/ton
F_{sc}	1.04	1.06	1.02	1.03	1.01	1.02

(c) Parameter Matching Techniques

Various parameter matching techniques were developed and used to estimate the effective thermal properties of the ground and the thermal resistance of the heat exchanger from the results of thermal conductivity tests (Austin, 1998; Berberich et al., 1994; Monzó, 2011; Shonder and Beck, 1999, 2000; Wagner and Clauser, 2005). These techniques are based on us ing assumed values for the various design parameters, i.e the effective ground thermal properties and the thermal resistance of the heat exchanger, to estimate the change of the average fluid temperature over time using analytical or numerical models. T he estimated average fluid temperature is compared to that measured in-situ; the assumed values for the design parameters are varied if the approximated fluid temperature does not represent the measured fluid temperature. The accuracy of the predicted temperatures is examined using an objective function attempting to optimize the error between the approximated and the measured fluid temperatures. Iterations with different values of the parameters are performed and the parameters that provide the best accuracy are the most representative values for the site conditions.

Various parameter matching techniques differ from one another in; (1) the chosen objective function for error optimization, (2) the used optimization technique, (3) the selected analytical or numerical model to estimate the fluid temperature, and (4) parameters to optimize for (Li and Lai, 2012). The following sections discuss these differences in details and focus more on the parameter matching technique proposed by Li and Lai (2012). This parameter matching technique is selected because it provides a robust procedure to estimate the required design parameters. Furthermore, this procedure is used as the basis to account for the effect of the heat exchanged with the ambient air while processing the test results as discussed in Section 7.5.2.

i. Optimization Parameters

Theoretically, the independent variables for optimization may be any combination of parameters used in the selected analytical or the numerical model including the undisturbed ground temperature, the effective ground thermal conductivity, the effective ground thermal diffusivity, the radius of the heat exchanger, the spacing between the legs of the ground loops, the thermal conductivity of the filling material, the thermal resistance of the heat exchanger, and the applied heating load (Li and Lai, 2012). Li and Lai (2012) conducted a sensitivity analysis considering the parameters listed above in order to select the ones that have a significant effect on the optimization results. This sensitivity analysis was conducted by differentiating the cylindrical source model with respect to each one of the listed parameters to obtain respective sensitivity coefficients. These sensitivity coefficients are used to infer the effect of varying each parameter on the estimated fluid temperature. The results of this sensitivity analysis showed that the significance of including various parameters in a descending order is as follows;

1) The undisturbed ground temperature (T_o),
2) The applied heating power (q) and the effective ground thermal conductivity (k_s),
3) The thermal resistance of the heat exchanger (R_b),
4) The spacing between the legs of the ground loops (D) and the thermal conductivity of the filling material (k_{fill}),
5) The effective ground thermal diffusivity (α_s).

The spacing between the legs of the ground loops (D) and the thermal conductivity of the filling material (k_{fill}) were concluded not to be of a significant impact should the thermal resistance of the heat exchanger is optimized since they contribute to this resistance (Li and Lai, 2012). T herefore, the thermal resistance of the heat exchanger is used as an optimization parameter rather than these two factors while processing Virginia tech test results. Furthermore, the effective ground thermal diffusivity (α_s) showed insignificant impact on the optimization results and thus it was not included while processing Virginia Tech test results.

ii. Objective Function

The ordinary least squares method (OLS) is the objective function that is commonly used to infer the accuracy of the predicted average fluid temperatures compared to the measured temperatures (Austin, 1998; Bandos et al., 2011; Kavanaugh and Rafferty, 1997; Li and Lai, 2012). In the OLS method, the square of the error between the estimated and the measured average fluid temperatures is summed over the considered testing period as shown in Eq. 7-25. The representative design parameters are the one corresponding to the trial that minimizes the least squared error as in Eq. 7-24. Thus, the optimization process is a minimization problem.

Min. $SE(T_o, q, k_s, R_b, D, k_{\mathbf{fill}}, \alpha_s)$ Eq. 7-24

$\text{SE} = \sum_{i=1}^{n}\left(T_{f-model,i} - T_{f-test,i}\right)^2$ Eq. 7-25

Where;

SE : Squared error of the estimated average fluid temperature,

$T_{f-model,i}$: Average inlet and outlet fluid temperatures estimated from the selected analytical model for time step i,

$T_{f-test,i}$: Average inlet and outlet fluid temperatures measured in the in-situ thermal conductivity test for time step i,

n : Number of time steps included in the optimization process.

This objective function is utilized when the parameter matching technique is used to process the results of various thermal conductivity tests conducted at Virginia Tech.

iii. Selected Model

Different analytical models can be incorporated with the parameter matching techniques including the infinite line source model and the cylindrical source model presented in previous sections. Other models such as the finite line source model presented in Chapter 2 can also be used.

iv. Optimization Algorithm

A robust optimization algorithm is required to fulfill the objective function rather than manually optimizing for the least squared error. Li and Lai (2012) examined the performances of two advanced iterative algorithms; the Levenberg-Marquardt method and the interior trust region method subjected to bounds. They showed that the inverse heat transfer problem solved to estimate the effective ground thermal properties is generally very ill-conditioned especially near the initial guessed values for the optimization parameters. This ill-condition makes the interior trust region method subjected to bounds more powerful and reliable than the Levenberg-Marquardt method (Li and Lai, 2012; Yuan, 2000). Thus, the interior trust region is utilized to analyze the results of thermal conductivity tests conducted at Virginia Tech.

The trusted region method assumes an initial guess for various optimization parameters which is treated as a guess for the solution of the optimization problem, thus an approximate model is constructed near the current guess point. This approximate model is trusted in a neighborhood region centered at the current point called the trust region. The size of the trust region is modified from iteration to another using a variable known as the trial step. The trial step is increased causing an enlargement of the trust region if the approximated model fit the original optimization problem well. Otherwise, the trial step is reduced causing the trust region to shrink around the current guess (Yuan, 2000). The trial step represents the solution of the approximate model within the trust region corresponding to a given guess. The trust region of the following iteration is modified using the estimated trial step from the preceding trust region using a merit function. The mathematical details of this method can be found elsewhere including Deng et al. (1993), Moré (1983), Powell (1970a, b). Matlab® (2011) was used to implement the trusted region optimization algorithm while analyzing the results of various thermal conductivity tests reported in this study. Reasonable lower and upper bounds for various optimization parameters were used while optimizing for the ground thermal properties at Virginia Tech test site. These bounds were selected according to the typical range for the type of the soils and the heat exchanger that exist at the test site.

v. Parameter Estimation

Since the trusted region optimization algorithm proposed to be used here depends strongly on the initial guess of various optimization parameters, the final results of the optimization is highly related to the initial assumed values of various parameters (Yuan, 2000). Li and Lai (2012) proposed to use Monte-Carlo simulations to account for the dependency of the results of the initial guess of the optimization parameters. In their work, different error distributions were considered including normal distribution and uniform distribution. The results were found to be independent from the assumed error distribution (Li and Lai, 2012). Thus, the normal distribution of the error is used here. The Monte-Carlo simulation for processing the results of thermal conductivity tests are summarized in the following steps (Li and Lai, 2012);

1. The average fluid temperature measured during the thermal conductivity tests are treated as the true values,
2. Assume initial values for various optimization parameters included in the processing. These initial values are used to estimate the average fluid temperature over time using a selected analytical model. Then, the squared error between the estimated and the measured average fluid temperatures is approximated,
3. Lower and upper bounds for each optimization parameter are assumed according to the typical range expected for the considered parameter. The trust region method is then used to minimize the squared error between the estimated and the measured average fluid temperatures by varying the optimization parameters within the respective bounds. The results of the optimization are a set of values for the optimization parameters that minimizes the objective function provided in Eq. 7-24,
4. Steps 2 and 3 are repeated *M* trials with varying the initial values for each parameter using a selected error distribution bounded by the lower and the upper bounds. Thus, each trial represents a set of values for various optimization parameters and the obtained optimization results correspond to the initial set,
5. The final expected value of each optimization parameter is estimated as;

$$\overline{\beta_i} = \frac{1}{M}\sum_{n=1}^{M}\beta_{in} \qquad \text{Eq. 7-26}$$

Where β_{in} is the i^{th} optimization parameter found on the n^{th} trial.

Li and Lai (2012) examined the proposed Monte-Carlo simulation using various number of trials *M* ranging from 5 to 2000. It is shown that the results of different optimization parameters does not vary significantly as long as the number of trials is more than 100, thus 500 trials were used while processing the results of Virginia Tech thermal conductivity tests.

7.3. Virginia Tech Thermal Conductivity Tests

Five thermal conductivity tests were performed as part of Virginia Tech in-situ testing program. Four of these tests were performed according to the ASHRAE procedure discussed in Section 7.2.1. Each one of these four tests was performed in a different heat exchanger that has a unique ground loop type, configuration, and/or backfilling material including; single and double ground loops, high density polyethylene loops (HDPE) and cross-linked polyethylene loops (PEX-a), and cement paste backfilling and sand backfilling. All the heat exchangers were 30.5 m (100 ft) in length and 25.4 cm (10 inches) in diameter. Table 7-3 summarizes the set up and the procedure used in each of these four tests. As presented in this table, the fifth test follows the

Dutch procedure and was conducted to improve the thermal conductivity practice as discussed in Section 7.7. The carrier fluid in all these tests was water with no antifreeze since the tests were performed using heating thermal loads which do not require the use of antifreeze.

This chapter focuses on the four thermal conductivity tests performed according to the ASHRAE standard in order to compare the effect of loop type and configuration, and the backfilling material on the estimated thermal properties of the ground and, more importantly, on the thermal resistance of the heat exchanger. In each of these tests, the tubes connecting the testing trailer and the tested ground loops were insulated. The amount of the insulation used in each test varies since more awareness of the effect of the ambient air on the test results was gained after performing TCT 1 which just had the typical insulation used with deep geothermal boreholes as shown in Figure 7–3(a). Due to the short length of the Energy Piles used in these tests, low heat rates were applied. Thus, the small effect of the heat exchanged with the ambient forms a s ignificant percentage of the applied heat and therefore affects the test results significantly. The connecting tubes in TCT 2 were attempted to be as short as possible to reduce the length over which the heat is exchanged with the ambient air. Furthermore, significantly more insulation was used in this test to reduce the heat loss to the ambient as shown in Figure 7–3(b). For TCT 3 and TCT 4, the length of the connecting tubes could not be reduced due to the presence of the mechanical loading frame. However, better insulation was used in these tests including aluminum tubes as shown in Figure 7–3(c).

(a) Test TCT 1

(b) Test TCT 2

(c) Tests TCT 3 and TCT 4

Figure 7.3. Thermal insulation used to reduce the heat exchanged with the ambient in each test.

Table 7-3. List of Virginia Tech thermal conductivity tests.

Test	Heat exchanger*	Loop type	Loop configuration	Backfilling	Testing procedure	Duration (hrs)		Applied Power (kW) using Eq. 7-4			Notes
						No heat	Test	(a)	(b)	(c)	
TCT 1	Pile 3	PEX-a	Single	Cement/Sand	ASHRAE	2.22	59.86	2.022 (9.6%)	2.186 (18.5%)	1.845 (ref.)	--
TCT 2	Pile 4	PEX-a	Double	Cement/Sand	ASHRAE	2.26	58.48	2.004 (8.2%)	2.171 (17.2%)	1.852 (ref.)	--
TCT 3	Pile 2	HDPE	Single	Cement/Sand	ASHRAE	2.35	59.38	1.995 (10.2%)	2.162 (20.6%)	1.810 (ref.)	--
TCT 4	Test Pile (Pile 1)	HDPE	Single	Cement	ASHRAE	1.53	3.35	4.930 (13.4%)	5.117 (17.7%)	4.346 (ref.)	--
						1.57	47.55	2.910 (11.8%)	3.085 (18.5%)	2.603 (ref.)	Thermal load, T-MT 3
TCT 5	Test Pile (Pile 1)	HDPE	Single	Cement	Dutch	3.73	48.94	Details in Section 7.7			Thermal load, T-MT 4

* refers to titles shown in Figure 6-3 for different element constructed as part of Virginia Tech testing facility.

At the beginning of each test, the carrier fluid was circulated for an initial time period over which no heating was applied. This initialization was performed to estimate the undisturbed ground temperature as discussed in Section 7.3.3. The length of the initialization period used in each test in presented in Table 7-3. After the initialization phase, constant heat rate was applied using electrical heaters. The amperage and the voltage applied to the operational heaters and the circulation pump were regulated and recorded. The test duration over which the heat was applied ranged between 48 to 60 hours as shown in Table 7-3. Moreover, each test was performed using a constant applied heat that differs from other tests. Table 1-3 presents the heat applied in each test estimated using the three techniques described in Eq. 7-4. Appendix XI presents the temperature at different depths along the center of Pile 3 and the Test Pile during TCT 1 and TCT 3, respectively.

As appears in Table 7-3, TCT 4 was intended to be performed using a 5kW heat rate to investigate the effect of the high thermal load on the test results and the estimated effective ground thermal properties. This high heat rate caused the system to heat up to the maximum allowable temperature so rapidly forcing a test termination. The loop temperature was checked after 24 hours and confirmed to be within the acceptable range of 0.3℃ (0.54°F) from the initially measured undisturbed ground temperature. Thus, the test was restarted using a 3kW (10.25 Btu/hr) heat rate that extended about 47.5 hours. The results of the second phase, i.e. 3 kW (10.25 Btu/hr), are the ones included in the data processing for this test.

Eq. 7-4(c) provides the most accurate applied power as discussed in Section 7.3.1. Thus, the power estimated using this equation for each test is treated as the reference power and used to approximate the error in the effective thermal conductivity of the ground and the thermal resistance of the heat exchanger should the other two equations were used. The errors of the applied power estimated using Eq. 7-4(a) and Eq. 7-4(b) compared to that estimated using Eq. 7-4(c) are shown between parentheses in Table 7-3. The estimated errors are all positive referring to more estimated power using Eq. 7-4(a) and Eq. 7-4(b) compared to that estimated using Eq. 7-4(c). Also, it is noticed that Eq. 7-4(b) provides the higher error in the estimated power which is expected since this power accounts for additional heat added to the system by the circulation pump.

According to Eq. 7-19 and Eq. 7-20; the higher the power used while processing the results of a given thermal conductivity test, the higher the estimated effective ground thermal conductivity and the lower the estimated thermal resistance of the heat exchanger. This higher ground thermal conductivity and lower thermal resistance of the heat exchanger refers to a more efficient system overall which will result in a shorter ground loops. Thus, less conservative ground and system properties would be estimated if Eq. 7-4(a) and Eq. 7-4(b) were used to process the results of any thermal conductivity test. Therefore in addition to being the most accurate power estimate, the power estimated using Eq. 7-4(c) results in a longer ground loops and thus it is used to process the results of all the tests reported in this chapter.

7.3.1. Undisturbed Ground Temperature (T_o)

The undisturbed ground temperature is estimated as the average temperatures of the inlet and the outlet fluids at the end of the initialization phase over which no thermal load was applied as presented in Section 7.3.3. Figure 7–4 shows the change of the average fluid temperature over the initialization period for each of the ASHRAE tests considered here.

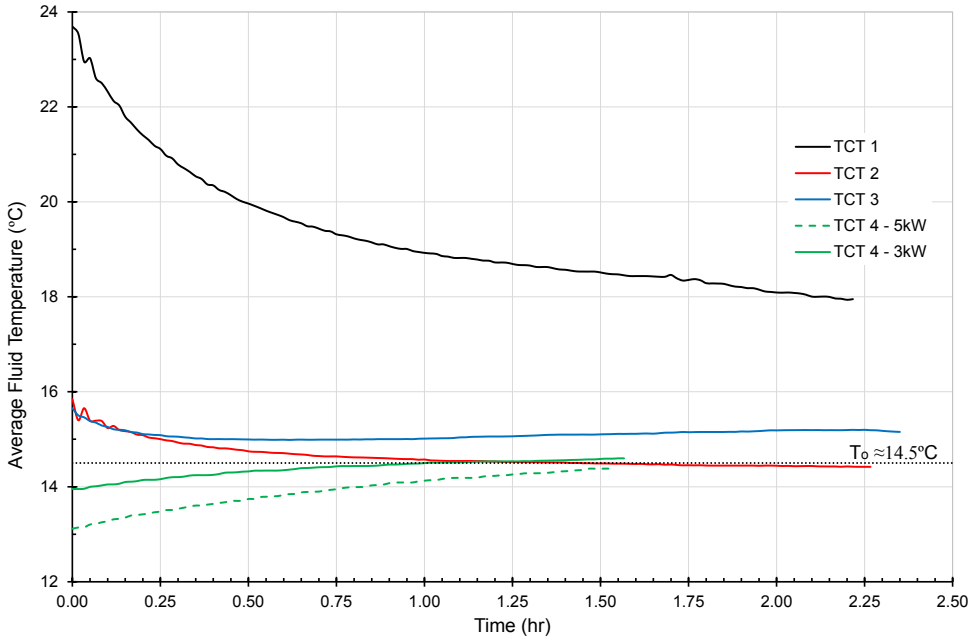

Figure 7.4. Estimating the undisturbed ground temperature from the average fluid temperature during the initialization phase of each thermal conductivity test.

The average fluid temperature for TCT 1 did not converge to a constant temperature even after the 2.25 hours initialization period as shown in Figure 7–4. This is attributed to the high initial water temperature at the beginning of the initialization phase. This high water temperature was affected by the hot ambient temperature during the test since this test was performed in the summer. Longer initialization period was required to have the fluid temperature coverage to the actual undisturbed ground temperature. Furthermore, it is observed in Figure 7–4 that the average fluid temperatures for TCT 2 and TCT 4 converge to about 14.5°C (58.1°F). The 14.5°C (58.1°F) is considered the in-situ undisturbed ground temperature because it agrees with the ground temperature profiles measured at the test site prior to the beginning of the testing program as shown in Figure 7–5. More discussion about the ground temperatures presented in Figure 7–5 is provided in Chapter 8.

Moreover, the average fluid temperature measured in TCT 3 converged to a slightly higher temperature about 15°C (59°F). Test TCT 3 started a week after finishing the last thermal cycle of T-MT 2 conducted on the Test Pile at 2.5m (8.2 ft) away for Pile 2 as discussed in Chapter 6. This thermal cycle was performed by circulating a fluid at 28 °C (82.4°F) for 12 hours, then the inlet fluid temperature was increase to 35°C (95°F) for another 12 hours, then to 50°C (122°F) for 10.5 days. The ground temperature around the test pile is affected by the long period of this high thermal load. Thus, the fluid temperature in the initialization phase converged to higher value. Field measurements could not be used to check the validity of this reason due to the lack of having temperature gauges installed in Pile 2 which is the heat exchanger for TCT 3. Instead, a 2-D Finite element model was built to examine the extent of the temperature bulb after terminating the third thermal cycle of T-MT 2. The ground in this model was assigned a thermal conductivity of 2.28 W/m·°C (1.317 BTU/hr·ft. °F), a thermal diffusivity of 7.74e-7 m^2/sec (0.0258 ft^2/hr), a specific heat of 2906.2 ton/m^3. These thermal properties are the average for the soils at Virginia Tech test site as will be concluded in Section 7.5. The details of this 2-D finite

element model were presented in Chapter 5. The result of this model is presented in Figure 7–6 that shows a temperature buildup at the location of Pile 2. Even after terminating the thermal load applied in test T-MT 2, the temperature at the location of Pile 2 kept increasing due to the lag in the progression of the thermal wave in the ground. The temperature build-up approached 15°C (59°F) at the location of Pile 2 when TCT 3 was initiated. Thus, the reason discussed earlier for the higher undisturbed ground temperature measured in this test is valid.

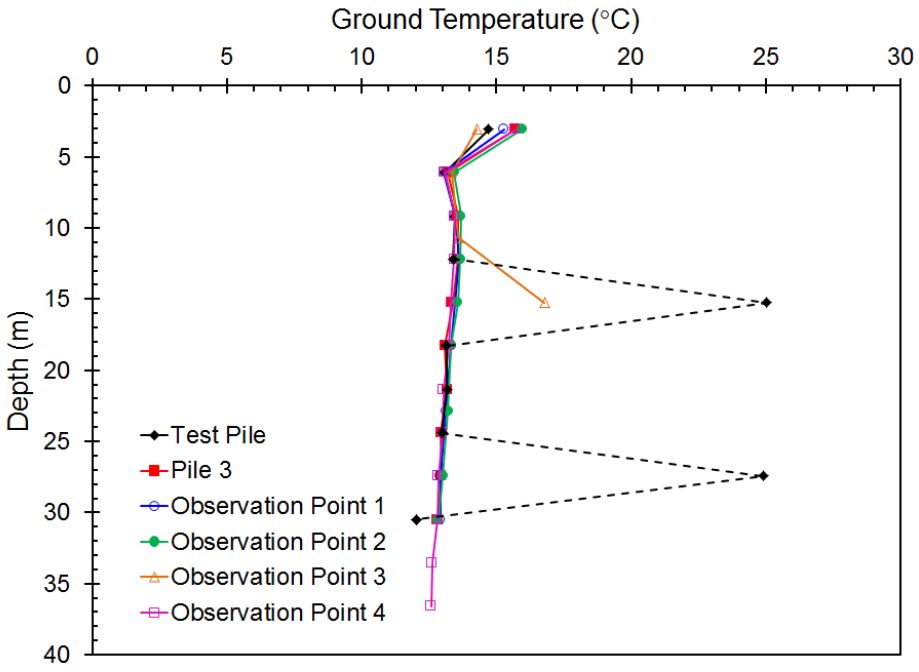

Figure 7.5. Undisturbed ground temperature measured before the beginning of the testing program.

It is desired to check if the undisturbed ground temperature measured in TCT 2 is affected by T-MT 1 since the former was performed 5 days after the end of the latter. Similar to TCT 3, a finite element model was conducted in which the third thermal cycle of the first thermo-mechanical test was modeled. In this model, water at 28ºC (82.4ºF) was circulated in the Test Pile for 24 hours, then at 35ºC (95ºF) for another 24 hours, and at last 50ºC (122ºF) for 18 hours. The same ground thermal properties were used and the ground temperature at the location of Pile 4 in which TCT 2 was performed was obtained and presented in Figure 7–6. As shown in this figure, the ground temperature at the location of Pile 4 was not affected by the thermal operation during T-MT 1. This is due to the large distance between the Test Pile and Pile 4 as well as the short thermal load duration of T-MT 1. Thus, the undisturbed ground temperature measured in TCT 2 was considered accurate and reliable.

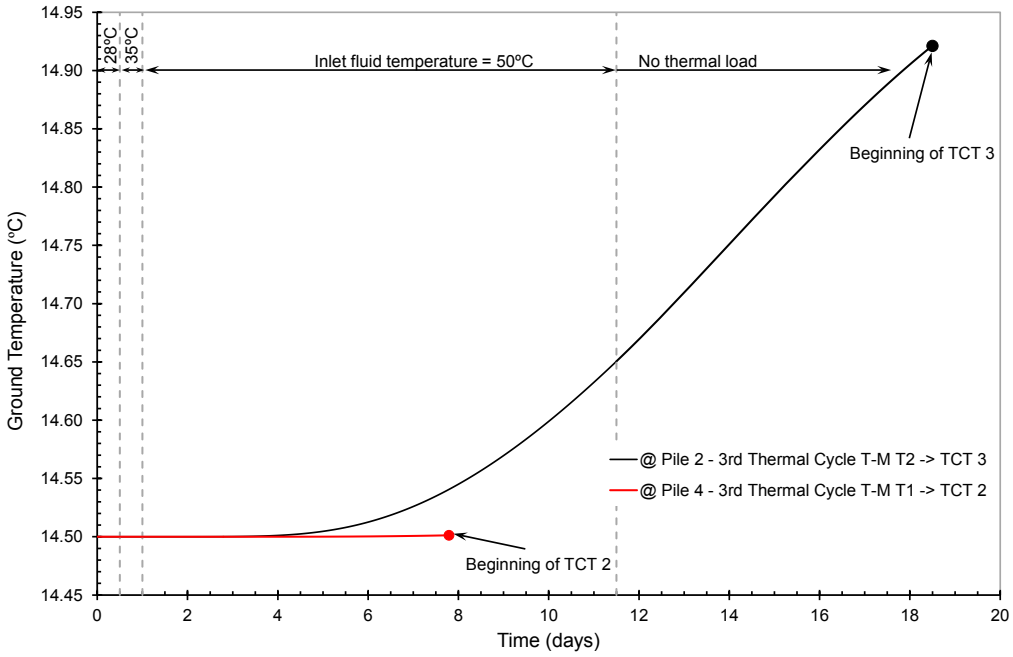

Figure 7.6. Effect of thermo-mechanical tests on the undisturbed ground temperature measured during TCT 2 and TCT 3.

7.3.2. Measured Fluid Temperatures (T_f)

The temperatures of the inlet and the outlet fluids were recorded in each of the considered tests every 1 minute. Figure 7–7 shows the measured fluid temperatures in each of these tests. It can be noticed in this figure that TCT 1 and test TCT 3 provide close fluid temperatures with slightly lower temperatures measured in TCT 3. The close agreement between the fluid temperatures in these tests was expected since these two tests were conducted on heat exchangers that were provided with single ground loop. The fluid temperatures measured in TCT 3 are slightly lower than those measured in TCT 1 due to the slightly lower applied power in TCT 3 compared to that applied in TCT 1 as shown in Table 7-3.

Despite the slightly higher power applied in TCT 2, the fluid temperatures measured in this test were significantly less than those measured in TCT 1 and TCT 3. The lower temperatures in TCT 2 are attributed to the less thermal resistance of Pile 4 which is the heat exchanger used in this test. Pile 4 was provided with double loops rather than the single loops used in TCT 1 and TCT 3. The use of double loops decreases the thermal resistance of the heat exchanger facilitating more heat exchange with the ground and consequently causing lower fluid temperatures if compared to the performance of single loops. Furthermore, the fluid temperatures measured during TCT 4 were significantly higher than those measured in other tests including those with identical loop type and configuration. This was expected since TCT 4 was performed using more applied power compared to all other tests.

More importantly, humps in the fluid temperature curves for all the tests were observed in Figure 7–7. The duration between the consequent humps for a given test is approximately about one day. The curves for the average fluid temperatures for each one of the considered tests are presented in Figure 7–8 in which the temperature humps were also observed. Figure 7–8 also shows the ambient air temperatures measured during each test. It can be inferred that the humps in the fluid temperatures occur when the ambient air temperature increases. As discussed earlier,

the applied power is estimated using the fluid temperatures measured inside the testing trailer. When this power increases, the temperatures of the inlet and the outlet fluids increase. When the ambient air temperature is less than the fluid temperature, the fluid losses heat to the air from the tubes connecting the testing trailer to the ground loops. The more the thermal gradient between the fluid and the air is, the more the heat losses. Due to this heat losses, the net power applied to the fluid and later injected to the ground is reduced causing the fluid temperature curves to flat out as seen over several time periods in Figure 7–8.

When the ambient air temperature increases and gets closer to the fluid temperature, the thermal gradient is reduced and so does the heat loss from the fluid to the air. Therefore, the net power injected into the ground increases relatively. This increase in the net applied power causes the fluid temperatures to increase. Thus, the humps in these figures were caused by; (1) the reduced net applied heat over the periods that have high thermal gradients between the fluid and the ambient air, and (2) the relative increase in this applied power over the periods of low thermal gradients.

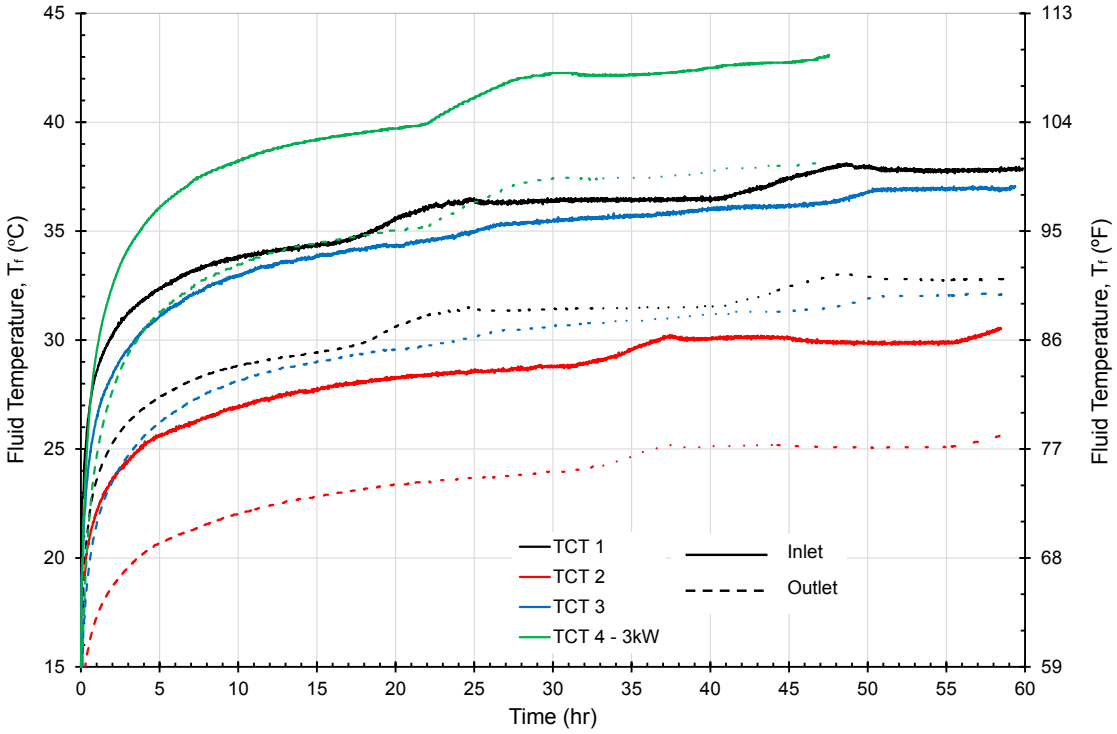

Figure 7.7. Measured inlet and outlet fluid temperatures for various thermal conductivity tests conducted following the ASHRAE procedure.

Figure 7–9 shows the calorimetric power estimated using the fluid temperatures measured inside the testing trailer for each test and the ambient air temperature. The calorimetric power is estimated using the measured inlet and outlet fluid temperatures in addition to the measured flow rate over the testing period as shown in Eq. 7-4.c. The standard deviation and the maximum spikes of the heating power applied to the electrical heaters were checked and found to comply with the ASHRAE restriction of 1.5% and 10% of the average power, respectively.

As shown in Figure 7–9, the calorimetric power in each test varies due to the slight variation of the flow rate. The calorimetric power was found to peak as the ambient air temperature

increases. These peaks suggest a decrease in the heat loss to the ambient and thus a relative increase in the net power applied to the fluid and the ground as discussed earlier.

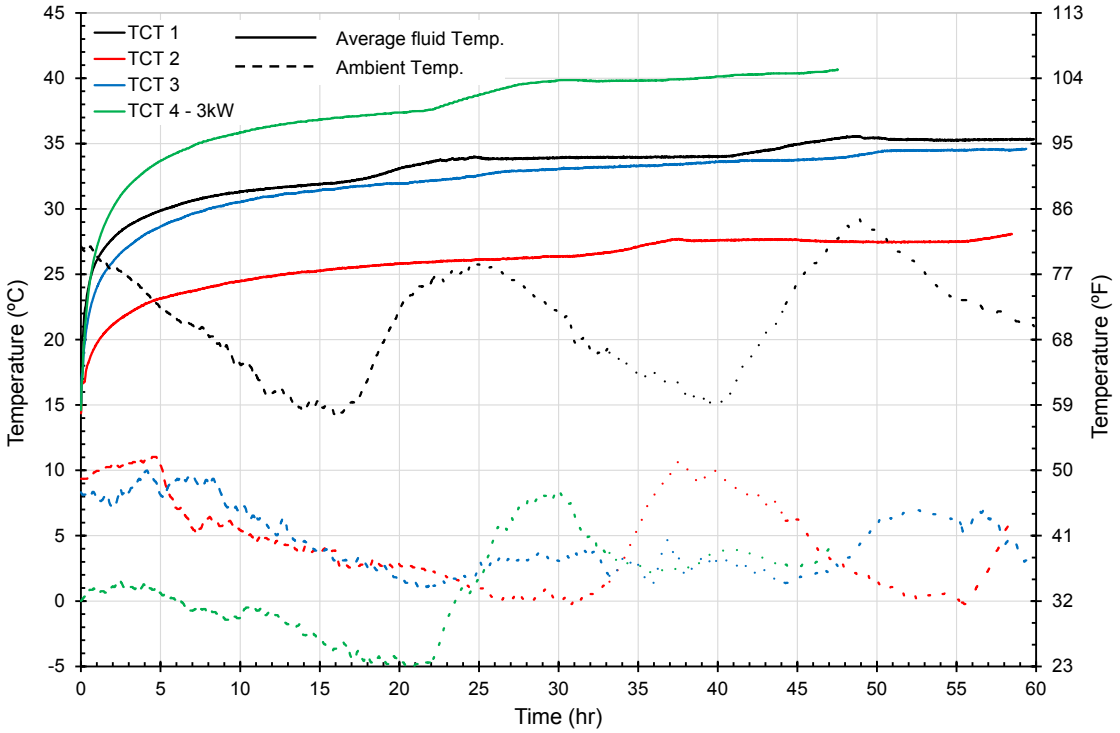

Figure 7.8. Averaged fluid temperature and ambient air temperature for various thermal conductivity tests conducted following the ASHRAE procedure.

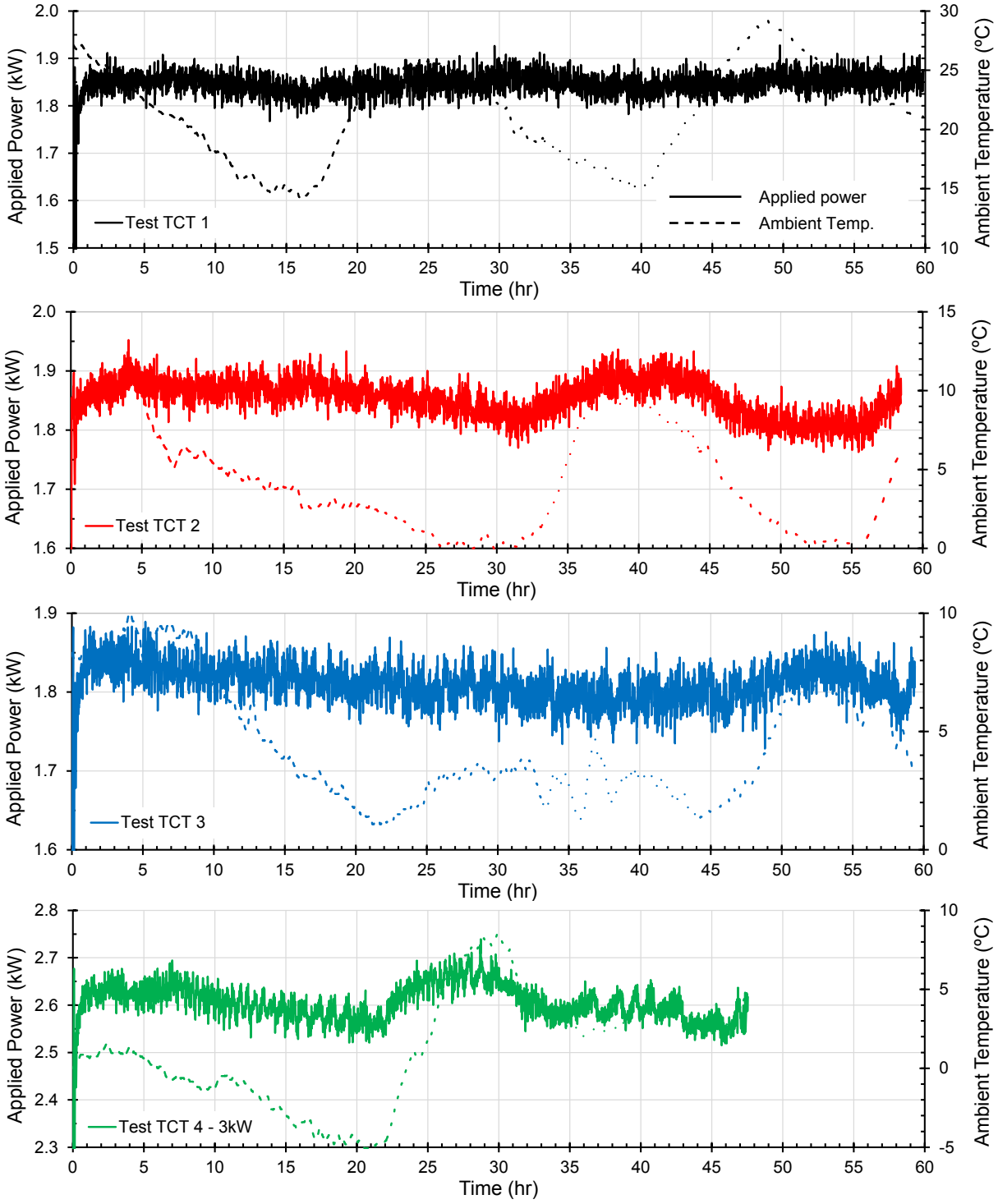

Figure 7.9. The calorimetric power applied to the fluid estimated using Eq. 7-4.c, and the ambient air temperature measured in each test.

7.4. Data Processing

In this section, the results of various thermal conductivity tests performed at Virginia Tech are processed initially without accounting for the heat exchanged with the ambient air followed

by processing the same results with accounts for the heat loss to the ambient using the correction proposed by Bandos et al. (2011). The results of the tests were processed twice to present the effect of ignoring the heat exchanged with the ambient air on the estimated results.

7.4.1. Ignoring the Ambient Temperature Interference

Due to its simplicity and popularity in practices, the infinite line source model presented in Section 7.3.4.a was used to process the results of all tests when the heat exchanged with the ambient is ignored. Furthermore, the parameter matching technique proposed by Li and Lai (2012) is used to process the data considering the infinite line source model, the finite line source model, and the cylindrical source model.

(a) Infinite Line Source Model

According to Eq. 7-18, the infinite line source model was used to process the results of thermal conductivity tests using the best-fit line for the average fluid temperature versus natural logarithm of time. This model assumes that the heat is transferred in the ground under steady state condition by conduction. Since reaching the steady state condition takes several hours, only the data after the initial few hours were used to develop the best-fit line. No precise period was recommended to be ignored at the beginning of thermal conductivity tests to account for the time needed to reach the steady state. However, the general agreement is to ignore at least the first 6 hours (Austin, 1998). Thus, two techniques to account for the time required to reach the steady state were used to process the results of thermal conductivity tests according to the infinite line source model;

- Forward Processing as shown in Figure 7–10(a): the time after which the test data were included while obtaining the best-fit line was varied from 6 hours after the beginning of the test till 10 hours from the end of the test. In this technique, the end of the test is fixed;
- Backward Processing shown in Figure 7–10(b): The time after which the test data were included while obtaining the best-fit line was fixed at 6 hours after the beginning of the test. While, the last time included in the processing decreases from the actual test termination time and backward.

Figure 7–11 shows the average fluid temperatures measured in the four thermal conductivity tests considered here using the natural logarithm of time. As observed in this figure, the average fluid temperatures for all tests converge to lines after an hour from the beginning of each test. However, the data during the first 6 hours are ignored while processing these results to comply with the general practice. It is seen in this figure that tests with higher applied powers produce steeper lines. According to Eq. 7-19 if two tests were conducted in the same soil formation with different applied power; it is expected to have steeper slopes of the average fluid temperature versus the logarithmic of time for higher applied powers. Moreover, the humps in the fluid temperature curves are more pronounced in this figure due to the logarithmic scale of the time. These humps affect the estimated thermal properties of the ground and the heat exchangers as will be discussed later.

The results of all these four tests were processed using the forward and the backward approaches. In the two approaches, a 2 hours time-step was used to change the start or the end times. Figure 7–12 and Figure 7–13 show the variation of the estimated ground effective thermal conductivity and the thermal resistance of the heat exchanger, respectively, with the number of hours included in the processing. The undisturbed ground temperature (T_o) required to estimate the thermal resistance of the heat exchangers in Eq. 7-20 was assumed to be 14.5ºC (58.1ºF) as

estimated in Section 7.4.1. Furthermore, the power used in the processing was estimated as the average calorimetric power over the considered test duration.

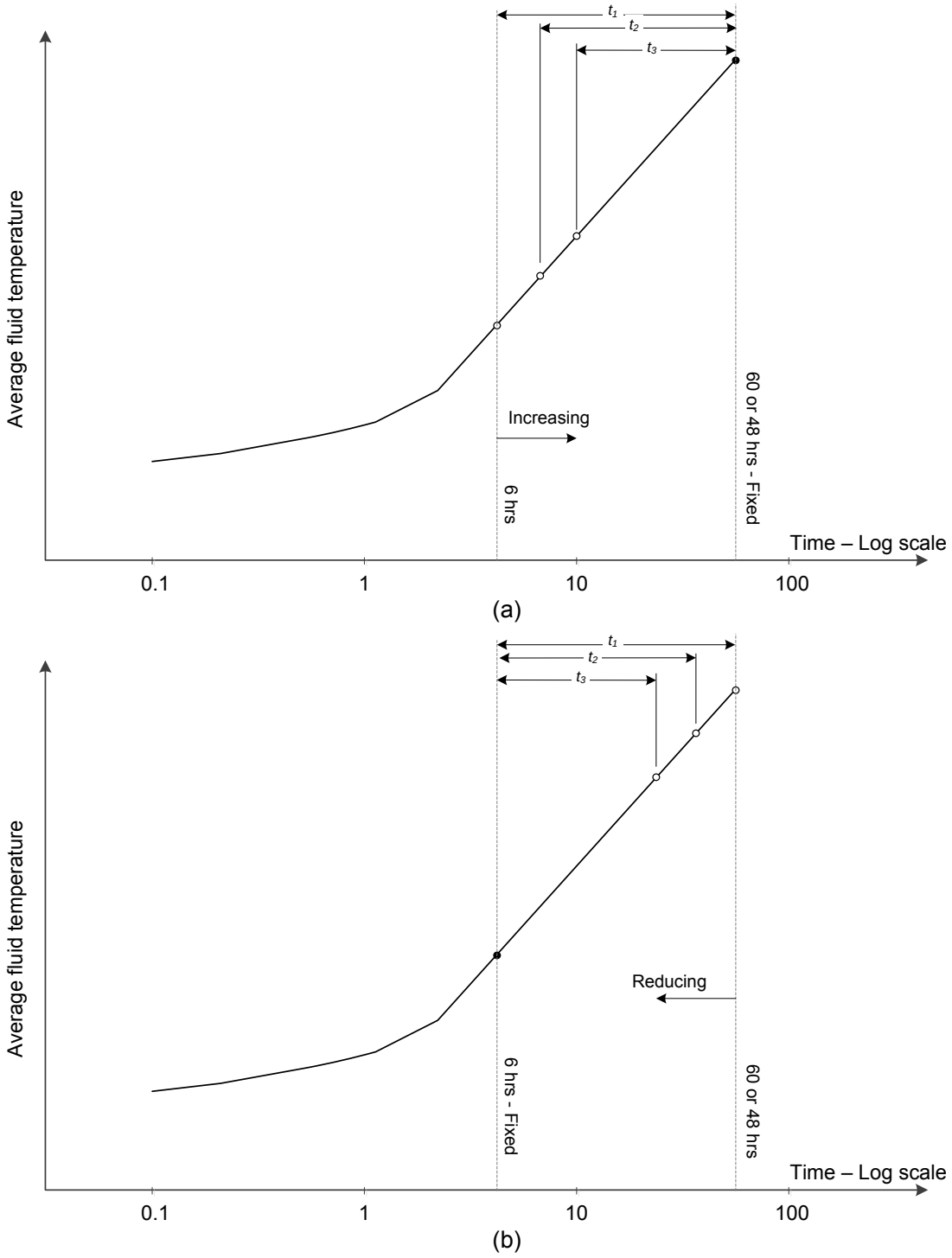

Figure 7.10. Processing the results of thermal conductivity tests using; (a) forward processing, and (b) backward processing.

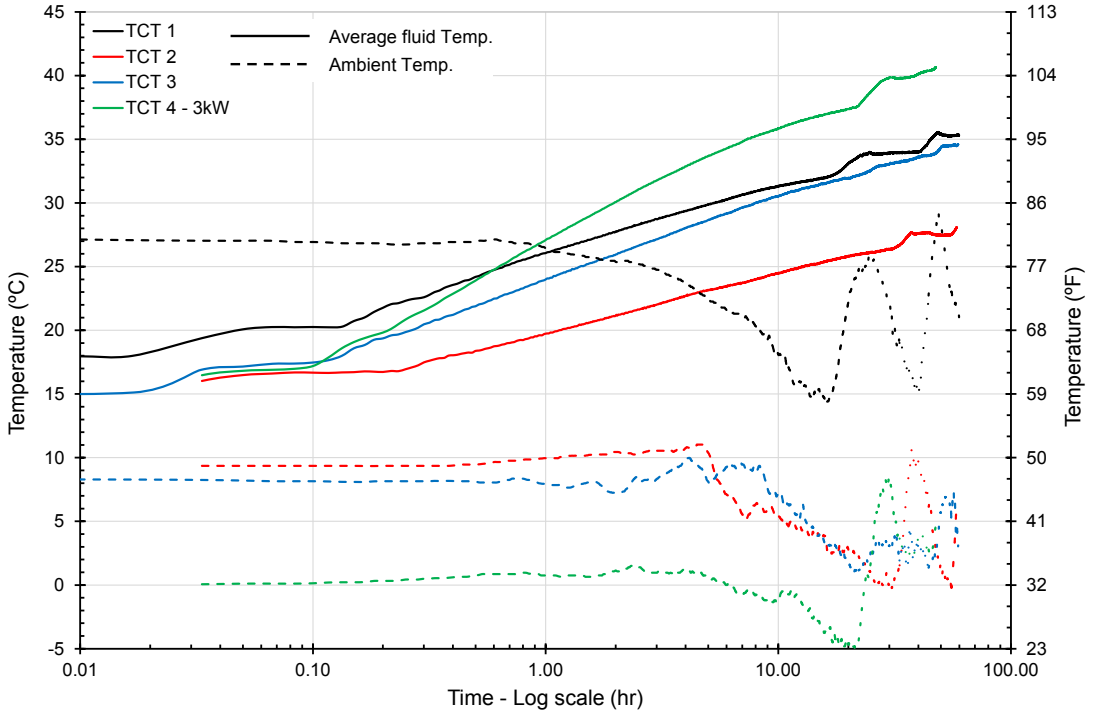

Figure 7.11. Results of the considered thermal conductivity tests using logarithmic scale for the time.

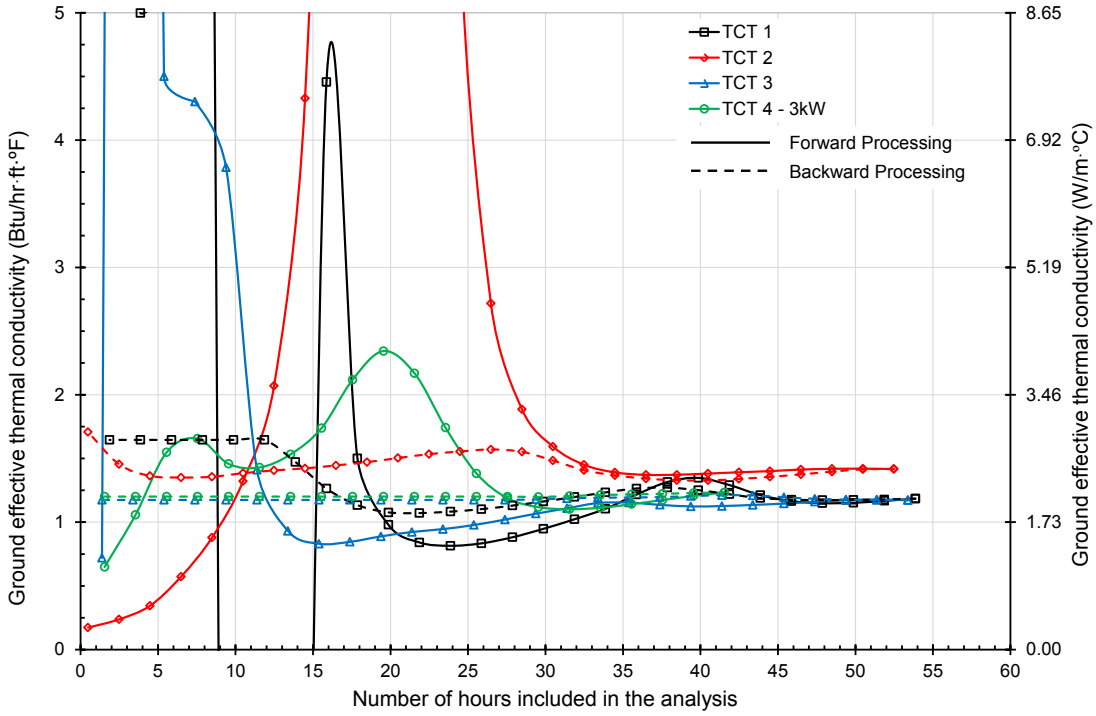

Figure 7.12. Ground effective thermal conductivity estimated using the infinite line source model for the forward and the backward processing.

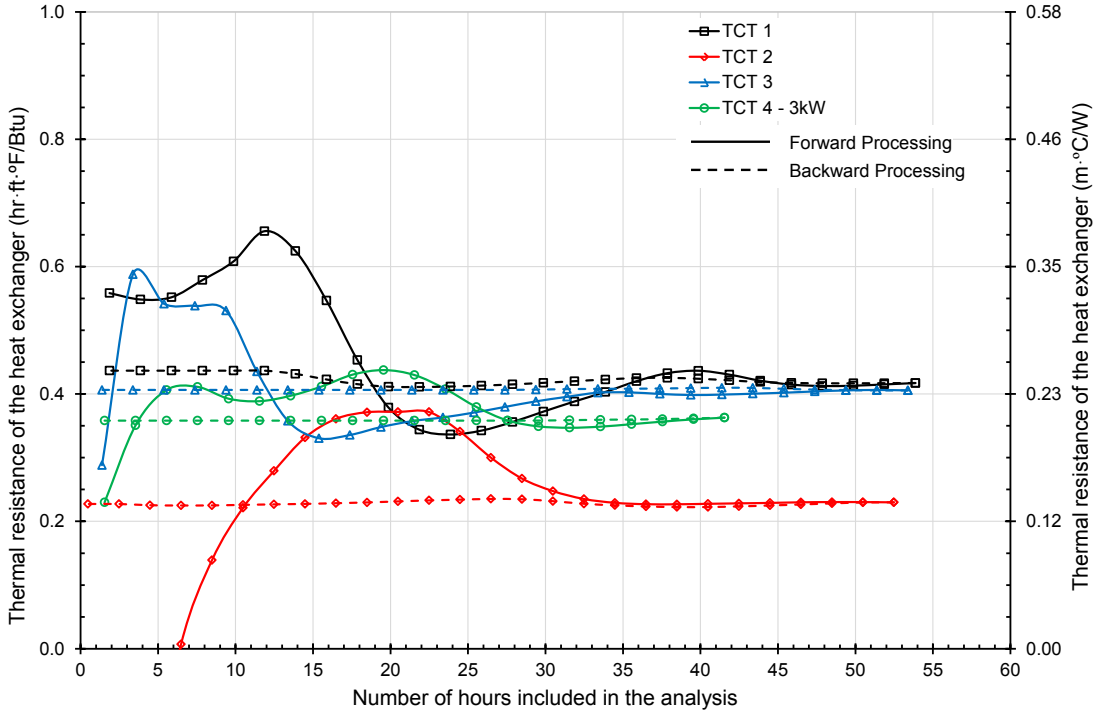

Figure 7.13. Thermal resistance of the heat exchanger estimated using the infinite line source model for the forward and the backward processing (T_o = 14.5ºC/58.1ºF).

As presented in Figure 7–12 and Figure 7–13, the forward processing produces considerable variation in the estimated ground thermal conductivity and the thermal resistance of the heat exchanger compared to the backward processing. It is also observed that the longer the time period included in the processing, the closer the results to their average values. It should be noticed here that, shorter time periods for forward processing refer to using only the data closer to the actual end of the tests; while for backward processing, the long periods refer to including the data closer to the actual end of the test. In fact, the reason for having more variation observed at shorter periods for forward processing is due to using just the data at the temperature humps in the processing. On the other hand, the variation in the parameters estimated using the backward processing is not as significant as that produced from the forward processing. This is because the humps at the end of the testing period are excluded from the data when the backward analysis is considered. This effect of the observed humps is discussed more in details in Section 7.5.2.

Furthermore, Table 7-4 summarizes the average and the standard deviation of the ground thermal conductivity and the thermal resistance of the heat exchanger estimated using the forward and the backward processing of the infinite line source model. The average for the ground thermal conductivity was estimated after excluding the outliers to obtain a reliable estimate. The forward processing produced higher average and standard deviation of the ground effective thermal conductivities in all tests compared to those estimated using the backward processing. While for the thermal resistance of the heat exchanger, the forward and the backward processing techniques gave very close estimates.

Since all these tests were performed at the same site and the ground stratification over the test site is quite uniform, the ground effective thermal conductivity was averaged to be about

2.41 W/m·°C (1.392 BTU/hr·ft·°F) using the results obtained from the forward and the backward processing techniques of all tests. The standard deviation for the average values of the ground thermal conductivity from all tests was also estimated to be about 0.35 W/m·°C (0.2 BTU/hr·ft·°F) which represents 15% deviation from the average value.

On the other hand, the thermal resistance of the heat exchanger was not averaged among all tests since each of these tests was conducted on a separate heat exchanger. However, it was noticed that the thermal resistance for Pile 4 which was used in TCT 2 is about half of that for other tests. This is attributed to the use of double ground loops in this test which reduces the thermal resistance of the heat exchanger. Moreover, the thermal resistances for Pile 3, Pile 4, and the test Pile are close to each other which is expected since all of these elements have single ground loop.

Table 7-4. Average and standard deviation of the ground effective thermal conductivity and the thermal resistance of the heat exchanger estimated using the infinite line source model for the forward and the backward processing.

Test	Ground thermal condctivity (W/m·°C)				Thermal resistance of heat exchanger (m·°C/W)			
	Average		Standard Deviation		Average		Standard Deviation	
	Forward	Backward	Forward	Backward	Forward	Backward	Forward	Backward
TCT 1 (Pile 3)	2.21	2.19	1.30	0.32	0.24	0.24	0.027	4.67E-03
TCT 2 (Pile 4)	3.18	2.46	2.08	0.13	0.13	0.13	0.039	2.17E-03
TCT 3 (Pile 2)	2.50	2.05	1.78	0.02	0.23	0.24	0.032	6.84E-04
TCT 4 - 3kW (Test Pile)	2.58	2.09	0.65	0.02	0.22	0.21	0.017	7.73E-04

(b) Parameter Matching

The benefit of using parameter matching over the simple infinite line source model is that it accounts for the effect of each optimization parameter on other parameters as well as providing an estimate of the undisturbed ground temperature since it is included as an optimization parameter. Furthermore, the parameter matching technique accounts for the variation in the actual applied power rather than using an average value as will be discussed later. In this section, the parameter matching technique proposed by Li and Lai (2012) and summarized in Section 7.3.4.(c).v was used to process the results of the four ASHRAE thermal conductivity tests conducted at Virginia Tech. The selected optimization parameters are; the undisturbed ground temperature, the ground effective thermal conductivity, and the thermal resistance of the heat exchanger. These parameters were considered the most important three as discussed in Section 7.3.4.(c).i. The heat rate was used as an input to the selected analytical model and thus it was not used as an optimization parameter. In the optimization reported here, the heat rate was estimated as the calorimetric power (Eq. 7-4.c) using the fluid temperatures measured inside the testing trailer. Thus, this heat rate does not account for the heat exchanged with the ambient air which will be discussed in the next section. The spacing between the legs of the ground loops and the thermal conductivity of the filling material were inherently accounted for in the thermal resistance of the heat exchanger and thus they were excluded from the optimization. Moreover, based on the findings of Li and Lai (2012), the thermal diffusivity of the ground does not affect the optimization results thus an average constant value of 7.75×10^{-7} m^2/sec (0.0258 ft^2/hr) was used with no optimization allowed for this parameter.

Three analytical models were used to estimate the average fluid temperature for any given set of initial values of the optimization parameters as mentioned in step 2 of the parameter matching procedure in Section 7.3.4.(c). These three models are; the infinite line source model,

the finite line source model, and the cylindrical source model. The parameter matching was performed using the forward and the backward processing techniques explained in the previous section for each of the considered tests. A time step of 2 hours was used in both forward and backward processing. Appendix XII shows the results of the parameter matching for the four tests including the forward and the backward processing using various selected analytical models. The results shown in Appendix XII are the three design parameters included in the optimization; i.e. the undisturbed ground temperature, the effective ground thermal conductivity, and the thermal resistance for the heat exchanger.

Table 7-5 presents a summary of the average and the standard deviation of the three optimization parameters estimated using the parameter matching technique using the forward and the backward processing for the four tests. The average undisturbed ground temperature was estimated to be about 14.4ºC which agrees with the value estimated from the initialization phase as discussed in Section 7.4.1. The effective average thermal conductivity of the ground estimated using the simple infinite line source model (i.e. 2.41 W/m·ºC) is about 25% higher than the one presented in Table 7-5 which was estimated using the parameter matching (i.e. 1.96 W/m·ºC). On the other hand, the standard deviation of the ground thermal conductivities estimated using the parameter matching for all the tests is significantly less than the one estimated using the simple line source model; i.e. 0.037 for parameter matching versus 0.35 for simple infinite line source. The estimated undisturbed ground temperature and the small variation of the approximated ground thermal conductivity imply that parameter matching provides better estimates of the optimization parameters than the simple infinite line source model.

Table 7-5. Summary of the parameter matching for the considered four tests using the infinite line source, the finite line source, and the cylindrical source model following the forward and the backward processing techniques.

Optimization parameter	Statistical parameter	Model	Test								Global estimates	
			TCT 1 (Pile 3)		TCT 2 (Pile 4)		TCT 3 (Pile 2)		TCT 4 - 3kW (Test Pile)		Average	Standard deviation
			Forward	Backward	Forward	Backward	Forward	Backward	Forward	Backward		
Undisturbed ground temperature (ºC)	Average	ILS	14.52	14.57	13.90	14.00	14.50	14.56	14.48	14.55	14.37	0.253
		FLS	14.59	14.54	14.01	14.00	14.56	14.53	14.53	14.56		
		CSM	14.47	14.48	13.84	13.90	14.42	14.41	14.44	14.45		
	Standard deviation	ILS	0.072	0.152	0.154	0.184	0.142	0.108	0.133	0.126		
		FLS	0.154	0.150	0.156	0.186	0.157	0.125	0.172	0.138		
		CSM	0.122	0.134	0.156	0.164	0.143	0.140	0.127	0.166		
Ground thermal conductivity (W/m·ºC)	Average	ILS	1.93	1.95	2.00	2.02	1.91	1.95	1.97	1.99	1.96	0.037
		FLS	1.93	1.96	1.98	2.02	1.93	1.96	1.96	1.98		
		CSM	1.90	1.94	2.02	2.03	1.91	1.92	1.96	1.96		
	Standard deviation	ILS	0.024	0.058	0.050	0.061	0.060	0.041	0.064	0.040		
		FLS	0.051	0.059	0.046	0.059	0.053	0.063	0.062	0.055		
		CSM	0.049	0.066	0.047	0.048	0.063	0.069	0.057	0.043		
Thermal resistance of heat exchanger (m·ºC/W)	Average	ILS	0.22	0.23	0.12	0.12	0.21	0.22	0.19	0.19		
		FLS	0.22	0.23	0.12	0.12	0.22	0.22	0.19	0.19		
		CSM	0.20	0.21	0.11	0.10	0.20	0.20	0.18	0.18		
	Standard deviation	ILS	2.74E-03	6.46E-03	4.19E-03	5.96E-03	5.83E-03	3.96E-03	5.49E-03	3.83E-03		
		FLS	5.16E-03	6.94E-03	3.83E-03	5.94E-03	5.86E-03	5.60E-03	5.78E-03	5.17E-03		
		CSM	4.52E-03	6.82E-03	4.58E-03	5.27E-03	6.30E-03	6.15E-03	5.06E-03	4.16E-03		

Whether implemented in the parameter matching framework or not, the infinite line source model attempts to minimize the square of the error between the measured and the estimated average fluid temperatures as shown in Eq. 7-24. The power averaged over the considered testing period is used in the simple infinite line source model to estimate the average fluid

temperature. In the parameter matching technique, the actual measured power was used to estimate the average fluid temperature. This is done by incorporating the superposition concept (Weibo et al., 2009) in the parameter matching framework so that the fluid temperature at any time is estimated using the actual power history prior to that time. Therefore, less reliable results are obtained from the simple infinite line source model due to; (1) the use of an average power value, and (2) simplifying the relation between the fluid temperature and the time logarithm using a linear relation. On the other hand; when the infinite line source is incorporated in the parameter match technique, the actual power was used forcing the shape of the predicted average fluid temperature to mimic the measured fluid temperature and thus the best-fit was performed using a more representative curve. This explains the discrepancy of the results of this model when the two approaches were used. The parameter matching estimates are considered more accurate because they account for the variation observed during the test in the applied power and the fluid temperature.

As mentioned earlier, the effective ground thermal conductivity estimated from the parameter matching is lower than this estimated using the simple line source model. This is expected to reduce the thermal resistance of various heat exchangers estimated using the former technique. This expected slight reduction is observed in the estimated thermal resistances for various heat exchangers as summarized in Table 7-5. Figure 7.14 explains the expected reduction using the simple infinite line source approach. For the same test results and assuming that the powers used while applying the two approaches are very close, the ground thermal conductivity decreases as the slope of the best-fit line increases. A reduction in the slope of the best-fit line reduces the intercept which is used to estimate the thermal resistance of the heat exchanger as presented by Eq. 7-20.

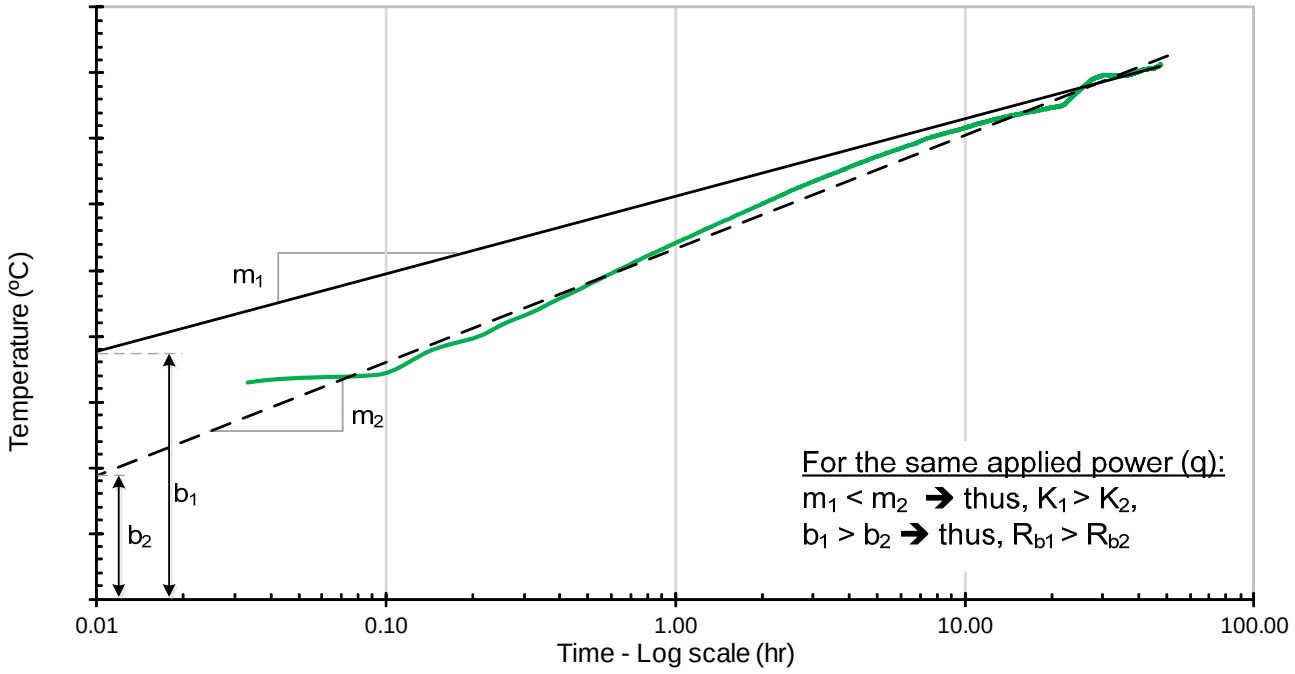

Figure 7.14. Effect of the ground thermal conductivity and the thermal resistance of the heat exchanger on one another.

7.4.2. Considering the Ambient Temperature Interference

The effect of the heat exchanged with the ambient air can also be incorporated in the parameter matching technique (Li and Lai, 2012). This is performed by combining the iterative procedure proposed by Bandos et al. (2011) for estimating the percentage of the heat exchanged to the ambient air with the parameter matching technique described by Li and Lai (2012). This newly combined approach is outlined as follows;

1. The percentage of the power exchanged with the ambient is included as an optimization parameter. The initial guess for p is assumed among the initial estimates for other parameters. An acceptable value for p is between 2 to 10%; this range can also be used as the bounds for p. Other optimization parameters included in this procedure are the effective thermal properties of the ground and the thermal resistance of the heat exchanger. No optimization for the undisturbed ground temperature is performed here; rather, the measured in-situ undisturbed ground temperature is used as a reference to estimate other optimization parameters. using the actual measured in-situ undisturbed ground temperature as a fixed parameter force the estimated values of various optimization parameters to provide the best estimate of the fluid temperature corresponding to this actual ground temperature,
2. Estimate the power injected to the ground using Eq. 7-11 corresponding to the assumed value of p,
3. The average fluid temperature is estimated using the power estimated in step 2, the initial values for other optimization parameters, any selected analytical model, and the measured in-situ undisturbed ground temperature,
4. The squared error between the estimated and the measured fluid temperatures is then estimated. The trust region method is then used to minimize this squared error by varying the optimization parameters within their respective bounds. The results of the optimization are a set of values for the optimization parameters, including p, that minimizes the objective function provided in Eq. 7-24,
5. Steps 1 through 4 are repeated M trials with varying the initial values for each parameter following a selected error distribution bounded by the lower and the upper bounds. Thus, each trial represents a set of initial values for various optimization parameters and the obtained optimization results correspond to this initial set,
6. The final expected value of each optimization parameter is estimated using Eq. 7-26.

The results of the optimization for the four considered tests are presented in details in Appendix XIII. Table 7-6 summarizes the optimization results for all these tests. It can be seen from this table that the percentage of the heat exchanged with the air in all tests is about 6-7%. This percentage was not expected to be very close for all the tests due to, for example, the higher thermal gradient between the fluid inside the connecting tubes above the ground and the ambient air in TCT 3 and TCT 4. These two tests were performed in the winter when the ambient air temperature was much lower than that of TCT 1 which was conducted in the summer. However, the use of more efficient insulation for TCT 3 and TCT 4 reduced the heat loss and therefore the estimated 6-7% heat loss in these two tests is an improvement since this percentage was expected to be more should the insulation used in TCT 1 was used in these tests. Furthermore, the percentage of the heat loss to the ambient air was reduced in TCT 2 due to; (1) the short length of the connecting tubes above the ground, (2) the use of relatively good insulation, (3) the lower thermal gradient between the fluid in the connecting tubes and the ambient air.

Table 7-6. Sum mary of the parameter matching using the corrected power for the considered four tests using the infinite line source, the finite line source, and the cylindrical source model following the forward and the backward processing techniques.

Optimization parameter	Statistical parameter	Model	Test								Global estimates	
			TCT 1 (Pile 3)		TCT 2 (Pile 4)		TCT 3 (Pile 2)		TCT 4 - 3kW (Test Pile)		Average	Standard deviation
			Forward	Backward	Forward	Backward	Forward	Backward	Forward	Backward		
Percentage of heat loss to the ambient air (%)	Average	ILS	93.84%	93.82%	93.90%	93.98%	93.83%	93.85%	93.72%	93.82%		
		FLS	93.84%	93.84%	93.95%	94.01%	93.96%	93.82%	93.81%	93.71%		
		CSM	93.81%	93.73%	93.86%	94.00%	93.68%	93.75%	93.73%	93.91%		
	Standard deviation	ILS	2.74E-03	3.09E-03	3.82E-03	4.54E-03	4.03E-03	3.15E-03	3.86E-03	3.17E-03		
		FLS	3.78E-03	3.89E-03	3.32E-03	3.10E-03	3.12E-03	3.28E-03	2.71E-03	3.57E-03		
		CSM	3.05E-03	2.99E-03	3.06E-03	4.21E-03	3.49E-03	3.36E-03	3.39E-03	3.45E-03		
Ground thermal conductivity (W/m·K)	Average	ILS	2.27	2.28	2.28	2.28	2.28	2.28	2.27	2.27	2.28	6.02E-03
		FLS	2.28	2.28	2.27	2.26	2.27	2.28	2.28	2.29		
		CSM	2.27	2.28	2.27	2.27	2.29	2.27	2.28	2.28		
	Standard deviation	ILS	0.041	0.039	0.035	0.039	0.036	0.038	0.038	0.036		
		FLS	0.034	0.036	0.034	0.031	0.039	0.040	0.038	0.045		
		CSM	0.044	0.034	0.034	0.033	0.034	0.041	0.030	0.040		
Thermal resistance of heat exchanger (m·K/W)	Average	ILS	0.26	0.26	0.15	0.15	0.26	0.26	0.24	0.24		
		FLS	0.26	0.26	0.15	0.15	0.26	0.26	0.24	0.24		
		CSM	0.25	0.25	0.14	0.14	0.25	0.25	0.23	0.22		
	Standard deviation	ILS	3.52E-03	3.55E-03	2.46E-03	2.91E-03	3.14E-03	3.40E-03	2.97E-03	3.09E-03		
		FLS	3.08E-03	3.39E-03	2.26E-03	2.25E-03	3.18E-03	3.14E-03	2.79E-03	3.57E-03		
		CSM	3.78E-03	2.80E-03	2.80E-03	2.61E-03	2.93E-03	3.71E-03	2.55E-03	3.64E-03		

The effective ground thermal conductivity estimated using the power corrected for the heat loss to the ambient air is higher than that estimated without correcting the applied power as show in Table 7-6. On the other hand, the standard deviation of the estimated thermal conductivity values is smaller compared to that estimated without correcting the power which suggest better estimate. As discussed earlier, increasing the thermal conductivity of the ground for the same power used to analyze the results of a specific test produces more thermal resistance of the heat exchanger as explained in Figure 7–14. For the analysis here, the power included in the analysis is reduced which should be accompanied with a significant decrease in the slope of the best-fit line to produce higher ground thermal conductivity. This reduction in the slope of the line gives more thermal resistances for the heat exchangers which are observed in Table 7-6 for all tests. Thus, the average ground thermal conductivity is estimated as 2.28 W/m·℃ (1.317 BTU/hr·ft·°F).

7.5. Validation

The 2.28 W/m·℃ (1.317 BTU/hr·ft·°F) estimated effective thermal conductivity of the ground and the percentages of the heat exchanged with the ambient air are validated using finite element models of the four tests. These models are 2-dimensional models in which the actual power injected to the ground is applied in the fluid domain. This actual power is estimated using Eq. 7-11 for the final average *p* for the considered test. Figure 7–15 shows the power corrected for the heat loss to the ambient air for each one of the considered tests. The details of the technique followed to build these models are presented in Chapter 3. As shown in Figure 7–16, the average fluid temperatures estimated from the finite element models agree very well with the results of the respective in-situ test.

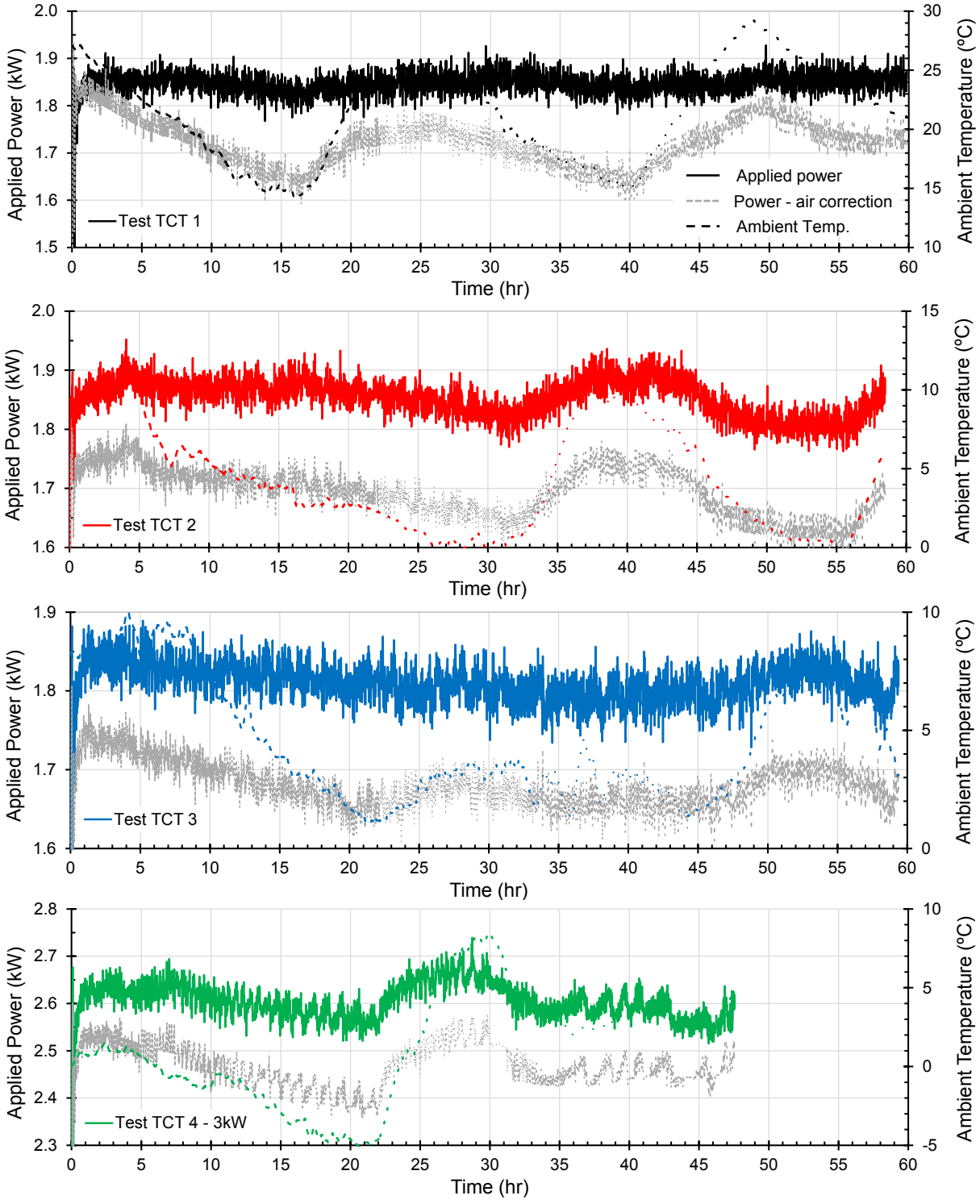

Figure 7.15. The actual applied power corrected for the heat lost to the ambient air versus the applied power with not correction and the ambient air temperature.

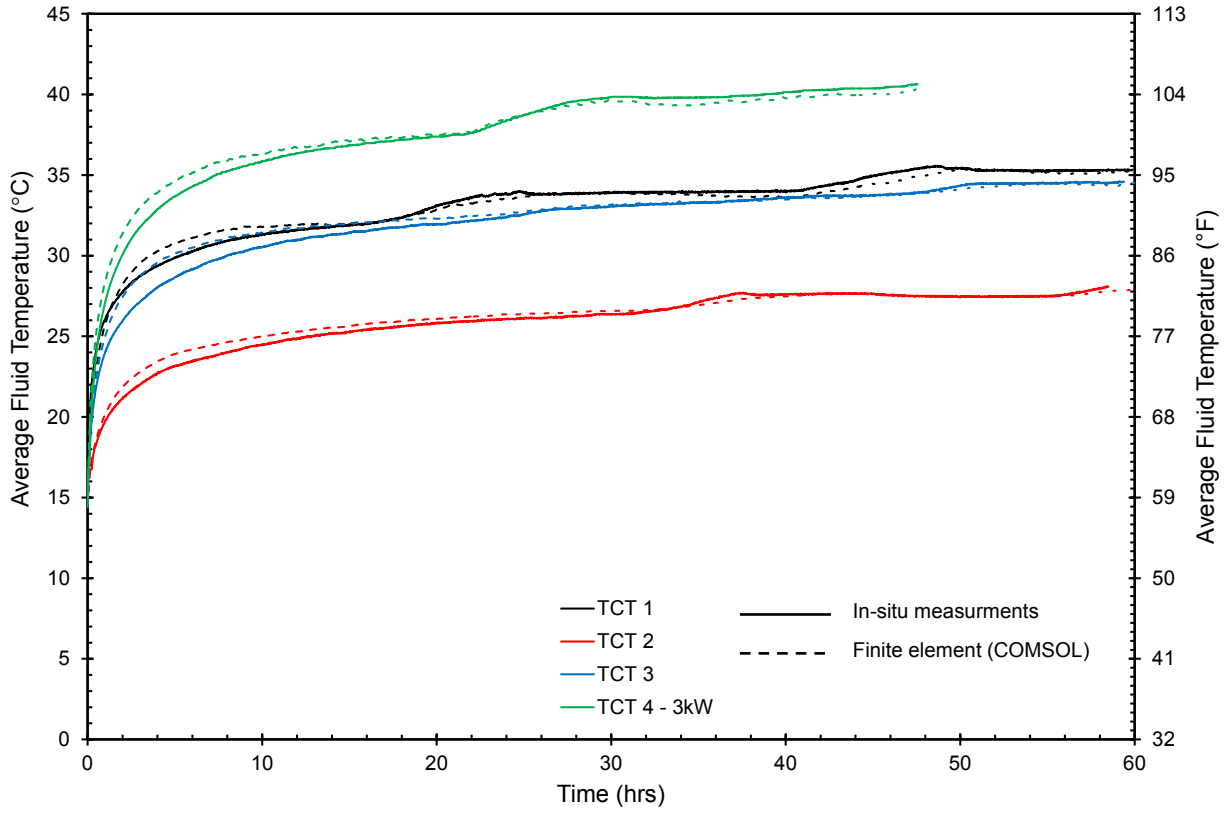

Figure 7.16. Validating the results of the parameter matching including the correction for the heat exchanged with the ambient air using finite element modeling of the four considered tests.

7.6. Modified Dutch Thermal Conductivity Test

The heat exchanged with the ambient air has a significant effect on the estimated effective ground thermal conductivity and the thermal resistance of the heat exchanger as discussed so far. The procedure proposed by Bandos et al. (2011) to estimate the amount of heat loss to or gain from the surrounding environment can be utilized to obtain reliable results as discussed earlier. It is, however, an approximation and relies on using a theoretical heat transfer analysis to account for the heat exchanged with the ambient by adjusting the measured fluid temperatures. Furthermore, this procedure requires the use of advanced processing techniques such as the parameter matching framework discussed.

In this section, a simple modification for the Dutch thermal conductivity procedure is proposed. This modification is to include the effect of the heat exchanged with the ambient in the measured fluid temperatures. This modification eliminates, or significantly reduces, the humps observed in the fluid temperature curves caused by the variation of the heat exchanged with the ambient air as discussed in the previous chapter. Thus, no need for advanced processing techniques exists. The simple line source model can be used to provide reliable estimates of the effective thermal conductivity of the ground and thermal resistance of the heat exchanger.

7.6.1. Theoretical Concept

The heating power in thermal conductivity tests performed according to the Dutch procedure is applied by maintaining a constant flow rate, and a constant difference between the inlet and

the outlet fluids as discussed in Section 7.2.2. Thus, a constant power is assured by setting the inlet fluid temperature (T^*_{in}) at any time (t_1) to the summation of the outlet fluid temperature (T^*_{out}) at the preceding time (t_0) and the desired constant temperature difference (ΔT) that provides the intended applied power, i.e. $T^*_{in}=T_{out}+\Delta T$. In practice, the inlet and the outlet fluid temperatures are measured inside the testing equipment. The testing equipment is connected to the ground loops using tubes. Heat exchange with the ambient occurs over the length of these tubes due to the thermal gradient between the carrier fluid inside the tubes and the ambient air. Therefore, the temperatures of the fluid at the entrance and at the exit of the loops near the ground surface differ from those measured inside the testing equipment. Thus, the temperature difference ΔT does not reflect the actual power applied to the ground.

Measuring the temperatures of the fluid at the entrance and the exit of the ground loops near the ground surface helps to estimate the actual power applied directly to the ground. In other words, the power estimated using these fluid temperatures accounts for the heat exchanged with the ambient. However, this power is not constant since it varies with the temperature of the ambient air as presented in Figure 7–15 for the actual power applied in the four ASHRAE thermal conductivity tests conducted at Virginia Tech. Thus, advanced processing techniques are required should this power be used to estimate the thermal conductivity of the ground.

In the proposed modification, the temperature of the fluid leaving the testing equipment and entering the ground loop is measured at two locations; (1) inside the testing equipment and before getting exposed to the ambient, T^*_{in}; and (2) near the ground surface before penetrating the ground, T_{in} as shown in Figure 7–1. The difference between these two temperatures (ΔT_{in}) refers to the heat loss/gain occurred along the tube connecting the loop inlet and the outlet of the testing equipment. Furthermore, the temperature of the fluid leaving the ground loop and returning to the testing equipment is measured near the ground surface (T_{out}), and inside the testing trailer (T^*_{out}). The difference between these two temperatures (ΔT_{out}) refers to the heat loss/gain occurred along the tube connecting the loop outlet and the return line of the testing equipment.

The average of the two estimated temperature differences along the legs of the tubes connecting the inlet and the outlet of the ground loops to their respective lines in the testing machine, i.e. ΔT_{in} and ΔT_{out}, is used when updating the set inlet temperature (T^*_{in}) using the online real-time updating as discussed earlier for typical applications. This average temperature difference ($\Delta T_{avg.}$) is incorporated in the updating process, as presented in Figure 7–17, for a given time (t_1) as;

$$T^*_{in}|_{t_1} = T_{out}|_{t_0} + \Delta T + \Delta T_{avg.} \qquad \text{Eq. 7-27}$$

Where; T_{out} : the temperature of the fluid leaving the ground loop measured near the ground surface at time (t_0),

ΔT : the temperature difference to be used to apply the desired heating power,

$\Delta T_{avg.}$: the average temperature difference measured along the tubes above the ground.

The fluid leaving the testing equipment, at temperature T^*_{in}, is expected to exchange some energy with the ambient. This heat exchange causes the temperature fluid at the inlet of the loops near the ground surface to deviate from the set inlet fluid temperature by a value equal and opposite to the average temperature difference, i.e. $T_{in} = T^*_{in} - \Delta T_{avg.} = T_{out} + \Delta T$. Thus, the net difference between the temperatures of the fluid leaving and entering the loop near the ground surface is maintained constant at ΔT. Figure 7–17 presents a chart for the steps used to implement the proposed modification within the Dutch thermal conductivity testing procedure.

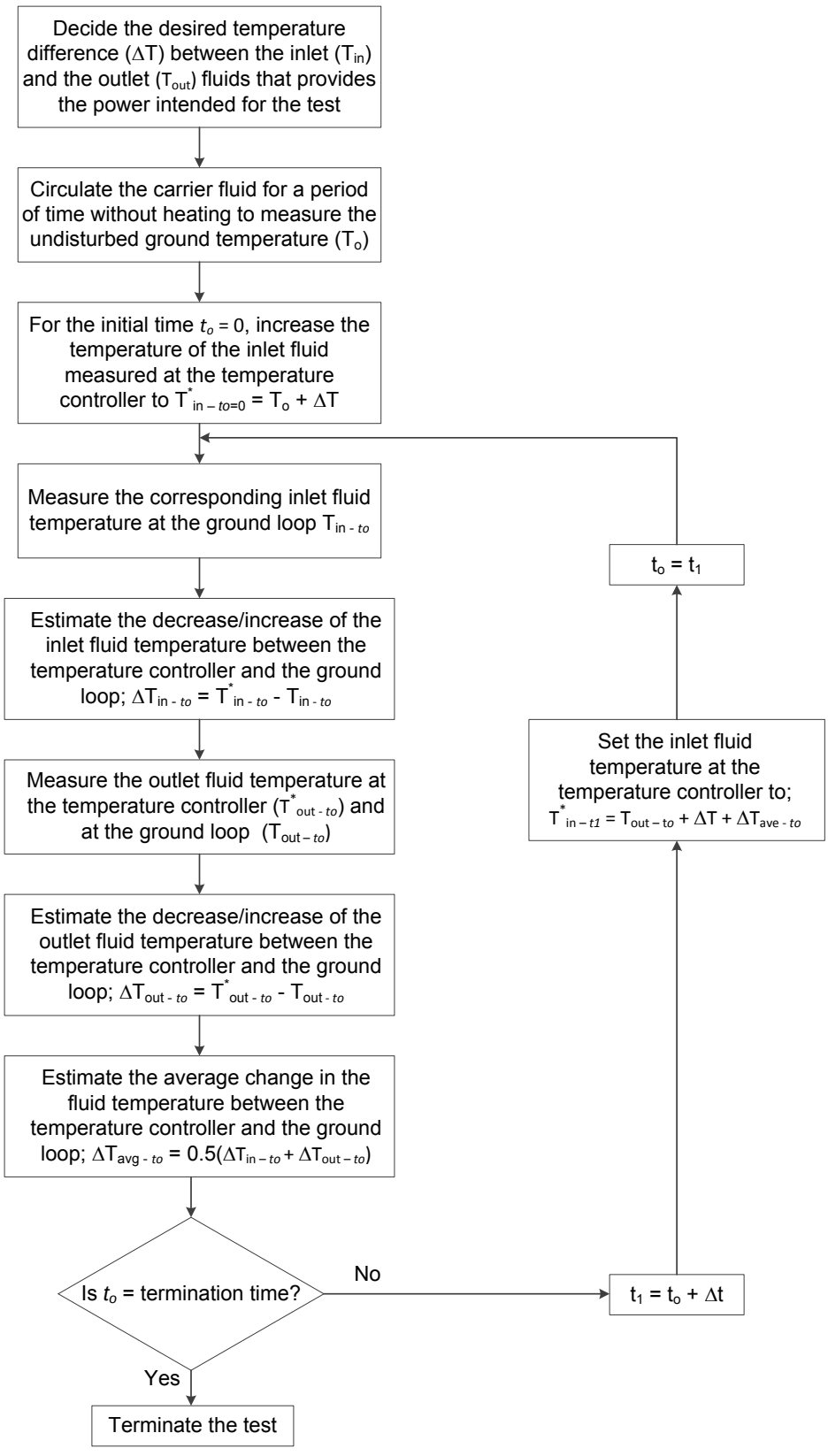

Figure 7.17. Proposed online modification of the inlet fluid temperature to account for the heat exchanged with the ambient air.

7.6.2. Virginia Tech Modified Dutch Thermal Response Test

The proposed modification was implemented in one of Virginia Tech thermal conductivity tests. In this test, the Dutch procedure with the proposed modification was followed to investigate its validity. The inlet fluid temperature controlling equipment discussed in Chapter 6 was utilized in this test to vary the inlet fluid temperature as desired during the test period. The test was performed on the test Pile when it was loaded mechanically, thus this test was considered as the thermal load of T-MT 4. The thermo-mechanical response of the test Pile in this test is presented in Chapter 8. The focus in this chapter is on the thermal equipment step up and testing procedure as well as the results of the thermal test in terms of the measured fluid temperature. Then, the measured fluid temperatures were used to estimate the effective thermal conductivity of the ground and the thermal resistance of the heat exchanger.

(a) Test Set Up

Two temperature gauges were installed in each of the inlet and the outlet connecting tubes to measure the respective fluid temperatures; one near the testing equipment and one near the ground surface. The fluid temperatures were collected every 2 minutes for the entire testing period. The carrier fluid used in this test was water that was circulated at a flow rate of 5.68 lit/min (1.5 gpm). The test was initiated by circulating the carrier fluid in the ground loop without applying any heat for a period about 4 hours to estimate the undisturbed ground temperature. Figure 7–18 shows the measured fluid temperature near the ground surface and inside the testing equipment. As seen in this figure, the fluid temperatures increase with time and at the end of the initialization phase they reach to 14.7 ºC (58.46ºF). This temperature represents the undisturbed ground temperature and it is consistent with the values estimated using other tests as discussed earlier.

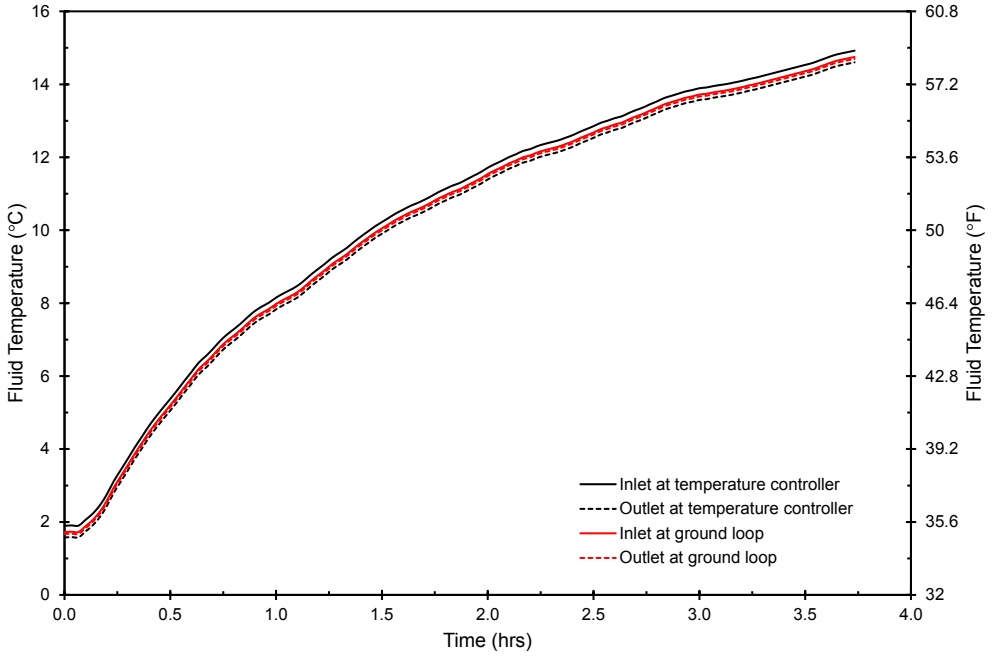

Figure 7.18. Fluid temperature during the initialization phase used to estimate the undisturbed ground temperature (T_o).

After the initialization phase, the thermal conductivity test was started by maintaining a 5.5ºC (10 ºF) of a temperature difference between the inlet and the outlet fluids measured near

the ground surface. This temperature difference and water flow rate correspond to an average applied power of about 2.2 kW or 72 W/m. This applied power is selected such that it is different from the power applied in the ASHRAE thermal conductivity test conducted on the same test Pile. This power difference is intended to check the reliability of the estimated results using various applied powers. The test was conducted for 48 hours over which the fluid temperatures were recorded every 2 minutes. The ambient air temperature was also measured during the test period using the temperature of the data logger which was kept uncovered to obtain representable air temperatures. Figure 7–19 presents the time variation of the inlet and the outlet fluid temperatures measured near the ground surface in red and close to the testing equipment in black along with the measured air temperature.

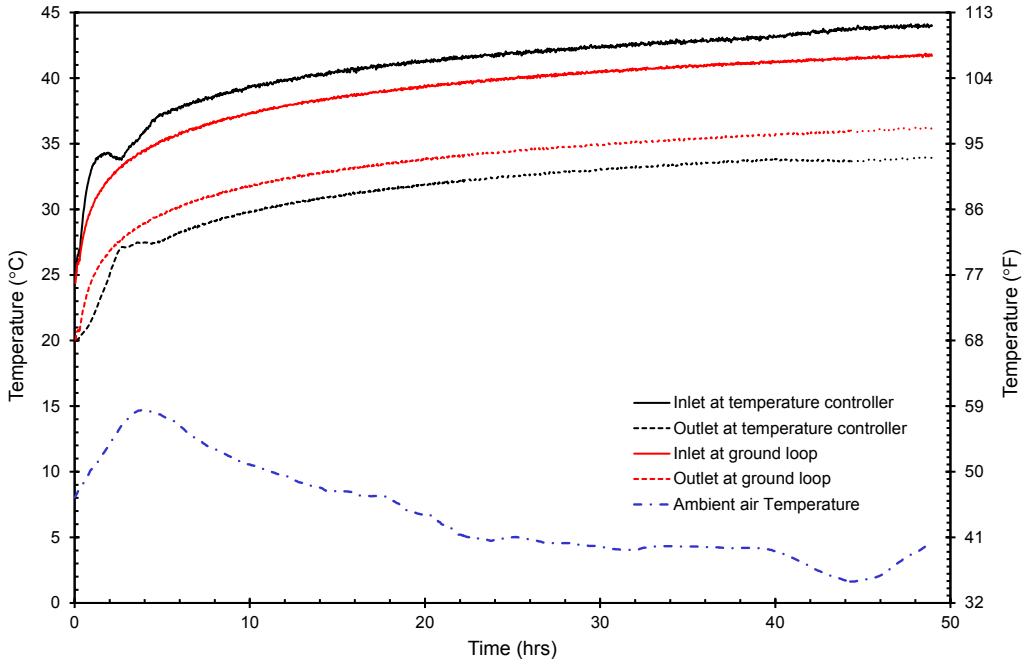

Figure 7.19. Measured fluid and air temperatures during the modified Dutch thermal conductivity test performed at Virginia Tech.

It can be seen in Figure 7–19 that the temperatures of the inlet and the outlet fluid measured near the testing equipment are affected by the variation of the ambient air temperature. For instance, the air temperature during test reached its highest value after 4 hours from the beginning of the test at which the thermal gradient between the fluid in the connecting tubes above the ground and the ambient air is minimized. Thus, the heat loss to the air at that point of time is the least which increases the power applied to the ground. Therefore, the minimum difference between the temperatures of the outlet and the inlet fluid measured near the ground surface and close to the testing equipment is observed at this time. Furthermore, the air temperature dropped near the end of the test, i.e. after 40 hours from the beginning of the test. This drop in the ambient temperature increases the heat loss from the tubes above the ground. And since the temperature difference between the inlet and the outlet fluid temperatures measured near the ground surface is maintained constant, this decrease in the applied power causes the observed decrease in the outlet fluid temperature as well as the increase in the inlet fluid temperature measured at the testing equipment.

The power estimated using the fluid temperatures measured near the testing equipment is compared to that estimated using the fluid temperatures measured near the ground surface as shown in Figure 7–20. In typical testing practices, the applied power is expected to increase as the ambient air temperature increases due to the reduction of the amount of the heat lost to the ambient. Similarly, the applied power is expected to reduce when the ambient air temperature drops. These two expected responses were observed in Figure 7–15 for the four ASHRAE thermal conductivity tests. However, the modified online adjustment of the inlet fluid temperature forced this response to be reversed. As shown in Figure 7–20, the power estimated using the fluid temperatures measured near the testing equipment (T^*_{in} and T^*_{out}) increases as the ambient air temperature decreases and vice versa. This reverse in the behavior assisted to successfully maintain the actual power applied to the ground, which was estimated using the fluid temperatures measured near the ground surface (T_{in} and T_{out}), constant at 2.2 kW over the entire testing period.

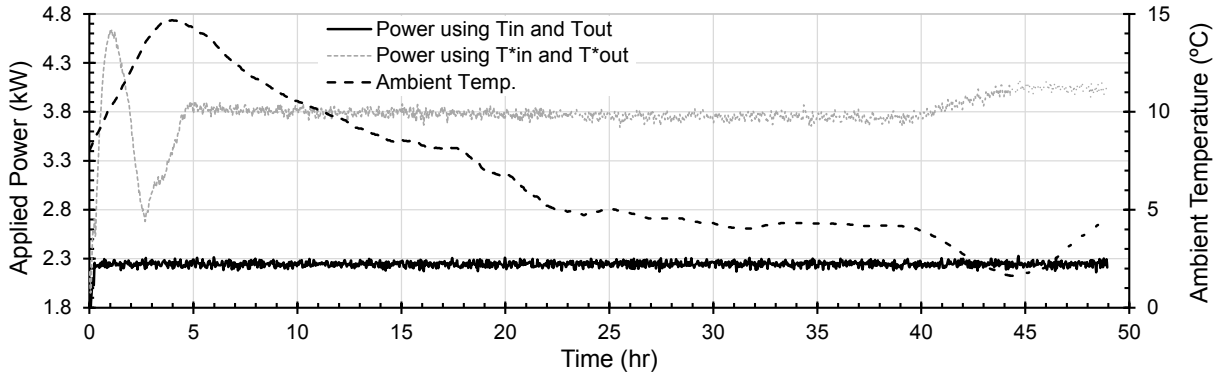

Figure 7.20. The ambient air and the power applied in the modified Dutch thermal conductivity test conducted at Virginia Tech, estimated using the fluid temperatures near the ground surface (T_{in} and T_{out}) and using the fluid temperatures near the testing equipment (T^*_{in} and T^*_{out}).

(b) Data Processing

Since the actual power applied to the ground was maintained constant and the fluid temperatures measured near the ground surface did not have humps, the simple line source model can be used to estimate the thermal conductivity of the ground and the thermal resistance of the heat exchanger. In order to do so, Figure 7–19 was redeveloped using a logarithmic scale for the time in the abscissa and shown in Figure 7–21. As presented in this figure, the fluid temperatures measured near the ground surface versus the logarithm of the time converge to a linear relation after the first hour. The relation between the average fluid temperature and the logarithm of the time is used to apply the simple infinite line source model. The slope of the relation between the average fluid temperature and the logarithm of the time does not vary with changing the considered testing period because no humps were observed. Furthermore, the actual power applied to the ground was constant during the entire testing period as shown in Figure 7–20. Therefore, the test data recorded starting from 6 hours after the beginning of the test till the end of the testing period were used once to estimate the effective thermal conductivity of the ground and the thermal resistance of the borehole. In other words, there is no need to use the forward and the backward processing with varying the considered testing period. The first 6

hours of the test data were ignored to comply with the ASHRAE requirement for processing thermal conductivity data.

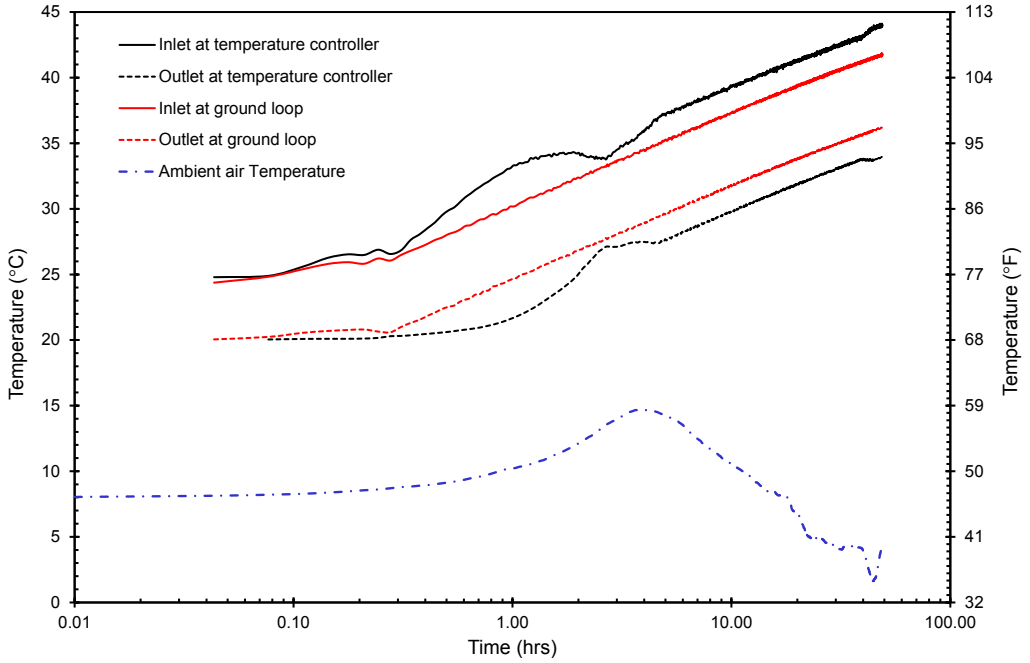

Figure 7.21. Measured fluid and air temperatures using logarithmic scale for the time.

The effective thermal conductivity of the ground and the thermal resistance of the test Pile were estimated to 2.23 W/m·℃ (1.288 BTU/hr·ft·ºF) and 0.24 m·℃/W (0.138 BTU/hr·ft·ºF), respectively. These values agree with those estimated using parameter matching for the four ASHRAE thermal conductivity tests. These results were used in a 2-dimensional finite element model similar to the one used for TCT 4 in Section 7.6. In this model, the actual power applied to the ground is used. The results of this model are presented in Figure 7–22 in which a comparison between the average fluid temperatures estimated using the finite element model and that measured in-situ is presented. Good agreement between the estimated and the measured average fluid temperatures is observed in this figure. Thus, it is concluded that the proposed modification for the testing practices assisted estimating reliable approximations of the ground thermal conductivity and the thermal resistance of the heat exchanger using the simple infinite line source model. Furthermore, parameter matching or any other advanced processing technique is not required to obtain reliable estimates of the ground thermal conductivity and the thermal resistance of the heat exchanger should the proposed modification is implemented in thermal conductivity tests.

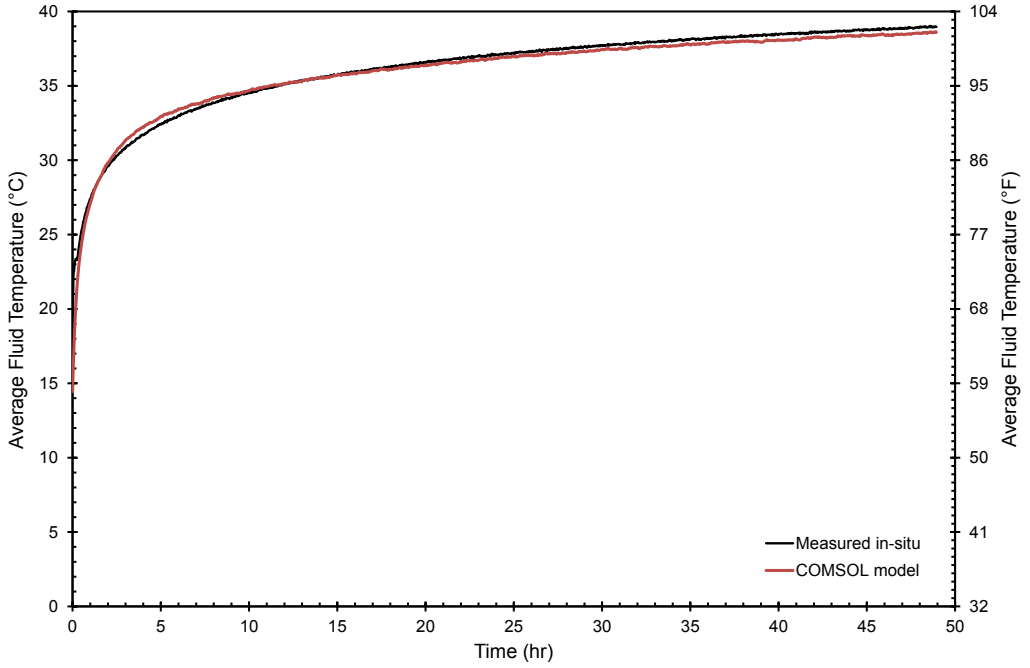

Figure 7.22. T he average fluid temperature estimated using the 2-dimensional finite element model versus the average fluid temperature measured in-situ.

References

American Society of Heating, Refrigerating, and Engineers Air-Conditioning (2009) "2009 ASHRAE handbook fundamentals." Atlanta, GA: American Society of Heating, Refrigeration and Air-Conditioning Engineers.

ASHRAE (2002) "Methods for Determining Soil and Rock Formation Thermal Properties from Field Tests," ASHRAE Research Summary - ASHRAE 1118-TRP: American Society of Heating, Refrigerating and Air-Conditioning Engineers.

Austin, W. A. (1998) "Development of an in situ system for measuring ground thermal properties," Mechanical Engineering. Stillwater, Oklahoma Oklahoma State University, p 177.

Bandos, T. V., Á Montero, P. Fernández de Córdoba, and J. F. Urchueguía (2011) "Improving parameter estimates obtained from thermal response tests: Effect of ambient air temperature variations," Geothermics, Vol. 40, No. 2, pp 136-143.

Berberich, H., N. Fisch, and E. Hahne (1994) "Field experiments with a single duct in water saturated claystone.," Proceedings of 6th International Conference on Thermal Energy Storage, Calorstock '94. Espoo, Finland.

Carslaw, H.S., and J.C. Jaeger (1986) Conduction of Heat in Solids: 2nd Edition, Oxford University Press, USA.

Deng, N.Y., Y. Xiao, and F.J. Zhou (1993) "Nonmonotonic trust region algorithm," JOTA, Vol. 26, pp 259-285.

Ingersoll, L.R., H.J. Plass, and M. Wis (1948) "Theory of the Ground Pipe Heat Source for the Heat Pump," Heating, Piping & Air Conditioning, Vol. 20, No. 7, pp 119-123.

Kavanaugh, S., and K. Rafferty (1997) Ground Source Heat Pumps: Design of Geothermal Systems for Commercial and Institutional Buildings, Atlanta, Georgia: American Society of Heating, Refrigerating, and Air-Conditioning Engineers, Inc.

Li, M., and A.C.K. Lai (2012) "Parameter estimation of in-situ thermal response tests for borehole ground heat exchangers," International Journal of Heat and Mass Transfer, Vol. 55, No. 9-10, pp 2615-2624.

MATLAB and Statistics Toolbox (R2011a), The MathWorks, Inc., Natick, Massachusetts, United States.

Mogensen, P. (1983) "Fluid in duct wall heat transfer in duct system heat storages," Proceedings of the International Conference on Subsurface Heat Storage in Theory and Practice: Swedish Council for Building Research.

Monzó, P.M. (2011) "Comparison of different line source model approaches for analysis of thermal response test in a U-pipe borehole heat exchanger," School of Industrial Engineering and Management, Division of Applied Thermodynamic and Refrigeration. Stockholm, Sweden: KTH Vetenskap och Konst, p 113.

Moré, J.J. (1983) "Recent developments in algorithms and software for trust region methods," In: A. Bachem, M. GrÄotschel, and B. Korte, Eds., Mathematical Programming: The State of the Art. Springer-Verlag, Berlin: Springer, pp 258-287.

Powell, M.J.D. (1970a) "A hybrid method for nonlinear equations," In: P. Robinowitz, Ed., Numerical Methods for Nonlinear Algebraic Equations: Gordon and Breach Science, London, pp 87-144.

Powell, M.J.D. (1970b) "A new algorithm for unconstrained optimization," In: J.B. Rosen, O.L. Mangasarian, and K. Ritter, Eds., Nonlinear Programming: Academic Press, New York, pp 31-66.

Shonder, J.A., and J.V. Beck (1999) "Determining effective soil formation properties from field data using a parameter estimation technique," ASHRAE Transactions, Vol. 105, No. 1, pp 458-466.

Shonder, J.A., and J.V. Beck (2000) "A new method to determine the thermal properties of soil formations from in situ field tests," ORNL Oak Ridge National Laboratory p40.

Wagner, R., and C. Clauser (2005) "Evaluating thermal response tests using parameter estimation for thermal conductivity and thermal capacity," Journal of Geophysics and Engineering, Vol. 2, No. 4, pp 349-356.

Weibo, Y., S. Mingheng, and C. Zhenqian (2009) "A variable heat flux line source model for boreholes in ground coupled heat pump," Power and Energy Engineering Conference, 2009. APPEEC 2009. Asia-Pacific, pp 1-4.

Witte, H. J. L., G. J. van Gelder, and J. D. Spitler (2002) "In situ measurement of ground thermal conductivity-A dutch Perspective," ASHRAE Transactions, Vol. 108, No. 1, pp 263-272.

Yang, H., P. Cui, and Z. Fang (2010) "Vertical-borehole ground-coupled heat pumps: A review of models and systems," Applied Energy, Vol. 87, No. 1, pp 16-27.

Yuan, Y.X. (2000) "A review of trust region algorithms for optimization," In: J.M. Ball, and J.C.R. Hunt, Eds., ICM99: Proceedings of the Fourth International Congress on Industrial and Applied Mathematics: Oxford University Press, pp 271-282.

Appendix XI

Temperature along Pile 3 during TCT 1 and along the Test Pile TCT 4.

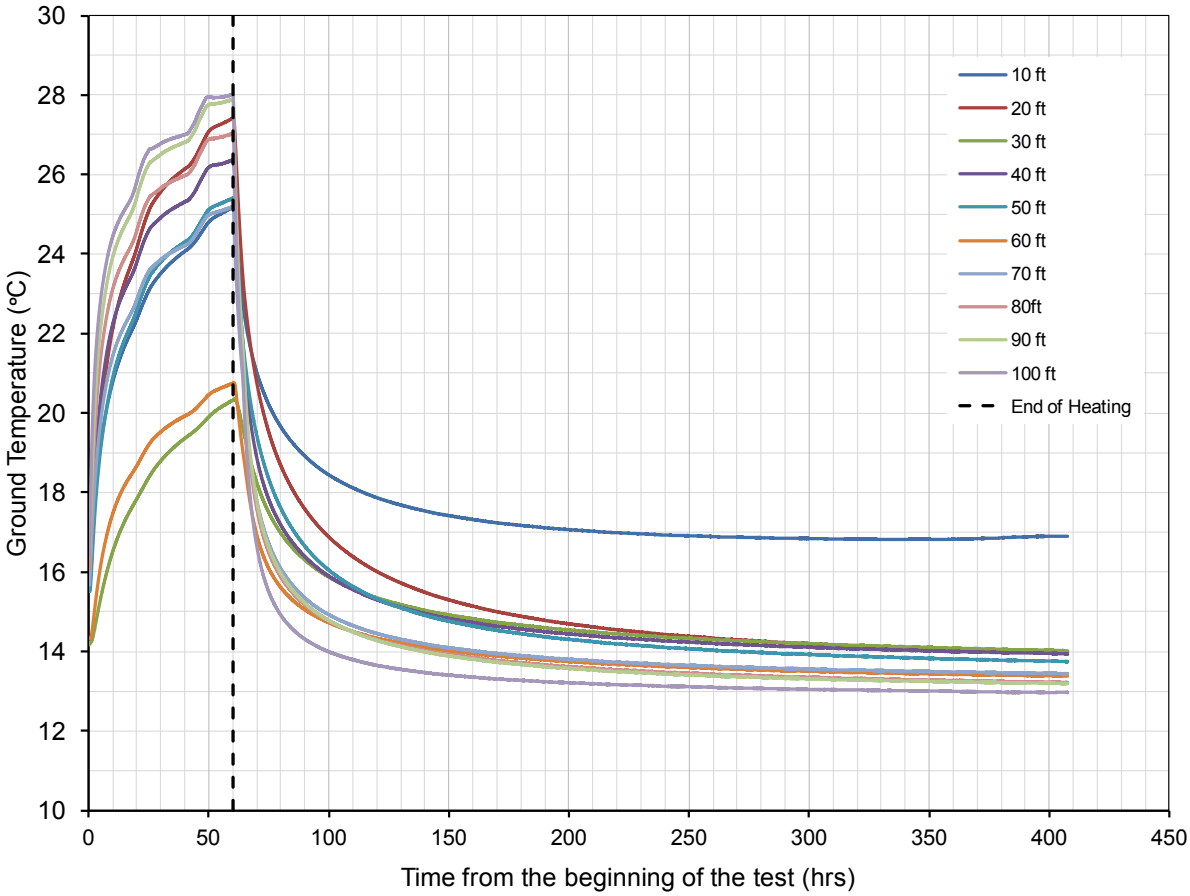

Figure XI.1. Temperature at different depths along the center of Pile 3 during TCT 1.

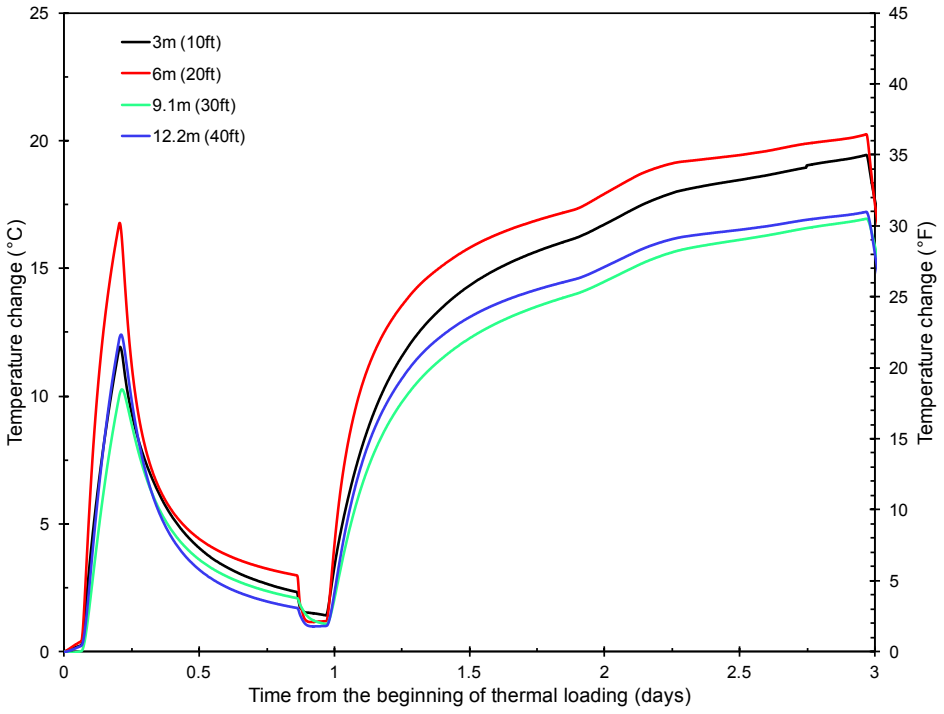

(a) Silty Sand Layer

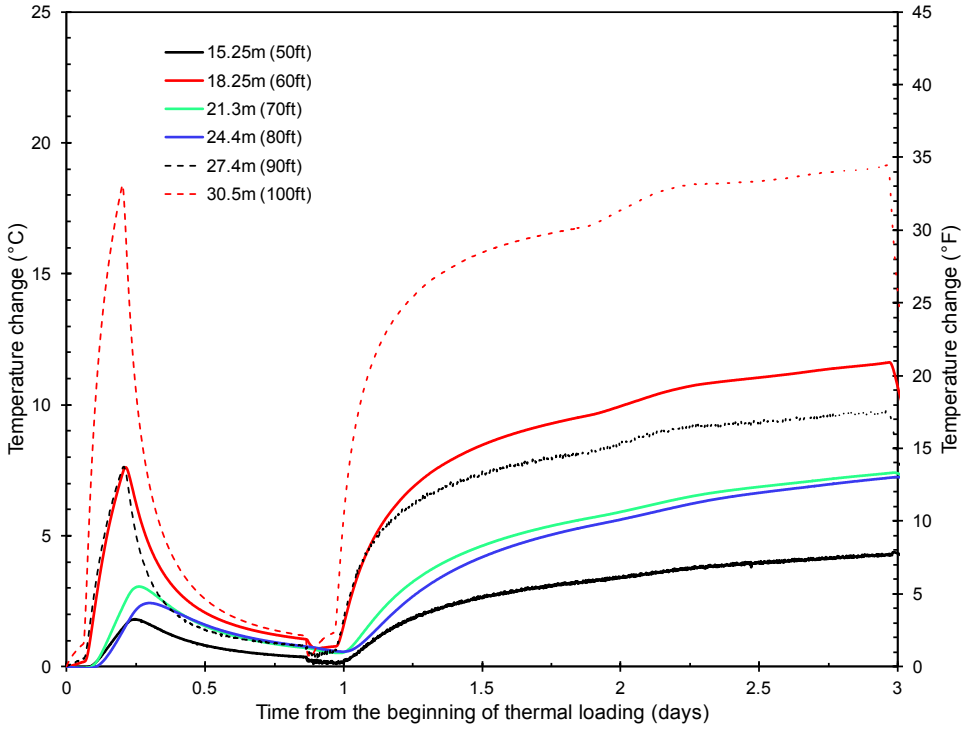

(b) Shale Layer

Figure XI.2. Temperature change at different depths along the Test Pile during TCT 3.

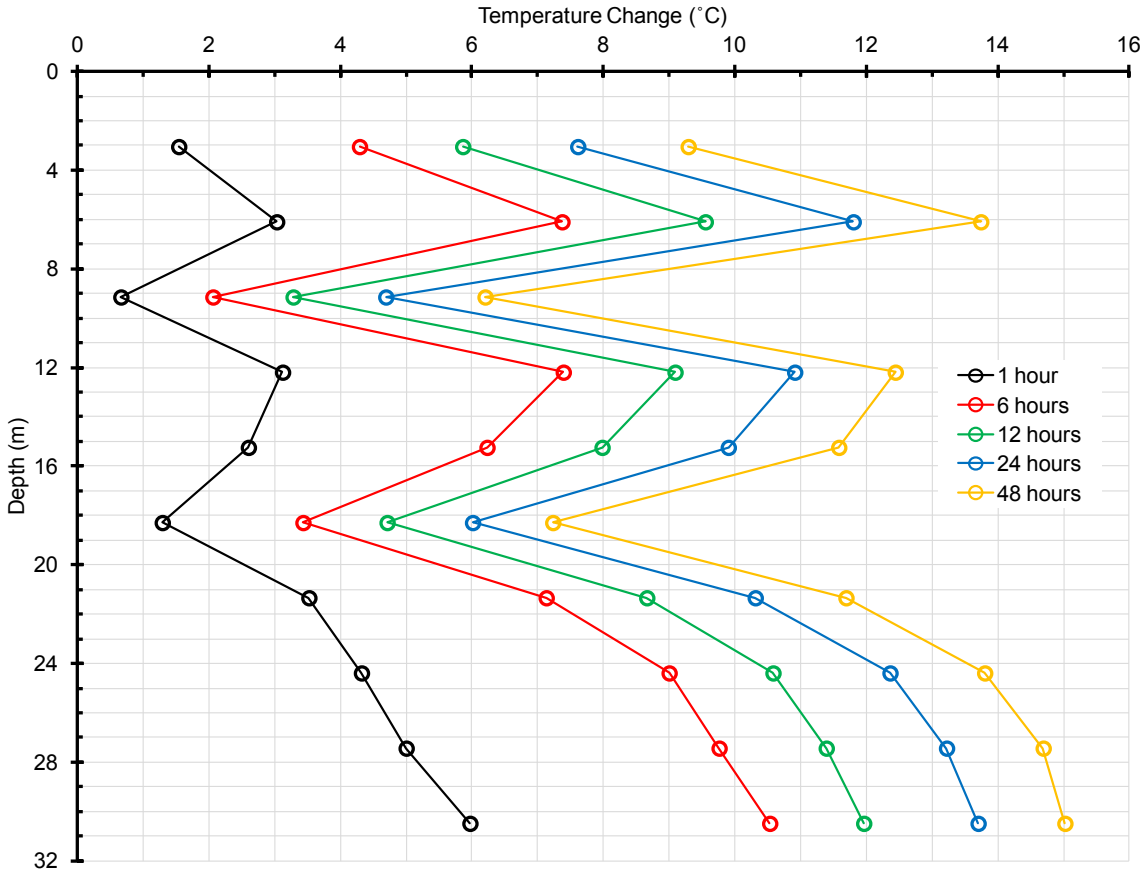

Figure XI.3. Temperature along the Pile 3 at different times during TCT 1.

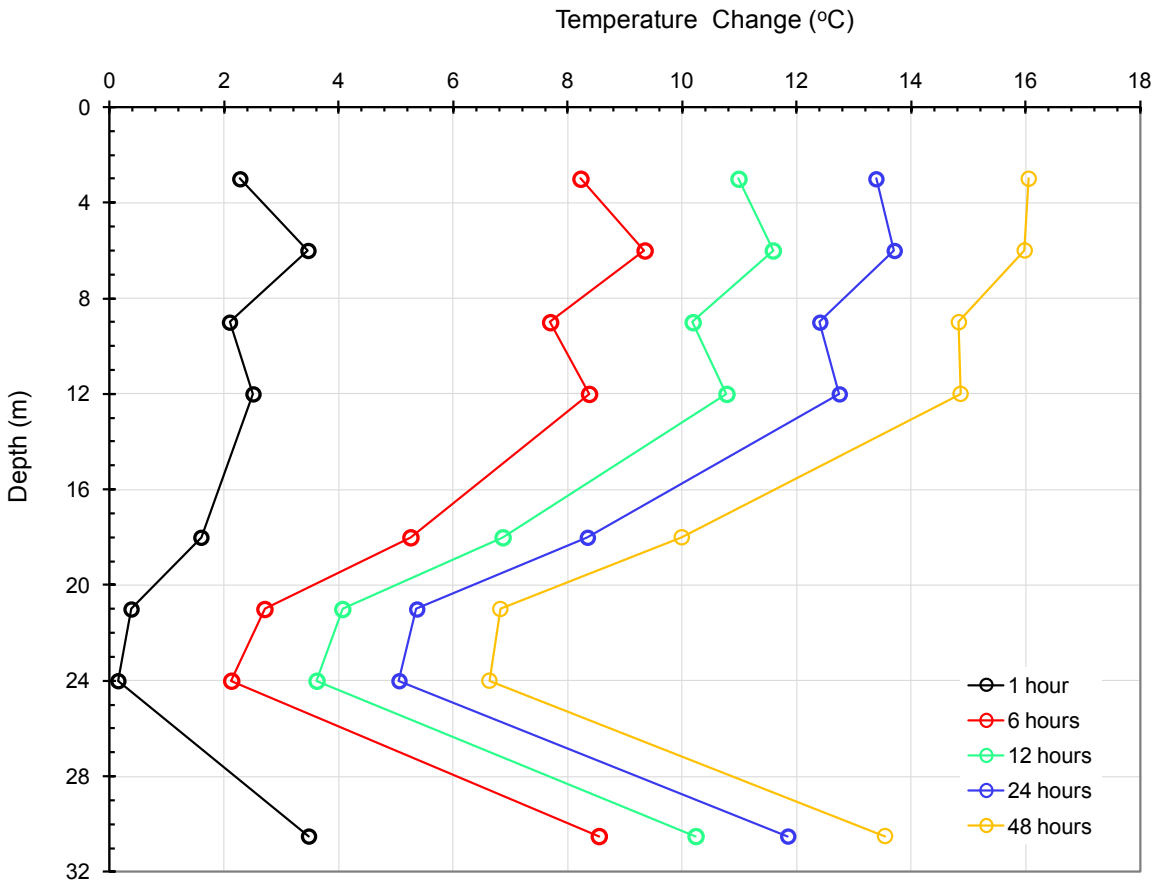

Figure XI.4. Temperature along the Test Pile at different times during TCT 3.

Appendix XII

Parameter matching with no ambient air correction using the infinite line source model, the finite line source model, and the cylindrical source model. Results include; undisturbed ground temperature, the effective thermal conductivity of the ground, and the thermal resistance of the heat exchanger.

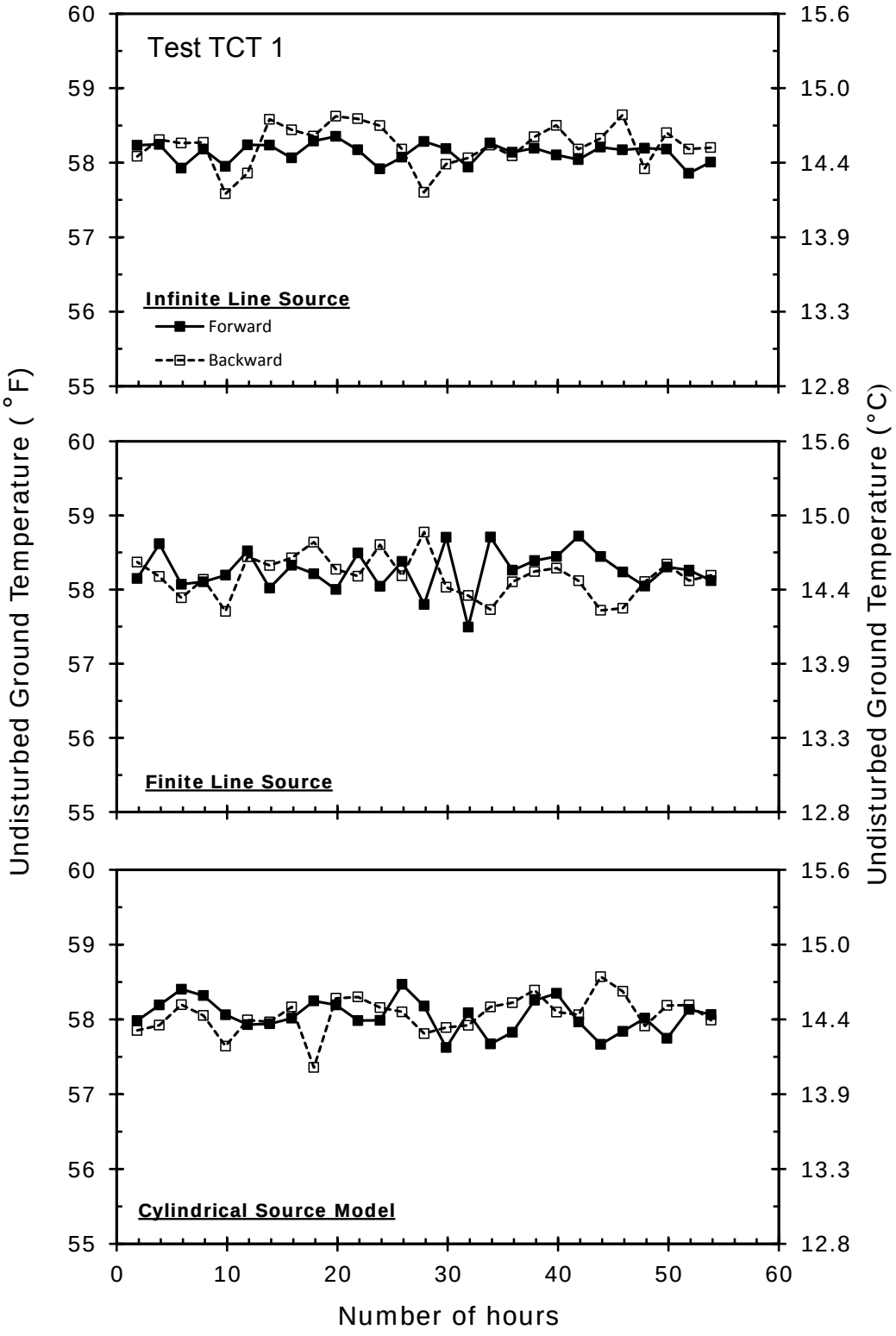

Figure XII.1. Undisturbed ground temperature estimated using various models incorporated in the parameter matching framework with no ambient air effects considered for TCT1.

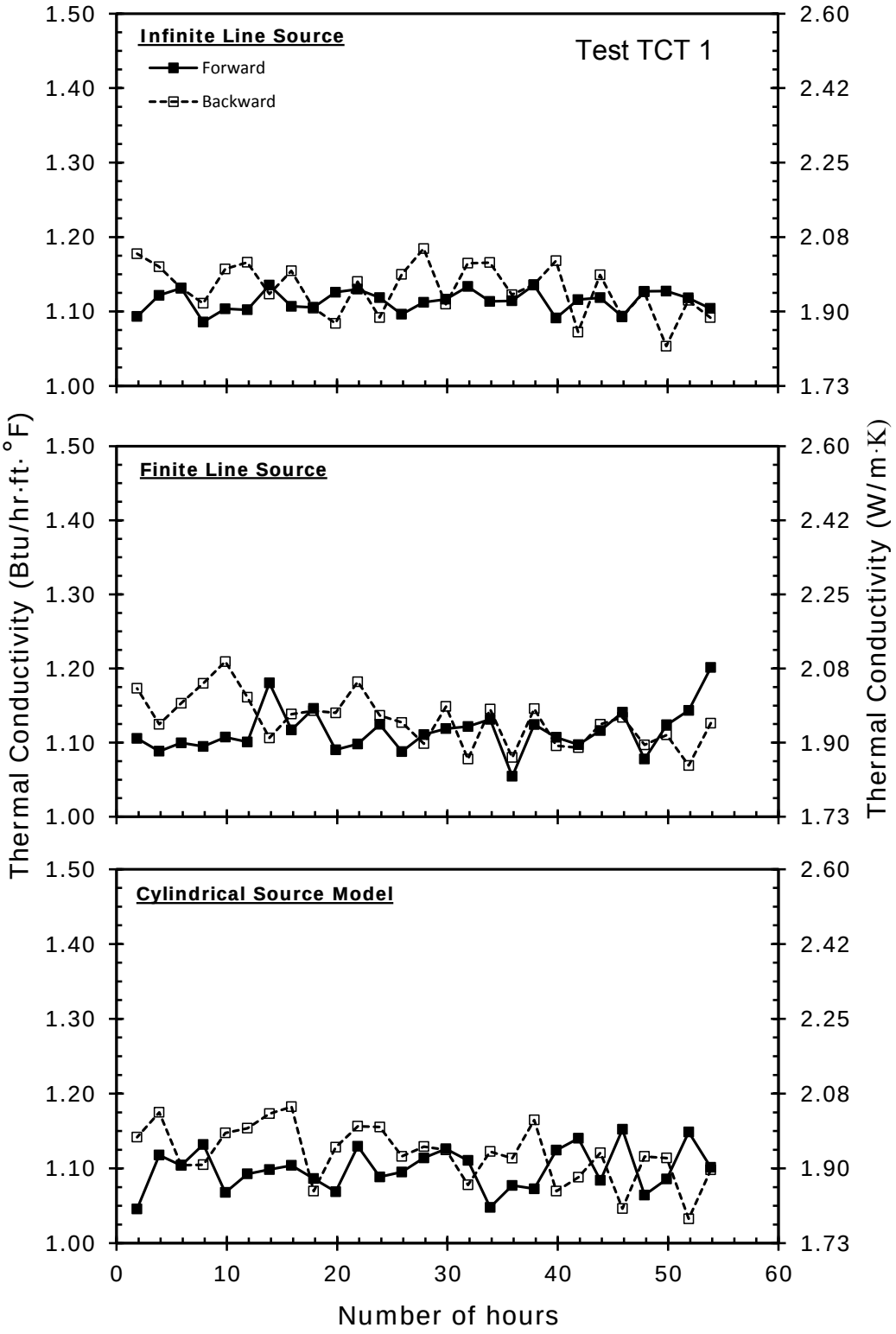

Figure XII.2. Ground effective thermal conductivity estimated using various models incorporated in the parameter matching framework with no ambient air effects considered for TCT1.

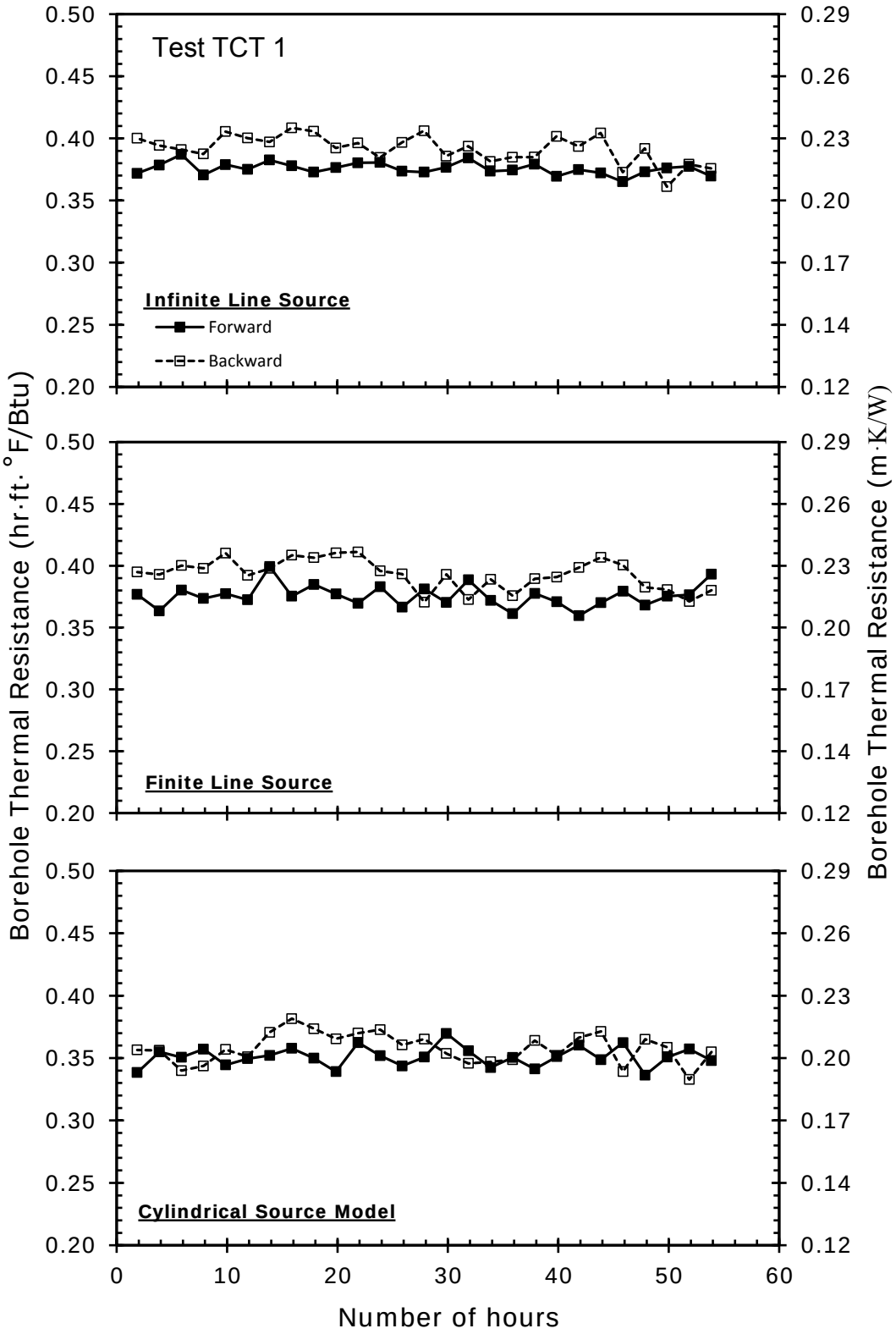

Figure XII.3. Thermal resistance of the heat exchanger estimated using various models incorporated in the parameter matching framework with no ambient air effects considered for TCT1.

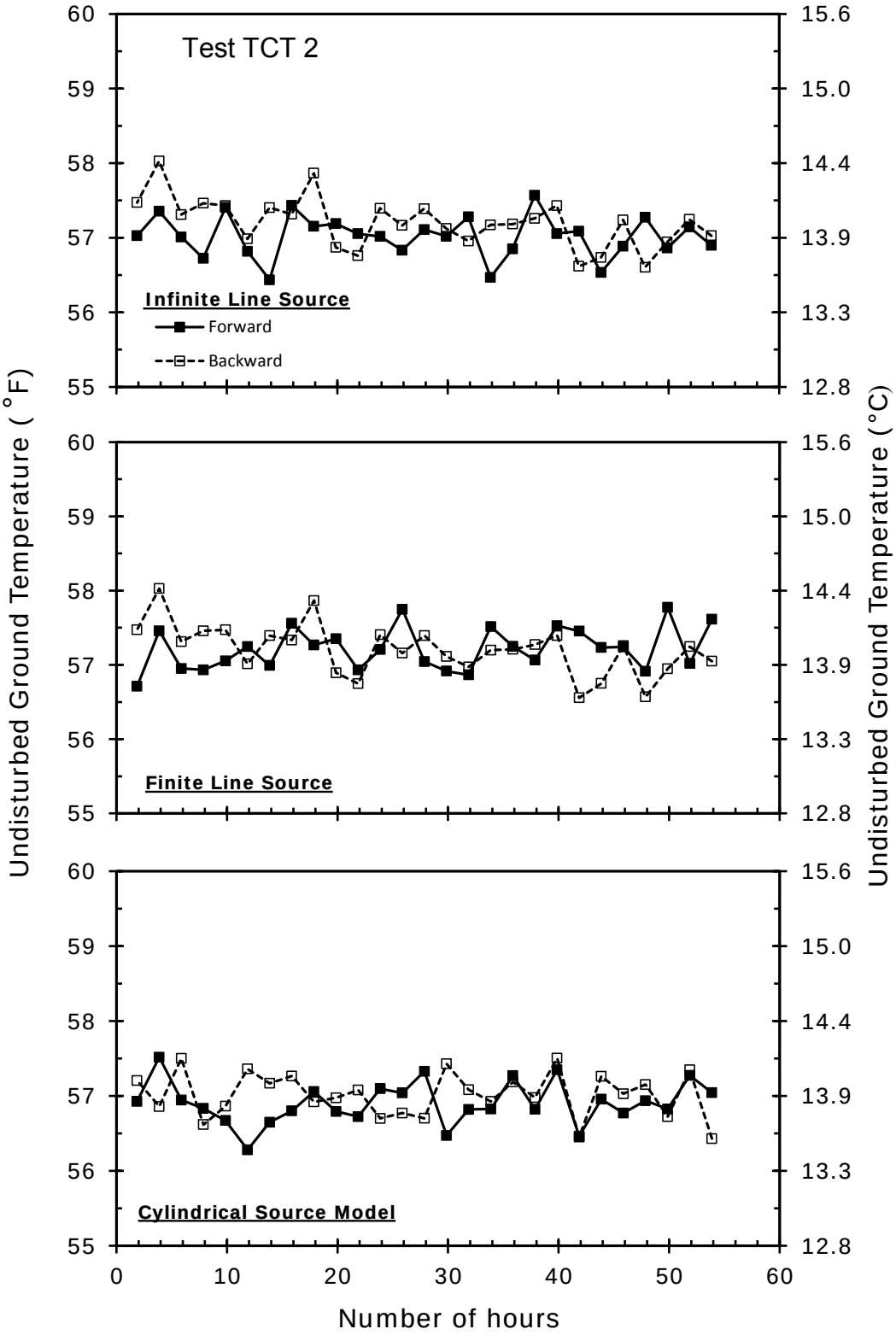

Figure XII.4. Undisturbed ground temperature estimated using various models incorporated in the parameter matching framework with no ambient air effects considered for TCT2.

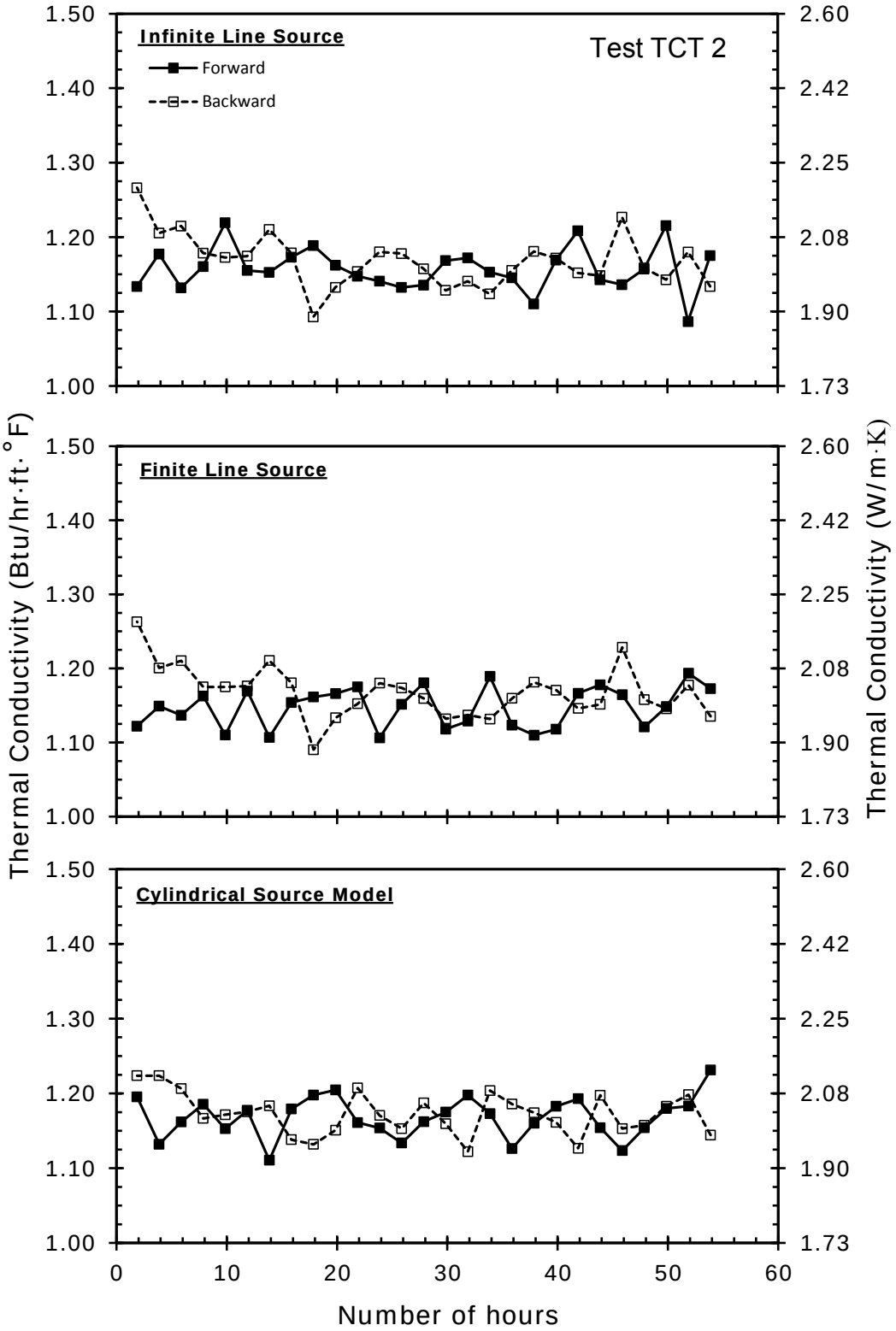

Figure XII.5. Thermal conductivity estimated using various models incorporated in the parameter matching framework with no ambient air effects considered for TCT2.

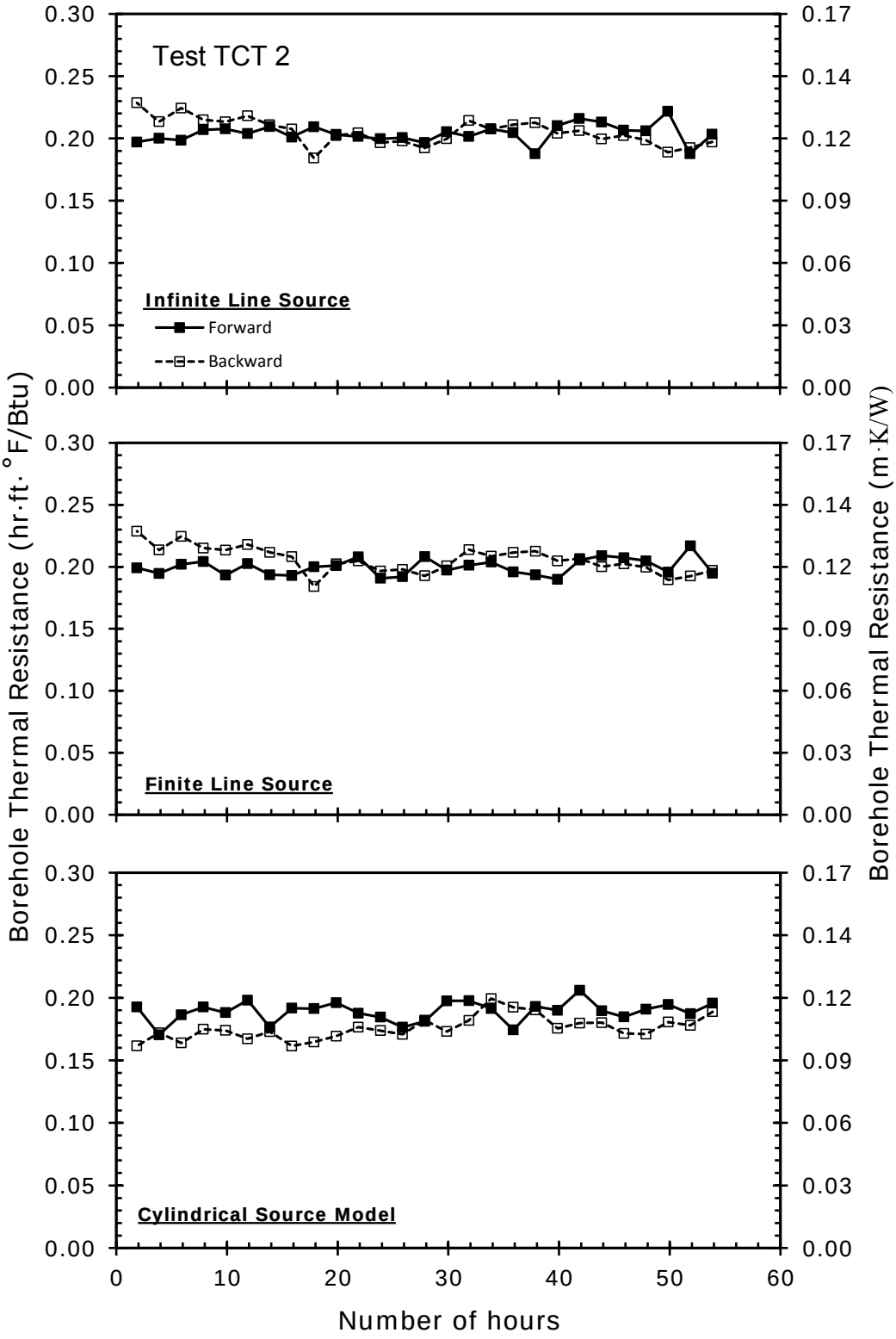

Figure XII.6. Thermal resistance of the heat exchanger estimated using various models incorporated in the parameter matching framework with no ambient air effects considered for TCT2.

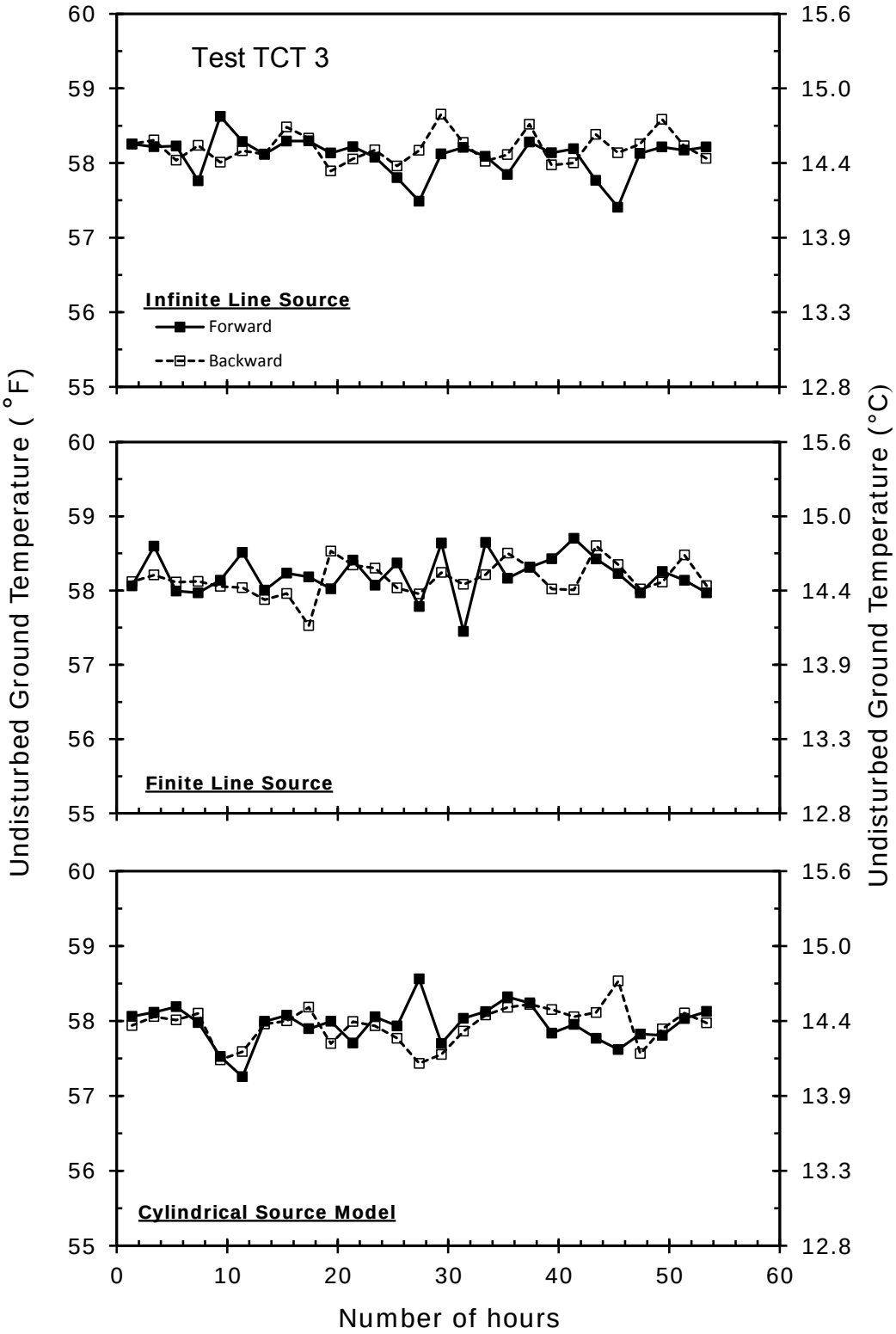

Figure XII.7. Undisturbed ground temperature estimated using various models incorporated in the parameter matching framework with no ambient air effects considered for TCT3.

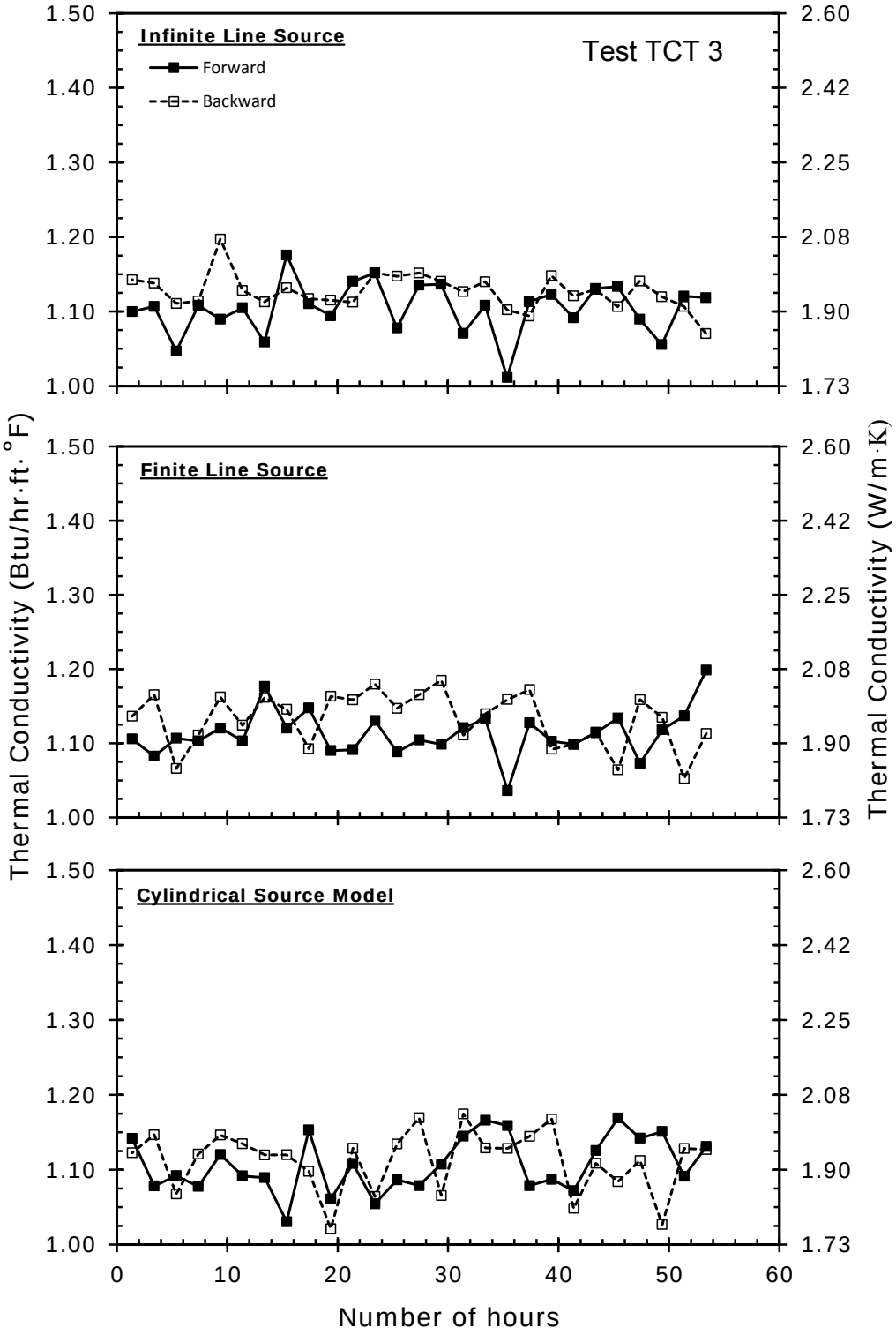

Figure XII.8. Thermal conductivity estimated using various models incorporated in the parameter matching framework with no ambient air effects considered for TCT3.

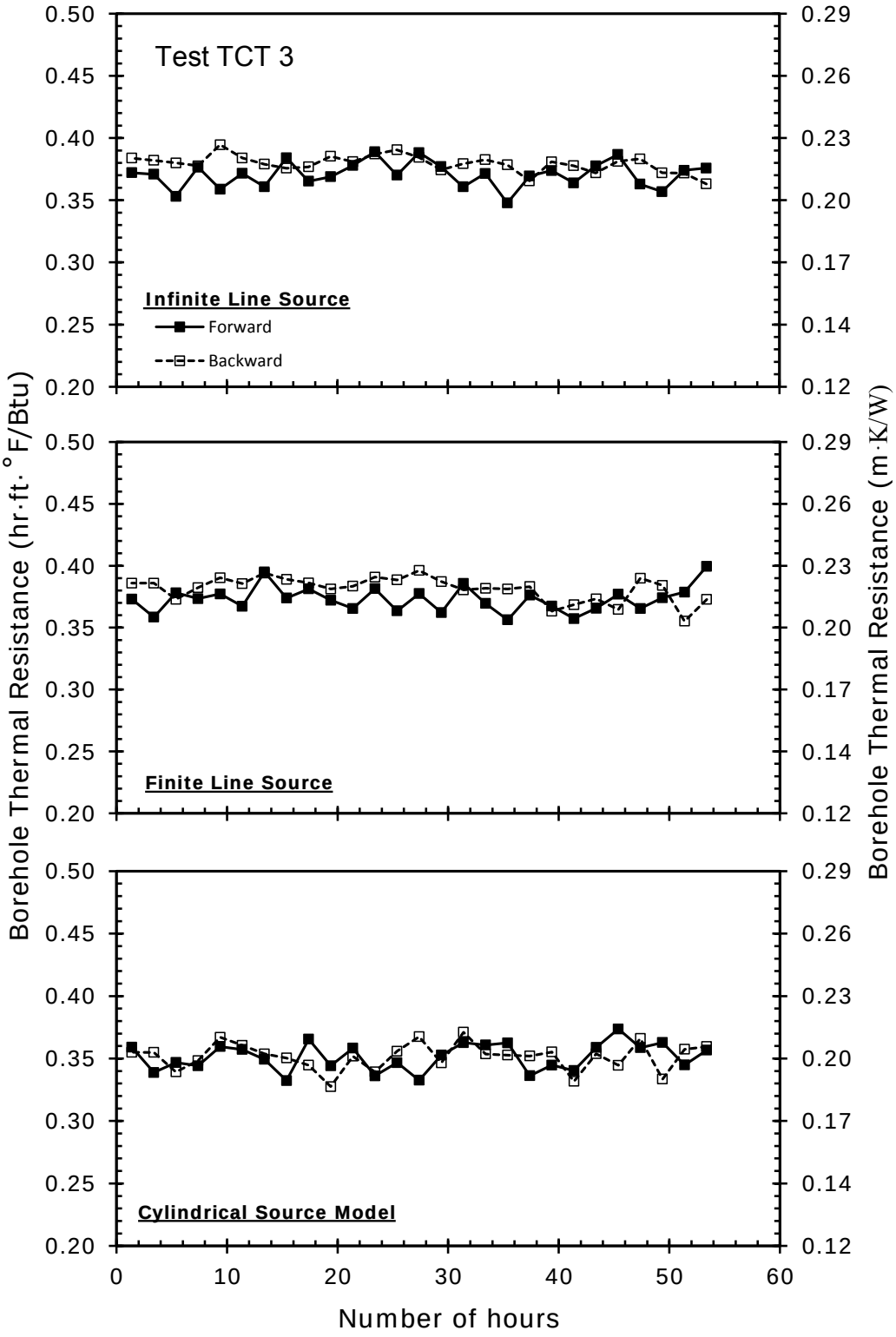

Figure XII.9. Thermal resistance of the heat exchanger estimated using various models incorporated in the parameter matching framework with no ambient air effects considered for TCT3.

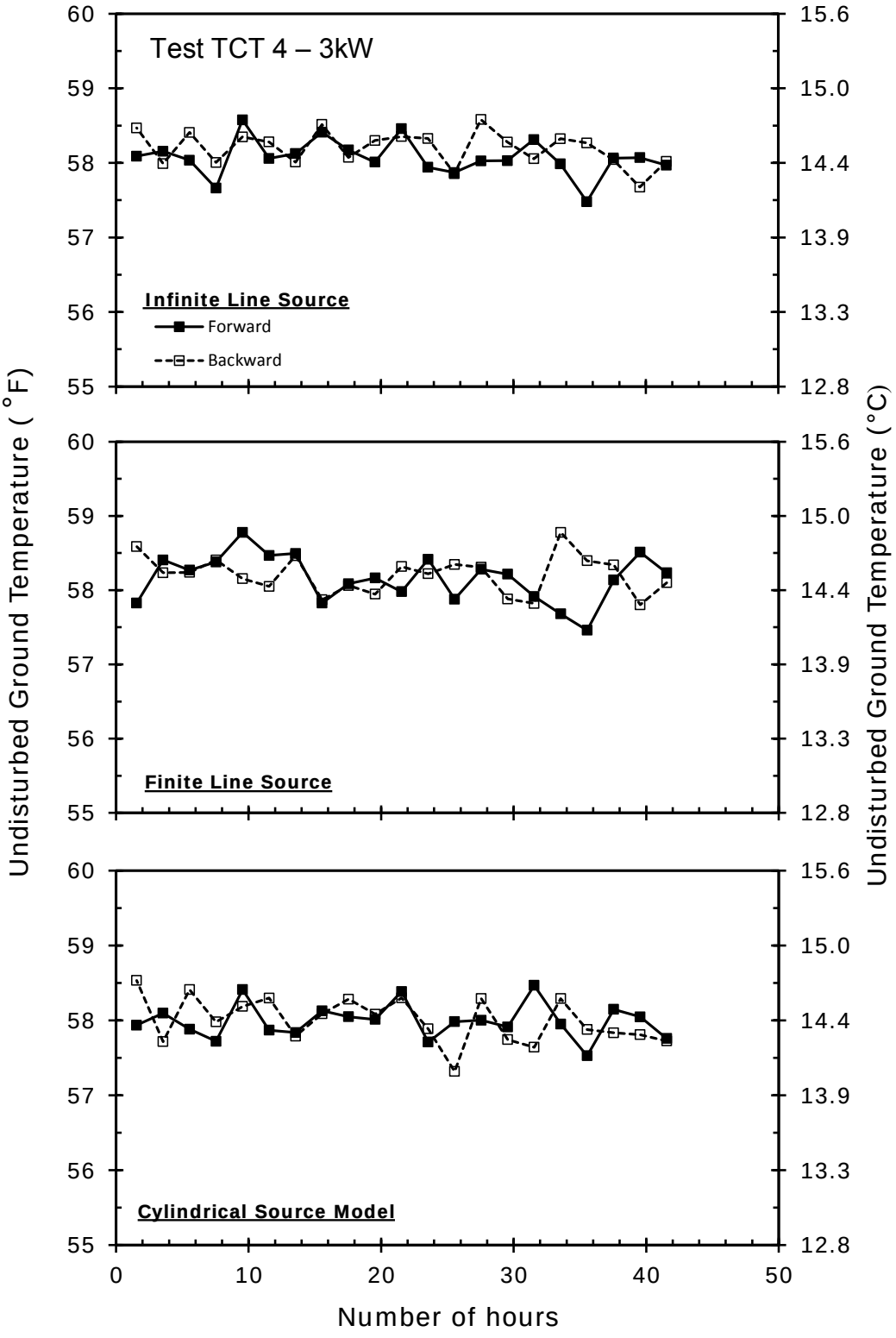

Figure XII.10. Undisturbed ground temperature estimated using various models incorporated in the parameter matching framework with no ambient air effects considered for TCT4.

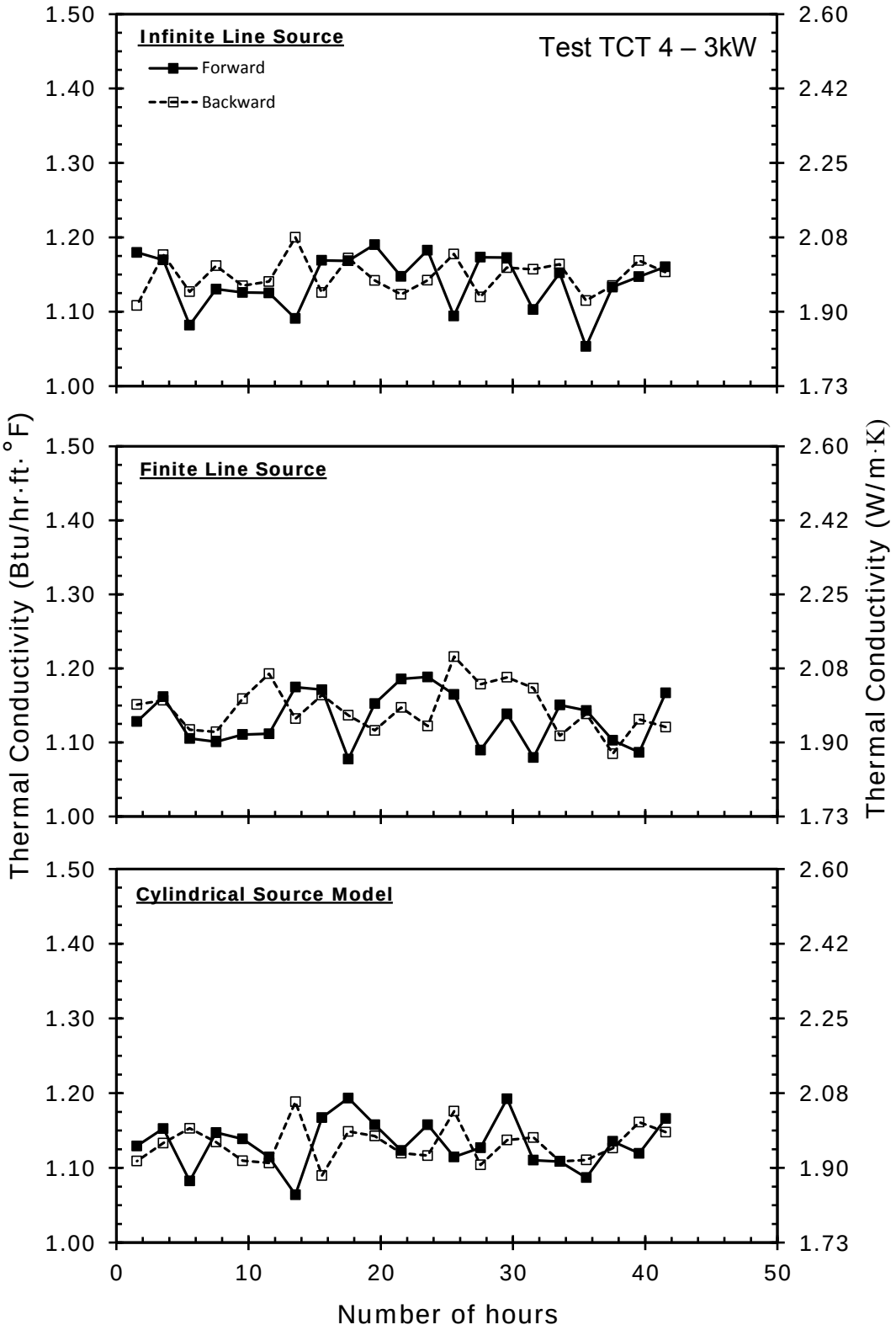

Figure XII.11. Thermal conductivity estimated using various models incorporated in the parameter matching framework with no ambient air effects considered for TCT4.

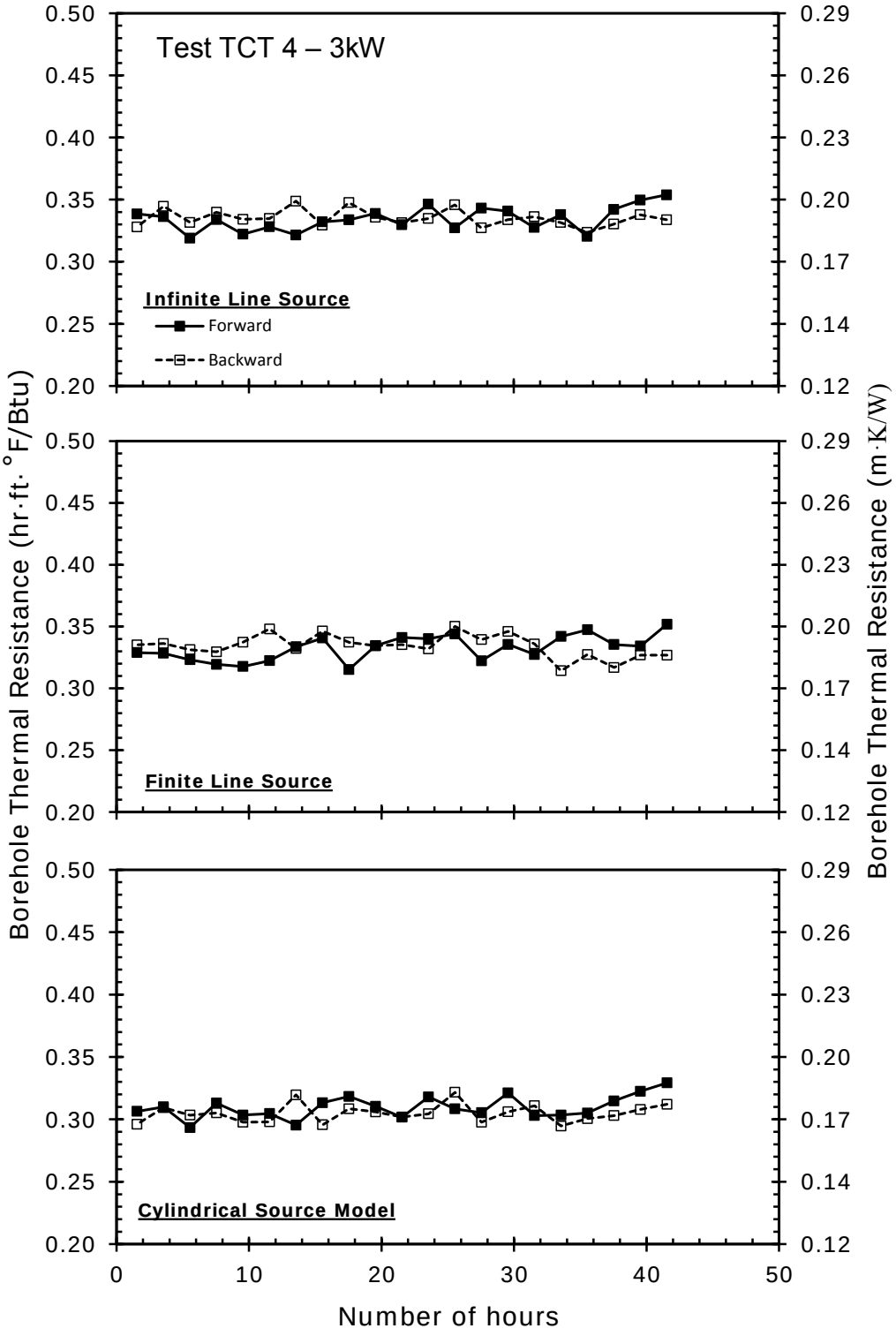

Figure XII.12. Thermal resistance of the heat exchanger estimated using various models incorporated in the parameter matching framework with no ambient air effects considered for TCT4.

Appendix XI

Parameter matching with ambient air correction using the infinite line source model, the finite line source model, and the cylindrical source model. Results include; percentage of the heat exchanged (loss) with the ambient air, the effective thermal conductivity of the ground, and the thermal resistance of the heat exchanger.

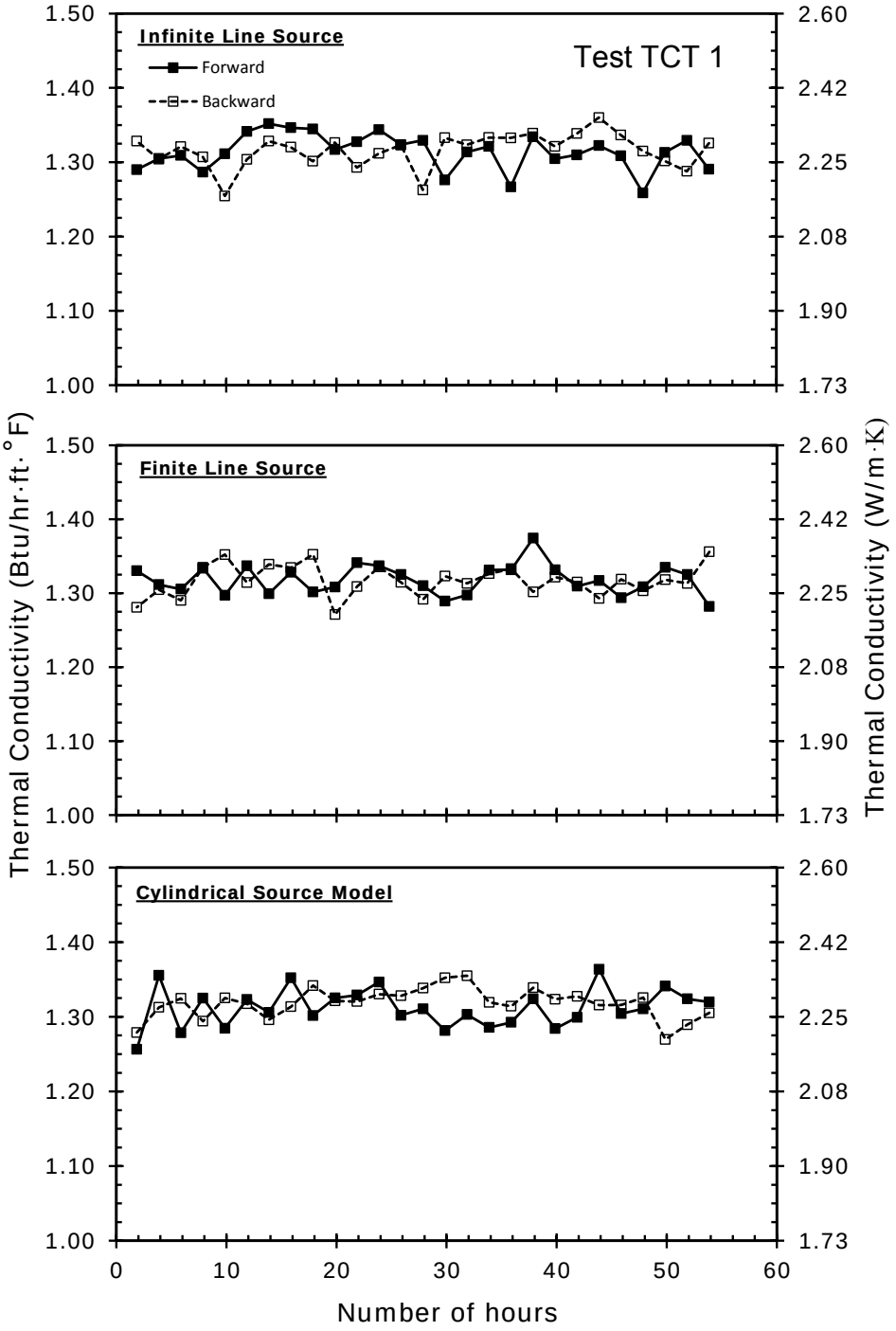

Figure XIII.1. Thermal conductivity of the ground estimated using various models incorporated in the parameter matching framework with no ambient air effects considered for TCT1.

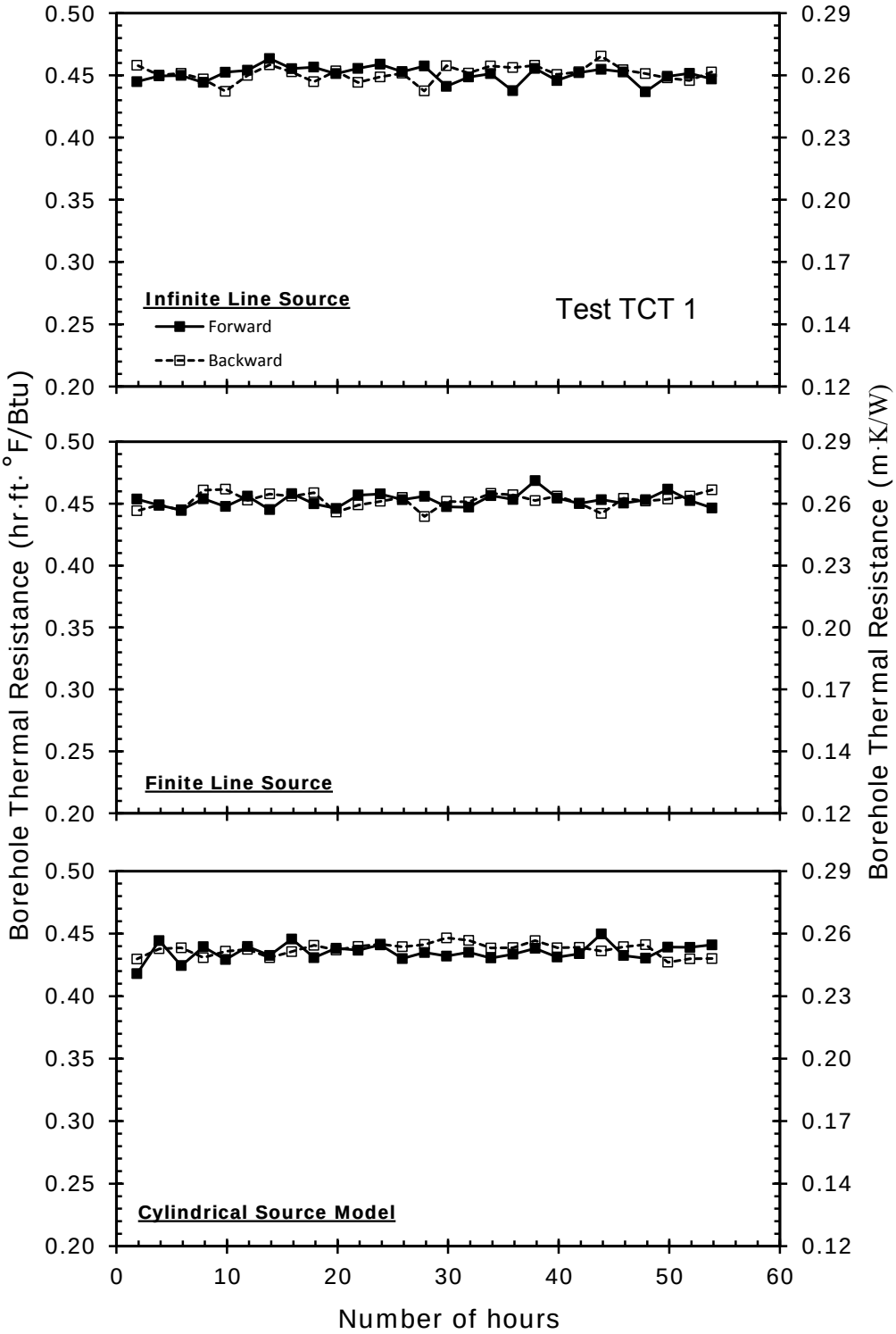

Figure XIII.2. Thermal resistance of the heat exchanger estimated using various models incorporated in the parameter matching framework with no ambient air effects considered for TCT1.

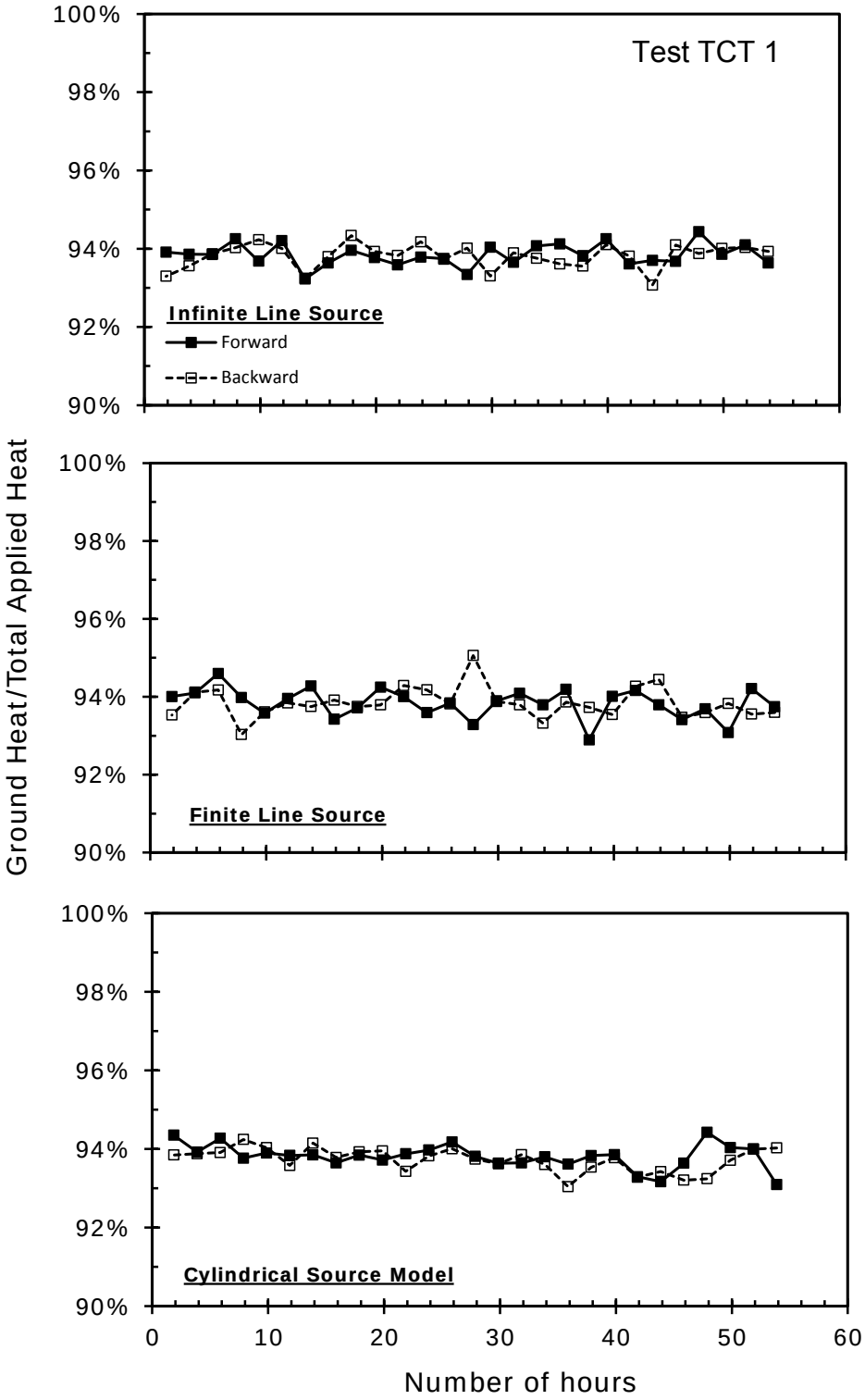

Figure XIII.3. Percentage of applied heat transferred to the ground estimated using various models incorporated in the parameter matching framework with no ambient air effects considered for TCT1.

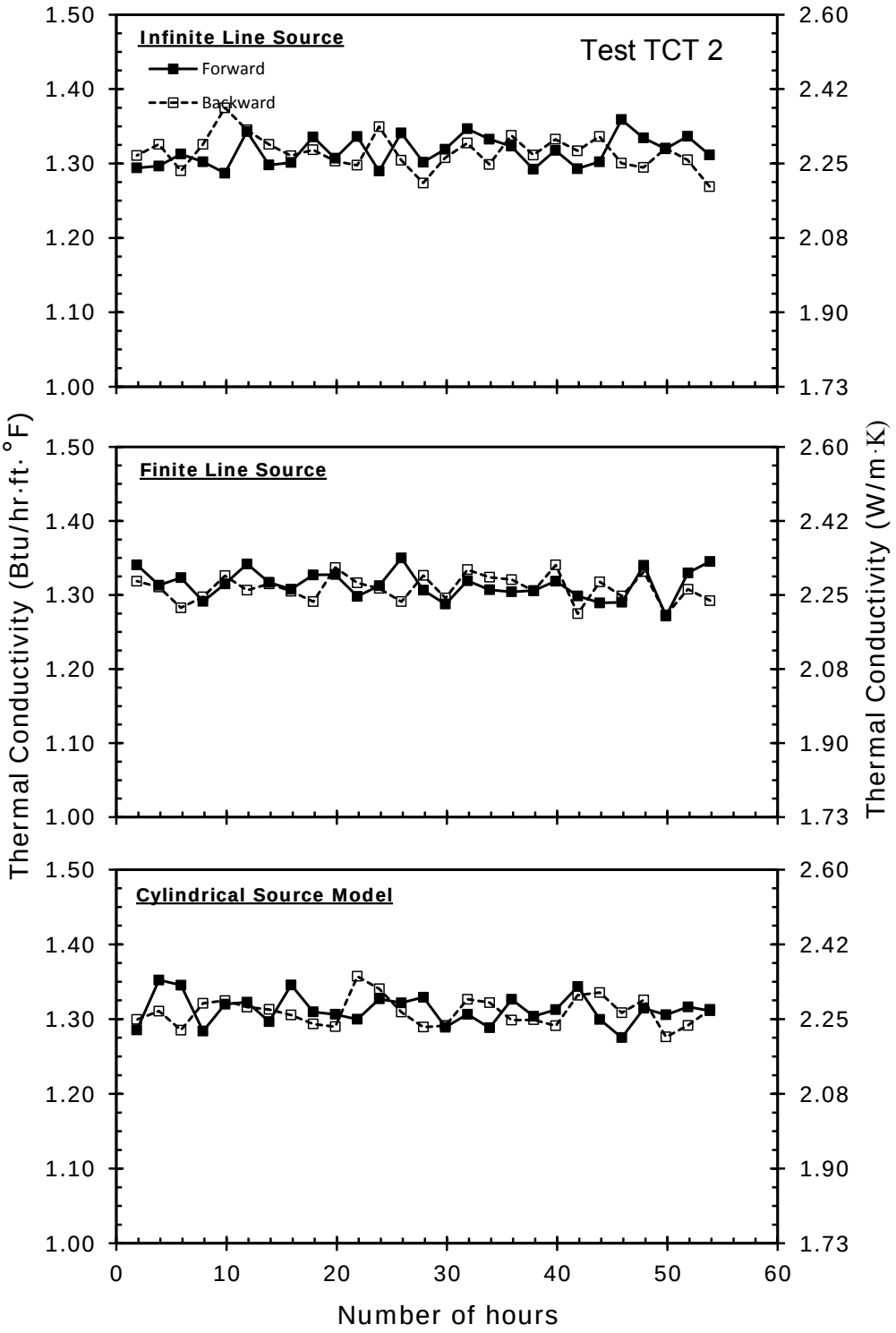

Figure XIII.4. Thermal conductivity of the ground estimated using various models incorporated in the parameter matching framework with no ambient air effects considered for TCT2.

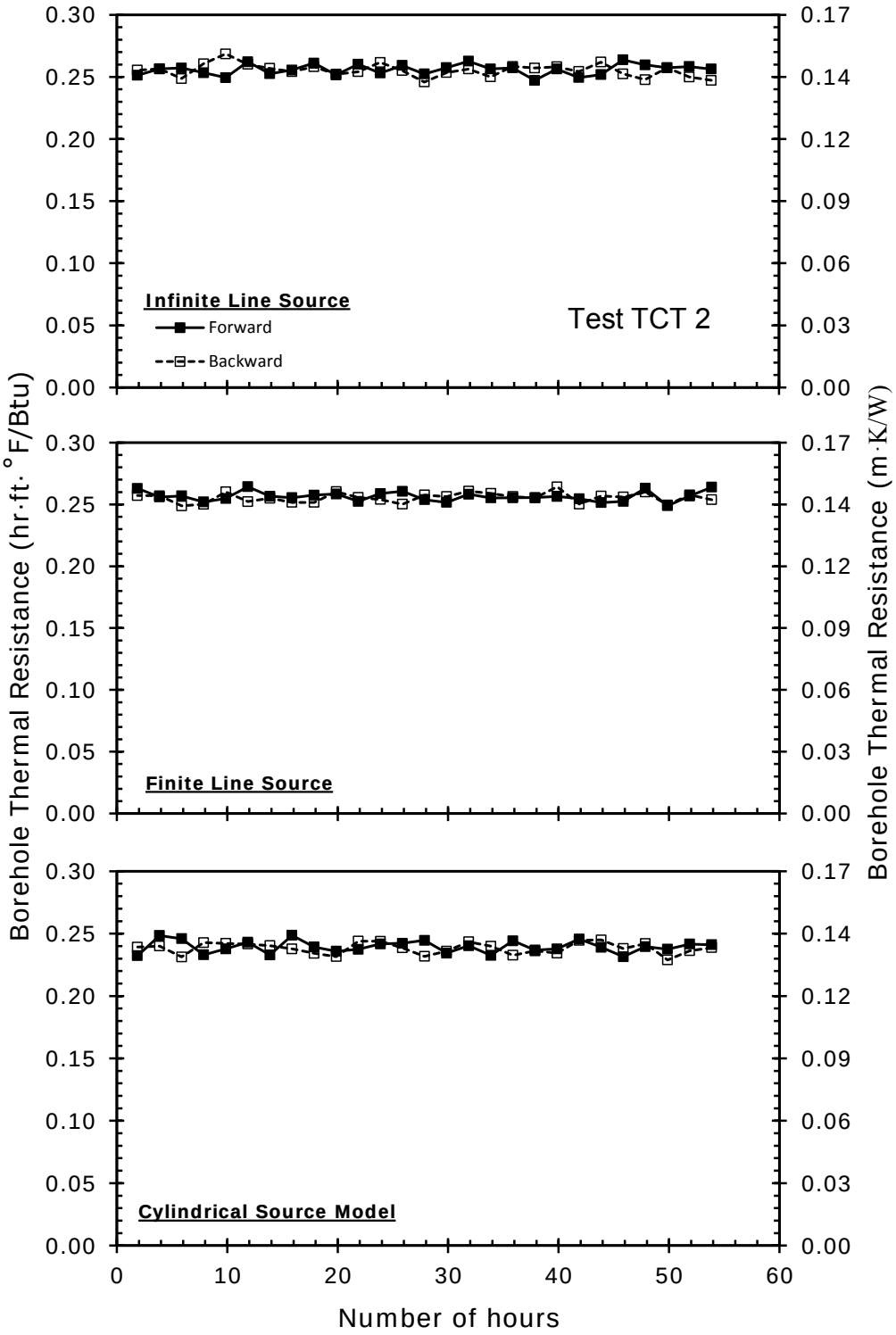

Figure XIII.5. Thermal resistance of the heat exchanger estimated using various models incorporated in the parameter matching framework with no ambient air effects considered for TCT2.

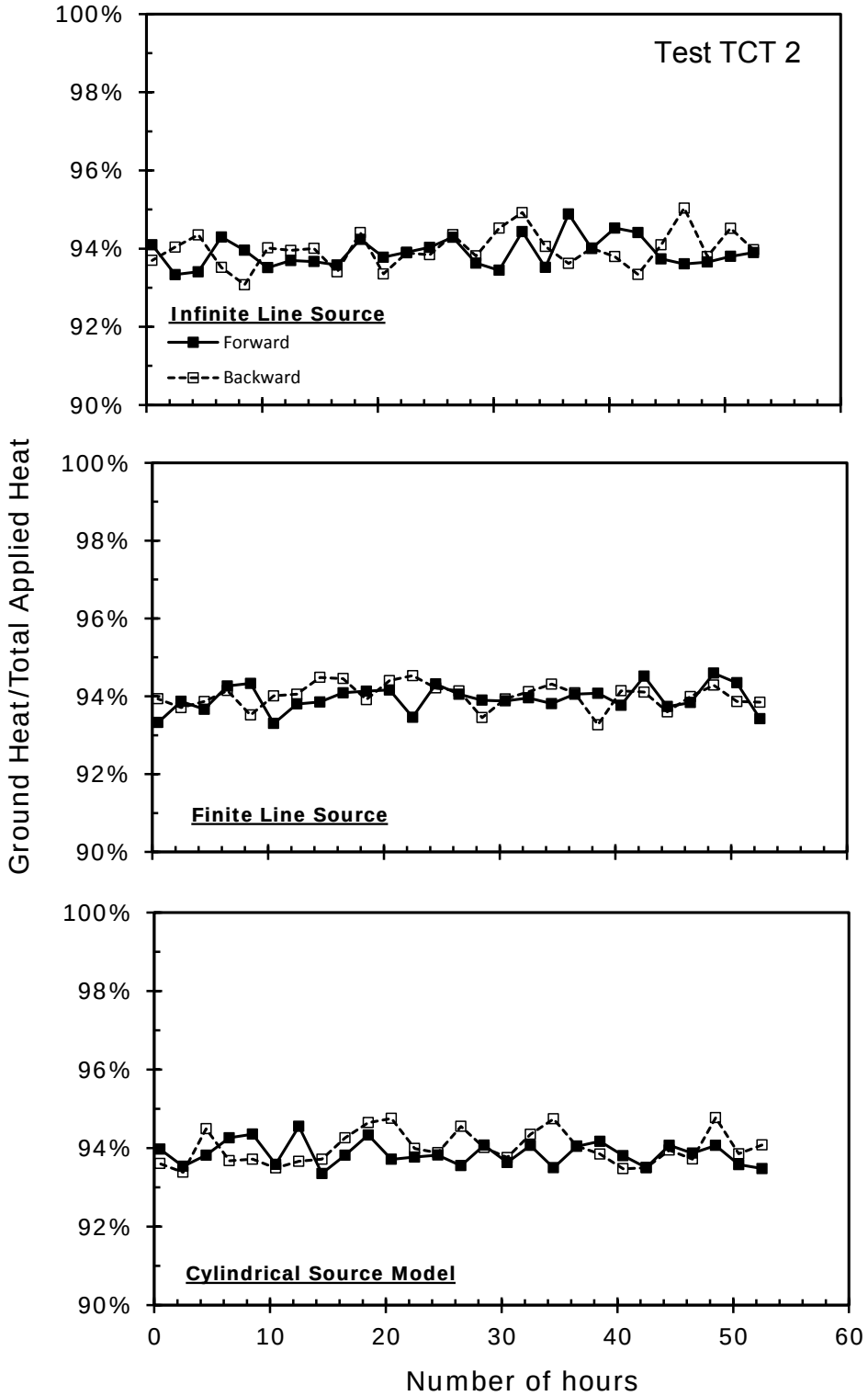

Figure XIII.6. Percentage of applied heat transferred to the ground estimated using various models incorporated in the parameter matching framework with no ambient air effects considered for TCT2.

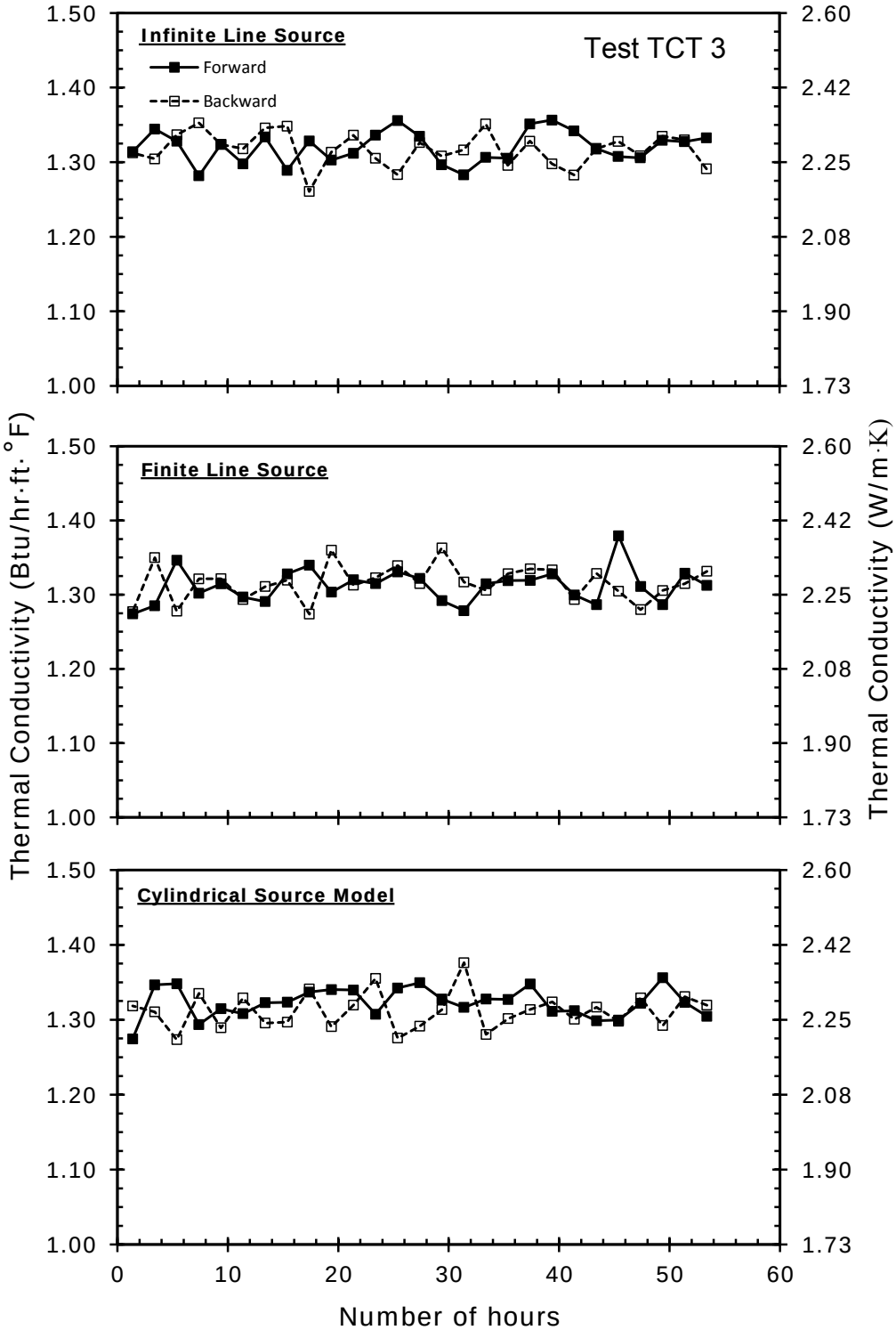

Figure XIII.7. Thermal conductivity of the ground estimated using various models incorporated in the parameter matching framework with no ambient air effects considered for TCT3.

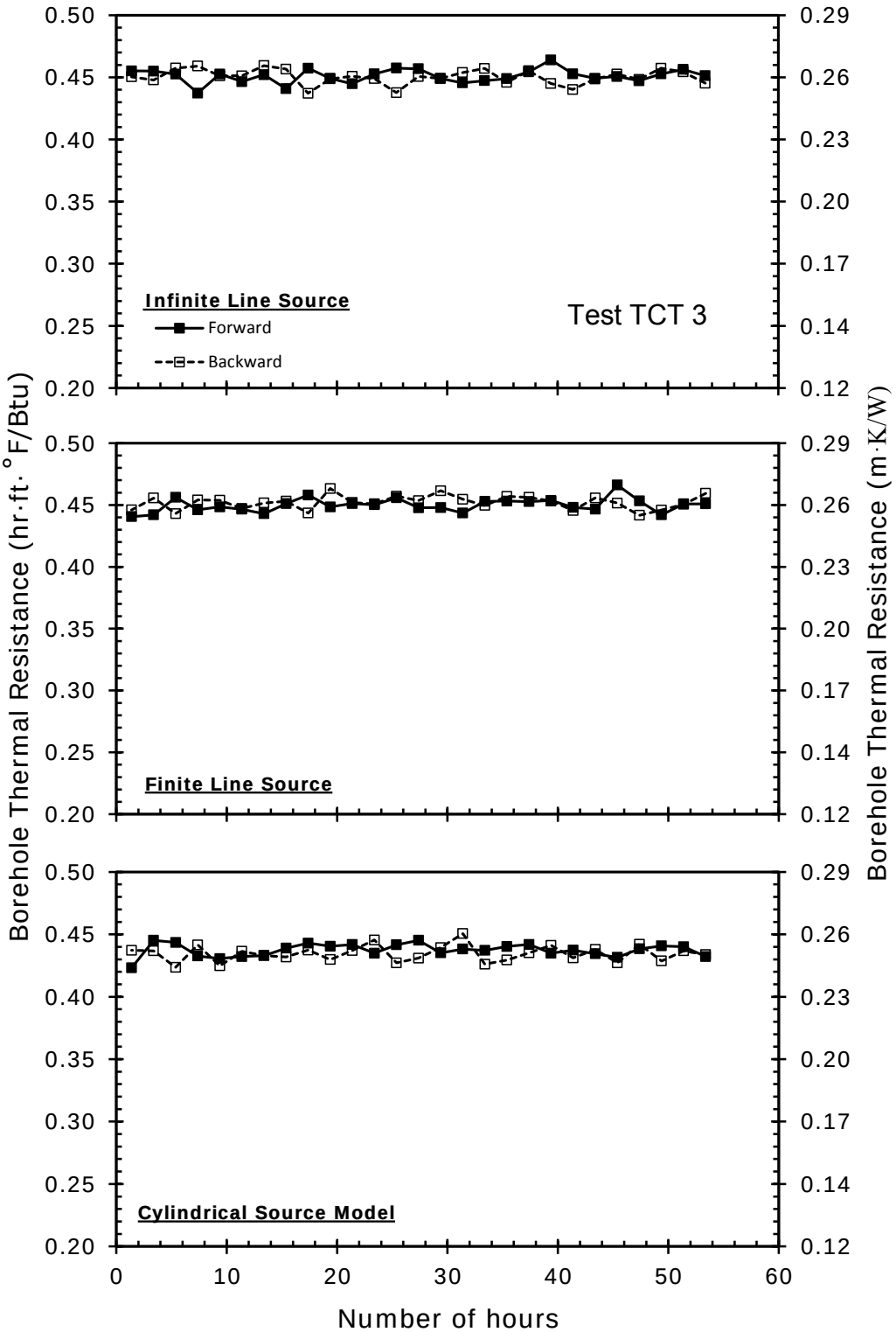

Figure XIII.8. Thermal resistance of the heat exchanger estimated using various models incorporated in the parameter matching framework with no ambient air effects considered for TCT3.

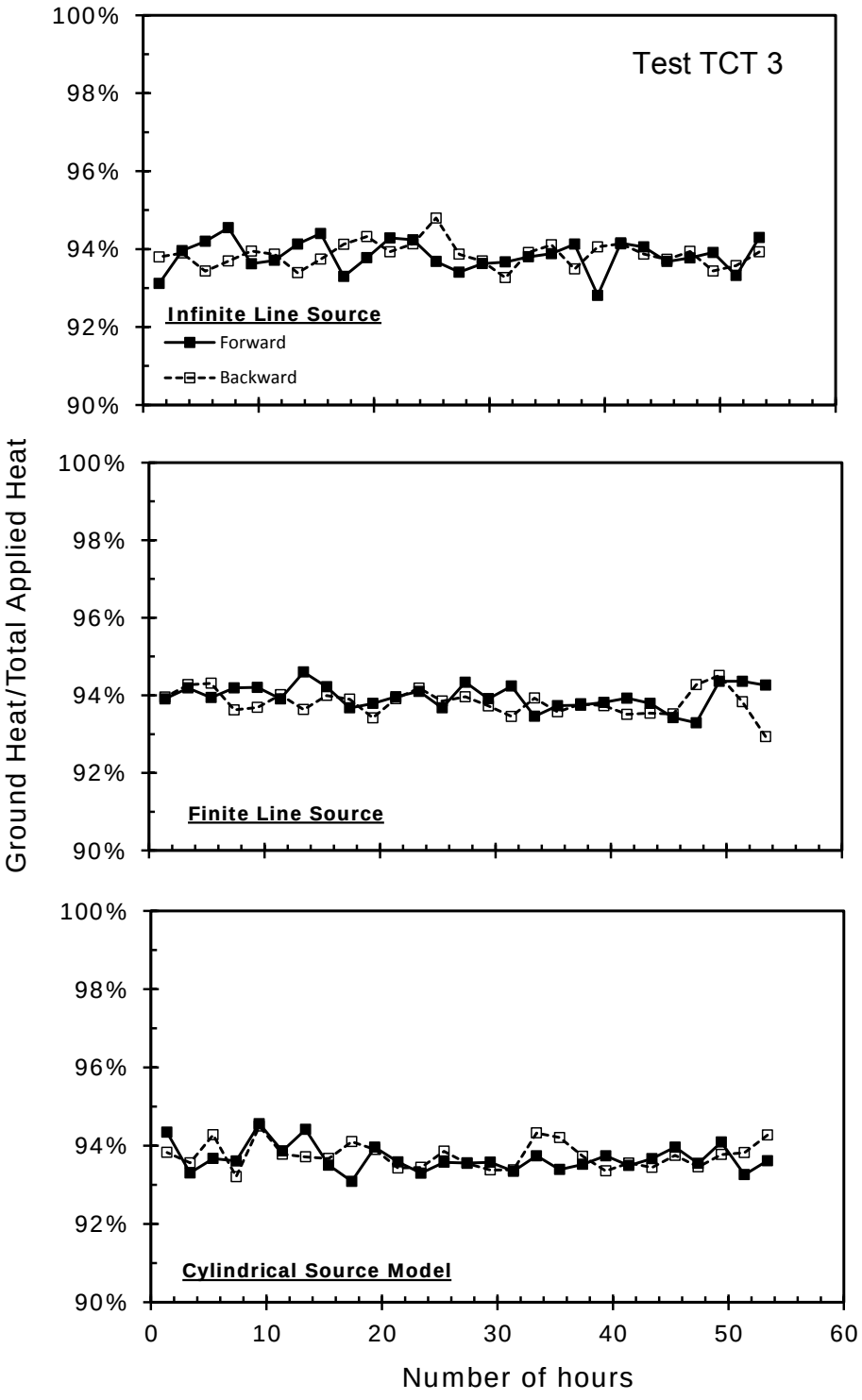

Figure XIII.9. Percentage of applied heat transferred to the ground estimated using various models incorporated in the parameter matching framework with no ambient air effects considered for TCT3.

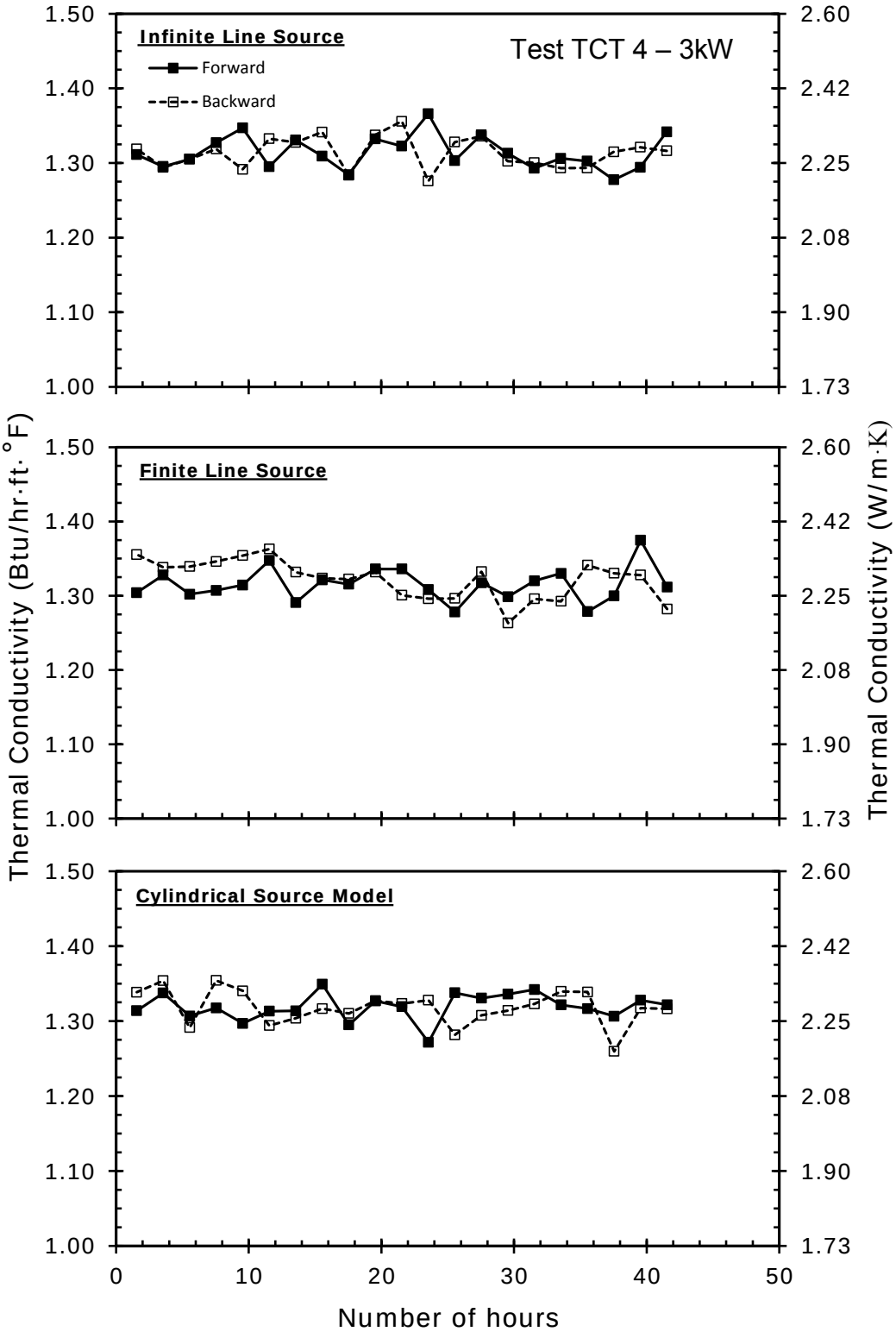

Figure XIII.10. Thermal conductivity of the ground estimated using various models incorporated in the parameter matching framework with no ambient air effects considered for TCT4.

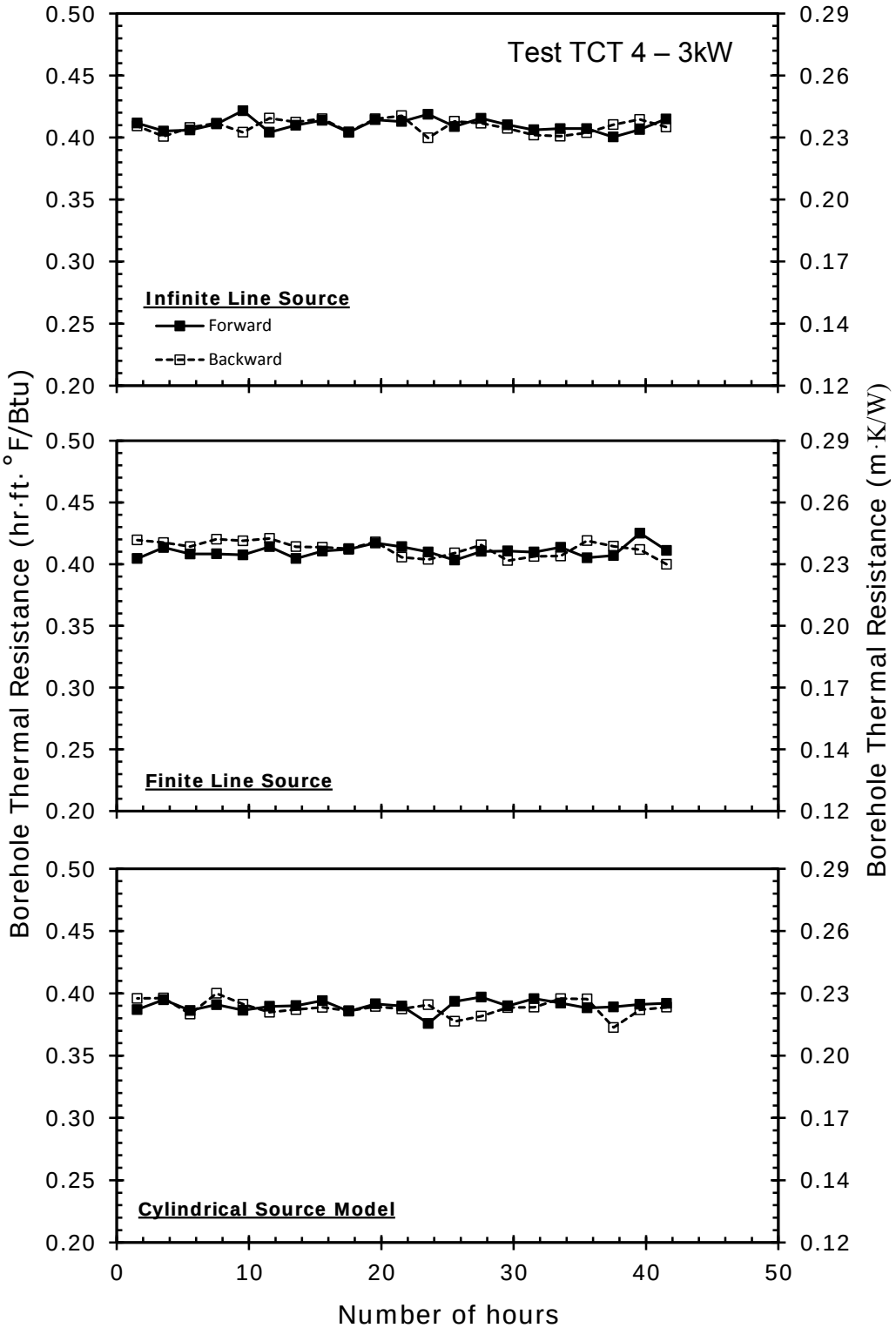

Figure XIII.11. Thermal resistance of the heat exchanger estimated using various models incorporated in the parameter matching framework with no ambient air effects considered for TCT4.

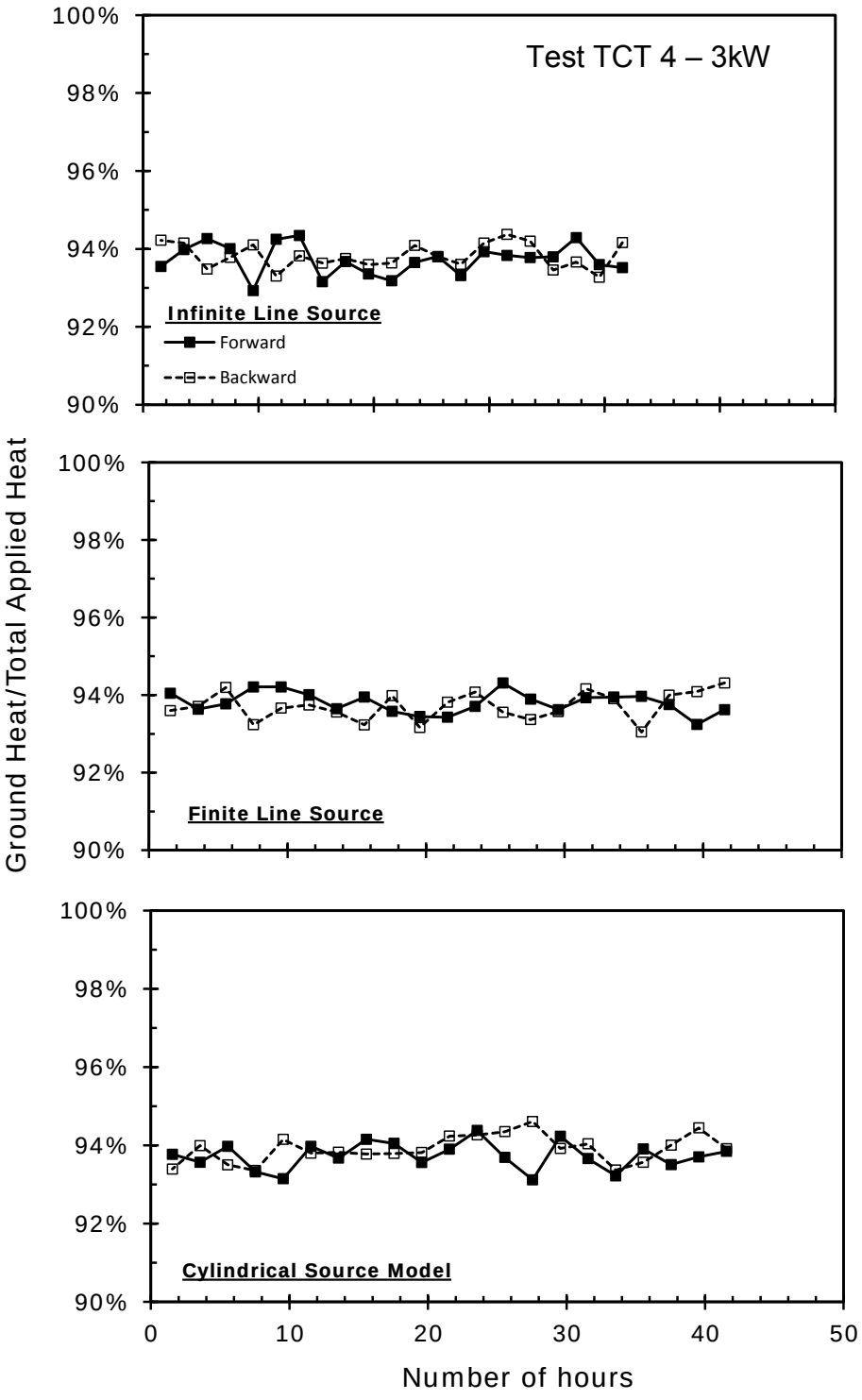

Figure XIII.12. Percentage of applied heat transferred to the ground estimated using various models incorporated in the parameter matching framework with no ambient air effects considered for TCT4.

CHAPTER 8. THERMO-MECHANICAL PILE LOAD TESTS

8.1. Introduction

Virginia Tech thermo-mechanical pile load testing program consisted of a mechanical loading phase and a thermal loading phase. The mechanical loading phase is essentially the same as a regular pile load test in which the pile is subjected to a compressive mechanical load. The thermal loading phase refers to subjecting the pile to a temperature change. The thermo-mechanical pile response is examined by subjecting the test pile to combined thermal and mechanical loading phases. The pile responses in each one of the phases were studied separately. Then the results of the thermal and mechanical phases are superimposed for understanding the overall thermo-mechanical behavior.

The test program included two mechanical phases and four thermal phases. The first mechanical phase was followed by a single thermal phase forming the first thermo-mechanical test named T-MT 1. After the end of this test, the mechanical and thermal loads applied on the Test Pile were released, and temperature and strain recovery was allowed. Thereafter, the second mechanical phase was initiated followed by three thermal phases forming T-MT 2, T-MT 3, and T-MT 4, respectively. Table 8-1 presents a list of the thermo-mechanical tests conducted as part of the testing program performed in this study.

Table 8-1. Virginia Tech thermo-mechanical tests performed on the Test Pile (Pile 1) as part of the testing program.

Test	Duration		Procedure and Equipment	General notes
	From	To		
T-MT 1	Oct. 27, 2011	Nov. 11, 2011	Temperature controlling equipment	--
T-MT 2	Nov. 21, 2011	Dec. 9, 2011		--
T-MT 3	Jan. 18, 2012	Jan. 20, 2012	Heat rate controlling equipment	Considered as TCT 4
T-MT 4	Feb. 18, 2012	Feb. 20, 2012	Temperature controlling equipment	Considered as TCT 5

*TCT: Thermal conductivity test, T-MT: Thermo-Mechanical test.

This chapter presents the testing procedures followed for different phases including the procedure for applying the mechanical load to the Test Pile (Pile 1), and procedures for applying the thermal loads by controlling the temperature of the inlet fluid or by controlling the applied heat rate. Moreover, the strains and stresses developed along the pile due to the applied mechanical and thermal loads are presented and discussed in Section 8.2. Temperature changes applied in the Test Pile, and its vicinity as well as the thermally induced strains along the Test Pile are presented in Section 8.3. Furthermore, a newly proposed finite element procedure to model the thermo-mechanical response of Energy Piles using decoupled analyses is presented and used to model thermo-mechanical load tests performed as part of this study.

8.2. Mechanical Loading Phase

This section presents the procedure followed to load the Test Pile mechanically. The pile head movement and strains along the Test Pile measured during each of the mechanical loading phases are presented afterwards. Pile head movement was measured using four dial gauges installed at the pile head while the strains along the Test Pile were measured using the strain

gauges installed in the pile. Also presented in this section is the distribution of the mechanical load along the Test Pile evaluated from the measured strains and the approximated pile modulus. The pile modulus was estimated using Fellenius (1989, 2001). Furthermore, the mechanical load distribution along the Test Pile was adjusted to account for the residual stresses using Fellenius (Fellenius, 2002a, b) for T-MT 1.

8.2.1. Loading Procedure

T-MT 1, was performed on the Test Pile (Pile 1) on October 27, 2011. After loading the Test Pile and monitoring its creep for 48 hours, the first thermal load was applied in the form of series of heating and cooling cycles as discussed later. A failure of one of the tube connections inside the hydraulic jack took place before finishing all the planned thermal cycles. This failure enforced an immediate release of the applied mechanical load in order to protect the hydraulic pump from the hot fluid. After fixing the failed connection, the second thermo-mechanical pile load test, i.e. T-MT 2, was initiated on November 21, 2011.

The quick pile load test procedure of the ASTM D-1143 (ASTM, 2007) was adopted while applying the mechanical load to the Test Pile in the two mechanical loading phases. The quick test is also known as procedure "A" in the ASTM D-1143 for testing deep foundations under static axial compressive loads (ASTM, 2007). Procedure "A" of the ASTM pile load standard indicates that; (1) the pile should be loaded in 5% increments up to the anticipated failure load but not to exceed the structural capacity of the pile, and (2) a constant time interval between 5-15 minutes for all loading increments should be used. For the Test Pile and as expected for a small diameter micropile embedded in rock, the structural capacity of the pile controlled the maximum load that can be applied on the pile. This maximum load for the Test Pile was estimated as 1334 kN (150 tons or 300 kips). Thus, twenty 66.7 kN (7.5 tons or 15 kips) increments were used to load the pile up to the 1334 kN (150 tons) ultimate load. Each load increment was maintained for 10 minutes during which readings of the four dial gauges at the pile head were recorded every 2 minutes. The pile creep was monitored for 48 hours after reaching the ultimate load and before the beginning of the thermal loading phase.

The time interval for each loading step was selected to assure minimal interaction between subsequent load steps. The limiting movement rate mentioned in the maintained pile load test procedure "B" of the ASTM D-1143 standard (ASTM, 2007) was used to estimate the loading time interval. The limiting movement rate mentioned in procedure B is 0.254 mm/hr (0.01 in/hr) referring to a small movement from the current loading step which will not affect the movement of the subsequent steps. As presented in the following sections, the axial movements observed during each loading step of the first and the second load tests were less than 0.3 mm/hr (0.012 in/hr).

8.2.2. Load-Displacement Relation

The readings of the four dial gauges placed at the pile head were recorded every 2 minutes during the first and the second load tests. These readings were used to evaluate the pile head displacement corresponding to different load levels. The displacement at the location of a dial gauge at any time is the difference between the current reading of the gauge and the initial reading. The pile head displacement was then calculated as the average of the four displacements of the dial gauges. Positive displacements refer to downward movements of the pile head while negative displacements represent upward movements of the pile head. The pile head movement versus the head load for T-MT 1 and T-MT 2 are shown in Figure 8.1.

It can be seen in Figure 8.1 that the pile head movement under the 1334 kN (150 tons) ultimate load is about 8 mm (0.3 inch). Moreover, the head load-displacement curves for the

first and the second load tests are similar when the load at the pile head is less than 667 kN (75 ton). When the loads at the pile head is more than 667 kN (75 ton), T-MT 2 showed a slightly stiffer response with less pile head movement than T-MT 1. Furthermore, the creep displacement at the pile head was less than 1 mm after 48 hours from applying the ultimate load for both of the load tests.

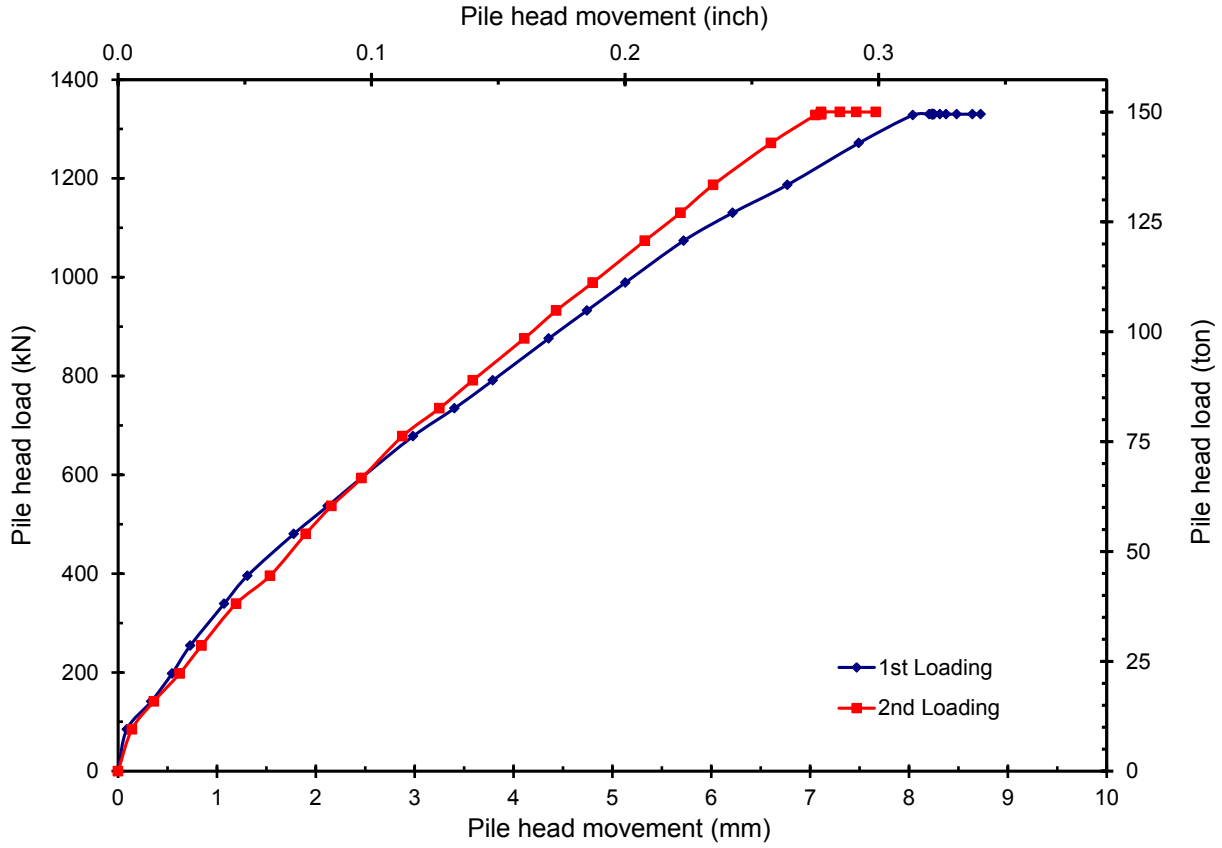

Figure 8.1. Pile head movement-load curves for 1st and 2nd load tests.

8.2.3. Measured Strain Profiles

Vibrating wire strain gauges are used to measure the strains along the Test Pile. These gauges measure the frequency of a vibrating wire tensioned between the two flanges. The change of the distance between the flanges causes the wire tension to vary which, consequently, results in different vibrating frequency of the wire. This dependency of the frequency on the distance between the flanges is the main concept behind measurement of deformation with vibrating wire strain gauges. The vibrating wire frequency is internally processed by the data logger and translated into a linear strain unit using various gauge constants provided by the manufacturer and confirmed by the gauge calibration process. The strain due to a mechanical load at the location of a gauge is measured in units of microstrain, i.e. $\Delta L/L \times 10^{-6}$.

The strains at different depths along the Test Pile were evaluated using the strain gauges following the procedure outlined earlier. Values of strains along the pile are plotted in Figure 8.2 for the first and second load tests. As seen in this figure, the strains along the pile segment embedded within the top silty sand layer are two orders of magnitude larger than those in the pile

segment embedded within the shale layer for both load tests. This is due to having no load transferred to the pile in this shale layer as discussed in the following section.

Furthermore as the depth increases, the load in the pile decreases due to the increased shaft resistance. This reduction in the pile load with depth generates smaller strains in the pile as depth increases for constant pile elastic modulus. In other words, it is expected to have larger strains at shallow depths because of the higher loads within the pile at these depths. This response is not observed in Figure 8.2 which shows less strains at 3 m (10 ft) and 6 m (20 ft) compared to the strains at 9 m (30 ft) and 12 m (40 ft). The contradiction between the observed and the expected responses is attributed to the composite section of the pile and its small cross-sectional area which caused the pile elastic modulus to decrease as the depth increases as explained in the following section.

Moreover, the strain-load relations in the top silty sand layer for T-MT 2 are more linear compared to those for T-MT 1. This response is expected for a reloading path of concrete elements. Furthermore, it can be seen in Figure 8.2 that for the range of the measured strain, the pile tangent modulus at depth 3 m (10 ft) did not change for both load tests while the second loading at depth 6 m (20 ft) has a slightly less tangent modulus compared to the first loading. On the other hand, the strain-load relations from the first and the second loadings at depths 9 m (30 ft) and 12 m (40 ft) are divided into an initial zone within which the first load test has a higher tangent modulus followed by a zone over which the response is reversed, i.e. the second load test has a higher tangent modulus. The transition between these two zones takes place at about 100 microstrain. The increase of the pile tangent modulus for depths 9 m (30 ft) and 12 m (40 ft) in the second load test agrees with the reduced pile head movement observed in this load test as shown in Figure 8.1. A more detailed discussion about the change of the pile modulus is presented in the following sections.

Additionally, the same strain-load relation at 15 m (50 ft) in the shale layer was obtained for both load tests as shown in Figure 8.2.b. In the second load test, the pile appears to be expanding within the shale layer rather than the small compressive behavior observed in the first load test. This pile expansion at depths below 21.3 m (70 ft) is due to the recovery of thermal strains produced by the thermal tests conducted as part of T-MT 1. As will be discussed in Section 8.3, part of the thermal strains produced when the Test Pile was subjected to thermal loads during T-MT 1 was locked in the pile. At depths below 70ft, these thermal strains developed during the thermal phase of T-MT 1 was not fully recovered when T-MT 2 was initiated. The recovery rate of these thermal strains was higher than the compression rate of the pile due to the applied mechanical load in the second loading. This difference in the recovery and compression rates showed final tensile measured strains for depths below 21.3 m (70ft).

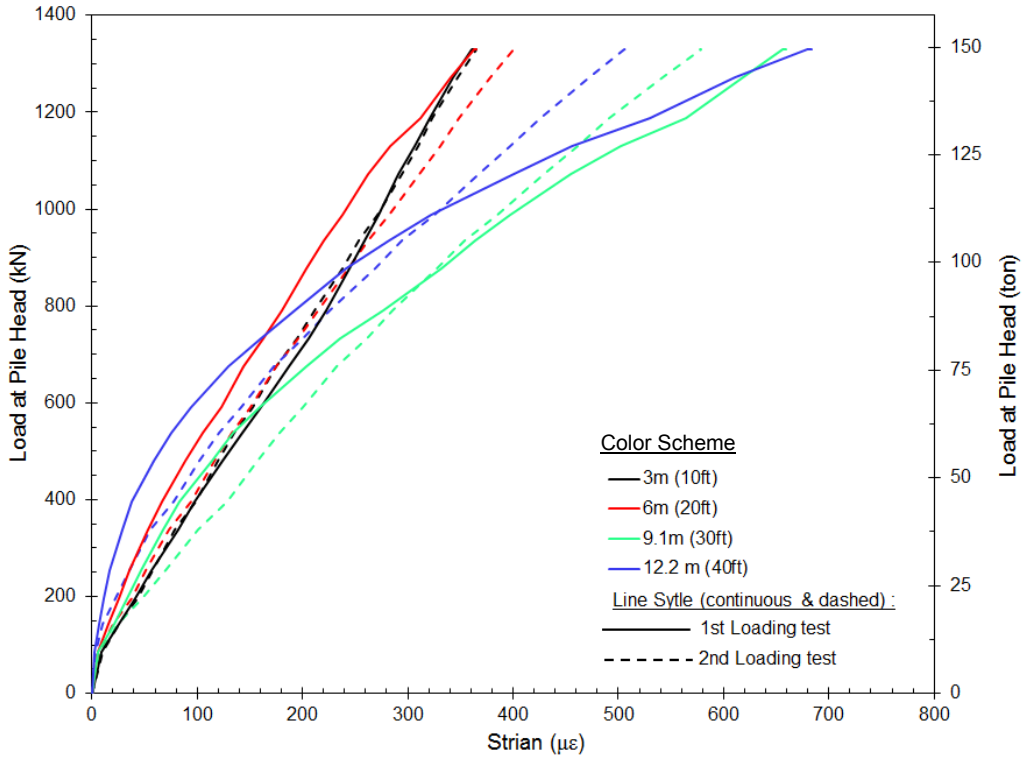

(a) for gauges in the top silty sand layer

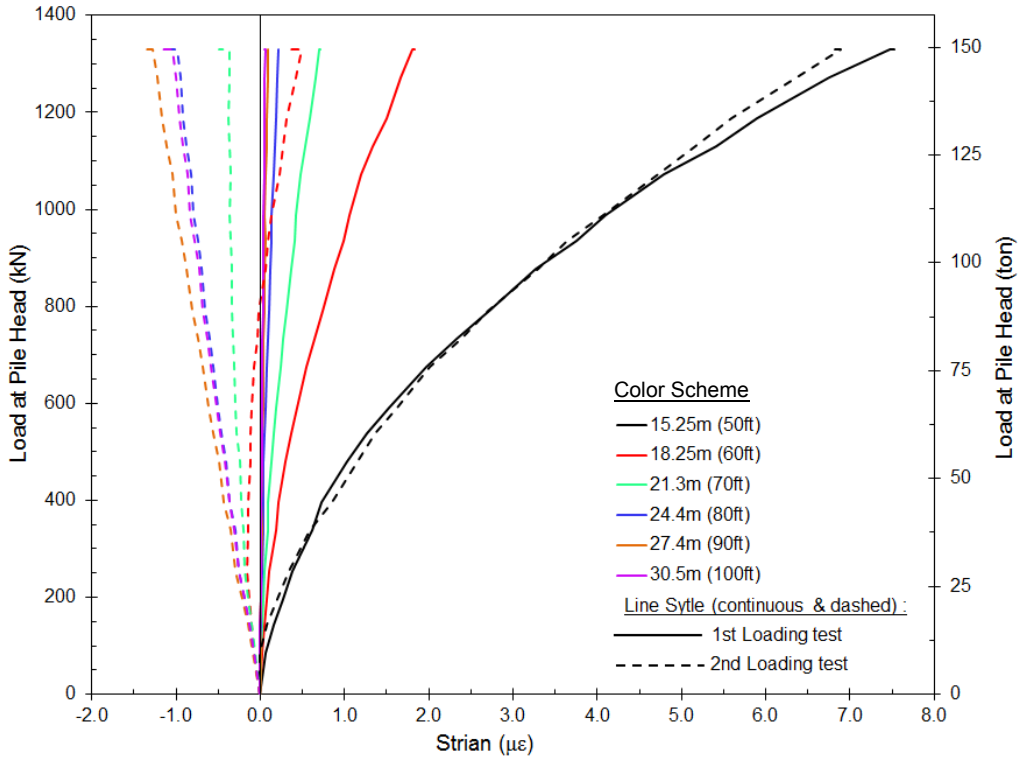

(b) for gauges in the bottom Shale layer

Figure 8.2. Measured strains along the pile during the 1st and the 2nd load tests.

8.2.4. Mechanical Load Profile

In order to analyze the effect of the thermal loads on the load carrying mechanism of the Test Pile, the mechanical load profile along the pile should be estimated. As discussed earlier, the strain gauges installed in the pile measure strains at various depths. A reliable estimate of the pile modulus is required to translate these measured strains into loads. This section presents the procedure followed to estimate the pile modulus at each depth and then estimating the true load profile along the pile.

(a) Pile Tangent Modulus

The pile modulus depends on the relative proportions and moduli of different materials forming the pile. For steel piles, the pile modulus is constant and equal to the steel modulus which results on a linear stress-strain relationship. For non-steel piles including concrete piles and composite piles such as the Test Pile, a second degree stress-strain relationship is expected which indicate that the tangent modulus is a linear strain-dependent (Fellenius, 1989). These linear stress-strain relation for steel piles and the strain-dependent modulus for composite piles are observed only when the ultimate shaft resistance was reached during a load test (Fellenius, 1989).

Fellenius (1989, 2001b) suggested a robust procedure to approximate the pile modulus form the measured strains in the pile. This procedure is to plot the tangent modulus in the y-axis versus the measured strain in the x-axis. The tangent modulus is estimated as the ratio between the applied incremental stress at the pile head and the measured incremental strain corresponding to such stress increment at the depth of interest. The pile modulus can be inferred when the tangent modulus–strain relation reaches either a constant value for steel piles or a linear relation for composite piles.

As described in Chapter 6, the tested pile has a composite section with a 25 cm (10 inch) diameter. The entire pile length has a centered 25.4 mm (1 inch) steel bar surrounded by the cement paste. The Test Pile is divided into two cross-sectional zones with respect to the existence of an external steel casing around the cement paste. The first zone is the top 9.75 m (32 ft) which has a 6 mm (0.25 inch) thick steel casing, and the second zone is the lower 20.7 m (68 ft) which has no steel casing. Due to this variation in the pile section, Fellenius procedure (1982, 2001b) was applied to determine the pile modulus for each strain gauge separately.

The tangent modulus–strain relations for strain gauges located at 3 m (10 ft), 6 m (20 ft), 9.1 m (30 ft), and 12.2 m (40 ft) for the first and the second load tests are shown in Figure 8.3. It is observed in this figure that for each of the load tests; (1) the pile tangent modulus decreases as the depth increases, (2) the pile moduli estimated from strain gauges at depths 3 m (10 ft), 6 m (20 ft), and 9.1 m (30 ft) converged to strain-independent constant values, and (3) a strain-dependent pile modulus was observed at depth 12.2 m (40 ft)).

Although the pile has a composite cross section, constant strain-independent pile moduli were observed at 3 m (10 ft), 6 m (20 ft), and 9.1 m (30 ft) which was attributed to having the linear stress-strain behavior of the steel dominate the pile response at these depths. The steel dominated the pile response because of the relatively high steel modulus compared to the cement paste modulus which affects the overall pile modulus. Moreover, the pile modulus at 6 m (20 ft) is slightly less than that at 3 m (10 ft) due to the varying consistency of the cement paste. On the other hand, a considerable reduction in the pile modulus was observed at 9.1 m (30 ft) which was attributed to the increased strains at this depth. The strains at 9.1 m (30 ft) were higher due to the weaker pile cement-section below 9.75 m (32 ft) at which the steel casing was terminated causing more strains to develop within this pile segment. Furthermore, the strain-dependent pile

modulus observed at 12.2 m (40 ft) was expected because at this depth only the cement paste controls the pile response.

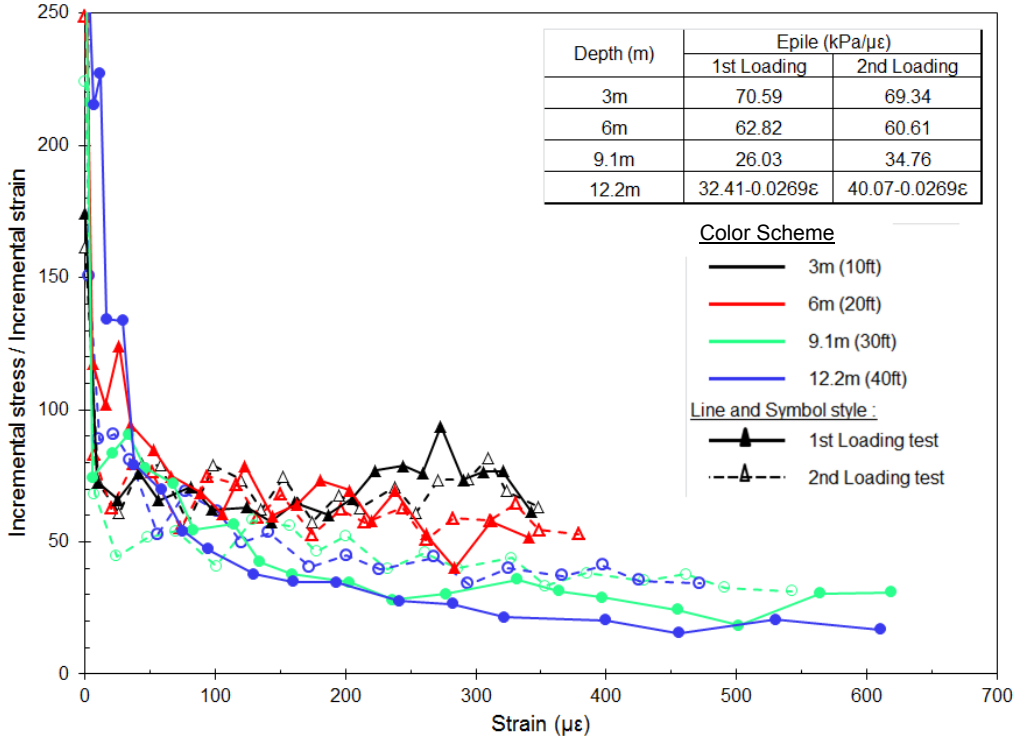

Figure 8.3. Tangent modulus for the Test Pile at different depths from the results of the 1st and the 2nd load tests.

It was not possible to estimate the pile modulus using Fellenius procedure for any of the strain gauges located below 12.8 m (42 ft) in the pile segment embedded in the shale layer because of the small measured strains which caused the modulus-strain relation to fluctuate over the measured strain range. Therefore, it was decided to use the pile modulus linear relation obtained at 12.2 m (40 ft) to translate the strains measured below 12.8 m (42 ft) into stresses in the pile.

Furthermore, pile moduli estimated from the second loading at 3 m (10 ft) and 6 m (20 ft) were not significantly different from those estimated from the first loading. On the other hand, pile moduli estimated from the second loading at depths 9.1 m (30 ft) and 12.2 m (40 ft) were found to be more than those estimated from the first loading. These changes are due to the expected elastic pile response in a loading-unloading-reloading cycle as in the second load test.

(b) Load Profile from Measured Strains

The estimated pile tangent moduli were used to translate the measured strains into loads in the pile. The load in the pile (P) was estimated as $P = EA\varepsilon$; where E is the estimated pile modulus at the considered depth, A is the cross sectional area of the pile and ε is the measured strain. Figure 8.4(a) shows the load distribution at the ultimate head load (150 tons) during the first load test. As seen in this figure, no load was observed in the pile below 15.25 m (50 ft). In other words, the majority of the load applied at the pile head was countered by the frictional resistances along the pile shaft in the top 12.8 m (42 ft) silty sand layer and the top 2.45 m (8 ft) of the shale layer.

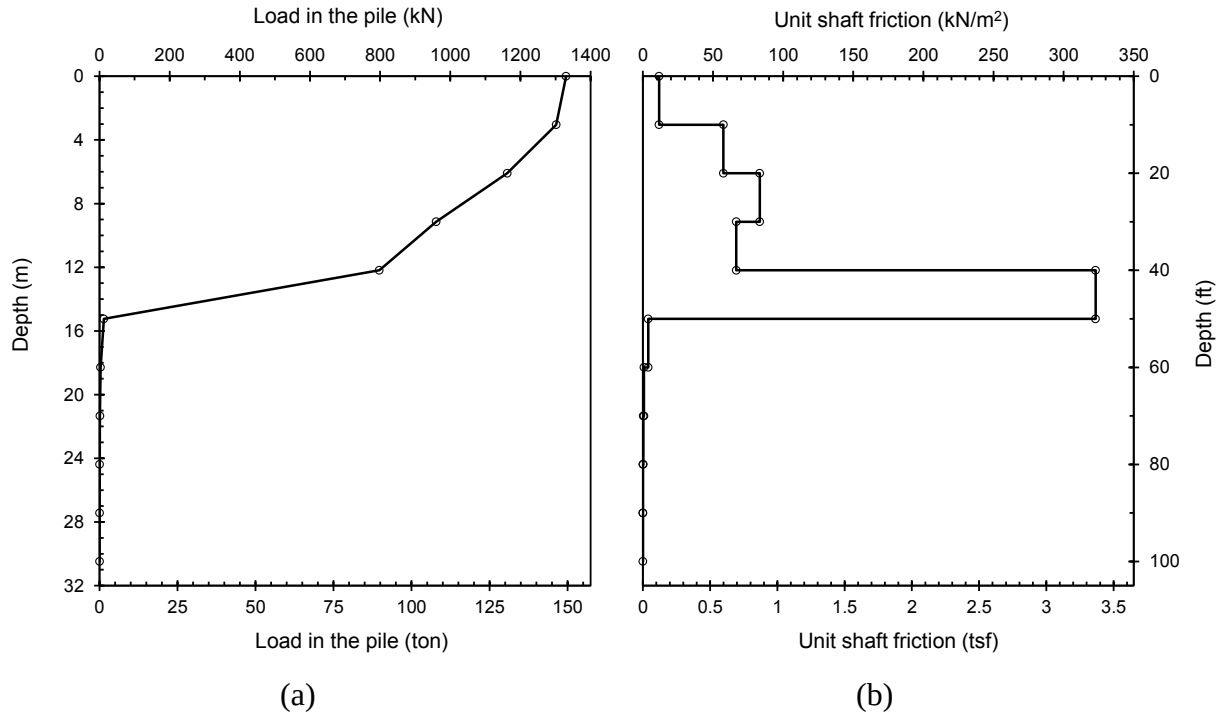

Figure 8.4. Estimated load profiles along the pile for each loading step of the first load test.

Moreover, the load in the pile is reduced as the depth increases because of the frictional resistance along the pile shaft. The load difference between any two points along the pile represents the frictional resistance developed along the segment of the pile shaft bounded between the considered points. The frictional resistance along a pile segment (R_s) is estimated as $R_s=q_sL_sA_s$, where q_s is the unit shaft friction along a pile segment of length L_s for a pile with A_s circumference. Therefore, the unit shaft friction along a pile segment (q_s) can be back-calculated as the slope of the load profile within this segment (R_s/L_s) divided by the pile circumference (A_s).

Thus, the Test Pile was divided into ten segments each is bounded by two strain gauges. The unit shaft friction along each segment was back-calculated as described earlier. Figure 8.4(b) shows the variation of the unit shaft friction along the Test Pile for the ultimate head load of the first load test. In this figure, the unit shaft friction increases with depth down to 9.1 m (30 ft), then less unit shaft friction between 9.1 m (30 ft) and 12.2 m (40 ft) was observed followed by a considerable increase till 15.25 m (50 ft) below which no significant friction was encountered. The existence of the shale layer below 12.8 m (42 ft) explains the increase of the unit shaft friction between 12.2 m (40 ft) and 15.25 m (50 ft) since more friction is expected at the pile-shale interface compared to that at the pile-sand interface.

(c) Residual Loads and the True Load Profile

Due to the expected increase in soil strength and confinement pressure as the depth increase, the unit shaft friction should increase with depth for homogeneous soils (Fellenius, 2011). This is in contrast with the observed reduction of the shaft friction between 9.1 m (30 ft) and 12.2 m (40 ft). This reduction was addressed in the literature and reported being due to residual loads in the pile prior to the load test (Alawneh et al., 2001; Briaud and Tucker, 1984; Fellenius, 2002a, b; Holloway et al., 1978). Residual loads in drilled shafts are attributed to the higher soil settlements compared to the settlement of the shaft under its self-weight. As shown in Figure

8.5, the soil settlement is reduced as the depth increases till a certain depth below which the soil settlement is less than the shaft settlement under self-weight. Therefore, a down-drag force along the soil-shaft interface is developed in the top segment of the shaft which is countered by the frictional forces along the lower segment of the shaft (Fellenius, 2002a, b).

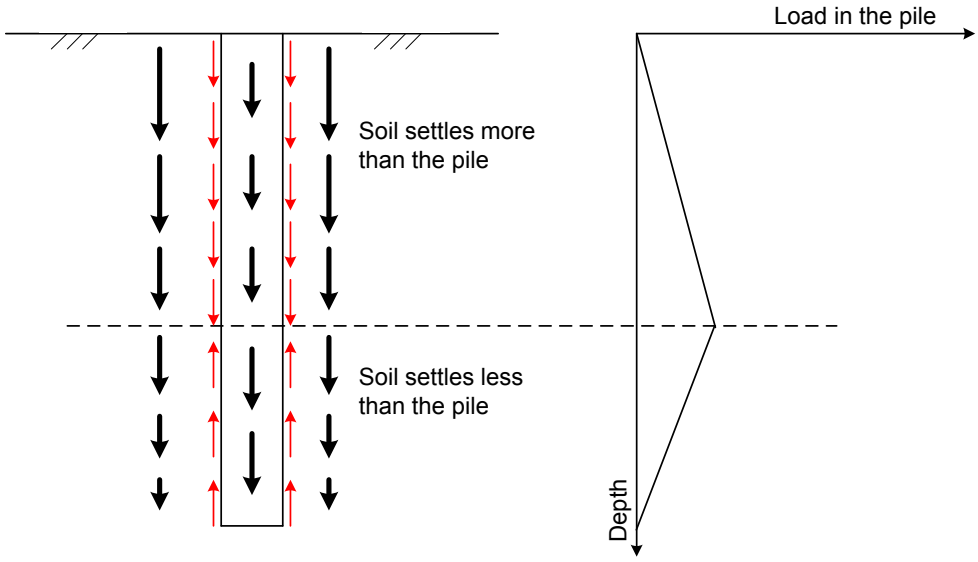

Figure 8.5. Residual load development in drilled shafts; black arrows show the relative magnitude of settlements for the soil and the shaft while red arrows show the direction of the frictional forces.

In order to estimate accurate and reliable true load and frictional resistances along the pile, the residual loads in the pile prior to the load test have to be considered (Fellenius, 2002a, b). Thus, it is recommended to start recording the linear strain units for the various gauges in the pile before casting the pile (Fellenius, 2002b). The difference between the linear strain units recorded right before the load test and that recorded before casting the pile is the strain that took place due to the curing of the concrete and the relative soil-pile deformations. This strain can be translated into a force in the pile due to the down-drag friction using an approximated pile modulus as discussed earlier. For VT load tests, the strains were recorded two months prior to the first load test which is about 15 months after casting the Test Pile. Therefore, estimating the residual load in the Test Pile prior to loading cannot be performed using this technique due to the lack of enough strain measurement.

Fellenius (2002b) presented an approach to estimate the residual loads in drilled shafts when no strain measurements prior to loading were available. This approach can be briefly explained as follows; the shaft friction in the upper segment of the drilled shaft due to the self-weight is downward while when the load is applied it reverses direction and becomes upward to resist the externally applied load. The direction of friction is gradually reversed from downward friction to an upward friction. Because the strains prior to the load test were not measured and consequently the reference for the friction due to loading is incorrectly assumed as zero, the measured friction is the summation of the downward and the upward frictions. Fellenius (2002b) assumed that the ultimate shaft friction was developed before and after loading regardless of the movement direction; thus the friction estimated from the loading data is, in fact, double the true

ultimate friction. Therefore, the true shaft resistance can be estimated as half of the measured reduction in the load along the pile.

Fellenius (2002b), then, suggested comparing this measured shaft resistance to a theoretical friction distribution based on an effective stress analysis. A match between the measured and the theoretical shaft resistances is possible to a certain depth below which the rate of increase of the measured resistance reduces while the rate of the theoretical resistance continues to increase. This depth is where the direction of the friction due to the self-weight is reversed, i.e. the dashed-line in Figure 8.5. Above this point, the true load in the pile is estimated by subtracting the true shaft resistance from the load at the pile head. In other words, the residual load in the pile above the point of reversal is half of the measured reduction in the load along the pile. The rate of the reduction of the load in the pile above the point of reversal is assumed constant below the point of reverse. This assumption assists to estimate the true load below the point of reversal by extrapolating the true load profile above the reversal point (Fellenius, 2002b). The residual load below the point of reversal is estimated by subtracting the measured load in the pile from the extrapolated true load.

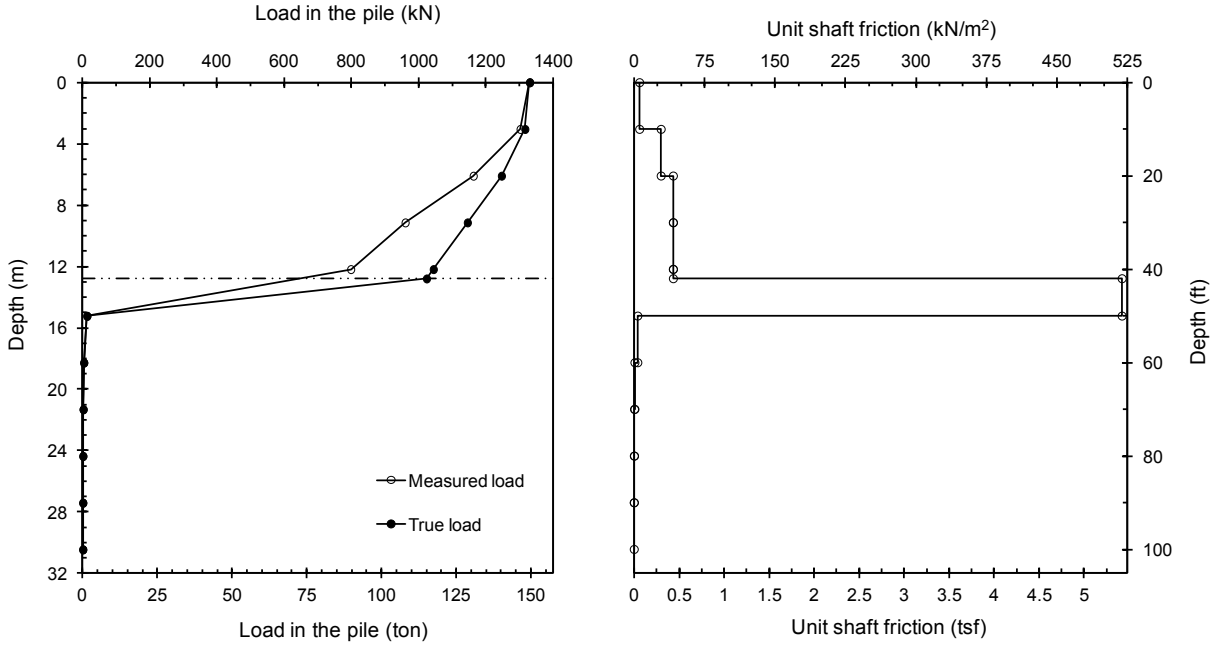

Figure 8.6. Measured, residual, and true load profiles along the Test Pile at the ultimate heat load of the first load test.

This approach is adopted to estimate the residual loads in the Test Pile prior to the first load test and consequently the true load profile in the Test Pile. Figure 8.6 shows the measured load and the true load profiles estimated using Fellenius (2002b) approach. In this figure, the true load and the shaft friction in the pile segment in the silty sand layer was developed till depth 12.8 m (42 ft) which is the interface between the silty sand and the shale. As appears from this figure, the unit shaft friction in the silty sand layer is constant and is not reduced as before.

The pile moduli for the second load test were used to obtain the load profile along the pile as shown in Figure 8.7. Similar to the first loading, the majority of the load applied at the pile head was countered by the frictional resistances along the pile shaft in the top 12.8 m (42 ft) silty sand

layer and the top 2.45 m (8 ft) of the shale layer. The residual load in the pile prior to the second loading is affected by the thermal cycles took place as part of T-MT 1. For simplicity, the effect of residual loads in the pile for the second loading and its following thermal loads is not considered within the discussion here. However, such effect is presented in Section 8.4.8.

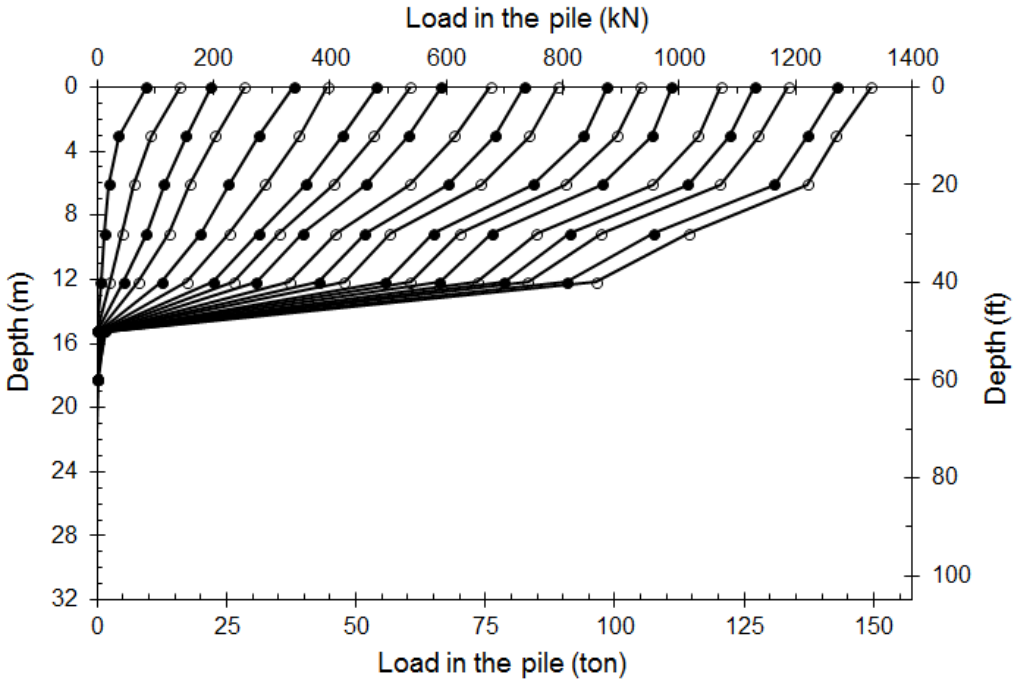

Figure 8.7. Measured load profiles along the pile for each step of the second load test.

8.3. Thermal Loading Phase

One thermal phase was applied to the Test Pile after the first loading phase while the Test Pile was subjected to three thermal phases after the second loading phase. Each thermal phase consisted of series of thermal cycles. In each thermal cycle; water was circulated in the ground loops with either a constant inlet temperature or a constant heat rate. Fixing the temperature of the inlet fluid to a constant value represents a reduction in the applied heat rate with time; on the other hand applying a constant heat rate produces an increasing inlet temperature with time. The fluid temperature controlling equipment was used to set the desired constant inlet temperatures in T-MT 1, T-MT 2, and T-MT 4. While, the heat rate controlling equipment was used to apply constant heat rates to the circulating water in T-MT 3.

This section discusses the procedure for applying the thermal loads using the temperature controlling equipment as well as the heat rate controlling equipment. Afterwards, the applied thermal loads in each test are discussed, followed by a detailed description of the temperature change in the tested elements and their vicinity.

8.3.1. Loading Procedure

Two different techniques were used to apply the thermal loads; (1) circulating a fluid with a constant inlet temperature, and (b) applying a constant heat rate to the fluid at the ground surface. The former thermal loads were applied using the fluid temperature controlling equipment; while the heat rate controlling equipment was used for the latter tests. The components of these machines were described in Chapter 6.

(a) Controlled Inlet Fluid Temperature Tests

The procedure outlined in this section for applying the thermal loads using the fluid temperature controlling equipment was followed in T-MT 1, and T-MT 2. In these two tests;

1. The thermal load was applied after monitoring the creep of the Test Pile under the ultimate mechanical load for 48 hours,
2. Three heating/cooling thermal cycles were applied in each test by varying the inlet fluid temperature,
3. For each heating/cooling thermal cycle;
    a. the heating load was applied prior to the cooling load,
    b. the heating load of each thermal cycle was applied using three equal heating steps starting from the preceding cooling till the maximum heating of the respective cycle,
    c. the cooling load of each thermal cycle was applied at once from the maximum heating of the preceding cycle,
    d. the thermal recovery from the maximum heating load of the final thermal cycle represents the cooling load for this cycle,
    e. identical heating/cooling thermal cycles and thermal steps for T-MT 1 and T-MT 2 were used to examine the repeatability of the results,
4. The duration of each thermal step was determined such that the temperatures and the strains along the Test Pile reach the equilibrium states. The equilibrium states of temperature and strain were reached after subjecting the Test Pile to a thermal step for about 6 hours as shown in Appendix XIV and Appendix XV. However, the thermal load steps were applied for 24 hours and 12 hours in T-MT 1 and T-MT 2, respectively. This additional time was considered to allow for more thermal interaction with the surrounding ground,
5. The pile head load was reset back to 150 tons after finishing each thermal step and before the beginning of the following step. Thus, the change of load at the pile head due to a thermal loading was cancelled at the beginning of the following step.
6. The pile head movement at the end of each thermal load was measured using four dial gauges installed at the pile head.

In addition to T-MT 1 and T-MT 2; T-MT 4 was also performed using the fluid temperature controlling equipment. In this test, the fluid temperature controlling equipment was used to perform a thermal conductivity test on the loaded Test Pile following the Dutch procedure (Witte et al., 2002). The thermal load for this test was applied in the form of an increasing inlet fluid temperature over a period of 48 hours. The inlet fluid temperature was increased such that the difference between the inlet and the outlet fluid temperatures is maintained constant over the entire test period. A detailed testing procedure is presented in Chapter 7.

(b) Controlled Heat Rate Tests

The procedure of using the heat rate controlling equipment being described in this section was followed in T-MT 3. This test was originally designed as a thermal conductivity test which was performed on the Test Pile following the ASHRAE standards (ASHRAE, 2009). It is

considered as a thermo-mechanical test because it was the thermal load was applied on the mechanically loaded Test Pile.

In this test; water was circulated without applying any thermal load from the heaters for 4 hours in order to evaluate the undisturbed ground temperature. Thereafter, a constant heat rate of 3kW was applied to the circulating water for 48 hours. This test was initiated using a heat rate of 5kW which, due to the short ground loop length, caused the fluid temperature to heat up to 49℃ (120°F) which is the maximum allowable temperature of the testing equipment in a short time. Thus, the test was terminated and initiated again after 24 hours using a reduced heat rate of 3kW.

8.3.2. Thermal Loads

As mentioned earlier; the thermal loads for T-MT 1, T-MT 2, and T-MT 4 were applied using the fluid temperature controlling equipment following the mechanical loading phase on the Test Pile while the heat rate controlling equipment was used to apply the thermal loads in T-MT 3. Figure 8.8 presents the measured inlet and outlet fluid temperatures for each of these tests. Appendix XIV presents the temperature along the Test Pile during the application of each thermal load for various thermo-mechanical tests considered in this study.

As presented in Figure 8.8; T-MT 1 included a single thermal phase following the mechanical phase. This thermal phase was performed by circulating water with constant inlet temperature at 5.3 lit/min (1.4 gpm) flow rate in the ground loops. Three thermal cycles were applied as part of this thermal phase; the first started with circulating water at 16℃ (61°F) for 48 hours after which the inlet temperature was reduced to 10℃ (50°F) for 24 hours then ending the cycle with water at 13℃ (55°F) for 24 hours. The second cycle started right after finishing the first cycle. In the second cycle, the water temperature followed a heating path of 20-28-35℃ (68-82-95°F) then a cooling path of 13-6℃ (55-42°F). Afterwards, the last cycle was initiated following a heating path of 13-28-35-50℃ (55-82-95-122°F). The thermal recovery at the end of the last thermal cycle is considered the cooling path for the cycle. Each thermal step in the second and the third cycles was applied for 24 hours except for the 50℃ (122°F) thermal step which was applied for 18 hours only. This is because one of the tube connections use to extend the ground loops to the top of the loading frame has collapsed. Fixing the failed connection was not possible due to limited accessibility and thus an immediate termination of the test and pile unloading was enforced.

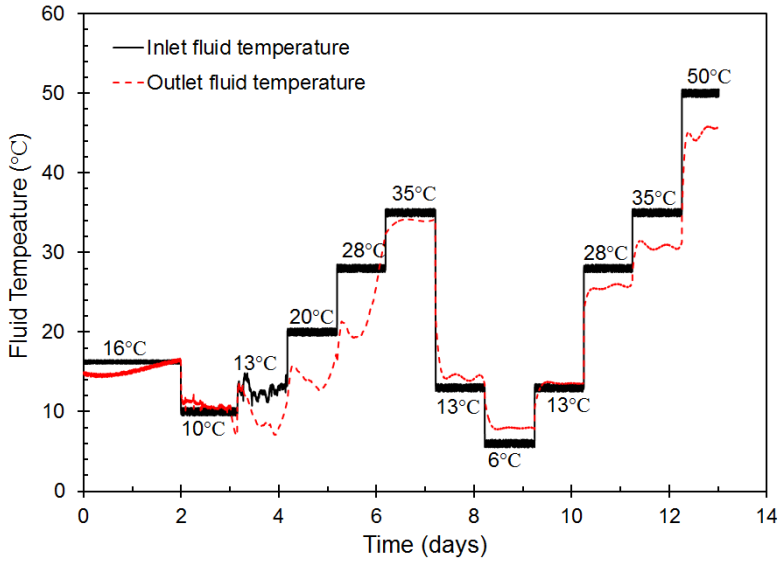

a) T-MT 1

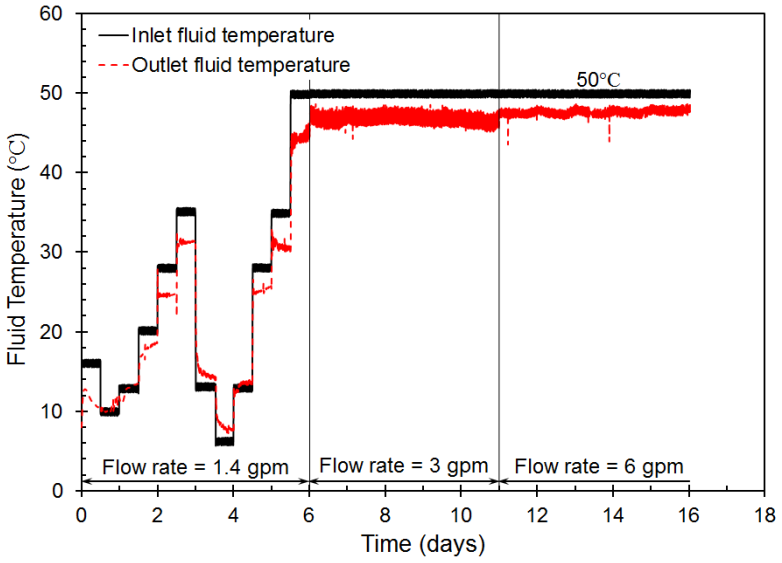

b) T-MT 2

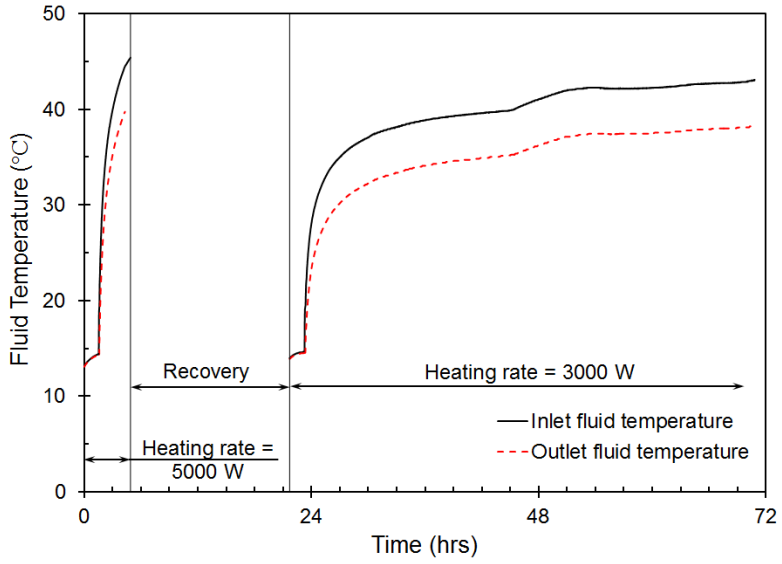

c) T-MT 3

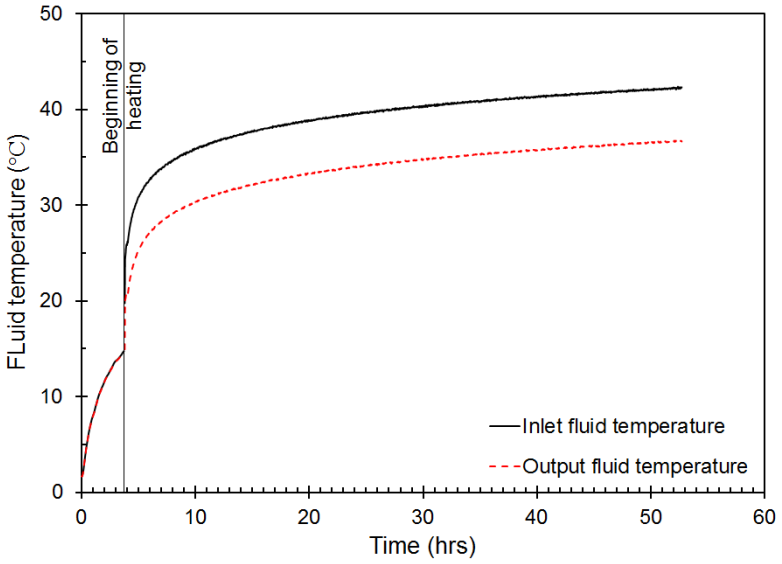

d) T-MT 4

Figure 8.8. Measured inlet and outlet fluid temperatures in each thermo-mechanical test.

The second mechanical loading phase was initiated by reloading the Test Pile mechanically after fixing the failed connection. After monitoring the pile creep for 48 hours; the thermal loading phase for T-MT 2 was initiated. As shown in Figure 8.8 (b), this thermal phase included circulating water in the ground loops using thermal cycles identical to T-MT 1. Since the temperatures and thermal strains measure in T-MT 1 reached their respective steady states in less than 10 hours, the duration of the thermal steps in T-MT 2 was reduced from 24 hours for T-MT 1 to 12 hours for T-MT 2. As for T-MT 1, a 5.3 lit/min (1.4 gpm) flow rate was used to apply all thermal steps. In order to investigate the effect of the flow rate on the thermal response of the Test Pile, the flow rate was increased from 5.3 lit/min (1.4 gpm) to 11.3 lit/min (3 gpm) then to 22.7 lit/min (6 gpm) for the 50℃ (122℉) thermal step. Each of the last two flow rates were applied for 5 days. At the end, the thermal phase of this test was terminated, but the mechanical load on the pile head was maintained.

One month after the end of T-MT 2, the thermal phase of T-MT 3 was performed. In this thermal phase and as shown in Figure 8.8 (d), the water was circulated in the ground loops for 2 hours with no applied thermal loads to evaluate the undisturbed ground temperature which was found to be about 14℃ (57℉). Then, a 5 kW constant heat rate was applied to the circulating water which due to the short length of the Test Pile caused a rapid increase in the water temperature to the maximum limit for the testing equipment in about 4 hours. Thus, the thermal load was shut down, and the ground temperature was allowed to recover overnight. On the following day, water was circulated with no thermal loads for 2 hours to confirm the recovery of the ground temperature. The undisturbed ground temperature was found to be 0.5℃ (0.9℉) more than the initially measured value referring to an acceptable thermal recovery to reinitiate the thermal test. A reduced 3 kW heat rate was applied for 48 hours. After the 48 hours testing period, the thermal phase was terminated, but the mechanical load on the pile head was maintained.

The thermal load of the fourth thermo-mechanical, i.e. T-MT 4, was started one month after the end of T-MT 3. T-MT 4 is considered a dual purpose test since it is used to; (1) improve the general thermal conductivity testing practice as discussed in Chapter 7, and (2) investigate the thermo-mechanical response of the Test Pile. In this test, the water was circulated for 4 hours with no thermal loads to confirm the undisturbed ground temperature which was found to be about 14℃ agreeing with the previous measured from T-MT 3. The thermal loads were then applied by assuring a constant difference between the inlet and the outlet fluid temperatures measured close to the ground surface where the loops penetrate the ground. A 5℃ temperature different was selected which provides a constant applied heat rate of 3 kW. The total testing period was 48 hours after which the thermal phase was terminated, and the pile was unloaded.

8.3.3. Thermal Response

The temperature changes in the Test Pile and its vicinity are vital to understand the thermo-mechanical behavior. The temperature change in an Energy Pile is used to estimate the amount of the "*blocked thermal strains*" which are the thermal strains prevented by the soil friction and the resistance at the pile toe and head. These *blocked thermal strains* are translated into thermal stresses in the pile. On the other hand, the temperature changes in the surrounding soils are also critical for estimating the extension of the thermal zone due to the operation of a single Energy Pile. This thermal zone is used to limit the minimum distance between adjacent Energy Piles to assure minimal interaction and better overall long-term performance. Moreover, the mechanical behavior of the soils around the pile depends strongly on temperature changes and thus a good measurement of the temperature change in the soil is required. This section focuses on the

observed temperature changes along the Test Pile and its vicinity for different thermo-mechanical tests.

(a) Undisturbed Ground Temperature

The undisturbed ground temperature was considered as the reference temperature for evaluating the temperature change in and around the Test Pile. For Virginia Tech site, the ground was subject to the first thermal load at the end of August 2011; therefore, the ground temperature measurements recorded early August 2011 and shown in Figure 8.9 were considered as the undisturbed ground temperature for the test site.

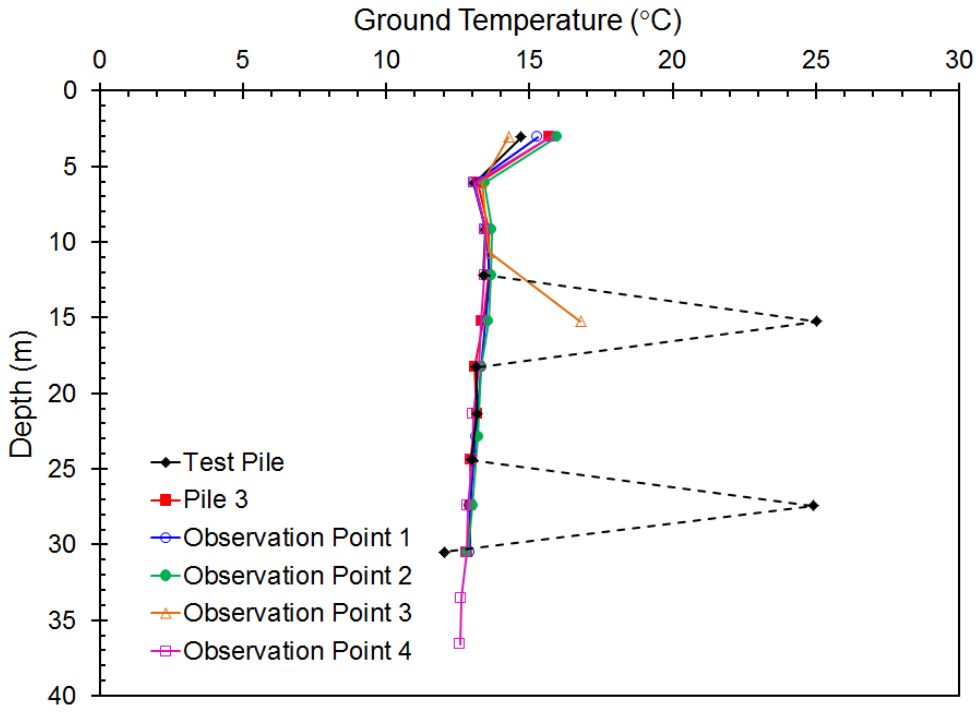

Figure 8.9. Undisturbed ground temperature measured in early August 2011 prior to any thermal activity at the test site.

As shown in Figure 8.9, the undisturbed ground temperature at the test site is uniform with depth and ranges from 13 to 14°C (55.4-57°F). This range agrees with the undisturbed ground temperatures measured from T-MT 3 and T-MT 4. Moreover, Figure 8.9 shows that the undisturbed ground temperature is consistent over the entire site since the profiles at all observation points match together.

Furthermore, Figure 8.9 shows that the measured ground temperatures at 15.25m (50ft), and 27.4m (90ft) in the Test Pile are considerably higher than the respective temperatures measured at other locations suggesting incorrect measurements. These incorrect undisturbed ground temperatures provide inaccurate reference temperatures when estimating the temperature changes at these depths. As presented later, the measured temperature changes at these depths were not significantly affected by the inaccurate reference temperatures. Thus, the temperature changes will be used in the following discussions since the thermo-mechanical response of Energy Piles depends on the temperature change rather than the temperature magnitude. On the other hand, the measured temperature at 15.25m (50ft) at observation well 3 is higher than the respective temperature at other locations. This high value is due to the fact that the gauges used

to instrument this observation point were concrete embedment strain gauges with built-in temperature sensors. The readings of this type of gauges are highly affected by the contact between the gauge and the concrete while the soil-embedment temperature gauges are less sensitive to the contact effects. Thus, the measured temperature may have been affected by an inadequate contact between the gauge and the backfilling sand which was used as a backfill in observation well 3.

(b) Reference Temperature and Thermal Recovery

A recovery period of about two weeks between T-MT 1 and T-MT 2 was introduced, while the recovery period between T-MT 2 and T-MT 3, and T-MT 3 and T-MT 4 was one month each. In order to measure an accurate temperature change in the Test Pile during a specific test, the reference temperature should account for the ambient and solar effects as well as the thermal effects of the preceding tests. The ambient temperature and solar energy are expected to affect the ground temperature at shallow depths over the entire site during the testing period. Thus, the undisturbed ground temperature is expected to vary over the four months testing period. Observation well 2 was drilled far away from all Energy Piles causing the temperature at this well to vary solely due to the ambient and solar effects. In other words, the thermal loads applied during testing will not affect the ground temperatures measured at observation well 2.

The recovery of the ground temperature at the Test Pile after each test was examined to quantify the effect of preceding tests on the measured temperature changes. For this purpose, the temperature profiles in the Test Pile at the beginning of each test, i.e. at the end of the recovery period from the preceding test, were compared to the respective temperature profile measured in the far-away observation well 2 as shown in Figure 8.10. The temperature profile in observation well 2 before any test represents the undisturbed ground temperature prior to this test considering the ambient and solar effects as discussed earlier. In Figure 8.10, the inaccurate temperature measurements at 15.25 m (50 ft) and 27.4 m (90 ft) in the Test Pile were eliminated. As shown in this figure, except for the top 5 m (16.4 ft), the ground temperature profiles along the Test Pile match the undisturbed ground temperature at observation well 2 for all tests. Thus, the temperatures along the Test Pile have fully recovered to the undisturbed ground temperature by the end of the recovery period for each test.

Moreover, Figure 8.10 shows that the temperatures over the top 5 m (16.4 ft) of the Test Pile deviate slightly from the undisturbed ground temperature with the latter temperature being higher. This is because the Test Pile was covered under a shed as mentioned in Chapter 6. The air temperature inside the shed is less than the outside ambient temperature since the shed reduces the solar effects. Thus, the temperature of the ground covered by the shed is lower than the temperature of the ground outside.

In conclusion, the temperature measured at a given location prior to a specific test is the best estimate of the reference temperature at that location for approximating the temperature changes due to the thermal operation of the considered test because as discussed earlier; (1) a full thermal recovery from any test took place prior to the beginning of the following test, and (2) this temperature considered the shed effects on the amount of the ambient and the solar interaction with the covered ground around the Test Pile.

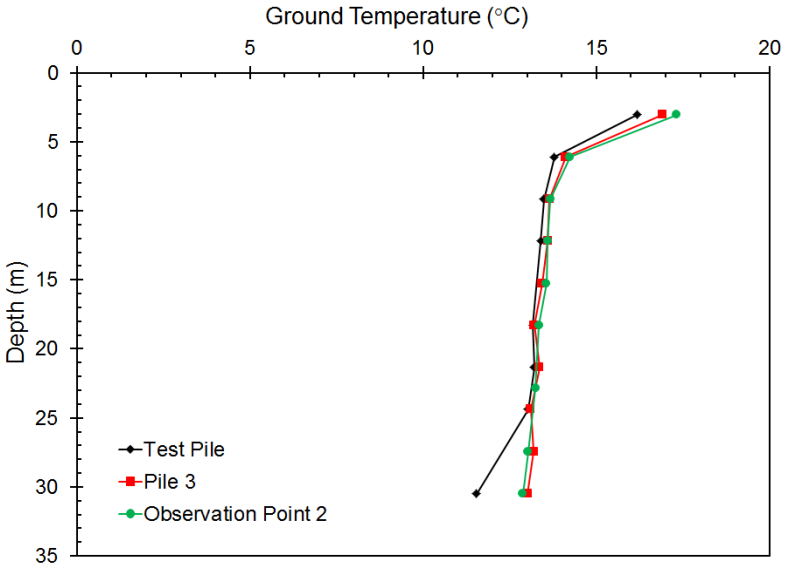

a) T-MT 1

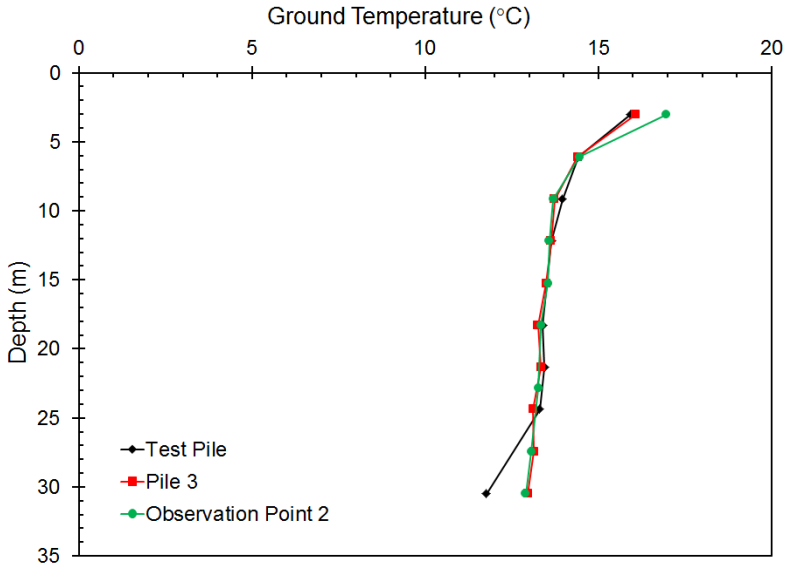

b) T-MT 2

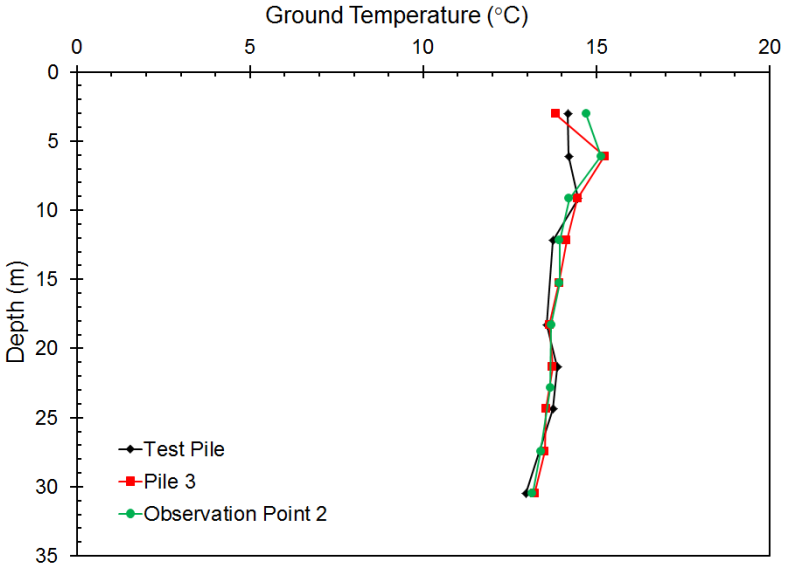

c) T-MT 3

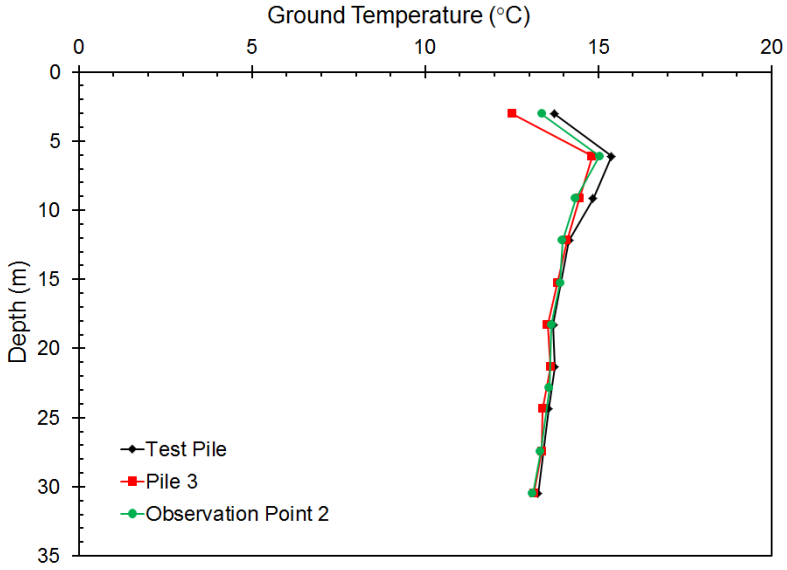

d) T-MT 4

Figure 8.10. Initial ground temperature for each thermo-mechanical test.

(c) Temperature Change Along The Test Pile

The selected reference temperature profile for each test shown in Figure 8.10 and the temperatures measured during the respective test were used to evaluate the temperature changes along the Test Pile. The temperature change at any location and depth was evaluated as the difference between the temperature measured during testing and the respective reference temperature. Positive temperature changes refer to ground heating while negative temperature changes indicate ground cooling. The temperature change profiles along the Test Pile are shown in Figure 8.11 for T-MT 3 and T-MT 4, and in Figure 8.12 at the end of each thermal step of T-MT 1 and T-MT 2. The temperature changes in the Test Pile at 15.25 m (50 ft) and 27.4 m (90 ft) was included in these figures, and they are consistent with the overall temperature changes along the Test Pile.

Figure 8.11 also presents the temperature change profile along Pile 3 at the end of a thermal conductivity test performed on this pile. The temperature change at the end of this test is considered here to explain the non-uniform temperature changes observed in the Test Pile during all thermo-mechanical tests. This test was performed following the ASHRAE standards (ASHRAE, 2009) for thermal conductivity tests with a heat rate of 2 kW applied for 60 hours in Pile 3. More details about this test are presented in Chapter 7.

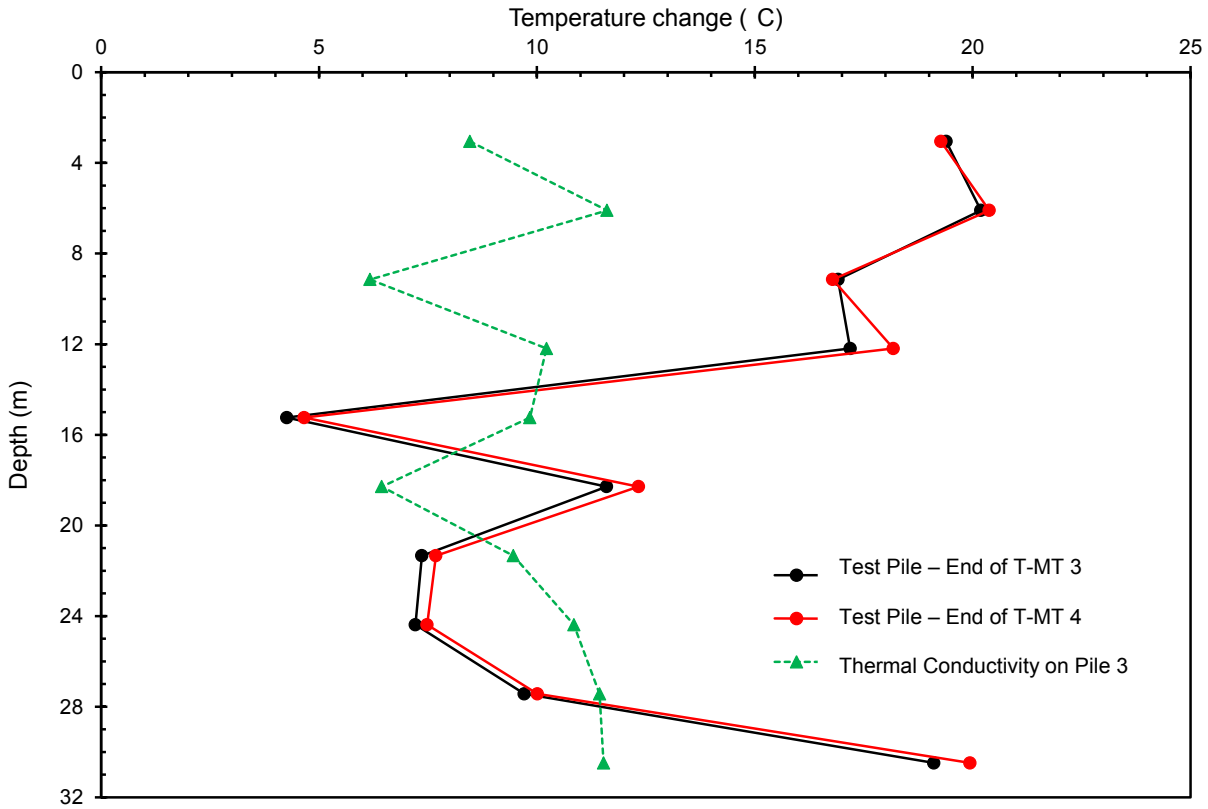

Figure 8.11. Temperature change along the Test Pile at the end of T-MT 3 and T-MT 4; and along Pile 3 at the end a thermal conductivity test.

It is noticed in Figure 8.11 that the temperature change is proportional to the applied heat rate providing that the thermal steady state has been reached. For instance; an average temperature change of 10-12℃ was observed at the end of the thermal conductivity test

performed in Pile 3 in which a heat rate of 2kW was applied while the average temperature change for the 3kW applied in T-MT 3 was about 17-18℃ (62-64°F). In these two tests; the thermal steady state was achieved since heat was applied for 60 hours in the former and 48 hours in the latter.

It is also noticed in Figure 8.11 that the temperature change profile along the Test Pile at the end of T-MT 3 agree with that obtained at the end of T-MT 4. These two tests were performed by applying 3kW heat rate to the Test Pile by controlling the inlet fluid temperature in T-MT 3, and controlling the heat rate in T-MT 4. Therefore, regardless of the heating technique, identical thermal responses are observed for the same applied heat rates.

Figure 8.12 shows similar temperature change profiles for all thermal steps performed as part of T-MT 1 and T-MT 2. The agreement between the temperature change profiles of respective thermal steps proves the replicability of the results and suggests that the reduced 12 hours duration used in T-MT 2 was sufficient to reach the thermal stability. The thermal stability was also confirmed by the temperature changes corresponding to 50℃ (122°F) in T-MT 2 since consistent measured temperature changes after 12 hours at 5.3 lit/min (1.4gpm), 5 days at 11.3 lit/min (3 gpm), and 5 days at 22.7 lit/min (6 gpm) were observed with 3℃ (5.4°F) of maximum difference.

As shown in Figure 8.11; a uniform temperature change profile was observed along Pile 3 at the end of the thermal conductivity test with a maximum variation of 5℃ (9°F). This temperature change variation is consistent with the variations reported by Bourne-Webb et al. (2009) and Laloui et al. (2006) on their Test Piles. On the other hand, the temperature change profiles along the Test Pile measured in T-MT 1, T-MT 2, T-MT 3, and T-MT 4 indicate a higher temperature change variation. This variation reached its maximum of about 15℃ (27°F) when the inlet fluid temperature was 50℃ (122°F) with the lower temperature changes at depths 15.25 m (50 ft), 18.25 m (60 ft), 21.3 m (70 ft), 24.3 m (80 ft), and 27.4 m (90 ft) below the ground surface. This was initially thought to be due to having the shale layer along the lower part of the pile compared to the silty sand layer along the upper part. This idea was questioned and rejected since the temperature change measured at 30.5 m (100ft) which is located within the shale layer agrees with those measured in the silty sand layer, and also the uniform temperature change profile in Pile 3. Numerical modeling was used to investigate the main reason for such unexpected large variation as discussed in the following section.

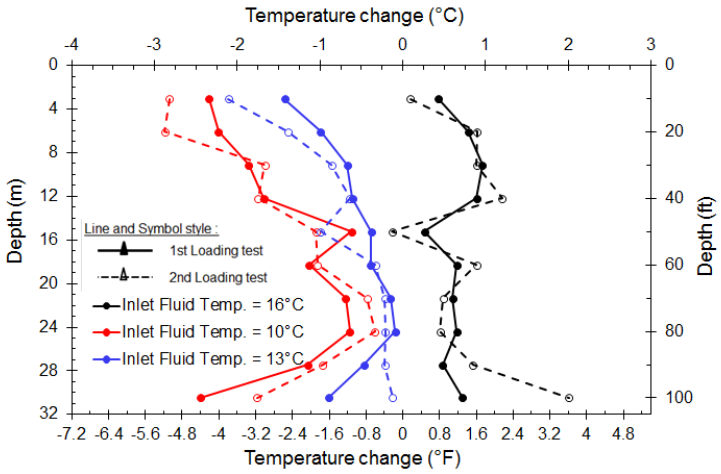

(b)1st thermal cycle

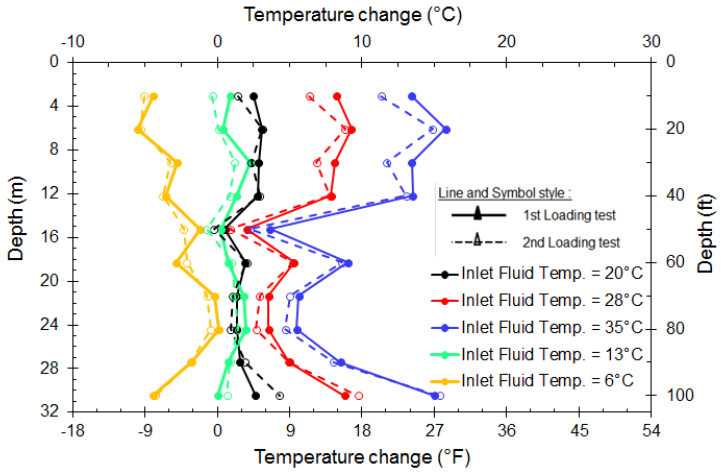

(c)2nd thermal cycle

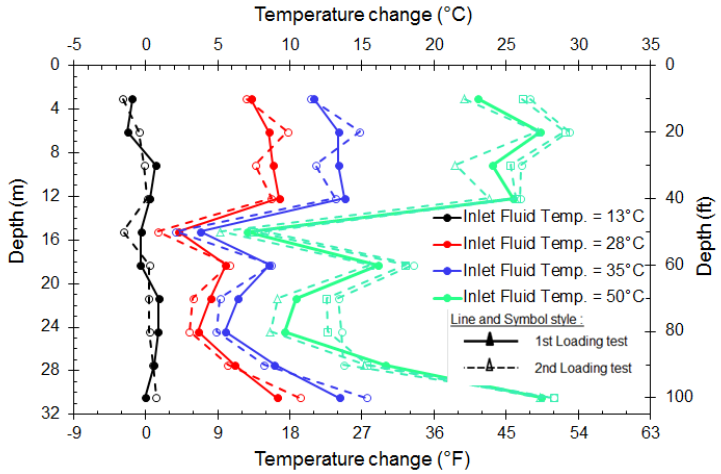

(d)3rd thermal cycle

Figure 8.12. Temperature change along the Test Pile at the end of various steps of the thermal load of T-MT 1 and T-MT 2.

(d) Location-Dependent Temperature Measurements

COMSOL multiphysics (COMSOL, 2011) was used to model an Energy Pile subject to an inlet fluid temperature at 50℃ (122 °F)applied for 48 hours. The modeling technique is as described in Chapter 7. In this model, the modeled pile was a 25 cm (10 inch) in diameter and 20 m (65 ft) in length. The initial undisturbed ground temperature was assumed to be 15℃ (59°F). A centered 25.4 mm (1-inch) single circulation loop was aligned along the centerline of the pile such that the spacing between the downward and the upward legs is 5 cm (2 inches). The thermal conductivity of the ground loops and the pile material were assumed to be 0.41 W/m·℃ (0.237 Btu/hr·ft·°F) and 1.44 W/m·℃ (0.832 Btu/hr·ft·°F), respectively.

Since it was initially thought that the unexpected variation of the temperature change along the Test Pile was due to the layered ground along the Test Pile, a two layers ground profile was considered in the model. These two layers are; a 10 m (32.8 ft) silty sand layer on top of a shale layer extending till the end of the model. Typical thermal properties for these layers were assumed and presented in Table 8-2.

Table 8-2. Thermal properties of the two ground layers considered in the numerical model.

Layer	Density, ρ (kg/m^3) ‖ (pcf)	Thermal conductivity, k (W/m·°C) ‖ (Btu/hr·ft·°F)	Specific heat, C_p (J/kg·°C) ‖ (Btu/lb·°F)
Silty SAND	1500 ‖ 93.6	1.5 ‖ 0.867	800 ‖ 0.191
Shale	2500 ‖ 156	4 ‖ 2.311	2000 ‖ 0.478

The temperature change profiles at the end of the modeled period are shown in Figure 8.13 for four different locations within the pile cross-section. The considered four locations are the pile center, a point centered between the pipe legs and located near the pile-soil interface (location 1), a point close to the pipe leg in which the fluid is moving upward (location 2), and a point close to the pipe leg in which the fluid is moving downward (location 3) as presented in Figure 8.13.

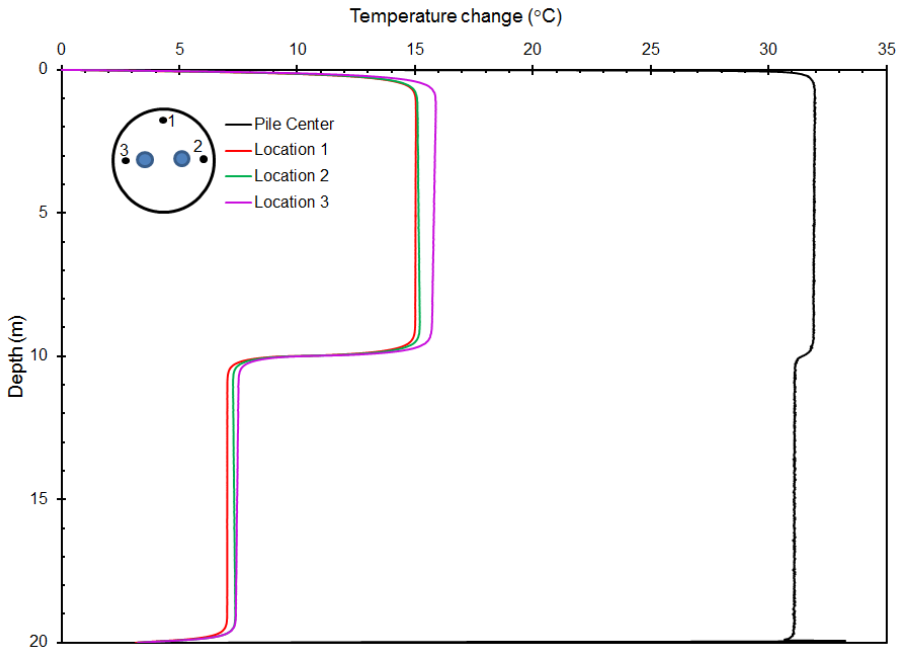

Figure 8.13. Effect of the relative locations of the temperature gauge and the ground loops on the measured temperatures.

Figure 8.13 shows a variation of about 1°C (0.5°F) in the evaluated temperature change profile at the center of the pile with the lower temperature change being in the layer with the higher thermal conductivity. This response was discussed in details in Chapter 4 when the multi-layer finite line source model was presented. Such small variation at the pile center suggests a minimal effect of the layered ground on the temperature change profile along the pile. Thus, the layered ground at the test site is confirmed not to be the main cause of the unexpected large variation in the observed temperature change along the Test Pile.

Furthermore, Figure 8.13 shows that the temperature change profiles at the three other locations agree together with a slightly higher temperature change near the pipe leg of the downward fluid flow. This is expected since the fluid in this leg has a higher temperature compared to the leg of the upward fluid flow. Moreover, it is noticed that for each one of these locations the temperature change measured in the silty sand layer is higher than the measured temperature change in the shale layer. The difference between the measured temperature changes in the silty sand and in the shale layer is about 7°C (12.6°F). Thus from the previous discussions, it can be concluded that as the distance from the pile center increases, the effect of the layered ground on the measured temperature profile increases.

More importantly, the temperature change measured at the pile center is higher than those measured at the other three locations with a difference of 16°C (28.8°F) and 22°C (39.6°F) in the silty sand layer and in the shale layer, respectively. Thus, the maximum difference between the temperature change measured by a gauge centered within the top silty sand layer and that measured by another gauge displaced from the pile center in the shale layer is about 23°C (41.4°F). This bounding difference agrees with the temperature change variations observed along the Test Pile shown in Figure 8.11 and Figure 8.12.

When constructing the Test Pile, the temperature gauges were installed in their exact locations by attaching them to the steel bar using strong struts, while the circulation loop was attached to the steel bar using duct tape as discussed in Chapter 6. Thus, a relative movement between the temperature gauges and the circulation loop can be expected especially as the depth increases causing the temperature changes along the Test Pile to vary.

In order to infer which temperature sensors were centered and which were not, the temperature change profiles measured in T-MT 1 and T-MT 2 for the 50°C (122 °F) thermal step were compared to the profile obtained from the finite element model. As presented in Figure 8.12, for the 50°C (122°F) thermal step the temperature changes measured in the silty sand layer and at depth 30.5 m (100 ft) in shale are about 30°C (54°F) which agrees with the 31°C (55.8°F)from the finite element model presented in Figure 8.13. The temperature gauges at 15 m (50 ft), 18.5 m (60 ft), 21 m (70 ft), 24 m (80 ft), and 27 m (90 ft) gave temperature changes along the Test Pile of about 10°C (18°F) suggesting some relative displacements at these depths. Thus, the temperature gauges located in the silty sand layer and at depth 30.5m (100ft) are considered centered while others are displaced.

i. Temperature Change Around The Test Pile

Estimating the thermal extent due to the operation of Energy Piles is mandatory for; (1) determining the minimum distance between adjacent Energy Piles such that minimal thermal interaction occurs and consequently achieving the maximum overall system efficiency, and (2) estimating the temperature-dependent mechanical behavior of the soils including the soil stiffness and strength. Figure 8.14 shows the change of the ground temperature in the vicinity of the Test Pile at the end of each thermo-mechanical test. For T-MT 1 and T-MT 2, the changes of the ground temperature at the end of the last thermal step, i.e. 50°C (122°F), are presented in

Figure 8.14(a). The temperature change at 6 m (20 ft) was selected to represent the silty sand layer and at 24.3 m (80 ft) to represent the shale layer. A linear transition in the temperature change was assumed between different locations at which the ground temperature was measured.

The temperature change along the Test Pile segment embedded in the shale layer was taken to be at the pile-soil interface as seen in Figure 8.14 since, as concluded in the previous section, all temperature gauges installed along this pile segment were displaced from the pile center. For T-MT 1, T-MT 3, and T-MT 4; the extension of the thermally disturbed zone around the Test Pile was about 1m (3 ft). While for T-MT 2 in which the thermal load was applied for 16 days with the last 10 days being continuous heating, 2.5m (8 ft) around the Test Pile was thermally affected. Moreover it is observed from Figure 8.14.a that for T-MT 2, the temperature change along the pile segment embedded in the shale layer was less than that along the pile segment embedded in the silty sand layer for nearby distances. As the distance increases, this response was reversed which is, again, agree with the findings of the multi-layer finite line source model reported in Chapter 4.

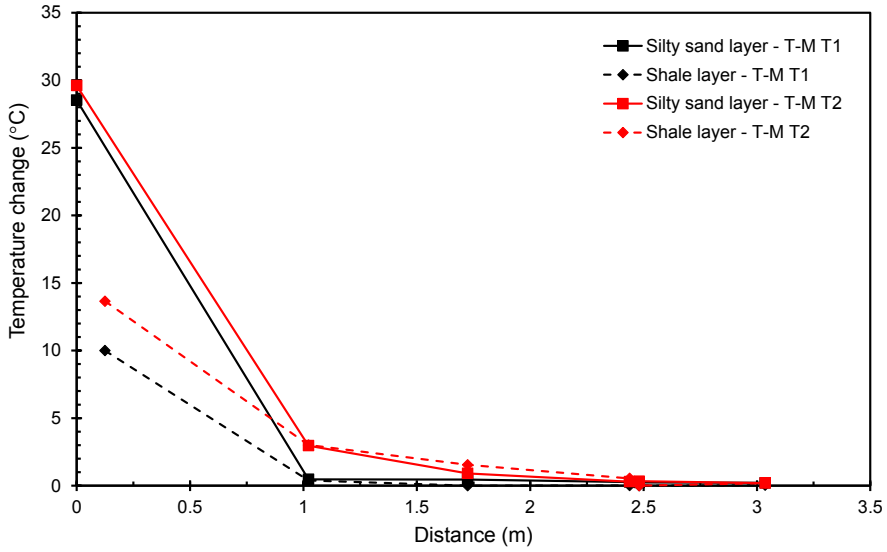

(a)

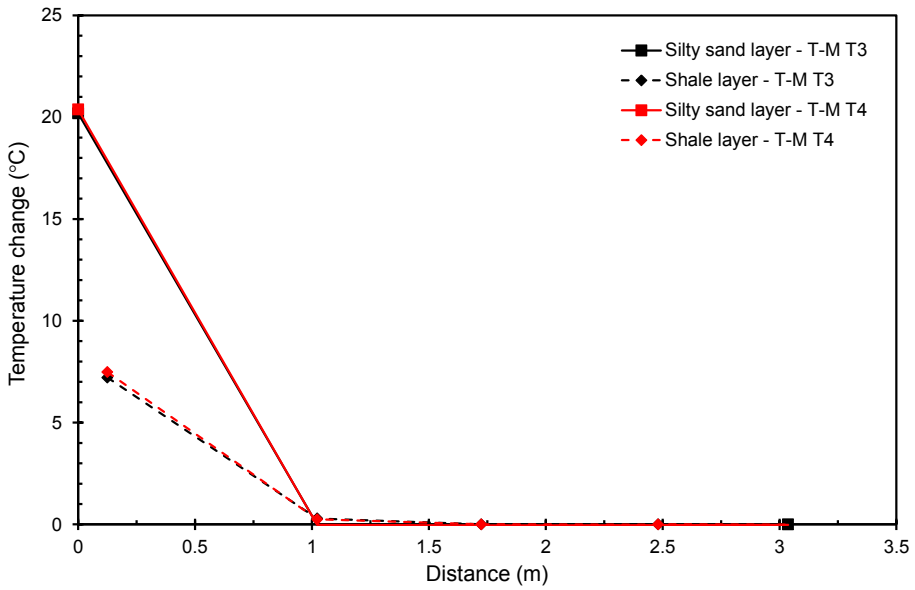

(b)

Figure 8.14. Temperature change around the Test Pile at the end of; (a) T-MT 1 and T-MT 2, and (b) T-MT 3 and T-MT 4.

8.4. Thermo-Mechanical Superimposed Effects

The strains measured along the Test Pile due to applying the mechanical load at the pile head were discussed in Section 8.2, while Section 8.3 discussed the temperature changes along the Test Pile and its vicinity. In this section; the thermal strains due to subjecting the Test Pile to various thermal loads are presented. A theoretical discussion about the development of the thermal strains and translating these strains into thermal loads are presented. Then, the effect of the gauge location in the pile cross-section on the measured thermal strains is discussed. And finally, the superimposed effect of the thermal and the mechanical loadings is presented.

8.4.1. Soil-Structure Interaction of Energy Piles

Subjecting an Energy Pile to a thermal load in the form of a temperature change causes it to undergo volumetric strains. These thermal volumetric strains are proportional to the temperature changes where the proportionality constant equals to the volumetric thermal expansion coefficient. The thermal volumetric strains can be divided into longitudinal strains and radial strains. Due to the small diameter of Test Pile, no instrumentations in the radial direction were provided in the pile. Thus, the radial thermal strains in the Test Pile cannot be analyzed. And therefore, the following discussion focuses only on the longitudinal thermal strains.

For a free Energy Pile which is not embedded in any soil, the pile will have a total change in length (ΔL_{free}) evaluated as;

$$\Delta L_{\text{free}} = \varepsilon_{\text{free}} \cdot L_o = \alpha \cdot \Delta T \cdot L_o$$

Where; $\varepsilon_{\text{free}}$: thermal strain for a free pile $= \alpha \cdot \Delta T$

α : the thermal expansion coefficient of the pile,

ΔT : the temperature change,

L_o : the pile initial length

Therefore, a 30.5m (100ft) concrete pile undergoes a change in length of about ±0.3 mm (±0.012 inch) when subjected to a ± 1 ℃ (± 0.5°F) temperature change assuming a typical concrete thermal expansion coefficient (α) of $1 \times 10^{-5}/$℃.

For the free Energy Pile, all the free strains (ε_{free}) are translated into changes in the pile length since the pile movements was not restricted. In order to prevent these thermal strains, external forces at the pile surface and ends should develop to resist the thermal deformations. When a pile is installed in the ground and upon subjecting it to a temperature changes, it attempts to change volume. The soil around the pile resists the thermal movements by generating a frictional resistance along the pile shaft. Furthermore, the soil at the pile toe and the building at the pile head resist the thermal longitudinal deformations by generating counteracting thermal toe and head forces (Bourne-Webb et al., 2009; Knellwolf et al., 2011). The thermally developed shaft, toe, and head resistances reduce the pile thermal deformations and consequently the thermal strains that took place along the pile. In other words, the actual observed thermal strains in the pile ($\varepsilon_{observed}$) are less than the theoretical free thermal strain (ε_{free}). The difference between the theoretical free strain (ε_{free}) and the observed strains ($\varepsilon_{observed}$) is the blocked thermal strains ($\varepsilon_{blocked}$). These blocked strains are the stress-dependent strains which can be used to back-calculate the thermally developed loads in the pile when multiplied by the pile modulus.

The observed strains decrease and the blocked strains increase for; (1) higher shaft resistances, and/or (2) higher fixity at the pile ends, i.e. head and toe. For instance when thermal loads are applied on a pile with completely fixed ends, no thermal deformations are allowed and thus all free strains are blocked $\varepsilon_{free} = \varepsilon_{blocked}$ (Bourne-Webb et al., 2009; Knellwolf et al., 2011). Moreover, all thermal strains can be blocked for cases where significantly high soil frictional resistances develop at the pile-soil interface even if for partially fixed pile ends. The latter case was observed in the thermo-mechanical tests performed on the Test Pile as discussed in the following sections.

8.4.2. Measured Thermal Strains

Since there are two complementing thermal strains named the observed thermal strain ($\varepsilon_{observed}$) and the blocked thermal strain ($\varepsilon_{blocked}$); it is desired to determine which one is being measured by the strain gauges used in the Test Pile for reliable analysis. Bridge Diagnostic Incorporate (Laman et al.) referred to the concept of having vibrating wire strain gauges that are self-compensating for temperature changes which theoretically do not record strains on structural members that are free to move under thermal loads. These strain gauges measure thermal strains that only cause thermal stresses in the tested elements. In other words, these strain gauges measure the blocked thermal strains ($\varepsilon_{blocked}$) rather than the observed thermal strains ($\varepsilon_{observed}$) as for the non-compensating gauges.

The temperature self-compensating concept is based on the fact that for a given temperature change ΔT, the change in the length of the vibrating wire installed inside the gauge is always consistent with the free thermal strain $\Delta L_w = \varepsilon_{th\text{-}free} \times L_o$, while the distance between the flanges is affected by the external resistances. As shown in Figure 8.15(b), when a gauge that is free to move with an initial length L_o is subjected to a temperature change ΔT; the change in the wire length is $\Delta L_w = \alpha \times \Delta T \times L_o$, where α is the thermal expansion coefficient of the material of the vibrating wire which, for simplicity, is assumed equal to the thermal expansion coefficient of the pile material. The distance between the flanges for this gauge and the wire length vary consistently producing the same vibration frequency and consequently give the same linear strain unit reading. Thus, no thermal strains are measured for such free-moving gauge. When the

gauge movement is restricted as in Figure 8.15(c); the change in the wire length is still $\Delta L_w = \alpha \times \Delta T \times L_o$ but the change in the distance between the flanges is less. The difference between the change in the wire length and the change in the distance between the flanges represents the blocked thermal strains since $\varepsilon_{th\text{-}blocked} = \Delta L_{th\text{-}blocked}/L_o$. The tension in the wire changes proportional to the net difference between the length of the wire and the distance between the flanges. Consequently the vibrating frequency differs allowing the measurement of the thermal strains.

In order to better understand which thermal strain is being measured, two approaches of looking at the blocked strains are adopted. The first; assuming that no temperature changes took place and that the initial length of the gauge and its wire was $L_o + \Delta L_{th\text{-}free}$. Then, when a load P_{th} is applied on the gauge, the distance between the flanges is compressed while the wire length is maintained the same $L_w = L_o + \Delta L_{th\text{-}free} = L_o (1+\{\alpha \times \Delta T\})$ as shown in Figure 8.15(d). For this case the measured change in the linear strain units refers to the mechanically developed strain which is $\Delta L/L_o$. Thus when the applied load produces a change in the distance between the flanges equal to $\Delta L_{th\text{-}blocked}$, then the measured strains refer to the blocked thermal strain $\varepsilon_{th\text{-}blocked}$. And since the two analysis approaches are analogues in producing the same change in length, then it can be concluded that the measured thermal strains are the stress-dependent strains which are the blocked strains. Moreover, the load P_{th} is known as the thermally developed load in the pile which can be back-calculated using the measured blocked thermal strains providing the pile modulus.

The other way to explain the self-compensating concept is by studying the extreme cases which are;

(1) when the gauge is free to move, the changes in the length of the wire and the distance between the flanges are consistent producing the same vibrating frequency and therefore the same linear strain unit reading. Thus, the change in the length of the gauge is the maximum or in other words, the observed strains reach the ultimate free strain while no thermal strains were blocked,

(2) when the gauge movements are completely blocked, the change of the wire length is consistent with the applied temperature change while the distance between the flanges are fixed; thus, a change in the vibrating frequency and the linear strain reading will be observed. For this case, no observed strains exist and the blocked strains reach to the ultimate free strain.

Since the gauge measure strain due to the changes in the vibrating frequency of the wire, then no thermal strains will be measured in the former case while an ultimate value for the thermal strain will be measured in the latter case. Thus, it can be concluded that the measured strains are the blocked strains.

It is important to notice that for the pile is heated, the flanges are attempting to move away from each other while the equivalent thermal load is resisting such movements which produce compressive blocked strains. On the other hand when the pile is cooled, the flanges are attempting to shrink towards each other but the equivalent thermal load is resisting producing a tensile blocked strains.

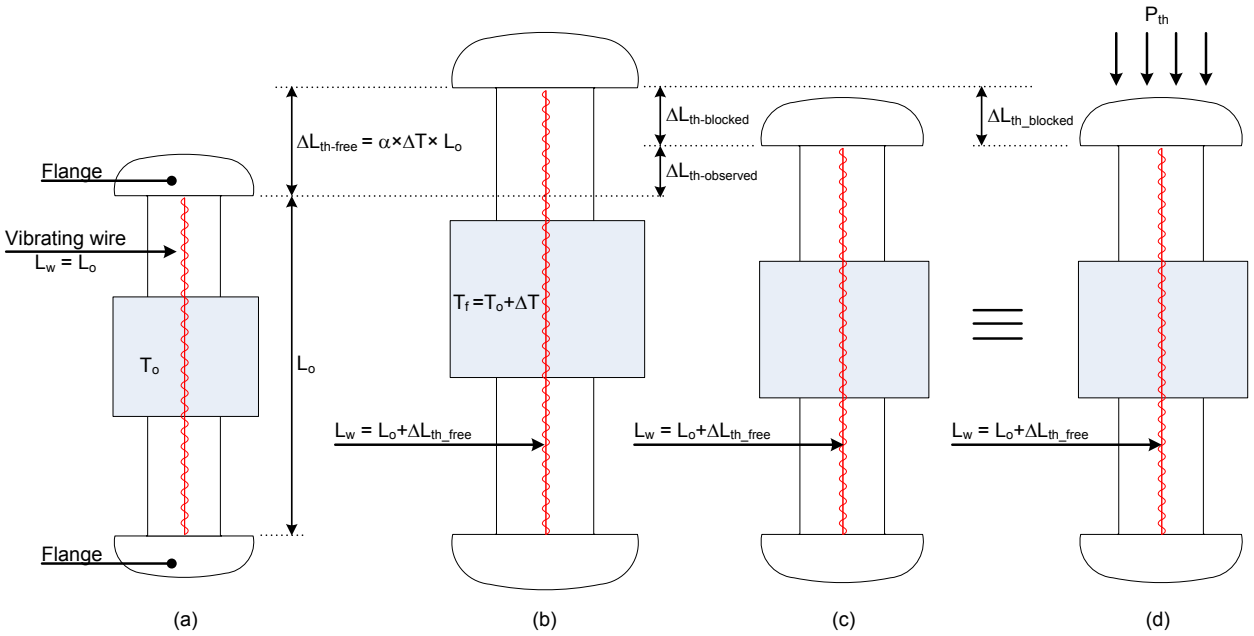

Figure 8.15. Concept of temperature self-compensating strain gauges.

Two indicators were used to inform if the strain gauges used in the Test Pile were self-compensating for temperature changes or not; the first is a simple test in which one of the leftover strain gauges was submerged in a hot water with the flanges free to move. The readings of this strain gauge showed a significant increase in the measured temperature ($\Delta T \approx 35^{o}C$) while no pronounced change in the linear strain unit reading was observed. This result suggests a self-compensating vibrating wire gauge.

The second indicator is the measured thermal strains during various thermo-mechanical tests. Although heating the Test Pile is expected to cause tensile strains due to the pile expansion, the measured thermal strains upon heating refers to compression. Similar reversed measurements were noticed for cooling since for this case tensile stresses were measured rather than the expected compression strains. This reversed behavior of measured thermal strains agrees with the expected response of self-compensating gauges explained earlier. Based on these two indicators, the used gauges were confirmed to be self-temperature-compensating gauges.

8.4.3. Location-Dependent Thermal Strains

Section 8.3(c) presented how the measured temperatures were affect by having the temperature gauges displaced from the center of the circulation loops. As presented in this section, the measured temperatures were affected significantly by the relative location of the gauges and the circulation loops within the pile cross-section. This section discusses the effect of this relative location on the measured thermal strains since the same displaced gauges were used to measure the temperatures and the strains.

Figure 8.16 shows a schematic of a longitudinal cross-section along half of the pile with four points at which a gauge may locate. All these points are at the same elevation but at different radial distances from the pile center with the first point located at the pile center; while the last point located close to the pile-soil interface. The other two points are located in between the first and the last ones. As observed in Section 8.3(c), the measured temperature decreases as the distance from the center increases; thus in this figure $T_1 > T_2 > T_3 > T_4$.

For a constant initial undisturbed ground temperature, the temperature changes at these four points also decrease with increasing the radial distance from the pile center since the reference temperature is the same. The free thermal strains are proportional to the measured temperature changes as discussed in Section 8.4.1; thus higher free strains are expected at the center (point 1) compare to those expected near pile-soil interface (point 4) as shown in Figure 8.16. On the other hand, a uniform thermal strain ($\varepsilon_{observed}$) will occur in the pile at a given elevation if the pile integrity is assumed because the core of the pile will deform as much as the surface does. In other words, no thermal strain variations will be observed in the radial direction. This uniform thermal strain ($\varepsilon_{observed}$) is bounded by the minimum free strain in the pile which is expected at the pile-soil interface where the lowest temperature change takes place. But since the free strains decrease along the radial distance, then the blocked thermal strains vary and decrease with increasing the radial distance as shown in Figure 8.16.

As discussed in the previous section, the strain gauges used in the Test Pile are self-compensating for temperature changes measuring the blocked strains which, as discussed earlier, vary with the radial distance from the pile center. Thus, the measured strains are location-dependent strains that need to be corrected for a final location-independent thermal strain profile. A correction approach is described below based on adjusting the measured blocked strains to represent the blocked strains expected at the same reference point along the pile. The selected reference point for the proposed correction is the pile center. This correction is as follows;

1) The free thermal strain at a specific depth in the pile is estimated using the measured temperature change at the considered depth and the thermal expansion coefficient of the pile material,
2) Using the measured blocked strain at the considered depth and the free thermal strain estimated in step 1, the average observed strain can be estimated as the difference between the two,
3) The average observed strain ($\varepsilon_{average}$) estimated from step 2 is assumed to be uniform in the radial direction as discussed earlier,
4) An average temperature change along the pile is selected from the measured profiles.
5) Using the selected average temperature change, the corresponding free thermal strain is estimated,
6) The difference between the free strain from step 5 and the observed strain from step 3 is the blocked thermal strain at the pile center.

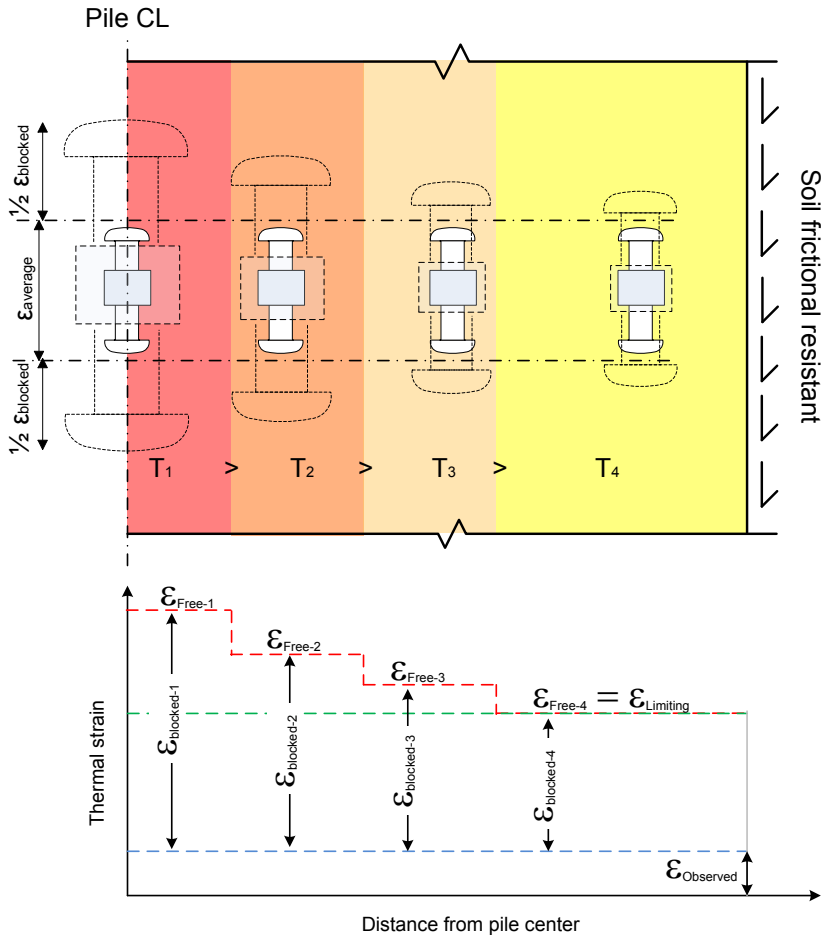

Figure 8.16. The effect of the gage's relative location within the pile cross-section on measured thermal strains.

The procedure outlined above was followed to correct the thermal strains measured in the pile segment embedded in the shale layer in all the thermo-mechanical tests; i.e. T-MT 1, T-MT 2, T-MT 3, and T-MT 4. For all these thermo-mechanical tests, the temperature measured at 30.5 m (100 ft) was selected as the average temperature since it agrees with the profile measured in the top silty sand layer. The thermal strains measured in the pile segment embedded in the silty sand layer were not correct since the uniform temperature changes that were obtain in this segment, as shown in Figure 8.11 and Figure 8.12, agree with the temperature changes measured at the pile center from the finite element model.

8.4.4. Measured Thermal Strain Profiles

The thermal strain measured by a specific strain gauge was estimated as the difference between the linear units measured at any time during testing and a reference unit of linear strain for the considered gauge. The reference unit of linear strain for T-MT 1, and T-MT 2 was taken after monitoring the creep of the Test Pile under the ultimate mechanical load for 48 hours and before the beginning of the thermal phase of the tests. The units of linear strain measured in the Test Pile right before applying the thermal loads of T-MT 3 and T-MT 4 were considered as the references strains for these tests. Positive thermal strains refer to compressive blocked strains; while negative thermal strains refer to tensile blocked strains. Appendix XV presents the

thermal strains developed within the pile segment embedded in the top silty sand layer during each thermo-mechanical test considered in this study.

Correcting the measured thermal strains for the difference in the thermal expansion coefficients between the steel of the vibrating wire and the pile grout paste is required for a reliable analysis of the thermal stresses in the pile (Geokon, 1986; Laman et al.). The thermal expansion coefficient for the vibrating wire steel is 12.2 με/℃, while for the cement paste is about 14.8 με/℃ (Cruz and Gillen, 1980). The mechanical strains measured while mechanically loading the pile were not corrected for the difference in the thermal expansion coefficients since the temperature at each depth along the pile was constant over the short loading period and thus the measure strains were the true mechanical strains. The correction for the difference in the thermal expansion coefficients between the vibrating wire and the grout paste was performed as (Geokon, 1986);

$$\varepsilon_{\text{true}} = \varepsilon_{\text{measured}} + (T_o - T_f)(C_{\text{vw}} - C_{\text{cm}})$$

Where;

C_{vw} : the thermal expansion coefficient of the vibrating wire = 12.2 με/℃,

C_{cm} : the thermal expansion coefficient of the cement mortar = 14.8 με/℃,

T_o : the initial temperature in ℃,

T_f : the final temperature in ℃.

The thermal strains measured during various thermo-mechanical tests were corrected for the effect of the difference in the thermal expansion coefficient using the above formula. Afterwards, the adjusted thermal strains measured by gauges in the pile segment embedded in the shale layer were used to correct for the location of the gauges within the pile cross-section following the procedure outlined in Section 8.4.3. The thermal strain profiles after these two adjustments at the end of T-MT 3, and T-MT 4 are presented in Figure 8.17, while Figure 8.18 shows the strain profiles at the end of each thermal load step performed in T-MT 1 and T-MT 2.

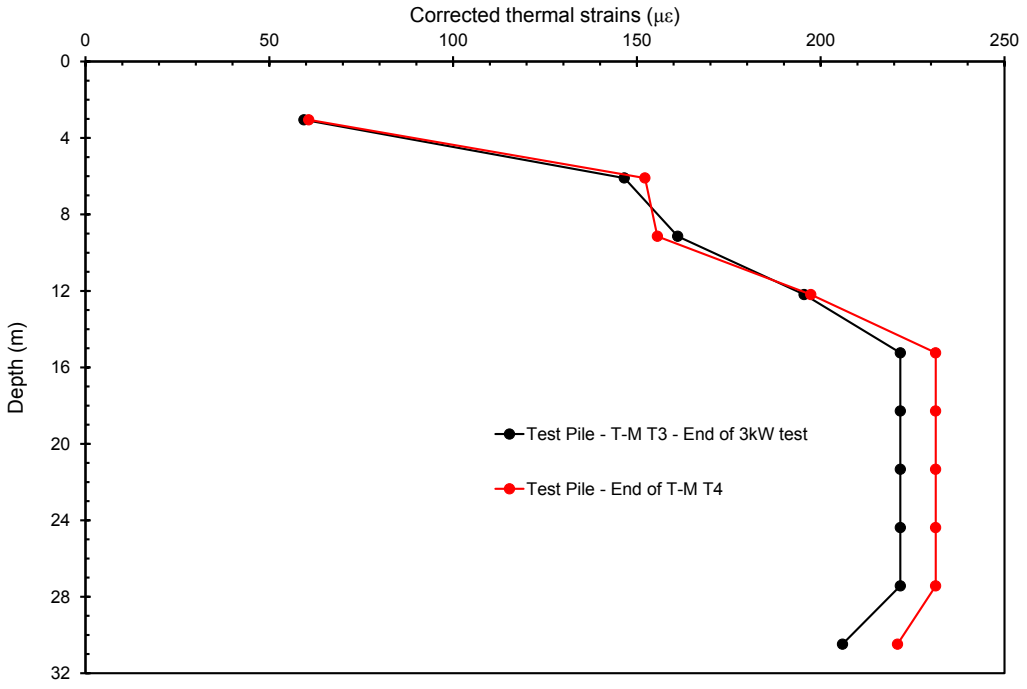

Figure 8.17. Blocked thermal strain profiles along the Test Pile at the end of T-MT 3, and T-MT 4.

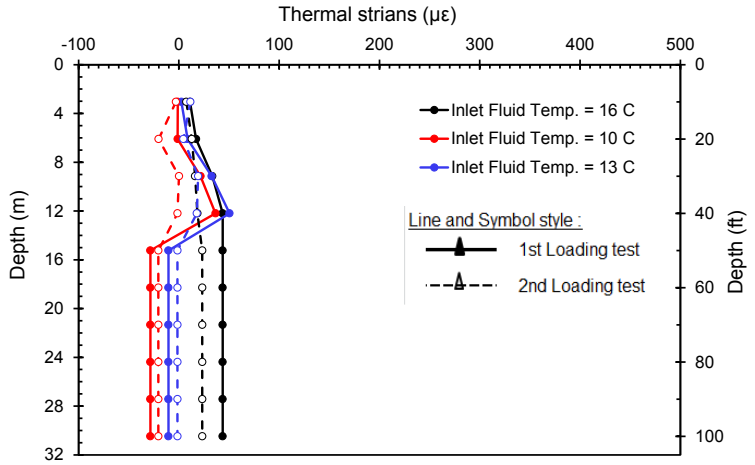

(c) 1st thermal cycle

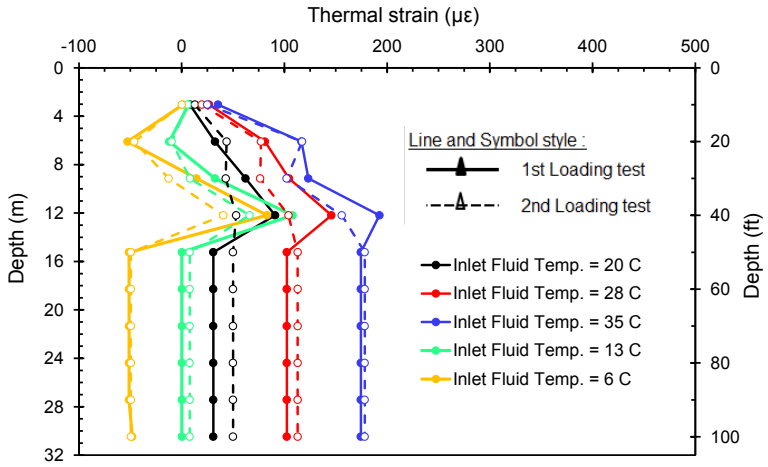

(d) 2nd thermal cycle

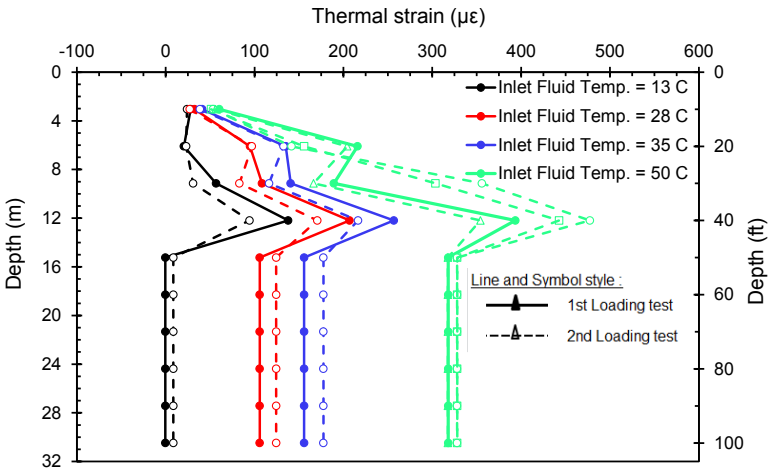

(e) 3rd thermal cycle

Figure 8.18. Blocked thermal strain profiles along the Test Pile at the end of each thermal load step of T-MT 1 and T-MT 2.

It is noticed from Figure 8.17 that the thermal strain profile at the end of T-MT 4 agrees with that obtained at the end of applying a heat rate of 3kW in T-MT 3. This observation was expected since the fluid temperatures from both tests were identical as shown in Figure 8.8. This also proves that the thermal strains in Energy Piles are not function of the technique used to apply the thermal load since this was the only difference between T-MT 3 and T-MT 4. Moreover, it is shown in Figure 8.18 that as the temperature of the inlet fluid increases, more blocked thermal strains in the Test Pile were observed. This is because for more inlet fluid temperatures, higher temperature changes were developed producing more thermal strains.

Furthermore, Figure 8.18 shows that the thermal strain profile of a specific thermal load step in T-MT 1 agrees with the respective profile in T-MT 2. In the segment of the Test Pile embedded in the silty sand layer, the thermal strains for all heating loads in T-MT 1 and T-MT 2 were increasing with depth till reaching the maximum value at 12 m (40 ft). Since the lowest blocked strains take place at the pile head, then the maximum thermal movements occurred at this point. At 12 m (40 ft) which is very close to the interface between the silty sand layer and the shale layer, the blocked thermal strains reached its maximum value suggesting the lowest thermal movement at this depth. This refers to having the neutral point close to 12 m (40 ft) as discussed in the Section 8.4.5and Section 8.5.

Moreover, it is observed that the thermal strain profiles for all thermo-mechanical tests in the pile segment embedded in the shale layer are uniform. A further investigation revealed that the uniform blocked strain profile for any given thermal load step is equivalent to the free strain corresponding to the considered thermal load. Thus, all thermal strains in the shale were blocked by the fixations at the pile toe and at the top of the shale layer in addition to the high frictional resistance of the shale. As discussed in Section 8.4.1, uniform thermal strains are expected when the pile head and toe are completely fixed or in the case of strong frictional or bonding resistances along the shaft as presented schematically in Figure 8.19. As suggested in Figure 8.19, uniform thermal strains will develop in the pile if its head and toe are completely fixed regardless of the type of the surrounding soil assuming that lateral deformations are also prevented by the soil mass. On the other hand to have a uniform thermal strain profile in a pile with partially fixed head and/or toe, the frictional resistant between the pile and its surrounding soils should be significantly high to prevent any desired thermal movements.

For the first thermal cycle in T-MT 1 before which the Test Pile and the ground were thermally undisturbed, applying a very small heating load using a circulating fluid at 16^{o}C (60.8°F) produced thermal strains in the silty sand layer that increase with depth till an ultimate value close to the soil-shale interface. These strains were not recoverable when the thermal load was reversed to cooling by circulating fluid at 10^{o}C (50°F) and 13^{o}C (55.4°F). The thermal strains developed in the pile segment embedded within the shale layer were recoverable with the applied fluid temperature. On the contrary, the thermal strains along the entire Test Pile were recoverable with the inlet fluid temperature for the first thermal cycle in T-MT 2. This change in behavior between T-MT 1, and T-MT 2 was attributed to the thermal history introduced to the ground after T-MT 1.

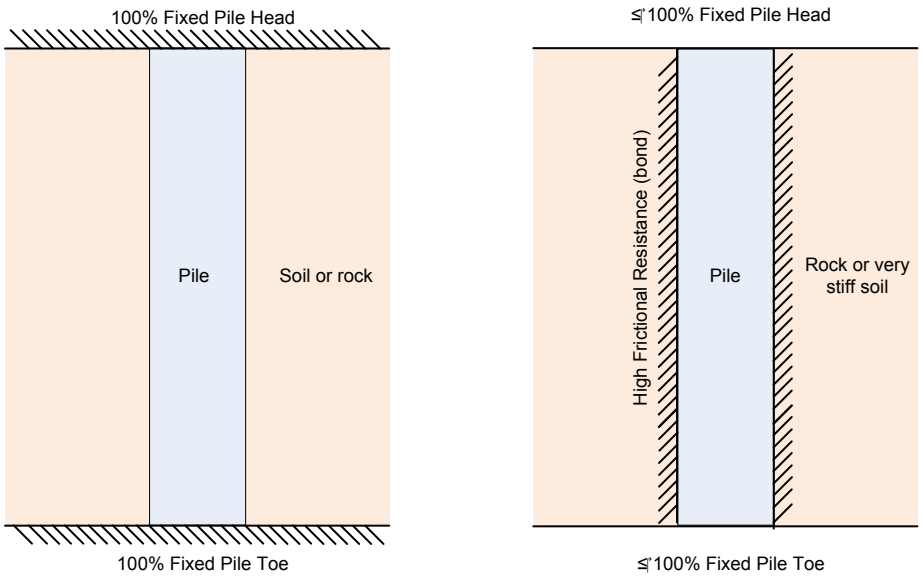

Figure 8.19. Schematic for cases where uniform thermal strains are expected.

The second thermal cycles in the two tests superimposed their thermal strains to those locked in from the first thermal cycle. In the 20-28-35°C (68-82.4-9°F) heating path of T-MT 1, the thermal strains increased at all depths as the inlet fluid temperature increases. In the pile segment embedded in the silty sand layer, the thermal strains increased with depth till 12 m (40 ft) below which uniform thermal strains were observed in the shale. It should be noticed that the peak thermal strains at 12 m (40 ft) for all heating step in this thermal cycle exceeded the uniform strains in the shale layer which, as mentioned earlier, is the free thermal strains. This unexpected behavior was due to having some strains locked-in the pile in the silty sand layer at the end of the first thermal cycle. For the heating path in T-MT 2, the thermal strains increased with depth in the silty sand layer and reached the uniform free thermal strain in the shale layer. In this test, the ultimate thermal strain did not exceed the free thermal strain in the shale layer since not much thermal strains were locked in the pile after the first cycle. When the 13-6°C (55-42.8°F) cooling path was applied, the thermal strains in the pile segment in the shale layer were recovered and became tensile for the two tests. On the other hand, a partial recovery of the thermal strains in the silty sand layer was observed in the cooling path of the two tests which again left some locked-in strains in the pile near the soil-shale interface.

The third thermal cycle in the two tests show similar behavior as the second thermal cycle in which; (1) the thermal strains increased at all depths as the heating load increases, (2) the thermal strain profile for a given heating load increased with depth till reaching to its ultimate value at 12 m (40 ft) below which the uniform free thermal strain was observed in the shale layer, and (3) the locked-in strains in the silty sand layer caused the ultimate thermal strains at 12 m (40 ft) to exceed the free thermal strain observed in the shale layer.

For 50ºC (122°F) thermal step in T-MT 2 in which the flow rate of the circulating fluid was increased from 5.3 lit/min (1.4 gpm) to 11.3 lit/min (3 gpm) then to 22.7 lit/min (6 gpm), it is noticed in Figure 8.18 that more thermal strains were observed at 9 m (30 ft) and 12 m (40 ft) for the last two flow rates compared to the former one. On the other hand, no significant additional thermal strains were observed during circulating the fluid at 11.3 lit/min (3gpm) and 22.7 lit/min (6 gpm) in the shale layer. This is because the temperature change in the shale layer did not change much as presented in Figure 8.12. Moreover, at 3 m (10 ft) and 6 m (20 ft) the thermal

strains at the end of the 5.3 lit/min (1.4 gpm) and the 11.3 lit/min (3 gpm) periods are less than this at the end of the 5.3 lit/min (1.4 gpm). This does not agree with the observed temperature changes shown in Figure 8.12 at these depths since more temperature change were observed for higher the flow rates. This is expected to produce more thermal strains. The reason for the observed unexpected behavior is that the thermal loads developed at the pile head due to circulating the fluid at a specific flow rate was released before increasing the flow rate to the next level. In other word, the load at the pile head was reset back to 150 tons. This load release caused some thermal strain relaxation at shallow depths.

8.4.5. Pile Head Movements and Neutral Point

The pile head movement was monitored using the four dial gauges placed at the pile head for all the thermal steps performed during T-MT 1, and T-MT 2. Figure 8.20 presents the measured pile head movements at the end of each thermal step. In this figure, positive sign refers to downward movements or pile shrinkage while negative sign refers to upward movements or pile elongation. A good agreement between the head movement from T-MT 1 and T-MT 2 is observed in this figure. Furthermore, the general response showed that the pile head moved upward when heating loads were applied indicating an overall pile expansion; while it moved downward when cooling loads were applied indicating an overall pile shrinkage.

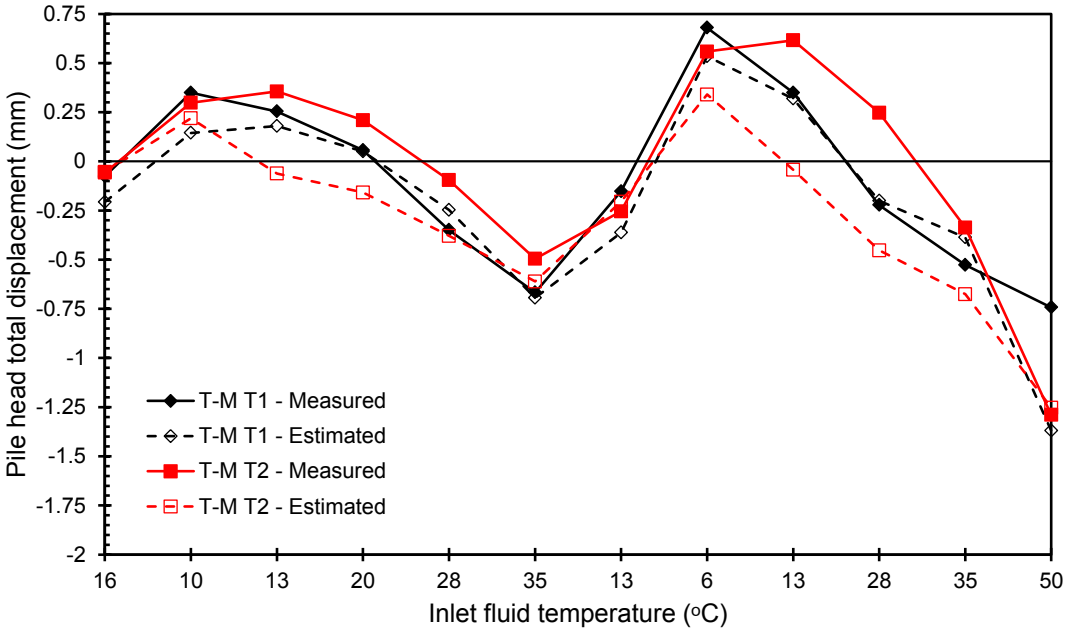

Figure 8.20. Pile head movement due to different thermal loads in T-MT 1 and T-MT 2.

The head movement curves and the blocked strain profiles were used to predict the location of the neutral point in the pile during heating and cooling. The neutral point is the point at which no thermal movements take place; in other words, all the thermal strains were blocked. This is performed by assuming that all thermal strains at depth 12 m (40 ft) were blocked which is supported by the previous conclusion that all the free strains in the pile segment in the shale were blocked. Thus, the observed strain at any depth above 12 m (40 ft) is calculated as the difference between the ultimate blocked strain at 12 m (40 ft) and the blocked strain at the considered depth. Thus, the change in the pile length between any two gauges was estimated by multiplying

the estimated observed strains by the initial length of the pile segment between the gauges. Figure 8.20 shows the measured head movements for T-MT 1 and T-MT 2 using the above procedure. As can be seen in this figure, good match between the estimated and the measured head movement curves is observed which suggest that the neutral point at which no movement occurs is located near to depth 12 m (40 ft). This is also confirmed with the finite element models reported in Section 8.5.

8.4.6. Thermal load profiles

The blocked thermal strains were translated into thermal loads in the pile using the pile moduli estimated in Section 8.2(d) . Pile moduli from the first load test were used to estimate thermal loads in the pile for T-MT 1. For thermo-mechanical load T-MT 2, T-MT 3, and T-MT 4, the pile moduli estimated from the second load test were used.

Figure 8.21 shows the thermal load profiles in the Test Pile at the end of T-MT 3 and T-MT 4. Similar to the thermal strains, uniform thermal loads in the pile segment embedded in the shale layer were observed. On the other hand, the thermal loads in the pile segment embedded in the silty sand layer follow the same trend of increasing with depth as the measured thermal strains shown in Figure 8.19 except at depth 6 m (20 ft) at which the thermal load was significantly magnified. This magnification is attributed to the higher pile modulus at 6 m (20 ft) compared to those at other depths.

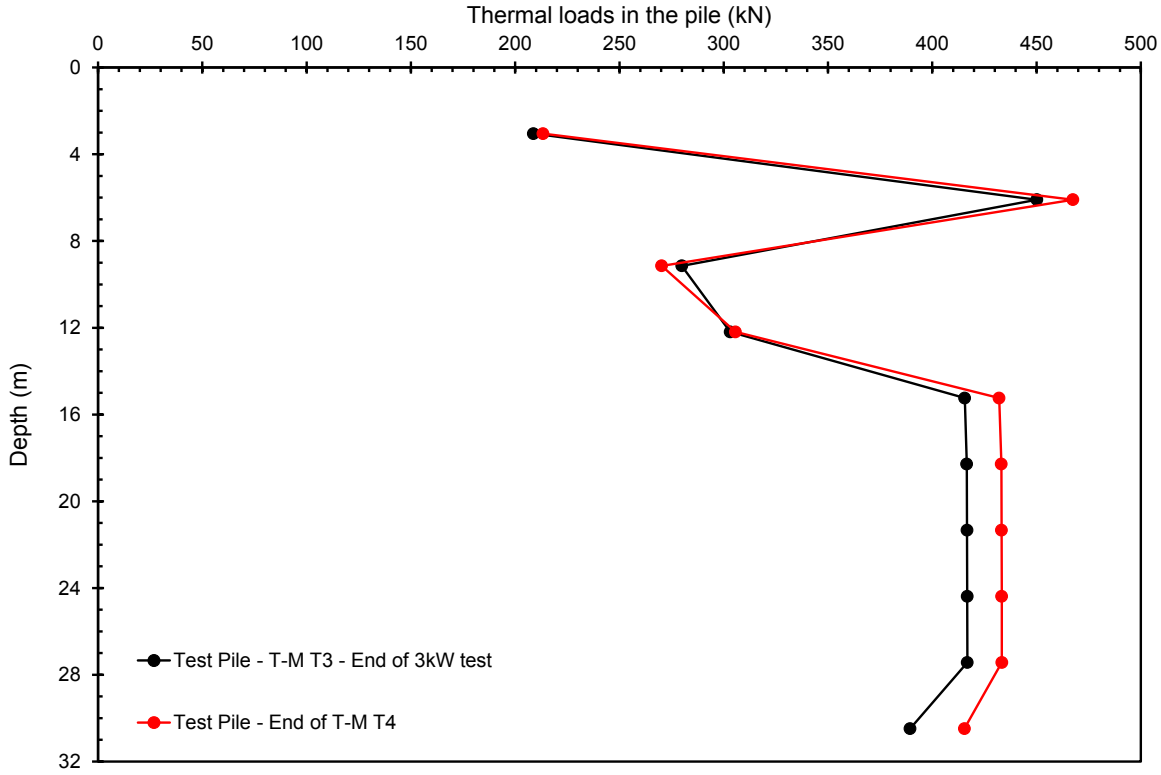

Figure 8.21. Thermal load profiles along the Test Pile at the end of T-MT 3, and T-MT 4.

Figure 8.22 shows that for the pile segment embedded in the silty sand layer; the thermal loads estimated from T-MT 1 agree with the respective loads estimated from T-MT 2 with load magnification at 6 m (20 ft) due to the higher pile modulus at this depth. While for the pile segment in the shale layer; similar to T-MT 3 and T-MT 4, uniform thermal loads were

developed in the T-MT 1 and T-MT 2 with more thermal loads developed for higher inlet fluid temperatures. It is also noticed from this figure that tensile thermal stresses were developed along the pile for the cooling steps of 10℃ (50°F) and 6℃ (42.8°F) inlet fluid temperatures. These tensile stresses agree with the previously observed tensile strains along the pile shown in Figure 8.18. Moreover, higher thermal loads were observed along the pile in T-MT 2 compared to those observed in T-MT 1 for a given thermal step. This was attributed to the higher pile moduli in the second load test as opposing to those obtained in the first load test as discussed in Section 8.2.d.

The observed thermal load magnification at 6 m (20 ft) presented in Figure 8.21 and Figure 8.22 can be confusing since this depth would be thought of as the neutral point. However, as discussed earlier, the neutral point from the strain perspective is expected to be at 12 m (40 ft) which is confirmed using finite element models in Section 8.5. Since the neutral point refers to the point of null observed strain or maximum blocked strains, then the location of the neutral point should be determined from the thermal strain profile not the thermal load profile especially when the pile modulus varies with depth.

It was also noticed that, the long thermal load duration of the last thermal step (i.e. 50℃) in T-MT 2 alters the shape of the thermal load profile along the Test Pile as shown in Figure 8.22 (c). In this figure, three thermal load profiles are presented for the 50°C (122°F) thermal step in T-MT 2; one profile for each flow rate used during this step. The thermal load profile for the lower flow rate 5.3 lit/min (1.4gpm) in T-MT 2 agrees with that obtained in T-MT 1 since both showed a thermal load magnification at shallow depths. This magnification is not observed for the other two flow rates 5.3 lit/min (1.4 gpm) and 11.3 lit/min (3 gpm); it was rather observed that the ultimate thermal load was at the 12 m (40 ft) instead of 6 m (20 ft) for flow rate of 5.3 lit/min (1.4 gpm). In order to infer if the alternation in the thermal load shape was due to the flow rate or the longer heating period, the heat injection rate produced while circulating each flow rate was calculated using as;

$$Heat\ injection\ (Watt) = M \times C_p \times |\Delta t|$$

where;

M : mass flow rate (kg/sec) = volume flow rate (m^3/sec) × water density (kg/m^3),

C_p : specific heat capacity of the water = 4180 J/(kg·°C),

Δt : difference between the inlet fluid temperature and the outlet fluid temperature (°C),

The average temperature differences between the inlet and the outlet fluids for 5.3 lit/min (1.4 gpm), 11.3 lit/min (3 gpm), and 22.7 lit/min (6 gpm) were 5.7℃ (10.3°F) , 3.1℃ (5.6°F) and 2.3℃ (4.1°F) respectively. These temperature differences produce average heat injection rates of 2.1kW, 2.4kW, and 3.6kW, respectively. About 15% increase in the heat injection rate was achieved when the flow rate was increased from 5.3 lit/min (1.4 gpm) to 11.3 lit/min (3 gpm), , and 50% increase when the flow rate was increased from 11.3 lit/min (3 gpm) to 22.7 lit/min (6 gpm) with a total increase of 70% from 5.3 lit/min (1.4 gpm). Thus, the alternation of the general shape of the thermal load profile is believed to be due to applying more heat injection rates corresponding to the higher flow rates for longer time periods.

Moreover, the thermal loads at 3 m and 6 m for the 50°C (122°F) thermal step in T-MT 2 are less when the flow rate was 5.3 lit/min (1.4 gpm) and 11.3 lit/min (3 gpm) compared to 5.3 lit/min (1.4 gpm). The reason for this was discussed in the thermal strain Section 8.4.4 and is attributed to releasing the thermal loads developed before every changing the flow rate.

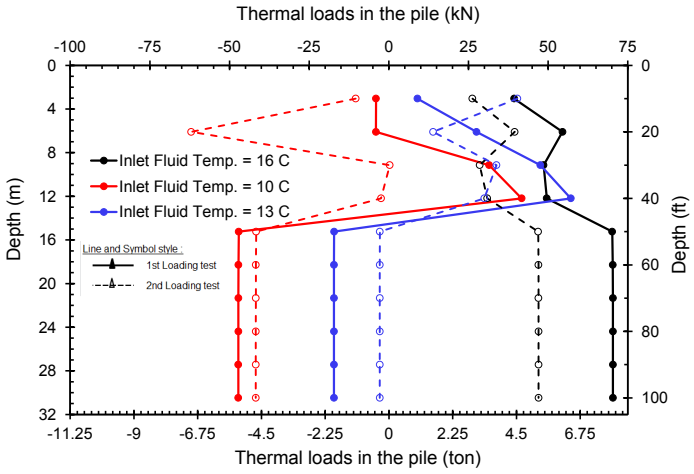

(f) 1st thermal cycle

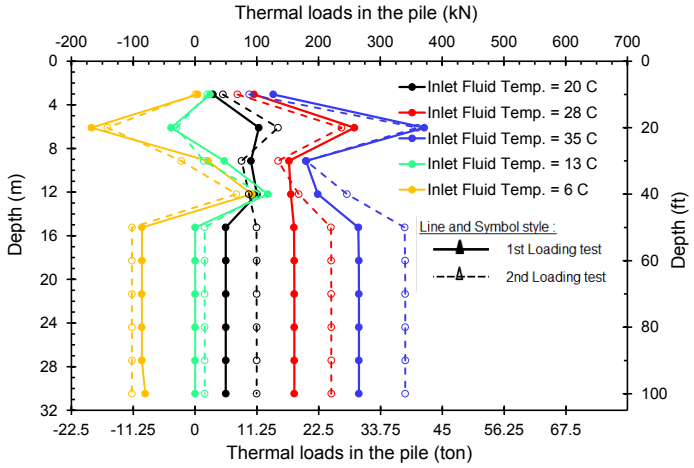

(g)2nd thermal cycle

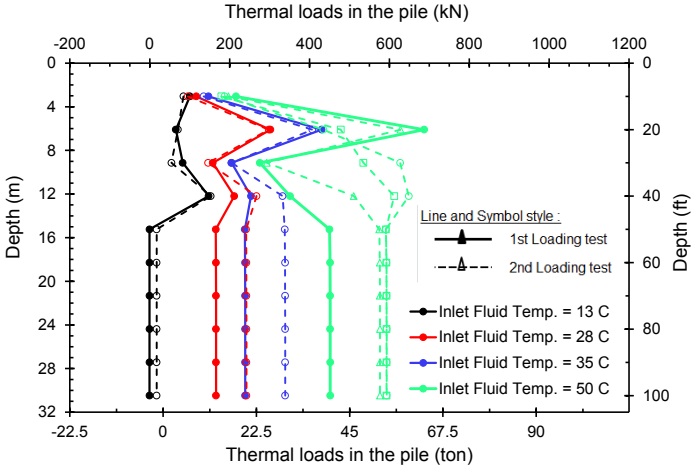

(h)3rd thermal cycle

Figure 8.22. Thermal load profiles along the Test Pile at the end of each thermal load step of T-MT 1 and T-MT 2.

8.4.7. Superimposed Thermo-Mechanical Load Profiles

The loads developed along the pile due to mechanically loading the pile head were superimposed to the thermal loads for evaluating the overall thermo-mechanical load in the pile. Figure 8.23 and Figure 8.24 show the thermo-mechanical load profiles along the Test Pile for each thermal step performed during T-MT 1 and T-MT 2, respectively. It is noticed from these figures that;

1) When the pile is subjected to heating loads, an increase in the load along the entire pile was observed with more load increase for higher inlet fluid temperatures. This is because the pile attempts to expand when heated, but as discussed earlier; the soil resists this expansion causing thermal compressive loads to build in the pile. The higher the applied fluid temperature, the more the desired thermal expansion of the pile and the more the restrained thermal movements which produces higher thermal loads.
2) On the other hand, tensile thermal loads were developed along the pile when subjected to cooling loads as discussed earlier. These tensile thermal loads reduce the overall load in the pile.
3) When the inlet fluid temperature was returned to the average undisturbed ground temperature 13℃ (55°F), the thermal loads in the pile segment in the top silty sand layer did not fully recover suggesting a stress build up in this pile portion after each thermal cycle. On the other hand, the thermal loads in the pile segment in the shale were fully recovered when the inlet fluid temperature was returned to 13℃ (55°F). More discussions about the recoverability of the thermal loads and strains are presented in the following section.

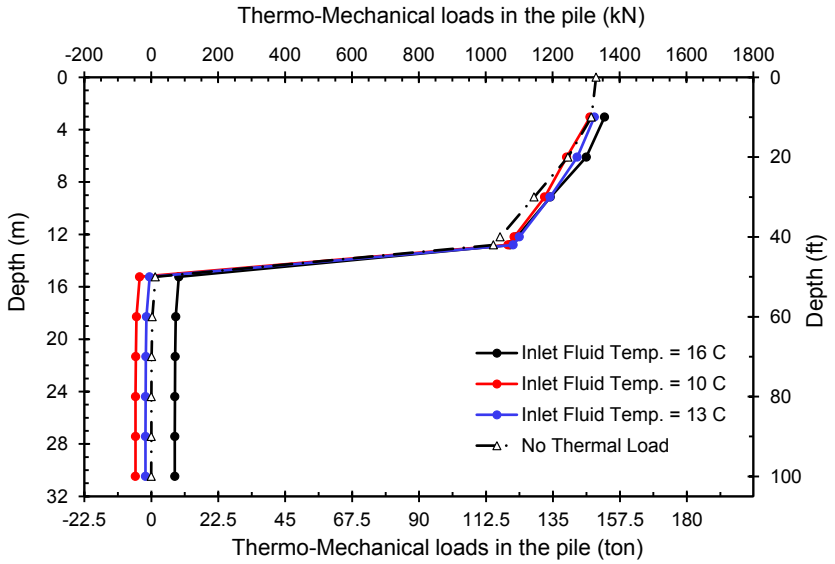

(a) 1st Thermal Cycle

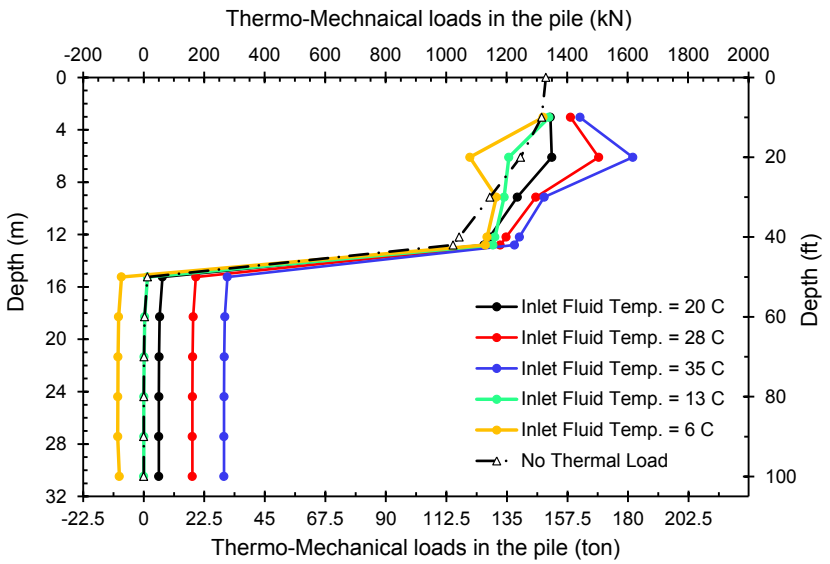

(b) 2nd Thermal Cycle

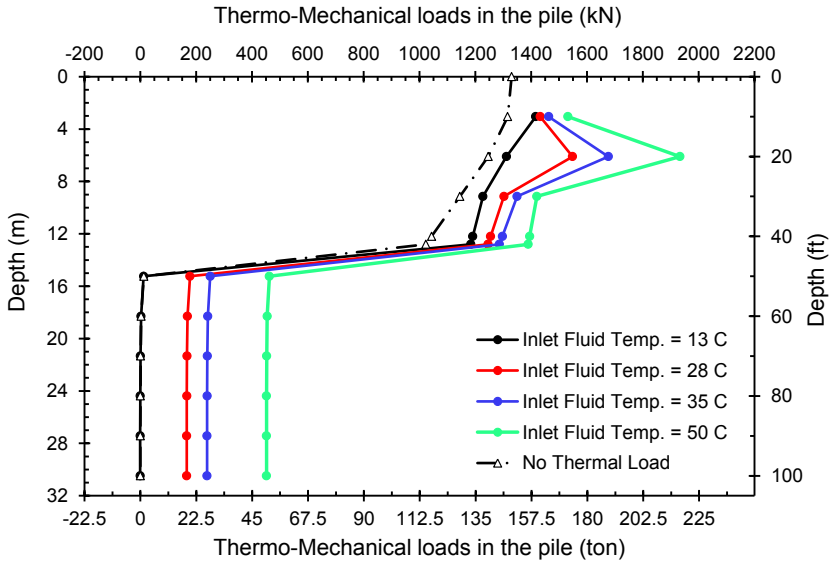

(c) 3rd Thermal Cycle

Figure 8.23. Thermo-mechanical load profile for each thermal step in T-MT 1.

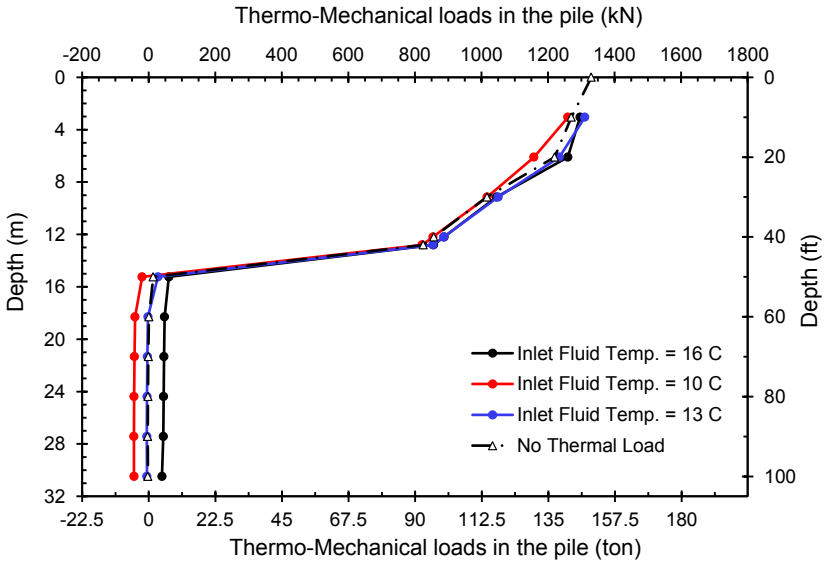

(d) 1st Thermal Cycle

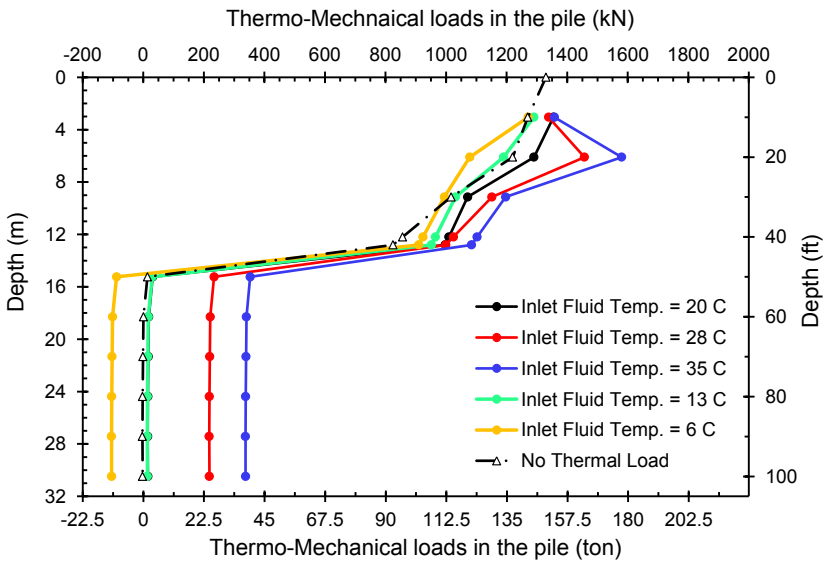

(e) 2nd Thermal Cycle

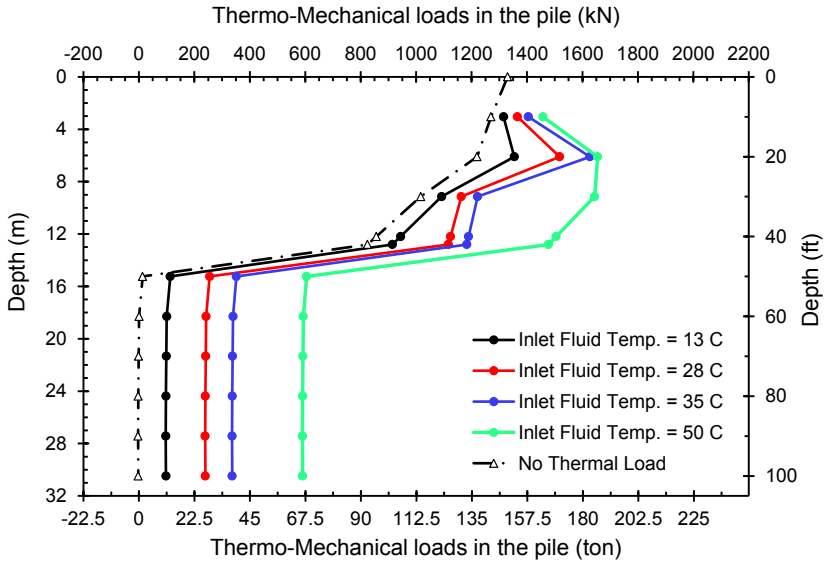

(f) 3rd Thermal Cycle

Figure 8.24. Thermo-mechanical load profile for each thermal step in T-MT 2.

8.4.8. Thermal Load Recovery

After each thermal cycle, some of the thermal loads are locked in the pile which, If not considered, can cause a structural failure of the pile when the total thermo-mechanical stresses exceed the compressive strength of the pile. No much attention was given to the locked in thermal loads in Energy Piles in the reported thermo-mechanical field tests in the literature (Bourne-Webb et al., 2009; Laloui et al., 2006). As part of the study reported here, the profiles for the load along the pile after each thermo-mechanical test were investigated to check if thermal loads were locked in or not.

Figure 8.25 presents the recovery of the thermal and structural loads in the pile after T-MT 1. The residual load distribution along the Test Pile prior to the first loading, $P_{residual}$ – T-MT 1 discussed in Section 8.2.d, is presented in this figure; in addition to the thermal load distribution ($P_{recovery}$ – T-MT 1) at the end of the thermal recovery period before unloading the pile. This thermal load at the end of the recovery period indicates that some of the thermally developed load along the pile was locked in after recovering the temperature. The superimposed residual and locked in thermal loads ($P_{residual}$ + $P_{recovery}$) is also presented in Figure 8.27 showing a significant increase in the load along the pile due to the first thermal test.

Additional loads were locked in the Test Pile after unloading the mechanical load from the pile head. These additional loads were added to the superimposed residual and thermal locked in loads to form the residual load profile encountered in the Test Pile prior to T-MT 2 ($P_{residual}$ – T-MT 2). As can be seen, the effect of the locked thermal loads in the pile in the top silty sand layer is larger than the locked structural stresses due to unloading. Moreover, there are no significant locked in thermal or structural loads in the pile segment embedded in the shale layer.

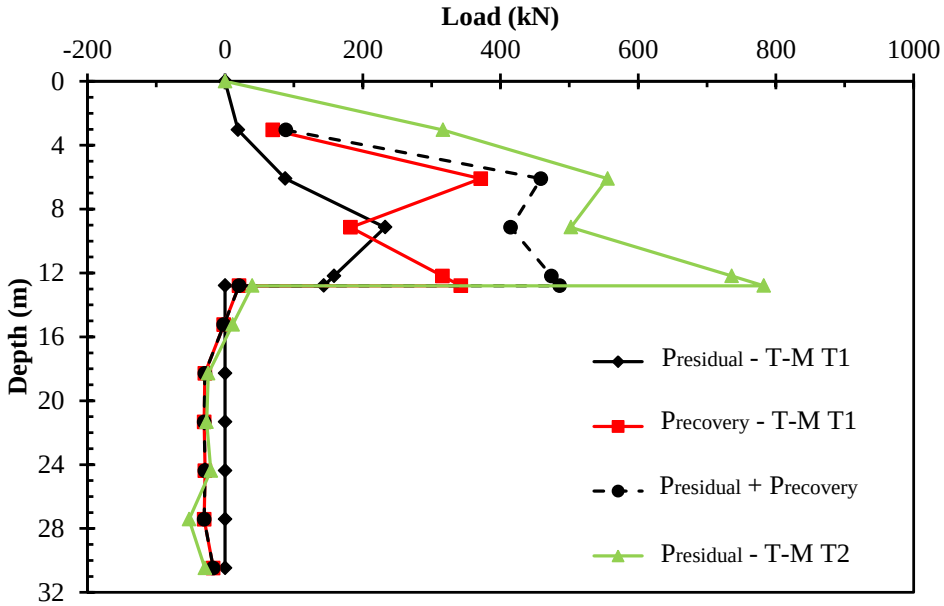

Figure 8.25. Thermal and structural load recovery after T-MT 1.

Similarly, the thermal load recovery after T-MT 2, T-MT 3, and T-MT 4 is presented in Figure 8.26. Again, there are no locked in thermal loads in the pile segment embedded in the shale layer. Moreover, the locked in thermal loads increase after each thermal load in the top silty sand layer. Therefore, the effect of consequent thermal cycles can cause the pile to reach to its structural capacity if the locked in thermal loads were ignored in the design.

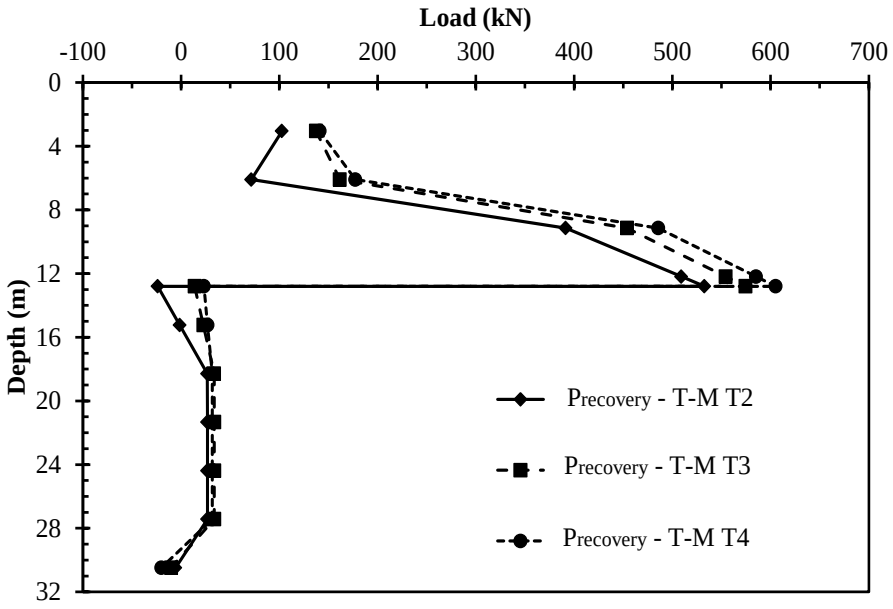

Figure 8.26. Thermal load recovery for T-MT 2, T-MT 3, and T-MT 4.

8.5. Numerical Modeling of Field Tests

The numerical models for Virginia Tech thermo-mechanical field tests are presented in this section. In these models, the strains and stresses generated along the Test Pile due to the mechanical load were decoupled from those developed by thermal loads. The overall thermo-mechanical response of the pile was then estimated by superimposing the decoupled mechanical and thermal strains and stresses to one another. The following discussions include; (1) the general concept for decoupling the thermal and the mechanical effects on an Energy Pile, (2) the analytical procedure proposed by Knellwolf et al. (2011) and its limitations, and (3) the proposed finite element modeling technique that implement the decoupled analysis and overcome the limitations of Knellwolf approach, and (4) results and discussions about the numerical models.

8.5.1. Concept of Uncoupled Thermo-Mechanical Modeling of Energy Piles

Two approaches can be followed for modeling the thermo-mechanical behavior of Energy Piles; (1) fully coupled thermo-mechanical modeling, and (2) decoupled thermal and mechanical analyses with the use of superposition for the overall thermo-mechanical behavior. The former approach is based on measuring the temperature changes in the soil due to the thermal operation of the ground loops. Then, these temperature changes are used to estimate the change in the soil stiffness and strength through various thermo-mechanical fully coupled soil constitutive models (Abuel-Naga et al., 2009; Cui et al., 2000; Hamidi and Khazaei, 2010; Hueckel and Baldi, 1990; Hueckel and Boretto, 1990; Hueckel et al., 1987; Hueckel et al., 2009; Hueckel et al., 1994; Hueckel and Pellegrini, 1991; Laloui, 2001; Laloui and Cekerevac, 2003, 2008; Laloui et al., 2001; Laloui et al., 2006; Modaressi and Laloui, 1997; Robinet et al., 1996; Seneviratne et al., 1993). The effect of the thermal loads on the mechanically loaded Energy Piles is estimated using numerical analysis codes that accounts for temperature-dependent soil parameters, as well as the thermal expansion of the pile. Thus, the soil gets weaker or stronger as its temperature varies allowing the numerical code to estimate the change in deformations and loads in the pile due to such variations. This approach is novel but estimating the parameters required to calibrate the selected constitutive model is a difficult task that requires special lab tests. These thermo-

mechanical lab tests are not widely available in the general practice which restricts the ability to use these models for the design of Energy Piles. Moreover, these constitutive models were all based on several assumptions that are not assured at the time due to the lack of enough lab tests on the thermo-mechanical response of soils.

The second approach which is based on the use of decoupled thermal and mechanical analyses and the superposition concept for estimating the thermo-mechanical response is adopted here. The use of this concept to analyze the thermo-mechanical behavior of Energy Piles was originally proposed by Bourne-Webb et al. (2009) and Knellwolf et al. (2011) presented the details of implementing the approach. The main advantage of this approach is its simplicity and ability to be implemented in practice using the currently available tools in addition to its acceptable accuracy. The following discussions outline clearly how this analysis is performed.

(a) Mechanical Analysis

When subjecting a pile to a mechanical load, the soil around the pile shaft generates frictional resistance to the applied load. For instance, as shown in Figure 8.27(a), the soils around the pile develop upward frictional forces ($R_{friction}$) when a compressive mechanical load is applied on the pile head. These upward frictional forces resist the applied downward compressive load ($P_{comp.}$). Similarly when the pile head is subjected to a tensile mechanical load as presented in Figure 8.27(b), the downward frictional forces are generated around the pile shaft resisting the applied load. This frictional resistance along the pile shaft is generally estimated as $R_{\text{friction}} = f_c A_p$; where f_c is the unit shaft friction, and A_p is the pile surface area $=2\pi rL$ for a circular pile with radius r and length L.

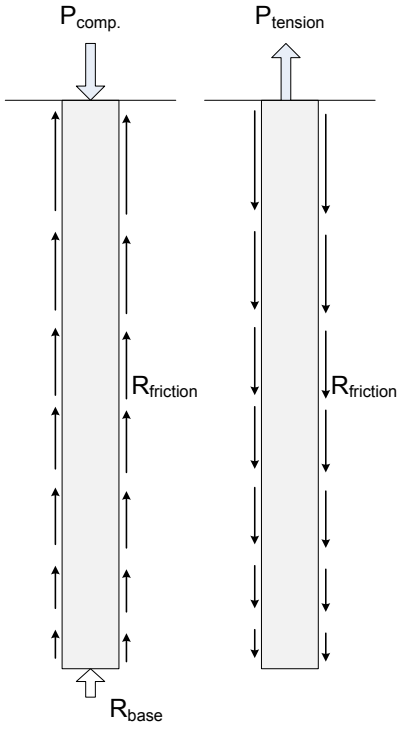

(a) Compressive loads (b) Tensile loads

Figure 8.27. Load carrying mechanisms of piles under mechanical compressive and tensile loads.

Furthermore, the soil underneath the toe of the pile react against the compressive load by applying a base resistance force (R_{base}) as shown in Figure 8.27(a). This base resistance force is estimated as $R_{\text{base}} = q_b A_b$; where q_b is the unit base resistance while A_b is the area of the pile cross-section $= \pi r^2$ for a circular pile with radius r. It should be noticed that, no base resistance is developed when the applied mechanical load is tension as shown in Figure 8.27(b) since the tensile strength of soils is neglected in general geotechnical engineering.

The magnitudes of the unit shaft friction and the unit base resistance are proportional to the displacement along the pile-soil interface and at the pile toe, respectively. For the unit shaft friction, higher frictional resistances are expected near the pile head as presented in Figure 8.27 with the longer arrows since more relative displacements between the pile and its surrounding soils are expected near the head.

Load-transfer curves (f-z for shaft; and q-z for base resistances) define the relationships between the displacement and the unit resistances of the base resistance and the shaft friction. Several load-transfer curves were reported in the literature such as Randolph and Wroth (1978), Frank and Zhao (1982), Armaleh and Desai (1987), and Frank et al. (1991). The curves for the shaft friction and the base resistance proposed by Frank and Zhao (1982) are presented in Figure 8.28. The finite element models reported in the following discussions are based on this set of load-displacement curves.

The initial part of the load-transfer curves shown in Figure 8.28 represents a linear response with slope of K_s and K_b for the shaft friction and the base resistance, respectively. These two slopes are function of the Menard pressuremeter modulus E_m (Knellwolf et al., 2011) and are generally estimated as;

$K_s = \frac{2E_m}{D}$ and $K_b = \frac{11E_m}{D}$ Where; D is the pile diameter.

This elastic response is assumed valid till the displacement corresponding to half of the ultimate unit shaft/base resistances. This displacement is considered as the first limiting displacement. After this displacement, the slope of the curve is reduced to one-fifth (20%) of the initial slope extending till the displacement corresponding to the ultimate value of the resistance as shown in Figure 8.28. The latter displacement is known as the second limiting displacement.

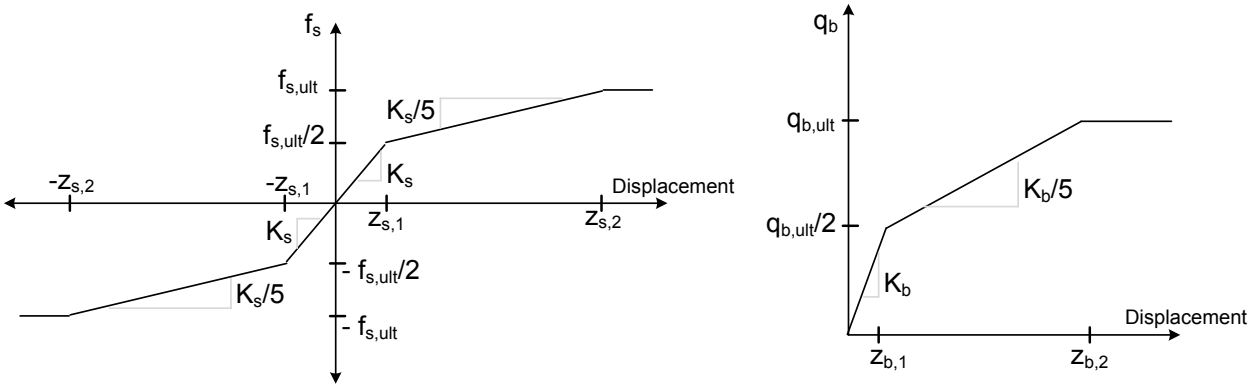

(a) Unit shaft friction (b) Unit base resistance

Figure 8.28. Load-transfer curves for the unit shaft friction and the unit base resistance (Frank and Zhao, 1982 - used under fair use, 2013)

The distribution of the mechanical load along a pile is estimated using the spring analogy in which the pile is divided into several elements connected to each other using linear elastic springs. The stiffness of the spring connecting any two pile elements of length h_n is given by $K_{pile,n} = E_{pile}/h_n$; where E_{pile} is the pile modulus. The soils around the pile shaft and at the pile toe are also modeled as springs acting on different pile elements with spring stiffness defined by the load-transfer curves shown in Figure 8.28.

Figure 8.29 shows the spring analogy for a pile subjected to compressive head load. In this figure the pile is divided into four elements. To estimate the load profile along the pile in Figure 8.29 under a given applied mechanical load ($P_{mech.}$);

1. A specific toe displacement ($z_{mech,t}$) is assumed. This toe displacement represents the displacement at the bottom of element 4 in Figure 8.29.

2. This assumed toe displacement is used to obtain the force at the bottom of element 4 which represents the base resisting force (R_{base}). The base resisting force is obtained by multiplying the area of the pile base by the unit base resistance (q_b) corresponding to the assumed toe displacement from the load-transfer curve for the foundation soil.
3. Afterwards, the displacement at the mid-length of element 4 ($z_{\text{mech,M}}$) is assumed equal to that at the base ($z_{\text{mech,t}}$) and the unit shaft friction along the bottom half of this element (f_s) is estimated using the load-transfer curve.
4. Then, the assumed displacement at the mid-length of element 4 is checked to satisfy the following formula;

$$z_{\text{mech,M}} - z_{\text{mech,t}} - \left(R_{\text{base}} + \frac{h_n \pi r}{2} \cdot f_s\left(z_{\text{mech,M}}\right) \right) \cdot \frac{h_n}{2AE_{pile}} = 0$$

If the above formula is not satisfied, the displacement at the mid-length of element 4 is varied and the unit shaft friction is re-estimated and the above condition is rechecked until satisfaction.

5. Once satisfied, the load at the mid-length of element 4 is estimated as;

$$F_M = R_{\text{base}} + h_n \pi r \cdot f_s\left(z_{\text{mech,M}}\right)$$

And the force (F_h) and the displacement ($z_{mech,h}$) at the top of element 4 are then estimated as;

$F_h = R_{\text{base}} + 2(F_M - R_{\text{base}})$, and $z_{mech,h} = z_{\text{mech,t}} + \frac{F_M}{AE} h_n$

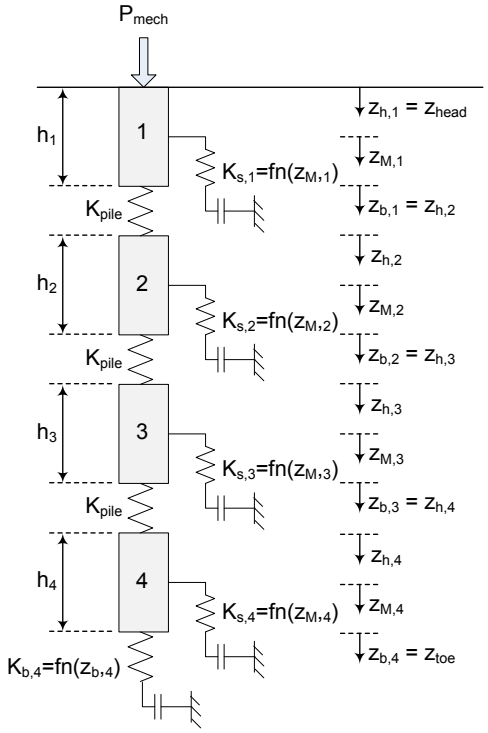

Figure 8.29. Spring analogy for analyzing the mechanical response in a pile foundation (Knellwolf et al. 2011- under fair use, 2013).

6. The force and the displacement at the top of element 4 are used as the force and displacement at the bottom of element 3 and the previous steps are repeated for element 3.
7. The procedure is repeated for all elements until reaching to element 1 at the pile head for which the estimated force at the top of the element is compared to the applied mechanical load;
   a. If these two loads are within an acceptable error margin, then the assumed toe displacement is correct and the load distribution in the pile is obtained from the estimated frictional and base resistances.
   b. If the error between the two loads is not acceptable, then the toe displacement is varied and the whole procedure is repeated until reaching to the acceptable accuracy in the pile load.

(b) Thermal Analysis

As discussed earlier in Section 8.4.1, Energy Piles tend to change volume when subjected to thermal loads. Only the change in the pile length due to thermal loads is considered here since the radial strains were not measured in any of the Virginia Tech thermo-mechanical tests. For simplicity, it is assumed that the Energy Pile considered here is not subjected to any mechanical load at its head. The following section discusses incorporating the mechanical load in the thermal analysis.

If a heating load is applied in an Energy Pile, it increases the temperature of the pile causing it to elongate. On the other hand, cooling loads reduce the temperature of the pile which causes the pile to shrink in length. If the pile was not embedded in the ground meaning that it is free to move, then the thermal deformations will take place around the point at the mid-length of the pile at which no thermal displacements occur as shown in Figure 8.30(a). This point is known as the neutral point. The thermal displacements increase linearly from the neutral point to its maximum values near the pile ends.

On the other hand, if the thermal displacements at the pile head or the pile toe were prohibited due to full fixation, then this fixed pile end represents the neutral point with null thermal displacements. For this case, the maximum thermal displacement will correspond to the free thermal strain as $\Delta L_{max} = \varepsilon_{free} \cdot L_{pile} = \alpha \cdot \Delta T \cdot L_{pile}$. This maximum displacement will occur at the other non-fixed pile end as shown in Figure 8.30(b) for fixed pile head and Figure 8.30(c) for fixed pile toe. Generally, the pile toe can be fixed if it is embedded on a very stiff soil or rock formation, while the pile head can be fixed when connected to a large pile cap or building element. Furthermore in case of having both of the pile ends fixed as shown in Figure 8.30.d, no thermal displacements will be observed at any point along the pile. Thus, all the thermal strains are blocked which will be translated into uniform thermal loads along the pile as discussed in Section 8.4.4.

When a pile installed in the ground with partially fixed ends is subjected to a heating load, it exhibits some thermal elongations which are less than this corresponding to the free thermal strain. The pile head moves upward while the pile toe moves down as shown in Figure 8.30(e). The opposite is true for cooling in which the pile shrinks with its head moving down and its toe moving up as in Figure 8.30(f). The direction of the thermal deformations is reversed at the neutral point located at some distance near the more fixed pile end. The deformations above and below the neutral point increase until reaching to the ultimate values at the pile ends. The expected profiles of the thermal displacements along the pile are presented in Figure 8.30 for each considered case. Moreover, the hatched areas in this figure represent the blocked displacements for each case. The blocked thermal strains are estimated through dividing the blocked displacements by the initial length of the pile.

The stresses and loads developed along the pile due to the applied thermal loads are proportional to the blocked thermal strains. Therefore, the maximum thermal stress occurs at the neutral point; while less thermal stresses are expected near the pile ends as shown in Figure 8.30(e) for heating and Figure 8.30(f) for cooling for a pile with partially fixed ends. Knellwolf et al. (2011) proposed to use the spring analogy to analyze the response of Energy Piles under thermal loads. To estimate the thermal load at the pile head, Knellwolf et al. (2011) proposed to use an elastic spring with stiffness (K_h) selected to best match the predicted thermal load and the one observed during field tests.

Figure 8.31 shows the Energy Pile presented earlier which was divided into four elements. This pile was assumed to be affected by a uniform temperature increase of ΔT over its entire

length. Therefore, the maximum pile elongation is limited to $\Delta L_{max} = \alpha \cdot \Delta T \cdot L_{pile}$ corresponding to the free thermal strain $\varepsilon_{free} = \alpha \cdot \Delta T$. Some of the free strain will be blocked by the soil friction and the fixity of the pile ends, thus the actual observed elongation will be less than ΔL_{max}. In Figure 8.31, the neutral point was assumed at the mid-length of the pile. Therefore, the top two elements will have upward thermal displacements while the lower two will have downward thermal displacements.

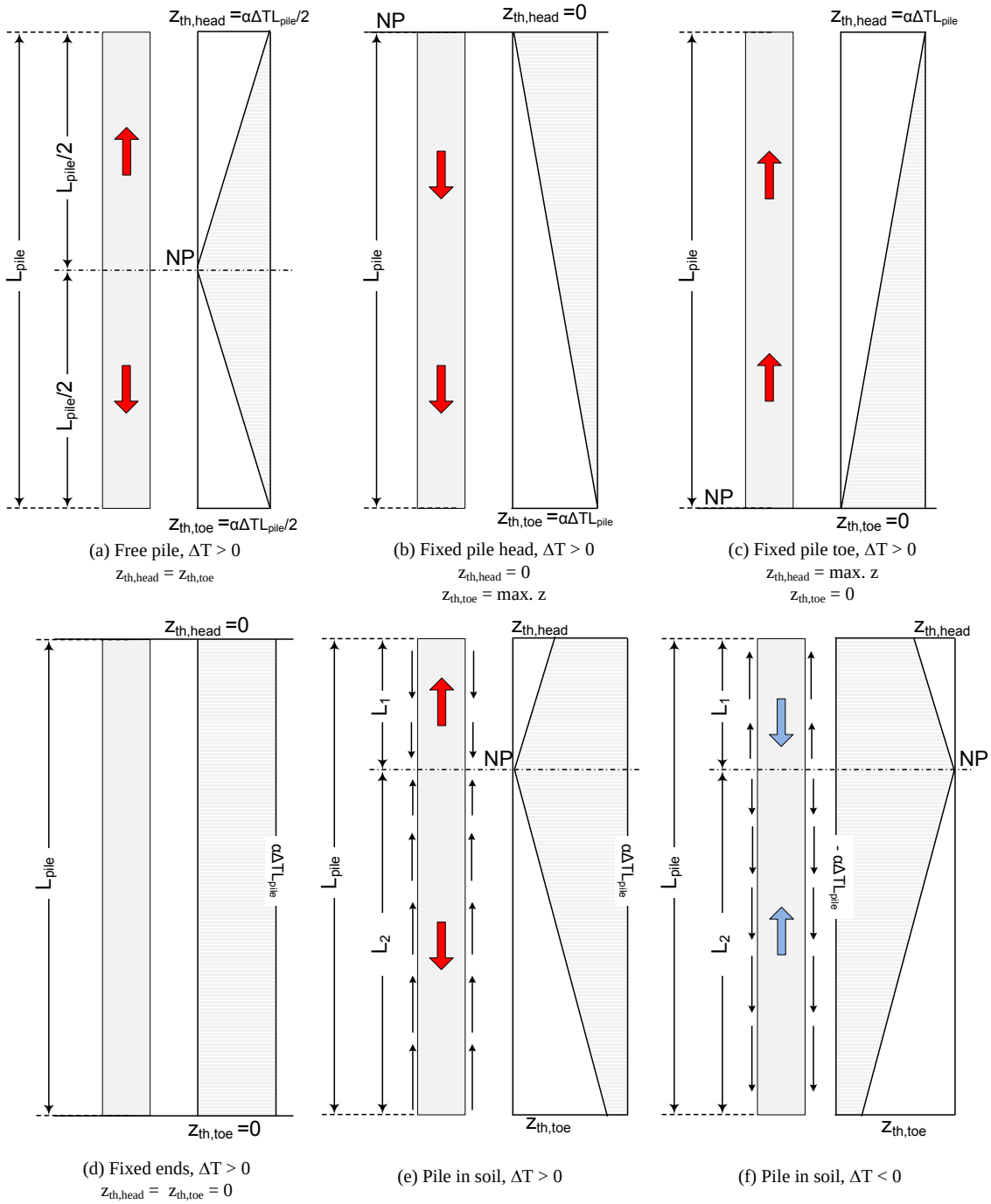

(a) Free pile, $\Delta T > 0$
$z_{th,head} = z_{th,toe}$

(b) Fixed pile head, $\Delta T > 0$
$z_{th,head} = 0$
$z_{th,toe} = \max. z$

(c) Fixed pile toe, $\Delta T > 0$
$z_{th,head} = \max. z$
$z_{th,toe} = 0$

(d) Fixed ends, $\Delta T > 0$
$z_{th,head} = z_{th,toe} = 0$

(e) Pile in soil, $\Delta T > 0$

(f) Pile in soil, $\Delta T < 0$

Figure 8.30. Effects of fixity of pile ends on the thermal displacement along the pile.

The steps listed below are followed to estimate the thermal strains, displacements, stresses along an Energy Pile subjected to a thermal load without having any mechanical on the pile head;

1. A neutral point (NP) is selected at the border between any two consequent elements,
2. All pile elements are assumed to undergo the free thermal strain $\varepsilon_{th,i} = \varepsilon_{\text{free}} = \alpha \cdot \Delta T$,

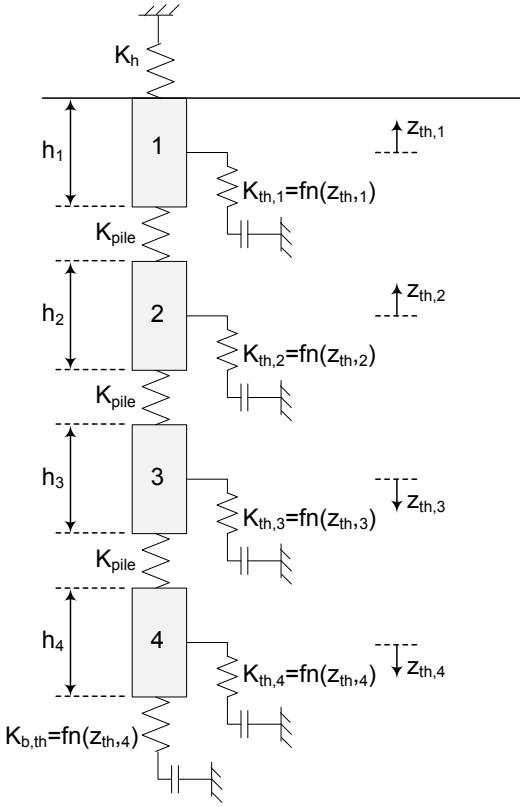

Figure 8.31. Effect of thermal heating load on Energy Piles (Knellwolf et al. 2011 - used under fair use, 2013).

3. The thermal displacements for each element is estimated as;

   $z_{th,i} = z_{th,i+1} - h_i \varepsilon_{th,i}$ for elements above NP

   $z_{th,i} = z_{th,i-1} + h_i \varepsilon_{th,i}$ for element below NP

   It should be noticed here that the downward movements are assumed positive while the upward movements are assumed negative.

4. Using the estimated displacements for each element along the shaft and the load-transfer curve for the unit shaft friction presented in Figure 8.28(a), the friction along each element is estimated,
5. Similarly at the pile toe, the displacement of the pile toe and the load-transfer curve for the unit base resistance presented in Figure 8.28(b) are used to estimate the thermal load at the toe. It should be noticed that the thermal load at the pile toe cannot be negative because the tensile strength of the soil is neglected,
6. The thermal load at the pile head is equal to the stiffness of the elastic spring (K_h) times the thermal displacement of the pile head,
7. Knowing all these thermally developed loads along the shaft and at the pile ends, the mobilized thermal stress in each element ($\sigma_{th,i}$) are estimated by summing the forces in the pile starting from either the pile toe or the pile head till the mid-point of the considered element,
8. The blocked thermal strains are estimated from the mobilized thermal stresses ($\varepsilon_{th\_b,i}$) as;

   $\varepsilon_{th\_b,i} = \sigma_{th,i} / E_{pile}$

9. The observed thermal strains ($\varepsilon_{th\_o,i}$) are then estimated by subtracting the blocked strains from the free strain; i.e. $\varepsilon_{th\_o,i} = \varepsilon_{\text{free}} - \varepsilon_{th\_b,i}$
10. Steps 2 through 9 are to be repeated until the observed strains for all elements converge. The final values of the observed strains after converging represent the actual strains,

11. For the thermal loads in the pile to reach to the equilibrium state, all the thermally developed frictional forces, and thermal loads at the pile head and toe should cancel each other. If these thermally developed forces do not vanish, then another NP is assumed and all the above steps are repeated until reaching to one NP that achieve the thermal equilibrium in the pile.

(c) Superimposed Thermo-Mechanical Analysis

If the thermal loads were applied on a mechanically loaded Energy Pile, the thermal strains and stresses along the pile will be superimposed to the preexisting mechanical strains and stresses, respectively. The thermal and the mechanical loads may produce displacements in the same direction or in opposite directions. For instance; downward mechanical displacements are generated along a pile subjected to a compressive mechanical load. If heated, all pile elements above the neutral point move upward while downward thermal displacements are observed in all elements below the neutral point. Thus, the total thermo-mechanical displacements for elements above the neutral point are less than the mechanical displacements, while the total displacements for elements below the neutral point are more than the mechanical displacements. Therefore, the pile above the neutral point is analogues to unloading the pile mechanically which causes the pile to recover some of the displacements. Similarly, the pile below the neutral point is analogues to an increase in the mechanical load. The opposite behavior is expected if the pile is cooled. For this case, the pile above the neutral point behave as if it is subjected to an increase in the mechanical load since the thermal and the mechanical displacements are downward. While, the pile below the neutral point acts as if it is mechanically unloaded because of the opposite thermal and mechanical displacements.

The superposition is achieved through treating the point representing the mechanical displacement and the corresponding resistances in the load-transfer curves as the reference from which the thermal displacements are measured. After superimposing the thermal displacements to the mechanical displacements, the total thermo-mechanical unit shaft and base resistances are estimated from the load-transfer curves. The thermal unit friction and base resistances are than estimated as the difference between the mechanical friction and base resistances and the respective total thermo-mechanical resistances. At last, the procedure outlined in the previous section to estimate the thermal response of the pile is followed using the estimated thermal unit resistances. Thus, an additional step is performed within the procedure outlined in the previous section to analyze thermal response of Energy Piles. This step is, for every neutral point trial, the thermo-mechanical unit resistances are estimated using the total thermo-mechanical displacement, and then the mechanical resistances are subtracted from these thermo-mechanical resistances to estimate the thermal resistances which are then used in the procedure.

Figure 8.32 shows a way to estimate the thermo-mechanical unit shaft friction by superimposing the mechanical and the thermal displacements in an Energy Pile initially subjected to a compressive mechanical load. The downward displacements are taken positive and the upward movements are assumed negative in this figure. According to Knellwolf et al. (2011) for the shaft friction, the load-transfer curve when the thermal and the mechanical displacements are opposing one another is assumed linear with a slope of K_s until half of the ultimate unit shaft friction after which the slope is reduced to 20% of K_s till reaching to the ultimate unit shaft friction. Similarly, Figure 8.33 shows the thermo-mechanical unit base resistance for an Energy Pile subjected to a compressive mechanical load. For the base resistance, the slope of the load-transfer curve is assumed equal to K_s for cases where the thermal

and the mechanical displacements are in opposite directions. This recovery line is limited to zero base resistance since the soil is assumed to have no tensile strength (Knellwolf et al., 2011).

It should be noticed that the thermal strains and stresses developed in a mechanically loaded pile due to a specific temperature change differ from those estimated if the pile was subjected to the same temperature change with no mechanical load. This is because for the latter case, the thermal displacements are measured from the origin of the load-transfer curves shown in Figure 8.28. While for the case of loaded pile and as discussed earlier, the thermal displacements are measured from the mechanical displacements which will change the amount of the predicted thermal resistances and the displacements required to mobilize them.

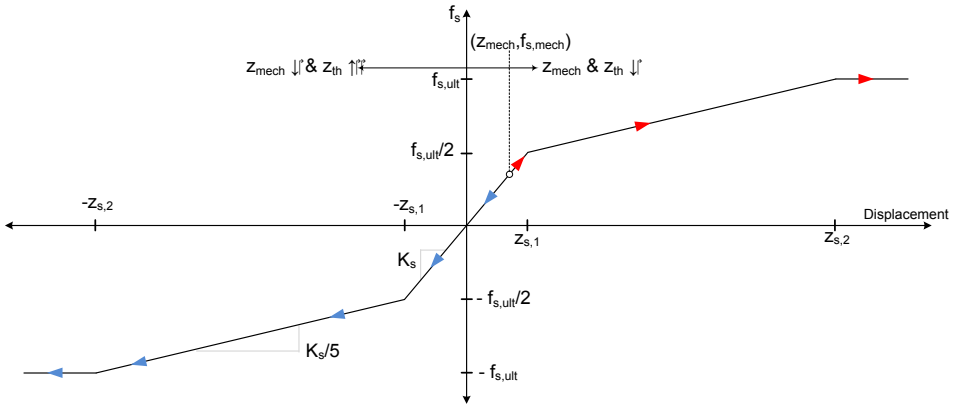

(a) $z_{mech} \leq z_{s,1}$

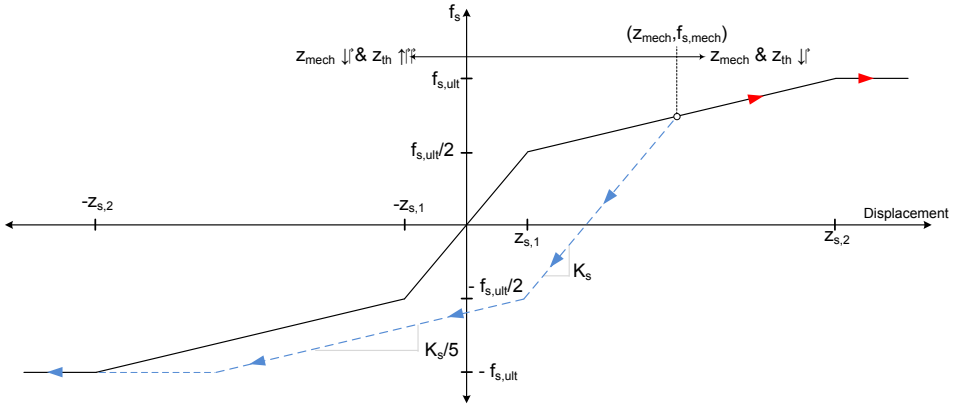

(b) $z_{s,1} \leq z_{mech} \leq z_{s,2}$

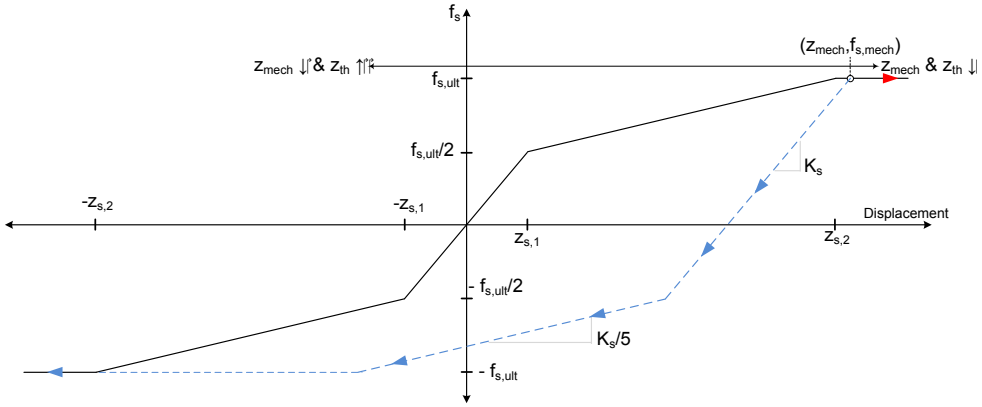

(c) $z_{s,2} \leq z_{mech}$

Figure 8.32. Thermo-mechanical response for the pile shaft friction.

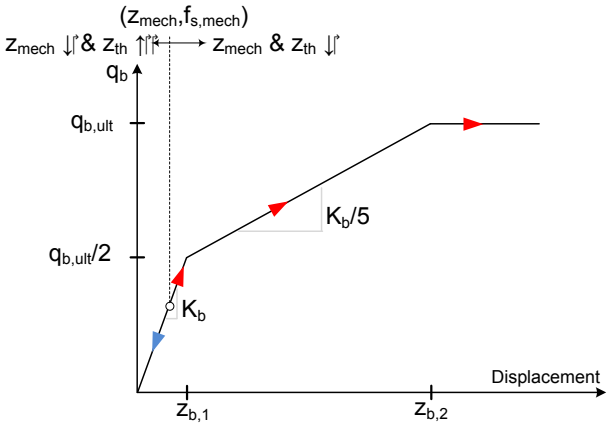

(a) $z_{mech} \leq z_{b,1}$

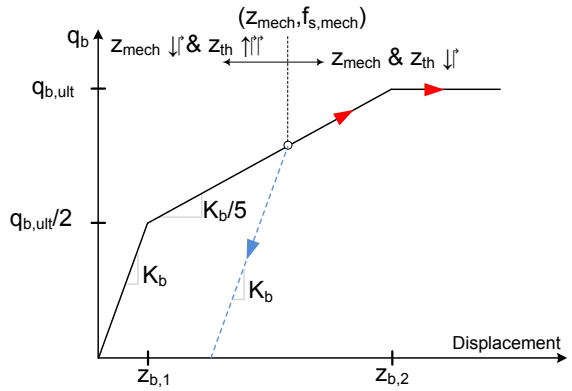

(b) $z_{b,1} \leq z_{mech} \leq z_{b,2}$

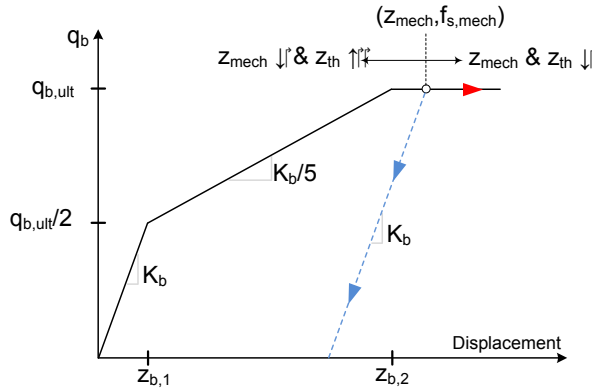

(c) $z_{b,2} \leq z_{mech}$

Figure 8.33. Thermo-mechanical response for the base resistance.

(d) Limitations of The Analytical Approach

The spring analogy described in the above sections and used to analyze the thermo-mechanical performance of Energy Piles has three limitations;

1. The assumption that the load-transfer curves do not vary with varying temperature. This contradicts that fact that the soil strength and stiffness are affected by the temperature of

the soil which consequently is expected to affect the spring stiffness representing the soil in the load-transfer curves. However, temperature-dependent load-transfer curves can be easily incorporated into the spring analogy, if known. In the thermo-mechanical analysis performed in this chapter, constant temperature-independent load-transfer curves are used due to the lack of information about the dependency of the strength and the stiffness of the soils at Virginia Tech site on temperature. Future research will include building temperature-dependent load-transfer curves to relax this limitation.

2. To perform the thermal analysis, the stiffness of the elastic spring assumed at the pile head is required. This stiffness depends of the connection between the pile head and the pile cap or the foundation system. It is difficult to estimate such stiffness and Kne1lwolf et al. (2011) selected the stiffness for the head spring such that a match between the field strain and the estimated strains is achieved. This process is time consuming since it requires a lot of iterations to reach to a good match. As presented in the following section, the use of COMSOL Multiphysics finite element allows optimizing for the stiffness of the head spring automatically.
3. The mechanical analysis in the spring analogy is a toe-head analysis in which the displacements and loads in the pile are solved from the pile toe to the pile head. The right displacement and loads in the pile are found iteratively as discussed in Section 8.5.1.a. This toe-head analysis does not work if the toe or any intermediate point along the pile is fixed since fixation is represented with a very high spring stiffness which produces high loads in the pile. These high loads cause the estimated load at the pile head to diverge significantly from the actual applied load. This limitation can be relaxed by incorporating the spring analogy in numerical models (finite element or finite difference) which are based on solving a matrix of degrees of freedoms rather than element wise toe-head analysis.

8.5.2. Decoupled Finite Element Approach for Energy Piles

Due to the limitations of the analytical method proposed by Knellwolf et al. (2011) for applying the spring analogy to analyze the thermo-mechanical response of Energy Piles, COMSOL Multiphysics finite element package (COMSOL, 2011) is utilized to relax these limitations and develop a robust modeling procedure for Energy Piles.

8.5.3. Load-Displacement Curves

Using the finite element analysis to implement the spring analogy is performed by modeling the soil at the pile surface as springs. The forces in the soil springs are estimated from the spring displacement as defined by the load-transfer curves for the unit shaft friction and the unit base resistance. Thus, the load-transfer curves discussed in Section 8.5.1 should be incorporated in the finite element framework. These curves cannot be implemented directly in finite element models since a spring in finite element is defined by its stiffness. The load-transfer curves do not provide the spring stiffness directly; they rather provide relationships between the displacement of a spring and the corresponding stress in the spring.

The stiffness of a spring is the ratio of the stress in the spring to the displacement required to develop that stress. For the load-transfer curves, the stiffness of the soil springs (K_{soil}) varies over a displacement range within these curves as shown in Figure 8.34 for the shaft and base resistances. This is because the load-transfer curves are defined as linear piece-wise relations over specific displacement ranges. Therefore, the load-transfer curves should be translated into stiffness-displacement curves to be able to utilize them in a finite element framework.

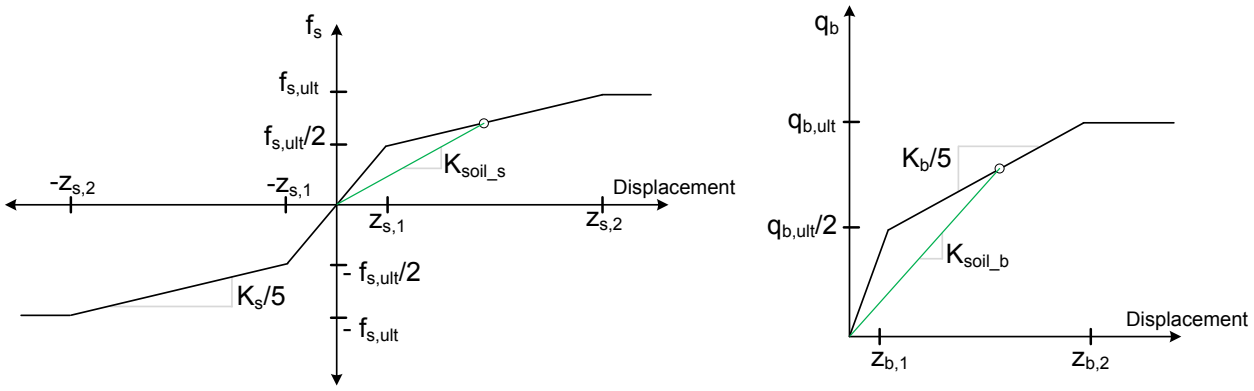

(a) Unit shaft friction

(b) Unit base resistance

Figure 8.34. Stiffness of the soil springs (K_{soil}) for finite element modeling of the load-transfer curves.

i. Mechanical Analysis

For the mechanical analysis, the load-transfer curves proposed by Frank and Zhao (1982) are translated into stiffness-displacement curves as follows;

- For the unit shaft friction load-transfer curve:

$$K_{\text{soil\_s}} = \begin{cases} K_s \ \ldots\ldots\ldots\ldots\ldots\ldots\ldots\ldots\ldots\ldots\ldots\ldots\ldots\ldots\ldots\ldots \text{ for } \left|z_{\text{mech,s}}\right| \le z_{\text{s,1}} \\ \dfrac{\left(f_{\text{s,ult}}/2\right)\left(1+\frac{\left|z_{\text{mech,s}}\right|-z_{\text{s,1}}}{z_{\text{s,2}}-z_{\text{s,1}}}\right)}{\left|z_{\text{mech,s}}\right|} \ldots\ldots\ldots\ldots\ldots \text{ for } z_{s,1} \le \left|z_{\text{mech,s}}\right| \le z_{s,2} \\ \dfrac{f_{\text{s,ult}}}{\left|z_{\text{mech,s}}\right|} = \dfrac{K_s}{3} \ \ldots\ldots\ldots\ldots\ldots\ldots\ldots\ldots\ldots\ldots\ldots\ldots\ldots \text{ for } z_{s,2} \le \left|z_{\text{mech,s}}\right| \end{cases}$$

Where;

$$z_{\text{s,1}} = \frac{f_{\text{s,ult}}}{2\,K_s} \quad \text{and} \quad z_{\text{s,2}} = z_{\text{s,1}} + \frac{5\,f_{\text{s,ult}}}{2\,K_s} = 6\,z_{\text{s,1}}$$

It should be noticed that this formulation holds true if the pile displacement is upward or downward as long as the absolute value of the mechanical displacement, $\left|z_{\text{mech,s}}\right|$, is used. The reason for this is that even though the displacement is negative for upward movements but the slope of the line connecting a point along the negative portion of the load-transfer curve and the origin which is the spring stiffness is positive.

Figure 8.35 shows the stiffness-displacement curve for the springs representing the soil along the pile shaft which is obtained using the transformation formulas presented above for the unit shaft friction. As appears in this figure, the shaft springs will have a constant stiffness until the mechanical displacement reaches its first limiting value, $z_{\text{s,1}}$. After that, the stiffness of the shaft spring reduces dramatically with increasing displacement until the second limiting value, $z_{\text{s,2}}$, after which the reduction continues but at a different rate.

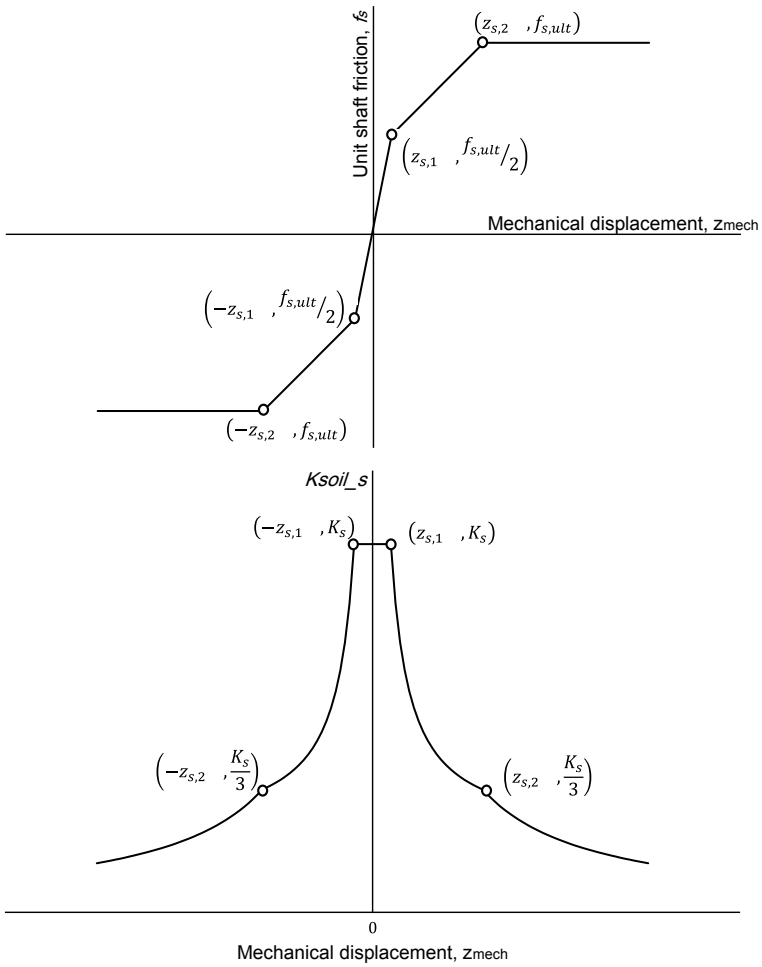

Figure 8.35. Spring stiffness-displacement curve from the load-transfer curve of the unit shaft friction.

- For the unit base resistance load-transfer curve:

$$K_{\text{soil\_b}} = \begin{cases} K_b \ \ldots\ldots\ldots\ldots\ldots\ldots\ldots\ldots\ldots\ldots\ldots\ldots\ldots\ldots\ldots\ldots \text{ for } \mathrm{z_{mech,b}} \le z_{\mathrm{b,1}} \\ \dfrac{\left(q_{\mathrm{b,ult}}/2\right)\left(1+\frac{\mathrm{z_{mech,b}}-z_{\mathrm{b,1}}}{z_{\mathrm{b,2}}-z_{\mathrm{b,1}}}\right)}{\mathrm{z_{mech,b}}} \ldots\ldots\ldots\ldots\ldots \text{ for } \mathrm{z_{b,1}} \le \mathrm{z_{mech,b}} \le \mathrm{z_{b,2}} \\ \dfrac{q_{\mathrm{b,ult}}}{\mathrm{z_{mech,b}}} = \dfrac{K_b}{3} \ \ldots\ldots\ldots\ldots\ldots\ldots\ldots\ldots\ldots\ldots\ldots\ldots\ldots\ldots \text{ for } \mathrm{z_{b,2}} \le \mathrm{z_{mech,b}} \end{cases}$$

Where;

$$z_{\mathrm{b,1}} = \frac{q_{\mathrm{b,ult}}}{2\,K_b} \quad \text{and} \quad z_{\mathrm{b,2}} = z_{\mathrm{b,1}} + \frac{5\,q_{\mathrm{b,ult}}}{2\,K_b} = 6\,z_{\mathrm{b,1}}$$

The load-transfer curve for the unit base resistance does not require the use of the absolute value of the mechanical displacement since no tensile base resistances will develop if the displacements are upward.

Figure 8.36 shows the stiffness-displacement curve for the springs representing the soil at the toe of the pile which is obtained using the transformation formulas presented above for the unit base resistance. This figure looks like the one presented in Figure 8.35 for the shaft soil springs except it only has the side of the curve representing the positive downward displacements.

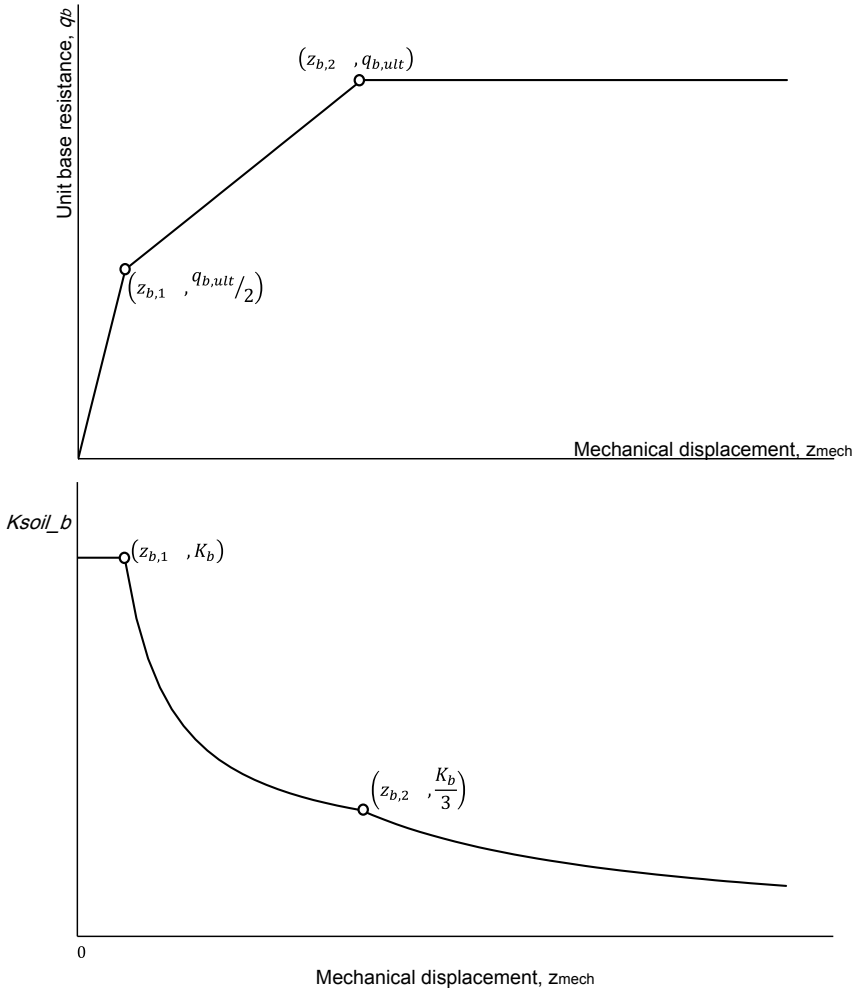

Figure 8.36. Spring stiffness-displacement curve from the load-transfer curve of the unit base resistance.

ii. Thermal Analysis

The change in the stiffness of the springs representing the soil around the pile shaft and at the pile toe due to the thermal operation of the Energy Pile is considered as the thermal stiffness of the springs (K_{soil_th}). This thermal stiffness is defined as the ratio between the changes in the unit resistance due to the thermal loads and the thermal displacement (z_{th}). As discussed in Section 8.5.1, the thermal unit shaft and base resistances are estimated as the difference between the unit resistances corresponding to the total thermo-mechanical displacement ($z_{mech}+z_{th}$) and the respective resistances corresponding to the mechanical displacement (z_{mech}). Thus, the thermal unit resistances depend on; (1) the mechanical displacement and unit resistances, and (2) the total thermo-mechanical displacement which depends on the direction and the magnitude of the thermal displacement. The direction of the thermal displacement determines if the thermal

load causes addition loading of the pile or if it releases some of the mechanical load as explained in Section 8.5.1 and discussed more below.

Figure 8.37 presents the concept of estimating the thermal unit shaft friction using the load-transfer curves proposed by Frank and Zhao (1982) and modified for the unloading path by Knellwolf et al. (2011). The thermal unit shaft friction for consistent directions of the thermal and the mechanical displacements is shown in Figure 8.37.a. For this scenario, the thermal displacement increases the frictional resistance along the pile shaft. Thus, the loading path of the load-transfer curves is followed and the thermo-mechanical stiffness of the soil spring, $K_{soil\_s}(z_{mech}+z_{th})$, is estimated using the total thermo-mechanical displacement ($z_{mech}+z_{th}$) in lieu of the mechanical displacement (z_{mech}) in the K_{soil_s} formula presented in the previous section. The thermal spring stiffness $K_{soil\_s\_th}$ is then estimated as the difference between the mechanical spring stiffness and the thermo-mechanical stiffness as;

$$K_{\text{soil\_s\_th}} = \frac{K_{\text{soil\_s}}\left(z_{\text{mech,s}} + z_{\text{th,s}}\right) * \left|z_{\text{mech,s}} + z_{\text{th,s}}\right| - K_{\text{soil\_s}}\left(z_{\text{mech,s}}\right) * \left|z_{\text{mech,s}}\right|}{\left|z_{\text{th,s}}\right|}$$

When the thermal displacement (z_{th}) releases the mechanical frictional resistance as shown in Figure 8.37.b, the unloading path is traced to estimate the thermal spring stiffness. The slope of the unloading path of the load-transfer curve is generalized here as the $K_{s\_unloading}$ rather than assuming it equal to the slope of the loading path as proposed by Knellwolf et al. (2011). The generalization is proposed since it is expected to have an increase in the soil stiffness after loading-unloading cycles. The ratio between the loading and the unloading spring stiffness are estimated using optimization techniques as discussed in Section 8.5.2.d. When the generalized unloading path of the load-transfer curves is traced and based on the magnitude of the thermal displacement, there are three cases for the thermo-mechanical point (*i*) in the figure; (1) point *i* is located within the first linear segment of the unloading path which is sloped at $K_{s\_unloading}$, (2) point *i* is located within the second linear segment which is sloped at 20% of $K_{s\_unloading}$, i.e. $K_{s\_unloading}/5$, and (3) point *i* is located in the loading segment corresponding to the ultimate unit friction ($f_{s,ult}$). The thermal stiffness of the soil spring is estimated as follows for each one of these cases;

- Case (1): $\left|z_{\text{th,s}}\right| \le \frac{\left(\text{f}_{\text{s,ult}}/2\right)+K_{\text{soil\_s}}\left(z_{\text{mech,s}}\right)*\left|z_{\text{mech,s}}\right|}{K_{\text{s\_unloading}}}$

$$K_{\text{soil\_s\_th}} = K_{\text{s\_unloading}}$$

- Case (2): $\frac{\left(\text{f}_{\text{s,ult}}/2\right)+K_{\text{soil\_s}}\left(z_{\text{mech,s}}\right)\left|z_{\text{mech,s}}\right|}{K_{\text{s\_unloading}}} \le \left|z_{\text{th,s}}\right| \le \frac{3\text{f}_{\text{s,ult}}+K_{\text{soil}_\text{s}}\left(z_{\text{mech,s}}\right)\left|z_{\text{mech,s}}\right|}{K_{\text{s\_unloading}}}$

$$K_{\text{soil\_s\_th}} = \frac{1}{5}\left(K_{\text{s\_unloading}} + \frac{4\,K_{\text{soil\_s}}\left(z_{\text{mech,s}}\right) * \left|z_{\text{mech,s}}\right| + 2\text{f}_{\text{s,ult}}}{\left|z_{\text{th,s}}\right|}\right)$$

- Case (3): $\left|z_{\text{th,s}}\right| \ge \left(\frac{\left(\text{f}_{\text{s,ult}}/2\right)+K_{\text{soil}_\text{s}}\left(z_{\text{mech,s}}\right)*\left|z_{\text{mech,s}}\right|}{K_{\text{s\_unloading}}} + \frac{5\,\text{f}_{\text{s,ult}}}{2\,K_{\text{s\_unloading}}}\right)$

$$K_{\text{soil\_s\_th}} = \frac{K_{\text{soil\_s}}\left(z_{\text{mech,s}}\right) * \left|z_{\text{mech,s}}\right| + \text{f}_{\text{s,ult}}}{\left|z_{\text{th,s}}\right|}$$

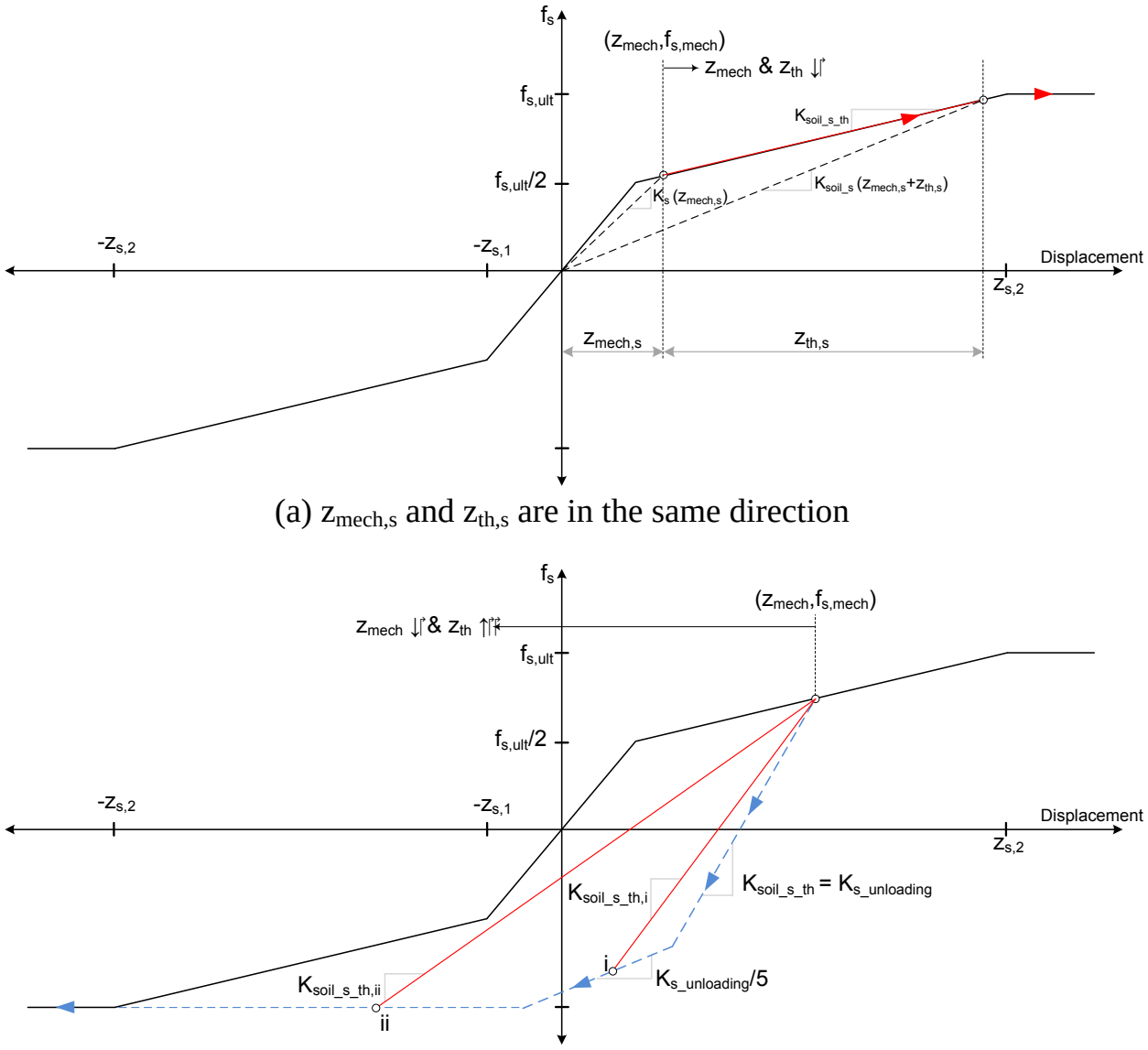

Figure 8.37. Thermal stiffness of soil springs along the shaft of Energy Piles.

The above formulas of the thermal spring stiffness for the two scenarios of opposing and consistent directions of the thermal and the mechanical displacements were incorporated into COMSOL finite element package (COMSOL, 2011). The variation of the thermal spring stiffness with respect to ranges of the thermal and mechanical displacements produces a surface are shown in Figure 8.38(a) which is plotted for initial slopes of the loading and the unloading paths of K_s =25.7 MPa/m, $K_{s\_unloading}$ = 5K_s, respectively; an ultimate unit shaft friction $f_{s,ult}$ = 28.7 kPa; and the two limiting mechanical displacements $z_{s,1}$ = 0.56mm (0.022 inch), and $z_{s,2}$ = 3.34mm (0.13 inch). Two-dimensional cross sections showing the relationship between the thermal spring stiffness and the thermal displacement for various given values of the mechanical displacement are presented in Figure 8.38(b) to better explain the three-dimensional surface.

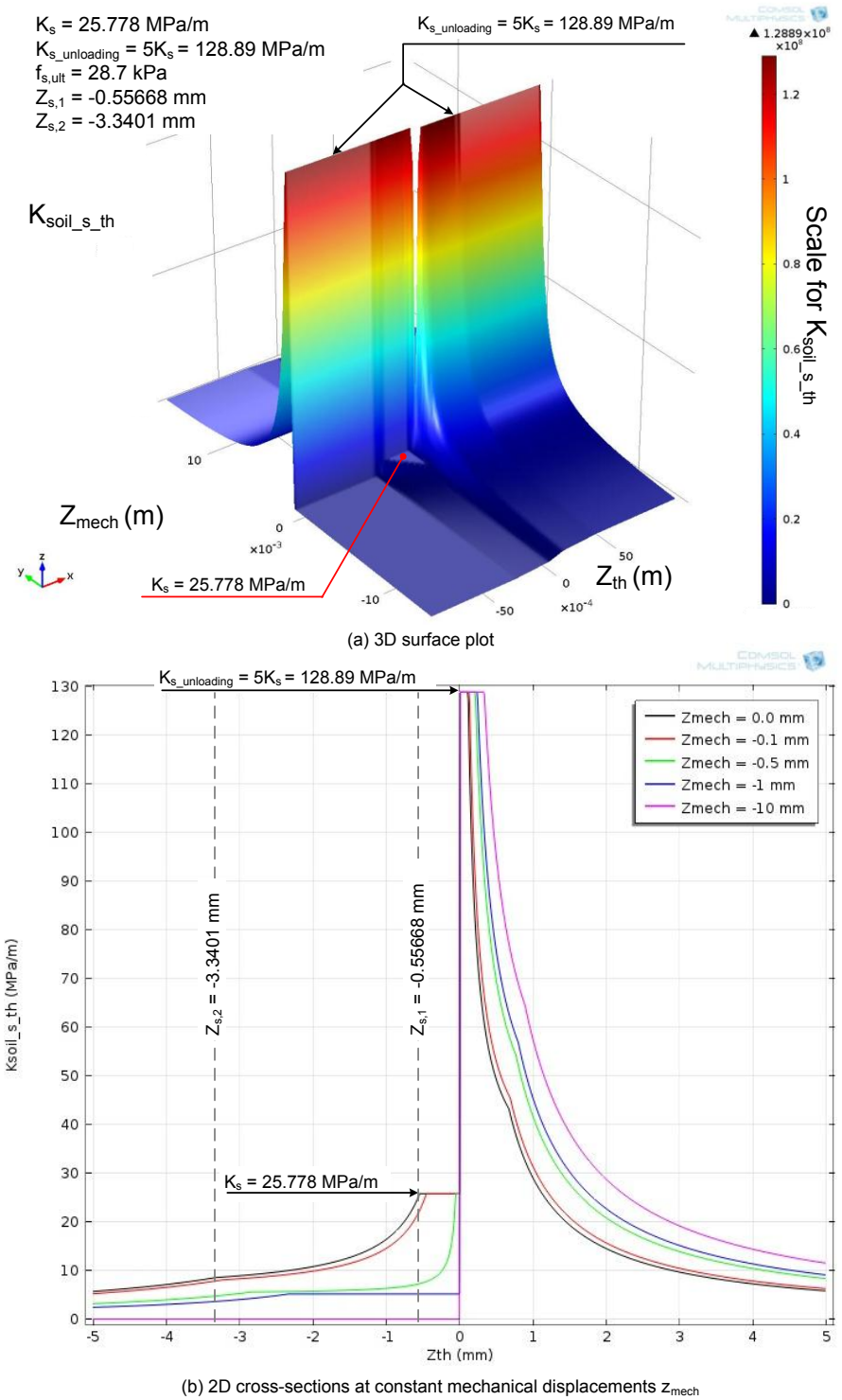

Figure 8.38. Thermal stiffness of the soil springs along the pile shaft for finite element modeling.

Figure 8.38(b) shows that the general shape of the variation of the thermal spring stiffness with respect to the thermal displacement is similar to that shown in Figure 8.35 for the mechanical spring stiffness. However, the thermal spring stiffness response is divided into two

sides; one is for consistent directions of the thermal and mechanical displacements (both negative in this figure), while the other is for opposing thermal and mechanical displacements. For the scenario of consistent thermal and mechanical displacements, the maximum thermal spring stiffness is equal to the loading stiffness K_s. This maximum thermal spring stiffness occurs when the total thermo-mechanical displacement is less than the first limiting displacement, $z_{mech}+z_{th} < z_{s,1}$. Thus for more mechanical displacements, the range of the thermal displacement over which this maximum thermal stiffness (K_s) occur is narrower. When the total thermo-mechanical displacement exceeds the first limiting displacement, the thermal spring stiffness is reduced. This response was observed in Figure 8.38(b) for mechanical displacements of 0.0, -0.1, and -0.5 mm.

When the mechanical displacement is more than the first limiting displacement and less than the second limiting displacement ($z_{s,1}<z_{mech}<z_{s,2}$), the thermal spring stiffness starts with a constant value until the thermo-mechanical displacement reaches to the second limiting displacement after which it decreases. The initial constant thermal spring stiffness for this case represents the second linear segment of the loading path of the load-transfer curve which is sloped at $K_s/5$. This response is observed in Figure 8.38(b) for -1 mm mechanical displacement. For mechanical displacements more than the second limiting displacement, the thermal spring stiffness is zero over the entire thermal displacement range as seen for mechanical displacement of -10 mm in Figure 8.38(b). This is because the mechanical and the thermo-mechanical point will lay on the horizontal line of the load-transfer curve meaning that the spring resistance has reached its ultimate value and that zero thermal stiffness.

On the other side of the thermal stiffness-displacement curves shown in Figure 8.38(b) which is when the thermal and the mechanical loads produce displacements in opposite directions, the general shape is maintained as before but the maximum thermal stiffness and the limiting displacements are different. The maximum thermal stiffness for this case is the slope of the unloading path of the load-transfer curve ($K_{s\_unloading}$). Furthermore, the first limiting thermal displacement below which the thermal spring stiffness is $K_{s\_unloading}$ increases as the mechanical displacement increases. This is because as the mechanical displacements increase, more opposing thermal displacement is required to have the total thermo-mechanical displacement reach to the point corresponding to half the ultimate unit friction. Similarly, the second limiting thermal displacement increases as the mechanical displacement increases since more thermal displacements are required for the total thermo-mechanical displacement to reach to the point of ultimate unit friction.

The formulation for the base unit resistance was developed following the same analogy as for the unit shaft friction as shown in Figure 8.39. The final formulas for the thermal stiffness of the base springs are; <u>when $z_{\mathrm{mech,b}}$ and $z_{\mathrm{th,b}}$ are in the same direction:</u>

$$K_{\mathrm{soil\_b\_th}} = \frac{K_{\mathrm{soil\_b}}\left(z_{\mathrm{mech,b}} + z_{\mathrm{th,b}}\right) * \left|z_{\mathrm{mech,b}} + z_{\mathrm{th,b}}\right| - K_{\mathrm{soil\_b}}\left(z_{\mathrm{mech,b}}\right) * \left|z_{\mathrm{mech,b}}\right|}{\left|z_{\mathrm{th,b}}\right|}$$

<u>While for $z_{\mathrm{mech,b}}$ and $z_{\mathrm{th,b}}$ in the opposite directions:</u>

- <u>Case (1): $\left|z_{\mathrm{th,b}}\right| \leq \frac{K_{\mathrm{soil\_b}}\left(z_{\mathrm{mech,b}}\right) * \left|z_{\mathrm{mech,b}}\right|}{K_{\mathrm{b\_unloading}}}$</u>

$$K_{\mathrm{soil\_b\_th}} = K_{\mathrm{b\_unloading}}$$

- Case (2): $|z_{th,b}| > \frac{K_{soil\_b}(z_{mech,b}) * |z_{mech,b}|}{K_{b\_unloading}}$

$$K_{soil\_b\_th} = \frac{K_{soil\_b}(z_{mech,b}) * |z_{mech,b}|}{|z_{th,b}|}$$

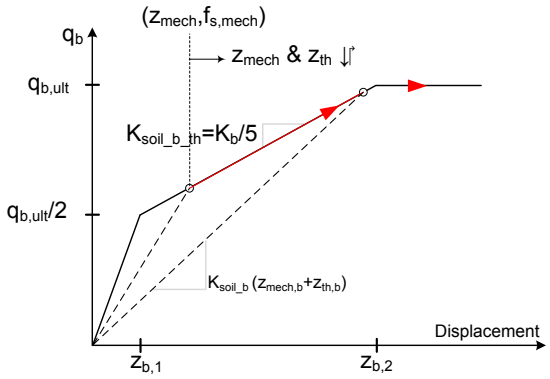

(a) $z_{mech,b}$ and $z_{th,b}$ are in the same direction

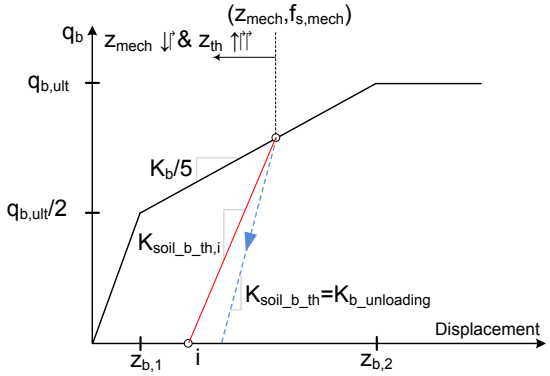

(b) $z_{mech,b}$ and $z_{th,b}$ are in the opposite direction

Figure 8.39. Thermal stiffness of soil springs at the base of Energy Piles.

(a) Boundary Conditions, Initial Conditions, and Meshing

In order to model the thermo-mechanical response of Energy Piles using decoupled analysis, the mechanical response should be modeled initially to estimate the profiles of the mechanical displacement and load in the pile. Afterwards, the thermal analysis is performed using the results of the mechanical analysis as an initial condition. In this sense, both the analytical method proposed by Knellwolf et al. (2011) and the finite element approach described here are similar. The only difference is the way each method solves for the displacements, and loads in the pile. Knellwolf et al. (2011) solves the problem from the toe of the pile till the head of the pile analytically as discussed earlier, while the finite element approach solves a matrix of the displacements of all nodes in the model at once. Solving a matrix assists relaxing the limitations of the analytical procedure as discussed in Section 8.5.1.

Since the pile is axisymmetric around its centerline, only half of the pile is modeled with an axis of symmetry set at the pile centerline as shown in Figure 8.40, and Figure 8.41. Also, it is shown in these figures that the pile domain was discretized into rectangular elements.

Figure 8.40 shows the boundary conditions and meshing used to perform the mechanical analysis of an Energy Pile with radius r and length L_{pile}. For the mechanical analysis and as presented in this figure, the boundary condition at the pile head was set to a uniform downward stress $\sigma_{mech} = Q_{mech}/\pi r^2$ which is the applied mechanical stress. The boundaries conditions at the soil-pile shaft were assigned as springs with displacement-dependent stiffness defined as shown in Figure 8.35. If different soil layers exist along the pile shaft, the soil-pile boundary for each layer is assigned a different displacement-dependent stiffness curve which is based on the ultimate unit shaft friction ($f_{s,ult}$) and loading stiffness (K_s) for the considered soil layer. Furthermore, the boundary condition at the toe of the pile is modeled as springs with the displacement-dependent stiffness for the foundation soil layer as shown in Figure 8.36. The initial conditions for this analysis are zero displacements everywhere.

The results of the mechanical analysis in terms of mechanical displacements at each node in the model were then used as initial conditions for the thermal analysis. In the thermal analysis, the pile head boundary condition was set to an elastic spring with stiffness of K_{head}, while the boundary conditions for the soil-pile interface along the shaft and at the pile toe were set to springs with displacement-dependent thermal stiffness as the one defined in Figure 8.38. The change in temperature was assigned for the entire pile therefore, the selected temperature change is the average observed during the thermo-mechanical load test or expected during the actual operation of the Energy Pile. For this analysis, the thermal expansion coefficient of the pile should be defined so that the thermal strains and displacements can be estimated.

If the pile toe and/or any point along the pile shaft are fixed, the soil springs representing the fixation boundary were assigned a very higher loading and unloading stiffness and unit shaft and base resistances. Since complete fixation does not take place in reality, using high spring stiffness and ultimate resistances is preferred over assigning a completely fixed boundary which is doable in finite element.

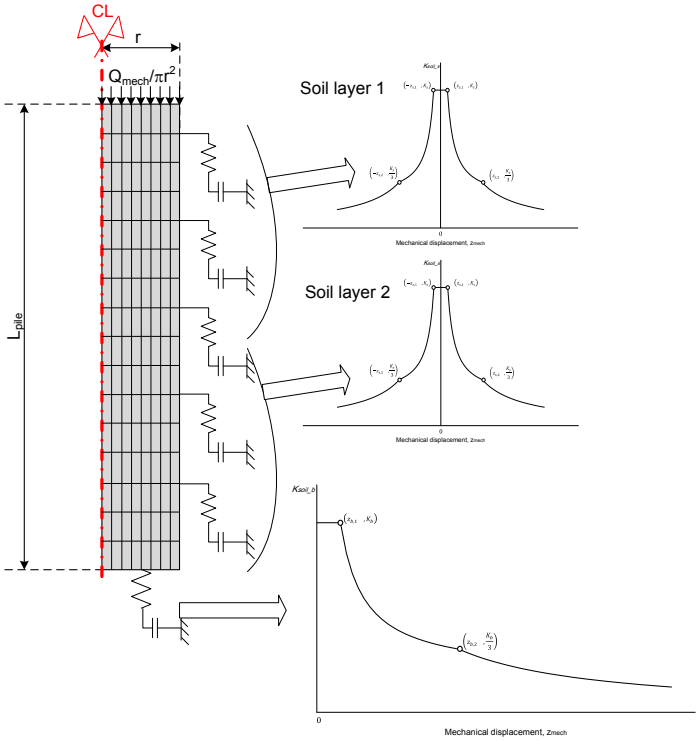

Figure 8.40. Mechanical analysis of Energy Piles in decoupled finite element models.

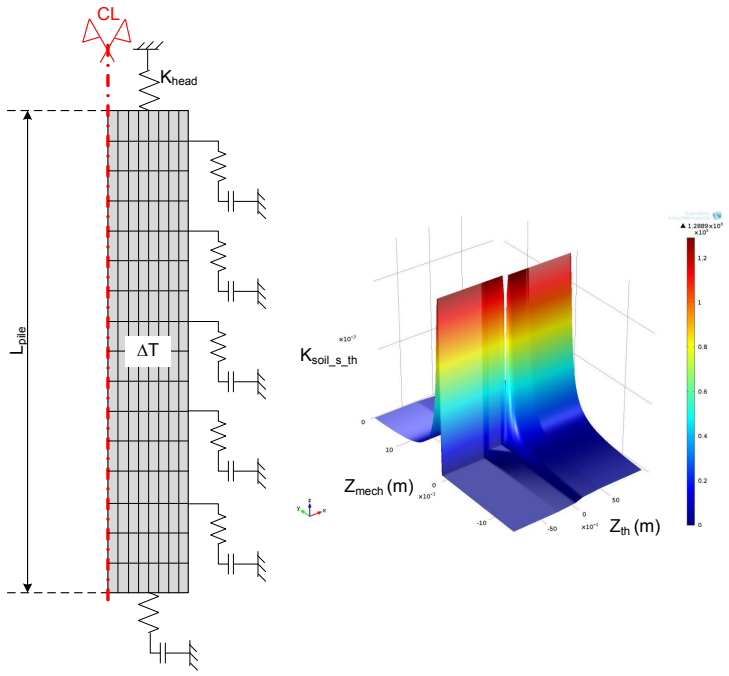

Figure 8.41. Thermal analysis of Energy Piles in decoupled finite element models.

(b) Model Validation

The proposed transformation of the load-transfer curves into spring stiffness-displacement curves and the modeling technique described in the previous sections are validated using the results of the two in-situ thermo-mechanical tests performed at the Swiss Federal Institute of Technology 1n Lausanne (EPFL) (Laloui et al., 2006) and at Lambeth College (Bourne-Webb et al., 2009). Knellwolf et al. (2011) modeled these two tests using the analytical methodology of implementing the spring analogy described in Section 8.5.1. Table 8-3 presents the soil and pile properties used by Knellwolf et al. (2011) while modeling these two tests. These properties were also used to model these tests using the proposed finite element technique.

Two tests were performed at the EPFL; the first test was for free pile head with no mechanical load, while the second test was for a pile supporting a building. The thermal load in first test was increased gradually going through 7.5-14.2-17.4-21.8 ºC (45.5-57.5-63.3-71.2°F) heating path. As shown in Figure 8.42(a), the finite element model was able to capture the thermal strains developed in the pile for each one of these thermal steps. Figure 8.42 was developed using the same parameters used by Knellwolf et al. (2011) in order to compare the results of the analytical method with those obtained from the finite element. For clarity purposes, the results of the analytical approach predicted by Knellwolf et al. (2011) were not shown in the figure, however the results from the finite element models match those estimated using the analytical model (Knellwolf et al., 2011) with a 1% maximum error. Moreover, Figure 8.42(b) shows the degree of freedom estimated using the proposed finite element model as well as the measured degree of freedom for the second test in which a 14.3ºC (25.7°F) temperature increase was applied. The degree of freedom is referred to as the ratio between the observed thermal strains to the free thermal strains. A good agreement between the estimated and measured degrees of freedom over the entire length of the pile is observed in Figure 8.42(b). For these tests, the observed strains are the ones that were measured in-situ since the measured

strains agree with the strains directly obtained from the finite element models. Thus, the strain gauges used at this test site were not self-compensating for temperature.

Also, the results from the Lambeth College tests were used to validate the proposed finite element approach. Figure 8.43 shows good agreement between the measured distributions of the mechanical load, the mechanical plus heating, and the mechanical plus cooling and the respective estimate load distributions obtained from the finite element models. The data over the top 6.5 m (21.3 ft) were ignored because the measured strains over this pile length were affected by the eccentric loading at the pile head which caused significant strain variations (Knellwolf et al., 2011). It should be noticed that when the measured thermal strains were found to be opposing the thermal strains directly estimated by the finite element models which represent the observed strains. Thus, the comparison was held with the blocked thermal strains in these tests which showed good match in the response. It is, therefore, the strain gauges used in this test were self-compensating for the temperature.

Table 8-3. Soil properties for different soils encountered at the test sites of Laloui et al. (2006) and Bourne-Webb et al. (2009).

Model input			EPFL	Lambeth College
Pile diameter (D), m			0.88	0.6
Pile length (L_{pile}), m			25.8	22.5
Pile modulus (E_{pile}), GPa			29.2	40
Thermal expansion coefficient (α),$^oC^{-1}$			1×10^{-5}	8.5×10^{-6}
Tests	Test 1	Mechanical (P), kN	0	1200
		Thermal (ΔT), ^oC	+7.5, +14.2, +17.4, +21.8	-19
		Head stiffness (K_{head}), GPa/m	0	0.1
	Test 2	Mechanical (P), kN	1000	1200
		Thermal (ΔT), ^oC	+14.3	+10
		Head stiffness (K_{head}), GPa/m	1.5	10
Soil layers (top to bottom)	1	Thickness, m	6	6.5
		K_s (MPa/m)	16.7	0
		q_s (kPa)	102	0
		$z_{s,1}$ (mm)	3.05	0
		$z_{s,2}$ (mm)	18.32	0
	2	Thickness, m	6	4
		K_s (MPa/m)	10.8	150
		q_s (kPa)	70	60
		$z_{s,1}$ (mm)	3.24	0.20
		$z_{s,2}$ (mm)	19.44	1.20
	3	Thickness, m	9.8	6
		K_s (MPa/m)	18.2	150
		q_s (kPa)	74	70
		$z_{s,1}$ (mm)	2.03	0.23
		$z_{s,2}$ (mm)	12.20	1.40
	4	Thickness, m	4	6
		K_s (MPa/m)	121.4	150
		q_s (kPa)	160	80
		$z_{s,1}$ (mm)	0.66	0.27
		$z_{s,2}$ (mm)	3.95	1.6
	Base soil	K_b (MPa/m)	1335.4	825
		q_b (kPa)	11000	460
		$z_{b,1}$ (mm)	4.12	278.79
		$z_{b,2}$ (mm)	24.71	1672.7

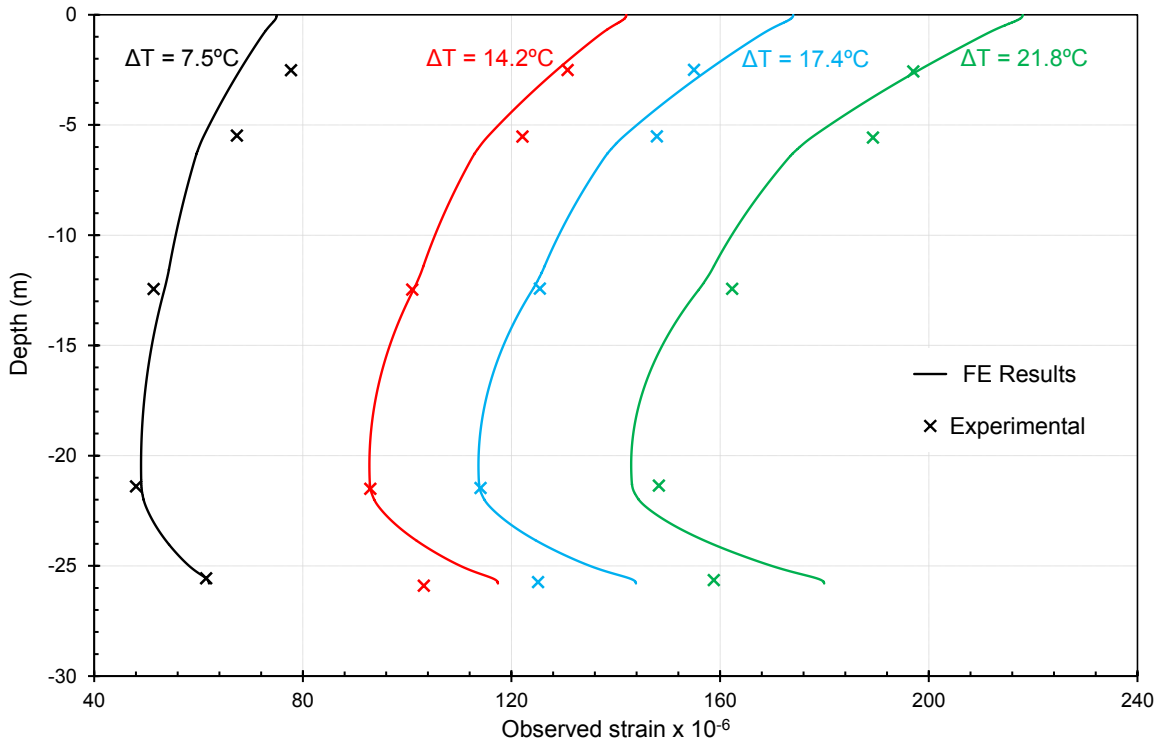

(a) Test 1 – Mechanical load = 0.0 kN

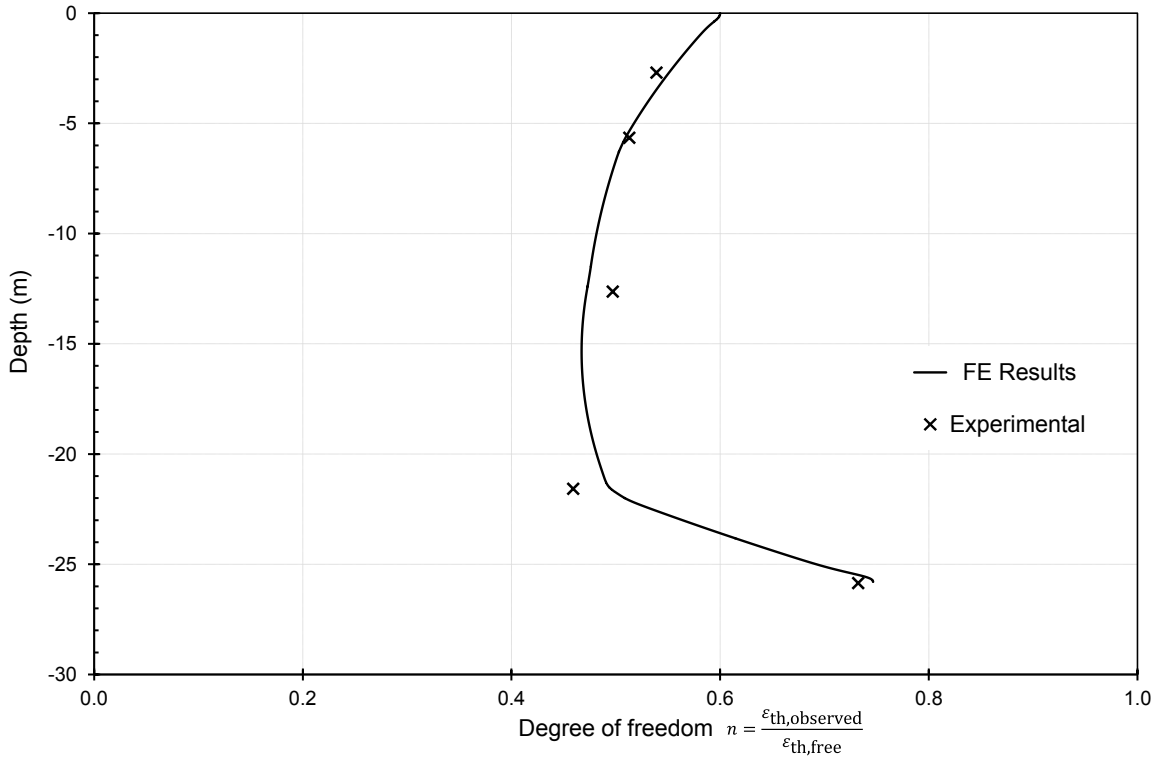

(b) Test 7 – Mechanical load = 1000.0 kN

Figure 8.42. Validating the proposed finite element approach with the EPFL thermo-mechanical in-situ test results (Laloui et al., 2006 - used under fair use, 2013).

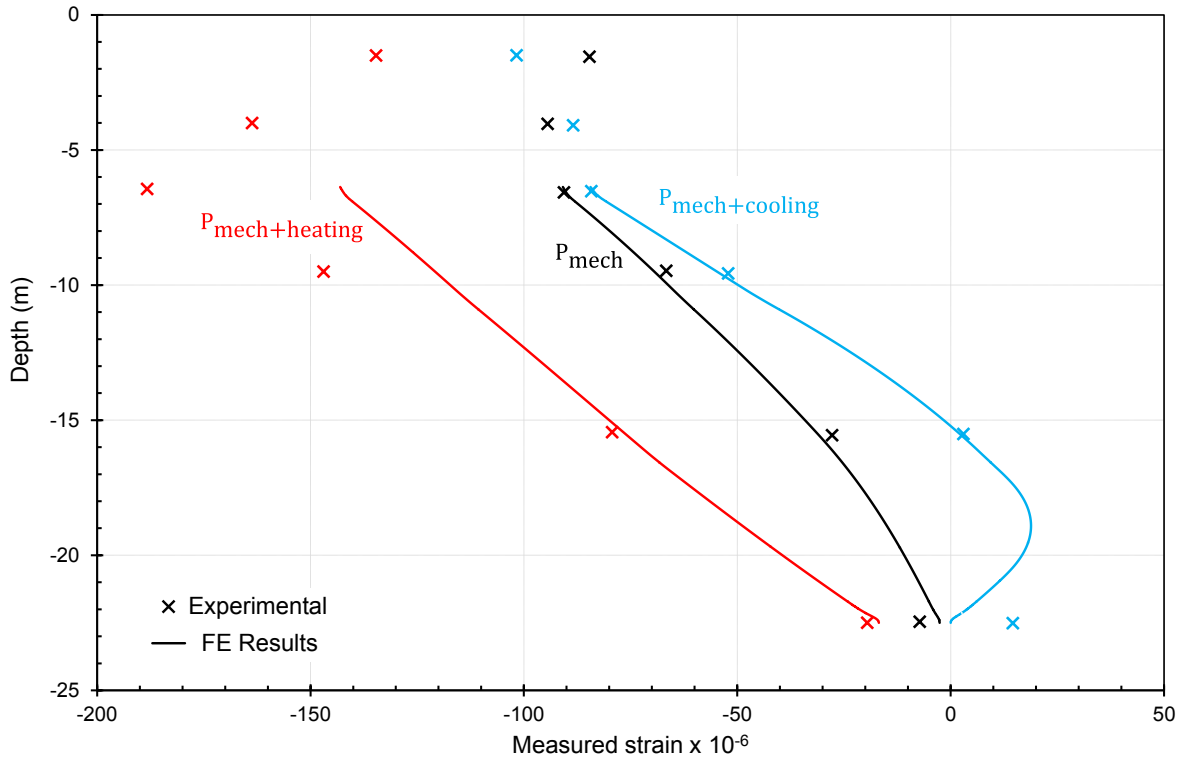

Figure 8.43. Validating the proposed finite element approach with the Lambeth College thermo-mechanical in-situ test results (Bourne-Webb et al., 2009 - used under fair use, 2013).

8.5.4. Modeling Virginia Tech Thermo-Mechanical Tests

The finite element procedure presented and validated in the above sections is used to model the two thermo-mechanical tests performed at Virginia Tech. The Test Pile was modeled using 2-dimensional axisymmetrical models representing the 3-dimensional nature of the pile and its surrounding soils. Even though the ground at the test site consists of two soil formations referred to as the silty sand and the shale formations; six soil layers were used in the finite element models. The silty sand layer was divided to four sublayers; the first layer extends from the ground surface till 3 m (10 ft) which is the depth of the first strain gauge in the Test Pile. The second silty sand sublayer extends from 3 m (10 ft) till the location of the second strain gauge at 6 m (20 ft) after than the third sublayer is encountered till the location of the third strain gauge at 9 m (30ft). The fourth silty sand sublayer extends from 9 m (30 ft) till the interface between the silty sand and the shale at depth 12.8 m (42 ft). Moreover, two sublayers were considered in the shale formation; the first extends from the interface of the two soil formations at 12.8 m (42 ft) and extends till 15.25 m (50 ft). The second covers the remaining length of the pile. These sublayers were selected such that the distributions of the mechanical load along the pile can be used to estimate the ultimate unit shaft frictions along the pile shaft.

The Test Pile was divided using rectangular nine-node elements. These elements were selected to improve the accuracy of the estimated strains along the pile. However, meshes with various element types and sizes were used to assure that the obtained solution is mesh-independent. These analyses showed that the results are independent of the number of elements used in the model as well as the element type. This conclusion was expected since the spring

analogy to model piles is, in fact, a 1-dimensional technique which produces mesh-independent models should it modeled in 2 or 3-dimensions. One-dimensional models could not be used because COMSOL does not support these models.

Several parameters are needed to define the displacement-dependent spring stiffness representing the soils around the pile shaft and at the pile toe. These parameters are; (1) the initial loading stiffness (K_s), (2) the two limiting displacements ($z_{s,1}$, and $z_{s,2}$), (3) the ultimate unit shaft and base resistances, (4) the unloading stiffness for the soil ($K_{unloading}$), and (5) the thermal elastic stiffness of the head spring (K_{head}).

The stiffness of the soil around the pile shaft in the top silty sand layer was plotted versus the displacements for the first and the second load tests as shown in Figure 8.44 in order to estimate the initial loading stiffness (K_s) and the two limiting displacements ($z_{s,1}$, and $z_{s,2}$). For a specific pile segment, the stiffness of the soil spring corresponding to each mechanical loading step is estimated as;

$$K_{s,i} = \frac{(P_{1,i} - P_{2,i})/A_{s,i}}{\Delta L_i}$$

Where;

$P_{1,i}$: Load in the pile at the top of the considered pile segment,

$P_{2,i}$: Load in the pile at the bottom of the considered pile segment,

$A_{s,i}$: Area of the pile shaft in layer $i = 2\pi r L_i$ for a pile segment with radius r and length L_i

ΔL_i *:* The change of the length of the considered pile segment.

It appears from Figure 8.44 that the two limiting displacements are equal for each pile segment within the silty sand layer. Therefore, a best fit displacement-dependent stiffness was defined for each silty sand sublayer. The initial spring stiffness and limiting displacement is provided in the tables in Figure 8.44. Furthermore, Table 8-4 summarizes the ultimate unit shaft friction for each of these silty sand sublayers were estimated as, where all the variables are as defined earlier;

$$f_{s,ult} = (P_{1,i} - P_{2,i})/A_{s,i}$$

Table 8-4. Ultimate unit shaft friction for each silty sand sublayers estimated for T-MT 1 and T-MT 2.

Silty sand sublayer	$f_{s,ult}$ (kPa) from T-MT 1	$f_{s,ult}$ (kPa) from T-MT 2
1 (ground surface – 3m)	5.8	20.83
2 (3 m – 6 m)	28.7	31.05
3 (6 m – 9 m)	41.7	83.48
4 (9 m – 12.8 m)	41.7	44.48

The Test Pile is fixed at its toe and at the interface between the shale and the silty sand layers as discussed in previous sections. The fixation of the pile at these locations was modeled by assigning high values for the loading and unloading stiffness. The stiffness was assigned to 10^{100} MPa/m while the value of the ultimate unit shaft and base resistance equal to 1000 MPa. The stiffness of the spring modeling the shale layer between the two fixation points was selected to be 1000 MPa/m which is a typical value for shale (Mitchell and Soga, 2005).

The obtained values for these parameters were used to model the mechanical loading of the Test Pile during T-MT 1 and T-MT 2. Figure 8.45 shows that the mechanical load distributions along the pile obtained from the finite element model for these two tests agree with the measured loads confirming that the values used for different parameters are valid.

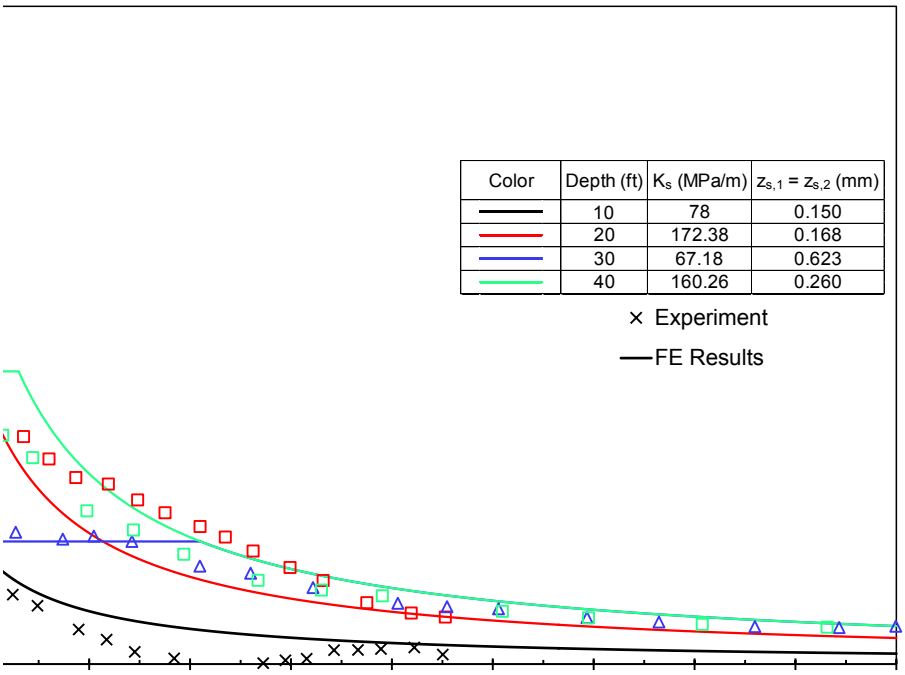

(a) T-MT 1

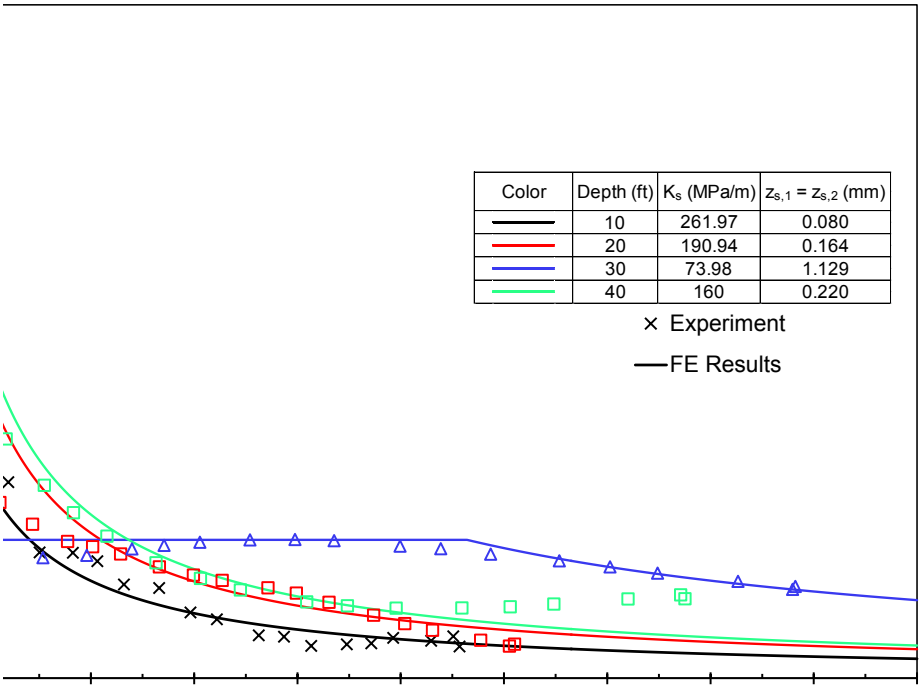

(b) T-MT 2

Figure 8.44. Displacement-dependent soil spring stiffness.

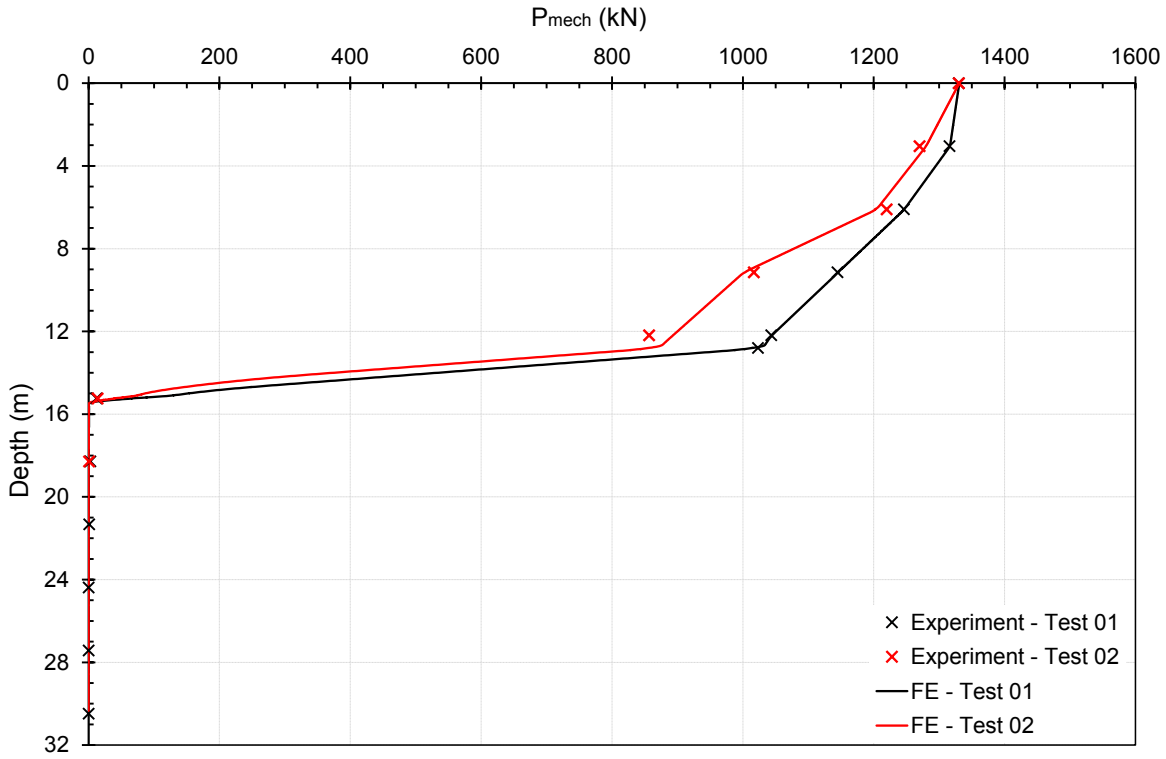

Figure 8.45. Comparison between the distributions of the mechanical load along the Test Pile from the finite element models and the in-situ measurements.

COMSOL optimization was utilized to estimate the unloading spring stiffness for different silty sand sublayers and the elastic stiffness of the head spring. The objective of the optimization was to minimize the summation over various thermal steps for the difference between the measured thermo-mechanical loads along the pile and the finite element results. Including all thermal steps of the same thermo-mechanical test in the objective function of the optimization assisted to estimate a unique value for the unloading stiffness of each silty sand sublayer which is applicable for all thermal steps. The results of the optimization suggest that; (1) the stiffness of the elastic spring was found to be 2 GPa/m for both load tests, and (2) the unloading stiffness for all silty sand sublayers are higher than the initial loading stiffness. Higher unloading stiffness is expected since the response of the pile under loading-unloading cycles is not elastic. COMSOL suggested that the stiffness of the soil spring for unloading is 5 times the loading stiffness for all silty sand sublayers.

The results of the COMSOL optimization were used to model the thermo-mechanical response of the Test Pile. Table 8-5 shows the value of the temperature change used to model every thermal step. It should be noticed that for the same thermal step in T-MT 1 and T-MT 2, unique temperature change is used. However, since the mechanical strains in the two tests are not exactly equal, the thermal response in the two tests is modeled separately.

Figure 8.46 and Figure 8.47 present the estimated thermal strains along the pile for each thermal step in tests T-MT 1 and T-MT 2, respectively. As shown in these figures, the finite element model provides good estimates for the thermal strains along the pile in general. However, it is noticed that when the Test Pile is subjected to thermal cooling after heating by reducing the temperature of the inlet fluid, such as in the first and in the second thermal cycles,

the finite element does not capture the strains looked in the pile after heating. Moreover; less agreement between the finite element strains and the measured strains is observed for the thermal cycles performed at the end of the tests. This is because the proposed finite element models do not account for the effect of the locked in thermal stresses in the pile.

Figure 8.48 and Figure 8.49 show the predicted thermo-mechanical loads along the pile shaft and compare them to the measured loads. In general, good agreement is observed in the estimated results except for cooling after heating. The lack of agreement between the predicted thermo-mechanical loads and the measured loads for cooling after heating is again attributed to the lack of estimating the locked strains and loads in the pile after each thermal cycle.

Table 8-5. Temperature change for modeling various thermal steps.

T_{fluid} (ºC) - Cycle	ΔT (ºC)	T_{fluid} (ºC) - Cycle	ΔT (ºC)
16 ºC – 1st cycle	+ 2	13 ºC – 2nd cycle	+ 2
10 ºC – 1st cycle	- 1	6 ºC – 2nd cycle	- 5
13 ºC – 1st cycle	- 0.5	13 ºC – 3rd cycle	+ 1
20 ºC – 2nd cycle	+2.5	28 ºC – 3rd cycle	+ 10
28 ºC – 2nd cycle	+ 10	35 ºC – 3rd cycle	+ 15
35 ºC – 2nd cycle	+ 15	50 ºC – 3rd cycle	+ 27

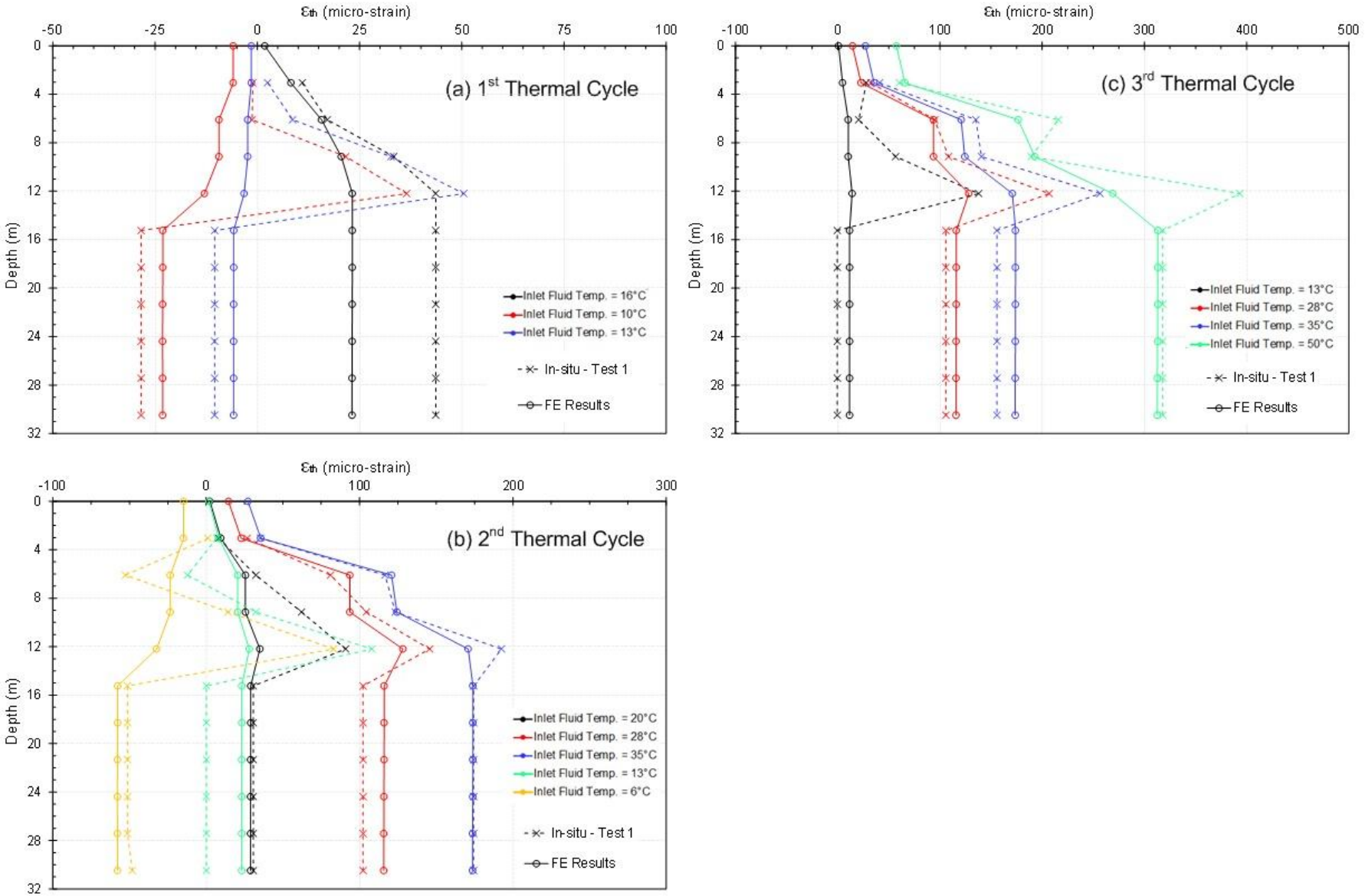

Figure 8.46. Comparison between the thermal strains from the finite element model and the in-situ measurements for T-MT 1.

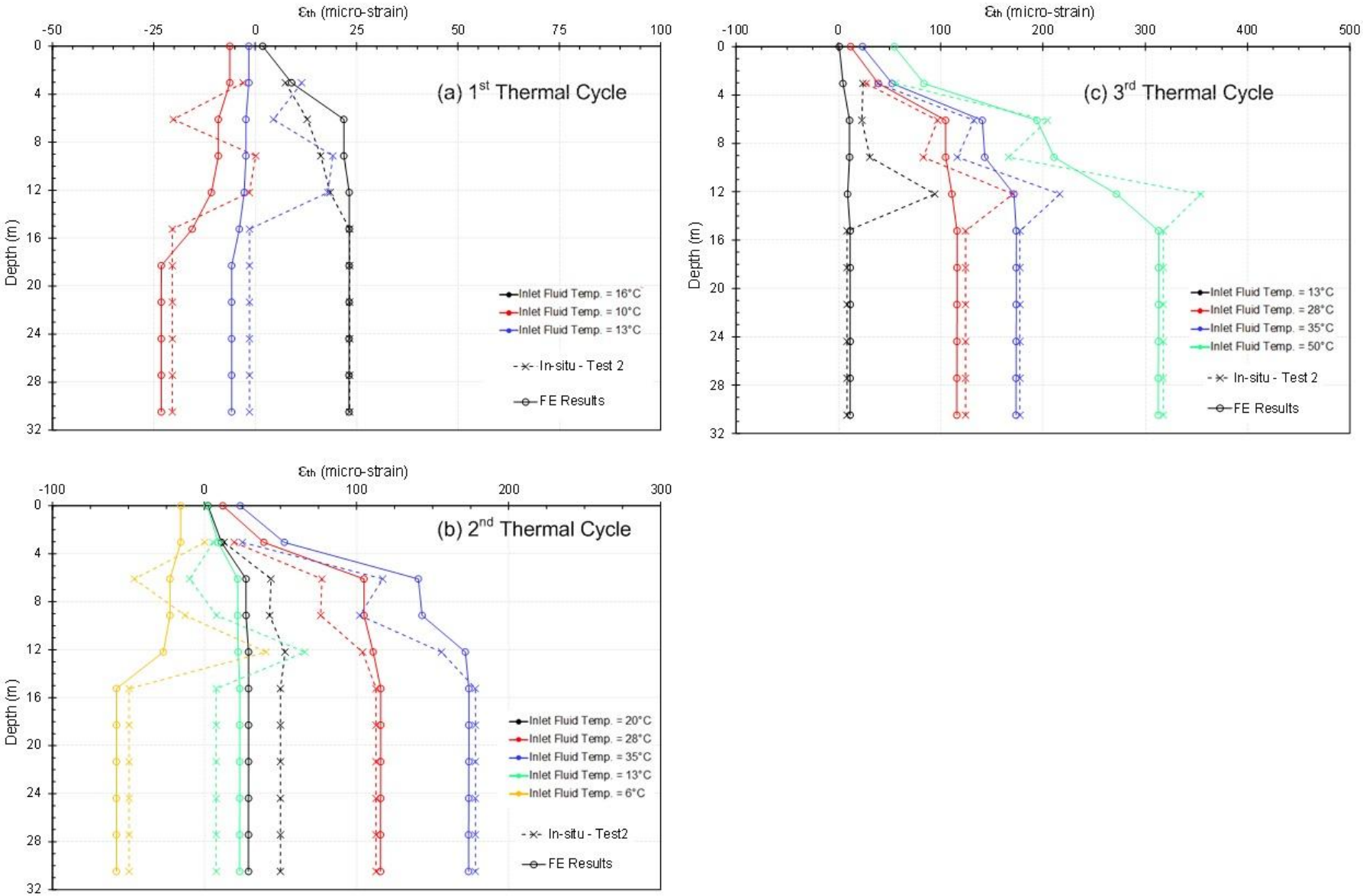

Figure 8.47. Comparison between the thermal strains from the finite element model and the in-situ measurements for T-MT 2.

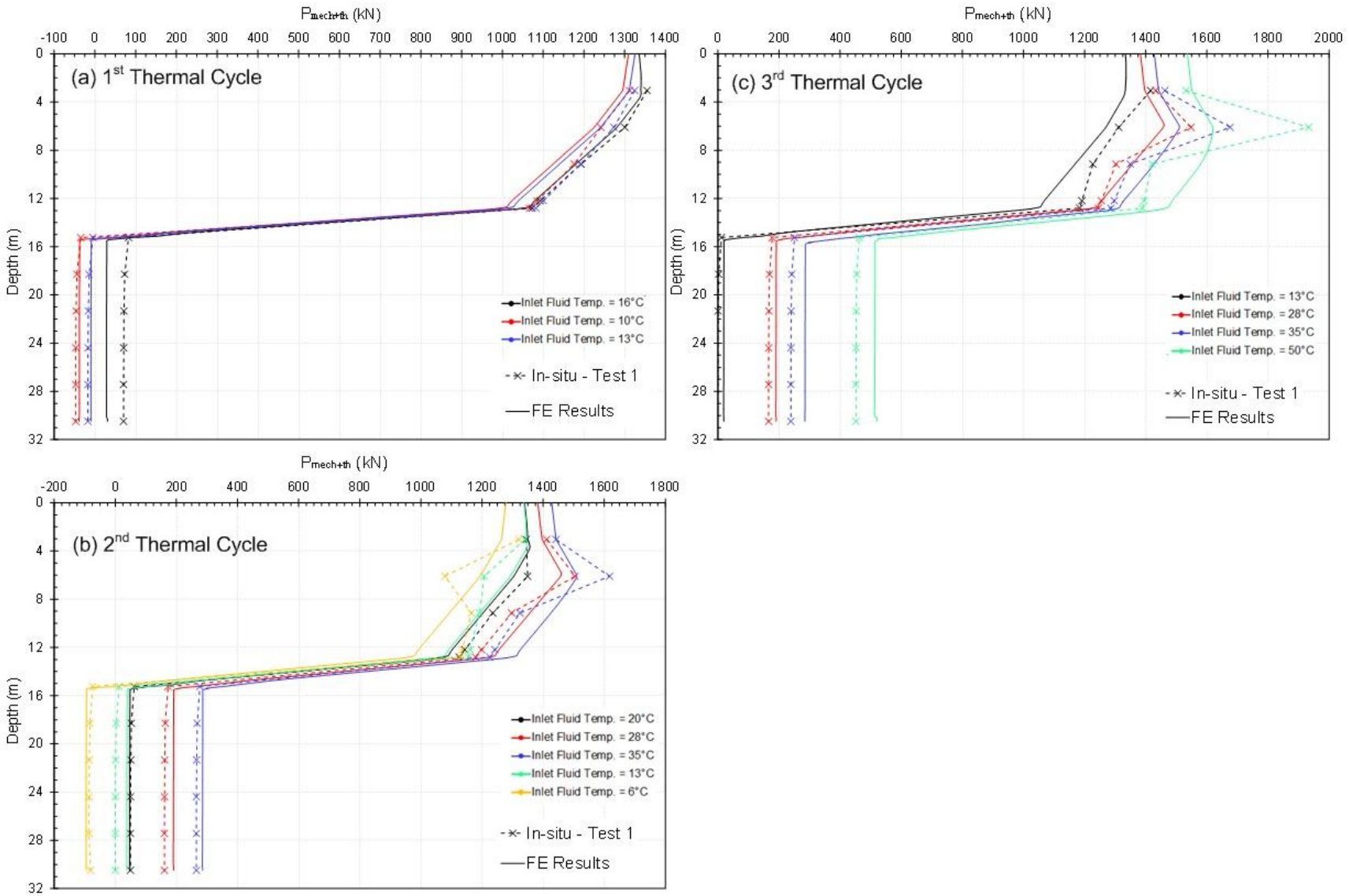

Figure 8.48. Comparison between the thermo-mechanical loads from the finite element model and the in-situ measurements for T-MT 1.

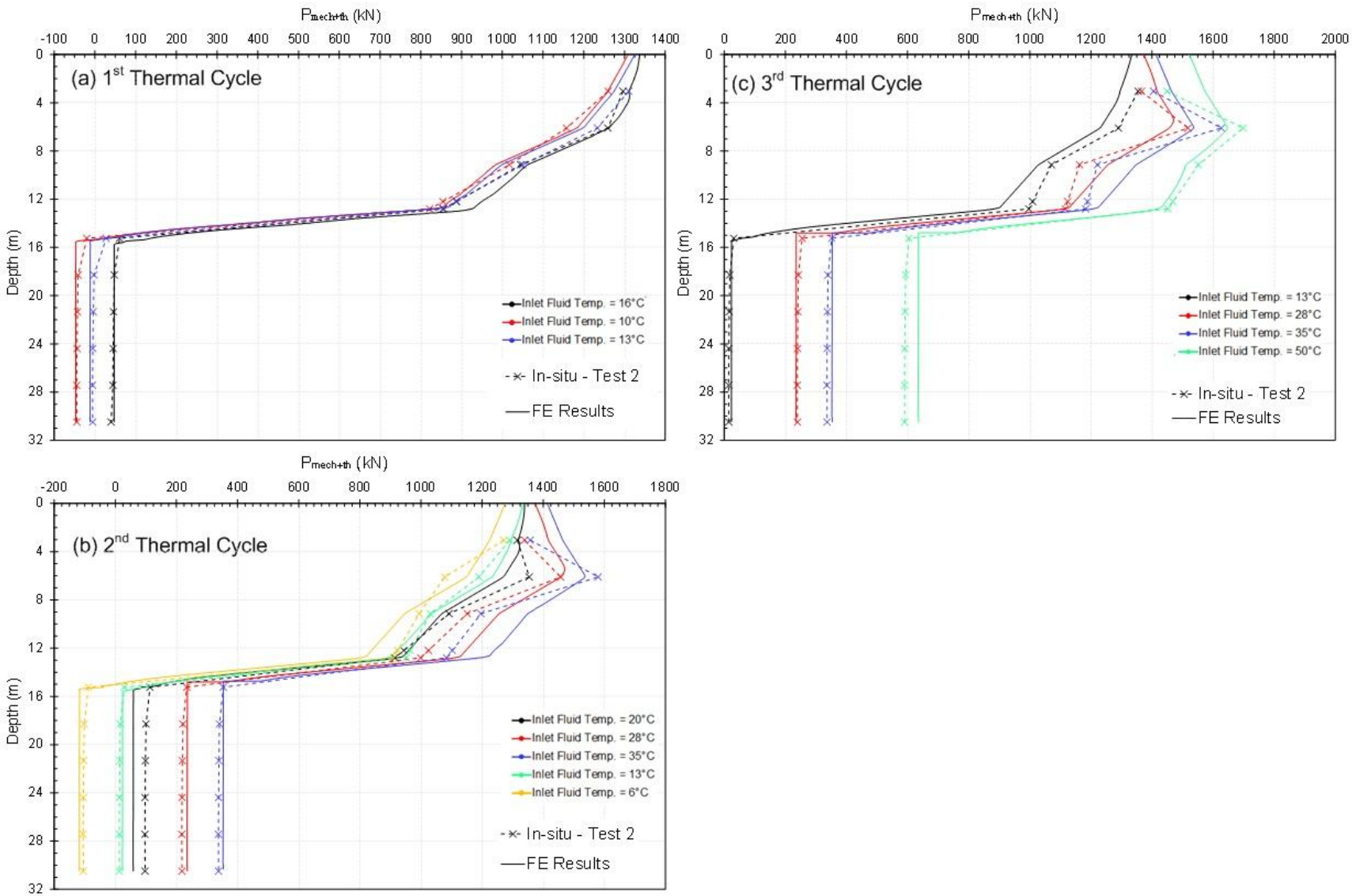

Figure 8.49. Comparison between the thermo-mechanical loads from the finite element model and the in-situ measurements for T-MT 2.

References

Abuel-Naga, H. M., M. Pender, D. T. Bergado, and A. Bouazza (2009) "Thermomechanical model for saturated clays," *Géotechnique*, Vol. 59, No. 3, pp 273-278.

Alawneh, A.S., O.K. Nusier, A.I.H. Malkawi, and M. Al-Kateeb (2001) "Axial compressive capacity of driven piles in sand: a method including post-driving residual stresses," *Canadian Geotechnical Journal*, Vol. 38, No. 2, pp 364-377.

American Society of Heating, Refrigerating, and Engineers Air-Conditioning. "2009 ASHRAE handbook fundamentals." American Society of Heating, Refrigeration and Air-Conditioning Engineers. Site Date: Access: <http://www.knovel.com/knovel2/Toc.jsp?BookID=2809>.

Armaleh, S., and C. S. Desai (1987) "Load-defromation response of axially loaded piles," *Journal of Geotechnical Engineering*, Vol. 113, No. 12, pp 1483-1500.

American Society for Testing Materials (2007) "D1143: Deep Foundations Under Static Axial Compressive Load." ASTM International, West Conshohocken, PA, 2007, DOI: 10.1520/D1143-07E01, www.astm.org.

Bourne-Webb, P. J., K. Soga, T. Amis, C. Davidson, P. Payne, and B. Amatya (2009) "Energy Pile test at Lambeth College, London: geotechnical and thermodynamic aspects of pile response to heat cycles," *Géotechnique*, Vol. 59, No. 3, pp 237-248.

Briaud, J.L., and L. Tucker (1984) "Piles in sand: A method including residual stresses," *Journal of Geotechnical Engineering*, Vol. 110, No. 11, pp 1666-1680.

COMSOL (2011) "Introduction to COMSOL Multiphysics: version 4.2," *Reference Manual and Tutorial, COMSOL Inc, Burlington MA.*

Cruz, C.R., and M. Gillen (1980) *Thermal expansion of Portland cement paste, mortar, and conrete at high temperatures*: Skokie, III : Portland Cement Association.

Cui, Y. J., N. Sultan, and P. Delage (2000) "A thermomechanical model for saturated clays," *Canadian Geotechnical Journal*, Vol. 37, No. 3, pp 607-620.

Fellenius, B.H. (1989) "Tangent modulus of piles determined from strain data," In: F.H. Kulhawy, Ed., *Geotechnical Engineering Division, 1989 Foundation Congress*: The American Society of Civil Engineers, ASCE, pp 500 - 510.

Fellenius, B.H. (2001) "Determining the true distribution of load in piles.," In: M.W. O'Neill, and F.C. Townsend, Eds., *International Deep Foundation Congress, An International Perspective on Theory, Design, Construction, and Performance*. Orlando, Florida: American Society of Civil Engineers, ASCE, pp 1455-1470.

Fellenius, B.H. (2002a) "Determining the resistance distribution in piles. Part 1: Notes of shift of No-Load reasing and residual load.," *Geotechnical News Magazine*, Vol. 20, No. 2, pp 35-38.

Fellenius, B.H. (2002b) "Determining the resistance distribution in piles. Part 2: Method for determining the residual load.," *Geotechnical News Magazine*, Vol. 20, No. 3, pp 25-29.

Fellenius, B.H. (2011) *The Red Book_Basics of Foundation Design*: Electronic Edition. www.Fellenius.net.

Frank, R., N. Kalteziotis, M. Bustamante, S. Christoulas, and H. Zervogiannis (1991) "Evaluation of performance of two piles using pressuremeter method," *Journal of Geotechnical Engineering*, Vol. 117, No. 5, pp 695-713.

Frank, R., and S.R. Zhao (1982) "Estimation par les paramètres pressiométriques de l'enfoncement sous charge axiale de pieux forés dans des sols fins," *Bulletin de Liaison des Laboratoires des Ponts et Chaussées*, Vol. 119, pp 17-24.

Geokon (1986) "Instruction Manual for Model 4200/4202/4210 Vibrating Wire Strain Gages," Lebanon, New Hampshire, p 24.

Hamidi, A., and C. Khazaei (2010) "A thermo-mechanical constitutive model for saturated clays," *International Journal of Geotechnical Engineering*, Vol. 4, No. 4, pp 445-459.

Holloway, D.M., G.W. Clough, and A.S. Vesic (1978) "The effects of residual driving stresses on pile performance under axial loads," *Proceedings Offshore Technology Conference*, Vol. 4, pp 2225-2236.

Hueckel, T., and G. Baldi (1990) "Thermoplasticity of Saturated Clays: Experimental Constitutive Study," *Journal of Geotechnical Engineering*, Vol. 116, No. 12, pp 1778-1796.

Hueckel, T., and M. Boretto (1990) "Thermoplasticity of saturated soils and shales: Constitutive equations," *Journal of Geotechnical Engineering*, Vol. 116, No. 12, pp 1765-1777.

Hueckel, T., M. Borsetto, and A. Peano (1987) "Modelling of coupled Thermo-elastoplastic-hydraulic response of clays subjected to nuclear waste heat," In: R. W. Lewis, E. Hinton, P. Bettess, and B. A. Schrefler, Eds., *Numerical methods in transient and coupled problems*: John Wiley.

Hueckel, T., B. François, and L. Laloui (2009) "Explaining thermal failure in saturated clays," *Géotechnique*, Vol. 59, No. 3, pp 197-212.

Hueckel, T., A. Peano, and R. Pellegrini (1994) "A constitutive law for thermo-plastic behaviour of rocks: an analogy with clays," *Surveys in Geophysics*, Vol. 15, No. 5, pp 643-671.

Hueckel, T., and R. Pellegrini (1991) "Thermoplastic modeling of undrained failure of saturated clay due to heating," *SOILS AND FOUNDATIONS*, Vol. 31, No. 3, pp 1-16.

Knellwolf, Christoph, Hervé Peron, and Lyesse Laloui (2011) "Geotechnical Analysis of Heat Exchanger Piles," *Journal of Geotechnical and Geoenvironmental Engineering*.

Laloui, L. (2001) "Thermo-mechanical bahaviour of soils," *Revue française de Génie civil*, Vol. 5, No. 6, pp 809 - 843.

Laloui, L., and C. Cekerevac (2003) "Thermo-plasticity of clays An isotropic yield mechanism," *Computers and Geotechnics*, Vol. 30, No. 8, pp 649-660.

Laloui, L., and C. Cekerevac (2008) "Non-isothermal plasticity model for cyclic behaviour of soils," *International Journal for Numerical and Analytical Methods in Geomechanics*, Vol. 32, No. 5, pp 437-460.

Laloui, L., C. Cekerevac, and L. Vulliet (2001) "Thermo-mechanical modelling of the behaviour of MC clay," In: Desai, Ed., *Computer Methods and Advances in Geomechanics*, pp 829-835.

Laloui, Lyesse, Mathieu Nuth, and Laurent Vulliet (2006) "Experimental and numerical investigations of the behaviour of a heat exchanger pile," *International Journal for Numerical and Analytical Methods in Geomechanics*, Vol. 30, No. 8, pp 763-781.

Laman, J.A., J.B. Sellers, and J.L. Schulz. "Influence of temperature on highway bridge strain measurements using vibrating wire gages." BDI Bridge Diagnostics Inc. Site Date: Feb. 13, 2012. Access: May 24, 2012. <http://bridgetest.com/products/vw-strain-gages/>.

Modaressi, H., and L. Laloui (1997) "A Thermo-viscoplastic constitutive model for clays," *International Journal for Numerical and Analytical Methods in Geomechanics*, Vol. 21, pp 313-335.

Randolph, M. F., and C. P. Wroth (1978) "Analysis of deformation of vertically loaded piles," *Journal of the Geotechnical Engineering Division*, Vol. 104, No. GT12, pp 1465-1488.

Robinet, J-C., A. Rahbaoui, F. Plas, and P. Lebon (1996) "A constitutive thermomechanical model for saturated clays," *Engineering Geology*, Vol. 41, No. 1, pp 145 - 169.

Seneviratne, H. N., J. P. Carter, D. W. Airey, and J. R. Booker (1993) "A review of models for predicting the thermomechanical behaviour of soft clays," *International Journal for Numerical and Analytical Methods in Geomechanics*, Vol. 17, pp 715-733.

Witte, H. J. L., G. J. van Gelder, and J. D. Spitler (2002) "In situ measurement of ground thermal conductivity-A dutch Perspective," *ASHRAE Transactions*, Vol. 108, No. 1, pp 263-272.

Appendix XIV

Temperature along the Test Pile During Various Thermo-Mechanical Tests

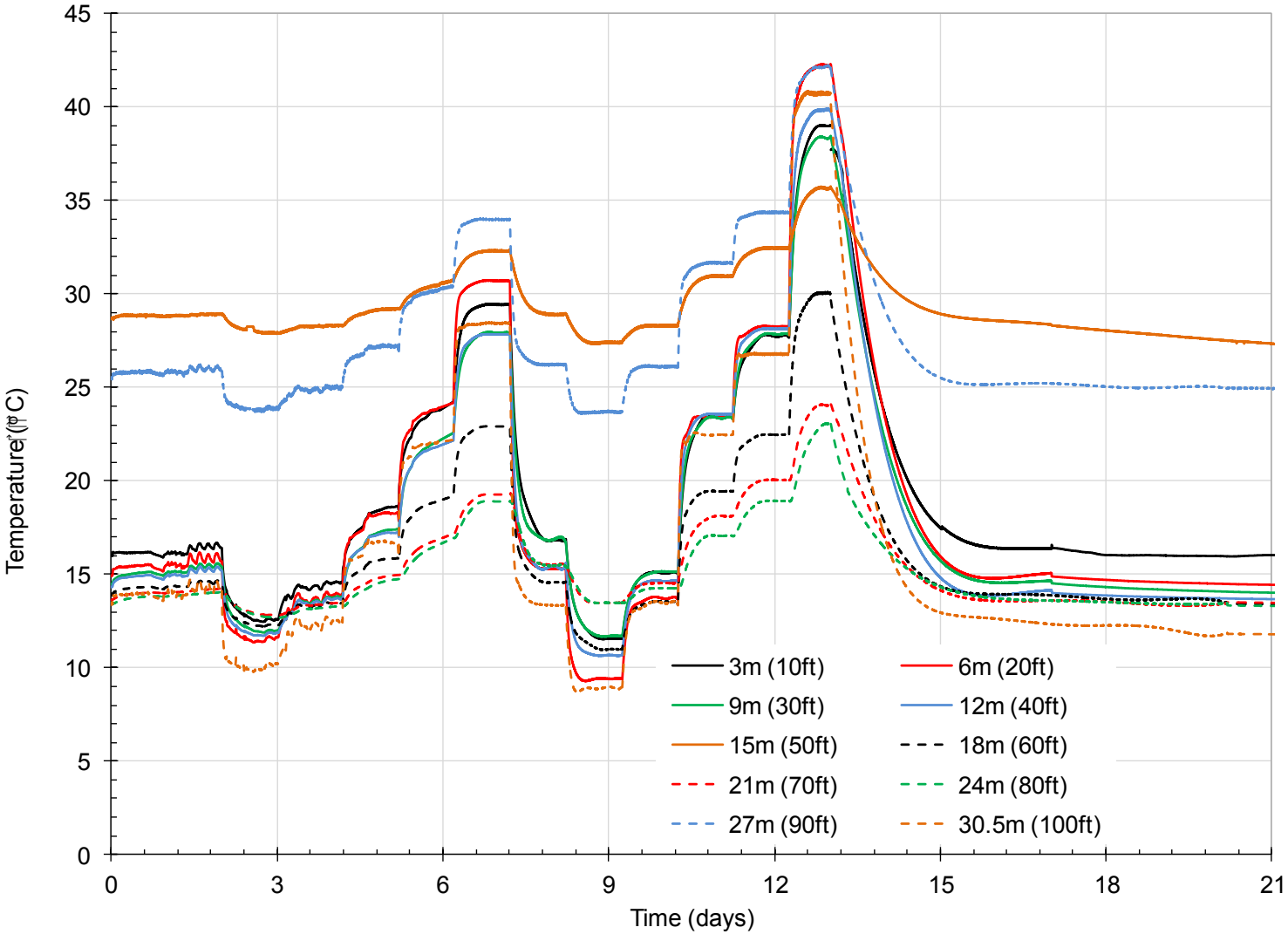

Figure XIV.1. Temperature along the Test Pile during T-MT 1

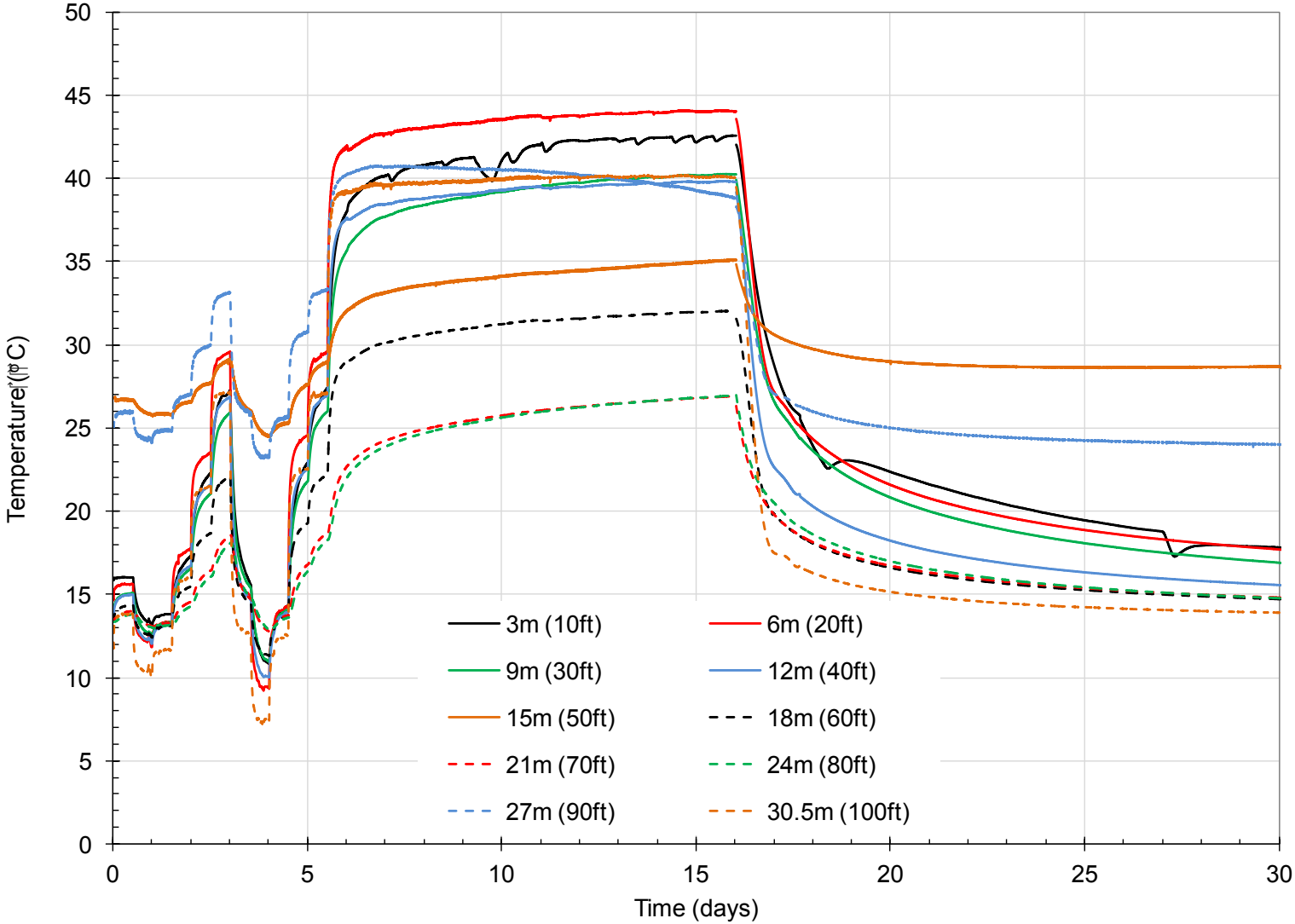

Figure XIV.2. Temperature along the Test Pile during T-MT 2

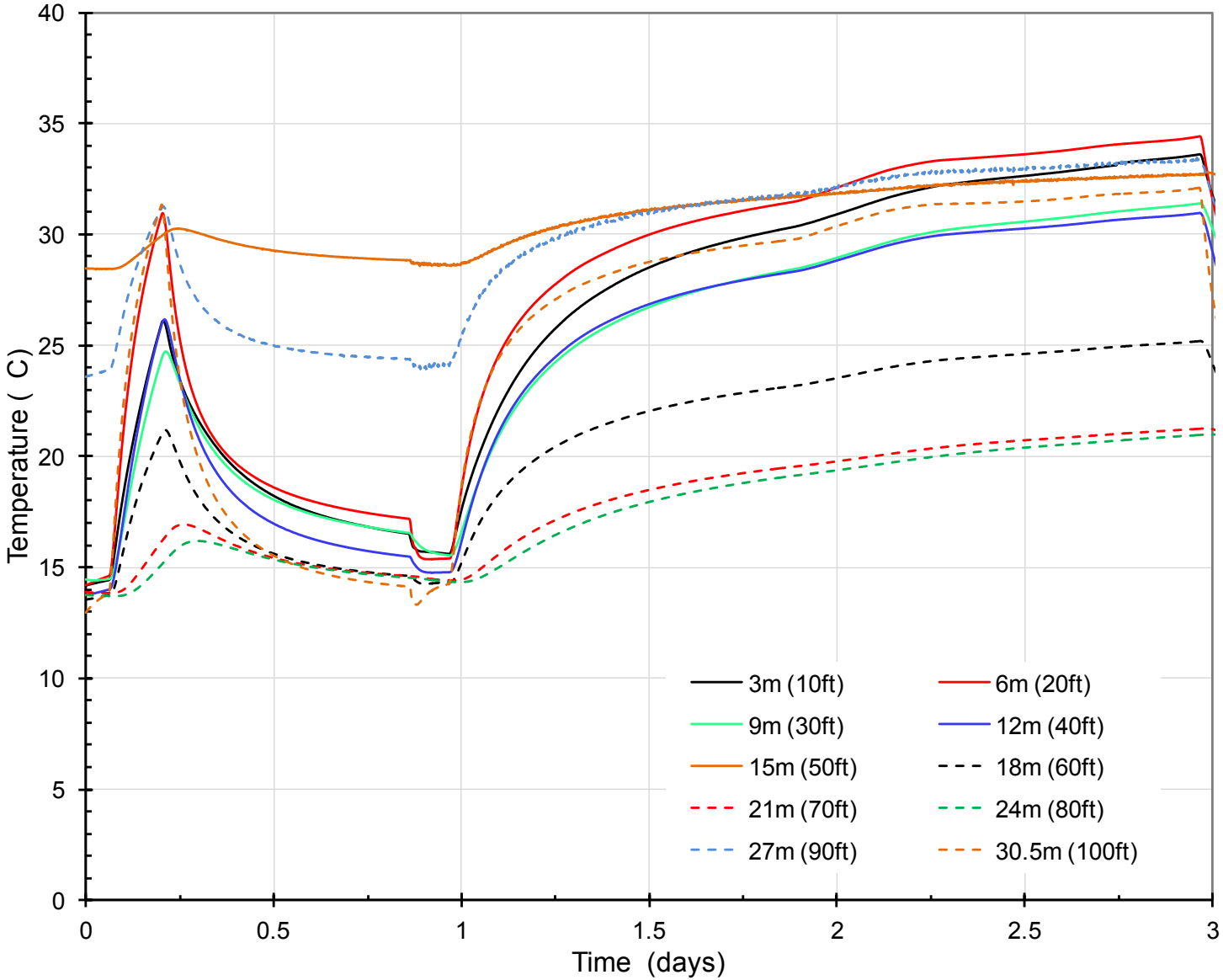

Figure XIV.3. Temperature along the Test Pile during T-MT 3

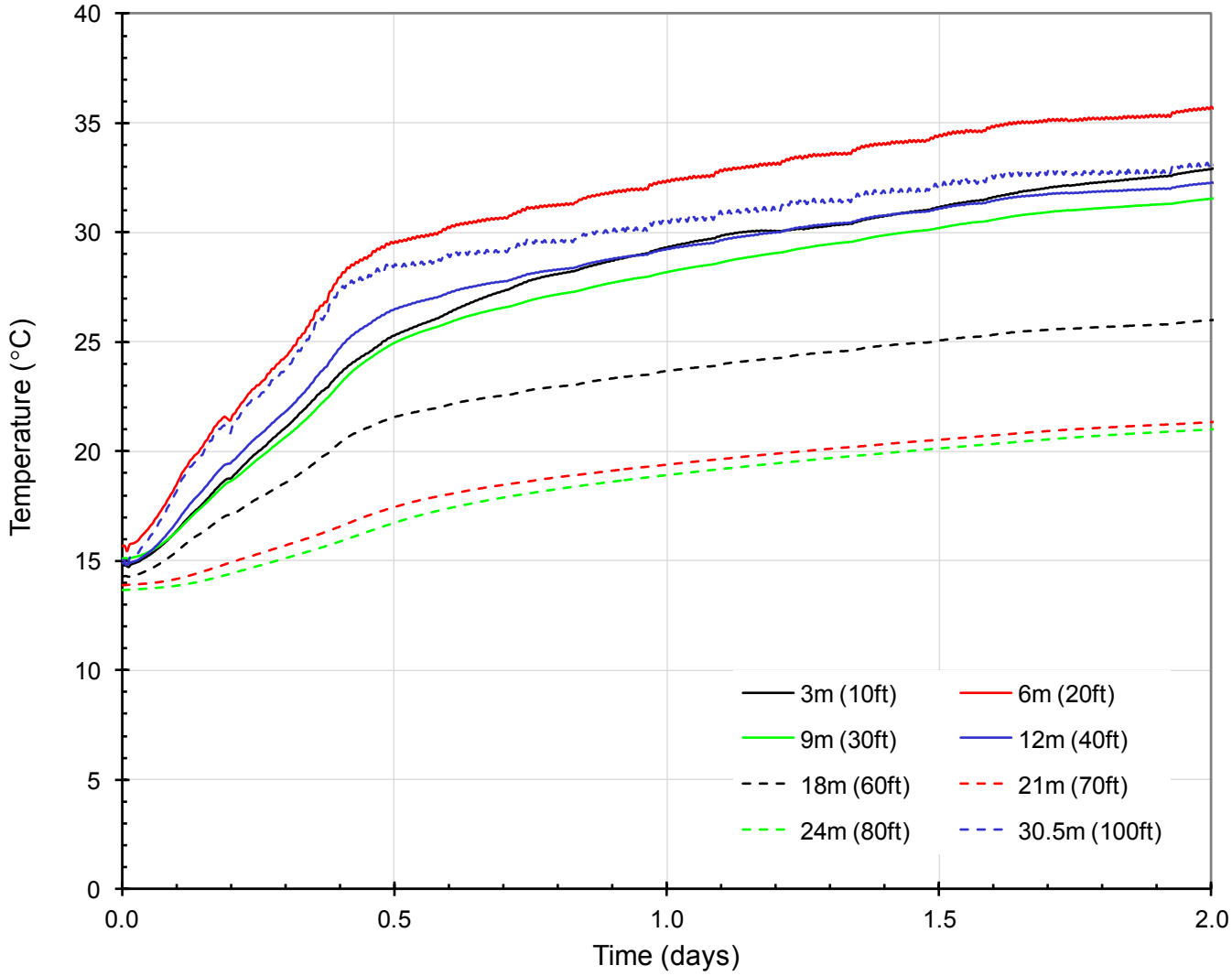

Figure XIV.4. Temperature along the Test Pile during T-MT 4

Appendix XV

Thermal strains along the pile segment embedded in the silty sand layer during various thermo-mechanical tests

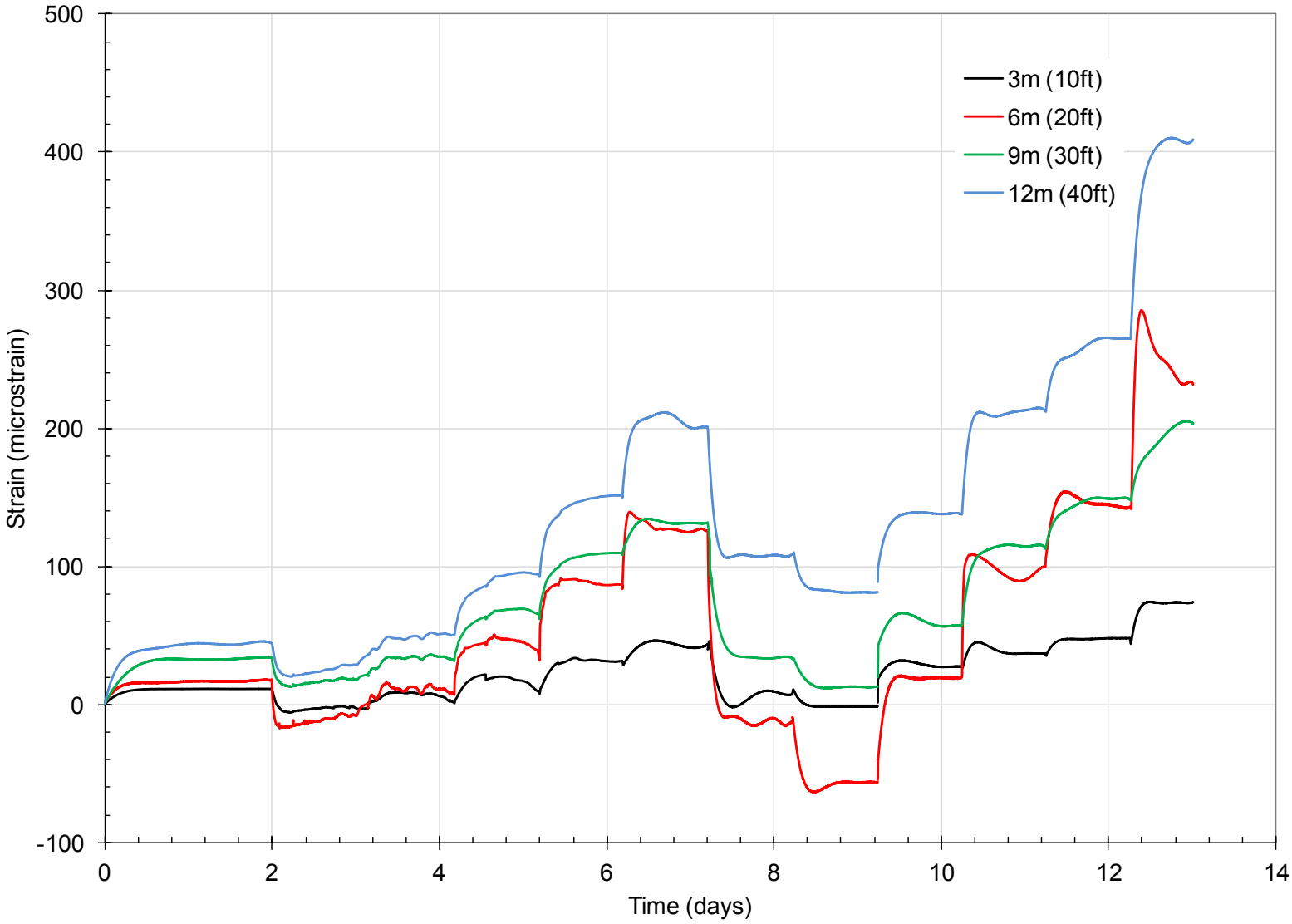

Figure XV.1. Thermal induced strains along the Test Pile during T-MT 1

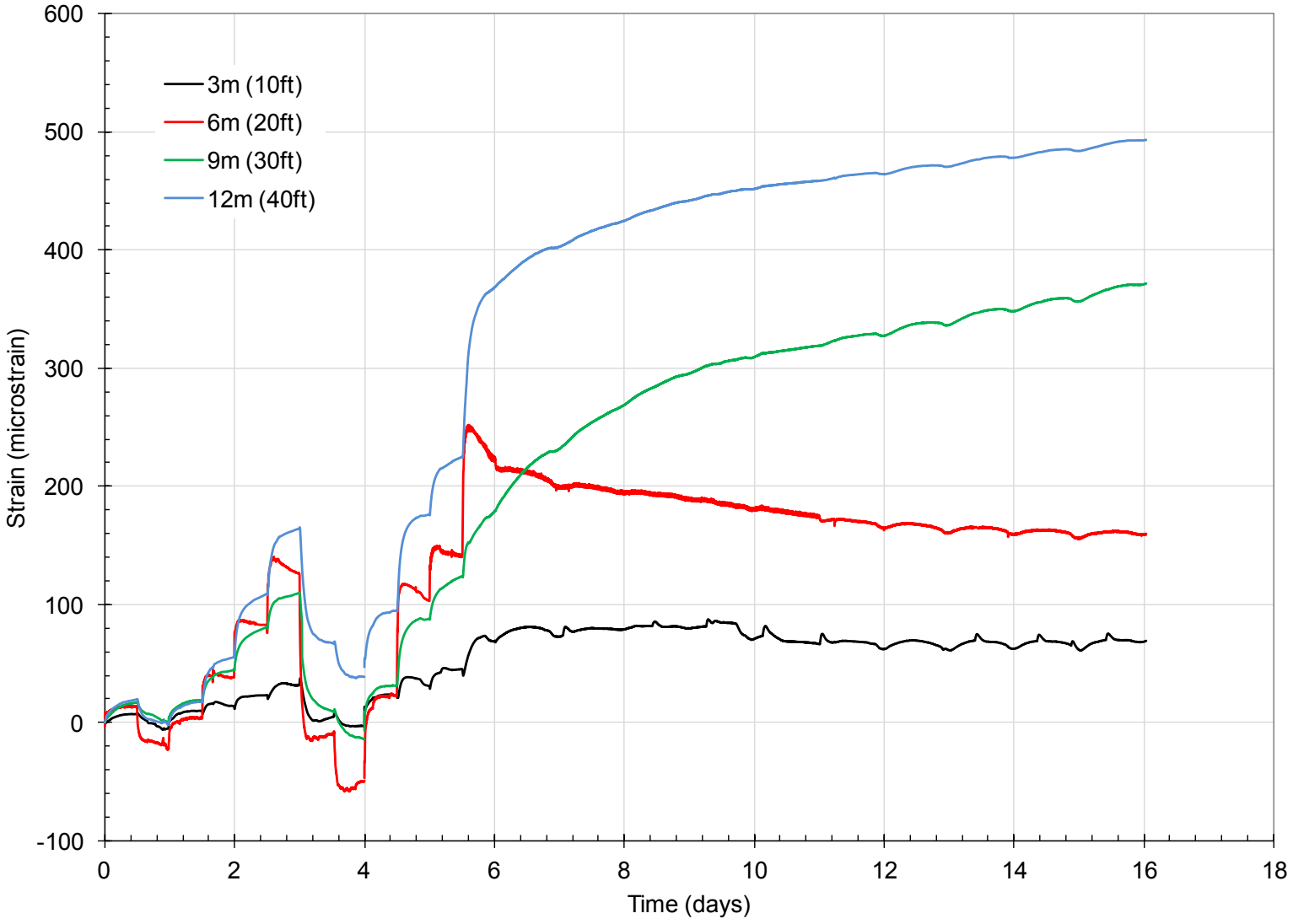

Figure XV.2. Thermal induced strains along the Test Pile during T-MT 2

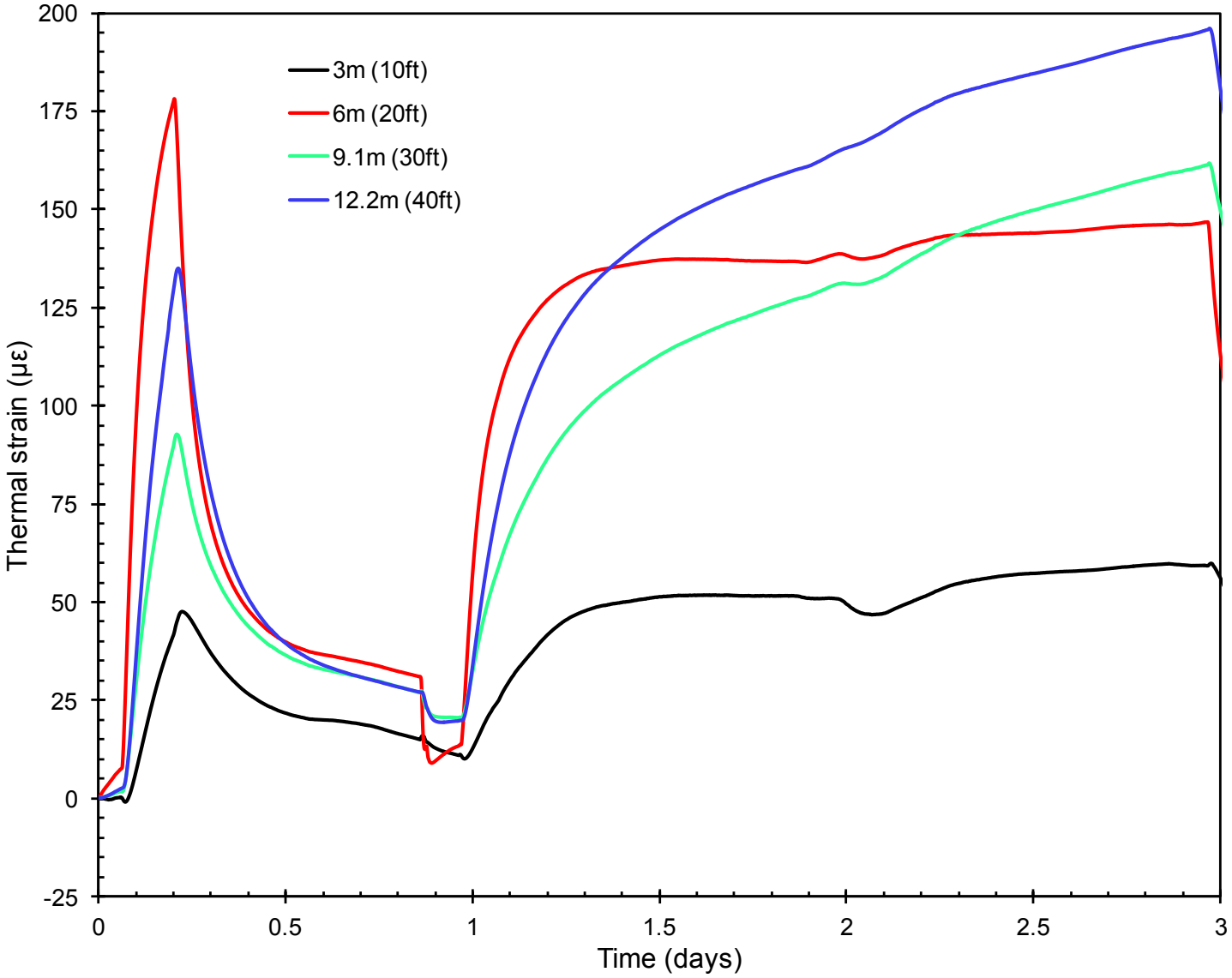

Figure XV.3. Thermal induced strains along the Test Pile during T-MT 3

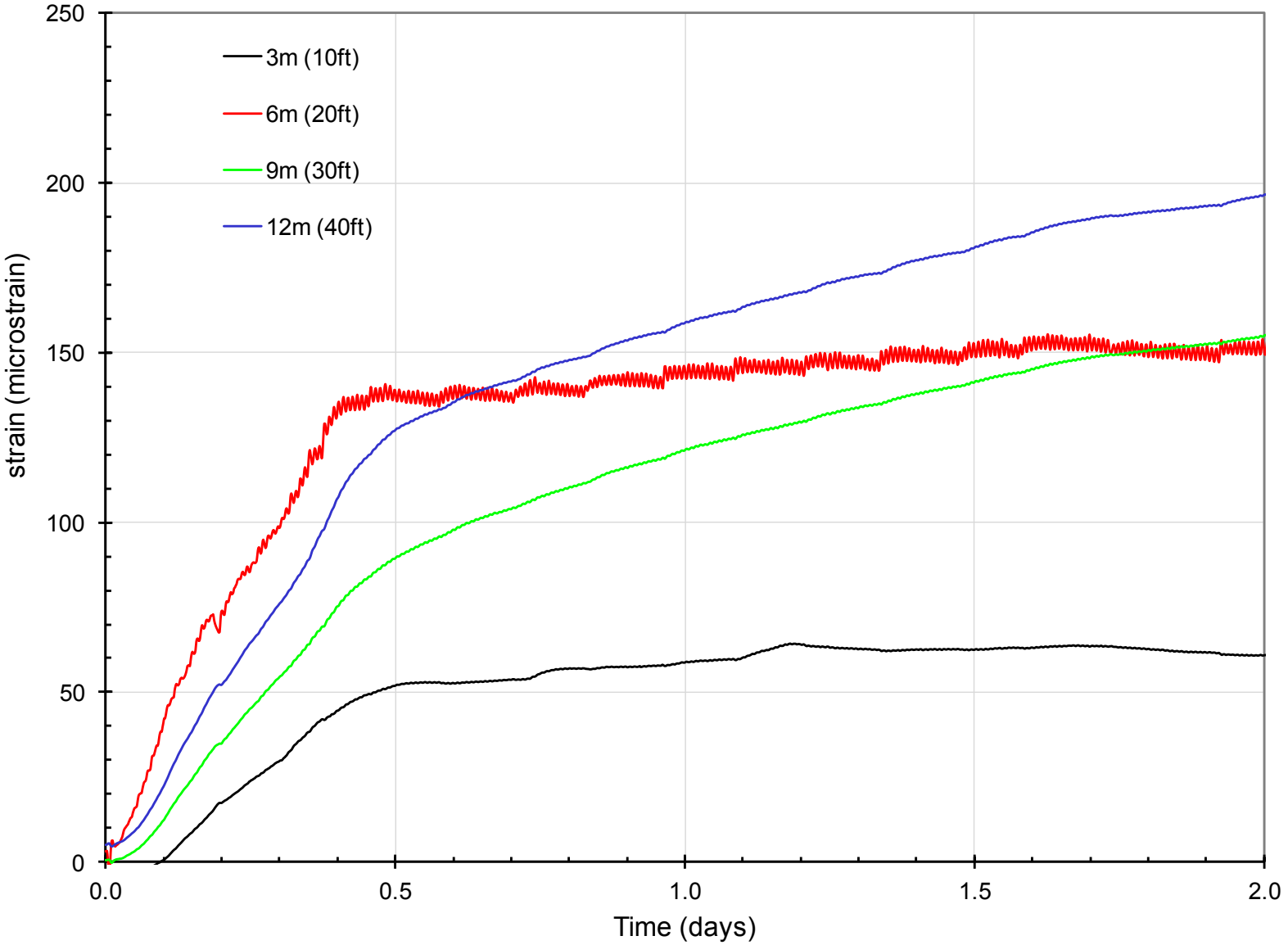

Figure XV.4. Thermal induced strains along the Test Pile during T-MT 4

CHAPTER 9. CONCLUSIONS AND POTENTIALS FOR FUTURE RESEARCH

9.1. General

The general findings of the conducted research are summarized in this chapter. The main concern of the research reported in this dissertation is to provide handful tools for the design of the Energy Piles. The research questions mentioned in the introduction chapter were addresses one at a time in each chapter of the dissertation within which newly developed analysis techniques, and testing approached and results are presented.

The design of energy piles requires the ability of estimate the design temperatures as well as the design mechanical loads. The design temperatures should account for the long-term temperature changes in the pile and its surrounding soils since the mechanical behavior of soils is temperature dependent and consequently the thermo-mechanical response of energy piles. Thus, the long-term thermal performance of energy piles should be investigated. One of the most fruitful approaches to investigate the long-term approach of energy piles is modeling either numerically or analytically.

The dissertation started with investigating the available analytical models to estimate the temperature changes in the ground including the infinite and the finite line source models, and the hollow and the solid cylindrical source models. It was found that all the available analytical models assume homogeneous soil layer; in other words, they cannot be used in case of stratified ground. Thus a new analytical model was developed based on the finite line source model to estimate the temperature changes in the stratified ground. The summary of the proposed model and its findings is presented in section 9.2.

The proposed multi-layer finite line source model as well as other analytical models cannot handle sophisticated conditions such as a ground water flow in layered soils subjected to varying heating rates over long time periods. Thus, a robust finite element model is need which was discussed in details in Chapter 3 and summarized in section 9.3.

The proposed finite element model is then used to conduct the long-term analysis for energy piles. However, the approach followed in practice about approximating the hourly variation of the thermal loads using a sine wave showed extremely unrealistic temperature changes in and around the pile. Thus, a newly developed methodology to obtain the sine wave that better represents the system was developed as discussed in Chapter 5 and summarized in section 9.4.

The design temperatures could be estimated using the finite element models and the newly proposed sine wave approximation. However, good estimate of the thermal properties of the ground and the thermal resistance of the piles are needed for reliable modeling results. Thus, the effect of the material (HDPE versus PEX-a) and the configuration (double versus single) of the ground loop on the thermal performance was investigated. In order to evaluate the effect of these factors, all other factors have to be maintained constant including the heating rate. Thus, thermal conductivity tests are performed in various energy piles which were provided with different loop types and configurations. The details of the tests performed are presented in Chapter 7 and summarized in section 9.5.

Finally, the effect of the thermal loads in the response of energy piles is investigated using in-situ testing. In this testing program, an energy pile is subjected to various cycles of heating

and cooling and the stains are measured at different elevations along the pile. The details of this test are presented in Chapter 8 and summarized in section 9.6.

9.2. Multi-Layer Finite Line Source Model

The proposed multi-layer model is based on the finite line source model and is simply using the superposition concept to estimate the temperature change in a layered ground. The heat exchanger/Energy pile is divided to segments correspond to the soil layers and the temperature change produced by each segment at the location of interest is estimated using the thermal properties of a transformed composite section. The transformed section is a representation of the various soil layers that the energy wave propagates through and is obtained using the laws of composite materials.

The proposed model adjusts the heating rate in each soil layer based on the thermal resistance of the soil for the propagation of the thermal waves. This adjustment has been validated against the results of 3-D models considering layered soil profiles with varying thermal properties. Furthermore, the proposed model accounts for the heat exchanged between layers due to developing a thermal gradient between such different layers.

The proposed model was validated using 3-D finite element models and proved accurate. The temperature changes in different soil layers at various distances and operation times were compared and a good agreement between the two models was found. Thus, the proposed model can be utilized to analyze the temperature changes in stratified grounds due to the operation of heat exchangers/Energy piles with a much less computational cost.

9.3. Numerical and Analytical Modeling of Energy Piles

As mentioned earlier, modeling the thermal performance of Energy Piles is mandatory for assessing the thermo-mechanical response of the piles and for approximating the expected design temperatures after long-term operation. However, considering all the pile components such as the ground loops and the carrier fluid in the 3-D numerical models is a challenge since these components have high aspect ratios which require significant computational powers to conduct the analysis. Therefore, simplifications were proposed to account for the carrier fluid and the small wall thickness of the ground loops in the finite element models without physically modeling them.

Furthermore, the selection of reliable and accurate initial and the boundary conditions for the finite element model is desired. Thus, the effect of using different acceptable initial and boundary conditions was investigated. The considered initial conditions included constant ground temperature, and actual varying ground temperature due to the annual change of the ambient air. While the considered boundary conditions included; constant ground surface temperature, the annual varying ambient temperature, and surface insulation. The use of constant surface and initial temperatures was considered due to its simplicity. The varying annual ambient surface temperature and the respective initial ground temperature are considered the most realistic and representable conditions for heat exchangers and energy piles which are not covered by an insulated building. In case of energy piles supporting buildings, thermal surface insulation is the more realistic. The 3-D finite element models considering these initial and boundary conditions were compared to one another and it was found that the general response in terms of temperature change in the ground does not change significantly for using different conditions.

Moreover, the effect of modeling energy piles as thermal anisotropic material was investigated. Energy piles are generally constructed using steel bars and concrete. The reinforcement is placed in the longitudinal direction of the piles which enhances the thermal properties of the composite section in this direction over the transverse direction. Accounting for this thermal anisotropy was found to be not of a significant importance. Thus, it was concluded that energy piles can be modeled as thermally isotropic material using the thermal properties of the transverse direction as the global properties.

In addition, it is found that the temperature changes are uniform along the pile and at the same distance in the surrounding homogeneous soil. Thus, it was concluded that 2-D cross sectional modeling is sufficient should the ground is homogeneous. These 2-D models were utilized in modeling the long-term thermal performance of the piles.

9.4. Long-term Thermal Performance

To investigate the long-term thermal performance of the energy piles, the hourly thermal operation of the heating/cooling system is simplified into a sine wave. It is found that the since wave the is typically used in practices which is based on the maximum design heating rate per unit length of the pile produces unrealistic temperature changes in and around the pile. Thus, a new approach was developed to provide the most accurate sine wave for the long term analysis. This approach is based on using the change point statistical analysis to estimate the duration for the heating and the cooling episodes. Thereafter, the magnitude of the sine wave covering the thermal loads is obtained by equating the sine wave area to the area under the rate-time history. This proposed approach was used to analyze the long term performance of three locations in the United States using 2-D finite element models. The temperature changes obtained from these equivalent sine waves for the three locations agree well with modeling the hourly variation of the heating rate for one year recommending that these waves are a better representation of the actual operation.

The equivalent sine waves were later used to analyze the long-term performance of energy piles installed at the three selected locations. In these analyses, it was assumed that the thermal loads are repeated for the 30 years considered operational period. Furthermore, the models were conducted for a 150 years to investigate the recovery of the ground temperature after terminating the system operation.

It was concluded that;

- The average ground temperature increases for the case where the ground heating load is more than the ground cooling load,
- The average ground temperature decrease for the case where the ground heating load is less than the ground cooling load,
- For balanced heated and cooling loads, no change in the average ground temperature was observed,
- The recovery of the ground temperature takes significantly less time when the thermal loads are balanced. Thus, it is recommended to use a hybrid system which allows to balances the thermal loads should the design ground thermal loads are originally imbalanced.

9.5. Thermal Conductivity Testing

Four thermal conductivity tests following the ASHRAE standards were conducted at Virginia tech on different energy piles. Each of the tested piles was provided with different

ground loop type and/or configuration. The scope of these tests was to investigate the effect of using different loop type and configuration on the estimated thermal properties of the ground and the thermal resistance of the pile. Two loop types were considered; HDPE and PEX-a. Additionally, single and double loops were tested.

It was found that humps in the measured inlet and outlet fluid temperatures take place in all the tests. These humps occurred at times when the ambient air temperature gets closer to the fluid temperature inside the loops. This is attributed to the reduction in the heat exchanged with the ambient air at these times due to the reduced thermal gradient. Due to the short length of the ground loops installed in energy piles, the heat rate applied during the thermal conductivity tests is quite lower than the typically used rates for geothermal boreholes. These relatively heat rates are significantly affected by the heat exchanged with the ambient air causing the observed humps. Thus, it was concluded that better thermal insulation is needed when conducting thermal conductivity tests on energy piles to reduce the thermal interference with the ambient temperature as much as possible.

The four conducted tests were found to provide a varying effective thermal conductivity of the ground should the effect of the heat exchanged with the ambient air is ignored while processing the testing results. When accounted for this heat gain/loss to the air, the four tests provide about the same ground thermal conductivity revealing the significance of this heat loss/gain of the test results. Furthermore, it was found that the loop type and configuration does not affect the estimate ground thermal conductivity. The ground configuration, however, showed a great impact on the thermal resistance of the energy piles. Piles that were provided with double loops had less thermal resistance than those provided with single loops.

Furthermore, another thermal conductivity test was conducted following the Dutch standards. This test, however, was modified to account for the heat exchanged with the ambient air while testing and thus obtain more accurate fluid temperatures. This test was implemented and its results were compared to those estimated using the ASHRAE tests considering the ambient effect and found consistent.

9.6. Thermo-Mechanical Behavior of Energy Piles

Four thermo-mechanical tests were conducted on a test pile at Virginia Tech to investigate the effect of the thermal loads on the mechanical response of the piles. The test pile was embedded about 60 ft into a shale layer which is a unique feature in this test compared to other field tests reported in the literature. Various levels of the thermal loads were applied to the test pile including heating- cooling loads. Compressive thermal stresses were found to develop in the test pile upon heating which increase the total thermo-mechanical stress in the pile. On the other hand, tensile thermal stresses develop in the pile upon cooling which reduce the total thermo-mechanical stresses in the pile. Furthermore, the thermal stresses along the pile portion embedded in the shale layer were uniform for both heating and cooling thermal loads. This is attributed to the high shear resistance at the interface of the pile-shale layer. In addition, the thermal stresses and strains developed in the pile portion embedded in the shale layer is recoverable while those in the pile portion in the top soil formation was not completely recoverable.

It was also observed from the results of the thermo-mechanical testing program that the measured thermal strains are significantly affected with the relative location of the strain gauges with respect to the ground loops in the pile. For future research, it is recommended to assure that the location of various strain gauges is fixed for more reliable testing results.